THE FIRST YEAR OF HST OBSERVATIONS

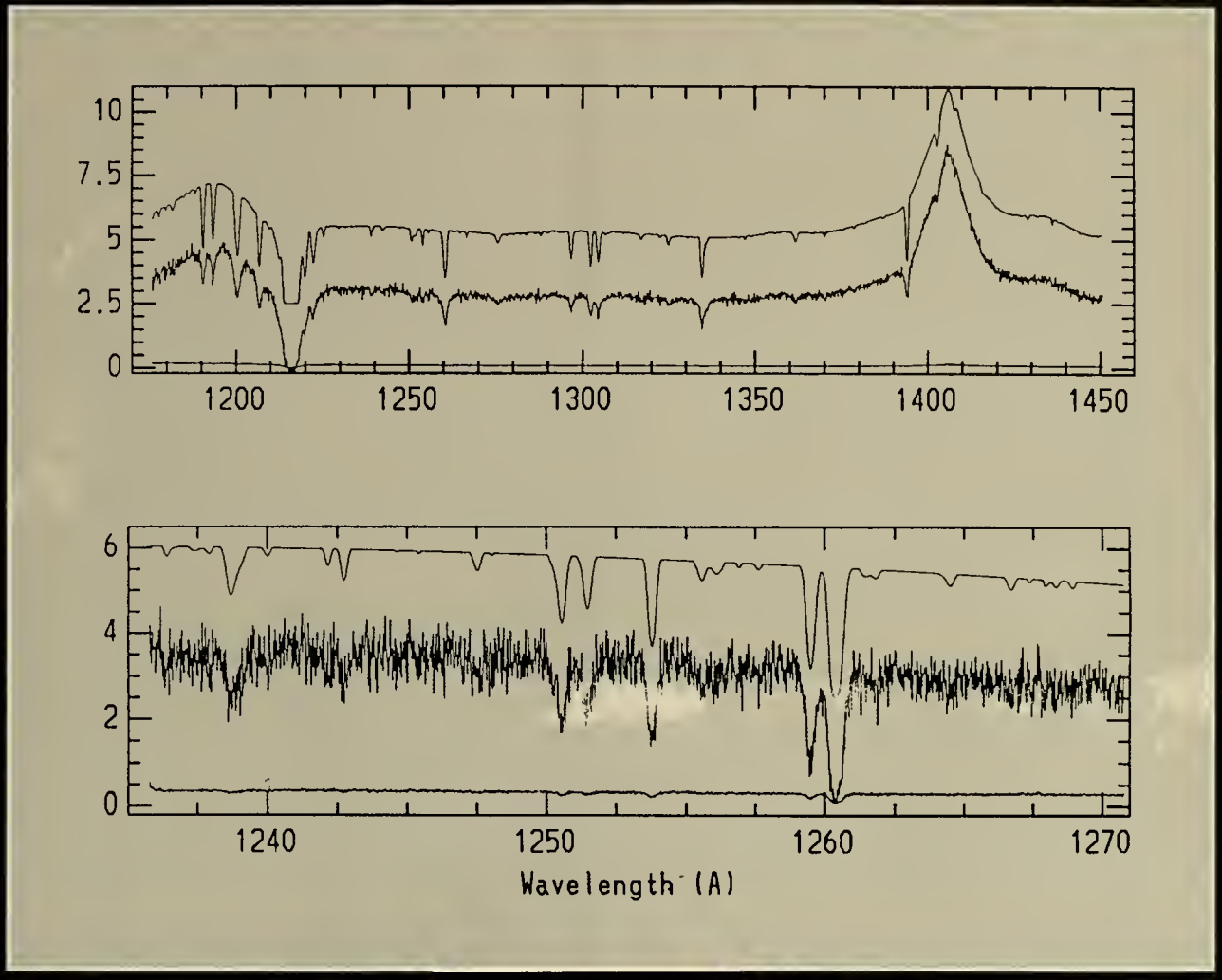

Proceedings of a Workshop held at the
Space Telescope Science Institute
Baltimore, Maryland
14-16 May 1991

Edited by A.L. Kinney and J.C. Blades

SPACE TELESCOPE SCIENCE INSTITUTE

NASA
National Aeronautics and Space Administration

The upper plot shows the spectrum of 3C273 in the GHRS G140L; raw data (below) and deconvolved data (above). The lower plot shows the spectrum of 3C 273 in the GHRS G160M; raw data (below) and deconvolved data (above). From the paper by R. J. Weymann.
(See also Morris S. L., Weymann, R. J. Savage, B. D., and Gilliland, R. L. 1991, *Ap.J.* 377, L21.

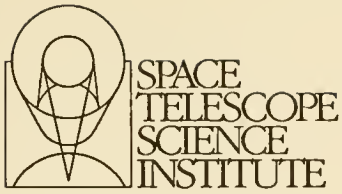

NASA
National Aeronautics and
Space Administration

THE FIRST YEAR OF HST OBSERVATIONS

Proceedings of a Workshop held at the
Space Telescope Science Institute
Baltimore, Maryland

14-16 May 1991

Editors:

A. L. Kinney and J. C. Blades
Space Telescope Science Institute
Science and Planning Division

Published and distributed by the Space Telescope Science Institute
3700 San Martin Drive, Baltimore, MD 21218

The Space Telescope Science Institute is operated by the Association of Universities for Research in Astronomy, Inc., under NASA contract NAS5-26555

CONTENTS

POSTERS

APPENDIX
Scheduling of Science Observations and Subsequent Data Processing

PREFACE

This volume presents the proceedings of the meeting on the *Year of First Light*, held at the Space Telescope Science Institute in Baltimore on 1991 May 14-16. Cohosted by the HST Science Working Group and the Space Telescope Science Institute, the meeting took place at the close of the engineering commissioning period and the beginning of the Guaranteed Time and General Observer science programs. The goals of the meeting were to gather the collective experience of the scientists who were instrumental in preparing for the HST mission and analyzing the early science and calibration data, and to inform both the HST community and prospective observers of the scientific potential of the Observatory, even with its aberrated optics.

At the time of the meeting, routine science observations were being scheduled on HST for four of the six scientific instruments. Only the High Speed Photometer and the Fine Guidance System (as used for astrometry) were still in their early commissioning activities. As a result, we were able to invite and solicit presentations covering many astronomical fields and representing many of the HST capabilities. The presentations included topics such as planets, hot stars, cool stars, chemically peculiar stars, stellar systems, galactic phenomenon, gravitationally lensed quasars, and the absorption systems observed in nearby quasars.

Because HST is a unique and complex observatory, we had also invited presentations and poster papers on the spacecraft performance, including the improved understanding of the Optical Telescope Assembly and the resultant imaging quality. Posters on the planning and scheduling system, which are included as appendices in this volume, show how science observations are executed with the telescope.

The meetings Scientific Organizing Committee would like to thank all participants in the three day meeting and, in particular, the contributors to this volume. The Editors, Anne Kinney and Chris Blades have collected an outstanding compilation of scientific and technical manuscripts. As these offer excellent examples of the scientific capabilities of the Hubble Space Telescope, we are very grateful for the Editors' efforts and are pleased to distribute these early scientific results to the astronomical community. Readers are also directed to the dedicated editions of the Astrophysical Journal Letters (*Ap. J. Lett.* **369, No. 2** and **377, No. 1**) and several papers describing the performance of the scientific instruments (Greenfield *et al.* 1991 SPIE 1494, p. 16 for FOC, Harms, R., *et al.* 1984, *Instrumentation in Astronomy V.*, p. 410 for FOS, and Lauer, T.R. 1989, PASP, 101, p. 445 for WF/PC).

Scientific Organizing Committee:

Dr. Riccardo Giacconi, Space Telescope Science Institute (ST ScI)
Dr. Albert Boggess, Goddard Space Flight Center (GSFC)
Dr. H. S. (Peter) Stockman, ST ScI
Dr. David Leckrone, GSFC
Dr. Colin Norman, ST ScI
Dr. Michael Fall, ST ScI

HST AND DENSE STELLAR SYSTEMS

Ivan R. King
Astronomy Department
University of California
Berkeley, CA 94720
U.S.A.

1. INTRODUCTION

In this discussion of the capabilities of HST in observing dense stellar systems, I will take up globular clusters and galaxies, but not active galactic nuclei, since the AGN's will be discussed in another part of the workshop. Actually my talk will have three parts: globular clusters, nearby galaxies, and distant galaxies.

We of course have four cameras available. The WFC has a pixel of 100 milliarcseonds (mas) and a field size of 160 arcsec. The PC and the FOC f/48 each have a pixel of 45 mas; for the PC the field size is 67 arcsec, and for the FOC f/48 it is only 22 arcsec. (Its extended-field capability is not usable here, because the reduced counting capacity in that mode cannot accommodate the range of magnitudes that we encounter.) The FOC f/96, with its pixel of 23 mas, was designed to critically sample the diffraction-limited HST image down to about 520 nm. At shorter wavelengths it would have been somewhat undersampled. But its field is only 11 arcsec.

(I am not going to say anything about the f/288 mode of the FOC, partly because its field is so tiny and partly because the spherical aberration makes its use very limited.)

In the actual aberrated images the FWHM of the core is about 65 mas, a value that does not depend much on wavelength, so the f/96 does have sampling that is adequate to use the resolution that the sharp image core gives us. We have in fact lost about a factor of 1.5 in the visible, relative to a diffraction-limited image, but we nevertheless have nearly the resolving power that HST was intended to have. But what we have really lost is about 5/6 of the light, which is out in the halo, where it is of no use to us. Even worse, in dense stellar systems this light spreads over the neighboring objects that we would like to measure, thereby increasing the background in an unpleasant way. We lose not only the 2 magnitudes represented by only 1/6 of the light being in the core, but we probably lose another magnitude because of this spread-out light.

I should mention some other differences between the cameras, too. The two most important are the dynamic range and the PSF. The WF/PC CCD's have a quite large dynamic range, whereas the IPCS detectors of the FOC go non-linear, and then saturate, at count rates of only a couple of tenths up to 1 count/pixel sec. On the other

hand, the PSF in an FOC image is independent of position, whereas in both the WFC and the PC a central obscuration in the re-imaging optics causes the PSF to vary quite significantly with position in the image. (A third difference, the readout noise of the WF/PC, is almost always of no importance when imaging dense stellar systems.)

2. GLOBULAR CLUSTERS

Globular clusters are one of the places where HST has a real advantage, because of its large scale and its high resolving power. But at the same time we have a small field (especially if we want the highest resolving power, which is achieved with the FOC f/96). Globular clusters are big things, and we can sample only small parts of them.

The superior resolving power of HST allows us to study faint stars at the centers of globular clusters; at ground-based resolutions these are literally covered up by the merged outer envelopes of the images of brighter stars. Prior to launch I had calculated that the FOC f/96 should be able to see stars to the HST limit even at the center of 47 Tucanae, which is one of the densest globulars known. This may indeed be possible after COSTAR is in place. But at the present time we are frustrated by the overlapping halos of the bright stars, which saturate almost all the area of a visible-light image. The PC is of course not subject to this limitation, but those overlapping halos still keep us from the faint images.

But even in a cluster as dense as 47 Tuc we are able to work in the ultraviolet and avoid saturation. Thus Mike Shara will be reporting on the discovery of blue stragglers in the center of 47 Tuc (later published as Paresce *et al.* 1991).

Another application of resolving power is in the clusters whose cores have collapsed down to a radius too small to resolve reliably from the ground. An example is M15, for which Tod Lauer will report PC observations later in this symposium. (See also Lauer *et al.* 1991a.)

One problem that has always interested me is the degree of equipartition of energy that has been reached in globular clusters. As the stars encounter each other and their velocity distributions relax, the tendency is for each stellar type to take on a velocity dispersion that is inversely proportional to the square root of its mass. The relative velocity dispersions should manifest themselves as different core radii for the different species. This is an impossible problem from the ground, because the cores are impenetrable, but with HST I look forward to taking it on.

Another problem—unfortunately postponed to the COSTAR era—is the study of horizontal branches in the globular clusters of M31. They are all at the same distance modulus and can therefore be compared directly with each other. Observation of a sufficient number of them should clear up the question of the dependence of absolute magnitude on metallicity, and may go a long way toward solving the "second-parameter problem."

I should also mention here another headache that the spherical aberration has created for us when we try to do stellar photometry in globular clusters. A photometry program such as DAOPHOT groups stars in sets of mutually overlapping images, and does an iterative fitting of the individual images within each group. But with our present PSF, all the stars in a cluster field make a single horrendous group. In my view, the computing time then becomes prohibitive. My solution has been to do a deconvolution of the image by Fourier techniques, which preserves photometric integrity, and then measure the deconvolved image. This approach has its own problems, though. Prior to deconvolution, bright stars with saturated centers have to be laboriously subtracted

out, one by one, as do stars whose halos run beyond the edges of the image. And deconvolved images have statistical problems that are far from trivial.

2. THE MILKY WAY AND NEARBY GALAXIES

2.1 The Milky Way

Both the FOC team and the WF/PC team are doing studies of Baade's Window, in the Galactic bulge. In the latter case, higher-latitude fields are also being studied. Here again we have a problem that benefits greatly from the resolving power of HST. Terndrup's (1989) pioneering ground-based study of Baade's Window was stopped by crowding around 19th or 20th magnitude; HST should go faint enough to study the main-sequence turnoff, below 22nd magnitude.

2.2 The Magellanic Clouds

The study of the R136 cluster in 30 Doradus, in the LMC was, I believe, the first scientific achievement of HST. (For a more recent treatment, see Weigelt *et al.* 1991.) Also, we shall hear during this Workshop from Francesco Paresce about the resolution of the expanding shell around Supernova 1987A. (See also Jakobsen *et al.* 1991.)

Here is another pair of systems in which high-resolution problems abound: star clusters, dense regions such as the bar of the LMC, etc.

2.3 The M31 Group

The bulge of M31 is a fascinating place, and a number of us will be delving into it. I hope to be able to see the low-metal-abundance Baade giants quite close in to the center, and thus determine the core radius of the M31 halo. And I know that Mike Rich will be studying these same stars in the near infrared.

I have already mentioned the globular clusters, but I should also note that when they are observed with the FOC, parallel exposures with the WFC will study the M31 halo population better than ever before.

Perhaps the most exciting problem associated with these galaxies is the centers of M31 and M32, both of which are very dense. First, direct imaging of the center of M32 will be very interesting. In an observation that was never published, Stratoscope saw a steady rise of brightness to a peak at least as sharp as its resolving power of 0.2 arcsec (Schwarzschild, private communication). Even more provocative, however, are the central rotations, whose angular velocity surpasses ground-based resolving power (Kormendy 1987, 1988). After COSTAR is installed, the long-slit spectrograph of the FOC will be able to tell just how high these angular velocities are. Simple dynamical reasoning shows that the central mass densities are directly proportional to the angular velocities.

And there is the problem of the origin of the ultraviolet light. At the moment of this writing, colleagues and I are struggling to interpret what we see in a far-UV image of the center of M31.

Finally (but I doubt it, really), there are problems of the disk population. M31 is a very crowded object, and all sorts of studies of the disk population will benefit from

the resolving power of HST.

2.4 Other Nearby Galaxies

Most of the observations I have mentioned are in the future. But we will hear today from Tod Lauer about the discovery of a sharp nucleus in NGC 7457. (See also Lauer *et al.* 1991b.) And other not-too-distant galaxies are amenable to all sorts of new studies.

One problem that has interested me in particular is the cores of elliptical galaxies. At the distances of the nearest giant ellipticals, cores such as those of M31 and M32 would be completely unresolved; and, in fact, Schweizer (1976) has suggested that many ellipticals that seem to have barely resolved cores are indeed in this situation. I am personally relieved, however, to find that in at least one Virgo elliptical HST imaging has shown the core radius to be just the 2 arcsec that I had estimated from ground-based images (King 1978).

3. DISTANT GALAXIES

For more distant galaxies our main concern is morphology. Here the resolving power of HST is crucial. The diameters of distant galaxies depend somewhat on the cosmology, but the important point is that they never get very small, so that HST resolving power can be used to study morphology at any distance. The only drawback at large distances is the dimming factor of $(1+z)^4$, which holds in all cosmologies. This can make the needed exposure times quite long, especially because of the long focal ratios of our cameras.

We have carried out one test on middle-distance galaxies, among the Scientific Assessment Observations. Single-orbit exposures were made with the FOC f/48 and with the WFC. The results (King *et al.* 1991) included a successful study, with the FOC, of a galaxy at magnitude 20.5 and good morphological assessments, with the WFC, of galaxies ranging from 17.5 to 19.8. Deconvolutions were made in all cases. One important conclusion, however, was that for really good results many orbits of exposure would be needed.

4. CONCLUSION

Contrary to many misguided early prophecies, imaging with HST is far from dead. For globular clusters and galaxies, a number of quite interesting results have already been obtained, and many more are in the offing.

REFERENCES

Jakobsen, P., Albrecht, R., Barbieri, C., Blades, J. C., Crane, P., Deharveng, J. M., Disney, M. J., Kamperman, T. M., King, I. R., Macchetto, F., Mackay, C. D., Paresce, F., Weigelt, G., Baxter, D., Greenfield, P., Jedrzejewski, R., Nota, A., Sparks, W., Kirshner, R. P., and Panagia, N. 1991, *Ap. J. (Letters)*, **369**, L63.

King, I. 1978, *Ap. J.*, **222**, 1.

King, I., Stanford, S. A., Seitzer, P., Bershady, M. A., Keel, W. C., Koo, D. C., Weir, N., Djorgovski, S., and Windhorst, R. A. 1991, *A. J.*, **102**, 1553.

Kormendy, J. 1987, in *Structure and Dynamics of Elliptical Galaxies* (I.A.U. Symposium 127), ed. T. de Zeeuw (Dordrecht: Reidel), p. 17.

Kormendy, J. 1988, *Ap. J.*, **325**, 128.

Lauer, T. R., Holtzman, F. A., Faber, S. M., Baum, W. A., Currie, D. G., Ewald, S. P., Groth, E. J., Hester, J. J., Kelsall, T., Light, R. M., Lynds, C. R., O'Neil, E. J., Schneider, D. P., Shaya, E. J., and Westphal, J. A. 1991a, *Ap. J. (Letters)*, **369**, L45.

Lauer, T. R., Faber, S. M., Holtzman, F. A., Baum, W. A., Currie, D. G., Ewald, S. P., Groth, E. J., Hester, J. J., Kelsall, T., Kristian, J., Light, R. M., Lynds, C. R., O'Neil, E. J., Shaya, E. J., and Westphal, J. A. 1991b, *Ap. J. (Letters)*, **369**, L41.

Schweizer, F. 1976, *Ap. J. Suppl.*, **31**, 313.

Paresce, F., Shara, M., Meylan, G., Baxter, D., Greenfield, P., Jedrzejewski, R., Nota, A., Sparks, W., Albrecht, R., Barbieri, C., Blades, J. C., Crane, P., Deharveng, J. M., Disney, M. J., Jakobsen, P., Kamperman, T. M., King, I. R., Macchetto, F., Mackay, C. D., and Weigelt, G., 1991, *Nature*, **352**, 297.

Terndrup, D. M. 1988, *A. J.*, **96**, 884.

Weigelt, G., Albrecht, R., Barbieri, C., Blades, J. C., Crane, P., Deharveng, J. M., Disney, M. J., Jakobsen, P., Kamperman, T. M., King, I. R., Macchetto, F., Mackay, C. D., Paresce, F., Baxter, D., Greenfield, P., Jedrzejewski, R., Nota, A., and Sparks, W. 1991, *Ap. J. (Letters)*, **378**, L21.

THE CENTRAL DYNAMICS OF 47 TUCANAE

Ivan R. King
Astronomy Department
University of California
Berkeley, CA 94720
U.S.A.

Abstract. The blue stragglers recently discovered in 47 Tucanae have an excess concentration in the very center of the cluster that is statistically significant at a marginal level. Studies of the distribution of the ordinary stars (mainly near the main-sequence turnoff) may imply the presence of a population of massive remnants near the center of the cluster, although more extensive observations will be needed to confirm such a hypothesis.

1. INTRODUCTION

In an ingenious use of engineering data—an HST focal run that happened to be made, at ultraviolet wavelengths, at the center of of the globular cluster 47 Tucanae—Paresce *et al.* (1991) reported the discovery of 21 blue stragglers in a central field that spanned only 44 arcsec. Blue stragglers had been seen at the centers of globular clusters before (Nemec and Harris 1987, Nemec and Cohen 1989, Aurière *et al.* 1990), and a suspicion was growing that they might be concentrated there; but the high resolving power of HST gave the first opportunity to examine the center of a dense cluster—and there they were. It is an easy guess that the blue stragglers concentrate to the center because they have a greater mass than that of the dominant main-sequence stars. What I want to do here is to pursue this reasoning further, and to examine some of the statistics of their detailed density distribution—which will lead to a more general excursion into the dynamics of the cluster center.

Whenever one finds a particular stellar species concentrated to the center of a globular cluster, the presumption becomes strong that the stars are there because they have a higher mass, have relaxed into equipartition, and therefore have lower velocities. In principle one ought to be able to use their degree of central concentration to estimate their mass. In practice this is not so easy, because of small numbers, because of the smallness of the field that we have covered, and because of some complications that I will discuss below. Unfortunately I began looking at this problem only the week before the workshop [and have not been able to return to it since], so this is going to be only a sketchy discussion.

2. THE CENTRAL CONCENTRATION OF THE BLUE STRAGGLERS

Not only are the blue stragglers concentrated relative to the outer parts of the cluster; they are centrally concentrated even within our small field. Of the 21 stars, 9 fall within the f/96 field, which is only 1/4 of the total. Unfortunately this is not what I would call a strongly significant result. In a binomial distribution where each object has a 1/4 probability of falling in the inner field, the probability that 9 or more will do so at random is 0.056.

Another test is their cumulative radial distribution. Here I wanted to compare with various distribution laws and did not have time to calculate the areas of annuli that did not lie completely within the f/48 field; so I considered only the stars out to the largest circle around the Meylan center that lies completely within the field. (The Paresce *et al.* paper gives three alternative centers; I believe that the Meylan center is a good estimate of the true center, because of the way in which he determined it. But I don't want to go into those details here, and the exact choice of center probably does not matter a great deal either.) The largest such circle had a radius of 217 pixels; unfortunately it left me with only 14 of the blue stragglers.

The distribution of light near the center of a cluster as concentrated as 47 Tuc is well represented by the formula

$$f = \frac{f_0}{1 + (r/r_c)^2}\,, \tag{1}$$

where f is surface brightness and the core radius r_c for 47 Tuc is a little over 25 arcsec. (In the present units, I used 610 pixels.) I converted this into a cumulative distribution function and compared with the blue stragglers by means of a Kolmogorov–Smirnov test. The probability of a deviation at least this large, at random, came out 0.053—again a quite marginal result.

But intuitively the c.d.f. for the blue stragglers really does look different, so I asked the question, "with what mass group *does* it agree best?" For modeling the distribution of groups of various stellar mass, I adopted a simple line of reasoning. Deep in a potential well a relaxed velocity distribution is quite close to Gaussian, and its density distribution is consequently quite close to a Boltzmann law, in which spatial densities are proportional to $\exp(-mU)$, where m is the mass of a star in the group and U is the potential. This behavior has the consequence that for the relative distributions of two mass groups,

$$n_{m_2} \propto (n_{m_1})^{m_2/m_1}\,, \tag{2}$$

where the n's represent spatial number densities.

Distributions of the form of the one in Eq. (1) have the property that the spatial distribution has the same form, except that the power of the quantity in the denominator becomes larger in magnitude by 1/2. For example, the projected distribution in Eq. (1) corresponds to the spatial distribution

$$n = \frac{n_0}{\left[1 + (r/r_c)^2\right]^{3/2}}\,. \tag{3}$$

If we take Eq. (1) to represent the turnoff stars (since the red giants and the subgiants have nearly the same mass, and all these stars together are responsible for nearly all of the light), and if we take the turnoff mass as the unit of mass, then we quickly find

that the projected distribution of stars of mass m is

$$f = \frac{f_0}{\left[1 + (r/r_c)^2\right]^{(3m-1)/2}}. \tag{4}$$

What I did then was to compute these curves for various values of m, integrate them into c.d.f.'s, and compare them with the c.d.f. of the blue stragglers. No statistical tests here; just, which one gave the best fit? The answer came out 7 times the turnoff mass. This seemed *a priori* such an implausible result that I decided to look further.

3. THE DISTRIBUTION OF TURNOFF-MASS STARS

It occurred to me to ask, are the ordinary stars distributed "right"? That is, do they fit the curve expressed by Eq. (1)? The answer was resoundingly that they do not. In this case there was no question of small-number statistics; I had 369 stars in the circle of radius 217 pixels. The Kolmogorov–Smirnov comparison gave a probability of 5×10^{-4}.

What is wrong here? We had always considered 47 Tuc to be a showcase-model of a smooth, relaxed cluster, with no suspicion of 0.0005-probability shenanigans going on at its center.

One possibility, of course, is that the data are wrong. We know that our flatfielding isn't yet perfect, the star-detection thresholds might not have been everywhere uniform, and we observed through some pretty weird bandpasses that might be doing something funny to us.

But if we accept the data, there is a line of reasoning that leads to an interesting interpretation of what we see. First, note that no one else has ever had a chance to look at this phenomenon before. Ground-based density distributions near the center of 47 Tuc have had to depend on photoelectric photometry of the integrated light of all the stars in any area that we study. This light is dominated by that of the red giants, and they are so few in number that the light distribution is statistically very much noisier than the distribution of the much more numerous faint stars that HST allows us to study. For the stars we see a resounding statistical effect, but in the distribution of integrated light it would not show up at any significant level at all.

Furthermore, the distribution that we see makes good physical sense. A cluster like 47 Tuc must contain a number of massive remnants—the presence of more than 10 pulsars is ample evidence of that—and because of their mass they should congregate at the center. They create an additional potential well there, and Boltzmann tells us that that deepening of the potential should increase the density in the center.

To make this more quantitative I computed some models. They have the observed mass function of 47 Tuc (as verified by a projection of the model at the radius at which the mass function was determined), and they have the additional property that I can arbitrarily add massive remnants, in the equipartition density distribution that their mass implies. They do indeed concentrate very strongly to the center. For a plausible value, I took their mass to be 1.4 $\mathcal{M}_\odot$. I haven't tried very many models, nor fitted them in great detail, but it looks as if a proportion of about 2–3% of the stars as massive remnants will cause the visible stars to have a distribution such as the one that we observe.

Such a model would also make a significant change in the fitting of the radial distribution of the blue stragglers. With part of their concentration at the very center

explained by the extra potential well due to the massive remnants, the distribution of the blue stragglers would no longer imply such implausible individual masses.

But let me emphasize again that this discussion is based on a single field, observed in unconventional color bands, and possibly subject to systematic errors. Whereas I believe that the reasoning given above is sound, and that massive remnants should be expected *a priori*, I would be very reluctant to make any strong assertions until we have a larger radial range in 47 Tuc, and, hopefully, other clusters observed at HST resolution.

4. CONCLUSIONS

It would be tempting to follow this line of reasoning, in order to find out how many massive remnants lie hidden at the center of 47 Tucanae, and then to use the model to determine from their distribution the masses of the blue stragglers. But at that point we would be out on the end of a long, shaky limb of reasoning. For the time being, I would prefer to regard this as a provocative non-result, to be taken up again when better data become available. What we see and deduce may be real and correct; but on the other hand, the moral of the story may be that a person who squeezes too hard on rough data will only end up by hurting his hands.

REFERENCES

Aurière, M., Ortolani, S., and Lauzeral, C., 1990, *Nature*, **344**, 638.

Nemec, J. M., and Cohen, J. G., 1989, *Ap. J.*, **336**, 780.

Nemec, J. M., and Harris, H. C., 1987, *Ap. J.*, **316**, 172.

Paresce, F., Shara, M., Meylan, G., Baxter, D., Greenfield, P., Jedrzejewski, R., Nota, A., Sparks, W., Albrecht, R., Barbieri, C., Blades, J. C., Crane, P., Deharveng, J. M., Disney, M. J., Jakobsen, P., Kamperman, T. M., King, I. R., Macchetto, F., Mackay, C. D., and Weigelt, G., 1991, *Nature*, **352**, 297.

A TALE OF THREE JETS

F. Macchetto*
and the FOC Investigation Definition Team
Space Telescope Science Institute
3700 San Martin Drive
Baltimore, Maryland, 21218
USA
* *Associated with the Space Science Department of ESA*

1. INTRODUCTION

The study of the optical counterparts to radio jets will be the subject of an intensive investigation program with the European Space Agency's Faint Object Camera first proposed 10 years ago (Macchetto 1981, Miley 1981). It has been known for a long time that radio jets are widespread in active galaxies (e.g. Miley 1980, Bridle & Perley 1984) and that they must play a fundamental role in galaxy activity and in the transport of energy from the nucleus to the radio-emitting lobes (Rees 1971, Blandford & Rees 1974). The jet radiation is believed to be synchrotron emission, but there are still only a few cases where the optical counterparts of radio jets have been detected (e.g., Butcher, van Breugel & Miley 1980, Fraix-Burnet, et.al., 1991). These extragalactic optical jets have a number of unfavorable observational characteristics that make it very difficult to understand their physical nature. The jets are rare, very faint, relatively small and are embedded in the bright stellar background of the parent galaxy.

Nevertheless, since the optical emission appears to be the continuation of the radio synchrotron spectrum, optical observations are essential to define the physical parameters and constrain the jet emission models. Observations with the Faint Object Camera allow many of the observational disadvantages to be overcome. The much greater spatial resolution provided by the FOC, compared to even the best ground based optical telescopes, means that the relative contrast of the jet to the underlying stellar background is improved by at least an order of magnitude. In addition observations in the ultraviolet provide another order of magnitude improvement in contrast, since the brightness of the starlight falls rapidly into the UV, while the steepness of the jet emission is typically flat ($\alpha \simeq 0.5$).

Furthermore, high spatial resolution observations in the visible and ultraviolet, offer the possibility to determine the precise location where particle acceleration occurs, since the electron lifetime for optical emitting electrons is extremely short. Finally, comparison of radio and optical morphologies obtained with similar resolution will

allow the investigation of confinement mechanisms and diffusion processes within the relativistic plasma.

To date, the FOC has observed at high spatial resolution the optical counterparts to the radio jets in PKS 0521-36; 3C66B and M87. The results show unexpected features and point at different physical mechanisms at work. In the next section, I will tell the tale of these three jets.

2. PKS 0521-36

One of the most prominent radio and optical jets is that found in the elliptical galaxy PKS 0521-36, a relatively isolated radio galaxy at a redshift z = 0.055 which also harbors a bright V = 16 BL Lac nucleus and extended optical line emission. Detailed spectroscopic and morphological studies have been carried out by Danziger et al. (1979, 1983); Cayatte & Sol (1987); and Boisson, Cayatte, & Sol (1989). Recently Sparks, Miley, & Macchetto (1990) reported optical polarization measurements of the jet and nucleus, which confirmed the expected high polarization if the emission is due to synchrotron radiation.

Images of PKS 0521-36 were obtained on 1990 August 25 with the FOC using the F430W and F320W filters and f/96, 512 × 512 mode (Paresce 1990) with a corresponding pixel size approximately 0".022. Pointing was defined using the radio VLBI position obtained by Morabito et al. (1986).

The galaxy has a very bright, $V \approx 16$, BL Lac nucleus which severely tests the ability of HST and the FOC to detect faint structure in the vicinity of bright objects. Accurate knowledge of the point-spread function appropriate to the data is essential to remove the halo around the nucleus which arises from the presence of spherical aberration in the HST primary mirror.

Various techniques were tried to remove the effects of the nucleus, from straightforward substraction of a scaled pointspread function (PSF), direct Fourier deconvolution, maximum entropy deconvolution, and Lucy's (1974) iterative deconvolution technique. A combination of point source subtraction and Lucy's method gave the best results. Specific PSF observations were obtained of the star BPM 16274, a UV flux standard (Bohlin et al. 1990; Turnshek et al. 1990).

An example of the resultant deconvolutions is shown in Figure 1. This uses Lucy's (1974) iterative deconvolution technique which constrains the result to be positive.

The VLA contour data as published by Keel (1986) is shown superposed on the FOC data in Figure 2. It is immediately obvious that the FOC data has a resolution very similar to that of the VLA data, but shows considerably more morphological information that the ground-based optical data.

The FOC image shows a bright knot located $\approx 1\farcs8$ to the NE and clearly resolved as in the VLA data. The width of the knot is $\approx 0\farcs8$. Beyond this bright knot, the jet has approximately constant surface brightness and a morphology similar to the VLA image with a total length of $6\farcs5$. The jet is also resolved in width, $0\farcs6$ wide in the fainter regions of the jet, with little or no evidence of structure on a scale of $\leq 0\farcs1$. The FOC data appears to show more flux than the VLA data in the region at slightly larger radius from the nucleus but close to the southern tip of the knot.

There is a second component seen in the deconvolution at $0\farcs36$ from the nucleus, Figure 2. It is visible in the raw data, although by no means as clearly as in the deconvolved image. Such a source would be completely within the core of the highest resolution VLA contour map published by Keel. We believe we have detected a pre-

1. The jet in PKS 0521-36 as observed by the FOC. An elliptical model of the galaxy has been subtracted. The jet is approximately 6.″5 long.

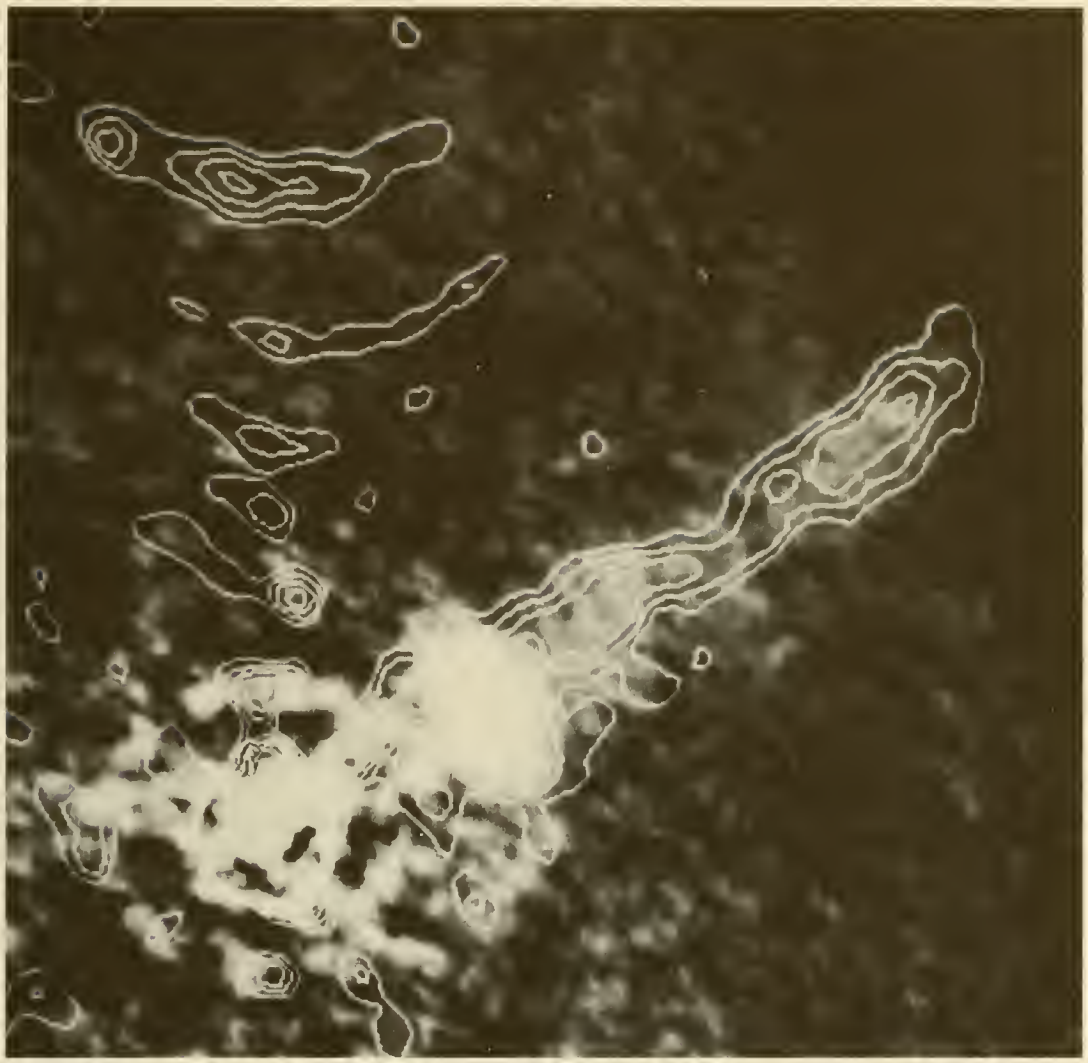

2. The VLA contour data of Keel (1986) is shown superposed on the FOC data. Note the excellent agreement of the two data sets.

viously unseen inner jet structure at a distance corresponding to 300 pc, $H_o = 75$ km s^{-1} Mpc^{-1}.

FOC observations of the nucleus of PKS 0521 - 36 seem to have resolved it into a bright nucleus and an inner jet extension. Presumably, the optical polarization measured by Sparks, Miley & Macchetto (1990) comes from both these components. The fact that the nuclear polarization is large and perpendicular to the jet direction (Sparks et al. 1990; Angel & Stockman 1980; Bailey, Hough & Axon 1983; Bridle et al. 1986) is consistent with what has been observed in other quiescent blazars and quasars. The second component close to the nucleus may be an inner extension of the jet, since it lies on the geometrical projection of the jet toward the nucleus. However, since this extension falls entirely within the VLA radio core, there is no independent way of confirming its existence. If real, it could be a site of electron acceleration along the jet due to transverse shocks (Drury 1983; Blandford & Eichler 1987).

The large bright knot further along the jet is a clear counterpart to the radio knot. The radio and optical polarization position angles (Keel 1986; Sparks et al. 1990) suggest a magnetic field aligned along the jet direction. This knot is unresolved in the optical polarimetric measurements, but the general sense of the magnetic field is still along the jet direction at that position. The bright knot is clearly an important site where particle acceleration is occurring.

The general optical morphology of the jet does not exhibit any significant degree of clumpiness even at FOC resolution.

Using the standard formula of Rybicki & Lightman (1979), we derive a mean lifetime for the electrons:

$$t_{1/2} = 16.4 \frac{1}{B^2 \gamma} \text{ yr}$$

where B is the magnetic field in Gauss and γ is the Lorentz factor. The mean distance for electron difussion is

$$D_{1/2} \approx \frac{5.5}{B^{3/2} \nu^{1/2}} \text{ kpc}$$

where $\nu = 120 B \gamma^2 / 10^{-4}$ is the cut-off frequency. With typical value $B \approx 10^{-4}$, the electron difussion distance is D $\approx$ 200 pc in the optical and D $\approx$ 100 kpc in the radio region. The corresponding lifetime for the optical electrons is $t_{1/2} \approx 600$ yr.

This implies that there must be continuous acceleration along the jet of the electrons responsible for the optical emission, since electron diffusion from the bright knot could not account for the observed optical extent.

3. 3C 66B

3C 66B is a relatively nearby bright radio source associated with a 13th magnitude galaxy at a redshift of 0.0215 (Matthews, Morgan, & Schmidt 1964). The galaxy lies in a small group close to the cluster Abell 347, at a distance of 86 Mpc. At this distance an angular scale of $0''.1$ corresponds to a projected linear size of 41 pc.

The radio source has been the subject of several comprehensive studies (e.g., Northover 1973; Miley & van der Laan 1973; van Breugel & Jägers 1982; Leahy, Jägers, & Pooley 1986). Its structure is intermediate between that of an edge-darkened double and a head-tail morphology, indicating that the morphology may be affected by motion of the parent galaxy through an ambient medium (Miley et al. 1972). When mapped

at sufficient resolution, the radio emission from the nuclear "head" apears jetlike and one-sided. An optical counterpart of the jet in 3C 66B was detected by Butcher et al. (1980) and further studied by Fraix-Burnet et al. (1989b).

Images of 3C 66B were obtained with the Faint Object Camera (FOC) on 1990 September 23 using the F320W filter in the f/96 512 × 512 mode (Paresce 1990) and reduced as in Macchetto et al. (1991). The filter bandpass is about 900 *Å* FWHM centered at 3360 *Å*. The pixel size after correction for geometric distortion is approximately 0.″022, ≈ 10 pc, and the field size approximately 11" ≈ 4 kpc. Two exposures of 1500 s duration were made with this filter, both in fine lock, resulting in a tracking accuracy of 0.″007 rms.

The galaxy was clearly visible in the raw data, but in order to investigate the jet alone, a model of the underlying galaxy light was substracted from the deconvolved image (Fig. 3) The model was obtained by fitting ellipses to isophotes and creating an image with exactly elliptical isophotes having the same parameters as those of the galaxy. This process removed some flux from the nucleus and is responsible for the residual "arc" opposite the bright knot in the jet, which slightly distorted the fitting of the ellipse and, therefore, led to an incomplete galaxy subtraction opposite it.

In order to compare our HST image with the best VLA map of 3C 66B, we smoothed the deconvolved and galaxy-subtracted optical image with a circular Gaussian function having $\sigma = 3.1$ binned pixels (FWHM ≈ 0.″35; Fig. 4a). Figure 4b shows a contour map of the "A-configuration" VLA map of 3C 66B obtained at 6 cm wavelength by Leahy et al. (1986).

Several conclusions can be drawn from these figures.

1. The similarities between the jet as seen in the "raw" and deconvolved images gives us confidence that the deconvolution process is not introducing any severe artifacts.

2. The similarities between the smoothed optical image and the radio map imply that on a scale of 0.″3 the radio and optical emission have very much the same radio-to-optical spectral index all along the jet.

3. On the scale of the HST resolution, the jet of 3C 66B is filamentary. *Filamentary structure has not previously been seen for optical jets,* although it has been observed on a scale of 0.″1 for the M87 jet in the radio (Owen et al. 1989), (and now with the FOC, see Section 4)

4. Two distinct "strands" appear in the HST image. These can be traced from ≥ 3.″7 (1.5 kpc) from the nucleus out to a distance of 7.″6 (3 kpc), where they disappear into the noise.

5. The separation between the strands varies between about 0.″3 and 0.″4, that is, about 150 pc.

6. The strands appear to undergo sharp "kinks" at distances of 2.″5 (1.0 kpc) and 6.″2 (2.5 kpc) from the nucleus.

7. An additional small bright feature is visible in the HST image off the jet, 5.″5 (2.3 kpc) to the north of the nucleus. It is unclear whether this is radiation from a compact region within the 3C 66B galaxy or whether it is due to an unrelated object. It may be related to the "blue knots" found by Fraix-Burnet et al. (1991).

It is interesting to compare our observations of 3C 66B with the high-resolution radio data of Owen, Hardee & Cornwell (1989) and our FOC high resolution observations of

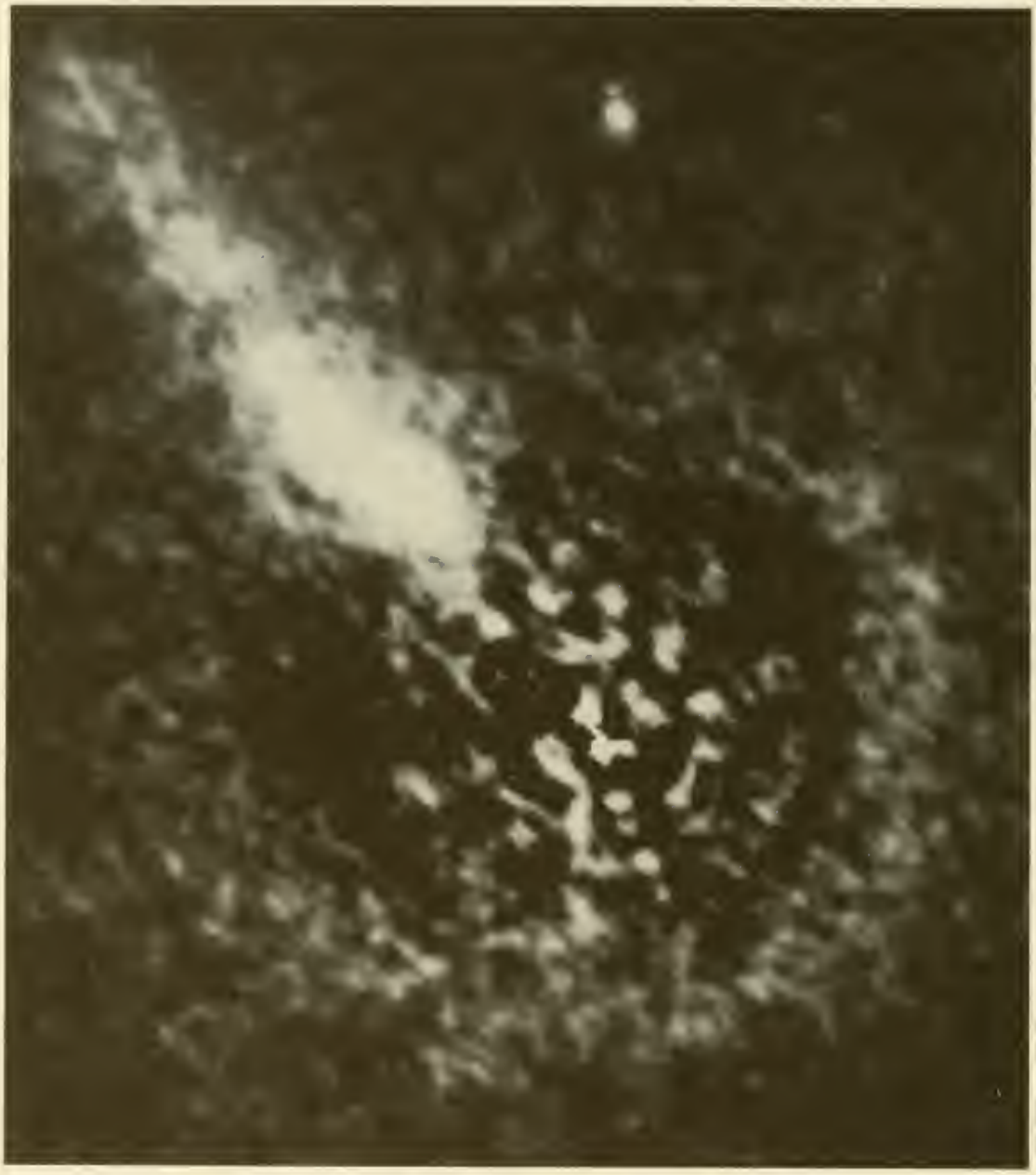

3. Deconvolved and galaxy-subtracted image of the jet of 3C 66B. The jet is 7.″6 (3 kpc) long. The FOC resolution of 0.″1 corresponds to 40 pc at the distance of the galaxy.

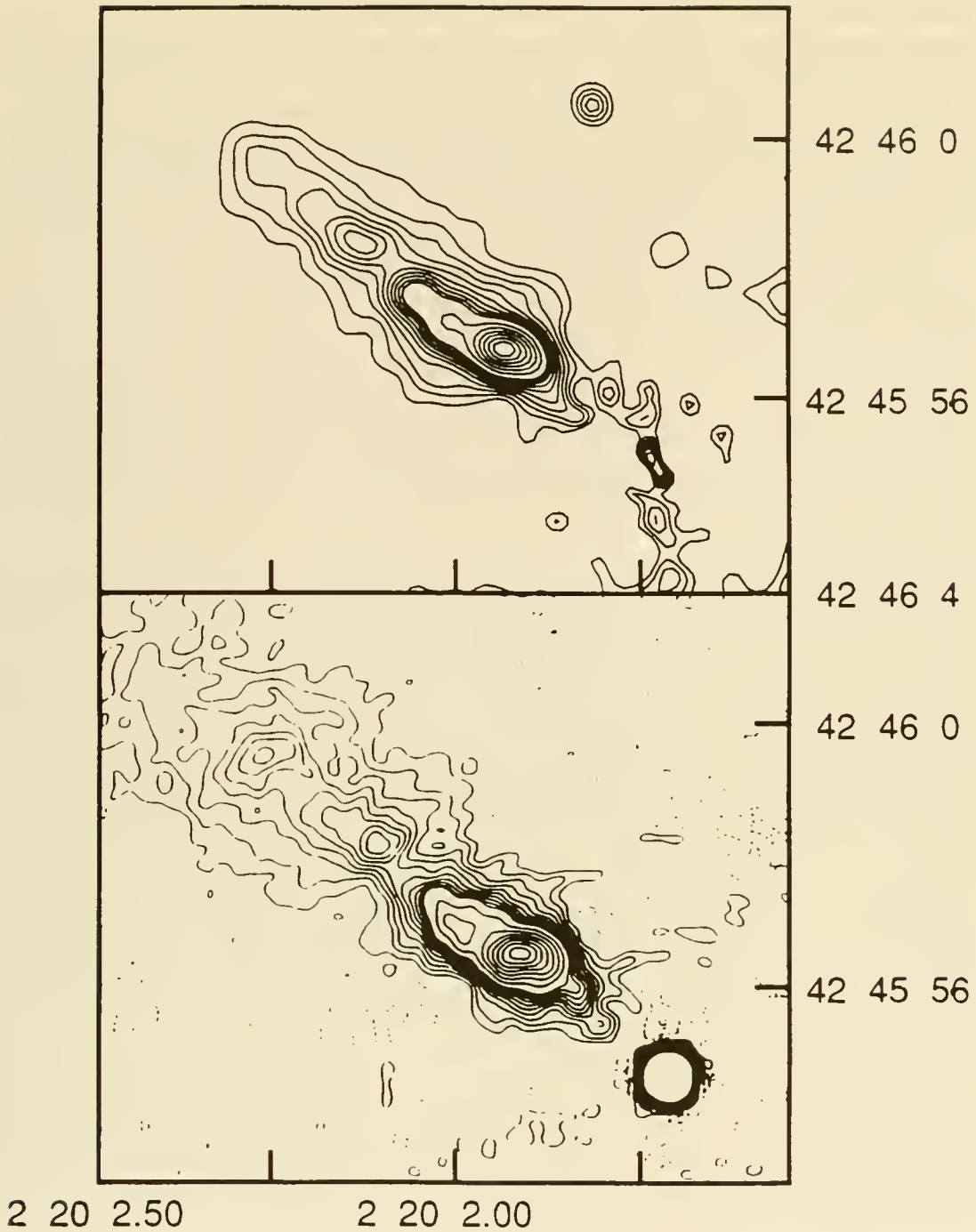

4. Contour map of 3C 66B jet smoothed with a Gaussian "beam" with σ = 3.1 pixels (0.″44 each). The contours are at intervals of 1.12 counts from 1.12 to 11.2 counts and intervals of 3.73 counts from 14.92 to 37.3 counts, corresponding to the contours of Leahy et al. 1986 for a nominal flux conversion and spectral index α = 1.1. Note that the spatial registration and scale are only approximate for the HST data. The coordinates' R.A. and Decl. axes are from Leahy et al. *(bottom)* The 5 GHz VLA map at comparable resolution to the optical image of *(top)* (from Leahy et al. 1986).

M87 (next section). The M87 jet also shows complex filamentary structure, with limb brightening over most of its length. However, it appears to be more sharply bounded than the jet in 3C 66B.

Although, unlike M87, 3C 66B is not a cD galaxy at the center of a rich cluster, there are several similarities between M87 and 3C 66B. Their total radio luminosities are comparable, but the jet in 3C 66B is slightly longer and can be traced out to about 3 kpc from the nucleus, a factor of 2 farther than in M87. Both jets appear filamentary and edge brightened. However, in 3C 66B, although further measurements are needed to confirm the fainter features, the double-stranded filaments appear to be embedded in a broader structure, which is not accurately colinear with the filaments. Also, although the 3C 66B jet is filamentary, the pitch angle of the filaments is quite different from that in the filaments in M87 - we do not see the tightly wound helix that the M87 shows.

A very basic question posed by these observations concerns constraints on the regions where the synchrotron-radiating electrons are accelerated. Does the presence of optical radiation along the jet imply that localized particle acceleration is required, or could the electrons be accelerated in the nucleus and transported to the sites of the radiation?

The average age of the radiating synchrotron electrons, with typical values for the magnetic field strength and cut-off frequency, is less than 1000 yr for the optical electrons, while the light travel time from the nucleus to the end of the observed optical jet is about 10^4 yr. Hence, at first sight, localized particle acceleration would be required.

However, as discussed later for M87, in situ acceleration is not needed in a two fluid model, (Pelletier and Roland 1989). In this case, a relativistic flow of electron-positron plasma moves in a channel through the jet. The external non-relativistic jet of electron-positron plasma carries most of the mass and kinetic energy. A mixing layer occurs at the boundary of these two fluids, and synchrotron radiation can be produced at this in interface.

The other new features present in our observations are the sharp bends or "kinks" in the double-stranded filaments. The origin of these kinks is unclear. The fact that they are mimicked in more than one filament suggests that they are not due to an instability mode in an individual filament. They may well trace out irregularities in the ISM of the galaxy and/or be due to time-dependent variations in the power of the nuclear machine responsible for producing the jet.

Another possibility is that these bends and kinks are the result of observing a jet which contains magnetic field modes which are at an angle to the jet. Models for force-free magnetized jets have been calculated by Königl & Choudhuri (1985) containing two magnetic field orientations, one parallel to the jet axis and the other a double helix twisted field. Both our observed filamentary edge-brightened configuration and the presence of bends are at least consistent with their model.

4. M87

The EO galaxy M87 harbours the prototypical and most studied example of an optical jet. First observed by Curtis in 1918, it remained little more than a curiosity, until Baade and Minkowski studied it in 1954 and first used the term "jet" to describe the sequence of optical knots extending to about 20" from the nucleus. Since then, the jet has been observed at radio (Owen, Hardee & Cornwell, 1989, Biretta, Stern & Harris 1991), optical (de Vaucouleurs & Nieto 1979, Keel 1988, Fraix-Burnet, Le Borgne & Nieto 1989) and X-rays wavelengths (Schreier, Gorenstein & Feigelson, 1980).

The radio and optical morphologies and polarization structure of the jet are similar (Schlötelburg et al, 1988) to within the resolution limits of the ground based observations. These results are best explained by emission from synchrotron radiation. In addition, the emission detected at x-ray wavelengths in the jet region also suggests that the synchrotron spectrum extends to high frequencies.

The origin of the optical continuum emission in radio jets can best be tested in M87, since it is the only jet which shows both a spectrum break and x-ray emission. Observations in the ultraviolet will help determine the exact frequency at which the break occurs. This, in turn, determines the value of the magnetic field and turbulences.

Optical and ultraviolet polarization observations at high resolution when compared to equivalent radio data will help determine the precise location and nature of the acceleration process, since the lifetime of these electrons, and therefore, their travel distance, is very small.

Images of M87 centred on the nucleus and positions along the jet were obtained with the FOC, utilizing the following filters in the f/96 512 $\times$ 512 modes: F120M, F140W, F220W (direct and with polarizers POL0,POL60,POL120), F430W (with polarizers only) and F501N. Additionally, a zoomed acquisition image was made with the F372M filter. The exposures were made in fine lock, with an expected tracking accuracy of $0\overset{''}{.}007$. The F120M image has low signal and is very noisy, but all other images of the nucleus were useful; adequate signal strength to give a significant impression of the jet were obtained only with the F140W, F220W, F372M and F430W filters. The F220W images are particularly valuable, because of the high contrast of the jet against the light from the stellar population of the galaxy which is very weak in the ultraviolet region.

The F220W exposures were corrected using the Lucy (1974) deconvolution technique to produce the final deconvolved images with minimum beam size $0\overset{''}{.}2$ FWHM. The results of this restoration are shown in Figure 5. This figure shows side-by-side the deconvolved FOC and VLA data. As is easily observed, two FOC frames (each of 11" $\times$ 11") are needed to cover the jet which extends for over 20" in length.

The complex structure and the wide range of intensities make it very difficult to display all the features in a single picture. Furthermore, the value of the relative intensity of the ultraviolet and radio data is arbitrary and was chosen only to show the most prominent features. Detailed intensity comparisons and determination of spectral indices as a function of position along the jet will be carried out in the near future.

The FOC observations demonstrate for the first time that the radio and ultraviolet brightness distribution is generally the same over a scale of about $0\overset{''}{.}1$ or about 10 pc (M87 presents 78 pc arcsec^{-1} at an assumed distance of 16 Mpc).

The FOC data shows that all the prominent optical knots (A,B,C, etc) have now been fully resolved and show the same remarkable structure as the radio data. (See Owen, Hardee and Cornwell, 1989, also for the knot notation). The jet is limb brightened, shows very well-defined edges along its conical structure with an opening angle of $\sim 6.5^o$ and has a tight filamentary structure. The appearance of this structure indicates that the filaments are wrapped around the jet with pitch angles of about 30^o - 40^o between the nucleus and knot I. At knot A, and between knots A and B, the filaments are more tightly wrapped with a pitch angle between 80^o and 90^o and decreasing from knot A towards knot B. The pitch angle may increase again towards knot C.

Slices taken across the jet at different locations show prominent limb brightening similar, but not identical, to the radio data. Detailed comparisons are beyond the scope of this paper, but this general agreement provides strong evidence in favor of the two fluid model for this jet. (Pelletier & Roland, 1988, Owen, Hardee & Cornwell 1988).

5. Left. Deconvolved FOC image of the M87 jet. Two FOC images are needed to cover the length of the jet ($\simeq$ 20"), hence the small gap in the spatial coverage. Right. Deconvolved VLA image kindly supplied by F. Owen and J. Biretta. The images show the remarkable agreement of the ultraviolet and radio observations.

In this scenario, the jet consists of a cone around which one or more bright filaments are wrapped. The optical and radio emission comes mostly from a surface layer in which these filaments are embedded. The synchrotron lifetimes in the ultraviolet are typically only of the order of 100 yr, corresponding to light travel times of about 30pc. This is comparable to the width and presumably the thickness of the optical and radio strands.

The low emissivity in the jet's core indicates that the energetic particles are not suffering significant synchrotron losses. This is also compatible with the model in which the jet's core has a relatively low magnetic field. In this case, the high-energy particles can be produced in the central black-hole and propagate along the jet's interior in a low magnetic field region, thereby suffering only modest synchrotron losses. As they diffuse *across* the jet and into the high magnetic field boundary layer, they can produce the optical emission without the need for in situ acceleration.

Several mechanisms can be invoked to explain how the emission from this boundary layer is produced. Non-linear evolution of synchrotron instabilities has been proposed by Bodo et al, 1991, to explain the formation of filaments in jets out of equipartition, such as that in M87, where the energy of the relativistic electrons exceeds that of the magnetic field. They find that in a plasma subject to constant heating, after an initial phase in which the instability growth rate follows the linear model, the instability reaches a quasi equilibrium state on timescales of the order of several synchrotron timescales. This mechanism can explain the formation of filaments of enhanced emission observed in the lobes and jet of M87.

Optical synchrotron emission can also be produced through a diffusive shock acceleration mechanism (Fraix-Burnet, 1991). This process is so efficient that requires the magnetic field turbulence to be quite low. The source of energy of this turbulence could be the kinetic energy of the jet which can be transferred to the magnetic field (or to the plasma) through the interaction of the jet with the interstellar medium.

The answer to which of the competing mechanisms and scenarios are at work and the determination of the relevant physical parameters will have to wait further detailed analysis of the FOC optical, ultraviolet and polarization data.

5. CONCLUSIONS

The study of the optical counterparts to radio jets with the Faint Object Camera on board the Hubble Space Telescope has already produced new and unexpected results.

The jet in PKS 0521-36, which is the most distant, has been fully resolved. Because of its length, magnetic field configuration and optical morphology, it seems to require reacceleration sites for the optical electrons. These could well be provided by shocks at the site of the brighter knots observed.

For both 3C 66B and M87, we have observed, for the first time at optical wavelengths, a filamentary structure which is similar to the radio data. In this case, we conclude that the emission comes from a boundary layer where the filaments and the strong magnetic field are located.

One of the most puzzling, but fundamental, results that must be explained by models of particle acceleration is why within an object, over more than five decades of frequency and a large variation of physical conditions, the old and young electrons have similar spatial distributions, although large differences are observed from object to object.

Our FOC observations of PKS 0521-36, 3C 66B and M87 show that, even with its present aberration problems, the HST is a uniquely important instrument for studying

synchrotron jets. Future observations with the HST of other extragalactic jets should provide fundamental information about the nature of collimated activity in galaxy nuclei.

6. ACKNOWLEDGEMENTS

The FOC/IDT members are: Rudolf Albrecht, Cesare Barbieri, David Baxter, J. Chris Blades, Alec Boksenberg, Phil Crane, Jean Michel Deharveng, Michael J. Disney, Perry Greenfield, Peter Jakobsen, Robert Jedrzejewski, Theo M. Kamperman, Ivan R. King, F. Duccio Macchetto, Craig D. Mackay, Antonella Nota, Francesco Paresce, William Sparks, and Gerd Weigelt.

We wish to thank Drs. F. Owen and J. Biretta for making available to us the VLA radio data for M87, and Dr. Keel for the PKS 0521-36 data.

REFERENCES

Angel, J.R.P., & Stockman, H.S. 1980, *Ann. Rev. Astr. Ap.*, **18**, 321

Bailey, J., Hough, J.H., & Axon, D.J., 1983, *M.N.R.A.S.*, **203**, 339

Baade, W. & Minkowski, R. 1954, *Ap. J.*, **119**, 221

Biretta, J.A., Stern, C.P. & Harris, D.E. 1991, *A. J.*, **101**, 1632

Blandford, R.D., & Eichler, D., 1987, *Phys. Report*, **154**, 1

Blandford, R.D., & Rees, M.J., 1974, M.N.R.A.S. **169**, 395

Bodo, G., Ferrari, A., Massaglia, S., Rossi, P., Shibata, K., & Uchida, Y. 1991, *Astr. Ap.*, in press.

Bohlin, R.C., Harris, A. W., Holm, A.V., & Gary, C. 1990, *Ap. J. Suppl.*, **73**, 413

Boisson, C., Cayatte, V., & Sol, H. 1989, *Astr. Ap.*, **211**, 275

Bridle, A., & Perley, R.A. 1984, *Ann. Rev. Astr. Ap.*, **22**, 319

Bridle, C., Hough, J.H. Bailey, J., Axon, D.J., & Hyland, A.R. 1986, *M.N.R.A.S.*, **221**, 739

Butcher, H.R., van Breugel, W.J.M., & Miley, G.K. 1980, *Ap. J.*, **235**, 749

Cayatte, V., & Sol, H. 1987, *Astr. Ap.*, **171**, 25

Curtis, H.D. 1918, Lick Observatory Publ, **13**, 11

Danziger, I.J., Ekers, R.D., Goss, W.M., & Shaver, P.A. 1983, in *Astrophysical Jets*, ed. A. Ferrari & A.G. Pacholczyk (Dordrecht:Reidel), 131

Danziger, I.J., Fosbury, R.A.E., Goss, W.M. & Ekers, R.D. 1979, *M.N.R.A.S.*, **188**, 415

de Vaucouleurs, G., & Nieto, J.L. 1979, *Ap. J.*, **231**, 364

Drury, L. O. C. 1983, *Rep. Progr. Phys.*, 46, 973

Fraix-Burnet, D., Golombek, D., Macchetto, F., Nieto, J.L., Lelievre, G., Perryman, M.A.C., & di Sergo Alighieri, S. 1991, *A. J.*, **101**, (1), 88

Fraix-Burnet, D., Nieto, J.L., Lelievre, G., Macchetto, F., Perryman, M.A.C., & di Serego Alighieri, S. 1989b, *Ap. J.*, **336**, 121

Fraix-Burnet, D., Le Borgne, J.F., & Nieto, J.L., 1989, *Astr. Ap.*, **224**, 17

Fraix-Burnet 1991, Proceedings 7th IAP Meeting Extragalactic Radio Sources: from Beams to Jets, Paris, France, 2-5 July, 1991

Keel, W.C. 1986, *Ap. J.*, **302**, 296

Keel, W.C. 1988, *Ap. J.*, **329**, 532

Königl, A., & Choudhuri, A.R. 1985, *Ap. J.*, **289**, 173

Leahy, J.P., Jägers, W., & Pooley, G.G. 1986, *Astr. Ap.*, **156**, 251

Lucy, L.B. 1974, *A. J.*, **79**, 745

Macchetto, F. 1981, in *Proc. of ESO/ESA Workshop Optical Jets in Galaxies*, ed. F. Macchetto, G. Miley, & M. Tarenghi (Noordwijk:ESA), 15

Macchetto, F., et al. 1991, *Ap. J.*, **369**, L55

Matthews, T.A., Morgan, W.W., & Schmidt, M. 1964, *Ap. J.*, **140**, 35

Miley, G.K. 1981, in *Proc. of ESO/ESA Workshop Optical Jets in Galaxies*, ed. F. Macchetto, G. Miley, & M. Tarenghi (Noordwijk:ESA), 9

Miley, G.K., 1980, *Ann. Rev. Astr. Ap.*, **18**, 165

Miley, G.K., & van der Laan, H. 1973, *Astr. Ap.*, **28**, 359

Miley, G.K., Perola, G.C., van der Kruit, P.C., & van der Laan, H. 1972, *Nature*, **237**, 269

Morabito, D., Preston, R.A., Linfield, R.P., Slade, M.A., & Jauncey, D.L. 1986, *Ap. J.*, **91**, 546

Northover, K.J.E.D. 1973, *M.N.R.A.S.*, **165**, 369
Owen, F.N., Hardee, P.E., & Cornwell, T.J. 1989, *Ap. J.*, **340**, 698
Paresce, F. 1990, FOC Instrument Handbook, Space Telescope Science Institute
Pelletier, G., & Roland, J. 1988, *Astr. Ap.*, **196**, 71
Rees, M.J. 1971, *Nature*, **229**, 312
Rybicki, G.B., & Lightman, A.P. 1979, Radiative Processes in Astrophysics (New York: Wiley)
Schlötelburg, M., Meisenheimer, K., & Röser, H.J. 1988, *Astr. Ap.*, **202**, L23
Schreier, E.J., Gorenstein, P., & Feigelson, E.D. 1982, *Ap. J.*, **261**, 42
Sparks, W., Miley, G., & Macchetto, F. 1990, *Ap. J.*, **361**, L41
Turnshek, D.A., Bohlin, R.C., Williamson, R.L., Lupie, O.L., Koornneef, J., & Morgan, D.H. 1990, *A. J.*, **99**, 1243
van Breugel, W.J.M., & Jägers, W. 1982, *Astr. Ap. Suppl.*, **49**, 529

EARLY OBSERVATIONS OF GRAVITATIONAL LENSES WITH THE PLANETARY CAMERA OF HUBBLE SPACE TELESCOPE

Jerome Kristian
Carnegie Observatories

for the

Wide Field/Planetary Camera
Investigation Definition Team *

---

* S.P. Ewald, E.J. Groth, J.J. Hester, J.A. Holtzman, T.R. Lauer, R.M. Light, D.P. Schneider, E.J. Shaya, W.A. Baum, B.G. Campbell, A.D. Code, D.G. Currie, G.E. Danielson, S.M. Faber, J.G. Hoessel, D. Hunter, T. Kelsall, C.R. Lynds, G. Mackie, D.G. Monet, E.J. O'Neil, Jr., P.K. Seidelmann, B. Smith and J.A. Westphal.

During Cycle 0, we obtained preliminary data for six "classic" gravitational lens systems, as part of the integrated WFPC IDT observing program. The lens observations were intended as a reconnaissance and evaluation program, to assess, with real data, what can usefully be done with the degraded point spread function (PSF) and to decide whether more extensive HST observations would be productive.

All observations were made with the Planetary Camera, in the team's standard V and I bands (F555W and F785LP). Two filters were used because the quasar images and the lensing galaxies have very different colors; the V band emphasizes the quasar images, and the I band the galaxies. Exposure times were chosen so as to not saturate the brighest

images, and also to fit within single dark-side orbits, to maximize spacecraft efficiency.

The general overall goals of our lens program are (1) To test the validity of gravitational imaging theories by observationally characterizing the lens systems as completely as possible [the mass distribution and redshift of the lensing galaxy and the intensities and geometry of all of the quasar images, including the expected but so far undetected (n+1)th images], and comparing the data with theoretical models. (2) To use individual lens systems as tools to obtain cosmologically interesting information - small and large scale galaxy mass distributions and mass/light ratios, H0, q0, etc.

The results of the Cycle 0 observations are rather encouraging. Useable data were obtained for all six systems, with at least modest new results for four of them, and it appears that many of the original objectives of the program can eventually be achieved, albeit with a considerable increase of exposure time. Lens observations are one of the few deep space programs suited to the telescope in its present condition: the most important information lies in the morphology and relative brightness of the images, rather than in their absolute magnitudes, which have so far proved difficult to measure with HST; there is structure on angular scales which requires HST resolution, but the structure is not so complex as to confuse the data with badly overlapping PSFs and the like; and the lens images are for the most part relatively bright, so the signal to noise is great enough to allow at least partial correction of the PSF.

The data are still being analyzed by the IDT; the results and the data themselves will be published elsewhere. Below we give just a few comments on each of the objects.

.....

Q0957+561

This, the first lens discovered, is still not well understood in spite of (or perhaps because of) the considerable amount of data available, both in the radio and optical. Optically, it has been known since the earliest days to consist of at least 3 components: two quasar images separated by 6 arc seconds and a lensing galaxy very close to one of the images.

The new HST data show the system in much better spatial detail. The three images are completely resolved for the first time, and the galaxy is bright enough that, even with the relatively short exposures, a rough core radius can be obtained, which should further constrain the theoretical models.

Deeper HST observations will provide detailed information on the structure of the lensing galaxy and, with luck, the location and intensity of the 3rd image, both of which will be of importance in finally understanding the system.

PG1115+080

PG1115, the "triple quasar", was the second gravitational lens discovered (Weymann et al 1980, Nature 285, 641), and the first and so far most interesting to be observed in our program. Over the decade following its discovery, some details of the system were found from the ground in a remarkable series of observational tours de force, using speckle techniques and direct imaging in extremely good seeing (see, e.g., Christian et al 1987, Ap.J. 312, 45, and references therein). Following a suggestion based on early imaging data and theoretical models, it was found that the brightest of the three components was itself double; the lensing galaxy was detected (although there is some disagreement in the literature as to its location); and variability between components, on a time scale of months, was seen.

The morphology was revealed in its full glory with the first raw HST pictures. The system is completely resolved, including the two bright components (separation 0.5 arc sec) and the lensing galaxy's location and brightness is easily and unambiguously seen in the raw data. The quality of the data, the accuracy and convincingness of the results, and the ease of obtaining them compared with the ground-based results, which are the product of formidable skill, expertise, dedication and labor, are a dramatic illustration of the power of HST for this kind of observation.

This system also provided a useful test case for various techniques to correct for the point spread function, in order better to see the lens galaxy. It was found that, at least in this case, the most effective technique was to remove the quasar images by subtracting a properly scaled bright image taken near the same time. This was found to be better than using theoretical PSFs or deconvolutions of various kinds, although in practice it was rather difficult to do (cf. the poster paper by E.J. Groth at this Workshop).

The 1115 system is relatively simple, as the known lenses go, and shows promise of being completely understood. Modeling of the Cycle 0 data by Schneider and Kristian suggest that the observed galaxy is capable by itself of producing the observed images, and what is required for a complete understanding of the system is a better knowledge of the distance and the mass distribution of the lens galaxy, and the location and brightness of the expected 5th image. Further HST observations will produce the second and third of these three data. The distance will have to await spectroscopy, perhaps with the FOS, but in the meantime, plausible and useful estimates can be made from the brightness and structure of the galaxy.

PG1115 is at present perhaps the best candidate for estimating the Hubble constant from measurements of time delays among the images. It and 0957 (which can be done from the ground), are the overall best candidates, and 1115 is better in some ways. It is simpler (0957 is complicated by the presence of a rich cluster, whose lensing effects are substantial and poorly known) and appears to be well on its way to being completely understood, and there are more images, which provide much tighter observational constraints and less ambiguity in matching intensity changes between images. Ground-based observations show

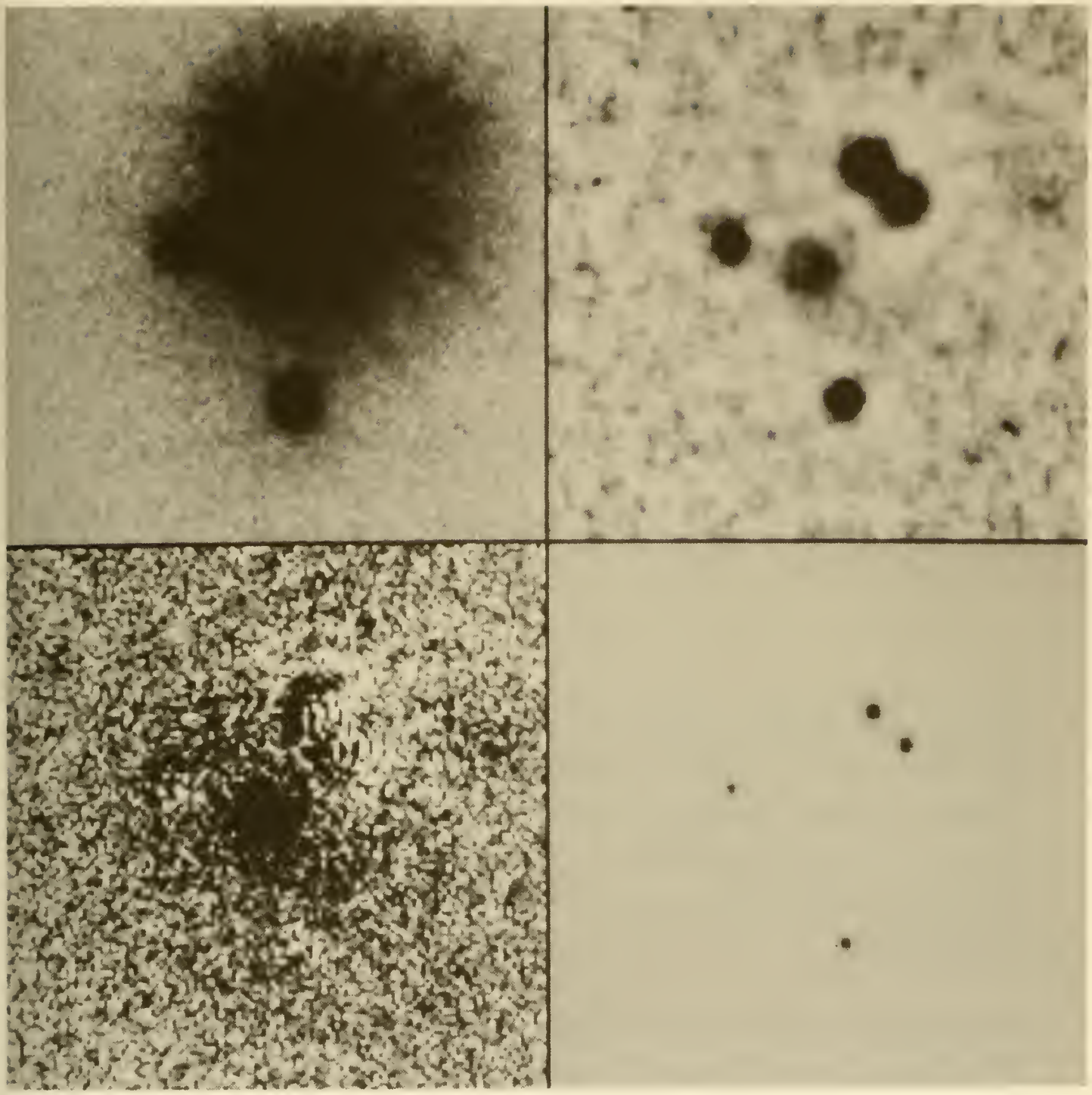

PG1115 - upper left,"raw" data; upper right, Lucy deconvolved; lower left, "raw" with quasar images subtracted; lower right, Lucy deconvolved with stretch set to display image cores.

variability in 1115 on time scales of months, which is consistent with theoretical predictions and convenient for measurement. The system is too compact and geometrically complex for accurate photometry from the ground, but the Cycle 0 data show that such measurements can easily be done with HST.

1634.9+267

This is a faint 4 arcsec quasar pair, which has been suggested as a lensed system on the basis of detailed similarities in the spectra, although no lens has been detected.

The Planetary Camera data shows two point sources with a possible very faint 3rd image whose reality remains to be verified.

MG2016+112

The lens system MG2016+112 was discovered in 1984 (Lawrence et al, Science 223, 66). Since then it has been observed extensively both in the visible and radio, mostly by Schneider and a host of distinguished colleagues in the MG lens survey group, who pushed ground-based techniques to their limits. It is now known to be composed of three radio sources and involves perhaps as many as 7 optical objects, 4 of them galaxies or extended emission regions.

Schneider et al saw evidence for a 3rd QSO image, which is one of the few even suggested in the literature, but it has never been confirmed.

Both ground-based and HST observations are difficult because of the small angular scale and faintness of the system. In spite of its observational difficulties, however, it is important because it provides a very stringent test of lensing theories.

Because of the faintness of the objects, our limited Cycle 0 data do not go deep enough to add anything new or substantive to the existing data, but they indicate that longer exposures will be able to do so. The two lens components are seen clearly in the V band, and faintly in the I band. Remarkably, the I band data also show D, one of the two potential lensing galaxies, at a redshift of 1. This is likely the most distant galaxy detected by HST in its early days.

2237+0305

Also known as the "Huchra lens" or the "Einstein cross", this famous system is composed of a distant QSO aligned almost precisely with the nucleus of a nearby galaxy. The galaxy splits the QSO into four images arranged in a rough square 1 arcsec on a side. A fifth image has been reported on the basis of ground-based data in a remarkable recent paper by Racine (A.J. 102, 454, 1991).

The system is completely resolved by the Cycle 0 PC observations. Unfortunately, the exposures are too short to definitively confirm or rule out the reported 5th image, although deeper exposures will be able to do so.

2345+007

There is an ongoing argument about whether or not this double quasar is a lens system. No lensing galaxy has been seen from the ground, although two groups have reported (somewhat different) small-scale structure in one of the images. The absence of an observable lens has led to a suggestion of imaging by dark matter. The system is of considerable interest because the 2 spectra have several Ly-alpha absorption systems in

common, which makes it a potentially powerful probe of Ly-alpha clouds.

The Cycle 0 PC data do little to resolve the uncertainty. They show only a pair of point sources, with no sign of any structure or other objects. The new data definitely rule out the presence of structure in either of the images such as has been reported earlier. The failure to detect a lensing galaxy was expected from the much deeper ground-based data which exists.

ULTRAVIOLET SPECTROSCOPIC STUDIES OF THE INTERSTELLAR MEDIUM WITH THE HUBBLE SPACE TELESCOPE

Blair D. Savage
Department of Astronomy
University of Wisconsin
475 N. Charter Street
Madison, WI 53706

1. INTRODUCTION

The study of the interstellar medium (ISM) is concerned with answering such questions as: 1.What is the three dimensional distribution of gaseous matter in the galaxy ? 2.What is the composition of that gas ? 3. What is the relationship between interstellar gas and dust ? 4. What are the physical conditions in the different phases of the interstellar medium? 5. What physical processes control these conditions ? 6. How does the ISM participate in basic Galactic processes ?

Satellite spectrographs make it possible to seek answers to these questions using the very significant diagnostic power of UV spectroscopy. Previous UV spectroscopic observations of the ISM were mostly obtained with the Orbiting Astronomical Observatory (OAO) series of satellites including OAO-2 and OAO-3 (the *Copernicus* satellite) and more recently with the *International Ultraviolet Explorer* (IUE) satellite. For a review of the OAO results and in particular those of the *Copernicus* satellite see Spitzer & Jenkins (1975) and Spitzer (1988). The IUE results relevant to the ISM are reviewed in a number of papers found in Kondo et al. (1987).

With the launch of HST a new suite of instruments has become available for the study of the ISM. These include two imaging cameras (WF/PC and FOC) and two spectrographs (FOS and GHRS) . The first HST imaging results are found in Astrophysical Journal Letters (1991 March 10). The imaging results for SN 1987A (Jakobsen et al. 1991) and the Orion Nebula (Hester et al. 1991) reveal that even though HST imagery is significantly impacted by the spherical aberration, important imaging science related to the ISM can still be pursued. The first HST spectroscopic results are found in Astrophysical Journal Letters (1991 August 20).

A discussion of the UV spectroscopic capabilities of the HST for studies of the ISM is the emphasis of this short review which is organized as follows: A brief overview of the diagnostic power of UV spectroscopy is found in § 2 while the spectroscopic capabilities of the HST are discussed in § 3. Examples of recent scientific results are found in § 4. Because of the author's affiliation with the GHRS science team and his access to GHRS data much of the emphasis will be on results from the GHRS.

2. THE DIAGNOSTIC POWER OF ULTRAVIOLET SPECTROSCOPY FOR STUDIES OF THE ISM

The spectrographic instrumentation on HST provides access to the rich UV region of the spectrum for absorption and emission line spectroscopy. The UV spectrographs aboard HST have high efficiency from 1150 to 3200 Å and limited capability from 1100 to 1150 Å. Table 1 lists some of the atomic and molecular species having their resonance lines or lines from low lying excited levels in the 1100 to 3200 Å region of the spectrum. Access to the UV makes possible the direct detection of absorption by such abundant atoms as C, N , O, Mg, Si, etc. in a number of ionization states including those found in cool neutral gas (C I, C II, N I, O I, etc) and those found in the hot interstellar medium (C IV and N V). In a number of cases, ions from adjacent ionization states are available which can be used to probe physical conditions in

interstellar clouds (e.g C I, C II, Mg I, Mg II, S I, S II, S III, P I, P II, P III, etc.).

The UV provides important tracers of cold neutral interstellar gas and permits studies of elemental abundances in that gas. With high spectral resolution and high signal to noise ratios it will be possible to begin to get information on many of the rarer elements such as those listed near the bottom of Table 1. In addition many molecules that play important roles in interstellar chemical reaction networks become available for direct study. The extension of some sensitivity to 1100 Å due to the selection of a LiF window for the short wavelength detector for the GHRS makes possible studies of the (0,0) and (1,0) Lyman band systems of H_2 and HD toward bright stars.

The UV provides important tracers of the hot ISM with the doublet of N V near 1240 Å being the most important among those accessible to HST. N V peaks in abundance in collisionally ionized gas with a temperature near $2x10^5$ K. Unfortunately the important O VI doublet near 1032 and 1038 Å is not observable with HST except in the spectra of QSO's with adequate redshift to shift the doublet to wavelengths longward of 1150 Å.

TABLE 1
ATOMS AND MOLECULES WITH UV RESONANCE LINES AND ATOMS WITH LINES FROM LOW LEVEL FINE STRUCTURE STATES WITH 1100 < λ < 3200 A

H I, D I	H_2 , HD
B I, B II , B III	
C I, C I*, C I**, C II, C II*, C IV	CO, C_2 ,CO^+,CH_2
N I, N V	N_2, CN^+, NO, NO^+
O I, O I*,O I**	H_2O
Na I	
Mg I, Mg II	MgH^+
Al I, Al II, Al III	
Si I, Si II,Si II*, Si III, Si IV	SiO
P I, P II, P III, P V	
S I, S II, S III	CS
Cl I	HCl
Sc II, Sc III	
Ti II, Ti III	
V I, V II, V III	
Cr I, Cr II	
Mn I, Mn II	
Fe I, Fe II, Fe II*, Fe III	
Co I, Co II	
Ni I, Ni II	
Cu I, Cu II	
Zn I, Zn II	
Ga I, Ga II	
Ge I, Ge II	
As I, As II	
Se I, Se II	
Kr I	

In addition to the direct detection of a wide range of atomic and molecular species for abundance studies, UV spectroscopy also permits measures of the physical conditions in interstellar clouds. Temperature information is available from the measured Doppler broadening of spectral lines or from the presence of certain species (i.e. N V suggests gas near $2x10^5$K). Interstellar gas density can be inferred by studying the excitation of fine structure levels or from measures of abundances of gas in adjacent states of ionization (i.e. Mg I/Mg II,

C I, C II, S I/S II, etc). In several cases, atomic isotope shifts are large enough to allow the direct study of important isotope ratios (i.e. D/H). In other cases isotope ratios can be inferred for atoms found in molecules (i.e. $C^{12}O/C^{13}O$, and HD/H_2) .

Figure 1 provides an example of the spectroscopic richness of the UV. The spectrum is of the bright rapidly rotating star Zeta Ophiuchi and was obtained with the GHRS Echelle A mode using the small science aperture. The spectral resolution is approximately 3.5 km s^{-1}. In the 6 Å region of the spectrum illustrated, interstellar absorption lines are found for Kr I λ1235.83, Ge II λ1237.059, Mg II λ1239.925 and Mg II λ1240.395. Kr I and Ge II have not been previously seen in the interstellar gas.

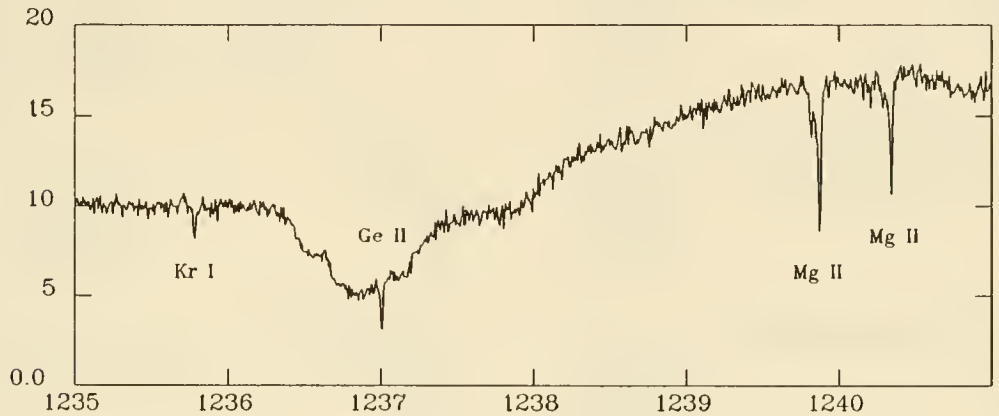

Figure 1. GHRS Echelle mode measurements of the far-UV spectrum of Zeta Ophiuchi from 1235 Å to 1241Å revealing interstellar absorption by Kr I, Ge II, and Mg II. The spectrum, obtained with the GHRS and the small (0.25"x0.25") entrance aperture, has a resolution of 3.5 km s^{-1}. The Mg II doublet lines reveal a two component structure with the strongest component at v(helio) = -15 km s^{-1} and a weaker component at -27 km s^{-1}. The signal to noise ratio in the spectrum is approximately 40/1.

3. HST SPECTROSCOPIC CAPABILITIES

Three HST instruments have spectroscopic modes that can be used for UV interstellar studies. The characteristics of these modes are listed in Table 2. The modes in the FOC and FOS can be used for low resolution (FWHM > 200 km s^{-1}) measurements of interstellar emission and or absorption lines and for the study of the continuous extinction due to interstellar dust. The FOS also has a spectropolarimetric mode that will permit important studies of the UV polarizing properties of interstellar and circumstellar dust .

It is expected that the primary instrument for studies of the interstellar gas will be the Goddard High Resolution Spectrograph (GHRS) which has modes providing low, medium and high spectral resolution operating in the UV from 1100 to 3200 Å.

The spherical aberration of the HST has adversely affected the spectrographs in several ways. To preserve spectroscopic resolution the small entrance apertures must be used which results in a substantial reduction in throughput. For example with the GHRS the estimated light loss when using the 0.25"x0.25" small science aperture (SSA) is approximately a factor of 3 for λ >1700Å and a factor of 4 for λ < 1700Å. The light loss is greater if the object is poorly centered on the aperture. The 2"x2" large science aperture (LSA) accepts more radiation but the resultant spectrum is degraded in resolution by about a factor of 2 to 3, depending on the mode.

TABLE 2
HST ULTRAVIOLET SPECTROSCOPIC CAPABILITIES

mode	wavelength range (Å)	resolution [a] ~FWHM (km s^{-1})		comment
Goddard High Resolution Spectrograph(GHRS)		LSA (2"x2")	SSA (.25"x.25")	
G140L	1100-1800	250 km s^{-1}	130 km s^{-1}	Side 1[b]
G140M	1100-1800	25	12	Side 1[b]
Echelle A	1150-1800	8	3.5	Side 1[b]
G160M	1150-2100	30	15	Side 2
G200M	1600-2300	25	13	Side 2
G270M	1900-3200	25	12	Side 2
Echelle B	1700-3200	8	3.5	Side 2
Faint Object Camera (FOC)		0.1" x 20" slit		
long slit spectrographic facility	3600-5400	260 km s^{-1}		first order
	1800-2700	260		second order
	1200-1800	260		third order
	1150-1350	260		fourth order
Faint Object Spectrograph (FOS) [c]		0.25" x 2.0" slit [d]		
G130H	1150-1608	210 km s^{-1}		G130H has low sensitivity
G190H	1576-2332	250		
G270H	2227-3306	250		
G160L	1150-2523	1200		

[a] The approximate resolution (FWHM [km s^{-1}]) is given for the various spectroscopic modes. The resolution depends on the aperture choice. When using the larger apertures a single number is a poor measure of the resolution. The spectroscopic spread function has a sharp core and very broad wings with a significant fraction of the energy going into the wings.

[b] At the time of writing (6 September 1991) side 1 of the GHRS was experiencing electrical problems with a low voltage power supply.

[c] The FOS has many other modes which operate at visual wavelengths. It also has a spectropolarimetric mode that can be used to study interstellar polarization in the ultraviolet.

[d] The FOS resolution is only listed for the 0.25" x 2.0" slit. A large selection of other aperture choices is available. However, the resolution will be degraded when using larger apertures.

When using the SSA, the GHRS intermediate resolution modes have a resolution comparable to the high resolution mode of the *Copernicus* satellite which is about a factor of 2 higher than the high resolution mode of the IUE observatory. The GHRS high resolution Echelle modes have a resolution about 3 times higher than the *Copernicus* satellite and 6 times higher than IUE. Figure 2 Illustrates absorption line measurements of the 2803.531Å Mg II line toward Mu Columbae obtained with the GHRS operating in several modes. Although the LSA Echelle-B spectrum appears to have somewhat higher resolution than the G270M -SSA measurement, the G270M measurement provides more wavelength coverage and a stable spectroscopic spread function. The appearance of the Echelle-B LSA measurement will vary with telescope pointing accuracy and with telescope focus.

Figure 3 compares LSA and SSA measurements of interstellar Fe II absorption obtained with the G270M grating. The degradation in resolution when using the LSA is substantial. Broad wings are apparent on the interstellar lines for the LSA measurements.

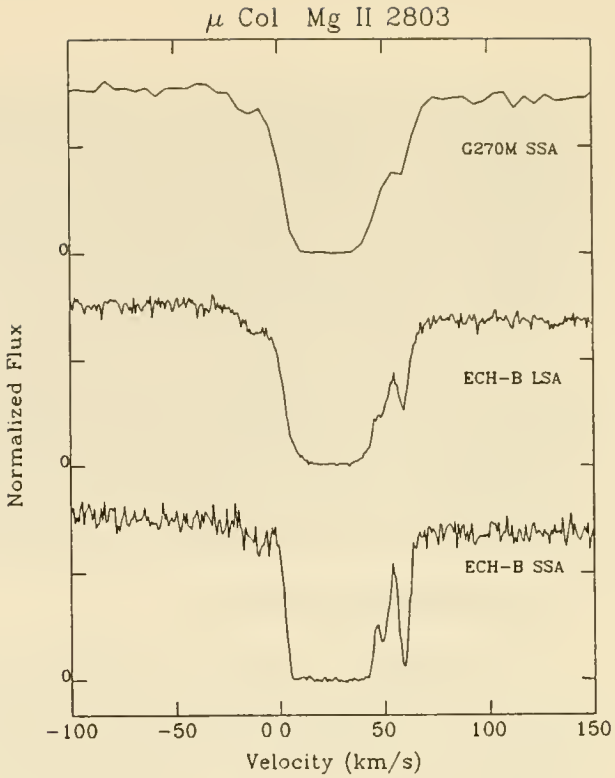

Figure 2. GHRS observations of the Mg II λ2803.531 interstellar absorption line toward μ Columbae in the G270M mode (with the SSA), in the Echelle-B mode (with the LSA), and in the Echelle-B mode (with the SSA). The multicomponent nature of the absorption which is readily apparent in the Echelle-B-SSA data is less apparent in the G270M-SSA measurement. The effective resolutions (FWHM) from top to bottom are approximately 12, 8 and 3.5 km s^{-1}.

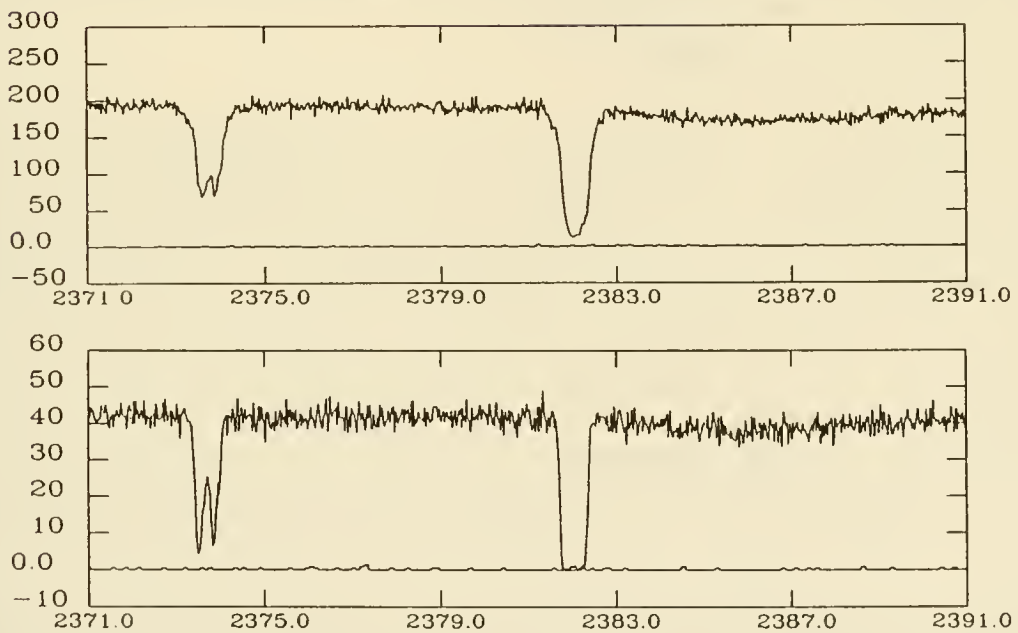

Figure 3. GHRS observations of interstellar Fe II λ 2374.461 and λ 2382.765 absorption toward HD 93521 as observed in the G270M mode with the large science aperture, LSA (top) and small science aperture, SSA (bottom). The degradation of spectral resolution when using the LSA at intermediate resolution is readily apparent. The effective resolution (FWHM) for the upper spectrum is 25 km s^{-1} compared to 12 km s^{-1} for the lower spectrum. However, the very broad wings on the spectroscopic spread function for the LSA measurement creates the broad wings on the resulting interstellar line profiles.

The principal advantages the GHRS offers over previous instruments for UV interstellar studies are: 1. *Higher spectral resolution.* The 3.5 km s^{-1} resolution will permit the study of conditions in individual interstellar clouds. 2. *Low noise photon counting detector* . The Digicon detectors are capable of very high S/N spectroscopy (S/N = 160 /1 has been demonstrated). The detectors can be used to observe objects well beyond the reach of IUE which is severely background noise limited. The combination of high resolution and high signal to noise permits the study of very weak interstellar features which are important for accurate abundance measurements.

At the time of writing, side 1 of the GHRS was experiencing intermittent electrical problems with a low voltage power supply. Side 1 contains the G140L, G140M and Echelle A modes while side 2 contains G160M, G200M, G270M, and Echelle B modes. If side 1 is lost for future use, the GHRS will still have wavelength coverage down to 1150 A with the G160M mode. However, the resolution is substantially reduced compared to that provided by Echelle A (15 versus 3.5 km s^{-1}). Echelle B on side 2 would provide a high resolution capability in the middle UV from 1700 to 3200 Å .

4. SCIENTIFIC RESULTS

This section overviews the principal results presented in several papers on interstellar absorption found in the special Astrophysical Journal Letters issue reporting the first HST spectroscopic results. Those papers involving the ISM concern the interstellar gas toward ξ Persei, the gaseous matter in the circumstellar environment of β Pictoris, and Milky Way absorption in the direction of the bright QSO 3C273. The results for β Pictoris are discussed elsewhere in this volume.

Several more recent HST results also pertain to the ISM. GHRS measurements of interstellar absorption by D and H toward Capella are discussed by Linsky(this volume). New GHRS measurements of weak absorption lines in the spectrum of ζ Ophiuchi from Cardelli, Savage & Ebbets (1992) are briefly described below.

4.1 Interstellar gas toward ξ Persei

The star ξ Persei (HD 24912) is an O7.5 III star at an estimated spectroscopic distance of 540 pc in the direction l = 160.4° and b = -13.1° The large vsini (216 km s^{-1}) and substantial reddening E(B-V) = 0.32 make ξ Persei well suited for studies of narrow interstellar absorption lines. Ultraviolet observations of interstellar absorption toward ξ Persei were obtained by the GHRS in October 1990 and January 1991. The measurements were obtained with the GHRS operating in the Echelle modes with the light of ξ Persei placed in the small (0.25"x0.25") entrance aperture. Observations were obtained at 26 different setup wavelengths with each observation providing approximately 5 to 10 Å coverage of the ultraviolet spectrum. The total integration time for each spectral region observed was typically 3 to 6 minutes. The signal to noise achieved in the reduced data ranges from 15 to 100 depending on the wavelength and the accuracy of centering the star in the small aperture. The results of the analysis of the GHRS data for ξ Persei are found in Cardelli et al. (1991), Savage et al. (1991) and Smith et al (1991). Cardelli et al. present gas phase abundance results for the diffuse clouds toward the star, Savage et al. discuss how elemental abundances vary with velocity, and Smith et al. consider physical conditions in the densest portions of the cloud toward ξ Persei where molecules are found. The data were processed using the techniques described by Cardelli et al. (1991). Sample interstellar line profiles plotted on a velocity basis are illustrated in Figure 4.

The GHRS setup wavelengths provided for the detection of interstellar absorption lines from the following ions: C I, C I*,C I**, C II, C II*, C IV, O I, O I*, Mg I, Mg II, Al III, Si II, Si IV, P II, S I, S II, S III, Cl I, Cr II, Mn II, Fe II, Ni II, Cu II, Zn II, and the CO molecule. The velocity structure of the absorption toward ξ Persei is as follows: 1. The diffuse clouds which are traced by the weaker absorption lines of neutral and once ionized atoms absorb between +5 and +15 km s^{-1}. 2. Ionized gas absorption is traced by the GHRS measures of Al III, S III, Si IV and C IV. The Al III and S III lines indicate broad absorption

extending from -20 to +20 km s^{-1}. The lines of Si IV and C IV also absorb in this velocity range although their profile shapes are considerably different than those for Al III and S III. N V λ1238 absorption was not detected in the low S/N spectrum obtained by the GHRS at 1238 Å. 3. The strong ultraviolet lines of species such as Fe II, Si II, O I, and C II reveal additional absorption at velocities different from those of the diffuse clouds. In particular, the lines of Fe II and Si II reveal components near -5 km s^{-1} and +25 km s^{-1}. These strong UV lines permit the detection of low column density gas with gas phase abundances very different than those found in the diffuse clouds toward ξ Persei.

Accurate measures of total column densities for a large number of atomic species have been determined from the ξ Persei absorption line measurements (Cardelli et al. 1991). A summary of the results is shown in Figure 5 which illustrates gas phase abundances relative to solar versus the condensation temperature for each element. The GHRS allows the measurement of very accurate column densities of not only abundant elements such as C, N, and O but also for many of the rarer elements such as Cr, Ni, Cu, and Zn.

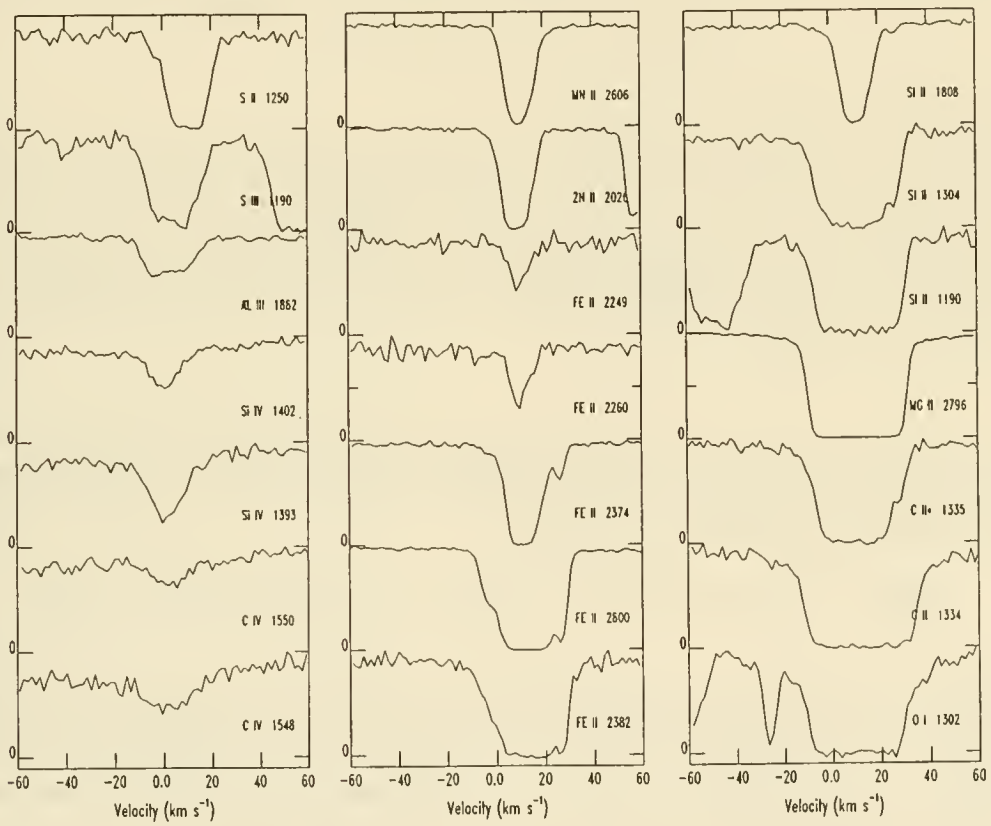

Figure 4. *Relative intensity versus heliocentric velocity for a sample of interstellar lines in the spectrum of ξ Persei. The zero-level of each line is indicated on the vertical axis in each panel. For Si II and Fe II the availability of absorption lines with a wide range of oscillator strength permits an evaluation of the nature of the absorption over a wide range of velocity. The low column density absorption components near -5 and +25 km s^{-1} are readily apparent in the sequence of Fe II λλ 2374.46, 2382.77, 2600.17 profiles illustrated. In several cases more than one absorbing species appears on the short portion of the ultraviolet spectrum illustrated. The measurements are from the GHRS Echelle mode with ξ Persei in the small aperture and have a resolution of approximately 3.5 km s^{-1}.*

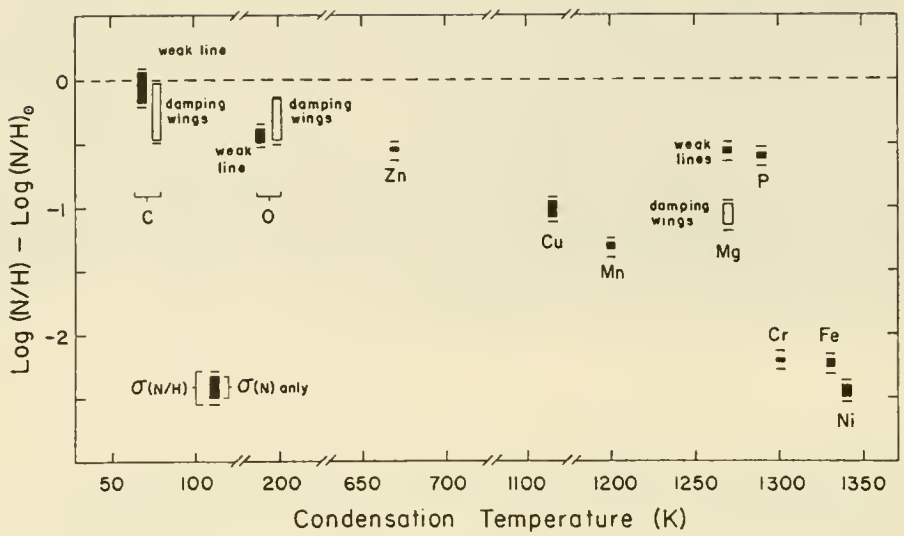

Figure 5. *Average depletion for dominant ions arising in the diffuse clouds toward ξ Persei plotted against the element's condensation temperature . The filled symbols illustrate depletions and their errors derived from weak absorption lines while the open symbols illustrate results from strong lines with Lorentzian damping wings. The extra error bars include the additional uncertainty associated with the errors in the reference hydrogen column density from Bohlin, Savage, & Drake (1978). The discrepancy between the open and filled symbols, especially for Mg II indicates potential errors in the adopted f values. This figure is from Cardelli et al. (1991)*

The 3.5 km s^{-1} resolution provided by the Echelle mode of the GHRS means that in many cases the absorption line measurements obtained by the spectrograph will be either fully resolved or close to being fully resolved. When an absorption line is fully resolved the observed optical depth of absorption is given by

$$\tau(v) = \ln [\, I_o(v) / I_{obs}(v) \,] = \frac{\pi e^2}{m_e c} f\lambda N(v) = 2.654 \times 10^{-15}\ f \lambda N(v),$$

where, $I_o(v)$ and $I_{obs}(v)$ are the continuum and observed intensity, respectively, N(v) is the column density per unit velocity in atoms cm^{-2} (km s^{-1})$^{-1}$, f is the oscillator strength of the line, and λ is the wavelength in Å. . When an absorption line is not fully resolved we refer to the optical depth as derived above as the apparent optical depth, $\tau_a(v)$, and the corresponding column density as the apparent column density, $N_a(v)$.

The high resolution absorption line data can be converted into measures of $N_a(v)$ extending over a large range of v by combining the absorption measurements for lines of different strength. The weak lines will determine $N_a(v)$ at velocities where the column density per unit velocity is large while strong lines will determine $N_a(v)$ at velocities where it is small. If a given species has a number of lines, it is possible to construct a complete $N_a(v)$ profile and use the empirical information in the region of velocity overlap from one line to the next to infer the presence or absence of unresolved saturated structures in the derived profiles. When $N_a(v)$ profiles derived from lines differing in the value of λf by more than a factor of 2 agree in a region where they overlap in velocity, the work of Savage & Sembach (1991) has demonstrated that it is reasonable to assume that unresolved saturated structures are not influencing the values of $N_a(v)$. Comparisons of curves of $N_a(v)$ for different elements

permits a study of how elemental abundances change with velocity due to the effects of differential depletion. Such a comparison is found in Figure 6 from Savage et al. (1991) which shows log $N_a(v)$ curves for O I , C II, Mg II, Si II, Fe II, S II, Mn II, and Zn II adjusted for solar abundance differences. At velocities where the curves for different elements coincide, the elements are found in the gas phase with the solar abundance ratio. At velocities where the curves differ one is directly viewing the effects of differential depletion. For example, in the velocity range from v = +5 to + 15 km s^{-1} the curve for Fe II in Figure 6 lies below that for O I by about 1.8 dex due to the incorporation of Fe into interstellar dust. In the cloud near v = +25 km s^{-1}, the various curves nearly overlap suggesting nearly solar abundance ratios for O I, Si II, Fe II, S II, Mg II. Evidently elements have been returned to the gas phase through some process like shock processing of interstellar dust in the medium absorbing near +25 km s^{-1}.

The interstellar line data for ξ Persei also provide significant diagnostic information about the physical conditions in the denser portions of the diffuse clouds along the sight line. Smith et al. (1991) have analyzed the data for C I, C I*, C I** , and CO to estimate the temperature, density, and pressure in the clouds. The highest density component near 6 km s^{-1} is estimated to have a very high pressure [log (P/k) > 4.3] while the component at 10 km s^{-1} has a pressure a factor of 10 lower. Such estimates are of great importance for detailed modeling of atomic and molecular conditions in diffuse clouds.

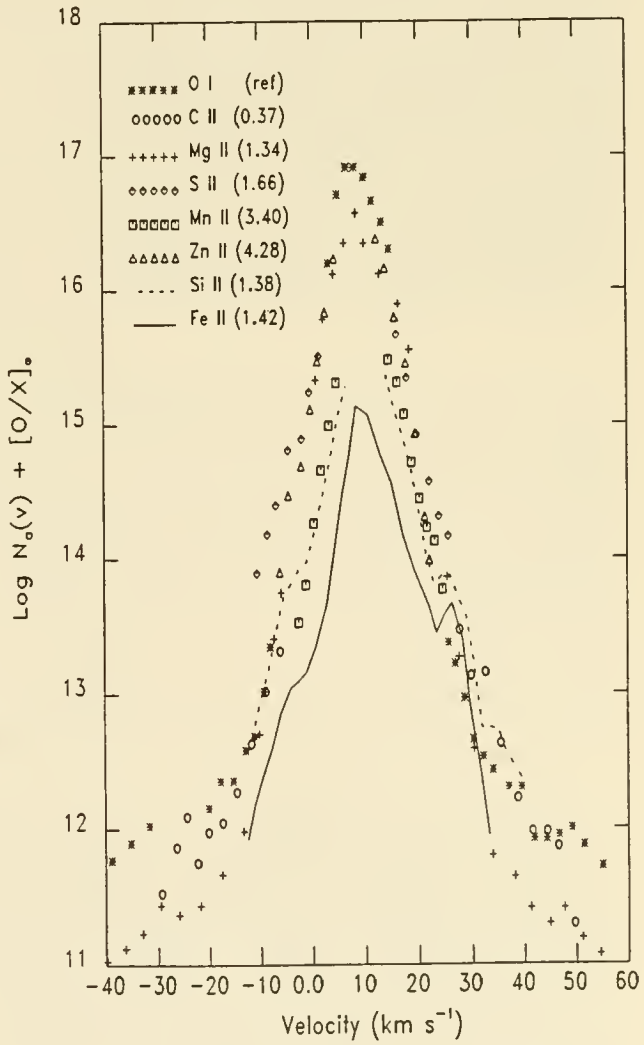

Figure 6. *Curves of apparent column density versus velocity adjusted for solar abundances for the sight line to ξ Persei for O I, C II, Mg II, Si II, Fe II, S II, Mn II , and Zn II. The value of $[O/X]_O$ for a given element was taken to be the logarithmic abundance difference for that element compared to oxygen and was obtained from the solar system abundances of Morton (1991). Thus, all the curves are corrected for solar abundance differences and are referenced to oxygen, a species that is only slightly depleted in diffuse interstellar clouds. At velocities where the curves for two species overlap, the two species therefore have solar abundance ratios. The large vertical separation of some of the curves at velocities corresponding to those of the diffuse clouds (v ~ +5 to +15 km s^{-1}) is caused by the depletion of the various elements into interstellar dust. Note that Lorentzian wings appear on the profiles for species with very strong lines (i.e. C II, O I and Mg II) . This figure is from Savage et al. (1991).*

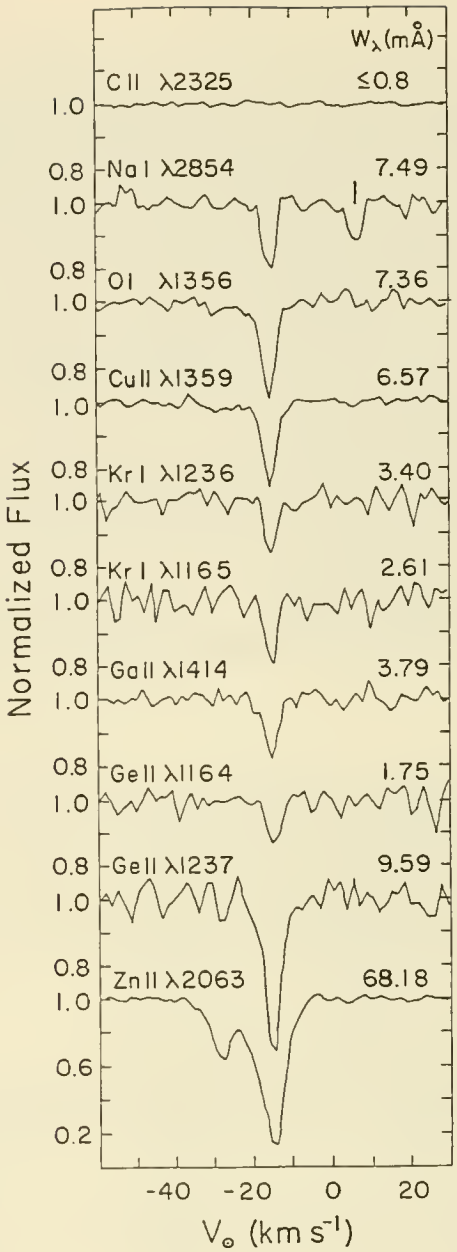

Figure 7. *Examples of weak absorption lines seen in Echelle mode observations of ζ Ophiuchi. The species and wavelengths are listed on the left while the observed equivalent widths in mÅ are listed on the right. The absorption for Zn II illustrates the two component structure seen in strong lines. The principal component is at -15 km s^{-1} with a weaker component near -27 km s^{-1}. The weak lines are only reliably detected in the -15 km s^{-1} component. C II] λ2325 is not detected with a 2σ upper limit of 0.8mÅ in a spectrum with S/N = 150/1. The detection of Kr I absorption is particularly significant since Kr is not expected to form bonds and will probably not be incorporated into the interstellar dust. Hence, measures of Kr provide direct abundance information about an important element created by a combination of r- and s-process nucleosynthesis. This figure is from Cardelli, Savage, & Ebbets (1992).*

4.2 Weak Absorption Lines Toward ζ Ophiuchi

In May 1991 the bright O star ζ Ophiuchi was observed with the Echelle modes in order to evaluate the scattered light in the spectrograph. Those science verification data are also providing important information about the ability of GHRS to detect weak absorption lines. The first scientific results from the analysis of the ζ Ophiuchi data is found in Cardelli, Savage & Ebbets (1992). Figure 7 provides a sample of the ζ Ophiuchi weak line measurements for lines of C II], Na I, O I, Cu II, Kr I, Ga II, and Ge II. In addition a strong line of Zn II is illustrated. The Zn II absorption reveals the two component absorption toward ζ Ophiuchi known from optical measurements with the principal absorption occurring near -15 km s^{-1} and weaker absorption near -27 km s^{-1}. The various weak lines only record absorption in the higher column density component near -15 km s^{-1} except for C II] which is

not detected with a small (2σ) upper limit of 0.8 mÅ. Ga, Ge and Kr represent the heaviest elements so far detected in the ISM. The derived column densities show that Ga is depleted by 1.2 dex from the gas phase while Ge is overabundant by 0.2 dex. The detection of Kr is particularly important since it is not expected to form chemical or mechanical bonds and should reside primarily in the gas phase. The 14.0 eV ionization potential of Kr I means that the neutral atom is the dominant ionization state in the neutral ISM. Assuming Kr to be undepleted, the measurements imply a logarithmic cosmic abundance of 2.95 on the scale where [H] = 12.00. Since Kr is produced by a mixture of s- and r-process nucleosynthesis, further observations in other sites will provide significant insights about nucleosynthesis and interstellar enrichment processes without the difficulty of understanding the complications produced by the presence of interstellar dust.

4.3 Absorption by the Galactic Corona Toward 3C273

Spectra of the bright QSO 3C273 were obtained by FOS (Bahcall et al. 1991) and by GHRS (Morris et al. 1991). Those spectra provided the important cosmological result that the Lyman alpha forest persists to zero redshift and that there is a significant decrease in the rate which the Lyman alpha forest thins out, occurring at some redshift less than about 2. The HST UV spectra of 3C273 also contain significant information about the gaseous halo or corona of the Milky Way. Lines associated with gas in the Milky Way disk and halo from H I, O I, C II, C II*, C IV, N I, N V, Si II, Si III, Si IV, S II, Mg II, Mn II, Fe II and Ni II are seen. Figure 8 shows the far-UV portion of the FOS spectrum obtained with the G130H grating (resolution ~ 250 km s^{-1}) and a small portion of the GHRS G160M spectrum obtained with the large aperture (resolution ~ 25 km s^{-1} but with wings extending to $\pm$ 70 km s^{-1}). The Milky Way lines seen in this 35 Å portion of the spectrum include: N V $\lambda\lambda$ 1238.82 and 1242.80, S II $\lambda\lambda$1250.58, 1253.81, and 1259.52 and Si II λ1260.42. The other lines, attributed to the Lyman alpha forest, appear at $\lambda\lambda$1242.17, 1247.54, 1251.46, and 1255.70 Å. The Lyman alpha line at 1251.46 is particularly strong with an equivalent width of 120 mÅ. A comparison between the FOS spectrum and the GHRS spectrum shows the high sensitivity of the GHRS to the detection of weak absorption lines.

The lines from abundant elements associated with the neutral ISM of the Milky Way are very strong and have widths (FWHM) extending from 110 km s^{-1} (O I) to 145 km s^{-1} (C II and Si II). These lines are tracing low column density high velocity dispersion neutral and weakly ionized gas toward 3C273 (l = 290° and b = 65°). The lines from the highly ionized gas (Si IV , C IV, and N V) are also very strong and broad. The direct detection of N V is quite significant because it traces collisionally ionized gas near 2×10^5 K. Gas at this temperature cools very rapidly. Its origin may be associated with the cooling gas of a Galactic fountain (Shapiro & Field 1976; Edgar & Chevalier 1986) or with thermal condensations in cosmic ray driven fountains (Hartquist & Morfill 1986).

The very strong Milky Way absorption toward 3C273 reveal a problem all extragalactic UV spectroscopic observers will face---that of allowing for the presence of Milky Way disk and halo absorption lines in the spectra of extragalactic objects.

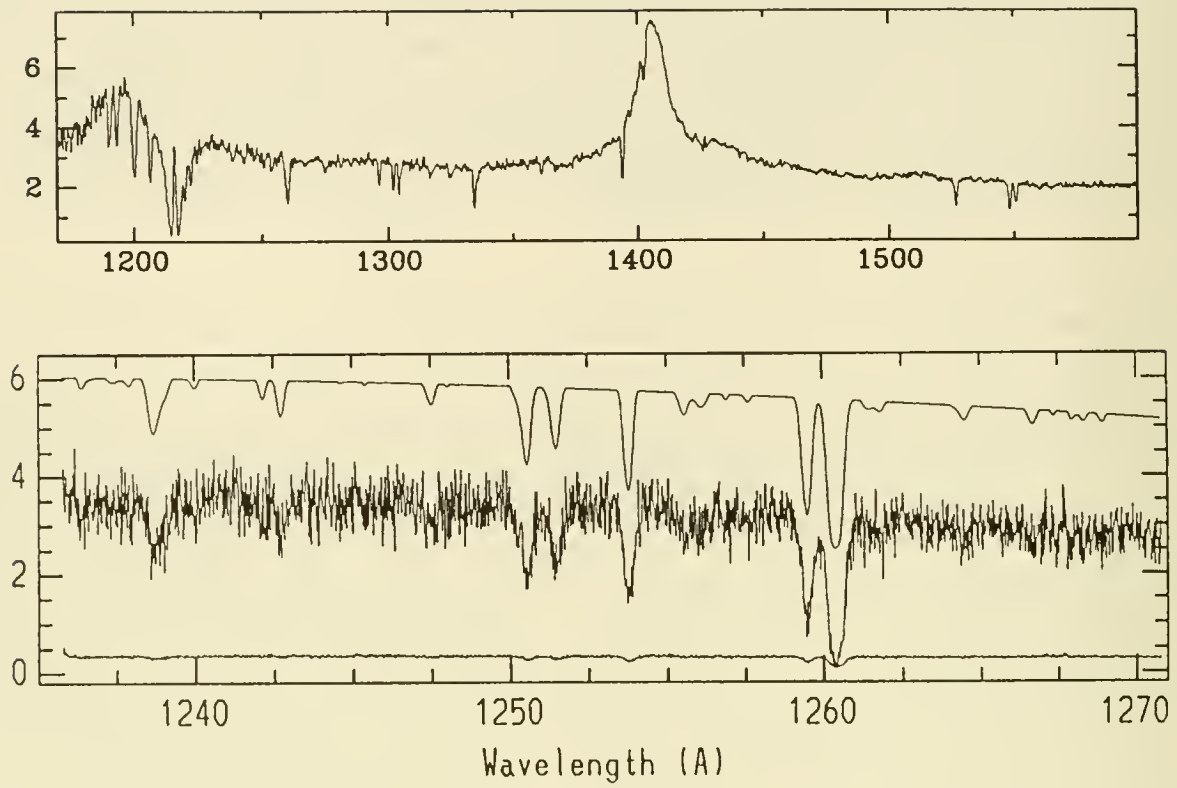

Figure 8. *FOS spectrum of 3C273 from Bahcall et al. (1991) and GHRS spectrum from Morris et al. (1991). The FOS spectrum (top) was obtained with the G130H grating using the 0.25"x2.0" slit and has a resolution of about 210 km s^{-1}. The GHRS spectrum (bottom) was obtained with grating G160M using the 2.0"x2.0" aperture and has a resolution of 30 km s^{-1} (FWHM) but with broad wings extending ±70 km s^{-1}. The lower curve in the bottom panel is the S/N in the spectrum shown as the middle curve. The upper curve in the lower panel illustrates a deconvolution of the original spectrum as described in Morris et al. Of particular significance for the Milky Way is presence of strong N V doublet absorption at λλ1238.80 and 1242.80 Å. This absorption may be produced by cooling 2x10^5 K gas in the Milky Way corona.*

Acknowledgements The efforts of many people have contributed to the success of the early HST spectroscopic program to study the interstellar medium with the FOS and GHRS. The author appreciates support from NASA through contract NAS5-29638.

References

Bahcall, J.N., Jannuzi,B.T., Schneider, D.P., Hartig, G.F. , Bohlin, R., & Junkkarinen, V. 1991, ApJ, 377, L5

Bohlin, R.C., Savage, B.D., & Drake, J.F. 1978, ApJ, 224, 132

Cardelli, J.A., Savage, B.D., Bruhweiler, F.C., Smith, A.M., Ebbets, D.C. Sembach, K.R., & Sofia, U.J. 1991, ApJ, 377,L57

Cardelli, J., Savage, B.D., & Ebbets, D.E. 1992, ApJ, (submitted)

Edgar, R.J, & Chevalier, R.A. 1986, ApJ, 310,L27

Hartquist, T.W., & Morfill, G.E. 1986, ApJ, 311, 518

Hester, J.J. et al. 1991, ApJ, 369, L75

Jakobsen , P. et al.1991, ApJ, 369, L63

Kondo et al. (eds), 1987, *Exploring the Universe with the IUE Satellite*, (D.Reidel Pub. Co.:Dordrecht)

Morris, S.L., Weymann, R.J., Savage, B.D., & Gilliland, R.L. 1991, ApJ, 377, L21

Morton, D.C. 1991, ApJS, (in press)

Savage, B.D., Cardelli, J.A., Bruhweiler, F.C. , Smith, A.M., Ebbets, D.C. & Sembach, K.R. 1991, ApJ, 377, L53

Savage, B.D., & Sembach, K.R. 1991, ApJ, (in press)

Shapiro, P.R., & Field, G.B. 1976, ApJ, 205,762

Smith, A. M., Bruhweiler, F. C., Lambert, D. L., Savage, B. D., Cardelli, J. A., Ebbets, D. C., Lyu, C.-H., & Sheffer, Y. 1991, submitted to ApJL

Spitzer, L. 1988, PASP, 100, 518

Spitzer, L. & Jenkins, E.B. 1975, ARAA, 13, 133

FOS Observations of the Absorption Spectrum of 3C 273 [1]

J.N. Bahcall [2], *B.T. Jannuzi* [2], *D.P. Schneider*,
Institute for Advanced Study
School of Natural Sciences, Princeton, NJ 08540

G.F. Hartig, R. Bohlin
Space Telescope Science Institute
3700 San Martin Drive, Baltimore, MD 21218

V. Junkkarinen
University of California, San Diego
La Jolla, CA 92093

Abstract

We describe the FOS observations of the absorption line spectrum of 3C 273 and compare the results with the GHRS observations of the same quasar. Three Ly-α lines appear to be produced by gas in the Virgo cluster or by the halos of galaxies associated with the Virgo cluster. We identify a total of seven Ly-α absorption systems with equivalent widths greater than 0.2 Å. The evolution of the number density of Ly-α clouds cannot be determined with confidence by comparing only 3C 273 observations with those of large redshift quasars. The inferred redshift-dependence of the number density depends critically upon whether or not the Virgo-cluster lines are included or upon an uncertain extrapolation of the equivalent width distribution for strong lines found at large redshifts.

1 INTRODUCTION

We report here on ultraviolet observations of 3C 273 made with the high resolution gratings of the Faint Object Spectrograph (FOS, see Ford 1985) as part of the science verification program of the Hubble Space Telescope. In §II, we summarize the observations and in §III we describe the measurement of the lines. In §IV, we discuss the identification of Ly-α lines. In §V we compare our results with those obtained by Morris *et al.* (1991) with the GHRS and in §VI we discuss the redshift evolution of the Ly-α systems. We summarize our main scientific results in §VII.

---

[1]Based on observations with the NASA/ESA Hubble Space Telescope, obtained at the Space Telescope Science Institute, which is operated by the Association of Universities for Research in Astronomy, Inc., under NASA contract NAS5-26555.

[2]Guest Observer with the *International Ultraviolet Explorer* satellite, which is sponsored and operated by the National Aeronautics and Space Administration, by the Science Research Council of the United Kingdom, and by the European Space Agency.

2 OBSERVATIONS

We observed 3C 273 on 14–16 January, 1991 using the three high resolution ($R = 1300$) gratings, G130H, G190H, and G270H, centered, respectively, on 1300 Å, 1900 Å, and 2700 Å. The spectra cover the region between 1150 Å and 3300 Å with a gap from 1600 to 1650 Å. Five apertures were used with each grating. They are the $0.25'' \times 2.0''$ slit, the three circular apertures with diameters of $1.0''$, $0.5''$, and $0.3''$, and the $4.3''$ by $4.3''$ square aperture. A paper currently in preparation (Jannuzi, Hartig, Bahcall, and Schneider 1992) will compare and analyze the data from all the apertures. In this talk, we use the data from different apertures to verify results obtained with the slit or to reject spurious features. The spectral resolutions (FWHMs) of the data obtained through the slit are 1.1, 1.5, and 2.0 Å for the three gratings. We also observed 3C 273 with the *International Ultraviolet Explorer* satellite on 7, 13, 15–17, and 23 January 1991 in order to set the zero point of the flux calibrations and to check upon possible flux variability.

Figure 1 of Bahcall *et al.* 1991 (hereafter, Paper I) shows the reduced HST slit data from all three gratings. The typical signal-to-noise ratio (SNR) is between 40 and 50 per diode in the G130H data (2000 s exposure), ≈ 60 per diode in the G190H data (1400 s exposure), and ≈ 100 per diode in the best-studied regions of the G270H data (1400 s exposure). The signal-to-noise ratios for the data are better than that expected to be obtained for the Key Project Quasar Absorption Line Survey, for which the signal-to-noise ratio will typically be 30 per diode in each of the gratings. Further details of the observations are given in Paper I.

We were fortunate in having observations through the five different apertures, which enabled us to reject a number of spurious features. For example, we rejected narrow features that had similar strengths and shapes when observed through the slit and the $4.3''$ aperture, since real lines have increased line widths (due to the degraded HST PSF) in the larger aperture.

3 MEASUREMENT OF ABSORPTION LINES

Details of the measurement of the lines are given in Paper I. For inclusion in the complete sample, we required that all lines be 3σ detections with observed EWs greater than 0.250 Å in the G130H or G190H data or greater than 0.150 Å in the G270H data and that the measured equivalent widths be consistent in the the slit and the $0.3''$ data.

Table 1 lists the complete sample of 36 absorption lines. The columns contain: the measured line center, equivalent width, error in equivalent width, identification, vacuum wavelength of identification, difference between observed and laboratory wavelength, and comments.

TABLE 1: Ultraviolet Absorption Lines

λ_{obs} (Å)	EW (Å)	σ_{EW} (Å)	Identification Ion	λ_0	$\Delta\lambda$ (Å)	Comment
1190.44	0.463	0.111	Si II	1190.42	0.02	
1193.35	0.414	0.102	Si II	1193.28	0.07	
1200.22	0.982	0.085	N I	1199.90	0.32	
1206.44	0.553	0.078	Si III	1206.51	−0.07	
1215.7:	7.0:	1.5:	Ly α	1215.67	0.06	EW uncertain:
1219.80	0.371	0.039	Ly α			$cz = 1020$ km s^{-1}
1222.12	0.414	0.092	Ly α			$cz = 1590$ km s^{-1}
1224.52	0.240	0.081	Ly α			$cz = 2185$ km s^{-1}; not in cpl. sp.
1238.60	0.183	0.076	N V	1238.81	−0.21	Not in cpl. sp.
1243.04	0.178	0.101	N V	1242.80	0.24	Not in cpl. sp.
1260.08	0.789	0.057	Si II	1260.42	−0.34	+ SII (1259.53) ?
1275.23	0.251	0.059	Ly α			$cz = 14,700$ km s^{-1}
1296.52	0.287	0.057	Ly α			$cz = 19,950$ km s^{-1}
1302.08	0.372	0.050	O I	1302.17	−0.09	
1304.40	0.395	0.060	Si II	1304.37	0.03	
1317.08	0.292	0.096	Ly α			$cz = 25,030$ km s^{-1}
1325.10	0.238	0.057	Ly α			$cz = 27,000$ km s^{-1}; not in cpl. sp.
1334.57	0.586	0.056	C II	1334.53	0.04	
1335.75	0.168	0.058	C II*	1335.70	0.05	Not in cpl. sp.
1361.53	0.146	0.072	Ly α			$cz = 35,990$ km s^{-1}; not in cpl. sp.
1393.86	0.479	0.036	Si IV	1393.76	0.10	
1402.69	0.261	0.042	Si IV	1402.77	−0.08	
1526.77	0.477	0.047	Si II	1526.72	0.05	
1548.26	0.561	0.049	C IV	1548.20	0.06	
1550.75	0.402	0.050	C IV	1550.77	−0.02	
1670.92	0.534	0.036	Al II	1670.81	0.11	
1855.63	0.281	0.053	Al III	1854.72	0.91	
1862.95	0.182	0.049	Al III	1862.78	0.17	Not in cpl. sp.
1878.03	0.259	0.068				Broad; Flat Field feature?
2026.55	0.266	0.035	Mg I	2026.47	0.08	
2065.09	0.440	0.061				
2344.16	0.727	0.031	Fe II	2344.21	−0.05	
2352.30	0.192	0.044				
2374.57	0.612	0.032	Fe II	2374.46	0.11	
2382.77	0.828	0.031	Fe II	2382.76	0.01	
2577.87	0.344	0.081	Mn II	2576.89	0.98	
2586.67	0.844	0.050	Fe II	2586.64	0.03	
2594.36	0.283	0.066	Mn II	2594.50	−0.14	
2600.25	0.980	0.051	Fe II	2600.18	0.07	
2606.71	0.155	0.026	Mn II	2606.47	0.24	
2796.27	1.098	0.025	Mg II	2796.35	−0.08	
2803.51	0.993	0.024	Mg II	2803.53	−0.02	
2852.85	0.392	0.027	Mg I	2852.97	−0.12	

4 LINE IDENTIFICATIONS AND IMPLICATIONS

For identifications, we used a standard set of ultraviolet absorption lines (Bahcall 1979) that correspond to the strongest allowed, one-electron, dipole transitions from ground or excited fine-structure states of abundant elements. Of the 36 observed lines in the complete sample, 28, or 78%, are identified at zero redshift with strong interstellar lines from the standard list. The rms wavelength difference between the measured and the 28 standard lines is 0.26 Å.

The characteristics of the interstellar lines towards 3C 273 that are inferred from our observations are discussed in Paper I (see also Ulrich *et al.* 1980).

Ly-α

absorption at small redshifts apparently produces 5 of the 8 lines in the complete sample that are not identified with Galactic absorption. The total range over which we have good observations exceeds 1770 Å. If the 8 unidentified lines were uniformly sprinkled over this entire range, then the Poisson probability is about 0.2% that 5 of 8 lines would be confined, as observed, into the 192 Å between the rest wavelength of Ly-α and the redshifted Ly-α emission line. One of the remaining three lines may be identified as a possible flat field artifact (at 1878.03 Å). In addition, there are three other real lines that are apparently Ly-α absorption systems but which have EWs too small to be in the complete sample. These lines, at 1224.52 Å (EW = 0.24 Å), at 1325.10 Å (EW = 0.24 Å), and 1361.53 Å (EW = 0.15 Å), are included in Table 1 and correspond to values of cz of 2,185 km s^{-1},27,005 km s^{-1}, and 35,995 km s^{-1}.

The Ly-α systems have H I column densities of $14 \lesssim \log N \lesssim 16$ for $b \approx 35$ km s^{-1}. The maximum EW that any line could have and not be in the complete sample (0.25 Å) limits the amount of metals present in the clouds to $\log N \lesssim 15$. The absence in our spectra of metal lines from the Ly-α systems (hereafter, called clouds) is not surprising; we would not expect to detect the metal lines unless the hydrogen is exceedingly highly ionized.

We emphasized in Paper I that the Ly-α lines at 1219.8 Å and 1222.1 Å are most likely caused by gas in the Virgo cluster or in halos of galaxies associated with the Virgo cluster. The heliocentric velocities of the two Ly-α systems are 1020 ± 17 km s^{-1} and and 1591 ± 45 km s^{-1}. The Virgo cluster has an average velocity of 1158 km s^{-1} (Huchra 1985) and contains galaxies with a broad range of velocities that bracket the two Virgo Ly-α clouds.

Figure 1 shows the spectrum in the region between 1203 Å and 1236 Å. The absorption line at 1224.52 Å (which was not included in the expanded part of the spectrum shown in Figure 2 of Paper I) has a measured equivalent width of 0.24 Å and is a real feature (approximately 3σ significance), although it is weaker than the lines at 1219.8 Å and 1222.1 Å. We believe that the line at 1224.52 Å is also caused by absorbing gas associated with the

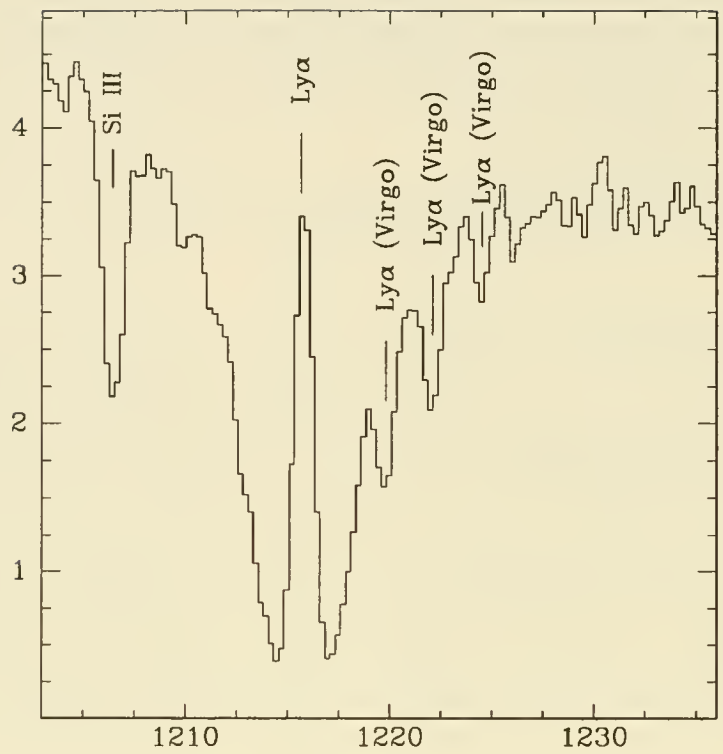

Figure 1. The region between 1203 Å and 1236 Å in the slit spectrum. The resolution is $\approx$ 1.1 Å. The most prominent feature is the strong Galactic Ly α absorption line. The geocoronal Ly α emission line is seen in the center of the Galactic absorption line. The absorption line shortward of Ly-α is produced by Si III in the Galactic interstellar medium. The three marked absorption features located on the red shoulder of the Galactic Ly α line are probably produced by gas in the Virgo Cluster or by halos of galaxies associated with the Virgo Cluster. The flux units are 10^{-13}erg s^{-1} cm^{-2} Å^{-1}.

Virgo cluster. Huchra (1985) notes that most of the galaxies in the direction of the Virgo cluster with velocities less than 3000 km s^{-1} are cluster members.

The large gas cloud H1 1225+01 discovered by Giovanelli and Haynes (1989) has a systemic velocity of 1275 km s^{-1} and may well be associated with the Virgo cluster. The center of H1 1225+01 is located about 250 kpc $\times$ d(H1 1225 + 01)/20 Mpc from the line of sight to 3C 273 and could be the source of one or more of the Virgo Ly-α absorption lines.

5 COMPARISON OF FOS AND GHRS OBSERVATIONS

Morris *et al.* (1991) identified absorption features in observations of 3C 273 that were taken through the Large Science Aperture of the Goddard High Resolution Spectrograph (GHRS). The results of the FOS and the GHRS observations were reduced independently.

A direct comparison of the FOS and the GHRS line lists is of great interest since it provides an objective estimate of the possible systematic errors in the measurements, in the data analysis, and in the interpretations.

Table 2 compares the wavelengths and equivalent widths measured by the group using the GHRS (Morris *et al.* 1991) and by the group using the FOS (Bahcall*et al.* 1991) for lines at zero redshift (lines arising from the galactic interstellar medium, ISM). Some regions of the spectrum were not observed with the GHRS and some weak lines reported by the GHRS group were not listed by the FOS group. There are 24 lines in common in the two lists. The agreement between the measurements for these lines is generally good. The root-mean-squared wavelength agreement is

$$< (\lambda_{\rm FOS} - \lambda_{\rm GHRS})^2 >^{1/2} = 0.33\text{Å} , \qquad (1)$$

and the root-mean-squared fractional difference between the equivalent widths is

$$< (EW_{\rm FOS} - EW_{\rm GHRS})^2 / EW^2_{\rm average} >^{1/2} = 0.34 , \qquad (2)$$

where $EW_{\rm average}$ is the average of the FOS and GHRS measured equivalent widths.

There is no evidence of any systematic displacement of measured line centers between the FOS and the GHRS data as a function of observed wavelength. In fact, almost half of the root-mean-squared wavelength discrepancy is contribute by only two lines.

Figure 2 shows that there are seven ISM lines with GHRS measured equivalent widths less than 0.200 Å. For all seven of these lines, the equivalent width measured with the FOS is larger than the equivalent width measured with the GHRS. Several different factors contribute to this skewed distribution. The most obvious explanation is a selection bias: GHRS lines with a measured equivalent width of less than 0.2 Å can *only* appear in the

TABLE 2: Comparison ISM Absorption Lines

GHRS λ	FOS λ	GHRS EW	FOS EW	Ident.
1190.5	1190.44	0.426	0.463	Si II
1193.5	1193.35	0.389	0.414	Si II
1200.4	1200.22	0.713	0.982	N I
1206.8	1206.44	0.445	0.553	Si III
1215.0	1215.7	7.8	7.0	H I
1238.75	1238.60	0.145	0.183	N V
1242.72	1243.04	0.052	0.178	N V
1250.53	....	0.164	....	S II
1253.78	....	0.183	....	S II
1259.50	....	0.274	....	S II
1260.40	1260.08	0.590	0.789	Si II
1302.07	1302.08	0.415	0.372	O I
1304.29	1304.40	0.385	0.395	Si II
1334.49	1334.57	0.622	0.586	C II
1335.72	1335.75	0.116	0.168	C II*
1370.09	....	0.079	....	Ni II
1393.64	1393.86	0.367	0.479	Si IV
1402.65	1402.69	0.217	0.261	Si IV
1423.04	....	0.043	....	
1526.66	1526.77	0.551	0.477	Si II
1534.71	....	0.078	....	
1548.16	1548.26	0.530	0.561	C IV
1550.72	1550.75	0.388	0.402	C IV
....	1670.92	....	0.534	Al II
1807.98	....	0.118	....	Si II
....	1855.63	....	0.281	Al III
....	1862.95	....	0.182	Al III
....	2026.55	....	0.266	Mg I
....	2344.16	....	0.727	Fe II
....	2374.57	....	0.612	Fe II
....	2382.77	....	0.828	Fe II
2576.71	2577.87	0.197	0.344	Mn II
2586.46	2586.67	0.747	0.844	Fe II
2589.98	....	0.033	....	
2594.27	2594.36	0.142	0.283	Mn II
2600.01	2600.25	0.942	0.980	Fe II
2606.28	2606.71	0.090	0.155	Mn II
2796.31	2796.27	1.167	1.098	Mg II
2803.49	2803.51	1.078	0.993	Mg II
....	2852.85	....	0.392	Mg I

FOS list if the equivalent width measured with the FOS data is greater than the GHRS measured equivalent width. This is because the minimum equivalent width for inclusion in the complete FOS sample was 0.250 Å. In addition, the higher resolution available in the deconvolved GHRS spectra permits the resolution of the FOS line at 1260.08 Å into two lines at line at 1259.50 Å and 1260.40 Å. Finally, it is possible that the two groups assumed different levels for the continuum.

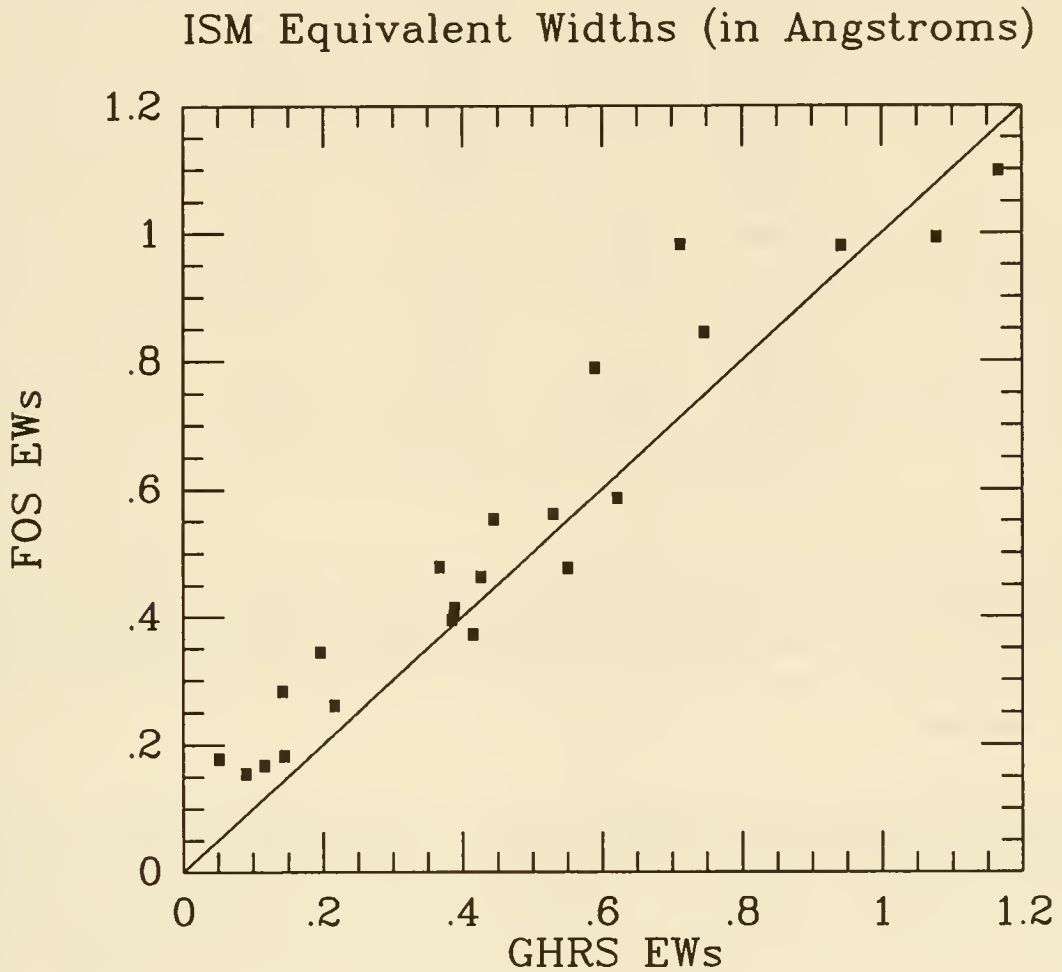

Figure 2. The measured equivalent widths (EWs) of ISM absoprtion lines from the FOS data (Bahcall *et al.* 1991) plotted against the results from the GHRS data (Morris *et al.* 1991).

Table 3 compares the Ly-α lines that were reported by the GHRS and the FOS groups. The agreement is generally good. No GHRS equivalent widths were reported for the three Virgo lines (two were detected). The only striking disagreement is the absence in the GHRS list of the line in the FOS list at 1317.08 Å. We reexamined two separate FOS flat-fields and verified that the feature in question is not created by our flat fielding. We also compared the

TABLE 3: Lyman Alpha Absorption Lines

GHRS λ	FOS λ	GHRS EW	FOS EW
1220.0	1219.80	....	0.371
1222.2	1222.12	....	0.414
....	1224.52	....	0.240
1242.17	....	0.027	....
1247.54	....	0.032	....
1251.46	....	0.120	....
1255.70	....	0.074	....
1275.19	1275.23	0.144	0.251
1276.54	....	0.068	....
1289.79	....	0.052	....
1292.84	....	0.063	....
1296.57	1296.52	0.302	0.287
....	1317.08	....	0.292
1322.16	....	0.075	....
1324.96	....	0.027	....
1325.22	1325.10	0.057	0.238
1361.63	1361.53	0.126	0.146
1393.86	....	0.333	....

strength of the feature in the observations through the five different apertures and verified that the 1317 Å line is, as expected if it is a real feature, strongest in the narrow slit and broader in the large 4.3″ aperture. We conclude that the 1317.08 Å line is an intrinsic feature of the spectrum.

The GHRS team analyzed lines with equivalent widths much less than the lower limit we adopted for inclusion in our complete sample. The lower limits adopted by the GHRS team were, respectively, 0.025 Å and 0.050 Å, for "weak" and "strong" lines. The equivalent width limit we adopted was 0.250 Å. This difference between the equivalent width limits is reflected in Table 3 by the presence of a number of weak lines reported by Morris *et al.* but not in Paper I. There are difficulties (see, e.g., the discussion of Morris *et al.* 1991) associated with including the small equivalent width lines. The signal to noise level decreases as one goes to smaller equivalent widths so that it becomes more difficult to be be sure that the weaker lines are not caused by flat-fielding or other sources of noise.

6 EVOLUTION OF Ly-α SYSTEMS

The number density and equivalent width distribution of Ly-α clouds at large redshifts has been determined by major surveys of many different sources. We compare with our observations of 3C 273 the number of Ly-α systems predicted for small redshifts by the

formulae used to fit the observations at large redshifts. Using the conventional parameterization (Sargent, Young, Boksenberg, and Tytler 1980; Murdoch, Hunstead, Pettini, and Blades 1986; Lu, Wolfe, and Turnshek 1991), the expected number, N, of Ly-α clouds in the spectrum of a nearby quasar may be written

$$N(z_{\rm em}, W > W_{\rm cutoff}) \;=\; A_0(1 \,+\, \gamma)^{-1}\left[(1+z_{\rm em})^{\gamma+1} \;-\; 1\right]\exp\left[-\left(\frac{W_{\rm cutoff}}{0.3\text{Å}}\right)\right], \qquad (3)$$

where $W_{\rm cutoff}$ is the minimum considered rest equivalent width. The values of A_0 that are determined by extrapolating large redshift observations are uncertain, but have been estimated recently by Murdoch *et al.* (1986) and by Lu *et al.* (1991).

The most direct comparison between expectation and observation is obtained by taking the ratio of predicted to observed number of systems assuming the *same* parameters, including minimum equivalent width, $W_{\rm cutoff}$, as for the large redshift surveys. Thus for the Murdoch *et al.* survey, with an equivalent width limit of 0.32 Å, one expects 0.76 systems for 3C 273 . For the Lu *et al.* analysis, one expects 0.506 systems with equivalent widths at least equal to 0.36 Å. We see that from Table 1 that there are exactly two lines that satisfy the equivalent width limits of the large redshift surveys, the Virgo lines at 1219.80 and 1222.12 Å. Including the Virgo lines, the ratio of observed to expected number of systems is 2.6 for the Murdoch *et al.* survey and 4.0 for the Lu *et al.* analysis. If we represent in the conventional way the evolution of the number density between small and large redshifts by a power law, $dN/dz \;\propto\; (1+z)^{\gamma}$, then we obtain

$$\gamma \;=\; 1.0 \text{ Murdoch } et\ al. \text{ parameters}; \quad \gamma \;=\; 1.2 \text{ Lu } et\ al. \text{ parameters}. \qquad (4)$$

We stress that for direct comparison with the analyses of large redshift samples only the two strong Ly-α systems (presumably) produced in the Virgo cluster can be used. Obviously, there are large systematic and statistical uncertainties in the value of γ that are not included in Eq. (4). A number of independent lines of sight must be studied before the evolution of the Ly-α clouds can be reliably determined.

We can obtain some additional information by considering Ly-α systems with EWs above 0.200 Å, since Murdoch *et al.* (1986) (see their Figure 3) have presented evidence that the equivalent width distribution has the canonical exponential form above this limit but changes shape for weaker lines. According to the FOS observations summarized in Table 1, the line of sight to 3C 273 contains seven Ly-α systems above 0.200 Å. The observed number of lines with equivalent widths greater than this value of $W_{\rm cutoff}$ is 6 times larger than predicted by the parameters determined by Murdoch *et al.* and is 12 times larger than predicted by the parameters of Lu *et al.* . Even ignoring the lines that apparently arise from the Virgo cluster, the number of observed Ly-α systems is larger than expected at the 90% confidence level.

The two strong Virgo Ly-α lines are not included in the GHRS analysis since they did not report the equivalent widths of these lines. As discussed by Morris *et al.* (1991), the determination of the evolution of the Ly-α clouds with the published GHRS observations requires additional information about the weak lines at large redshifts. Therefore, Morris *et al.* used the form and parameters derived by Murdoch *et al.* (1986) for the equivalent width distribution. However, Morris *et al.* also noted that the conclusions of Murdoch *et al.* referred to a domain of much larger EWs and therefore the GHRS group investigated other studies of weaker lines at large redshifts. The uncertainties and controversies involved in using weak lines include the difficulty of separating real lines from spurious features and the possibility that the shape of the equivalent width distribution changes with redshift for weak lines. The listener is referred to the papers of Morris *et al.* (1991), Murdoch *et al.* (1986), and Lu *et al.* (1991) for a discussion of these points.

7 SUMMARY AND DISCUSSION

Approximately a quarter of a century ago, before the discovery of any absorption features in the spectra of quasi-stellar sources, it was predicted (Bahcall and Salpeter 1966) that intergalactic gas in clusters of galaxies would produce ultraviolet quasar absorption lines. In the first direct test of this idea, we find in the direction of 3C 273 three Ly-α absorption systems that are probably associated with the Virgo cluster. It is not clear whether or not our observations confirm this hoary prediction since the lines could arise from individual clouds in large halos of galaxies within the cluster (see Bahcall 1975). One possible way of distinguishing between gas in halos of galaxies and gas between galaxies is in the width of the lines. Intergalactic gas might well produce broad absorption lines reflecting the velocity dispersion within the cluster potential, but there may also be localized clumps of gas between galaxies in the cluster that produce relatively narrow lines.

The observation of a larger-than-expected number of Ly-α absorption lines in the spectrum of 3C 273 is an encouraging sign for future HST studies of quasar absorption line systems. However, a reliable determination of the cosmic evolution of the Ly-α systems will require observations of a number of independent lines of sight.

We express our gratitude to the FOS instrument team for building a superb instrument. This work was supported in part by NASA contract NAS5-29225 and STSCI grant #2424.

REFERENCES

Bahcall, J. N. and Salpeter, E. E. 1966, Ap. J. Letters 144, 847.

Bahcall, J. N. 1975, Ap. J. Letters 200, L1.

Bahcall, J. N. 1979, in *Scientific Research with the Space Telescope*, IAU Colloquium 54, ed. M.S. Longair and J. W. Warner (superintendent of documents, U.S. Government Printing Office, Washington, DC, 20402.

Bahcall, J. N., Jannuzi, B. T., Schneider, D. P., Hartig, G. F., Bohlin, R., and Junkkarinen, V. 1991, Ap. J. Letters 377, L5, (Paper I).

Ford, H.C. 1985, *Faint Object Spectrograph Instrument Handbook*, (Space Telescope Science Institute: Baltimore).

Grady, C.A., and Taylor, M.A. 1989, IUE Data Analysis Guide, IUE Newsletter, No. 39.

Giovanelli, R. and Haynes, M.P. 1989, Ap. J. L., 346, L5.

Huchra, J. P. 1985, in *The Virgo Cluster of Galaxies*, eds. O.-G. Richter and B. Binggeli, (European Southern Observatory: Garching), p. 181.

Jannuzi, B.T. , Hartig, G. F., Bahcall, J. N., and D. P. Schneider 1992, in preparation.

Lu, L., Wolfe, A.M., and Turnshek, D.A. 1991, Ap.J., 367,19.

Lynds, C. R. 1971, Ap.J.(Letters) 164, L73.

Morris, S. L., Weymann, R. J., Savage, B. D., and Gilliland, R. L. 1991, Ap. J. Letters 377, L21.

Murdoch, H.S., Hunstead, R.W., Pettini, M., and Blades, J.C. 1986, Ap.J. 309, 19.

Sargent, W.L.W., Young, P.J., Boksenberg, A., and Tytler, D. 1980, Ap.J.Suppl. 42, 41.

Sargent, W.L.W., Boksenberg, A., Steidel, C. C. 1988, Ap.J.Suppl. 68, 539.

Ulrich, M. H., *et al.* 1980, M.N.R.A.S. 192, 561.

RESULTS AND SOME IMPLICATIONS OF THE GHRS OBSERVATIONS OF THE LYMAN α FOREST IN 3C273

Ray J. Weymann
Observatories of the Carnegie Institution of Washington
813 Santa Barbara Street
Pasadena, CA 91101
USA

Abstract.

The results of the first GHRS exposures of 3C273 and related observations are summarized, and their implications for our understanding of the Ly α forest assessed. The potential for further understanding of the Ly α forest and intergalactic medium through additional HST and ground-based programs is briefly discussed. The number of low redshift Ly α lines found is substantially higher than expected based upon extrapolation from ground-based data using current estimates of the slope of the log (dN/dz) vs. log (1+z) relationship. However, we consider the more significant results to be the small value of the slope ($\sim$ 0.80) between redshift 0 and 2 and the establishing of the very existence of low redshift Ly α clouds in numbers sufficient for their properties to be investigated in some detail.

1. INTRODUCTION

The discovery of numerous Ly α clouds in the line of sight between ourselves and 3C273 (Morris *et al.* 1991, hereafter MWSG; see also Bahcall *et al.* 1991, hereafter BJSHBJ) presents us with the opportunity of studying the evolution of the properties of the Ly α forest clouds (and possibly the intergalactic medium as well) for over about 90 % of the age of the Universe. Since an account of the observations and reductions has already been given in MWSG, in §2 we simply summarize the results of these observations and touch upon a few highlights. In §3 we discuss what can be inferred about the evolution of the Ly α forest based only upon some extremely scanty current data. Finally, in §4 we discuss some of the open questions concerning the Ly α forest, and some possible future observations, both space and ground-based, which may shed some light on these questions.

2. SUMMARY OF THE 3C273 OBSERVATIONS

In Table 1, collated from Table 1 of MWSG and Table 1 of BJSHBJ, we list all the possible Ly α absorption lines seen in either the GHRS or FOS observations. As described in MWSG, the quantity -log P is a measure of the probability, P, that the absorption feature arises by chance from photon statistics. Although an analysis of the noise properties of these exposures by Gilliland *et al.* (1991) suggests that the noise characteristics are well–approximated by Poisson statistics, the weaker absorption features should be viewed with some caution since some very weak features due to variations in photocathode response could still be present even though the FP-SPLIT mode was used. From inspection of Table 1 it is seen that the agreement in wavelength between the GHRS and FOS observations is quite satisfactory, though the agreement in equivalent widths between the GHRS and FOS observations is only fair and becomes poorer for the weaker lines. The following points deserve comment:

i) A line at λ1317.08Å was identified as Ly α in BJSHBJ but is almost certainly galactic Ni II. Curiously, this line was not seen in the GHRS G160M exposure, but is clearly visible in the deconvolved GHRS 140L exposure, with a measured wavelength differing by only 7 km s^{-1} from the FOS value. The corresponding Ni II line at λ1370 is present in the GHRS 160M exposure at the expected wavelength to within a few km s^{-1} . We therefore do not list the λ1317Å line in Table 1.

ii) There has been considerable discussion lately over the value of the minimum doppler parameter in the Lyman α forest clouds. (*cf.* Webb and Carswell 1991; Hunstead and Pettini 1991 and references therein.) It is thus of interest to examine the minimum doppler parameter found in the GHRS 3C273 data. The narrowest well-determined doppler parameter is for the line at λ1361Å. It is only "well–determined" in the sense that this line appears on two separate GHRS G160M exposures, and two separate Voigt profile fits yield column densities and doppler parameters in good agreement. After these two exposures are coadded we find the best value of b to be 22.0 km s^{-1} with a formal 1–σ uncertainty of 3.2 km s^{-1} and a value for χ^2 per degree of freedom of 1.035 with 50 degrees of freedom. In fact, the doppler parameter is not too well constrained. Fixing the doppler parameter at various values and allowing the fitting routine to fit the column density and redshift, we find that the χ^2 probability drops below 5% (*i.e.*, the fit starts to become discernably poor) only for b outside the range $12 \leq b \leq 37$ km s^{-1} . (In addition to the uncertainties due to photon counting statistics, since these observations were taken through the LSA and the PSF for this mode is somewhat uncertain (Gilliland *et al.* 1991), there is some additional uncertainty in the doppler parameter and the value for the doppler parameter just quoted differs from that given in MWSG because a slightly different PSF was assumed.)

iii) As noted in MWSG, the Si IV doublet arising in the galactic halo is anomalous in that we measure an equivalent width ratio of λ1394 to λ1403 of greater than 2.0. Moreover, the centroid of the λ1394 component is significantly discrepant in velocity compared to other high ionization galactic halo lines. This led MWSG to suggest that another line was blended with the Si IV λ1394 line, presumably another intervening Ly α line. As described in MWSG, one can infer the optical depth of the extra contributor by using the λ1403 line as a template for the Si IV column density vs. velocity and applying that to the observed λ1394 feature. Figure 1 shows the result of this procedure. The profile with the large equivalent width is the observed

Table 1: Lyman α Lines in 3C273

λ_{GHRS} (Å)	λ_{FOS} (Å)	EW_{GHRS} (mÅ)	EW_{FOS} (mÅ)	cz (km s^{-1})	b	log N (cm^2)	-log(P)	Note
1220.0	1219.80		371	1018			L	a
1222.2	1222.12		414	1591			L	a
1242.17		27		6535	23	12.87	6.0	b
1247.54		32		7859	49	13.01	5.2	
1251.46		120		8826	36	13.48	>7.5	
1255.70		74		9872	111	13.30	>7.5	
1275.19	1275.23	144	251	14678	24	13.55	>7.5	
1276.54		68		15011	17	13.04	>7.5	
1289.79		52		18278	63	13.06	5.9	
1292.84		63		19031	34	13.12	>7.5	
1296.57	1296.52	302	287	19950	28	14.13	>7.5	
1322.16		75		26261	56	13.23	>7.5	
1324.96		27		26952	45	13.05	5.9	c
1325.22	1325.10	57	238	27016	18	13.57	>7.5	c
1361.63	1361.53	126	146	35995	20	13.52	>7.5	
1393.86		331		43943	37	13.97	D	d

Probability code: L=GHRS observation with G140L only; D=not resolved; see text for explanation of -log(P) values.

cz values from GHRS wavelengths unless noted.

Notes:

a: on wing of galactic Lyman α, cz from FOS

b: line did not improve χ^2 of fit to NV doublet

c: parameters uncertain, dependent upon deblending; these two lines unresolved by FOS

d: Unresolved from Si IV λ1394 galactic halo line; see text for details

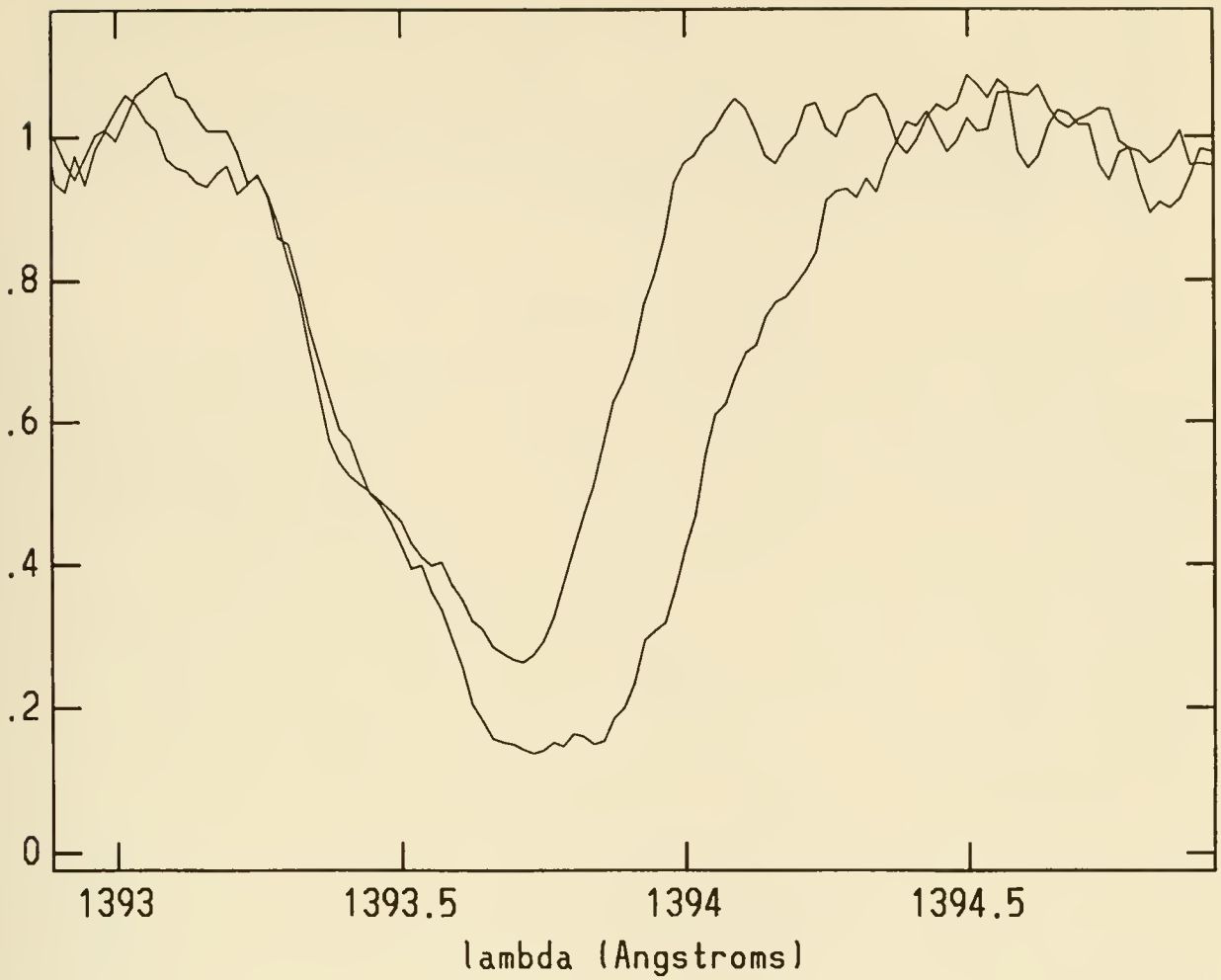

Fig. 1—The result of deblending the λ1394 complex into the Si IV contribution and the inferred Lyα contribution. The profile with the large equivalent width is the observed profile (after 5–smoothing) and the profile with the smaller equivalent width is the inferred Si IV. The large amount of residual absorption is attributed to a Lyα line.

blend (after 5–smoothing), while the profile with the smaller equivalent width is the predicted Si IV λ1394 profile. Evidently there is a very large residual amount of absorption. Alternatively, we may find the best fit to the observed profiles using Voigt profiles for the Si IV doublet and an additional feature at λ1394. The former method has the advantage that it does not require the assumption of a Voigt profile, but has the disadvantage that it does not take account of the finite PSF (at least as we have applied this method.) The Ly β line should be observable with the GHRS 140M grating as and when side 1 is operable.

3. THE EVOLUTION OF THE LY α FOREST

The justifiable excitement and gratification over the discovery that Ly α forest lines appear to exist at very low redshifts has led, in our view, to overemphasis of the degree to which the density of lines exceeded "expectations". There were really only two bases upon which predictions of the line density at very low redshift could be made: 1) Extrapolation of fits to the line density from ground–based data. 2) Models. Needless to say, both of these methods carried with them enormous uncertainties.

With respect to the extrapolation, not only must the extrapolation of the line density *per se* be carried out over a huge range in log (1+z), but one must tacitly assume that the distribution of equivalent widths also does not vary unless one is comparing samples whose limiting equivalent widths are the same. In addition, the data base for ground–based observations is weighted rather heavily to redshifts above 2, so that despite the very large number of lines, γ, (the slope of the log(dN/dz) *vs.* log (1+z) relation) is not that well determined. For example, in an analysis using over 900 lines and 38 QSOs, Lu *et al.* (1991) obtained a value of $\gamma = 2.75 \pm 0.29$ (when lines in the sample likely to be affected by the proximity effect are removed), but found some evidence that evolution steepened below a redshift of ~ 2.3, with a broken power law fit having a value of $\gamma = 4.21$ below this value. On the other hand Rauch *et al.* (1991), using a smaller number of lines, but based upon higher–resolution data (and heavily weighted to redshifts above 2) found $\gamma = 1.68 \pm 0.80$ for a sample having the same cutoff in line strength. It is possible that a global fit for γ over all redshifts might yield values not very different from the Rauch *et al.* value. In this sense the number of lines at low redshift is not "unexpected". On the other hand, it is clear that the predicted number of lines at low redshift is incompatible with the fit obtained by Lu *et al.* , for both the single power law and especially for the broken power law. More significantly, when a value of γ is determined from the HST data at z $\sim$0.05 and ground–based data at z$\sim$2.0, it is much flatter than either the Lu *et al.* or Rauch *et al.* value.

These results hold when objects other than 3C273 are considered. While it borders on the foolish to quote results based upon only 4 objects, especially when vastly more extensive data will be soon forthcoming (and indeed are already in hand), some results based upon the 4 objects available to the author at the time of writing are as follows:

i) For weak lines—*rest* equivalent width (REW) $\geq$ 50mÅ—we believe the 3C273 sample is probably complete. From Table 1 there are 10 such lines over the range from z=0.016 to z=0.151. (This includes the inferred line at λ1394 but not the two Virgo cluster lines, since the minimum z sampled by the G160M exposures does not include these lines. The upper limit is adopted, as in MWSG, to take account of the proximity effect from 3C273.) We compare this with a sample having the same REW cutoff taken from the data published by Carswell *et al.* (1991) for Q1101-264.

A simple linear fit to the two locally determined values of dN/dz gives a value of $\gamma = 0.82$, close to the maximum likelihood value quoted in MWSG.

ii) For lines of intermediate strength (REW $\geq$ 200mÅ—*cf.* BJSHBJ), we can adjoin to the G160M 3C273 list of 4 lines (we use the GHRS values of the equivalent widths) the two additional Virgo cluster lines seen in the FOS and G140L GHRS spectra. In addition, we judge the PKS2155-33 observations of Boggess *et al.* (1991) to also be complete to this limit. In this object, Maraschi *et al.* (1988) reported the presence of two absorption lines which they interpreted as intervening Lyα. However the HST observations show[1] that the feature measured at λ1237 and tentatively identified by Maraschi *et al.* as N V is at λ1236 which is sufficiently far from the galactic halo N V λ1238 line that we think it unlikely to be attributable wholly to N V. In addition, they show that the feature at λ=1285 consists of two well-separated (ΔV$\sim$600 km s^{-1}) features. The local value of dN/dz at z$\sim$2.0 for lines with REW $\geq$ 200mÅ is again taken from the Carswell *et al.* data for Q1101-264. In computing the local value of dN/dz for z$\sim$0 for this range of line strengths a matter of principle arises: It will be noted that the galactic Lyα line has not been included in the list, since it is clear that our preferred position in a spiral galaxy makes all lines–of–sight atypical at zero redshift. To what extent should our preferred position in the local supercluster and rather near the Virgo cluster cause us to give less than full weight to the Virgo cluster clouds? A large number of lines–of–sight not passing through the Virgo cluster will soon make this question moot, so we shall not dwell on it, but simply quote two values of γ for this range of line strength: With the two Virgo clouds we find $\gamma = 0.54$, and without the two Virgo clouds, $\gamma = 0.83$.

iii) Finally, for lines with REW $\geq$ 360mÅ—the threshold adopted by Lu *et al.* —we add lines from the two objects CSO251 and PG1211+143 (Burbidge *et al.* 1991). In these two objects there are an additional two certain and two probable Lyα lines with REW $\geq$ 360mÅ.[2] As in case ii) above, we considered both the cases in which the Virgo lines were and were not counted, and cases in which the two probable lines just mentioned were and were not counted. For the high redshift end of the fit we used the line density found by Lu *et al.* at z=2.3. The corresponding values of γ range between .73 and 1.24.

The actual values of γ thus determined are, of course, very uncertain due to the small number of lines in all three cases considered. Neverless, if one assumes the validity of the Lu *et al.* fit, the number of lines actually observed at low redshift would be extremely unlikely to occur by chance. In other words, the Lu *et al.* fit does not extend to low redshifts, but becomes much flatter.

With respect to whether the number of zero redshift lines was "unexpected" from the point of view of models, a number of authors have, after the fact, shown that such behavior can arise quite naturally. Indeed, the possibility of a flattening of γ or even of a turnup in the number of lines per unit redshift at low redshifts was explicitly noted several years ago by Bechtold *et al.* (1987; see their Figure 8) using a simple

[1] I thank Drs. Boggess and Bruhweiler for permission to quote this result in advance of publication.

[2] I thank Dr. V. Junkkarinen for communicating these two spectra and Drs. Burbidge and Junkkarinen for permission to quote these results in advance of publication.

pressure–confined quasi–static model with the confining pressure undergoing adiabatic expansion, together with their best estimate of the evolution of the intergalactic ionizing radiation field.

4. CURRENT PROBLEMS AND FUTURE OBSERVATIONS

A detailed review of models of the Lyα clouds and their evolution is beyond the scope of this paper. However, the following comments are relevant in connection with possible future observations, both ground–based and with HST.

It goes almost without saying that an important constraint on models will be provided by the detailed picture of the evolution of the Lyα forest line density over the entire range from 0.0 to $\sim$5.0 and the range from 0.0 to $\sim$1.6 will undoubtedly be provided by the Quasar Absorption Line Key Project provided only that the HST and spectrographs do not lose further capability. As noted in §3 however, there is still room for substantial improvement in delineating the line density as a function of both line strength and redshift, especially in the regime from $\sim$1.6 to $\sim$2.3. It would also be useful to devise a measure for the line density which is not sensitive to the decomposition into multiple components, perhaps along the lines pioneered by Webb *et al.* (1991) and Jenkins and Ostriker (1991) in the context of the Gunn-Peterson trough analysis.

In §2 we noted the interest in the possible existence of lines with very small values of the doppler parameter. However the question of the origin of doppler parameters with large formal values is also of interest (*cf.* Rauch *et al.* 1991). Values of up to 50 and even 60 km s^{-1} are derived even when based upon high resolution data. Such values surely cannot represent thermal widths, and the question is whether they are to be attributed to bulk motion or discrete components. If the latter, then as noted by Rauch *et al.* , the two–point correlation function will have a strong peak at velocities of order 20–50 km s^{-1} , though the interpretation presumably has nothing to do with gravitational clustering, but would more likely reflect fragmentation in a hydrodynamical process. Simulations show that it is generally possible to distinguish between these two origins for the super–thermal doppler parameters at resolutions now being employed for ground–based observations, but better signal–to–noise is required.

At least for 3C273 it is feasible to carry out such observations as well, and this should be done to see if the origin of the large formal doppler parameters is the same at low redshift as it is at high redshifts.

The question of the characteristic size of the Lyα clouds is still an important open question. The results of Foltz *et al.* (1984) on the pair of QSOs 2345+007A,B have been widely quoted as providing a characteristic size of the clouds of a few kpc. Subsequently, Steidel and Sargent (1990) examined this pair at lower resolution but higher S/N and concluded that it was unlikely to be a gravitational lens, but rather a true double QSO. This change in the geometry would imply that the characteristic size was as much as an order of magnitude larger than the value which Foltz *et al.* suggested. Most recently however, these same authors (Sargent and Steidel 1991), on the basis of further data, have concluded that the weight of the evidence favors the gravitational lens interpretation after all. However, they have discovered additional absorption systems exhibiting metals, and at least 3 of the 4 Lyα lines found by Foltz *et al.* to be common to the two lines of sight belong to these systems. Thus, only at most one of the lines in common to the two lines of sight is a Lyα-only system. The consequence of this is that the constraint on the sizes of the clouds is decidedly relaxed and becomes more in the nature of a lower limit. Intensive spectroscopic study of Q2345A,B should clearly

be a high priority project for the new generation of large telescopes, as also stressed by Sargent and Steidel.

In the meantime, at least one ambiguity in connection with the interpretation of the common lines in double or gravitationally lensed QSOs appears to have been cleared up. Until now, there has been no compelling reason to believe that lines in common represent the same physical cloud, as opposed to a swarm of small cloudlets. Recently however, Smette *et al.* (1991) have shown that the equivalent widths of the lines in common between the pair UM671A,B are strongly correlated, suggesting that single large clouds are involved and setting a firm lower limit of order 20 kpcs to the cloud sizes. This pair too should be studied at higher resolution and high S/N.

The characteristics sizes above refer to redshifts $\sim$2, and it would evidently be of considerable interest to place similar constraints on the characteristic sizes at very low redshifts. At least one pair, Ton 155/156 offers the possibility of examining this question with HST, although an IUE exposure (Malkan 1991) of Ton 155 suggests that a strong Ly limit system may be present at a redshift of about 1.2-1.4 which has absorbed most of the far UV flux.

A final question of considerable interest which can be readily investigated for the low redshift Lyα clouds towards 3C273 (and of course towards all other QSOs) involves the question of the association of the clouds with optical images (if any) and the statistical correlation of the clouds with galaxies and clusters of galaxies (if any).

As pointed out by MWSG, direct imaging of the clouds themselves by means of their recombination radiation does not appear feasible except for extremely high column densities, unless the clouds are exposed to UV radiation fields several orders of magnitude higher than the estimated value of the intergalactic radiation field at zero redshift. Direct "imaging" in 21 cm radiation is also not feasible. However, it could well be that the Lyα clouds are shreds of H I on the outer edges of, *e.g.,* dwarf galaxies which might have some Hα emission. Such dwarf galaxies may have extremely low surface brightnesses and would be very difficult to detect in continuum radiation, especially very near a bright object like 3C273. In a collaboration involving S. Morris, R. Schommer, R. Weymann and T. Williams, a very preliminary set of observations were obtained by Schommer and Williams at the CTIO 4m telescope using the Rutgers Fabry-Perot Interferometer, and scanning over the 1600 km s^{-1} and 1000 km s^{-1} regions with a FWHM of 2.5Å. No obvious features appear which are clearly above the noise (of a few electrons), although some faint emission filaments about 30-40 arcsec from the QSO may possibly be present at about the noise level (Schommer 1991). Before any decision can be made about the reality of such possible features, much more extensive data will need to be obtained. In a separate collaboration, custom narrow-band filters have been obtained to search for emission features at the two Virgo cloud redshifts as well as the redshift space around the feature at 1251Å, using the Smith-Terrile coronograph at the Las Campanas duPont telescope.

In addition to a search for emission features closely associated with the Lyα clouds, an obvious related program is to check for statistical correlations (or anti-correlations) between individual galaxies and groups and clusters of galaxies and the Lyα clouds. Indeed, preliminary investigations along these lines have already been carried out by Salzer (1991) and by Jaaniste (1991). In particular, Salzer has examined currently available redshifts in the neighborhood of 3C273 to identify those galaxies closest to the Virgo Lyα clouds and to look for structures which might be associated with some of the more distant clouds. Interestingly, one of the closest associations appears to be between one of the clouds and the large H I cloud 1225+01, a possible association

already noted by BJSHBJ. The data is still too scanty for any definitive conclusions to be reached concerning the extra–Virgo clouds. Collaborative programs are underway at LCO and CFHT to provide extensive redshift and color data on galaxies near the 3C273 line–of–sight.

As a final quasi–philosophical remark, it is certainly not clear that the Lyα systems found at very low redshift represent the same phenomenon seen at high redshift. There has been extensive debate over whether the low– and high–column density Lyα systems at high redshift are best regarded as members of a "single population" or should be considered two separate populations. Suppose the result should emerge that the low redshift Lyα clouds are indeed associated with galaxies and clusters of galaxies (we already know that two such clouds are.) There may then be a tendency to conclude that the low redshift clouds belong to a different population than the high redshift clouds, since the high redshift clouds "don't cluster like galaxies". (A more accurate statement is that the two point correlation function for the Lyα–only systems shows very little structure whereas that for the higher column density systems exhibiting C IV does.) This conclusion would be premature. In general, the existence of a property (*e.g.*, the correlation function) spanning a wide range as another parameter (*e.g.*, column density or redshift) varies is not an argument in and of itself for two populations. To make a convincing case for two populations, it will be necessary to trace the strength of the association between the Lyα clouds and galaxies (if such an association is found at low redshift) back to higher redshifts and then find other properties (*e.g.*, metal abundance) which discriminate between Lyα clouds which do and do not associate with galaxies. Only then could one consider the two–population case to have been made.

REFERENCES

Bahcall, J.N., Jannuzi, B.T., Schneider, D.P., Hartig, G.F., Bohlin, R., and Junkkarinen, V. 1991, *Ap. J. (Letters)*, **377**, L21. (BJSHBJ)

Bechtold, J., Weymann, R.J., Lin, Z., and Malkan, M.A. 1987, *Ap. J.*, **315**, 180.

Boggess, A., Bruhweiler, F., Kondo, Y., Urry, M., Grady, C., and Norman, D. 1991, *in preparation.*

Burbidge, E.M., Cohen, R., Junkkarinen, V. and several other FOS team members. 1991, *in preparation.*

Carswell, R.F., Lanzetta, K.M., Parnell, H.C., and Webb, J.K. 1991, *Ap. J.*, **371**, 36.

Foltz, C.B., Weymann, R.J., Roser, H.–J., and Chaffee, F.H. 1984, *Ap. J. (Letters)*, **281**, L1.

Gilliland, R.L., Morris, S.L., Weymann, R.J., Ebbets, D., and Lindler, D. 1991, *in preparation.*

Hunstead, R.W., and Pettini, M. 1991 in *Proc. of the ESO Mini-Workshop on Quasar Absorption Lines* ESO Scientific Report No. 9 Feb. 1991, p. 11.

Jaaniste, J. 1991, (preprint submitted to *Baltic Astronomy.*)

Jenkins, E.B. and Ostriker, J.P. 1991, *Ap. J.*, **376**, 33.

Lu, L., Wolfe, A.M. and Turnshek, D.A. 1991, *Ap. J.*, **367**, 19.

Malkan, M. 1991, *private communication.*

Maraschi, L., Blades, J.C., Calanchi,C., Tanzi, E.G., and Treves, A. 1988, *Ap. J.*, **333**, 660.

Morris, S.L., Weymann, R.J., Savage, B.D., and Gilliland, R.L. 1991, *Ap. J. (Letters)*, **377**, L21. (MWSG)

Rauch, M., Carswell, R.F., Chaffee, F.H., Foltz, C.B., Webb, J.K., Weymann, R.J., Bechtold, J., and Green, R.F. 1991, *submitted to Ap.J.*

Salzer, J.J. 1991, *submitted to Astron. J.*.

Sargent, W.L.W. and Steidel, C.C. 1991, *preprint*

Schommer, R. 1991, *private communication.*

Smette, A., Surdej, J., Shaver, P.A., Foltz, C.B., Chaffee, F.H., Weymann, R.J., Williams, R.E., and Magain, P. 1991, *submitted to Ap.J.*

Steidel, C.C. and Sargent, W.L.W. 1990, *A. J.*, **99**, 1693.

Webb, J.K., and Carswell, R.F. 1991 in *Proc. of the ESO Mini-Workshop on Quasar Absorption Lines* ESO Scientific Report No. 9 Feb. 1991, p. 3.

Webb, J.K., Barcons, X., Carswell, R.F., and Parnell, H.C. 1991, *preprint.*

Hot Stars and the HST

R.P. Kudritzki
Institute für Astronomie und Astrophysik der Universität München
Scheinerstr. 1
8000 München 80
Germany

Abstract.

The HST is ideally suited to the observation of hot massive stars which emit much of their prodigious energy output as radiation in the ultra-violet region of the spectrum. These most luminous of stars can be identified directly in galaxies as distant as the Virgo cluster or indirectly through their illumination of giant HII regions, such as the 30 Doradus complex in the Large Magellanic Cloud. They are therefore ideal standard candles and tracers of young populations providing important information about abundances, star formation, energetics of the ISM (radiation, stellar winds) and nucleosynthesis.

On the other hand, thanks to dramatic advances in NLTE model atmosphere techniques the methods of quantitative spectroscopy of hot stars have experienced great progress. Model atmospheres are now available that include the opacity of thousands to tens of thousands of lines fully in NLTE and take into account the radiation hydrodynamics of stellar winds. This has opened the door to determine precisely the stellar parameters of luminosity, effective temperature, gravity, mass, radius, distance, chemical composition as well as the stellar wind parameters, mass loss rate and velocity structure not only in our own galaxy but also in local group galaxies and somewhat beyond. In addition, new ionizing model atmosphere fluxes are becoming available that will allow a more realistic interpretation of nebular recombination spectra.

The crucial parameter determining the properties of hot stars is metallicity. It affects the ionizing energy distribution, the spectral appearance, the stellar wind properties and the formation and evolution of hot stars. With HST it will be for the first time possible to study quantitatively the physics of massive stars in galaxies of different metallicity, in particular by obtaining high quality ultraviolet spectra of hot stars in the Magellanic Clouds.

In this connection, we report first HST observations obtained with the GHRS of the O3f star Melnick 42 in the 30 Doradus complex of the LMC. A first analysis of the excellent spectra reveals that with a luminosity of $2.3 \times 10^6 L_\odot$ and a present mass of $100\ M_\odot$, the object is one of the most massive stars known. An estimate of abundances indicates that iron and oxygen are very likely reduced by a factor of four relative to the sun, whereas carbon is more strongly depleted and nitrogen is approximately solar. The terminal velocity of the stellar wind is 3000 km/sec. The mass-loss rate is

$4 \times 10^{-6} M_{\odot}$/year, with a large uncertainty.

Most of the content of this paper has been discussed in recent reviews by Kudritzki and Hummer (1990) and Kudritzki *et al.* (1991) and the very recent publication on first results obtained with the GHRS in the Ap.J. Letters by Heap *et al.* (1991). In consequence, to avoid simple duplication of paper, only this summary is published here.

REFERENCES

Heap, S.R., Altner, B., Ebbets, D., Hubeny, I., Hutchings, J.S., Kudritzki, R.P., Voels, S.A., Haser, S., Pauldrach, A., Puls, J., Butler, K., 1991, *Ap. J. (Letters),* **337**, L29.

Kudritzki, R.P., Hummer, D.G., 1990, *Ann. Rev. Astr. Ap.*, **28**, 303.

Kudritzki, R.P., Gabler, R., Kunze, D., Pauldrach, A., Puls, J., 1991, in *Massive Stars in Starbursts*, STScI Symp. Series No.5, eds. C. Leitherer *et al.* p. 59

GHRS FAR-ULTRAVIOLET SPECTRA OF CORONAL AND NONCORONAL STARS: CAPELLA AND γ DRACONIS

Jeffrey L. Linsky[1] and Alexander Brown
Joint Institute for Laboratory Astrophysics
University of Colorado
Campus Box 440
Boulder, CO 80309-0440
USA

Kenneth G. Carpenter
NASA Goddard Space Flight Center
Code 681
Greenbelt MD 20771
USA

Abstract. We report on the first GHRS spectra of two very different late-type giant stars – Capella and γ Dra. Capella is a 104 day period binary system consisting of two stars (G9 III and G0 III) each of which shows bright emission lines formed in solar-like transition regions and coronae. By contrast, γ Dra is a hybrid-chromosphere star with very weak emission lines from high-temperature plasma. Low-dispersion spectra of these stars covering the 1160 to 1717 Å spectral range show unresolved emission lines from neutral species through N V. The very different surface fluxes detected in the spectra of these stars suggest different types of heating mechanisms. Moderate dispersion spectra of Capella show intersystem lines of C III, N III, O III, O IV, Si III, and S IV, which are sensitive to electron density. Echelle spectra of hydrogen and deuterium Lyman-α, Fe II, and Mg II permit measurements of the cosmologically interesting D/H ratio and the properties of the interstellar medium on the 13 pc line of sight to Capella.

1. INTRODUCTION

The Goddard High Resolution Spectrograph on the HST places new observational capabilities in the hands of astronomers studying the atmospheres of stars and the interstellar medium. Both IUE and Copernicus have obtained ultraviolet spectra of bright sources in the 1170–3200 Å spectral region, but the GHRS will expand our observational capabilities enormously in at least four ways:

[1]Staff Member, Quantum Physics Division, National Institute of Standards and Technology

- The higher throughput of the GHRS and the low background of its Digicon detectors support photon-limited observations of much fainter sources than heretofore feasible and the measurement of weaker emission and absorption lines which are buried in the noise of existing ultraviolet spectra.
- The GHRS can obtain spectra with signal/noise well in excess of 100:1 (Carpenter *et al.* 1991), a major improvement over IUE. This is critical for measuring lines profile shapes, Doppler-imaging experiments, and for studying individual velocity components in interstellar absorption lines.
- Small science aperture (SSA) spectra are not noticeably degraded in spectral resolution by the spherical aberration. Wahlgren *et al.* (1991) determined that at 1940 Å moderate dispersion G160M spectra have a resolution of 28,000 and the echelle spectra have a resolution of 87,000. Large science aperture (LSA) spectra are degraded in resolution by a factor of 2 compared to prelaunch expectations, but spectral deconvolution techniques can recover most of the lost resolution for point sources when the signal/noise is sufficiently large. Except for echelle spectra of a few very bright sources obtained with a rocket instrument, the GHRS is the highest resolution and most sensitive ultraviolet spectrograph in operation.
- The very low scattered light level of the GHRS gratings and the solar-blind detectors make observations of the ultraviolet spectra of very red stars possible. These properties are essential for studies of interstellar deuterium, for example.

In this paper we provide examples of these new capabilities, which will yield major scientific benefits in the study of cool stars and the interstellar medium. At the same time, we should recognize that IUE beautifully complements the strengths of the GHRS by its broad spectral coverage in single exposures, its capability to monitor sources over many time scales, and its continuing success in observing targets of opportunity.

2. LOW DISPERSION SPECTRA OF COOL GIANTS

On 15 April 1991 we obtained GTO low dispersion G140L spectra of Capella, a 104 day spectroscopic binary system consisting of a slowly rotating G9 III primary (Capella Aa) and a more rapidly rotating G0 III secondary star (Capella Ab). (See Battan, Hill, and Lu 1991 for a discussion of the system parameters.) On the basis of IUE spectra, Ayres and Linsky (1980) showed that the G0 III star dominates the ultraviolet emission line spectrum of the system. During SV, we obtained on 6 April 1991 low dispersion spectra of the K5 III star γ Draconis, a member of the class of hybrid-chromosphere stars. The ultraviolet spectra of these stars are characterized by high-velocity blue-shifted absorption features due to a cool wind (75–200 km s^{-1}) and faint emission lines formed at temperatures up to 150,000K (Hartmann, Dupree, and Raymond 1980; Drake, Brown, and Linsky 1984).

Low dispersion spectra with the G140L grating provide a means of rapidly observing broad spectral regions (288 Å at one time) with enough spectral resolution (2,000 with the SSA and roughly 1,000 with the LSA) to measure the fluxes of most important emission lines, although higher resolution spectra are needed to separate close blends. We first inspect the low dispersion spectra to identify the major differences between an "active" star like Capella Ab and a very inactive star like γ Dra.

Figures 1 and 3, which display the 1170–1710 Å region of Capella, should be compared with Figures 2 and 4, which display the 1260–1740 Å region of γ Dra. We note immediately that the spectrum of Capella is dominated by bright emissions, including the resonance lines of C II, Si IV, C IV, and N V formed at temperatures of 20,000–150,000K (see Table 1). The brightest feature is Lyman-α, despite strong interstellar hydrogen absorption in its core (see below). In the Sun this line is formed at 40,000K as a result of ambipolar diffusion (Fontenla, Avrett, and Loeser 1991), and we suspect that the line is formed at similar temperatures in Capella. Emission lines of other neutral species are formed in the chromosphere at T $\leq$ 8,000K and are very weak, except for the C I multiplet near 1657 Å.

Table 1. Comparison of Emission Line Surface Fluxes (log units)

Multiplet	logT	Sat. Limit	V711 Tau (RS CVn)	Capella (G0III)	Sun (G2V)	γDra (K5III)	αBoo (K2III)
C IV 1549 Å	5.0	6.0	5.62	5.43	3.73	2.08	<2.00
Si IV 1400 Å	4.8		5.05	4.88	3.37	1.60	<2.00
Si III 1892 Å	4.6		4.68	5.26			1.82
C II 1334 Å	4.3		5.46	5.20	3.67	1.93	<2.00
O I 1304 Å	3.9		5.24	4.85	3.62	3.70	3.75
C I 1657 Å	3.8		5.07	5.01		2.51	2.84
Mg II 2800 Å	3.8	7.2	6.82	6.92	6.07	4.73	5.25

The low dispersion ultraviolet spectrum of γ Dra shows a very different appearance as both Lyman-α and the O I 1304 Å multiplet dominate over the high-temperature lines. The temperature at which the Lyman-α line forms in inactive K giants is not known, but the O I lines are formed in the chromosphere as a result of pumping by Lyman-β (Haisch *et al.* 1977). The other prominent emission lines are from neutral species and the fourth positive bands of CO, all formed at temperatures below 8,000K. While the CO bands could be identified in IUE spectra of Arcturus (Ayres, Moos, and Linsky 1981; Ayres 1986), the GHRS spectra are of much higher signal/noise and will permit more detailed analysis. The high temperature resonance lines of C II to N V are all present but very weak compared with the low-temperature emission lines.

This qualitative difference in the spectra of Capella and γ Dra can be made quantitative by measuring the observed emission line fluxes and converting them to surface fluxes by dividing by the square of the stellar angular radii. The latter may be inferred simply from the stellar visual magnitudes and colors (Linsky *et al.* 1979). The surface fluxes are given in Table 1, together with corresponding values for the more active RS CVn system, V711 Tau (Byrne *et al.* 1987), the quiet Sun (Ayres, Marstad, and Linsky 1981), and the slowly rotating K giant Arcturus (α Boo; Ayres, Simon, and Linsky 1982). Mg II and other chromospheric line fluxes were obtained from Ayres *et al.* (1982) and Simon, Linsky, and Stencel (1982). We also list the maximum observed C IV and Mg II surface fluxes for the youngest and most rapidly rotating stars without obvious circumstellar disks. Vilhu (1987) calls these fluxes "saturated" in the sense that they represent the maximum radiative emission from a star completely covered with "active regions", which are undoubtedly locations of strong magnetic fields.

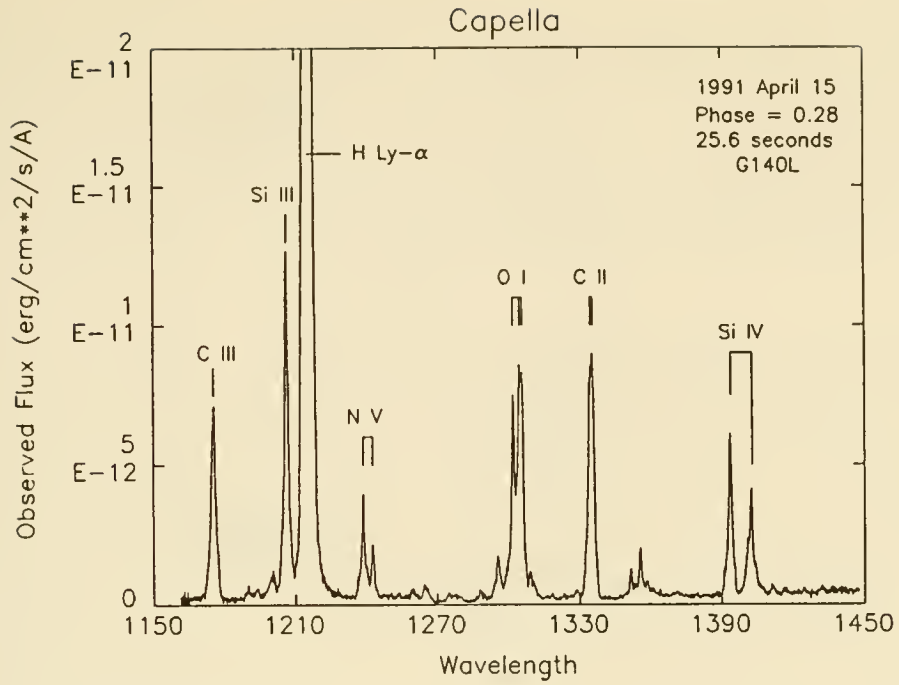

Figure 1.: The GHRS low dispersion spectrum of Capella obtained with the G140L grating. The 1170–1450 Å spectrum contains emission lines formed at 20,000–150,000K.

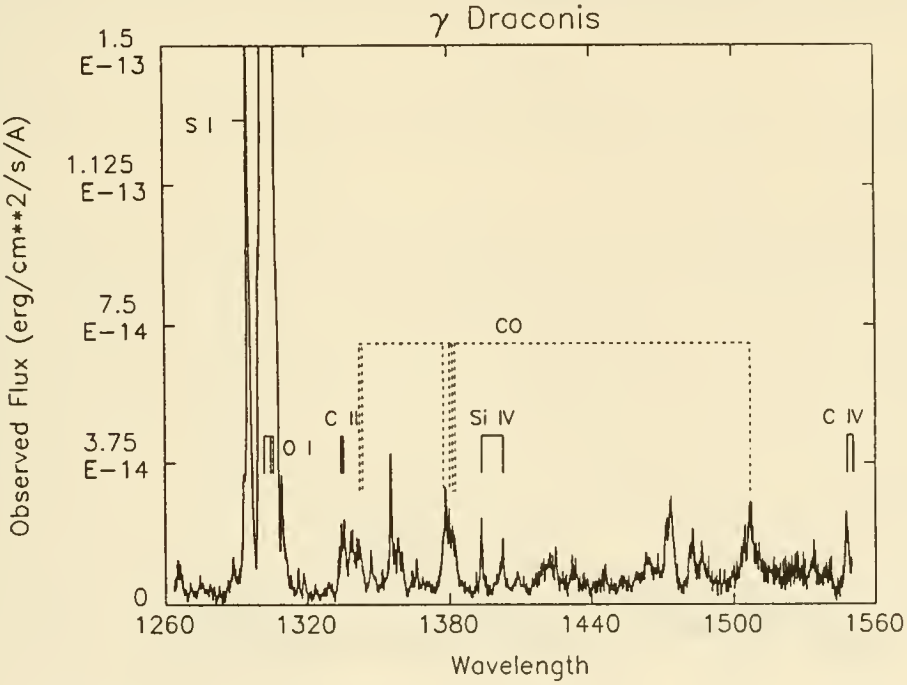

Figure 2.: The GHRS low dispersion spectrum of γ Draconis obtained with the G140L grating. The 1260–1550 Å spectrum contains the bright O I resonance line multiplet (1302, 1304, and 1306 Å) blended with S I lines. The high-temperature transition region lines are very weak compared to those in the Capella spectrum. The fourth positive bands of CO are indicated. There are many weak emission lines that are not identified here, but no evidence for photospheric or other continua.

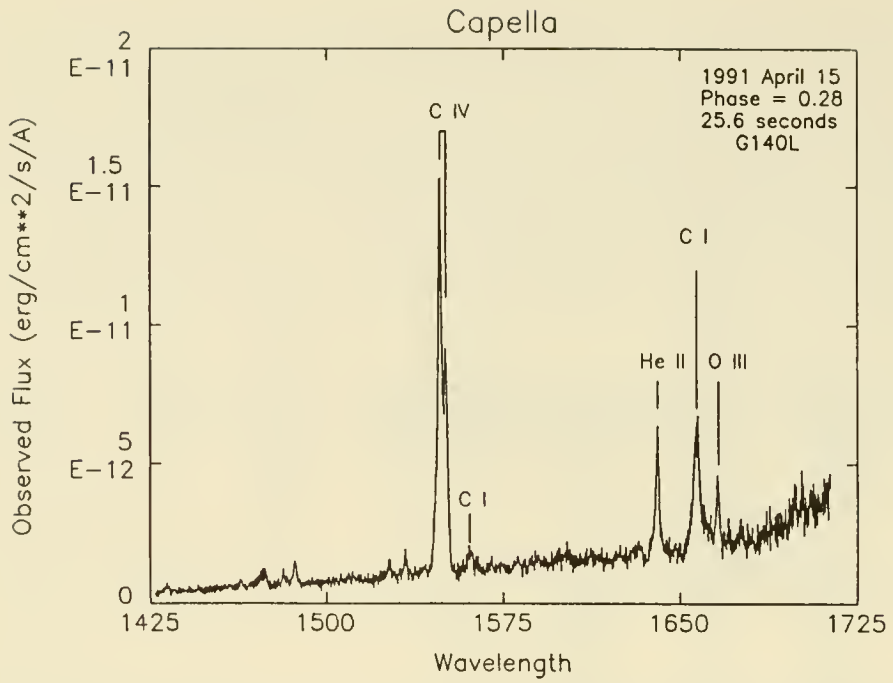

Figure 3.: Same as Fig. 1 except for the 1425–1710 Å region. This spectrum is dominated by the C IV resonance lines formed at 100,000K. Note the HeII 1640 Å line and the intersystem O III] line at 1666 Å, which is a part of a density-sensitive multiplet. The underlying continuum is from the G0 III star in the system.

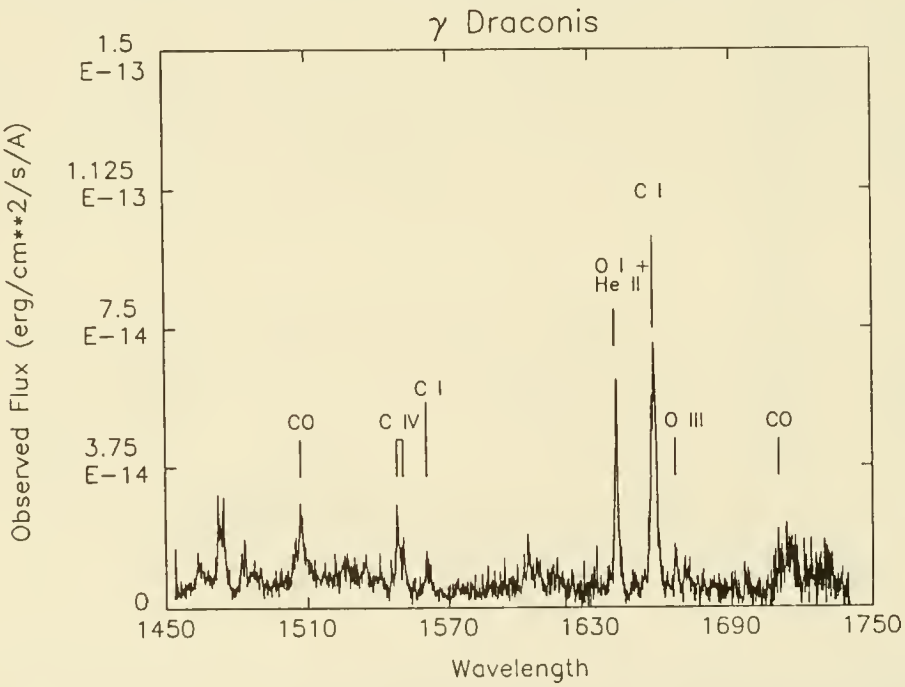

Figure 4.: Same as Fig. 2 except for the 1450–1740 Å region. Unlike the Capella spectra, low-temperature emission lines dominate over the high-temperature C IV lines. There is no evidence for the photospheric continuum in this spectrum or out to 1840 Å.

The data in Table 1 indicate that the surface fluxes of the high-temperature lines for Capella Ab lie about a factor of 3 below the saturated limit, and those for the shorter period V711 Tau system lie even closer to this limit. A natural explanation for this behavior is that a large fraction of the surface area of these active stars is covered by "plages" where the magnetic fields are strong and the heating rate is at or near its maximum possible value. Indeed, large plages have been identified on the surface of AR Lac by Doppler imaging techniques (Neff *et al.* 1989), and Linsky (1990) has shown that the surface fluxes in the plages of the RS CVn systems AR Lac, II Peg, and V711 Tau are near the "saturated" limit.

On the other hand, the surface fluxes for the high temperatures lines for γ Dra lie nearly a factor of 10,000 below the "saturated" limit. They are, in fact, the smallest surface fluxes ever measured on a cool star. Previously, the smallest values were the uncertain upper limits for α Boo listed in Table 1 obtained with IUE. One could interpret the very small surface fluxes of high-temperature lines on γ Dra as indicating that the fraction of the surface of such slowly rotating inactive stars covered by active regions is $\sim 10^{-4}$, less than 10% of the plage coverage of the quiet Sun. This hypothesis is possible but is not easily tested observationally. More likely heating mechanisms are acoustic waves generated by the known convective motions in the photosphere, or perhaps magnetoacoustic waves if weak magnetic fields are present. Cuntz (1987) and Cuntz and Luttermoser (1990) have computed models of the K giant star α Boo in which a stochastic distribution of acoustic wave periods leads to the occasional coalescence of individual shocks into very strong shocks that produce high-temperature plasma. Our observations of γ Dra and our proposed observations of α Boo and other stars will extend the measurement of surface fluxes to even smaller values to test these and other competing theories.

3. MODERATE DISPERSION SPECTRA OF COOL GIANTS

We now inspect the moderate dispersion spectra of Capella obtained through the LSA during our GTO program. These spectra have a nominal dispersion of 10,000 or 30 km s^{-1}. Figure 5 shows a spectrum containing the C IV resonance lines obtained with the G160M grating. These line profiles appear to be smooth Gaussians with no identifiable structure or splitting. Since the components of the Capella system have a radial velocity separation of 53.5 km s^{-1} at phase 0.28, the absence of splitting or line asymmetry confirms that one star, the G0 III star as determined in previous studies, contributes most of the flux. The absence of line structure indicates that no single bright plage was on the surface of the G0 III star. This also is consistent with earlier studies, but more active RS CVn systems like AR Lac show enhanced discrete features, superimposed on otherwise smooth line profiles, which are thought to be produced by bright plages that are Doppler-shifted by stellar rotation. We will observe the C IV lines in AR Lac at many phases to map the location of bright plages regions using the Doppler imaging technique.

The FWHM of the C IV 1548 Å line is 217 km s^{-1}, while for the 1550 Å line it is 186 km s^{-1}. These widths are much larger than the predicted thermal width, $\Delta\lambda_D = 14.4$ km s^{-1}, and the instrumental width of 30 km s^{-1}, but are consistent with IUE observations at quadrature (Ayres 1984). The line flux ratio $f_{1548}/f_{1550} = 1.77$ is significantly smaller than the ratio of gf values which is 2.0. These data indicate

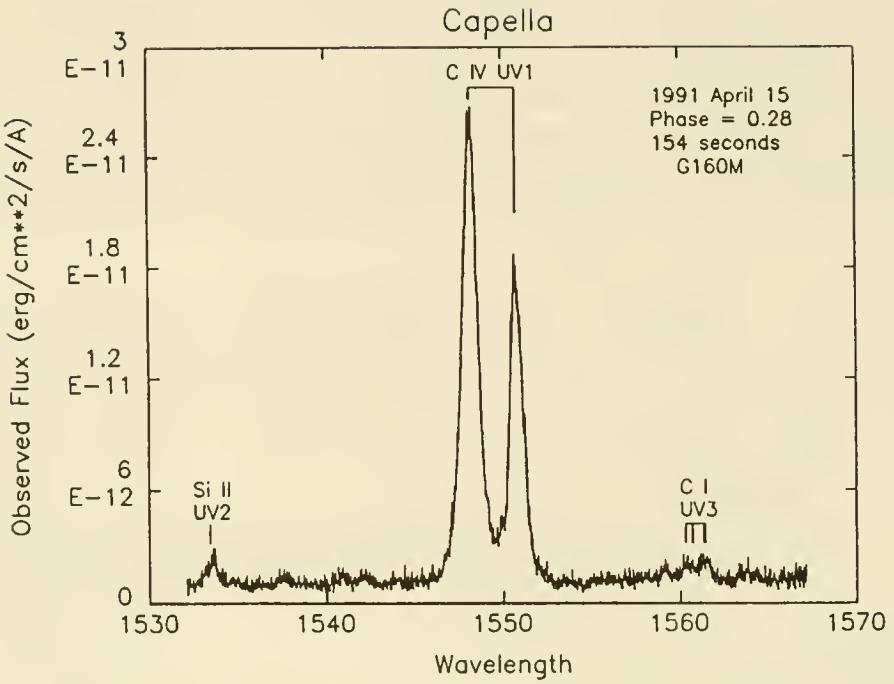

Figure 5.: A GHRS moderate dispersion spectrum of Capella obtained with the G160M grating. The C IV resonance lines are well-resolved in this spectrum. The profiles are smooth with no evidence for isolated plage regions on the surface of the G0 III star.

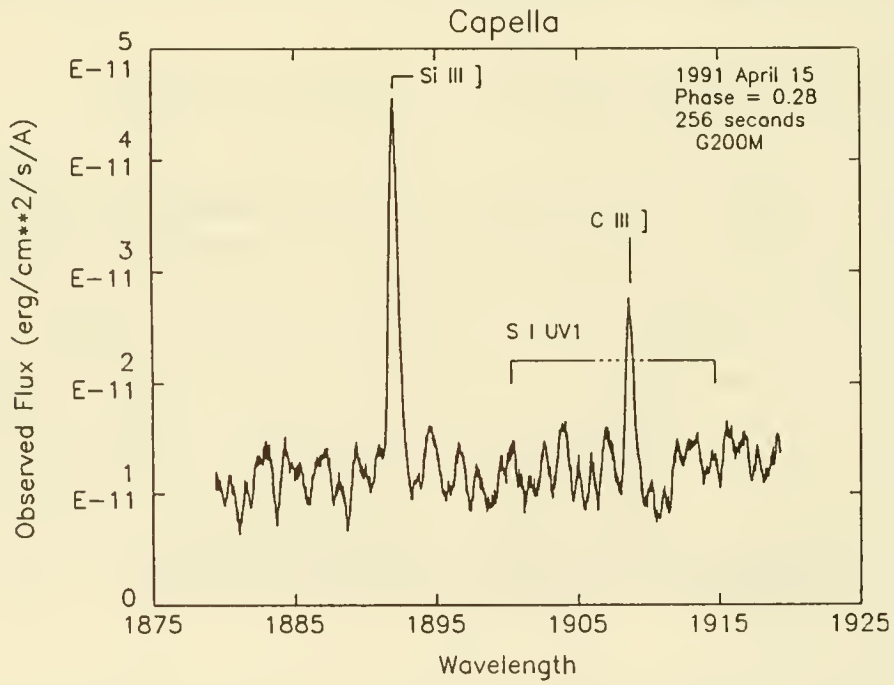

Figure 6.: A GHRS moderate dispersion spectrum of Capella obtained with the G200M grating. The intersystem lines of Si III and C III are in emission superimposed on the photospheric absorption line spectrum.

that both turbulence and opacity broaden these lines, and that the more opaque line is optically thick. Such data will provide new constraints on acceptable model atmospheres for Capella and other stars.

3.1 Density-sensitive Line Ratios

Figure 6 shows the presence of the Si III] and C III] intersystem lines in a moderate dispersion G200M spectrum. The line fluxes can be measured without too much confusion above the photospheric absorption line spectrum of the star. Intersystem lines of O III] at 1660 and 1660 Å are shown in Figure 7, and the intersystem lines of O IV] and S IV] are shown in Figure 8. To our knowledge, the S IV] have never been detected previously in a stellar spectrum, except for the Sun, while the other intersystem lines have been detected by IUE in the spectra of several stars but with poor signal/noise. Clearly the GHRS can measure accurate fluxes for these faint lines. We note that FWHM = 124 km s^{-1} for the Si III] line, while the predicted thermal width, $\Delta\lambda_D = 6.0$ km s^{-1}, and instrumental width is 30 km s^{-1}. The narrower width of this line compared to the C IV 1550 Å line is consistent with the Si III] line being turbulently broadened but with no opacity broadening, as is expected for intersystem lines that should be optically thin.

Intersystem lines are important, because they provide independent measures of the electron density at the plasma temperatures where the ions are abundant. This can be seen by considering a simple three-level atom in which level 1 is the ground state, transition 1-3 is allowed, and transition 1-2 is an intersystem transition. For example, in Si III the 1-3 transition would be the $3s^2\ ^1S - 3s3p\ ^1P$ resonance line at 1206 Å, and the 1-2 transition would be the $3s^2\ ^1S - 3s3p\ ^3P$ intersystem line at 1892 Å. The statistical equilibrium equations for this three-level atom are:

$$n_1 \left[n_e C_{12} + B_{12} \bar{J}_{12} \right] = n_2 \left[n_e C_{21} + A_{21} \right]$$

$$n_1 \left[n_e C_{13} + B_{13} \bar{J}_{13} \right] = n_3 \left[n_e C_{31} + A_{31} \right],$$

where n_i is the population of level i, C_{ij} is the collisional rate for the i-j transition, $\bar{J}_{ij}$ is the mean radiation field in the $i-j$ transition line, and A_{ij} and B_{ij} are the Einstein A and B rates. Since the observed flux, $f_{ij} \propto n_j A_{ji}$, the flux ratio of the permitted to the intersystem line is,

$$\frac{f_{31}}{f_{21}} \approx \frac{C_{13}/C_{12}}{\left[\frac{n_e C_{21}}{A_{21}} + 1 \right]}.$$

When the first term in the denominator becomes appreciable, i.e. when $n_e \geq 0.1 A_{21}/C_{21}$, then collisional de-excitation of the upper state of the intersystem line is important and the flux ratio depends explicitly on the electron density. At higher densities collisional de-excitation from the upper state of the allowed transition (not included in the above equation) also becomes important, and the flux ratio is no longer sensitive to density. Table 2 summarizes the density range over which the prominent ions with ultraviolet intersystem lines are density sensitive. Figures 6–9 demonstrate that the GHRS can provide beautiful spectra containing these lines that can form the observational basis for accurate numerical models of stellar chromospheres and transition regions for late-type stars. An example is the model of β Dra computed by Brown *et al.* (1984) on the basis of earlier IUE spectra.

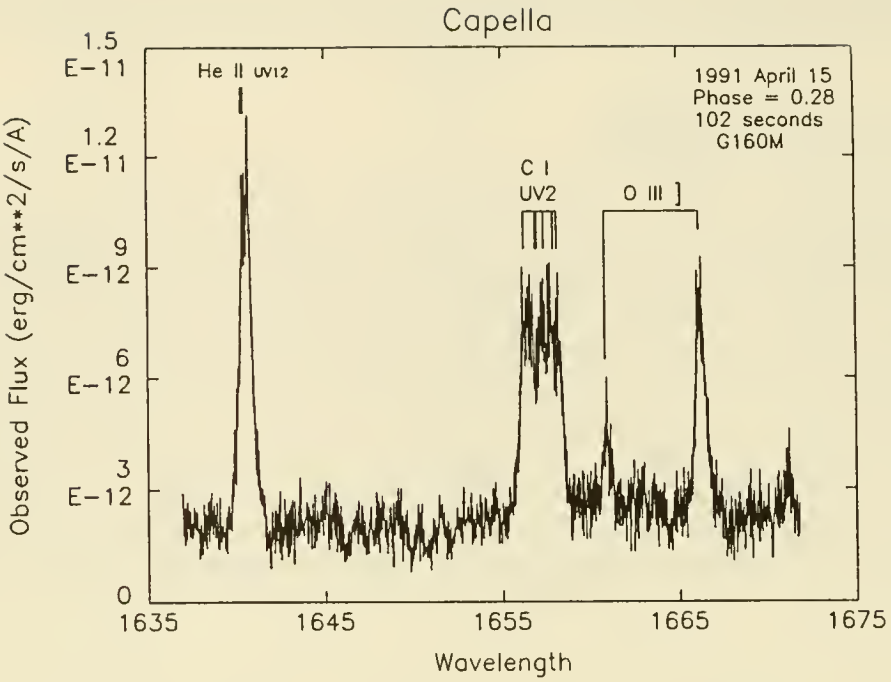

Figure 7.: A GHRS moderate dispersion spectrum of Capella obtained with the G160M grating. Note the intersystem lines of O III], which are density sensitive.

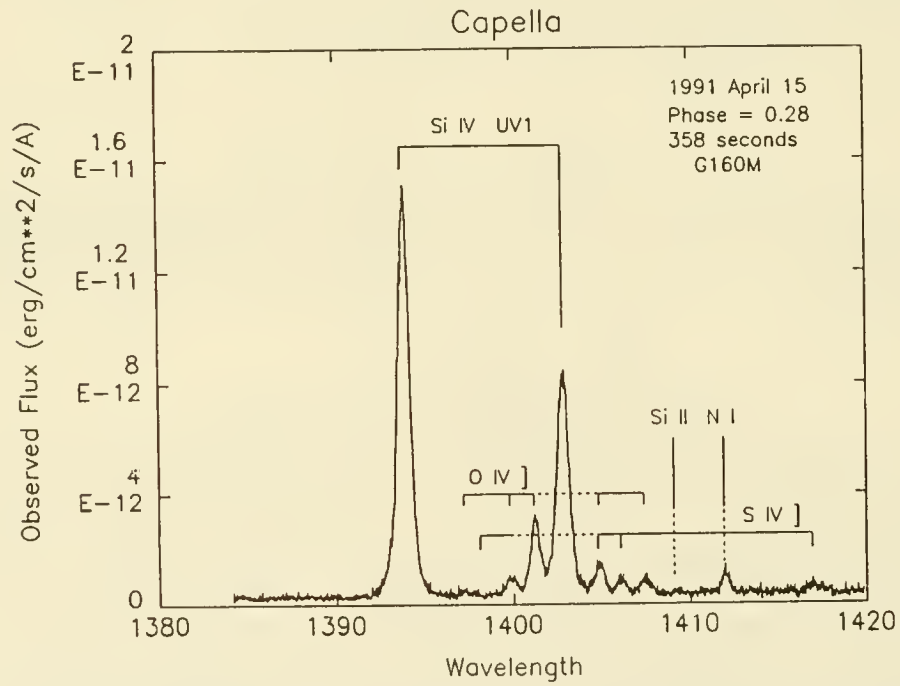

Figure 8.: A GHRS moderate dispersion spectrum of Capella obtained with the G160M grating. Note the intersystem lines of O IV] and S IV], which are density sensitive.

Table 2. Density-sensitive Line Ratios in the 1170–2350 Å Region

Ions	logT	Wavelengths (Å)	Range of log(N_e)
C II	4.0	2323.5, 2324.7, 2325.4, 2326.9, 2328.1	7–9
Si III	4.6	1294.5–1303.3 (6 lines), 1892.0	9–12
O III	4.6	1660.8, 1666.2	9–13
N III	4.8	1746.8, 1748.6, 1749.7, 1752.2, 1754.0	8–10
S IV	4.9	1404.8, 1406.0, 1416.9	10–13
O IV	5.1	1397.2, 1399.8, 1401.2, 1404.8, 1407.4	8–12
O V	5.4	1218.4	10–13

4. HIGH DISPERSION SPECTRA: THE INTERSTELLAR MEDIUM AND D/H RATIO FOR THE LINE OF SIGHT TOWARDS CAPELLA

We discuss finally our beautiful echelle spectra of Capella obtained through the SSA, which have a measured spectral resolution (Wahlgren *et al.* 1991) of 87,000, corresponding to 3.4 km s^{-1}. Our objective in obtaining these spectra was to determine the D/H ratio and the physical properties of the interstellar medium along the 13 pc line of sight towards Capella. For this purpose Capella is a bright emission line source against which we measure the opacity of resonance lines formed in the interstellar medium. These data are also useful for other purposes as we shall see.

Figure 10 shows the spectrum of the Mg II h (2803 Å) and k (2796 Å) resonance lines obtained with the Ech-B grating. These spectra show the narrow interstellar absorption lines, which are spectrally resolved and do not go to zero flux after correction for scattered light. The analysis of the line profiles provides information on both the line opacity and broadening. To the right of the interstellar lines one can see the self-reversal of the emission line from the G9 III star, and to the left one can see a portion of the self-reversal of the emission line from the G0 III star. These features are barely present in IUE spectra at this phase. The shape of the composite emission line will be useful in testing chromospheric models of these stars.

We show the Ech-A spectrum of the Lyman-α region in Figure 11. The broad stellar Lyman-α emission line is mutilated by the interstellar hydrogen Lyman-α absorption feature and a narrow interstellar feature due to deuterium Lyman-α centered at -0.32 Å relative to the hydrogen absorption line. The deuterium line has been seen in Copernicus and IUE spectra of Capella (e.g. Murthy *et al.* 1990) and other stars, but this spectrum is the first in which the line has been spectrally resolved. The small amount of instrumental scattered light can be measured from the minimum flux seen in the saturated interstellar core of the hydrogen absorption line. The central depth of the deuterium feature is a measure of its optical depth, and the shape of the hydrogen absorption feature can be used to measure its opacity. A detailed analysis of this spectrum, which is now under way, will provide a very accurate measurement of the D/H ratio along this line of sight. This will be important for inferring the primordial D/H ratio, which is a major constraint on models of the very early universe.

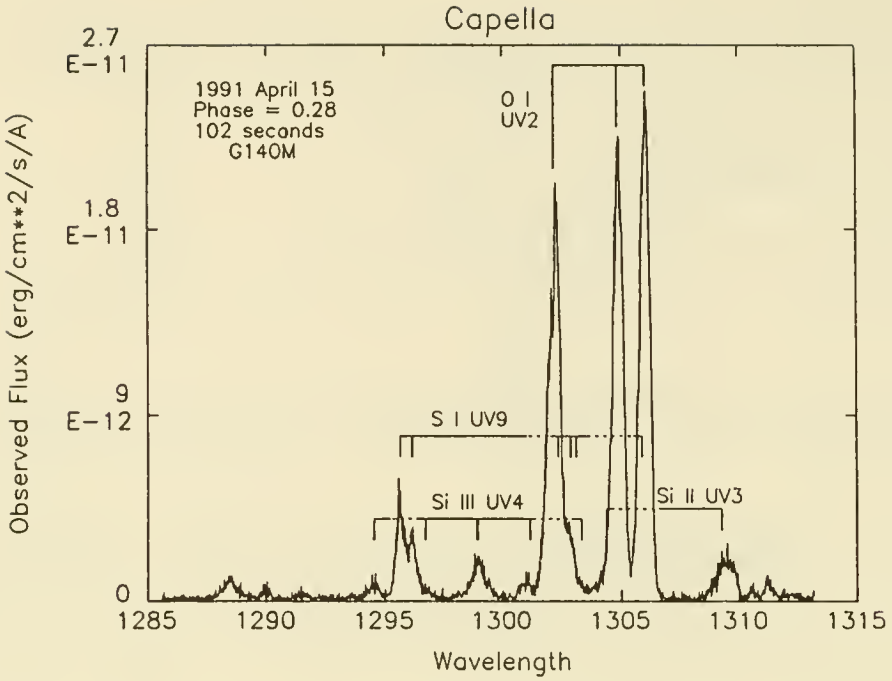

Figure 9.: A GHRS moderate dispersion spectrum of Capella obtained with the G140M grating. The Si III lines are density sensitive.

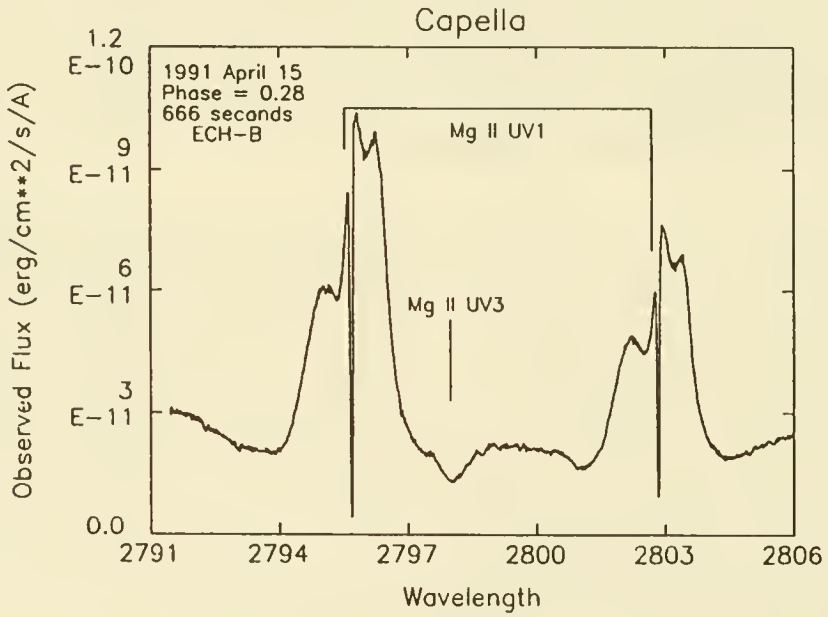

Figure 10.: A GHRS high-dispersion spectrum of Capella obtained with the Ech-B grating. Each of the Mg II resonance lines (2796 and 2803 Å) shows the narrow interstellar absorption line and self-reversed emission from the G5 III star (to the right) and the G0 III star (to the left).

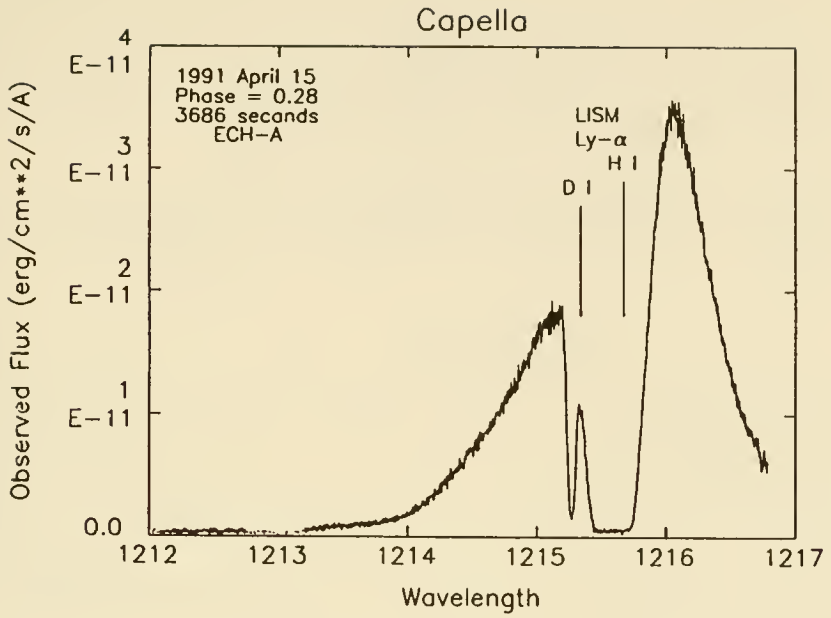

Figure 11.: A GHRS high-dispersion spectrum of Capella obtained with the Ech-A grating. Superimposed on the stellar Lyman-α emission line is interstellar absorption due to hydrogen and deuterium.

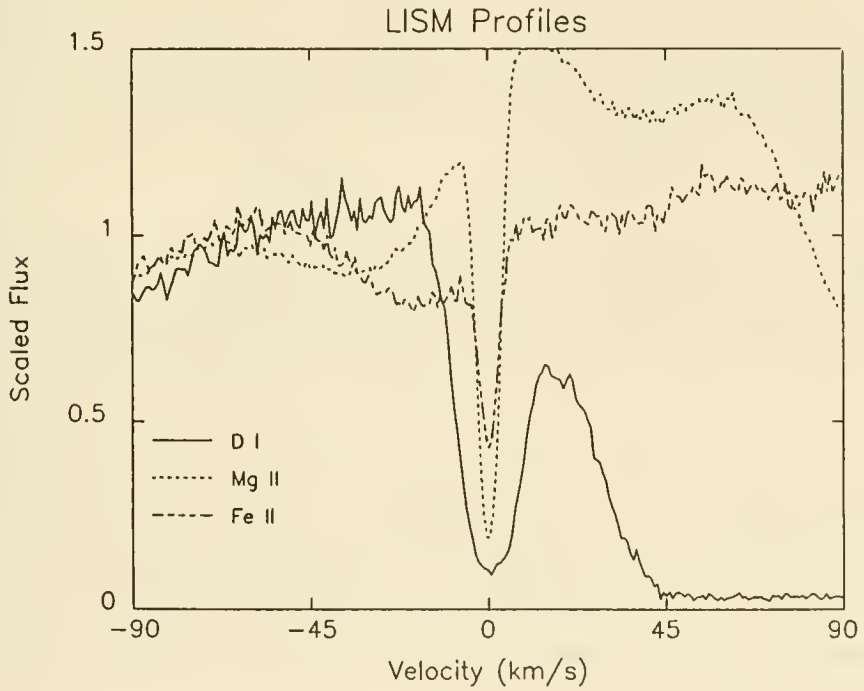

Figure 12.: Comparison of the interstellar absorption lines of deuterium, Mg II, and Fe II on a common velocity scale.

Figure 12 compares the interstellar absorption lines of Mg II h, Fe II 2600 Å, and deuterium on a common wavelength scale. Since the D and Fe ions differ by a factor of 28 in mass, the different line widths provide a means for separating thermal from turbulent broadening. There appears to be only one velocity component in this line of sight, but we are investigating whether the dip at the center of the deuterium line may indicate a second cooler velocity component. When the instrumental properties of the GHRS are better understood, we will publish what we hope will be a definitive value for the D/H ratio and interstellar properties for this line of sight.

This work is supported by NASA Grant S-56500-D to the National Institute of Standards and Technology. We wish to thank Tom Ayres for his suggestions.

REFERENCES

Ayres, T. R. 1984, *Ap. J.*, **284**, 784.
Ayres, T. R. 1986, *Ap. J.*, **308**, 246.
Ayres, T. R. 1988, *Ap. J.*, **331**, 467.
Ayres, T. R., Marstad, N. C., and Linsky, J. L. 1981, *Ap. J.*, **247**, 545.
Ayres, T. R., and Linsky, J. L. 1980, *Ap. J.*, **241**, 279.
Ayres, T. R., Moos, H. W., and Linsky, J. L. 1981, *Ap. J. (Letters)*, **248**, L137.
Ayres, T. R., Simon, T., and Linsky, J. L. 1982, *Ap. J.*, **263**, 791.
Batten, A. H., Hill, G., and Lu, W. 1991, *Pub. A.S.P.*, **103**, 613.
Brown, A., Jordan, C., Stencel, R. E., Linsky, J. L., and Ayres, T. R. 1984, *Ap. J.*, **283**, 731.
Byrne, P. B., Doyle, J. G., Brown, A., Linsky, J. L., and Rodono, M. 1987 *Astr. Ap.*, **180**, 172.
Carpenter, K. G., Robinson, R. D., Wahlgren, G. M., Ake, T. B., Ebbets, D. C., Linsky, J. L., Brown, A., and Walter, F. M. 1991, *Ap. J. (Letters)*, **377**, L45.
Cuntz, M. 1987, *Astr. Ap. (Letters)*, **188**, L5.
Cuntz, M. and Luttermoser, D. G. 1990, *Ap. J. (Letters)*, **353**, L39.
Drake, S. A., Brown, A., and Linsky, J. L. 1984, *Ap. J.*, **284**, 774.
Fontenla, J. M., Avrett, E. H., and Loeser, R. 1991, *Ap. J.*, **377**, 712.
Haisch, B. M., Linsky, J. L., Weinstein, A., and Shine, R. A., 1977, *Ap. J.*, **214**, 785.
Hartmann, L., Dupree, A. K., and Raymond, J. C. 1980 *Ap. J. (Letters)*, **236**, L143.
Linsky, J.L. 1990, in *Active Close Binaries*, ed. C. Ibanoglu (Dordrecht: Kluwer Academic), p. 747.
Linsky, J. L., Worden, S. P., McClintock, W., and Robertson, R. M. 1979, *Ap. J. Suppl.*, **41**, 47.
Murthy, J., Henry, R. C., Moos, H. W., Vidal-Madjar, A., Linsky, J. L., and Gry, C. 1990, *Ap. J.*, **315**, 675.
Neff, J. E., Walter, F. M., Rodono, M., and Linsky, J. L. 1989, *Astr. Ap.*, **215**, 79.
Simon, T., Linsky, J. L., and Stencel, R. E. 1982, *Ap. J.*, **257**, 225.
Vilhu, O. 1987, in *Cool Stars, Stellar Systems, and the Sun*, ed. J.L. Linsky and R.E. Stencel (Berlin: Springer-Verlag), p. 110.
Wahlgren, G. M., Leckrone, D. S., Shore, S. N., Lindler, D. J., Gilliland, R. L., and Ebbets, D. C. 1991, *Ap. J. (Letters)*, **377**, L41.

HIGH RESOLUTION UV SPECTROSCOPY OF THE CHEMICALLY PECULIAR B-STAR, CHI LUPI

David S. Leckrone
NASA, Goddard Space Flight Center

Sveneric G. Johansson
Department of Physics, University of Lund

Glenn M. Wahlgren
Astronomy Programs, Computer Sciences Corporation

Abstract. Science assessment observations of the bright, ultra-sharp-lined B-peculiar star, chi Lupi, with the GHRS have provided an ultraviolet spectrum of unprecedented detail and photometric accuracy. The observed profile of the resonance line of Hg II at 1942 A confirms the reality and extreme nature of the Hg isotope anomaly in this star. In the surrounding 10 A spectral interval we observe for the first time lines of Ru II, As I, Ge II and Zr III. The data provide an ample demonstration of the inadequacies of the currently available atomic data base for the quantitative interpretation of high resolution ultraviolet spectra.

1. INTRODUCTION

In the preceeding papers Rolf Kudritzski and Jeff Linsky have treated, respectively, the hot, massive OB stars with their powerful winds and turbulent atmospheres, and the cool, late-type stars with their convective envelopes and dynamic chromospheres. In this discussion we are concerned with the "lukewarm" stars in the intermediate effective temperature range between about 8500 K and 15,000 K, whose stable photospheres we observe for the express purpose of deriving accurate elemental abundances.

This interval of B and A spectral types constitutes an important "cut" through the HR diagram. It includes "normal" B and A dwarfs, whose main-sequence lifetimes are only a few hundred million years. Abundances derived for such stars presumably represent the composition of the interstellar medium, from which the stars formed, at a much more recent epoch than do solar abundances. Thus, they provide more suitable reference values, for example for studies of abundance depletion in the present interstellar gas, than do solar abundances. This temperature interval also includes a small number of relatively bright, highly evolved Population II field stars, which closely resemble blue horizontal branch stars in globular clusters. Elemental abundances determined for some species in these field horizontal branch (FHB) stars reflect the results of CNO processing and dredge-up on the red giant branch. For most elements, however, abundances provide a direct measurement of the composition of the interstellar medium at a very early epoch of galactic evolution.

Of primary interest for this paper are the 10 to 20 % of B and A main-sequence stars that are classified as "chemically peculiar" (CP) stars. There are two, apparently unrelated, sequences of such stars - those which possess magnetic fields, and those which do not. The nature and origin of the spectroscopic

anomalies in these stars has been an enigma for nearly a century (e.g. Lockyer and Baxandall 1906). The high resolving power and photometric integrity of the HST/GHRS offers the opportunity for a major advancement in our understanding of these bizarre objects.

The normal B and A stars, CP stars and FHB stars are apparently "well-behaved" subjects for analyses utilizing classical, LTE, plane-parallel model atmospheres and the associated spectral synthesis techniques. They are too hot to have convective photospheres and too cool to have significant winds, turbulence or mass loss. They emit sufficient ultraviolet flux to allow efficient UV spectroscopy down to Lyman-alpha. However, the derivation of meaningful elemental abundances for such stars may be complicated by processes of radiatively-driven diffusion, leading to chemical fractionation and an inhomogeneous radial distribution of the various ions present in their highly stable photospheres. It is this physical process, involving a competition between gravity and radiation pressure, that is currently the most widely accepted explanation for the peculiar abundances measured for the CP stars. It is a primary objective of our GTO program with the GHRS to critically test the quantitative predictions of diffusion models, as well as to evaluate alternative possibilities.

Access to ultraviolet wavelengths is critical to this work. Their is a paucity of lines in the visible spectra of B and A dwarfs, and only a small sample of the periodic table is represented in studies which rely on ground-based spectroscopy alone. At UV wavelengths one can observe numerous intrinsically strong lines of low-abundance elements. Combining UV and optical-wavelength spectra gives one access to transitions from multiple ionization states and to resonance or low-excitation lines, which minimizes the possibility of large systematic errors due to departures from LTE. Finally, the rich UV absorption line spectra of these stars provides both a challenge and an opportunity for atomic physics. Absorption-line spectra of singly or doubly ionized elements are essentially impossible to observe in the laboratory, but are easily observed in the stars. We demonstrate in this paper that in trying to quantitatively interpret the strengths of the UV transitions we have observed, we are pushing contemporary knowledge of atomic structure to its limits.

The following sections present the salient properties of our target, chi Lupi, and describe two scientific investigations - 1. an attempt to independently confirm the reality and magnitude of the isotope anomaly in Hg, first detected in ground-based observations of a single line, Hg II λ3984, and 2. a search for lines of elements whose abundances are unknown from optical-wavelength spectra. The former represents an important step prior to our extensive GTO program to thoroughly investigate the abundance and isotope anomalies in Hg, involving observations of strong resonance or low excitation UV transitions of Hg I, Hg II and Hg III in several stars. The latter begins the process of "filling in" the periodic table in order to systematically study the patterns of abundance anomalies from element to element as well as from star to star.

2. PROPERTIES OF chi Lupi

The target star for our observations, chi Lupi, is ideally suited to the purposes of the Science Assessment Program, that is to demonstrate the capabilities of the HST and GHRS in the presence of a severely aberrated point spread function. In addition to being bright (V = 3.9), so that integration times could be kept relatively short, chi Lupi possesses an exceedingly sharp-lined absorption spectrum containing a complex assortment of lines ranging from very weak to strong. Thus, it provides a good vehicle with which to assess the resolving power and effective S/N ratio of the GHRS. That chi Lupi is among the most sharp-lined of early-type stars results from its low projected rotational velocity, v sin i < 1.2 km/sec (Dworetsky and Vaughan 1973) and a "classical" microturbulent velocity parameter = 0.0 km/sec (Adelman, et al. 1991, in preparation). Chi Lupi is a double-lined spectroscopic binary. The primary has T_{eff} = 10,650 K, log g = 3.8, while for the secondary T_{eff} = 9,200 K, log g = 4.2. Near 1940 A, the wavelength region of interest here, the primary-to-secondary light ratio in the continuum is about 6.6. We see lines of the secondary in our observation, but they are generally very weak.

Chi Lupi is one of the more extreme members of the non-magnetic sequence of chemically peculiar stars of the "HgMn" class. Both ground-based and IUE spectra indicate that Mercury is approximately 100,000 times overabundant in chi Lupi's photosphere, with respect to the solar-system value, although it must be noted that the abundance of Hg in the solar system is itself poorly known (e.g. Leckrone 1984). Platinum appears to be about 10,000 times overabundant (Dworetsky, et al. 1984).

As mentioned previously, the shape and position of Hg II λ3984 suggests that Hg in chi Lupi's photosphere is dominantly in the form of ^{204}Hg, the heaviest isotope of Hg (White, et al. 1976). For comparison, only 7% of the Hg in the normal terrestrial isotope blend one finds in a thermometer is ^{204}Hg. Similarly, it appears that the heaviest isotopes of Pt are also overabundant in chi Lupi. The mercury anomalies are particularly important. Any physical model which seeks to explain the origin of the abundance anomalies in CP stars must be able simultaneously to reproduce a huge absolute overabundance of Hg and an extreme abundance distribution of the Hg isotopes in the line forming region of chi Lupi's atmosphere. Early attempts to create such theoretical models, based on radiatively-driven diffusion, may be found in Michaud, et al. (1974). To test these models, we must compare the strengths of lines from three ionization states, Hg I, II and III, in chi Lupi and in other Hg-rich stars of various effective temperatures. And to do that requires ultraviolet spectra of high quality. The present Science Assessment observations serve the additional purpose of providing an essential check on these seminal results, obtained from Hg II λ3984, prior to the commitment of further HST time to the extensive study of the Hg anomaly.

3. THE OBSERVED SPECTRUM

Figure 1 illustrates a GHRS Echelle spectrum of chi Lupi, centered on the Hg II resonance line at 1942.3 A. These Science Assessment data were obtained on

February 11, 1991. The 0.25 arcsec small science aperture (SSA) of the instrument was used for the observation. This transmitted the central peak of the OTA point spread function into the spectrograph, while rejecting the broad PSF "skirt", which results from spherical aberration. Consequently, the resolving power of the GHRS anticipated prior to launch ($\lambda/\delta\lambda \simeq 87{,}000$) is achieved in this mode, but with efficiency reduced by about a factor of four compared to pre-launch expectations. The total integration time was 2278 sec. To achieve proper sampling, the spectrum was quarter-stepped across the detector's diode array, so that one quarter of the total integration time was devoted to each of 2000 sample points in the spectrum. The S/N ratio per sample point near the continuum is approximately 100. The 1942.3 A Hg II line is plainly visible near the center of the displayed spectrum. Perhaps of even greater interest is the complex and remarkably detailed array of absorption lines seen in the surrounding 10.4 A interval.

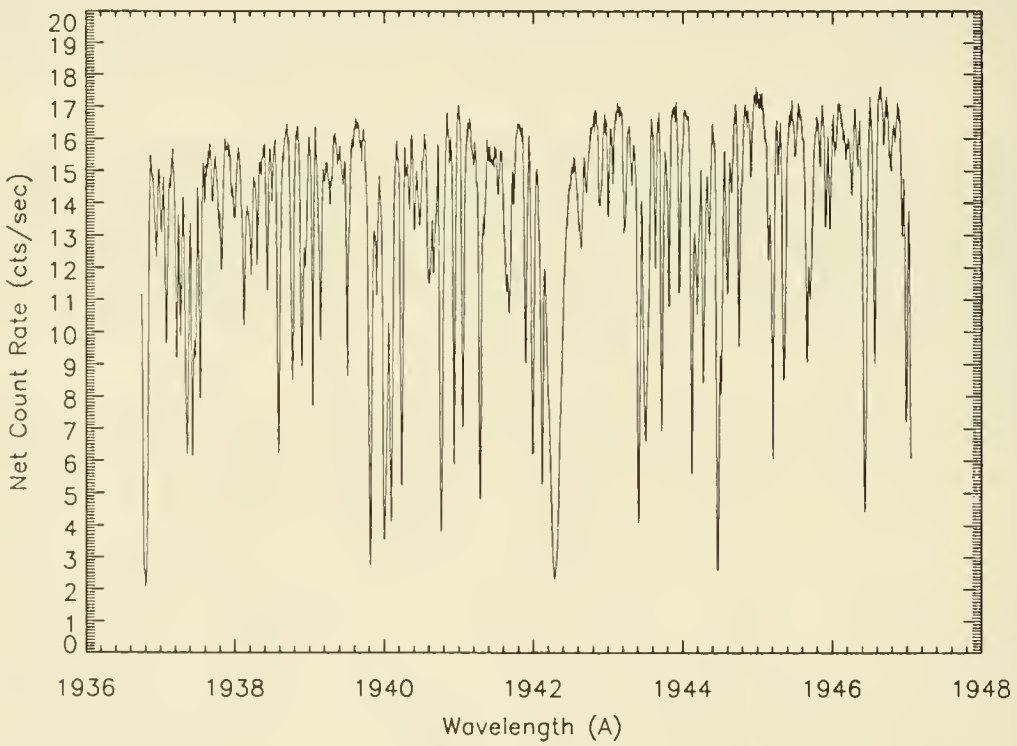

Figure 1. GHRS Small-Science-Aperture Echelle spectrum of chi Lupi, centered on the resonance line of Hg II at 1942.3 A.

4. THE MERCURY ANOMALY

In Figure 2 we have "zoomed in" on a one Angstrom segment of the spectrum, containing the Hg II line. The observed line profile has a well defined shape and appears to be relatively free of distortions due to blends. Figure 3

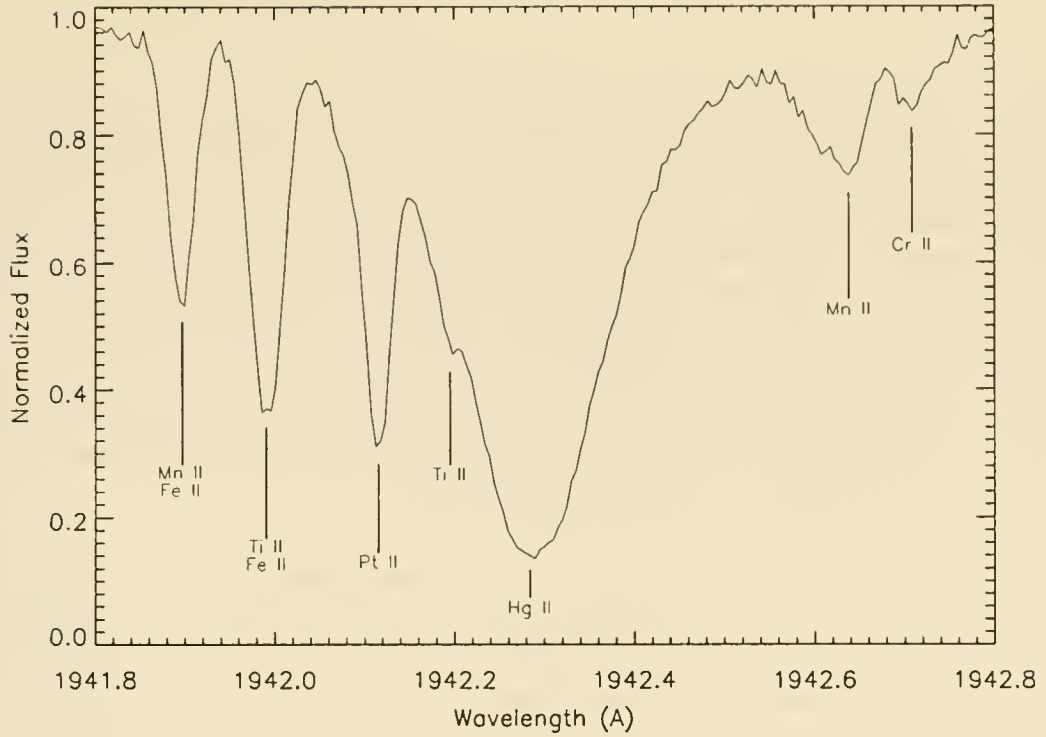

Figure 2. Profile of the Hg II λ1942.3 resonance line in chi Lupi, observed with the GHRS.

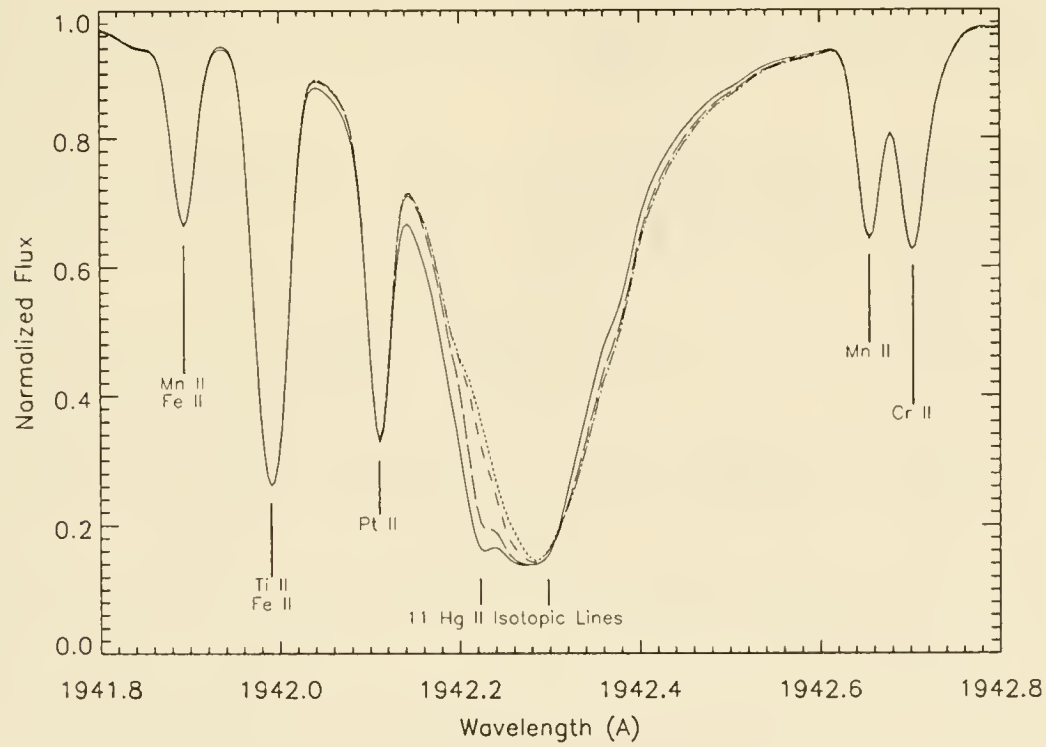

Figure 3. Theoretical profiles of Hg II λ1942.3, calculated for various mixtures of Hg isotopes. Solid - q = 0.0 (solar mix), long dashes - q = 1.0, medium dashes - q = 2.0, short dashes - q = 3.0 (value estimated from Hg II λ3984).

shows our theoretical spectrum calculations for this same interval. The Hg II line is in fact a composite of eleven individual isotopic and hyperfine components of diverse strength, with central wavelengths ranging from 1942.2240 to 1942.2994 A. For convenience we have chosen to calculate various isotope blends using a one-parameter model defined by White, et al. (1976). The logarithmic isotope mix parameter, q = 0.0 for the terrestrial blend of Hg isotopes. This corresponds to the solid curve in Figure 3. White, et al. estimated q = 3.0 for chi Lupi, based on their observations of Hg II λ3984. This case, plotted with small dashes in Figure 3, corresponds to a mixture made up of about 99% ^{204}Hg, about 1% ^{202}Hg, and tiny traces of the other isotopes. Two intermediate cases (q = 1.0 and 2.0) are also plotted in the figure. Our purpose in Figure 3 is to demonstrate that the shape, width and central wavelength of the Hg II λ1942 profile are sensitive to variations in the relative abundances of the Hg isotopes.

We can now simply superpose the observed and theoretical Hg II profiles, as shown in Figure 4. It is clear from this comparison that the mixture of isotopes in the line-forming region of chi Lupi's photosphere deviates

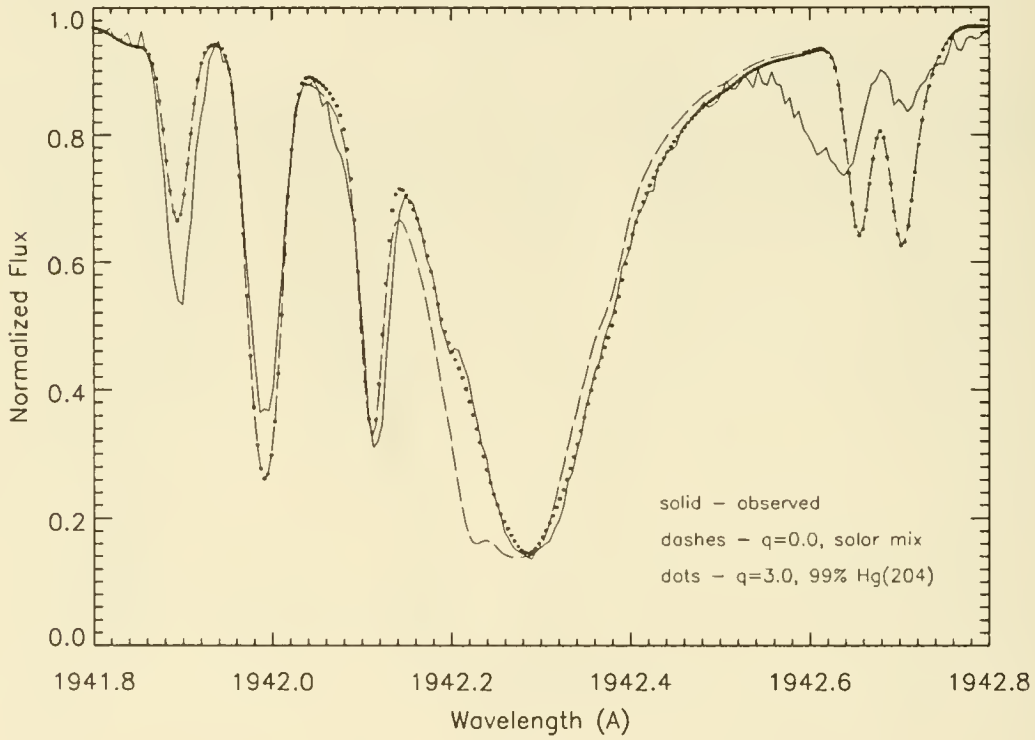

Figure 4. Comparison of observed and theoretical profiles of Hg II λ1942.3.

strongly from the solar-system isotope blend. The isotope anomaly is both real and extreme. The observed profile is reasonably well matched by the theoretical model with q = 3.0, but in fact is indistinguishable from the case of pure ^{204}Hg, to within the observational uncertainties. The one-parameter model used to describe the isotope mixture is somewhat arbitrary (although it has an empirical basis described by White, et al.). It must be emphasized,

however, that we are unable to define any alternative mixture of Hg isotopes that would lead to an equally good fit to the observed profile.

The fit to the observed Hg II profile is not perfect. In particular, we are unable to compute a profile which is quite as narrow as the observed one. Also, there are significant departures from a good fit at the deepest part of the line core. It is possible that we are observing subtle evidence that mercury is not homogeneously distributed, but is concentrated in higher, cooler atmospheric layers. A more sophisticated, non-LTE model atmosphere and rigorous treatment of the radiative transfer problem in the high photosphere are also called for. Details of the analysis of the Hg II λ1942 feature can be found in Leckrone, Wahlgren and Johansson (1991).

5. "FILLING IN" THE PERIODIC TABLE

The abundances of approximately eighteen chemical elements have been "reliably" determined from optical-wavelength spectra of chi Lupi's photosphere. For the present discussion we loosely define a "reliable" abundance as one that is based on at least two spectral lines that give more or less the same answer. In only six cases are abundances from ground-based data derived from lines of more than one ionization state of a particular element. Thus, in most cases it is difficult to assess the magnitude of systematic errors due to departures from LTE in the ionization equilibria. So we know relatively little about the patterns of elemental abundances in chi Lupi. We only know, on the basis of the study of a few elements, that its abundances are extremely anamalous in some cases.

It has been a long-standing objective of Space Astrophysics to remedy this kind of problem by extending the observations to ultraviolet wavelengths where one can find many intrinsically strong lines of trace elements and of ionization states which are not well represented in the visible. Of course the instruments flown on Copernicus and on the IUE have allowed considerable progress to be made. But as one can see in Figure 5, with the HST and GHRS we have stepped into a new, largely unexplored spectroscopic universe. The comparison shown here between an IUE high resolution spectrum of chi Lupi and the GHRS Echelle observation is not intended to belittle the capabilities of the IUE. The latter observatory has been and will continue to be an immensely important tool for astrophysics. Instead, the comparison illustrates a new capability, not available before from any instrument. The S/N ratio ($\simeq$ 15) of this single IUE observation could be improved perhaps to 40 or 50 by coadding multiple IUE images, obtained with the star properly offset in the IUE large aperture. However, the resolving power in the IUE observation cannot be improved beyond what is shown here. The GHRS observation of chi Lupi is, we believe, the most detailed ultraviolet spectrum of any star obtained to date, except perhaps for the Sun.

In the 2 A interval shown in Figure 5 are several examples of elements or ionization states seen for the first time. These include Zr III, As I, Ru II, and Ge II. Lines of Zr II are observed in ground-based spectra of chi Lupi and other CP stars, but Zr II is the minority ionization state, sensitive to departures from LTE. We have identified three well-resolved and unblended

lines of Zr III, the majority ionization state, in the observed 10.4 A interval.

We attribute the weak feature observed near 1937.6 A to As I λ1937.594, on the basis of close wavelength coincidence and the lack of any other candidates at that wavelength. Our wavelength scale registration is accurate to 1-2 mA (see discussion in Leckrone, et al. 1991). Moreover, only a small number of features in the 10.4 A interval do not have solid identifications. We will have to search for lines of Arsenic at other UV wavelengths to be certain of this identification. However, if verified, we believe this is the first detection of Arsenic in any star, including the sun.

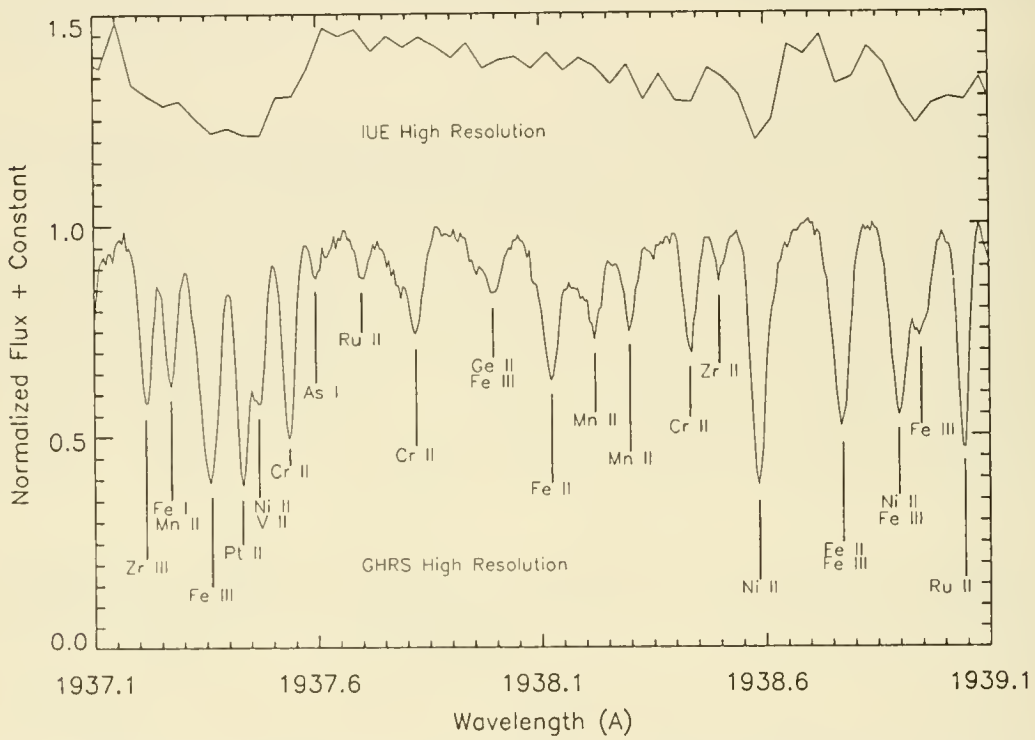

Figure 5. Comparison of IUE and GHRS Echelle observations of chi Lupi

The observed feature near 1938.0 A is, we believe, about a 50-50 blend of Ge II λ1938.007 and Fe III λ1937.990. A companion Ge II line in this resonance multiplet, at 1938.890 A, is unresolved from the blend with Ni and Fe lines seen in Figure 5. Thus, we must also look elsewhere in the UV to confirm the identification of Ge II. A few Ge I lines have been identified in the solar spectrum. But the present observations, if confirmed, constitute the first detection of Ge II, and hold out the promise that we will be able to derive Ge abundances in the sharp-lined early-type stars.

The detection of five well-resolved lines of Ru II in our 10.4 A interval is particularly exciting. Two of these lines are seen in Figure 5. Ru I is seen in the optical-wavelength spectrum of the sun and other late-type stars. Ruthenium is found to be about two orders of magnitude overabundant in the late-type, "heavy metal" or S stars, where it is a component of the s-process

neutron capture chain that leads to formation of the unstable element Technetium (see e.g. Wallerstein 1984). With the GHRS we now have the ability to measure the abundance of Ru in CP and other early-type stars. In chi Lupi Ru also is about two orders of magnitude overabundant, as we shall show in the following section. Given that models of the production of the abundance anomalies in CP stars based on nucleosynthesis are now very much out of favor, we are reluctant to suggest that the overabundance of Ru in chi Lupi results from recent s-processing, as it does in the S stars. However, prudence dictates that one should check the UV spectrum of chi Lupi for the lines of Tc II, and we plan to do so.

We also see in Figure 5 a moderately strong line of Pt II near 1937.4 A. Our spectrum of chi Lupi contains many line of Pt I and II. This should not have come as a surprise, since the star's photosphere is overabundant in Pt by a factor of 10^4, and given the well-known richness of the Pt spectrum in the ultraviolet. After all, we use Pt lamps as wavelength calibration standards on GHRS, FOS, IUE and other space instruments. But it is nevertheless interesting to see in the absorption line spectrum of chi Lupi a mirror image of the emission line spectrum produced by the GHRS Wavecal lamp.

6. THE ATOMIC DATA PROBLEM

The line density in the spectrum illustrated here is obviously high. The dominant contributors are transitions from the second spectra of the iron group elements, V, Cr, Mn, Fe and Ni. To accurately synthesize the spectrum, using codes such as Kurucz's SYNTHE routine, one needs comprehensive and accurate atomic data - wavelengths, transition probabilities, and line broadening parameters for all transitions which make a noticeable contribution to the line opacity in the observed wavelength interval. Even the spectra of ions which are not of direct astrophysical interest are important, because their lines may be blended with those of other species of primary scientific interest. Their inclusion in the calculated synthetic spectra facilitates the accurate estimation of the level of the line-free continuum. Moreover, a large number of unidentified lines, produced for example by iron group ions, would add great confusion to the process of identifying lines produced by rarer and more interesting elements.

The massive library of atomic data, calculated by Kurucz (1991) using the Cowan Code, provides the only reasonably comprehensive database with which one can begin to quantitatively interpret complex UV spectra. Although Kurucz has calculated data for over 50 million iron-group transitions, fewer than 2% of these involve atomic energy levels which have been accurately measured and classified, using laboratory spectra. It is this relatively small subset of transitions that have accurate enough wavelengths in the Kurucz database to be useful for computing synthetic spectra. Kurucz's library also includes compilations of transitions, calculated or measured, for elements both lighter and heavier than the iron group.

We now face a dilemma, an extreme example of which is illustrated in Figure 6. In this plot of 1.2 A of chi Lupi's spectrum there is virtually no agreement between the observed spectrum and the theoretical spectrum, calculated with

the Kurucz atomic data base. This is a problem both with the completeness of the atomic database and with our knowledge of atomic structure, level mixing and configuration interactions.

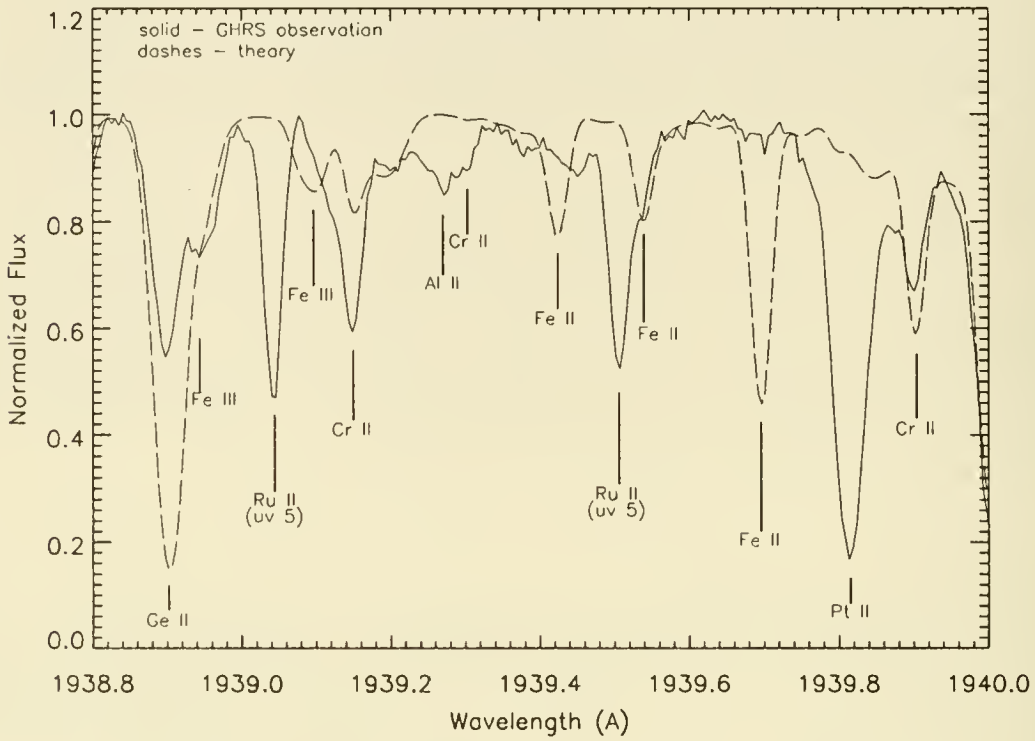

Figure 6. First attempt to theoretically synthesize a 1.2 A spectral interval of chi Lupi, using atomic data from most recent Kurucz calculations.

Kurucz has not yet included data for Ru or Pt, so that no calculated features appear at the wavelengths of these lines. He did include a "guess" for the transition probability of the Ge II line, apparently based on relative laboratory line intensities. This estimated gf-value is obviously much too large.

We see an extremely anomalous calculated Fe II feature near 1939.7 A. The transition is b $^2P_{1/2}$ - w $^2D_{3/2}$. Whenever we encounter Fe II transitions which involve this upper level, whether in analysing GHRS or IUE data, the Kurucz gf-values seem to be badly in error. We believe this results from the difficulties in accurately treating the mixing of closely coincident atomic levels in the Cowan Code calculations. In this case the Kurucz calculations produce a short-range perturbation between w $^2D_{3/2}$ and w $^2P_{3/2}$ which is not verified by laboratory line intensities. Less extreme examples of the same problem are seen in the two Cr II lines, λλ 1939.149, 1939.902, one of which is calculated much too weak and the other somewhat too strong.

There are also "simple" problems of wavelength accuracy. For example, the wavelength of the calculated Fe III line at 1939.105 A should now be increased by 10 mA, based on new measurements of the Fe III spectrum by J. Ekberg at the

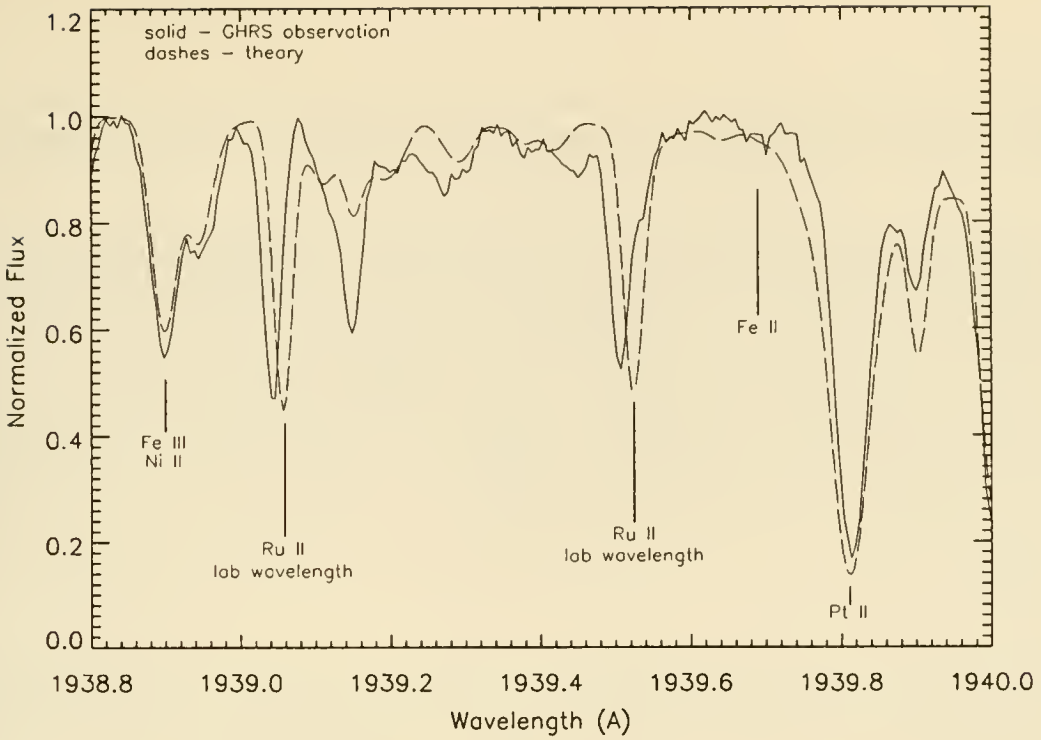

Figure 7. Improved spectrum synthesis, using published wavelengths for lines of Ru II.

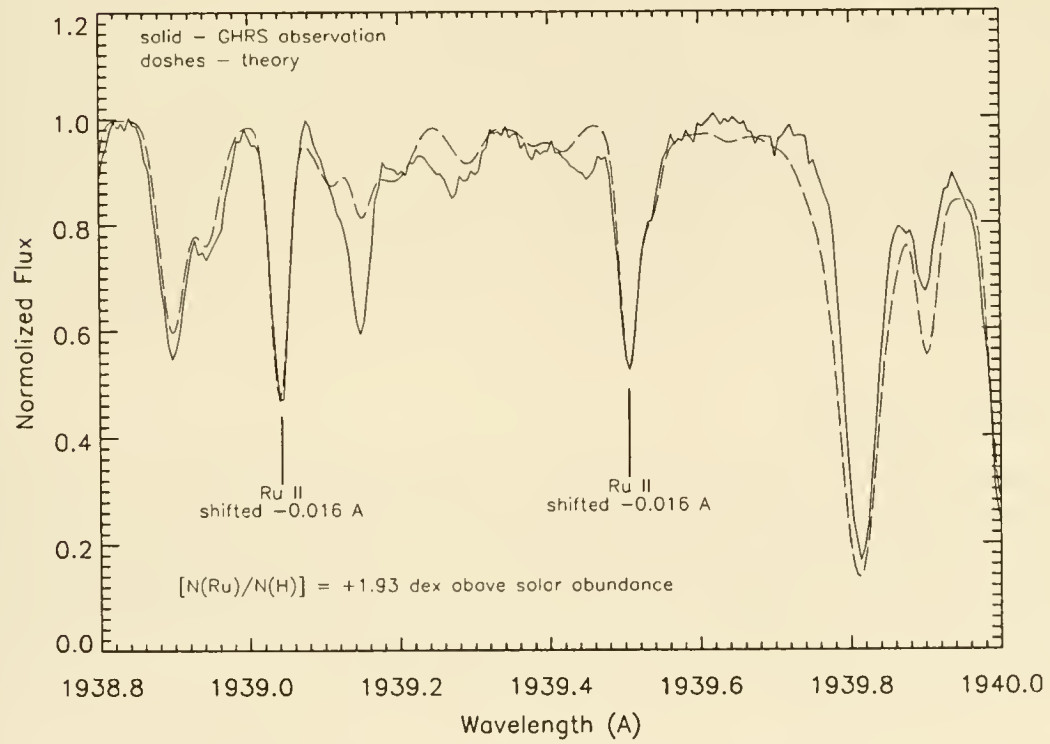

Figure 8. "Final" spectrum synthesis with calculated Ru II lines arbitrarily shifted by -0.016 A. Ruthenium is about 2 dex more abundant in chi Lupi's atmosphere than in the sun.

University of Lund. Such an apparently minor adjustment makes the difference between a clear discrepancy, and reasonable agreement, between theory and observations at the position of the Fe III line.

In Figure 7 we illustrate the first effort to resolve some of these problems. We obtained improved estimates for the transition probability of the Ge II λ1938.890 line, using calculated values for Si II, which is homologous with Ge II and checking these with measured values for other lines in the same multiplet in Ga I, which is isoelectronic with Ge II. These two approaches yield consistent values of log gf ≃ -3.6, instead of the value, 0.0, "guessed" in the Kurucz database. We added Pt lines to the database, with transition probabilities from Cowan-Code calculations for the classified transitions. As shown in Figure 7, the result is slightly too strong for the Pt II line near 1939.8 A. We simply eliminated the super-anomalous Fe II line at 1939.698 A from the calculation. And we shifted Fe III λ1939.1 to its refined laboratory wavelength.

Of special note in Figure 7 are the two lines of Ru II (UV multiplet 5). We estimated transition probabilities for these lines using the Cowan Code, and in fact these calculations converged to the measured log gf-values for the corresponding transitions of Fe II, which is homologous with Ru II. As shown in Figure 7, the calculated relative line strengths are approximately correct and the relative spacing of the two lines in wavelength corresponds to that observed in the stellar spectrum. However, the absolute laboratory wavelengths (which come from Shenstone and Meggers 1958) differ from those observed in the stellar spectrum by 16 mA. In fact all five well-resolved Ru II lines observed in our 10.4 A interval are shifted from their published laboratory wavelengths by -0.016 A. We do not know whether this discrepancy reflects a calibration problem in the laboratory measurements or an astrophysical phenomenon. New measurements of the Ru II spectrum will soon be made at Lund, using the new Fourier Transform Spectrometer there. For purposes of estimating the Ruthenium abundance in chi Lupi, however, we have simply shifted all of the calculated Ru II lines by -0.016 A. The result is illustrated in Figure 8. On this basis we conclude that Ru is overabundant by about 2 dex in chi Lupi relative to the solar value.

7. CONCLUDING REMARK

We cannot say at this moment whether the discovery of a particular, previously unobserved species, such as Ruthenium, Arsenic or Germanium, will ultimately provide the decisive clue about the origin of the truly bizarre abundance anomalies observed in stars such as chi Lupi. These new GHRS data do illustrate vividly, however, that with superb resolution and S/N ratios, we are beginning to realize the full potential of UV space spectroscopy as originally envisioned by its pioneers decades ago.

REFERENCES

Dworetsky, M.M., & Vaughan, A.H., Jr. 1973, ApJ, 181, 811.
Dworetsky, M.M., Storey, P.J., & Jacobs, J.M. 1984, Phys. Scripta, T8, 39.
Leckrone, D.S. 1984, ApJ, 286, 725.
Leckrone, D.S., Wahlgren, G.M., & Johansson, Se. G. 1991, ApJ, 377, L37.
Lockyer, N., & Baxandall, F.E. 1906, Proc. Roy. Soc. (London), 77, 550.
Michaud, G., Reeves, H., & Charland, Y. 1974, A & A, 37, 313.
Shenstone, A.G., & Meggers, W.F. 1958, J. Research Nat. Bur. Std., 61, 373.
Wallerstein, G. 1984, J. Opt. Soc. Am. B, 1, 307.
White, R.E., Vaughan, A.H., Jr., Preston, G.W., & Swings, J.P. 1976, ApJ, 204, 131.

Hubble Space Telescope Optical Performance

Christopher J. Burrows[1]

Space Telescope Science Institute, 3700 San Martin Drive
Baltimore, Maryland 21218, USA

ABSTRACT

The Hubble Space Telescope suffers from spherical aberration. Although much that is scientifically valuable can be done with the telescope in its present condition, we must install corrective optics on-orbit in order to enable many key programs. An analysis of imaging data obtained on-orbit gives the same results as measurements on the null lens used to fabricate and test the primary mirror, so such optics can be designed with confidence. The assumed conic constant on the primary mirror for all the corrective optics, -1.0139(5), is consistent with measurements by four major independent methods. Aligning the new optics will be very demanding, because of the large slope of the wavefront to be corrected. If the images are to be diffraction limited, the pupil at the corrective element must be aligned to better than one percent of its diameter. Some other residual effects of the spherical aberration will remain after installation of the corrective optics, primarily in the pointing and collimation of the telescope. We summarize the present imaging performance of the observatory, and compare it with the expected performance when corrective optics (COSTAR and WFPC 2) are installed on-orbit.

2. INTRODUCTION

This is a general review of the status of and prospects for the Hubble Space Telescope (HST) optics, and the current and projected imaging performance of the observatory, written one year into the mission. Despite the spherical aberration, HST is now routinely producing high resolution images and spectra. Nevertheless its performance is seriously degraded relative to expectations. It has almost completed an extensive commissioning period, made more difficult by the spherical aberration, so now is a good time to review what we have learned, and where we are going. We concentrate here on the optical performance of the various observatory subsystems. The scientific results have been discussed extensively elsewhere, [1,2] and in these proceedings. The present optical imaging performance, and pointing control system performance are generally well understood.[3] We choose not to repeat information given in (3). Instead, we concentrate on giving the reader some additional background on the imaging performance and how it can be modelled. We concentrate here on understanding

---

[1]Affiliated with the Astrophysics Division, Space Science Department of the European Space Agency.

physically the current imaging performance and compare it with the expected performance which should be substantially attained after the planned servicing mission.

The HST will be serviced on orbit with a shuttle visit presently scheduled for November 1993. At that time, the bulk of the problems caused by the spherical aberration will be fixed. That mission will involve the most ambitious on orbit satellite repair ever undertaken. It will probably include replacement of the solar panels, gyros, the High Speed Photometer and the Wide Field/ Planetary camera (WFPC). The solar panels are affecting the pointing performance primarily during terminator transits because thermal gradients across the bistem array supports are causing them to rapidly bend and then oscillate. There are also impulsive torques on the spacecraft at other times due to stiction in the tensioning mechanisms. One of six rate gyro assemblies failed after nine months on orbit. A second gyro has failed, and a third has shown evidence of possible failure since the workshop. The Faint Object Camera (FOC), Faint Object Spectrograph and High Resolution Spectrograph will probably be largely corrected by a replacement for the High Speed Photometer, COSTAR. COSTAR is designed to deploy corrective optics in front of the scientific instrument apertures.[4] Finally, but most critically, the Wide Field Planetary Camera (WFPC) which is the main scientific instrument of the observatory will be replaced by a similar instrument with internal correction.

3. MEASUREMENT OF SPHERICAL ABERRATION

In order for the corrective optical schemes to work, the spherical aberration must be precisely characterized. None of the schemes presently contemplated allows for on-orbit adjustment of the amount of compensating spherical aberration that they introduce. Measuring the amount of spherical aberration to the precision required has been a major challenge. It has been determined from historical optical test data, from recent measurements on the test equipment and from on orbit measurements with both the main cameras. Remarkably, these methods all agree to within about 1/45 wave, which is sufficient for the corrective optics. The loss of encircled energy in a 0.1 arcsecond radius resulting from such an error is only about 2%.

The on-orbit determination of the spherical aberration has evolved from low order phase aberration least squares fitting procedures (which were used to originally diagnose the spherical aberration), to involved procedures involving simultaneous solutions to the pupil phase map and pupil obscurations at three different focal settings as reported by Roddier in these proceedings. Many groups have developed such techniques but we only discuss our results here. The wavefront fitting procedure was first developed and applied within days of the WFPC first light images in May 1990. Since then it has evolved considerably by including the secondary mirror support spiders, primary mirror support pads and field dependent WFPC internal obscurations (which are misaligned in an unexpected but determined manner). The algorithm works best on well sampled out of focus images at long wavelengths with good pointing stability. Such images have been obtained in both the PC and FOC. Given the pupil

obscurations[3], the image is determined in the Fraunhofer approximation once the distribution of phase errors on the wavefront in the exit pupil is fixed. These errors can be expanded in a series of orthogonal polynomials, and the coefficients deduced by a least squares fit to the observed data at various focus positions. The rms wavefront error expressed in waves at 632.8 nm is converted to a change in the conic constant on the primary mirror by dividing by 35.3. (This factor is correct rather than the 36.03 one naively deduces by doubling the sag on the mirror primarily because the reflected ray does not exactly retrace its path). Our result is that the conic constant on the primary mirror is 1.01410(45), from fifteen measurements in the planetary camera (PC6), after subtracting a correction of 0.0010 due to a manufacturing error in the camera. The FOC gives 1.01394(85) from four measurements and no significant camera aberrations are believed to contribute. Figure 1 shows a comparison of an observed star image in PC6 with filter F547M at a focus setting close to the telescope paraxial focus, with the results from phase retrieval. These same techniques are now being applied to the telescope collimation, and should be applied to generate theoretical point spread functions at the adopted focus position for use in deconvolution.

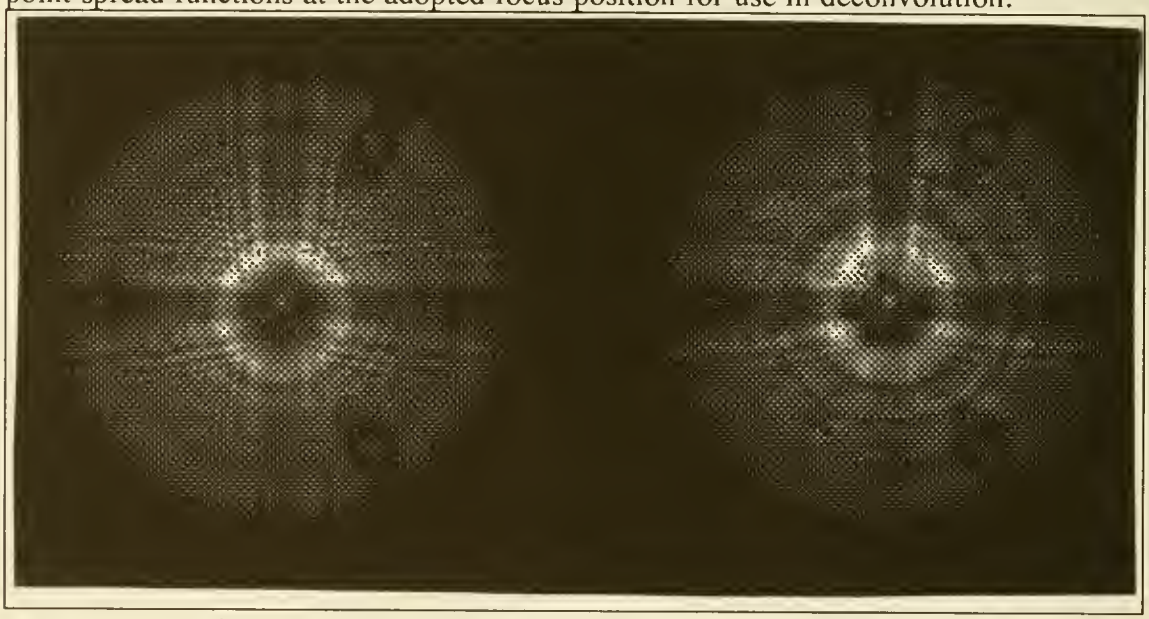

Figure 1 Comparison of fits to data for defocussed images

The on-ground determination at Hughes, Danbury (formerly Perkin Elmer) has proceeded by recertifying the null lens used in their manufacture of the primary mirror. The combination of null lens and primary mirror was designed to reflect a spherical wave exactly back on itself as illustrated in Figure 2. The autocollimated wavefront from the assembly as built was measured with an interferometer, and changes were made to the figure of the primary mirror in order to get straight fringes. As a result errors in the construction of the null caused a corresponding error in the primary, and recertifying the null now comes close to a direct measurement of the primary mirror figure. The null consists of two spherical mirrors, which reimage the interferometer focus onto the center of curvature of the HST primary, and introduce

most of the required optical path changes, together with a refractive field lens that images the interferometer pupil onto the primary mirror

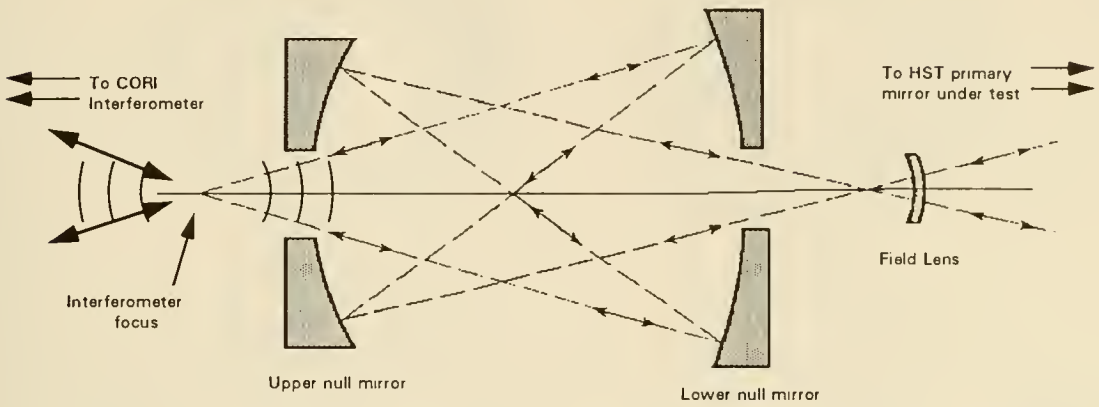

Figure 2. The null lens used in the manufacture of the HST primary mirror

The field lens positioning error primarily responsible for the spherical aberration in HST has now been measured as 1.305 mm and the cause of the error is believed to be understood[5]. In addition the two mirrors in the null lens have been remeasured as separated by an amount that differs from the design by 79 microns. This is also a significant error, and has recently been explained by measurements of the null mirror radii, which are in error by about the correct amount to explain the discrepancy, given the way they were positioned. The original spacing was set from the centers of curvature, while the recent measurement was from the surface vertices. After the remeasurement of the mirror radii, the reflective null lens data indicate that the conic constant on the primary is 1.01378(31).

Finally, a less precise (but more accurate!) refractive null lens was made that was used in place of the reflective null early in the testing. Archival interferograms from the period when the mirror was polished with this null indicate a conic constant of -1.01314(60). There is reason to believe that the secondary mirror was made correctly.

Figure 3 summarizes the status of all the above primary mirror conic constant estimates. All the measurements agree quite closely with the adopted value of 1.0139(5) which is being used in the design of the corrective optics. The nominal conic constant for the primary is -1.0022985. The difference between these values corresponds to an RMS wavefront error of -0.410 waves at 633 nm, and the edge of the primary is 2.2 microns too low. (which can be compared to its nominal sag relative to a sphere of 0.2mm)

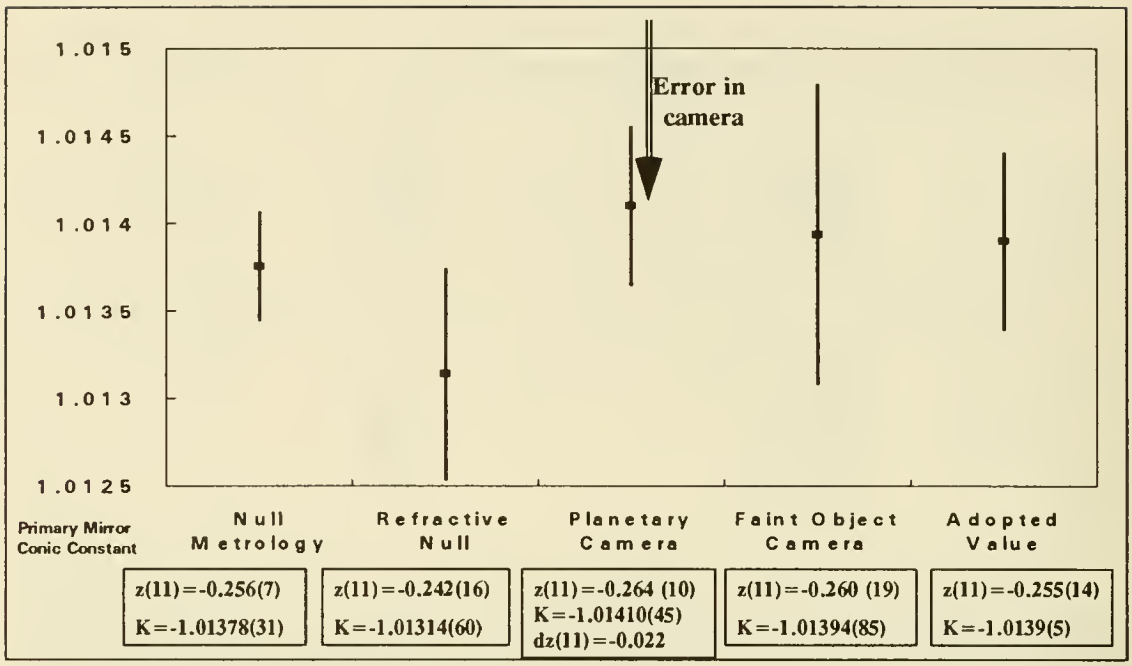

Figure 3. Estimates of the HST primary mirror conic constant.

4. CORRECTIVE OPTICS ERRORS

Because of the accuracy of our knowledge of the spherical aberration, on-orbit compensation for errors in the prescription is not planned. On the other hand, there are extremely tight positional tolerances for the corrective optics which will necessitate on-orbit centering adjustments. The reason for this is as follows. All the corrective schemes being pursued involve reimaging the primary mirror on to a corrective element which has exactly the opposite deformation to the primary mirror error. Thus the optical path delays at the edge of the pupil introduced by the primary mirror that presently cause marginal rays to focus 40 mm too far back are cancelled by compensating advances introduced by the corrective optic. The compensating term varies as the fourth power of the pupil radial position, and therefore changes rapidly near the edges. Slight misalignments then lead to large amounts of wavefront perturbation proportional to the derivative of the aberration (coma), and to the amount of misalignment. If the system is misaligned by as much as one percent, it will cease to be diffraction limited. A seven percent misalignment (which is about equal to the misalignments in the existing WFPC) would lead to as much RMS coma as we presently have in spherical aberration. Of course, the misalignments in the existing camera would not have significantly damaged the image quality, if the OTA wavefront had been nominal. Similarly, the scale of the pupil image must be right. If it is in error by 2 percent, we again fail to be diffraction limited. These issues are illustrated in Figure 4.

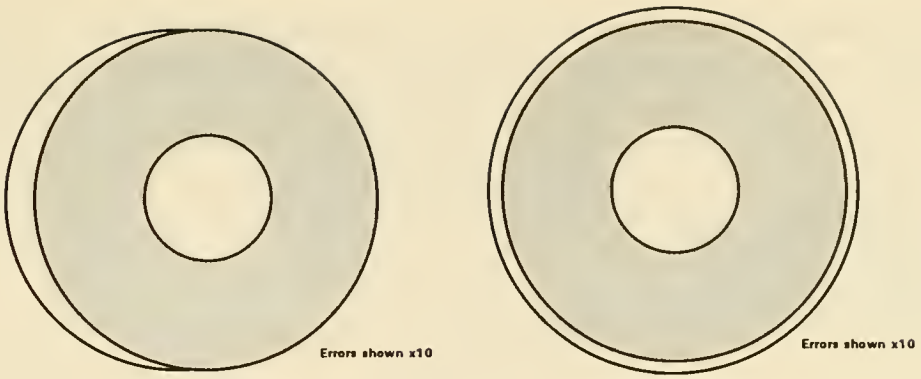

One percent diameter misalignment of the image of the primary mirror on the corrective optic gives 7/100 waves rms of coma.

Two percent diameter error of the image of the primary mirror on the corrective optic gives 7/100 waves rms of spherical.

Figure 4. Sensitivity of corrective optics to misalignments and scale errors.

5. GUIDING PERFORMANCE

The servicing mission will probably not include changeout of the three Fine Guidance Sensors (FGS). These detectors are affected by the spherical aberration both in their coarse track and fine lock modes but for different reasons. Each FGS consists of a large pickoff mirror that takes a quadrant of the field between 10 and 14 arcminutes off axis and directs the beam onto an aspheric collimating element. The beam is then steered by two sets of moveable prisms onto a beamsplitter and thence to one of two orthogonal Koesters prism interferometers. The faces of the Koesters prisms are reimaged onto photomultiplier tubes with square 5 arcsecond field stops.

In coarse track the field of the four PMT in a given FGS is nutated around the star image, so that the system works somewhat like a quadrant detector. Performance is degraded because the star image is aberrated, so the image on the field stops is not sharp. The result is that the pointing performance is degraded by about 2 magnitudes. It still scales at the square root of the number of photons, but the rms jitter expected for 14.5 magnitude guidestars of 20 milliarcseconds is only realized for 12.5 magnitude guidestars.

In fine lock the performance is limited by the transfer function of the interferometers. Because of the presence of misalignments in the FGS, the beam is not exactly centered on the Koesters prism at interferometer null. This would not affect performance appreciably in the absence of spherical aberration from the OTA, but the fringe visibility is drastically reduced by the position dependent phase errors that result.

Operational changes to planning, scheduling and pointing control system control loop gains are being made to mitigate the degraded performance of the FGS, and solar array

induced jitter. For bright stars, we have excellent pointing stability in fine lock away from terminator transitions. The changes are making such performance possible on fainter (and therefore more common) guide stars, and avoiding loss of lock at the terminator. However, it is not expected that acceptable fine lock performance will be achieved on stars with visual magnitudes fainter than about 13.5, so coarse track (with its associated larger pointing errors) will continue to be the only available guiding mode over much of the sky.

6. TELESCOPE COLLIMATION

The Optical Control System (OCS), contains a set of three radial shearing interferometers (WFS), one in each FGS. They were designed to collimate the telescope (ensure that the optical axes of the hyperbolic primary and secondary mirrors coincide). They do not work because of the spherical aberration. There is always some zone on the primary mirror with such a rapid rate of change of the wavefront that the fringe separation in the instrument is smaller than the instantaneous field of view of the image dissector tubes, so the fringe visibility drops. In principle, they therefore can only accurately measure aberrations with significant angular dependence (such as astigmatism), but are poor when measuring aberrations that only have radial dependences (such as focus and spherical aberration), or that have angular dependences that look like wavefront tilt over any narrow annulus (such as coma). As a result the present collimation of the telescope was set by tilting the secondary mirror until the camera images were symmetrical and decentering it (with compensating tilts) until the OCS indicated zero astigmatism.

Hughes Danbury and Pierre Bely at STScI have independently modelled the FGS in fine lock, and are able to predict the effects of differing telescope collimation on the FGS transfer functions. The results to date indicate that the performance of the FGS can be significantly improved at least for FGS 1 and 3, but at the cost of the images in the WFPC and FOC. Now that the effects of collimation on FGS performance are better understood, and the effort to numerically understand the spherical aberration is completed, the collimation will be revisited with a view to improving the FGS performance while compromising the camera images as little as possible. To this end, a systematic study of the phase retrieval results at numerous secondary positions is underway, together with a sequence of dedicated HST observations to perform a 'coma sweep'. So far, results from both cameras seem consistent, and it is believed that the telescope has been operating with about 1/15 wave of coma. Improved knowledge of the collimation can be used to generate better theoretical point spread functions.

6. IMAGING PERFORMANCE

The Science Working Group (SWG) has defined the focus setting of the secondary mirror to be used for HST observations by requiring that it gives the maximum encircled energy in 0.1 arcseconds radius for the FOC at 486 nm. Figure 5 shows a series of theoretical encircled energy curves as a function of focus setting, assuming the nominal conic constant. In practice the encircled energy is lower than these curves

indicate primarily because of microroughness scatter from the mirror surfaces, but the shape of the curves seems to agree with observations.

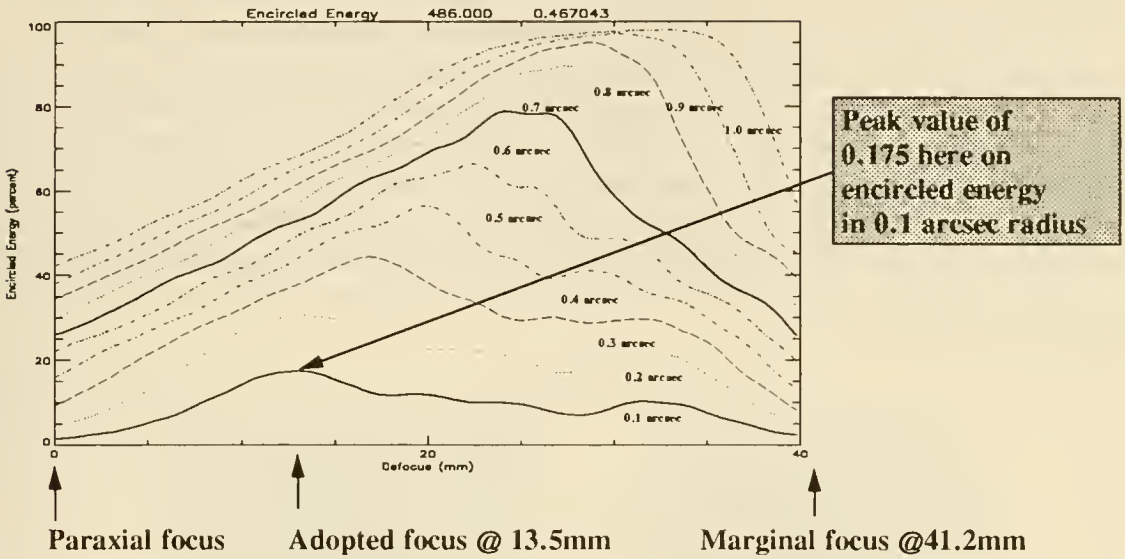

Figure 5. Predicted Encircled energy for the FOC as a function of focus position.

The peaks in the curves shift towards the paraxial focus as the wavelength is decreased. In the limit of short wavelengths, (neglecting microroughness), we get the ray trace limit which can be written in closed form, and is an adequate approximation for some purposes. The transverse aberration of a ray at fractional pupil coordinate x(with $0.33 < x < 1$) is then $T_m(x^3\text{-}xd)$, where T_m is the transverse spherical aberration, of a marginal ray in the paraxial focal plane (about 3.07 arcseconds), and d is the defocus as a proportion of the longitudinal spherical aberration - d is 0.327 at the SWG focus. At this focus, the geometric image radius is obtained by setting $x=1$ and comes out as 2.07 arcseconds. Further it is easy to see that the zone of the mirror that geometrically is in focus is at $x = 0.572$. From the fact that the effective aperture contributing to the core is roughly 2/3 the expected size,one might predict that the core would be about 50% broader than expected, and detailed diffraction calculations confirm this intuition. Specifically, the FWHM at 633 nm is 75 milliarcseconds, instead of 53 milliarcseconds, and it is proportional to wavelength to a reasonable approximation. (At longer wavelengths it oscillates somewhat about the linear trend due to interference phenomena, remaining constant between 850 and 950 nm for example.)

The WFPC differs slightly from the FOC in that the reimaging cameras contain secondary mirrors that obscure part of the center of the beam, and also contain about 1/30 wave of extra spherical aberration. The result is that the encircled energy curve for a 0.1 arcseconds radius aperture is shifted by 3.7 mm further from the paraxial focus, and the encircled energy at the SWG focus is about 12% instead of a possible peak value of 17%. The central obscuration in the cameras moves in a predictable way from ray trace calculations, although it is not centered at the center of each chip as one

might expect from the optical design. The result is that star images change in a predictable way as one changes field position. An example is shown in Figure 6 which compares predicted and observed PSFs at several field positions in PC6 through filter F547M. The theoretical predictions are parameter free being based entirely on the known pupil function of the camera, the measured spherical aberration of the OTA and the SWG focus definition. Obviously one could improve the agreement further by introducing known misalignments in the telescope (primarily coma), and modelling the measured phase errors on the primary and secondary mirrors. This work is ongoing, and hopefully will lead to better simulated PSFs for deconvolution purposes. In the meantime, a library of PSFs with the above nominal parameters has been produced by at the STScI, using the TIM software. Both the library and the software are available to interested researchers on request.

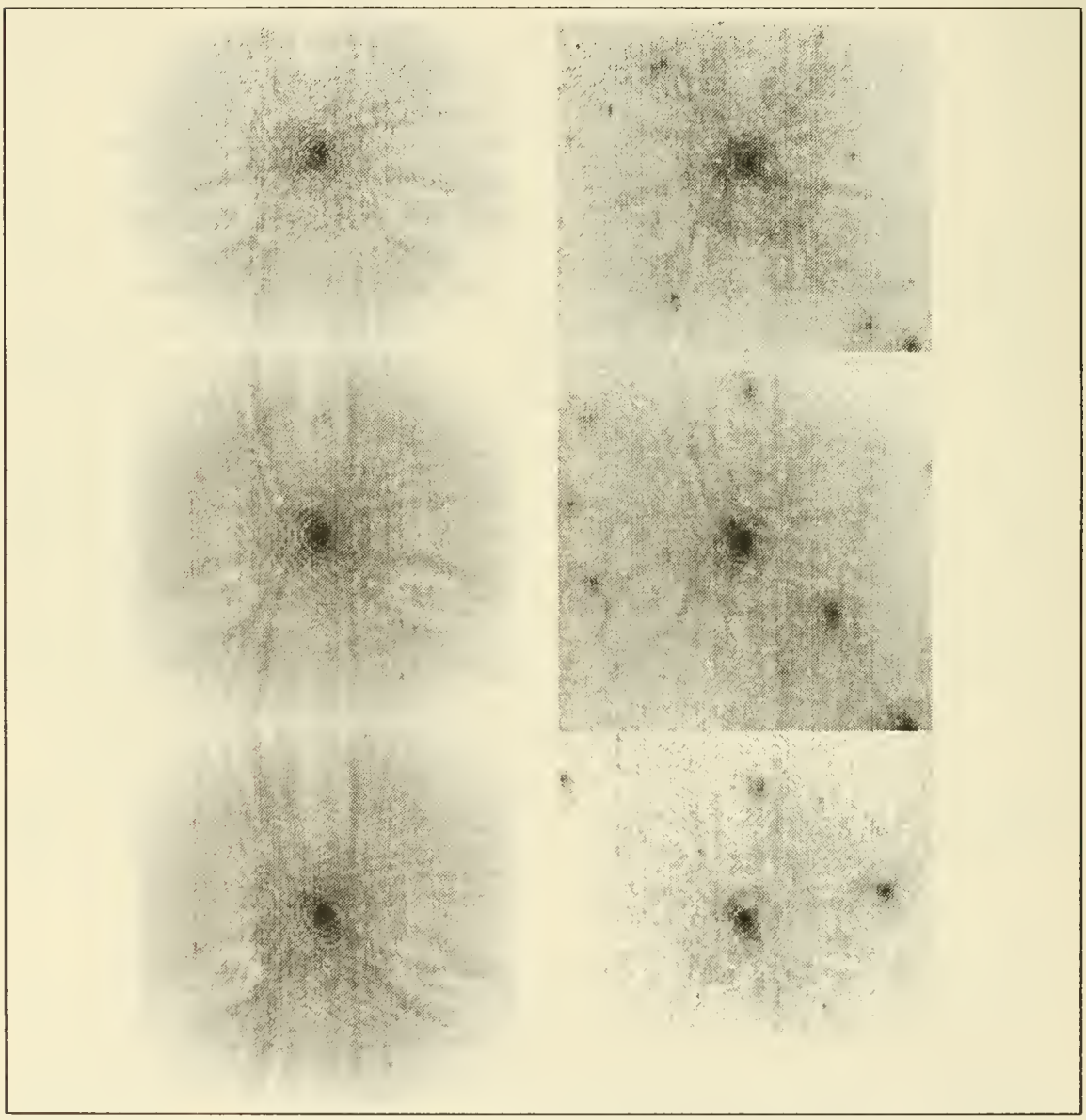

Figure 6 Comparison of predicted and observed PSFs at several field positions in PC6

7. REFERENCES

1. Astrophysical Journal (Letters) 369 (1991) (all papers)
2. Bulletin of the American Astronomical Society Vol 22 pp 1275-1284 (1990) (Abstracts to session 49 of the January 1991 AAS meeting)
3. Burrows, C.J. et al. "The imaging performance of the Hubble Space Telescope" Astrophysical Journal (Letters) 369, 21 (1991)
4 Brown, R. A. and Ford, H.C (Editors) " Report of the HST strategy panel" , Space Telescope Science Institute special publication (1991)
5. Allen, L. et al. "The Hubble Space Telescope optical systems failure report" NASA publication (November 1990)

INTRODUCTION TO THE GODDARD HIGH RESOLUTION SPECTROGRAPH (GHRS)

John C. Brandt

Laboratory for Atmospheric and Space Physics
University of Colorado
Boulder, CO 80309-0392
USA

The principal presentation on the Goddard High Resolution Spectrograph (GHRS, née HRS) and its status will be made by Dr. Dennis Ebbets in the following paper. This introduction presents the GHRS from the perspective of the Preliminary Design Review (PDR), which began on December 12, 1978. Some archival research has uncovered my notes and viewgraphs[1] from the "kickoff" talk for that meeting. Here, I review the materials presented at the PDR and comment where appropriate.

First, GHRS is very much a team effort requiring the cooperation of scientists, engineers, technicians, programmers, and support personnel. Because the scientific investigations to be carried out are from a variety of astronomical disciplines, the Science Team is large. It originally consisted of twelve members and now numbers sixteen; see Table 1.

Table 1
The GHRS Investigation Definition Team

John Brandt (PI) – University of Colorado, Boulder
Sara Heap (Co-PI) – Goddard Space Flight Center
Edward Beaver – University of California, San Diego
Albert Boggess – Goddard Space Flight Center
Kenneth Carpenter – Goddard Space Flight Center
Dennis Ebbets – Ball Aerospace
John Hutchings – Dominion Astrophysical Observatory
Michael Jura – University of California, Los Angeles
David Leckrone – Goddard Space Flight Center
Jeffrey Linsky – Joint Institute for Laboratory Astrophysics
Stephen Maran – Goddard Space Flight Center
Blair Savage – University of Wisconsin, Madison
Andrew Smith – Goddard Space Flight Center
Laurence Trafton – University of Texas, Austin
Frederick Walter – State University of New York, Stony Brook
Ray Weymann – Observatories of the Carnegie Institution of Washington

The areas of intended scientific investigation were summarized by the PDR viewgraphs shown in Figure 1. These objectives dictated an ultraviolet instrument (wavelength range ≈ 1100-3200Å) with the instrumental capabilities given by PDR viewgraph shown in Figure 2. We wanted to attempt a simple approach and design; see Figure 3. The GHRS has one major moving device, the "Carrousel," which is used to position the various gratings and acquisition mirrors.

MAJOR SCIENTIFIC OBJECTIVES

1. THE INTERSTELLAR MEDIUM
   - Very Local Gas in the Interstellar Medium
   - Molecule Formation and Selective Depletion of Heavy Elements in Dense Clouds
   - By Studying Distant Stars' Spectra, Determine Composition & Distribution of the Gas in Adjacent Spiral Arms, Galactic Halo, and Magellanic Clouds
   - Search for as Yet Undetected Simple and Very Complex Molecules in Space
2. MASS LOSS BY STELLAR WINDS AND THE EVOLUTION OF THE OUTER ATMOSPHERES OF STARS
   - OB Supergiants in the Magellanic Clouds
   - Coronal Winds in Late-Type Stars
   - Mass Loss, Chromospheres, Circumstellar Shells in Red Giants
   - Mass Transfer in X-Ray (& Other) Binary Stars
3. ABUNDANCES OF THE ELEMENTS AND STELLAR EVOLUTION
   - Abundances in Stars with Wide Age Range to Determine Chemical Evolution of the Galaxy
4. EXTRAGALACTIC SOURCES
   - Limited But Important Quasar Studies
   - Physical Investigation of Nuclear Regions of Seyfert Galaxies
5. THE SOLAR SYSTEM
   - Atmospheric Structure in Jovian Planets and Their Satellites
   - Auroral Activity on the Planets
   - Abundance of Deuterium in Comets

Fig. 1 - Summary of the scientific objectives for the GHRS.

DESIGN DRIVERS

- Ultraviolet Response - 1100Å - 3200Å
- Spectral Resolution - $R = 2 \times 10^4$ (15 km/s)
  $R = 1.2 \times 10^5$ (2.5 km/s)
- High Sensitivity
- High Photometric Precision
- Angular Resolution - none within field of view

Fig. 2 - Summary of the desired instrumental capabilities for the GHRS.

The detectors chosen were the 512-channel Digicons with (1) a LiF/CsI faceplate/photocathode combination for short-wavelength response and long-wavelength rejection; and (2) a MgF_2/CsTe combination for long-wavelength response. The Digicons have a very high dynamic range (~ 10^8).

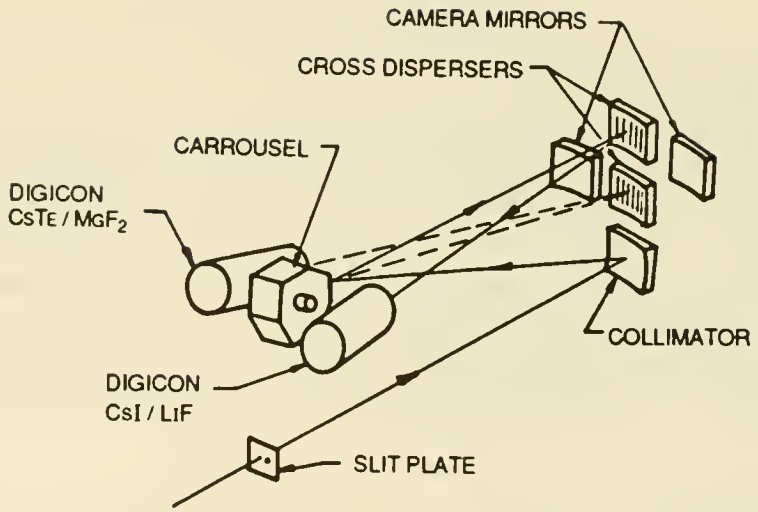

Fig. 3 - Cartoon of the GHRS.

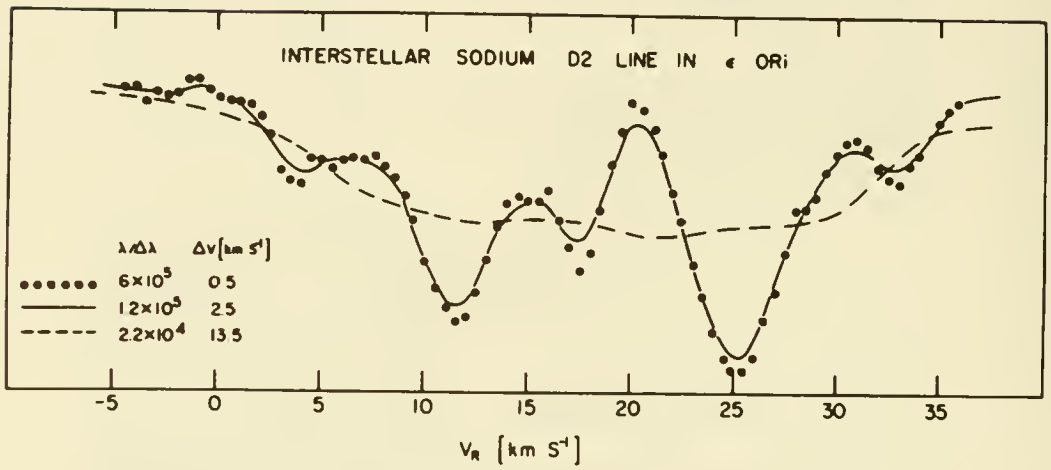

Fig. 4 - The interstellar D2 line at different spectral resolutions; the observations at R = 6 x 10^5 are from Hobbs (1969).

The R = 2 x 10^4 mode uses four first-order gratings. The highest-resolution mode uses an echelle grating and cross dispersers; it became the R ≈ 1.0 x 10^5 mode (instead of the R = 1.2 x 10^5 mode) when the desired echelle could not be fabricated. A replica of a grating was substituted. Finally, note that our R = 2 x 10^3 mode is not mentioned. At the time of PDR, it was in the design stage but not yet approved. We envisioned it as a reconnaissance mode and as a useful backup to the FOS in the wavelength range 1100-1750Å.

At the time of the PDR, we wished to stress that the inclusion of an R = 1.0 x 10^5 mode was not arbitrary. To establish this point, we showed (see Figure 4) the spectrum of the interstellar sodium D2 line at various values of R. This value of this inclusion has been completely confirmed.

The PDR presentation discussed some further details of the instrument, made comparisons with previous spaceborne ultraviolet instruments, and concluded with a summary of an instrument with major scientific capabilities. (Recall that the scientific instruments were originally selected provisionally and were subject to later confirmation). Some of these capabilities have survived the HST spherical-aberration problem intact.

Specifically, my PDR notes contain the assertions of a "... powerful instrument above the atmosphere" that "should produce a huge variety of astrophysical results and discoveries!" Even allowing for the "puffing" of a selling environment, things have turned out surprisingly well, as evidenced by the GHRS early results papers already in press.[2]

Notes

1. Some of these materials were from our original proposal, " A High Resolution Spectrograph for the Space Telescope," HRS-680-77-01, July 1977.

2. Ap J. Letters, **377**, No. 1, 10 August 1991 issue.

STATUS OF THE GODDARD HIGH RESOLUTION SPECTROGRAPH IN MAY 1991

Dennis Ebbets
Ball Aerospace Systems Group
PO Box 1062 AR1
Boulder, CO 80306

John Brandt
LASP University of Colorado
Campus Box 391
Boulder, CO 80309

Sara Heap
NASA Goddard Space Flight Center
Code 680
Greenbelt, MD 20771

Abstract. At the time of this workshop the Orbital Verification of the GHRS had been completed, and the Science Verification was well under way. This presentation summarized the state of our knowledge about HST pointing accuracy, target acquisition procedures, sensitivity, spectral resolution, stray and scattered light, wavelength calibration, photometric precision and time resolution.

1. ACCURACY OF INITIAL HST POINTING

In January, and again in February, 1991, a GHRS to FGS "Fine Alignment Test" was performed, whose goal was to measure the location of the GHRS science apertures in the coordinate system defined by the FGSs. The test executed properly, the expected data were obtained and analyzed, and the positions of the apertures were updated. Since that update there have been 22 successful target acquisitions, all of which found the star within +/-3 arc seconds of the initial pointing. Thirteen targets were found within +/- 1 arc second, including all 9 for which the celestial coordinates had been measured with the GASP system at STScI. It now appears that the geometrical alignments between the science instruments and the pointing control system are accurate enough to support routine target acquisitions. We recommend that observers use GASP coordinates whenever possible, and SAO positions for brighter targets. It is important to be careful about such details as Equinox (1950 or 2000), proper motions, and the epoch of the proper motion. When specifying a GHRS target acquisition, we recommend the use of "search-size=3" with GASP coordinates, and "search-size=5" otherwise. Figure 1 shows a histogram of initial pointing errors compiled between February and April 1991.

2. TARGET ACQUISITION OPTIONS

Three types of acquisitions have been exercised and found to work well. We have used "interactive acquisitions" with great success. The GHRS commands the HST to execute an outwardly growing spiral search pattern, and generates a "field map" of the 2x2 arc sec

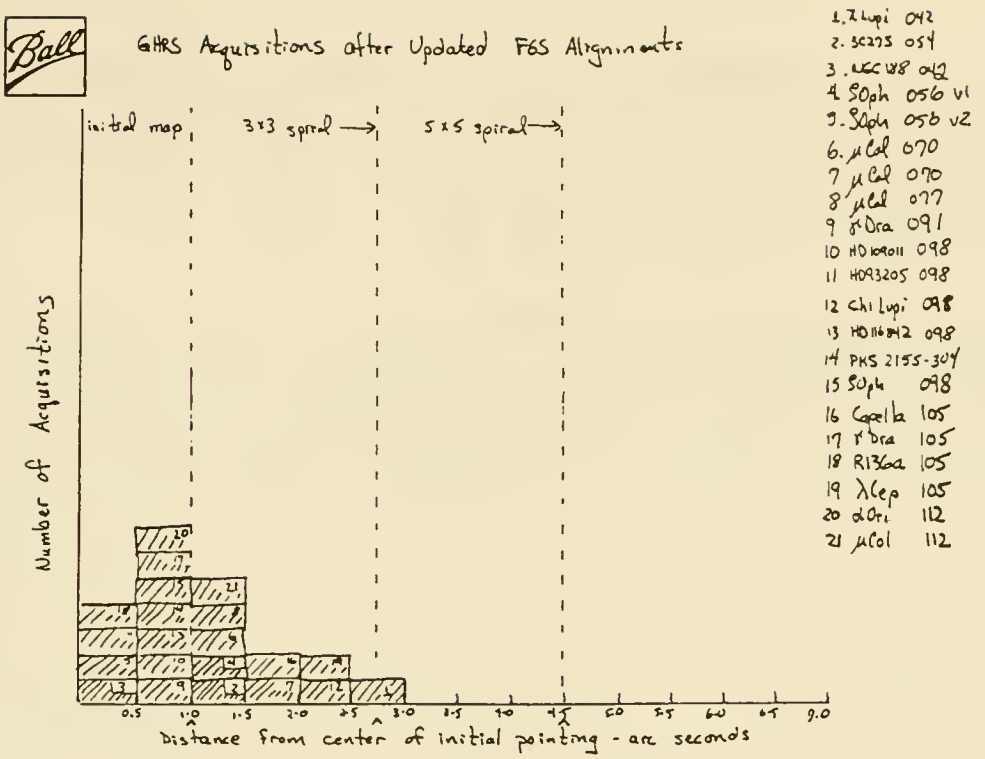

Figure 1. Accuracy of initial telescope pointing

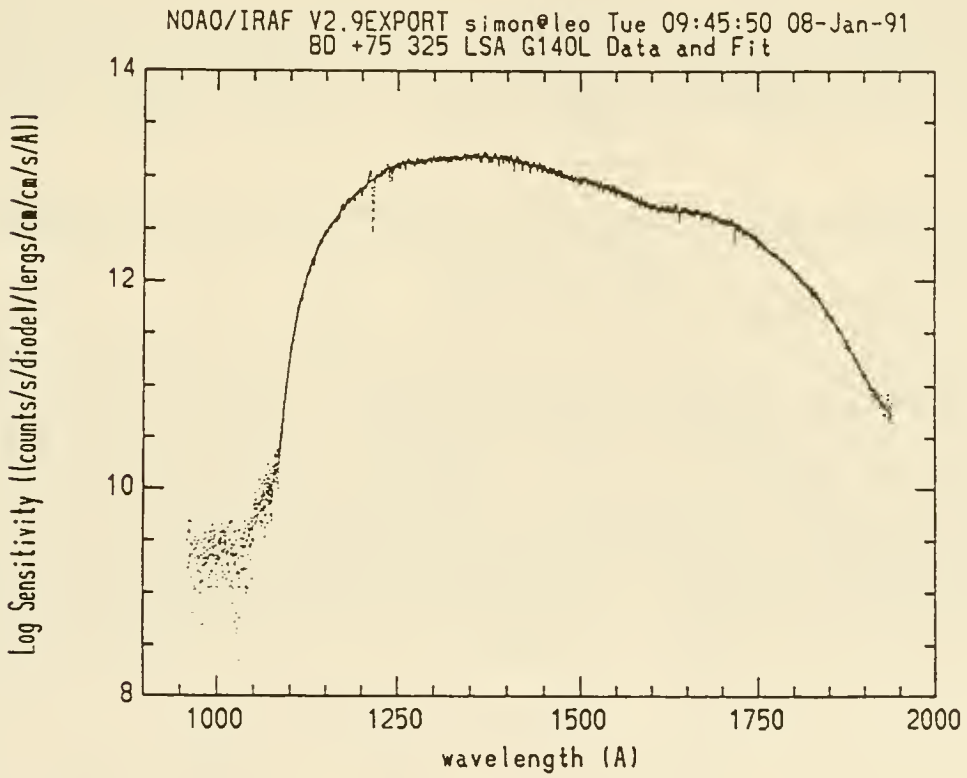

Figure 2. Sample calibration for grating G140L

aperture at each point. Software on the ground assembles the maps into a mosaic, from which the observer identifies the target. A slew request then moves the telescope to place the target at the center of the aperture. We have verified that all flight and ground software procedures are working properly, making interactive acquisitions a reliable option for many targets.

If the count rate can be accurately estimated for the proposal, an "onboard acquisition" will produce excellent results in a shorter time. Our standard procedure has either four or five steps. We first "search" until the target is detected, followed by a "locate" in the 2x2 arc sec aperture. We follow this by a second locate, to "peakup" in that aperture. A "map" then shows the final centering. If the smaller 1/4x1/4 arc sec aperture is desired, a blind offset is made, followed by a map of that aperture. Good coordinates, a proper "faint" limit, and use of the "double locate" ensures a successful onboard acquisition. We recommend a faint limit of approximately 40% of the best estimate of the count rate, and a "step time" chosen to produce at least 200 counts.

A third option is an initial acquisition of a nearby star followed by a blind offset to the real target. We tested this with a separation of approximately twenty arc seconds, and found the target within a few tenths of an arc second from the center after the offset. A "peakup" then improved the position.

We have found that the current algorithm for "peakup" in the small science aperture does not work well, and we do not recommend its use. The problems are a combination of the broad image structure, jitter, and inherent imprecision in the method. An improved algorithm has been designed for a future update to the flight software.

We had not attempted any acquisitions of moving targets, nor any WFC assisted acquisitions at the time of this workshop.

3. SENSITIVITY AND SPECTRAL RANGE

The photometric sensitivity of the GHRS has been calibrated using measurements of three UV standard stars - BD+75d325, HD93521 and Mu Columbae. The throughput for the 2x2 arc sec aperture has been well determined, and is 0.4 to 1.1 times the prelaunch estimates. Most of the discrepancies result from the 30% loss of light in the aberrated image, and errors in the ground based calibration at the shortest wavelengths. There is no evidence for deterioration of the sensitivity since 1984. The 1/4x1/4 arc sec aperture transmits 1/5 to 1/3 of the light captured by the 2x2 arc sec aperture. The recommended wavelength intervals for the first order gratings are:

GRATING	RECOMMENDED RANGE	COMMENT
G140L	1050 - 1900	
G140M	1050 - 1900	
G160M	1150 - 2300	2nd order overlap for lambda > 2300
G200M	1600 - 2300	2nd order overlap for lambda > 2300
G270M	2200 - 3300	2nd order overlap for lambda > 3300

Figures 2 and 3 show the large aperture calibration for grating G140L, and the ratio of small to large aperture throughput. Complete sensitivity information will be available in the Proposal Instructions, the GHRS Instrument Handbook, and in the IDT's End of SV Report. Figure 4 shows a spectrum of a starburst knot in a spiral arm of the Seyfert galaxy NGC 1068, obtained with G140L and calibrated with the data shown in Figure 2.

4. SPECTRAL RESOLUTION

The image of the small science aperture maps onto one diode in the GHRS detectors. For observations obtained with a star in this aperture, the spectral resolving power is unaffected by the OTA image structure. The two onboard spectral lamps have apertures and optical paths identical to the science aperture. The illumination is similar enough that the profiles of their emission lines serve as reliable proxies of the line spread function and resolution. We have measured the profiles of hundreds of calibration lines, and have verified that the GHRS internal optical focus is essentially perfect, and the full resolution planned for the instrument is available. Figure 5 shows a histogram of line widths for Echelle A, with a peak at 1.05 diode widths. We have verified that the line width is constant, showing no variation with wavelength, location on the detector, or echelle order. Figure 6 shows the line widths converted to resolving power for the Echelle.

Observations made with the target centered in the large aperture suffer a loss of resolution of approximately a factor 2. The line spread function has a sharp core and significant but truncated wings. Experiments by members of the GHRS science team and the STScI have demonstrated that deconvolution can be performed if the S/N of the raw data is adequate. Three techniques have been explored so far, a "block-iterative" restoration, the "Richardson-Lucy" algorithm, and a "Fourier Quotient" approach. All three preserve the location of features in the spectrum and greatly improve the contrast between blended features. Equivalent widths may not be preserved, so quantitative measurements may be better served by small aperture data. Figure 7 shows one example of a small aperture spectrum, and a deconvolved large aperture exposure for comparison.

We recommend the following observing strategies if spectral resolution is an important goal. Use the small science aperture with increased exposure time to compensate for the lower throughput. Use a "step-pattern" with four samples per diode width. Use the default "comb-addition" of four. Keep the duration of

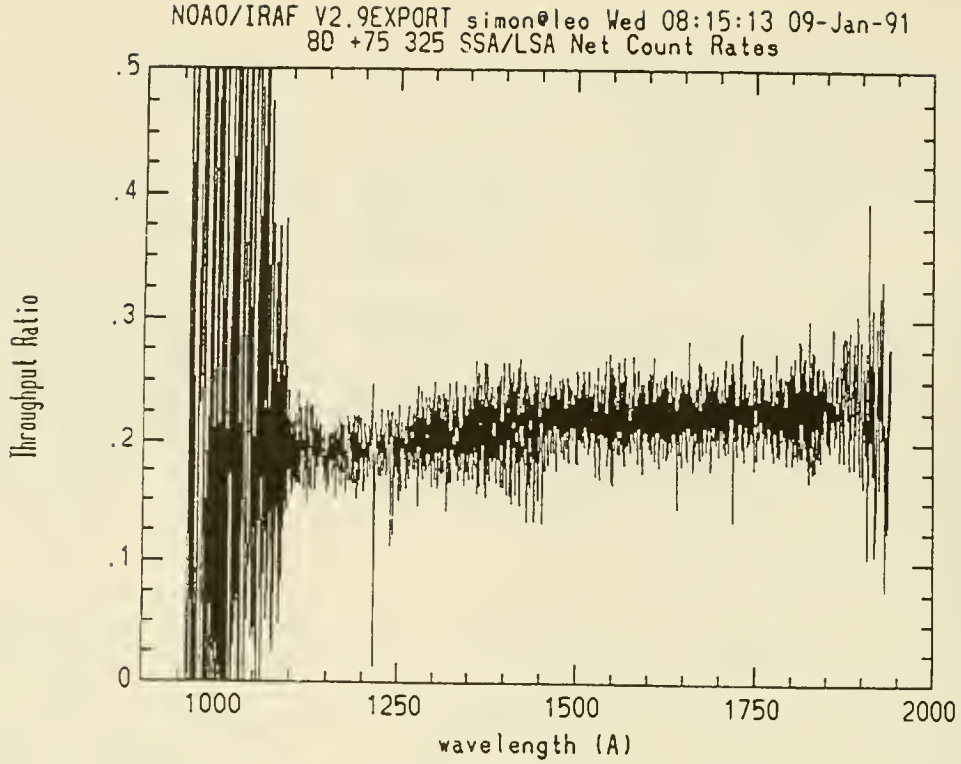

Figure 3. Small/large aperture throughput

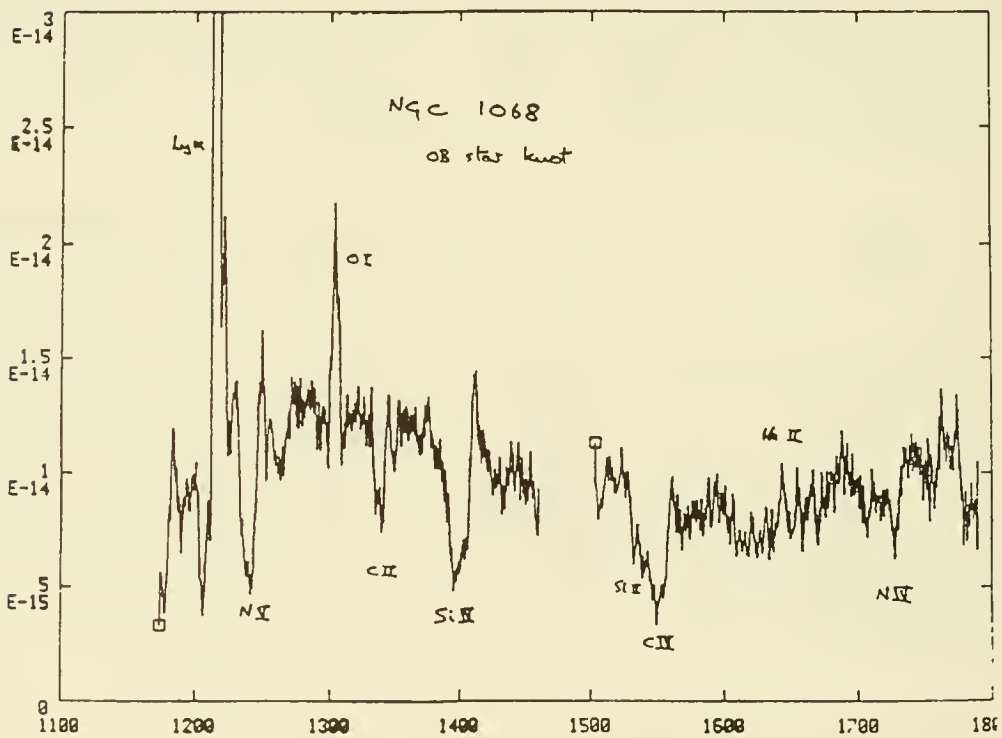

Figure 4. G140L spectrum of a starburst in NGC 1068

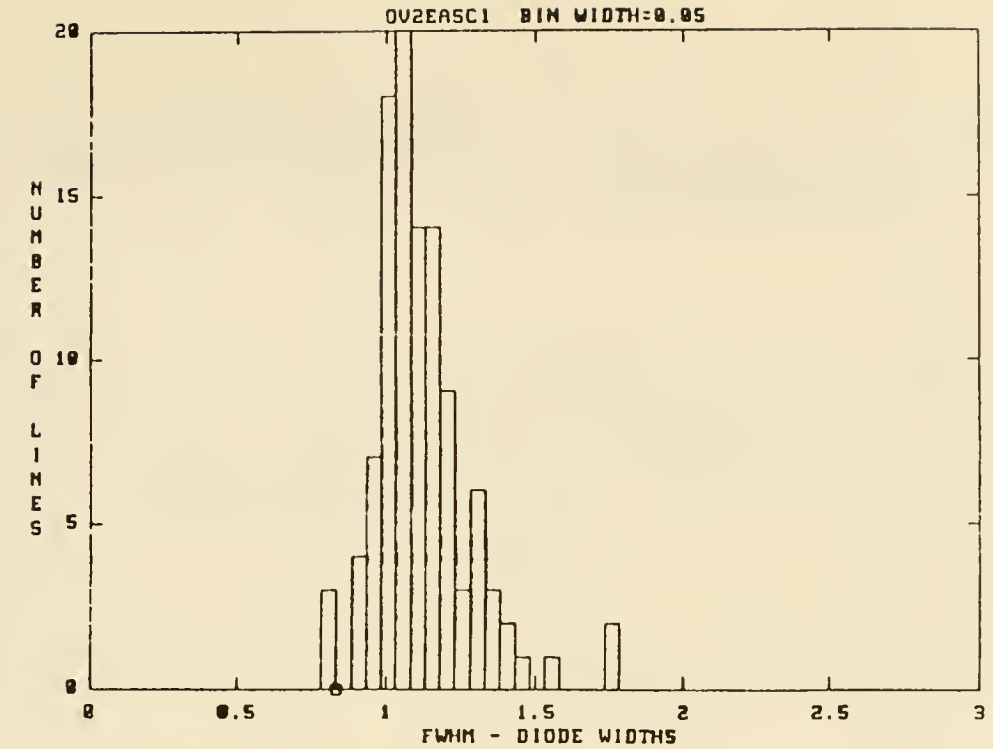

Figure 5. Echelle A emission line widths

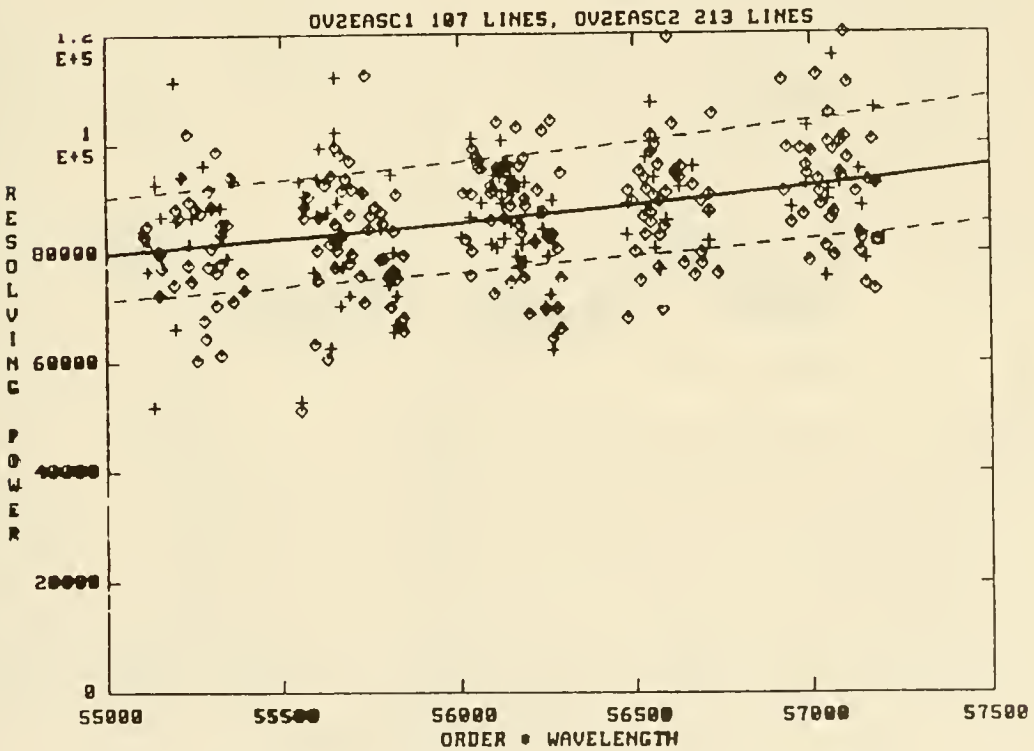

Figure 6. Echelle A resolving power

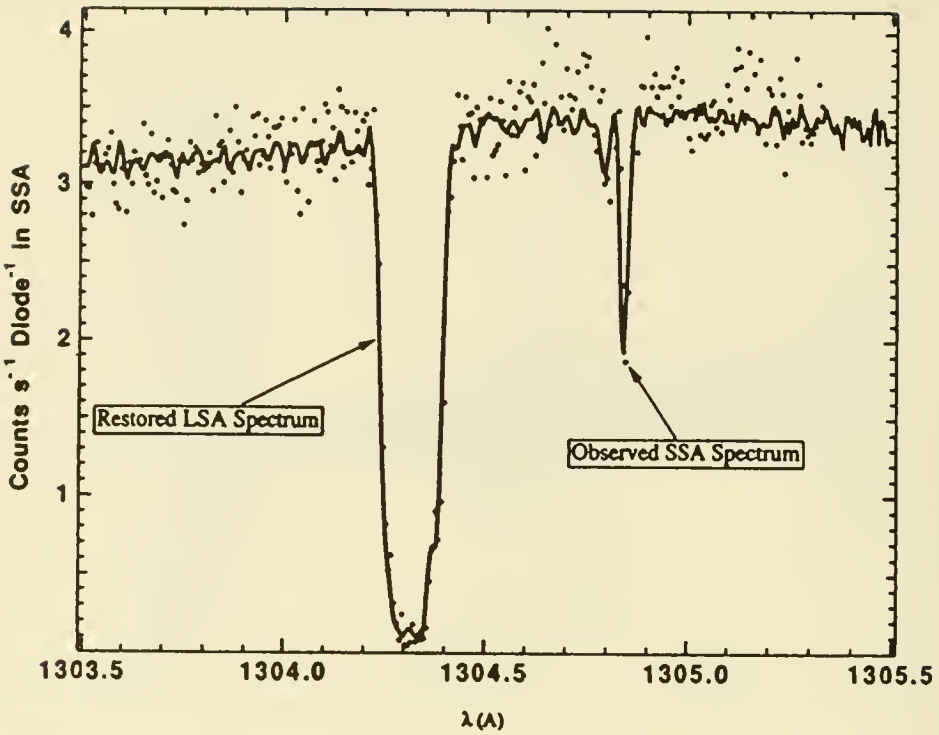

Figure 7. Deconvolution of large aperture spectrum

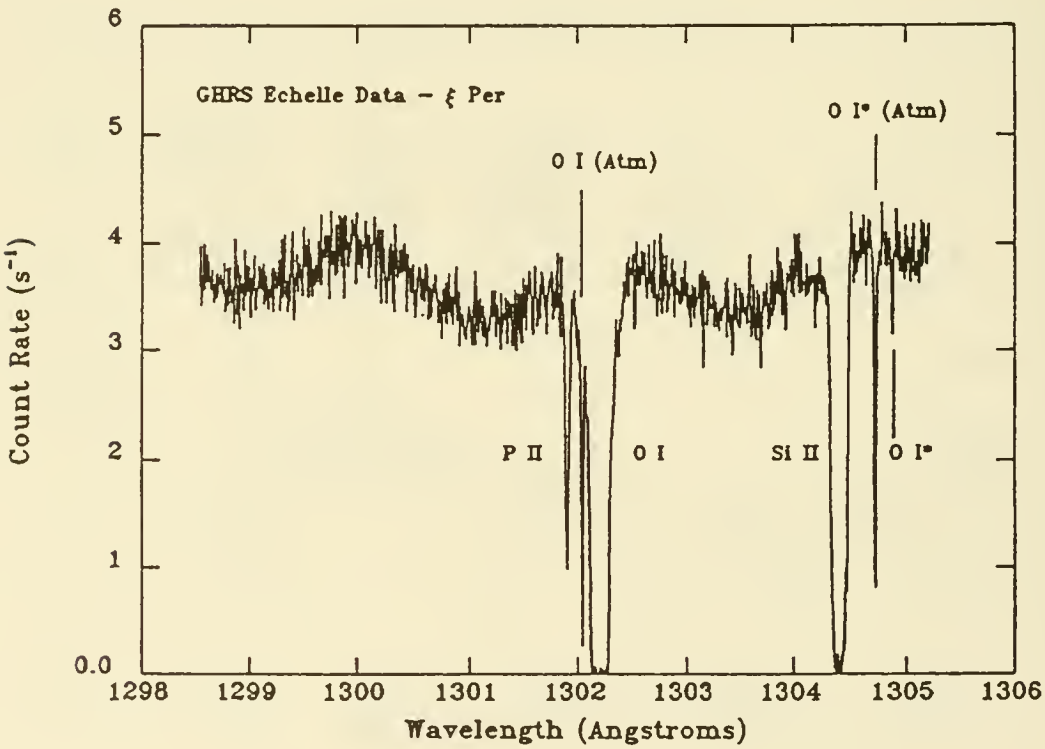

Figure 8. Removal of echelle scattered light

individual subexposures to no longer than ten minutes. Merge individual "fp-split" segments together carefully by coaligning spectral features. Figure 9 shows a short spectral interval of the star Chi Lupi observed with various combinations of apertures and gratings.

5. STRAY AND SCATTERED LIGHT

Many of the scientific programs of the GHRS require very precise measurements of line profiles. Accurate profiles in turn require that all background components be removed from the raw data. We investigated four possible types of scattered light. Near angle grating scatter is essentially the far wings of the instrumental line spread profile. For the low and medium resolution gratings this appears to be negligible beyond two diode widths or so from line center. In the high resolution modes both the Echelle and cross disperser gratings produce faint but broad wings which scatter light for many angstroms. Light is scattered both along the direction of dispersion, and into the interorder regions, and requires careful removal. We recommend using a "step-pattern" which samples the interorder light with the science diodes, especially for Echelle exposures. Figure 8 shows Echelle observations of saturated interstellar absorption lines in the spectrum of Xi Per. After removal of the background the cores of the lines show essentially zero residual intensity, as they should. A third effect is "red leak", in which longer wavelength light could be scattered into the field of view and superimposed on the true ultraviolet signal. We have observed uv emission lines from very cool stars, and detect no spurious "continuum" light between the lines. Side 1 modes in particular are extremely "solar blind." Figure 10 shows our observations of chromospheric emission lines from Gamma Dra at low, medium and high resolution. The fourth effect is telescope scattering, in which light from nearby bright stars is scattered into the aperture during observations of nearby fainter targets. We measured the signal as a bright standard star was stepped away from the GHRS aperture, and found a residual fraction of 2E-5 at 16 arc seconds off center.

6. PHOTOMETRIC PRECISION AND SIGNAL TO NOISE RATIO

We have quantified four effects which influence the photometric quality of GHRS data. Photon statistics dominate the signal to noise ratio, and exposure times should be based primarily on this. The dark noise in the detectors is less than 0.01 counts per diode per second. Dark noise is significant only if the source count rate is less than roughly five times this rate. Scattering in the Echelle creates another statistical noise source, which can be minimized with proper smoothing and removal of the background. Finally, small scale irregularities in the photocathode sensitivity, gradients, blemishes, granularity etc. contribute noise on spatial scales from the full detector width to pixel to pixel variations. These can be accommodated somewhat by using the "fp-split" procedure. Figure 11 shows signal to noise ratio achieved in some prelaunch calibration spectra. The data follow the

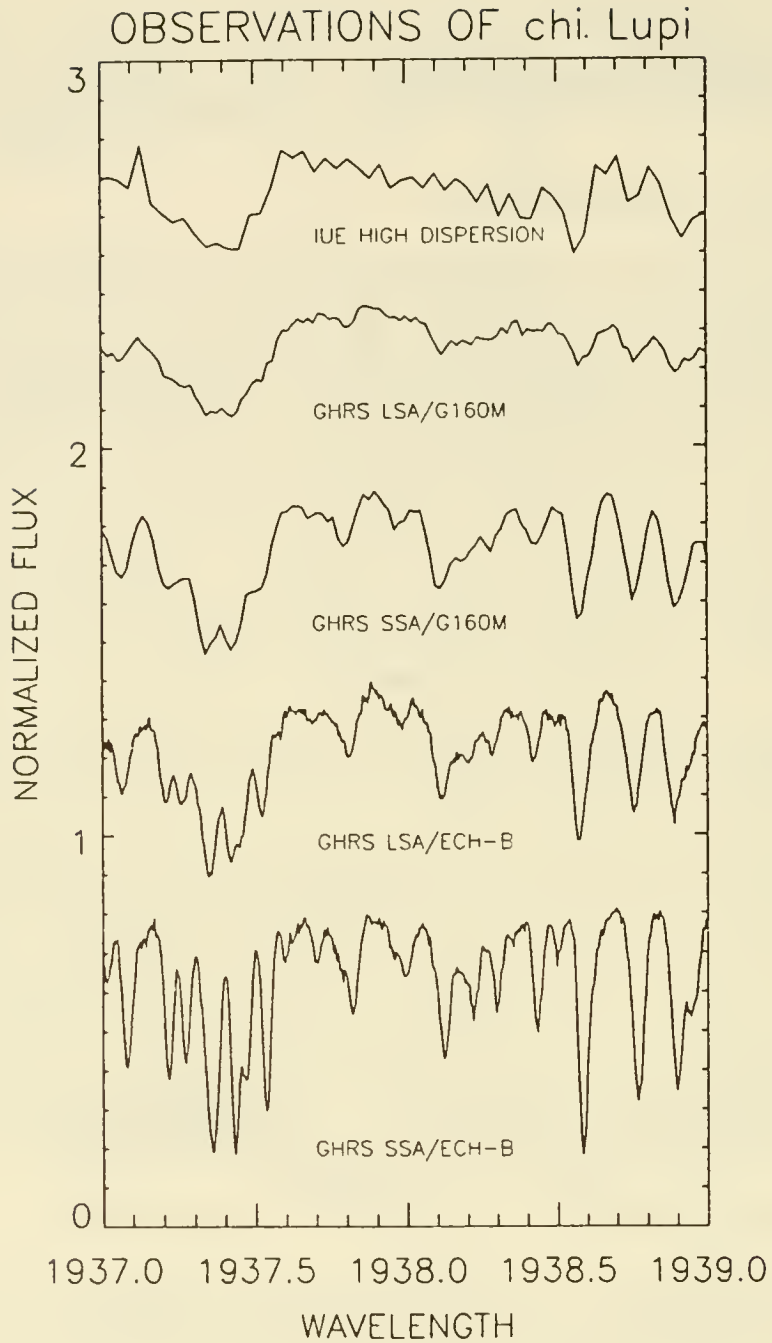

Figure 9. Comparison of resolving power with GHRS large and small science apertures, medium and high resolution gratings

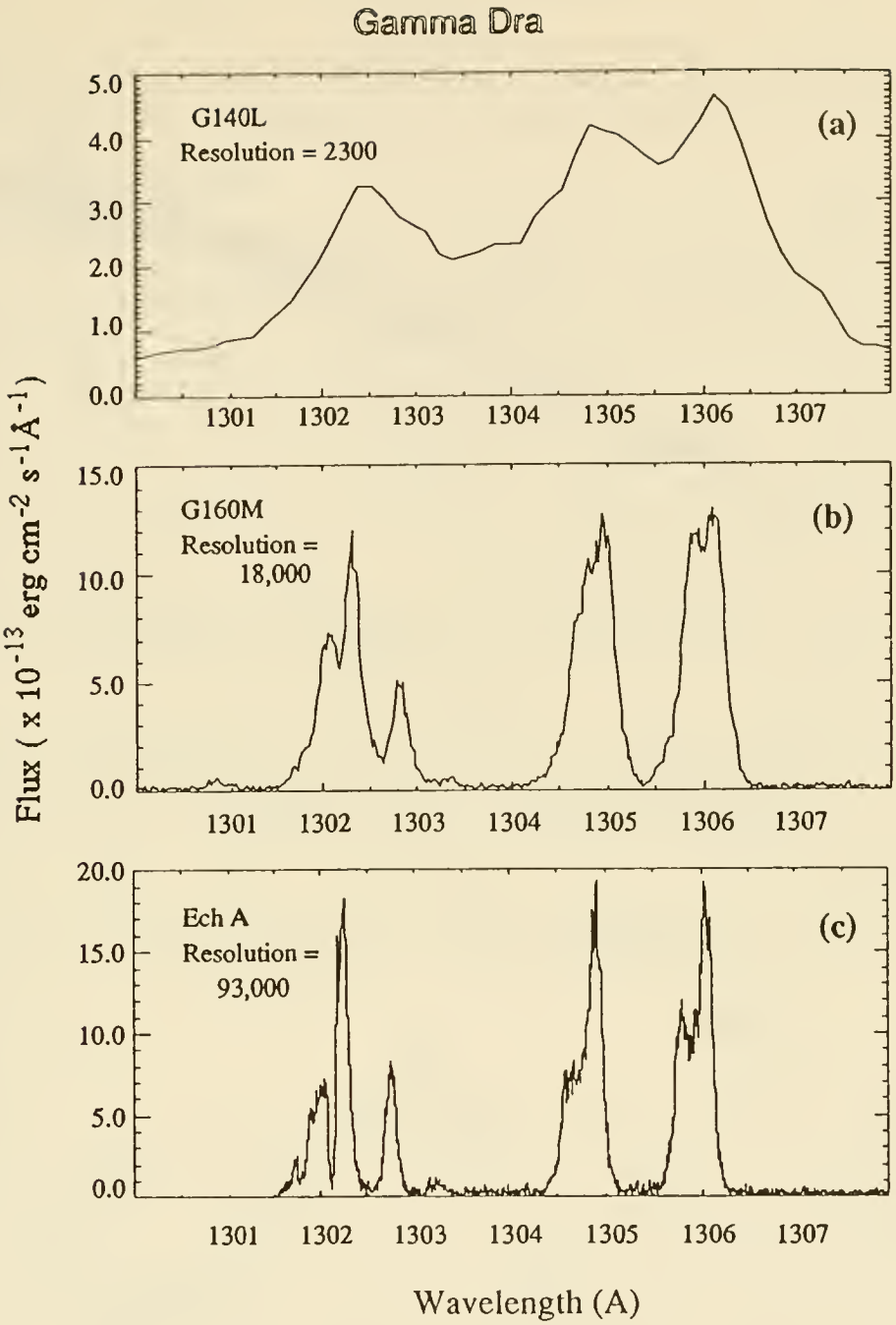

Figure 10. Emission lines from the chromosphere of Gamma Dra, a cool star with no ultraviolet continuum emission. The GHRS is "solar blind" to scattered long wavelength light, and produces no spurious "red leak" signal.

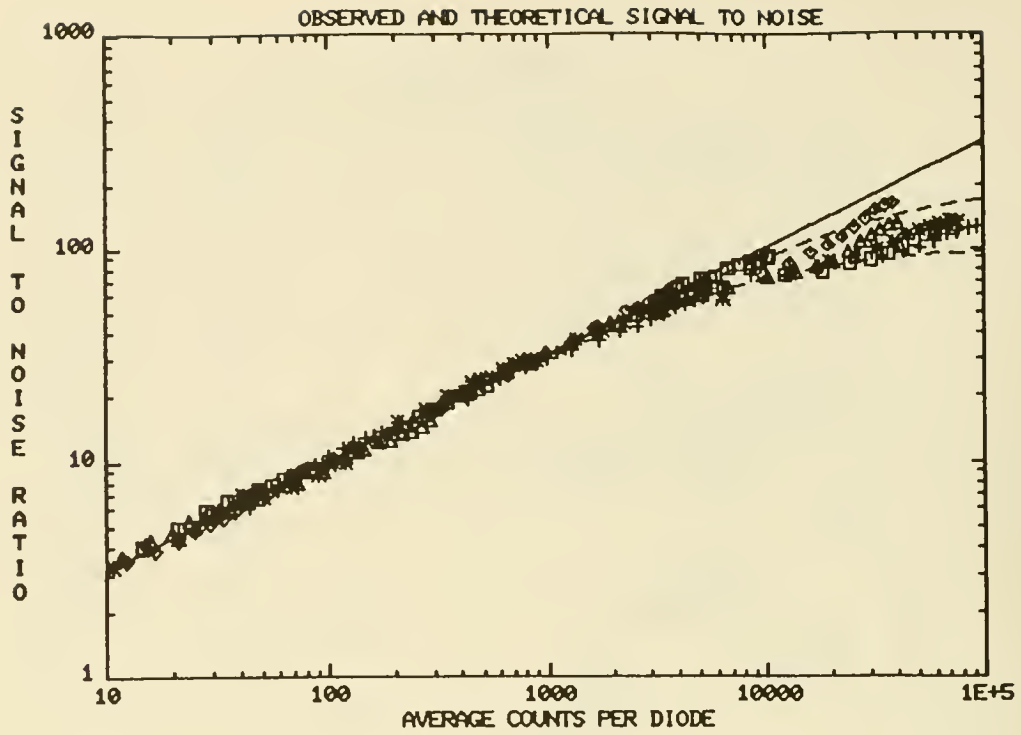

Figure 11. The signal to noise ratio is dominated by photon statistics at low signal levels, and by detector irregularities at high levels.

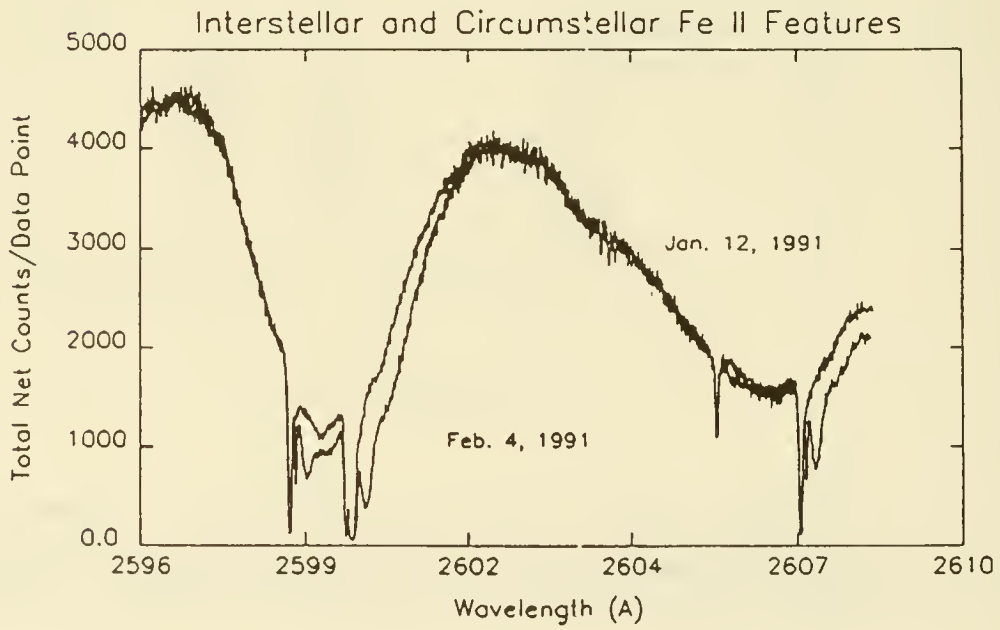

Figure 12. Variable and nonvariable features in the Beta Pic spectrum are easily distinguished with accurate wavelength scales and good photometric precision.

expected "root N" behavior up to S/N = 50. The departures at higher signal levels show that photocathode irregularities at the 1 - 3% RMS level dominate if they are not calibrated out of the data.

7. WAVELENGTH CALIBRATION

The GHRS contains two onboard Pt-Ne hollow cathode lamps, whose spectrum was calibrated for precise wavelengths at NIST. Observations of these reference spectra have been used to establish the relationships between wavelength and geometrical location for all grating and Echelle modes, at a wide range of carrousel positions. We formulate the problem is such a way that a polynomial describes the relationship at any given carrousel position, and the coefficients of the fit, the "dispersion constants" can be smoothly interpolated to carrousel positions not explicitly calibrated. We have settled on a cubic representation. Our data reduction process evaluates this basic step, and makes adjustments for offsets between the lamp and science apertures and a small systematic thermal drift. There are smaller errors associated with geomagnetic effects, miscentering of the star in the aperture, and carrousel repeatability that are not modelled at this time. Experiments with a large data base of lamp spectra, and a growing set of observations of interstellar absorption lines indicates that our wavelength calibrations are internally consistent to approximately +/- 1 km/sec, with an absolute zero point uncertainty of about 3 km/sec. Figure 12 shows two of our medium resolution spectra of Beta Pictoris,taken approximately three weeks apart. The excellent registration of the non-variable interstellar components illustrates the accuracy of the wavelength scale, and our confidence in measurements of the time variable circumstellar components.

8. TIME RESOLUTION

The two basic spectroscopic operating modes ACCUM and RAPID, can both produce data with higher time resolution than has been previously possible. ACCUM allows use of the full suite of flight software features, and can achieve approximately thirty seconds time resolution for the duration of target visibility. RAPID mode bypasses the flight software, so no substepping or data quality checking can be performed, but can achieve time resolution between 0.05 and 12.75 seconds. If the "sample time" is longer than 0.35 seconds very long observations can be accommodated by the tape recorder. Shorter sample times limit the duration to approximately 20 minutes. Our science team has used RAPID with 0.4 second sample time for observations lasting seven orbits.

9. SUMMARY - WHAT IS RIGHT, WHAT IS NOT?

At the time of this workshop, the initial pointing accuracy and target acquisition procedures were working very well. We had no serious difficulties getting stars into the large science aperture. Sensitivities had been calibrated and found to support use of the entire 1050 - 3300 A spectral range. The planned spectral resolution is achieved by placing the target in the small science aperture. Observing procedures and data reduction algorithms allow accurate removal of scattered light in the Echelle modes. The signal to noise ratio is dominated by photon statistics up to about S/N = 50. Routine wavelength calibrations are accurate to better than one pixel. All operations, commanding and flight software aspects appear to be working well.

Precise and reliable centering of targets in the small science aperture is still being worked on. Improvements to data base parameters and flight software algorithms will hopefully improve the utility of this aperture. The throughput of the small aperture has suffered significantly from the aberrated telescope image, but hopefully will be improved by the proposed COSTAR instrument. Unanticipated sensitivity to thermal and magnetic environments require some special care. The photocathode irregularities have not been fully calibrated, and their removal is not yet automatic.

Acknowledgement: The results discussed in this paper represent the work of dozens of individual scientists, engineers and managers. We gratefully acknowledge the contributions of the members of the Investigation Definition Team and their many colleagues. The tireless efforts of many individuals at HSTPG and the STScI were required to bring the OV and SV programs to fruition. The engineers from Ball Aerospace, and the HST operations staff contributed immensely to the development of the GHRS and the implementation of its scientific program.

Early Operations with the High Speed Photometer

J. W. Percival, R. C. Bless, and M. J. Nelson
Space Astronomy Laboratory
1150 University Avenue
Madison, WI 53706
USA

Abstract. The performance of the High Speed Photometer (HSP) during the Orbital Verification (OV) and the Science Verification (SV) programs of the Hubble Space Telescope (HST) is described. The HSP is operating as designed, and all hardware is fully operational. The HSP has been seriously affected by the degraded point spread function (PSF) of the telescope system, the telescope pointing calibration, and the jitter in the spacecraft pointing.

1. INTRODUCTION

The design and basic operation of the HSP has been described elsewhere (Nelson et al. 1991 and White, 1990). It can produce high speed (12 μS) photometry in 27 narrow, medium, and broad filters from 1200 to 7500 Ångstroms. The HSP has no moving parts, and selects targets and filters in a two step operation. First, to select a target, the HST is maneuvered so that the target image falls at a particular point in the focal plane, where it passes through the desired filter and a 1 arcsecond observing aperture. The filtered target image then falls on the face of an Image Dissector Tube (IDT). Next, the HSP acquires the target by magnetically steering the IDT's read beam to the point on the tube face on which the filtered image is falling. In practice, there is in intermediate operational step. The star is first acquired in a 10 arcsecond aperture, and an on-board target acquisition is performed that centers the star in the aperture of choice.

The large number of HSP apertures, and the need for precise, repeatable, and stable HST pointing to produce high quality photometry conspired to complicate and lengthen the HSP OV and SV activities. The HSP is nearing the end of these activities, and has begun to observe scientifically interesting targets, including a rapidly oscillating Ap star, and a stellar occultation by Saturn's rings.

2. INTERNAL CALIBRATIONS

The primary internal calibration for the HSP is to measure the magnetic deflection

currents that move the IDT read beam to the part of the tube face on which the desired filter/aperture combination is imaged. Initially, this was done using the bright earth as a flat field source, backlighting the aperture plate. We make a crude image by stepping the read beam through a grid, making a photometric measurement at each point. These images are analyzed to yield a deflection coordinate pair for any given aperture.

We discovered that the earth is not a very flat field. It is spikey on small (1 km) spatial scales, probably due to cloud tops and strips, and scattered sunlight from water. The spikes were 5-50 times the average expected brightness of the earth. Operational changes were made for the solar sensitive detectors to lower the tube gain when exposed to the bright earth, and Orion was selected as a flat field for some filters on these detectors. The operational changes and much longer exposure times delayed the calibration of these detectors by several months. The deflection calibrations for each aperture are now known to within about 0.05 arcseconds.

3. ALIGNMENT CALIBRATIONS

The other alignment critical to normal HSP operations is the calibration of the focal plane positions of the photometry apertures. This calibration is performed by scanning the HST in a grid pattern on the sky, while doing time-series photometry through the selected aperture. An analysis of the time-varying signal, combined with a post-test knowledge of where the spacecraft was pointing, yields a focal plane coordinate pair for each aperture.

Early in the mission, the fine guidance sensor (FGS) calibration was so poorly known that the alignment stars could not be positioned reliably within the diameter of the 10 arcsecond finding aperture. Reliable, repeatable FGS calibrations only began appearing in January 1991. Focal plane calibrations have proceeded smoothly since that time, and the HSP aperture positions in the HST focal plane are now known to within 0.02 arcseconds. Figure 1 shows contour plots of the same star in two different HSP photometry apertures.

4. OPERATIONS

4.1. Bright Earth

The bright earth problem discussed above resulted in operational changes for the two solar sensitive IDT's and for the photomultiplier tube (PMT). Whenever the current pointing is about to be occulted by the bright earth, the IDT gain is lowered by decreasing the high voltage. After the occultation, the voltage is restored to its normal observing value. The PMT has a less fragile reflective, rather than a transmissive, photocathode, so the operational change for it was simply to turn off the bright object protection software for this tube during the bright earth events. The bright object protection is reenabled after the occultation.

4.2. Target Acquisition

The HSP has an on-board target acquisition mode. A crude image, described in

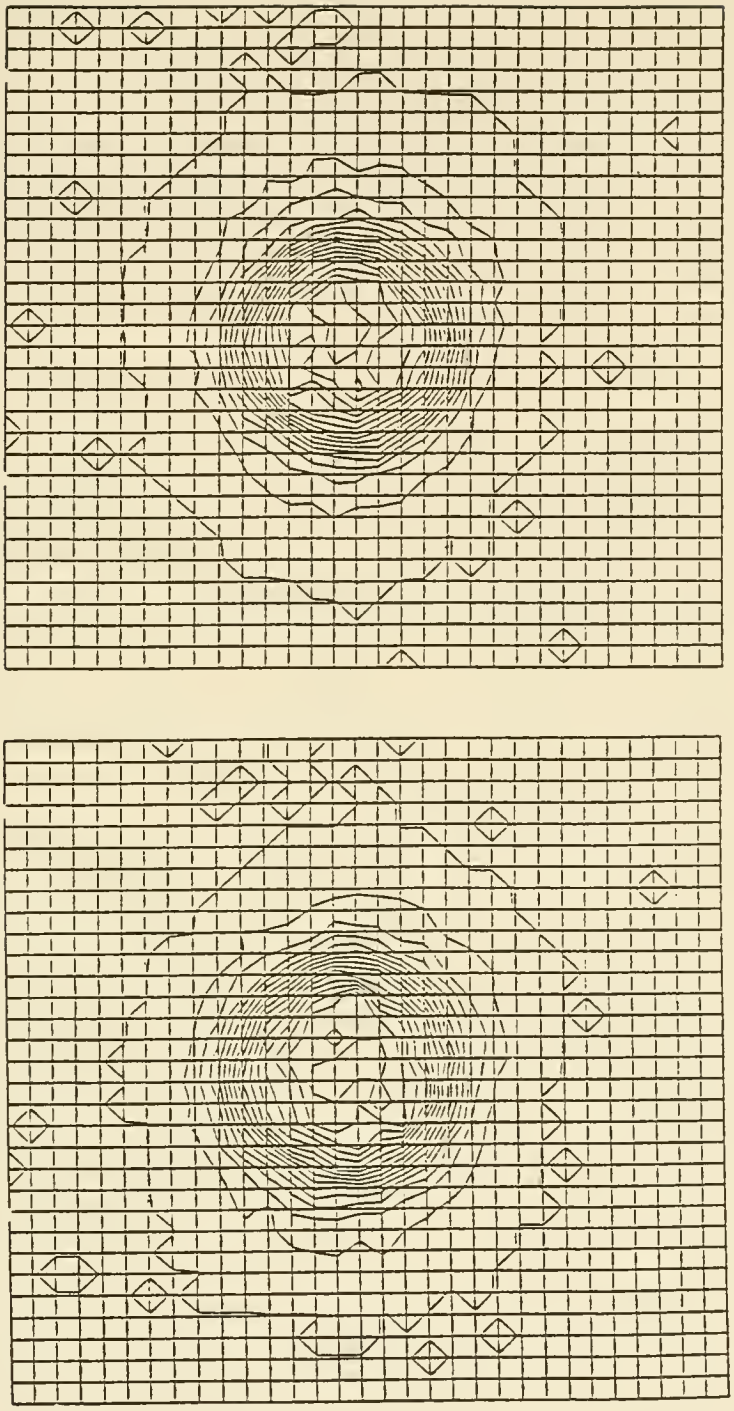

Figure 1: Centering in two HSP photometry apertures.

Section 2 above, is made of the 10 arcsecond finding aperture after moving the HST to place the target star within it. The image is sent to an on-board computer program that performs a simple centroid calculation on the target, and issues a small angle maneuver request to center up the target. The *relative* positions of the HSP apertures are known to great accuracy, so after the centering operation the target can be reliably moved to any photometry aperture with subsequent small angle maneuvers.

The image is oversampled with the 1 arcsecond read beam, and the original algorithm was designed to operate on the expected extremely narrow PSF. The much broader actual PSF presents a larger than expected image to the simple nearest-neighbor centroid algorithm, which results in a slightly less accurate centroid. We have found that doing the acquisition twice in a row causes an improvement in the net centering. We find that the target acquisitions converge rapidly (two is enough) and is repeatable to within 0.05 arcseconds. This is now done automatically. The proposer need not request the iterated acquisition.

4.3. Length of Exposures

The HST Science Data Formatter (SDF) protocol was designed with the imaging instruments in mind. The SDF operates in a three dimensional data space whose axes are words per line (WPL), lines per frame (LPF), and frames per observation (FPO). The idea is that WPL and LPF are determined by the image size, the image is integrated before the science data transfer is started, and that once begun, the transfer should proceed at a high rate. The SDF expects lines of data to follow each other in the LPF dimension within a strictly observed timeout period of 10 ms. The third, FPO, dimension represents successive frames so the SDF allows the science instrument to insert an arbitrary amount of time between frames.

The HSP does not collect a whole frame before sending. It has no buffers that large. It begins the transfer to the SDF as soon as the first line of data has been collected. Because of the 10 ms SDF timeout in the LPF dimension, the HSP must be prepared to transmit the next line of data within 10 ms of the previous one, which it can do only in the high-speed (MHz) photometry regime. For lower speed photometry, the HSP is forced to collapse the LPF dimension to unity, sending each line as a new frame. The final piece in this puzzle is that the HSP FPO counter is only an 8-bit quantity, which limits the HSP to 256 frames. This places an upper limit on the number of samples per science observation of 2 * WPL * FPO, or about a half million 8-bit samples (half as many 16-bit samples, of course). This constrains the sample time for long observations. As you lengthen the observation but keep the total number of samples fixed, then each sample must last longer to span the time. A detailed analysis can be found in White (1984).

One interesting observation has already been subjected to this constraint. In our 5.6 hour time series of a rapidly oscillating Ap star, the quarter million sample limit forced each sample to be no shorter than 82 milliseconds. We have proposed a simple commanding fix to eliminate this constraint. This fix, when implemented, will allow arbitrarily long data sets. This commanding fix is now being reviewed by the STScI.

5. PERFORMANCE

5.1. Throughput

The throughput of the HSP filters has been measured with stars during the FGS alignment activities. The results agree, with one exception, with HSP model predictions modified only for the broadened PSF. We find the expected 50% reduction for the 1 arcsecond photometry apertures, and a 75% reduction for the 0.65 arcsecond forward facing polarimetry IDT.

The exception is the 5500 Ångstrom filter (F551W) on the solar sensitive IDT. We find an unexplained 60-70% loss of light in each of the four apertures on that filter. We are investigating this curious result.

5.2. Linearity

In our linearity test, we looked at four stars between 5^{th} and 11^{th} magnitudes. Exposure times were chosen to produce a signal to noise (S/N) ratio of 50. Table 1 shows the known and measured V magnitudes. The measured value was derived from a magnitude-count relation with a linear color term. The agreement is satisfactory given the S/N of the HSP data.

Catalog M_v	Measured M_v
5.111	5.119
7.247	7.267
8.060	8.035
11.070	11.067

Table 1: HSP linearity.

5.3. Photometric Performance

The photometric performance of the HSP is affected by the HST spherical aberration because the broadened PSF has significant energy at the edge of the photometry aperture, a situation that the system was not designed to encounter. The presence of energy at the edge of the aperture increases our sensitivity to two effects, the ability to point the HST in a repeatable way, and the stability of the pointing during an exposure.

The repeatability of the pointing places a limit on our photometric accuracy. If a star is measured two different times, and the position of the PSF changes slightly from one time to the next, then we will measure a slightly different count rate as more or less light passes through the aperture. Figure 2 shows the predictions of a model that numerically integrated the energy under the flight PSF as a function of miscentering in the aperture. The target acquisition repeatability of about 0.05 arcseconds implies a lower limit of about a millimagnitude in absolute photometry.

The HST exhibits some pointing instability that is detectable by the HSP. The day/night terminator reaction can cause the stellar image to move nearly *completely* out of the photometry aperture, and the induced jitter can inject power into a time series at frequencies ranging from 0.1 Hz to 10 Hz. Figure 3 shows the 5.6 hour time series of the Ap star. Note the loss of light at the transition from night to day (the low part of the sinusoid). The sinusoidal variation occurs at the orbital period, and is a topic under investigation. It may have to due with thermal effects in the HSP or in

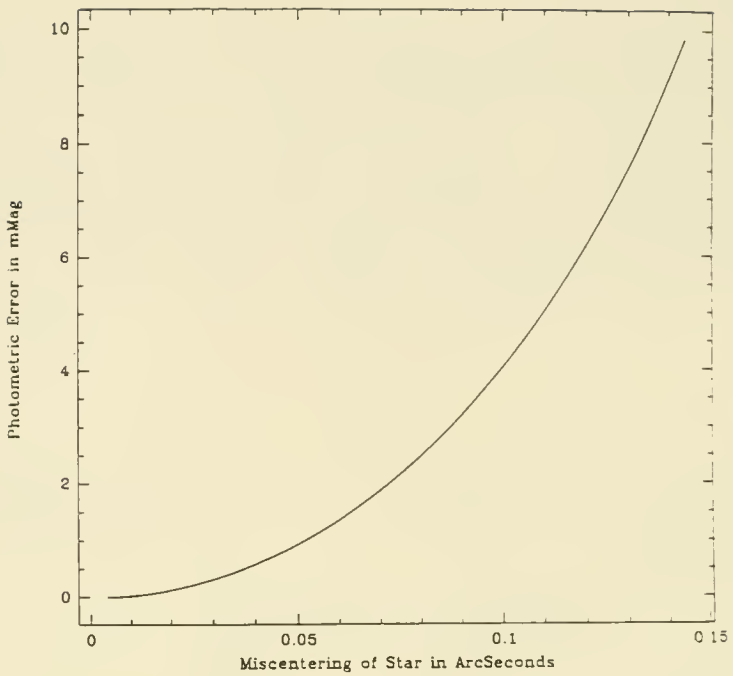

Figure 2: Photometric error vs. centering error for a 1" aperture.

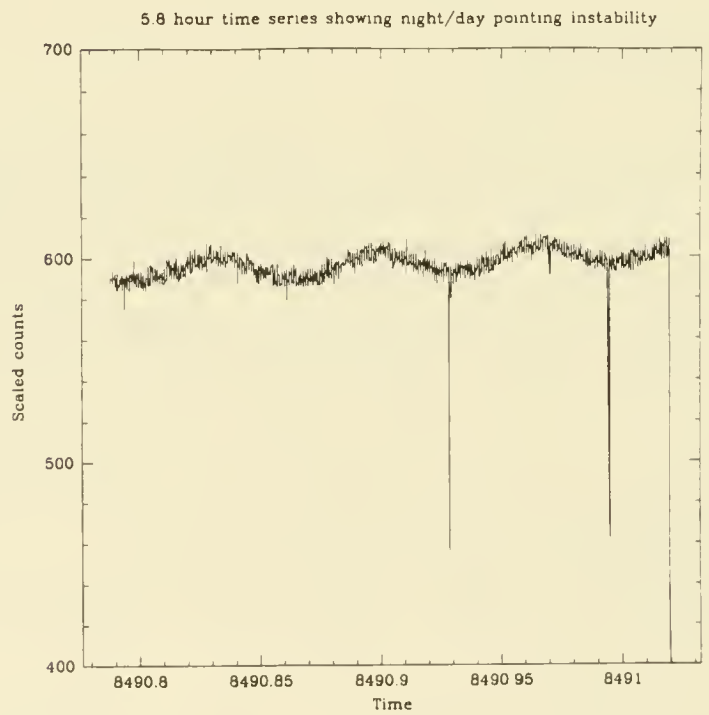

Figure 3: Data dropouts at night/day boundary.

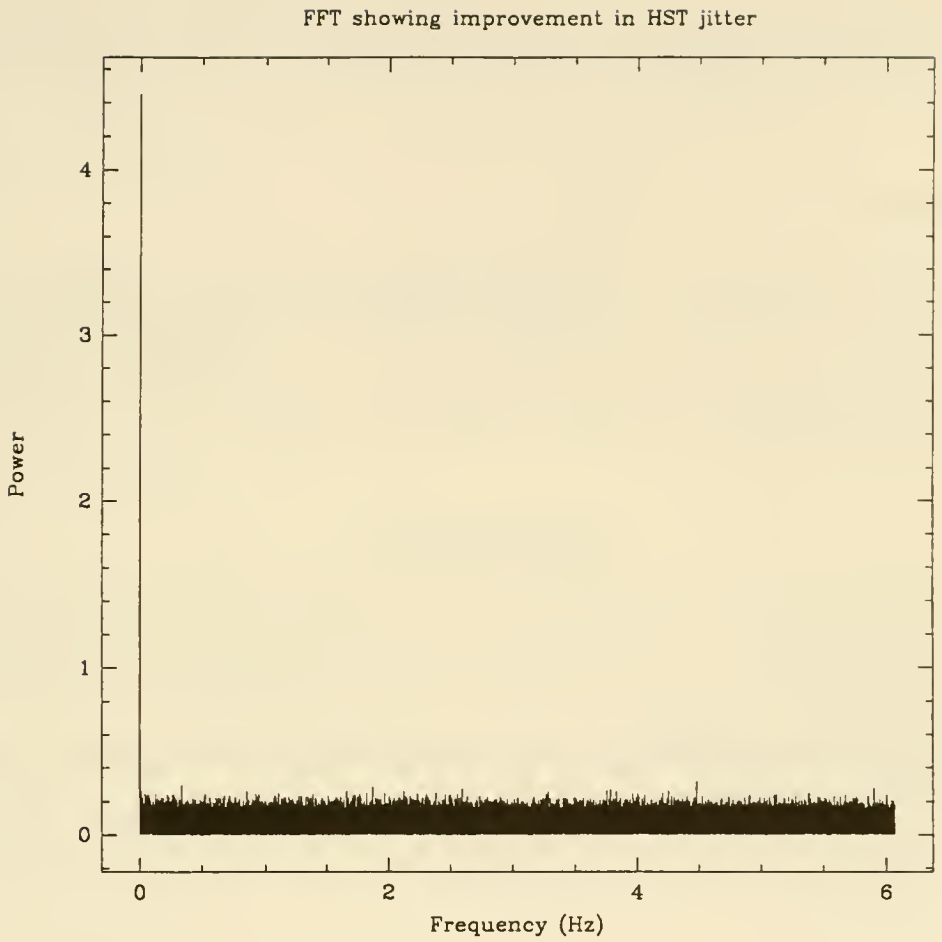

Figure 4: Improvement in HST jitter seen by the HSP.

the HST guidance system.

Figure 4 shows part of the Fourier transform of this time series. Note the lack of detectable power at 0.6 and 2 Hz, where power was earlier seen in HSP data. This improvement in the Fourier domain is apparently a result of the improved Solar Array Gain Augmentation (SAGA) software running in HST. This SAGA fix has improved the performance of the guidance system at the terminator crossings. The data glitches in Figure 3, while large in magnitude, are short in duration (seconds rather than minutes) and appear to die out quickly. A more extensive jitter test is being designed by the STScI.

6. SUMMARY

The HSP is performing as designed, except for the effects of the HST spherical aberration. The instrument is linear to within the 2% accuracy of the data. The on-board target acquisition is repeatable to within 0.05 arcseconds, which places a theoretical lower limit on the photometric accuracy at about 1 millimagnitude. The HSP has nearly completed its Science Verification activities, and is now beginning its GTO science program.

REFERENCES

Nelson, M. J., Bless, R. C, and Percival, J. W. 1991, *Photometry From Space*, ASP Meeting, June 1991.

White, R. L. 1990, *Hubble Space Telescope High Speed Photometer Handbook*, Space Telescope Science Institute.

White, R. L. 1984, Timing Considerations for HSP Data Collection, STScI Instrument Science Report HSP-001.

Early Commissioning Astrometry Performance of the Fine Guidance Sensors

G. F. Benedict, W. H. Jefferys, Q. Wang, A. Whipple, E. Nelan, D. Story, R.L. Duncombe, P. Hemenway, P. J. Shelus, B. McArthur, and J. McCartney
University of Texas
Austin, TX 78712

O. G. Franz, L. Wasserman, and T. Kreidl
Lowell Observatory
Flagstaff, AZ 86001

Wm. F. van Altena and T. Girard
Yale University
New Haven, CT 06511

L. W. Fredrick
University of Virginia
Charlottesville, VA 22903

Abstract. We discuss astrometry with the Fine Guidance Sensors and explore various factors limiting their performance. These results were obtained before starting either the Orbital Verification or Science Verification programs.

1. Astrometric Use of FGS

The Hubble Space Telescope contains three fine guidance sensors (FGS). While two are used for pointing control, the third is available for astrometric measurements. These measurements fall into two broad categories, position mode (POS) and transfer scan (TRANS) mode. A detailed discussion of these modes and the required post-observation processing can be found in Bradley et al. (1991). A principal goal of Astrometry Orbital Verification is the selection of the astrometer: which FGS of the three available will give the best performance in both position and transfer mode. Currently, this critical choice will be made in November 1991, after the final mirror moves to minimize coma and astigmatism are made.

1.1 Transfer scan mode

Since it affords us an introduction to the response function of the FGS, we shall first discuss TRANS mode. Fig.1 presents an example of the characteristic response of the FGS 1 Y-axis for Upgren 69 in NGC 188, a star thought to be without a companion. This curve (often referred to as an S-curve) is generated by scanning the 5 arcsec square FGS entrance aperture over the star. A similar curve will be produced for the x-axis. Positive attributes of any transfer function include large modulation, which is the left peak to right valley amplitude, and the detailed shape of the curve. A transfer function should ideally have only one positive peak and one negative valley. Comparing the ideal with the actual, we see three peaks and three valleys in Fig. 1. Minimizing these secondary peaks and valleys is a prime consideration.

A double star will produce a transfer function which is the sum of two overlapping single star transfer functions. It is obvious that the detailed shape of the single star transfer function will affect binary detection. The sample curve, for a V=9.58 star, will become very much noisier for a fainter star. This noise, too, will affect the detection limits for duplicity.

The pre-launch TRANS mode performance goal for binaries was 10 mas separation detectability for two stars differing in magnitude by less than 0.75 magnitudes. Unfortunately, the spherical aberration and lack of critical collimation of the telescope along with the internal mis-alignments within each FGS also affect the shape of the transfer function. The ultimate capability of the FGS for double star astrometry will not be known until the telescope is properly collimated.

1.2 Position mode

In POS mode, the fine guidance electronics searches for the first zero crossing in the FGS response curve after the first deep minimum, traveling right to left along the curve in Fig. 1. The positions of the star selector coordinates are averaged for some period of time while the fine guidance electronics keeps the star at this position, called the null point.

Fig. 2 illustrates the planning and the mechanics of a typical (but, as yet, unrealized) POS mode observation. The star selectors move the FGS entrance aperture to any location within the pickle-shaped region. To measure the position of a target relative to a field of reference stars, we

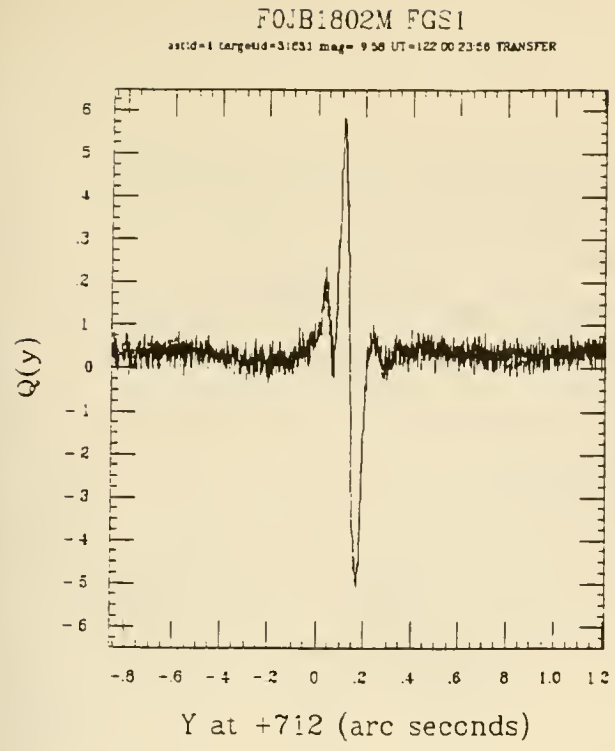

Figure 1 - An S-curve for the Y axis of FGS 1. The target star was Upgren - 69 in NGC 188.

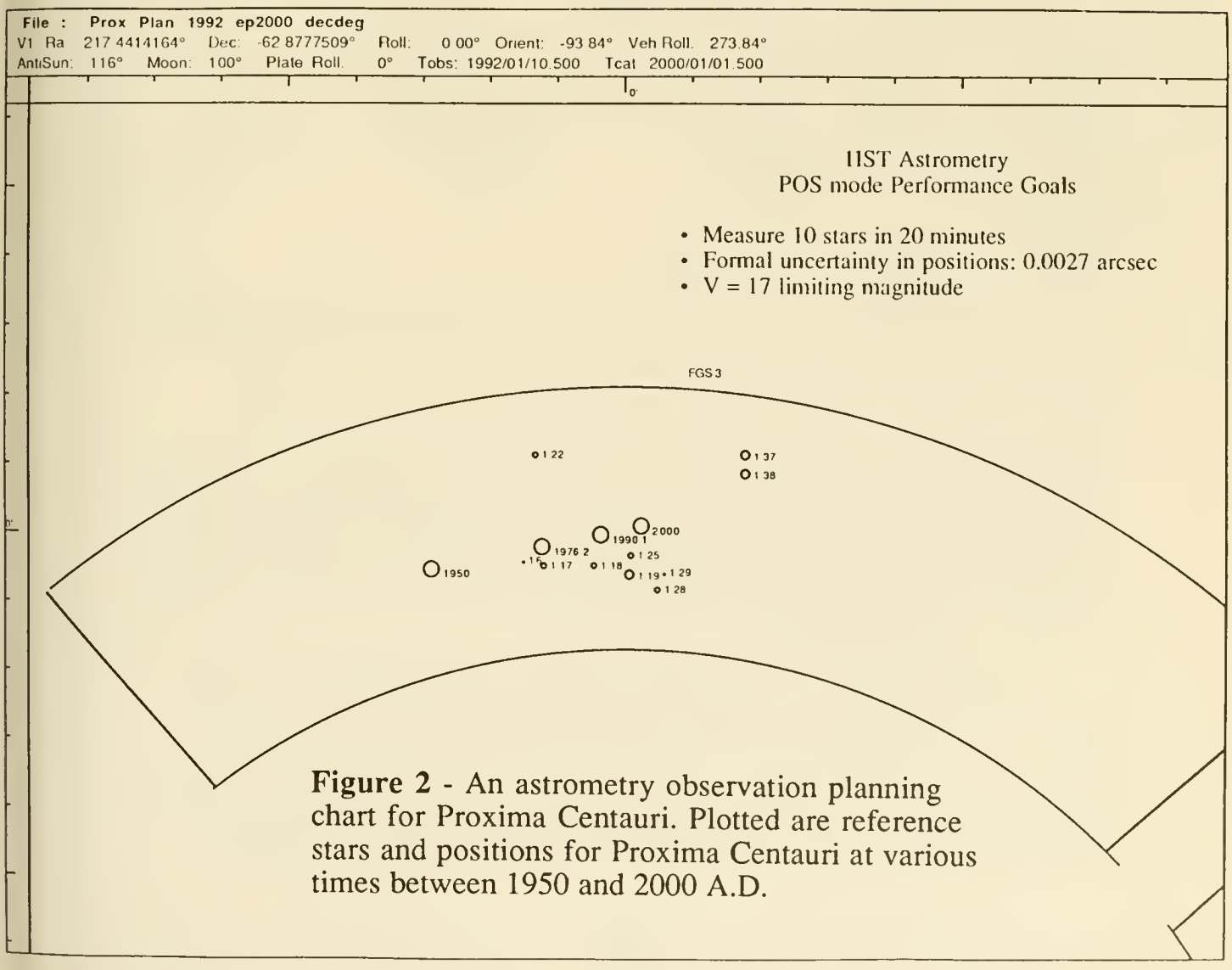

Figure 2 - An astrometry observation planning chart for Proxima Centauri. Plotted are reference stars and positions for Proxima Centauri at various times between 1950 and 2000 A.D.

command the star selectors to the predicted position of the target, obtain star selector readings averaged for some specified period of time depending on the star magnitude, then proceed to do the same for each reference star. The limiting magnitude will be determined primarily by the height of the peak-to-peak modulation of the transfer function (S-curve) because as the noise increases with fainter stars, the S-curve itself will become buried within the peaks and valleys of the background noise. The original pre-launch POS mode performance goal, 2.7 mas per measurement on a V=17 magnitude star, will require that many of the performance issues discussed in the next section be resolved. Aside from the scientific loss inherent in degraded astrometric performance, these issues, if unresolved, impact guiding.

2. Performance Issues

Both the environment of the FGS and the internal conditions of the FGS directly determine the interferometric response and hence the ability of the FGS to make astrometric measurements. This section describes these difficulties and in some cases identifies possible solutions. With a clear understanding of these extrinsic and intrinsic conditions, we can estimate our potential on-orbit performance.

2.1 Problems Extrinsic to FGS

2.1.1 Spherical Aberration

This major blow to HST performance has most often been discussed in the context of camera science (e.g., Hester, et al., 1991). For many months the FGS's were thought to be immune to spherical aberration. A series of 'N Points of Light' tests proposed by the Astrometry Science Team, in which the same star is observed in TRANS mode in 'N' locations within each FGS field of view, have demonstrated otherwise. The results for one such test (a Five Points of Light) for all FGSs are shown in Fig. 3, and will be discussed in greater detail below.

2.1.2 Collimation

Once it was determined that the Optical Control System Wavefront Sensors were not usable in the presence of spherical aberration, Hughes Danbury Optical Division and the Astrometry Science Team proposed to explore the secondary mirror tilt and decenter (collimation space) using the 'N Points of Light' tests. Coma, the result of misalignment of the HST

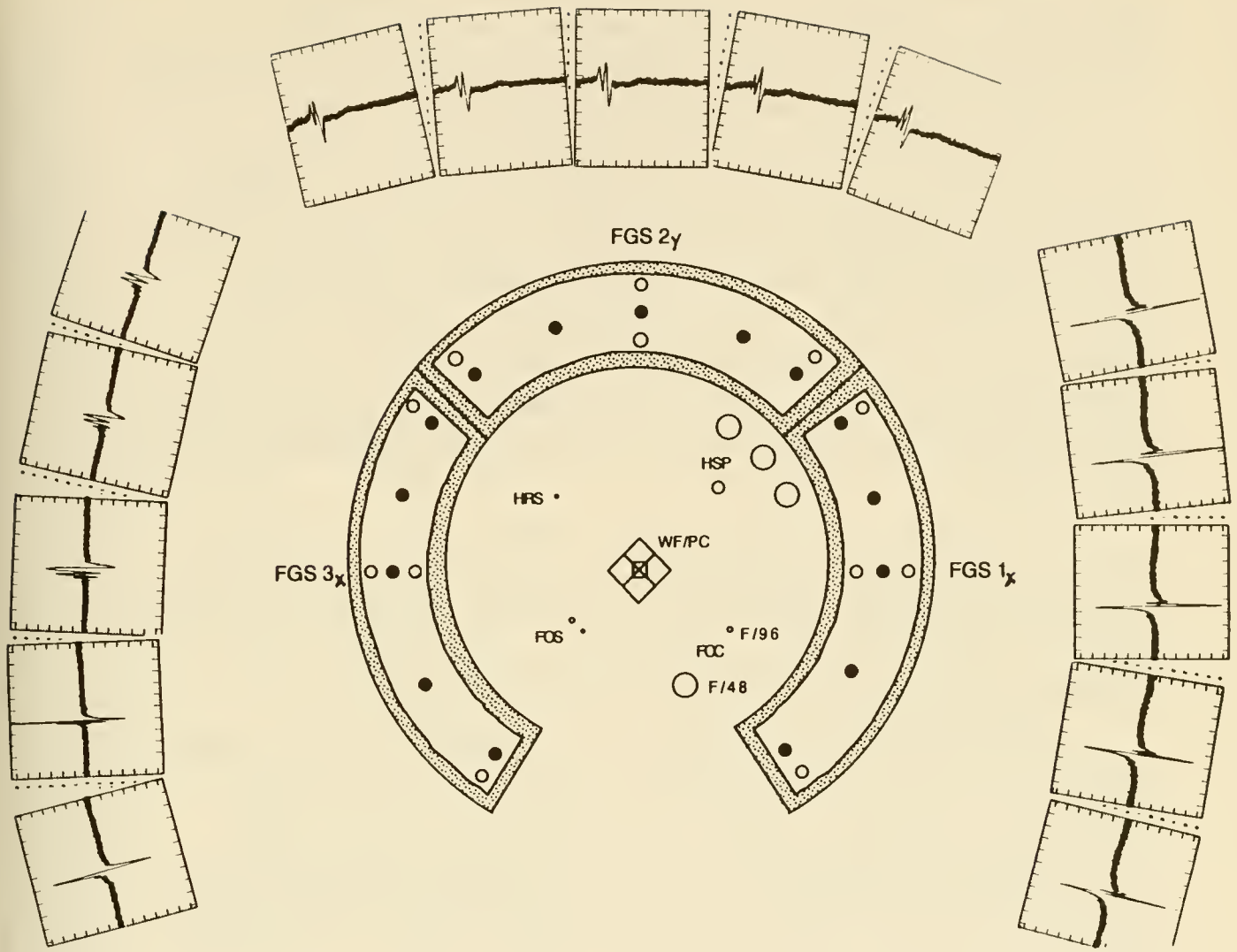

Figure 3 - Summary of a "5 Points of Light" test done day 066, 1991. Plotted are x-axis S-curves for FGS 1 and 3, y-axis S-curves for FGS 2. Positions within the FGS field of view are blackened within each FGS "pickle". Note the variation of modulation with position within the "pickle" for FGS 3.

secondary mirror relative to the primary, produces a characteristic deformation of the intrinsic transfer function of each FGS. This deformation can consist of some combination of modulation reduction and the introduction of additional and spurious peaks and/or valleys.

This very productive series of observations discovered as much about each FGS as about the state of collimation of HST. The unhappy conclusion, corroborated by ground testing of a flight-spare FGS, is that the large spherical aberration of the as-built primary mirror, in the presence of internal FGS misalignments, produces a signature in the transfer functions which mimics coma. The pair of transfer scans of the same star in the same FGS shown in Fig. 4 illustrates the problem. At one secondary mirror position the S-curve has far more modulation than at the other position.

The ultimate result of the 'N Points of Light' tests was to prove the existence of FGS internal misalignments, a not inconsequential reward, since the detailed shape of the transfer function influences binary detection. For FGS 3 (Fig. 3) the internal misalignments cause the shape of the transfer function to vary with location within the FGS.

Another conclusion from these tests was that the secondary mirror position itself can perturb the transfer function shape. It appears to be impossible to obtain high quality S-curves from all three FGS units simultaneously. It is hoped that the secondary mirror will eventually end up in a position which will provide very high quality S-curves from one FGS, lesser quality, but still usable S-curves from another, and guiding-quality S-curves in the third FGS.

The principal effect of lack of collimation for FGS astrometry at this point has been to delay our choice of astrometer. Once the WFPC and FOC have determined the best coma and astigmatism secondary mirror position, a final 'N Points of Light' test will be carried out to select the astrometry FGS. From transfer function variations seen as the secondary changes positions, it has become clear to us that a stationary secondary mirror is of prime importance.

2.1.3 Jitter

A major contributor to the FGS error budget, jitter, has its strongest source in the response of the Solar Arrays to terminator crossing. This stimulus occurs roughly eighteen times each 24 hours. The strongest modes

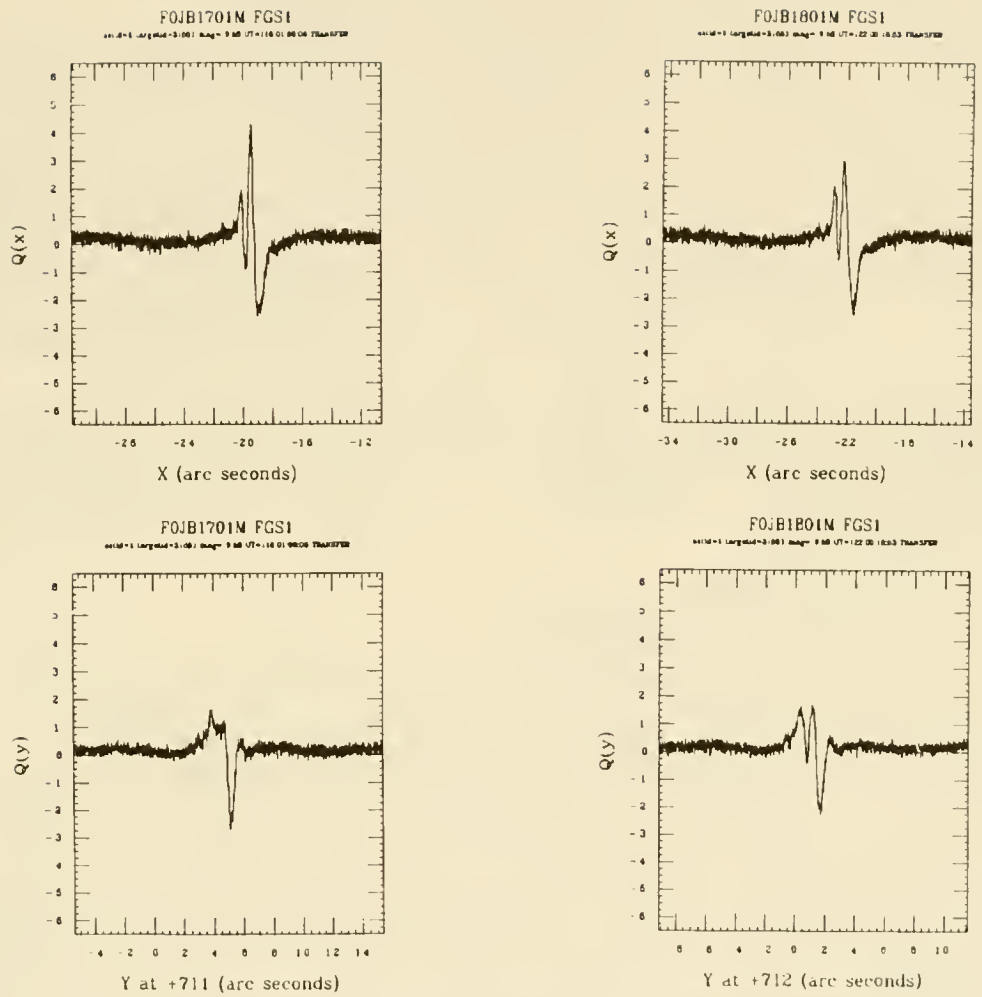

Figure 4 - S-curves for Upgren-69 for x (top) and y (bottom) axes for two different secondary mirror positions, day 116 (left) and day 122 (right) in 1991.

excited have frequencies near 0.1Hz and 0.6Hz. The effects are strongest for about 6 minutes after each terminator passage, although there are random 'quakes' throughout orbit night or day.

Fig. 5 displays an example of the jitter problem. We present TRANS mode data for a star observed as part of a preliminary thermal test. The five consecutive scans, each taking one minute, clearly indicate motion along the scan axis, especially in the third panel.

Fig. 6 shows what the guiding FGSs "see" at the terminator. We plot the sum of the two PMT channels on each axis against time. FGS 3 and FGS 2 are installed in HST such that the Y axis of FGS 3 is parallel to the X axis in FGS 2. The disturbances seen by the FGS seem highly correlated, which raises the possibility that they could be removed. Note the presence of both the 0.1Hz and 0.6Hz oscillations. These data were acquired before a partial fix via on-board software (SAGA) was installed. In an optimistic sense, jitter is a temporary problem, since NASA is committed to exchanging the flawed Solar Arrays with a redesign much less sensitive to temperature variations. This upgrade is scheduled to occur during the first refurbishment mission.

2.2 Problems Intrinsic to FGS

2.1.1 Internal misalignments

As discussed above, the 'N Points of Light' tests demonstrated conclusively that spherical aberration, coupled with internal FGS misalignments, can change the shape of the transfer function. For FGS 1 and FGS 2, the misalignments perturb the transfer function in a similar fashion throughout the FGS field of view. For FGS 3 (Fig. 3) the internal misalignments cause the shape of the transfer function to vary with location within the FGS.

Each FGS has a filter wheel installed near an aperture stop. One position in this wheel contains a 2/3 aperture stop. A partial, but for some projects most unsatisfactory, fix consists of observing with the FGS 2/3 aperture. This greatly reduces the consequences of FGS misalignment, often restoring the transfer function to a near normal shape and modulation. Unfortunately, the use of the 2/3 aperture reduces our limiting magnitude. Rare is the scientifically interesting target surrounded by bright reference stars! Relying on the 2/3 aperture to 'fix' misalignments also

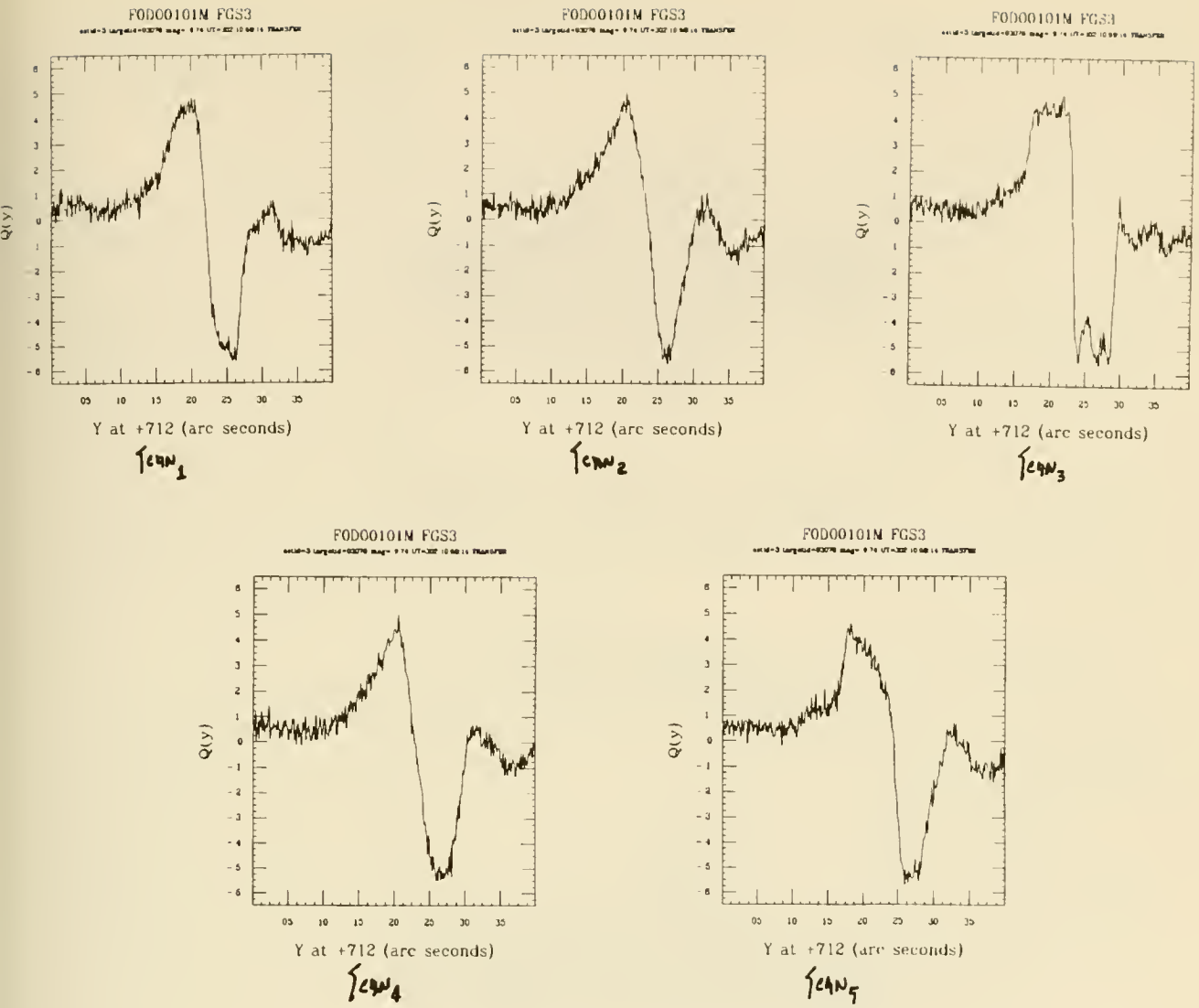

Figure 5 - A set of five TRANS mode scans for a star. Each scan duration was 100 seconds. Jitter affects all but scan 2. Multiple scans in TRANS mode are now standard procedure.

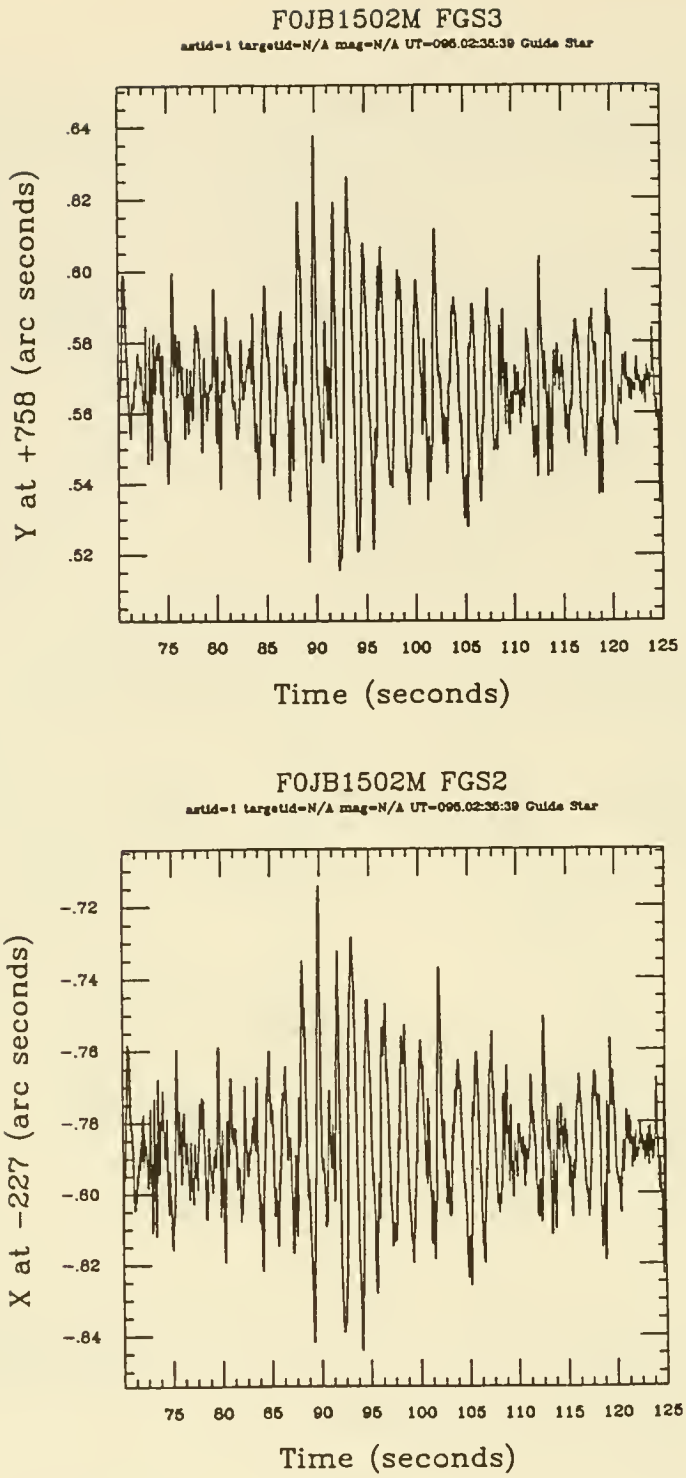

Figure 6 - Top, FGS 3 y-axis, bottom, FGS 2 x-axis. The sum of the two PMT channels on each axis is plotted against time. Easily seen are the 0.1Hz and 0.6 Hz components to the HST jitter. Note the correlation between FGS 3 and FGS 2. These are parallel axes, due to the placement of FGS 3 and FGS 2 within HST.

prohibits the use of the scientifically useful bandpass limiting filters installed in each FGS.

2.2.2 Optical Field Angle Distortion

Achieving the specified 2.7 mas relative positional measurement accuracy will require that we map and remove distortions known to be present in the FGS optical train. These distortions are caused by, for example, non-flatness in the pickoff mirror and figure imperfections in the FGS asphere. We lump all effects together and call them optical field angle distortion (OFAD). Ideally, one would like to simply observe a field of stars whose relative positions are known to 0.5 mas. Analyzing the residuals of a fit of FGS data to these known positions would give information on the intrinsic FGS distortions. Unfortunately, no such field exists. The FGS itself is the only device accurate enough to measure the effects of optical field angle distortion.

How then will we determine the distortion? We shall observe a rich star field (such as NGC 188 or NGC 5617) as follows. We obtain POS mode data for about 25 stars in each FGS. We do this fifteen times, varying the pointing by some fraction of the width of an FGS, to achieve significant overlap. Next, the data are corrected for known star selector encoder errors and HST orbit-induced velocity aberration. We finally subject these data to overlapping plate techniques using GaussFit (Jefferys et al., 1991), solving for star positions and distortion coefficients simultaneously. The constraint that the relative star positions are unchanged for each observation set allows us to determine the optical effects intrinsic to the FGS.

To demonstrate the overall correctness of the approach, we provide some results from a preliminary OFAD. These results (to be discussed at greater length in Wang et al., 1991) are not a sufficiently accurate mapping of positions and distortions to achieve our goal of 2.7 mas relative positions. The observations were done in coarse track rather than fine lock. We obtained only five pointings, rather than fifteen. Nonetheless, they do show that our methodology works.

For this sparse data set we restricted ourselves to a model with order five or fewer terms for the distortion coefficients. We also included ground-based astrometry as a check, knowing that if the approach was

viable, these would have far larger errors in position than did the HST data.

The results are encouraging, especially considering the non-optimal observing conditions and degree of overlap. Fig. 7 displays the x and y residuals (O-C) plotted against the x coordinate. The residuals plotted against the y coordinate have a similar distribution. Both residual plots are for the HST data. As expected, the ground-based residuals (not shown) were considerably larger. Fig. 8 presents the x and y residuals as a function of position within FGS 1, showing that we have mapped the distortions with 3 to 5 mas rms residuals. Note that the smaller residuals in y are probably due to the smaller jitter along this axis for this FGS unit. The y axis is perpendicular to the direction of the dominant flapping mode of the solar arrays. To obtain the full field 1-2 mas will require many more pointings, fine lock, and the scheduling legerdemain required to avoid terminator crossings.

Finally, each time the secondary mirror is moved, the milliarcsecond calibrations of the field distortions are obliterated. This stands as a compelling astrometric argument for a stable secondary mirror.

3. Transfer Scan Mode Scientific Results

While waiting for the telescope to be optimally collimated we have accomplished some early science using the transfer scan mode. By observing a presumed single star close in time to the observation of a suspected double, and by observing the presumed single star at the same location within an FGS as the target star, we have inspected a set of stars for duplicity and have measured the relative positions of the components of a known double.

3.1 Hyades Binary Search

As part of the Early Release Observation (ERO) program, S-curves for about a dozen stars in the Hyades were obtained and examined in an effort to detect previously unknown binaries. One star has a suspicious looking S-curve and may be double. The detailed results of this survey (Franz et al., 1991b) are to appear in The Astronomical Journal.

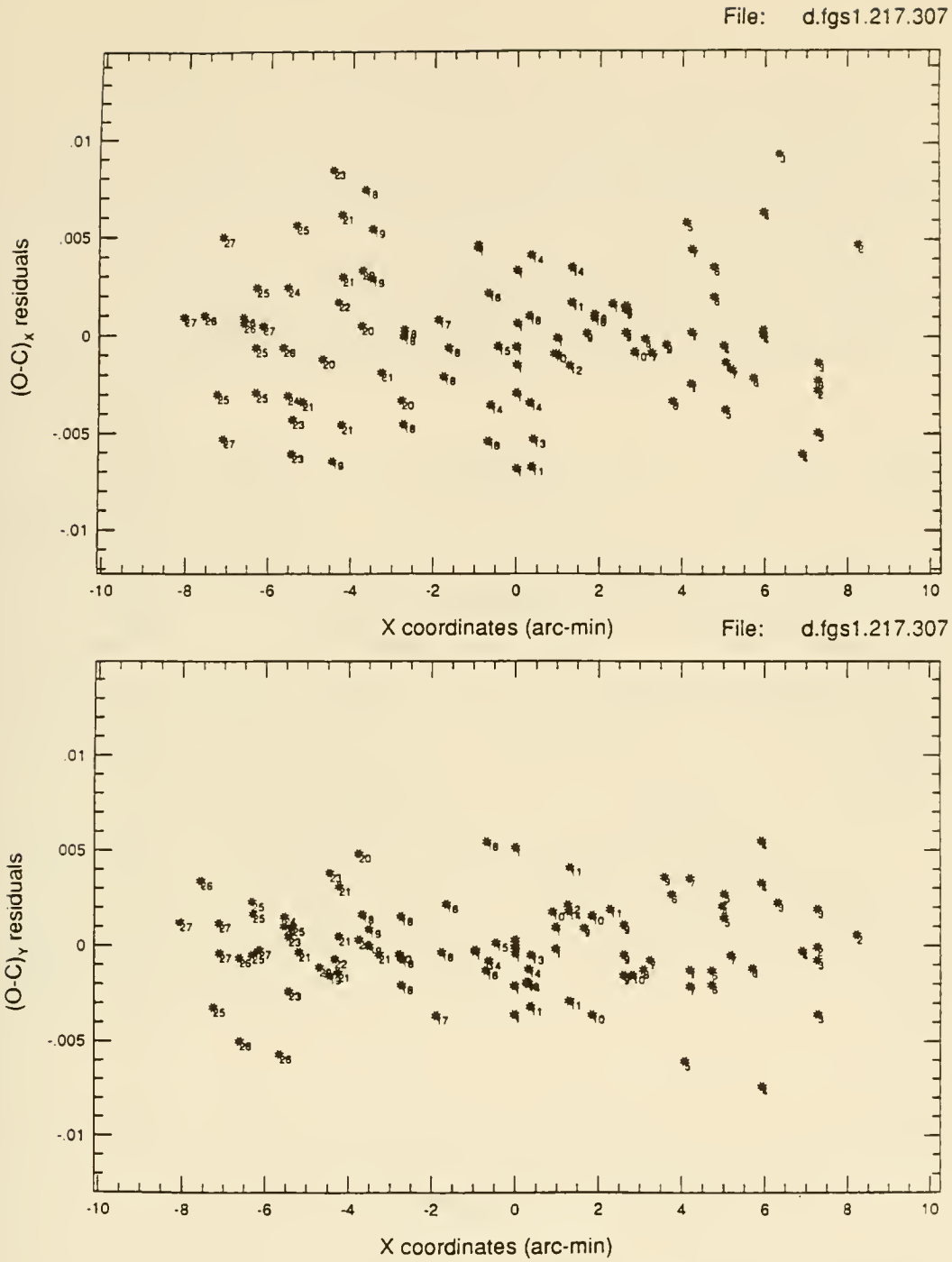

Figure 7 - X (top) and y (bottom) residuals (in arc seconds) plotted against x (in arc minutes) for a preliminary OFAD study. Note that the residuals are smaller for the y-axis, which for this FGS is perpendicular to the major flapping direction of the Solar Arrays.

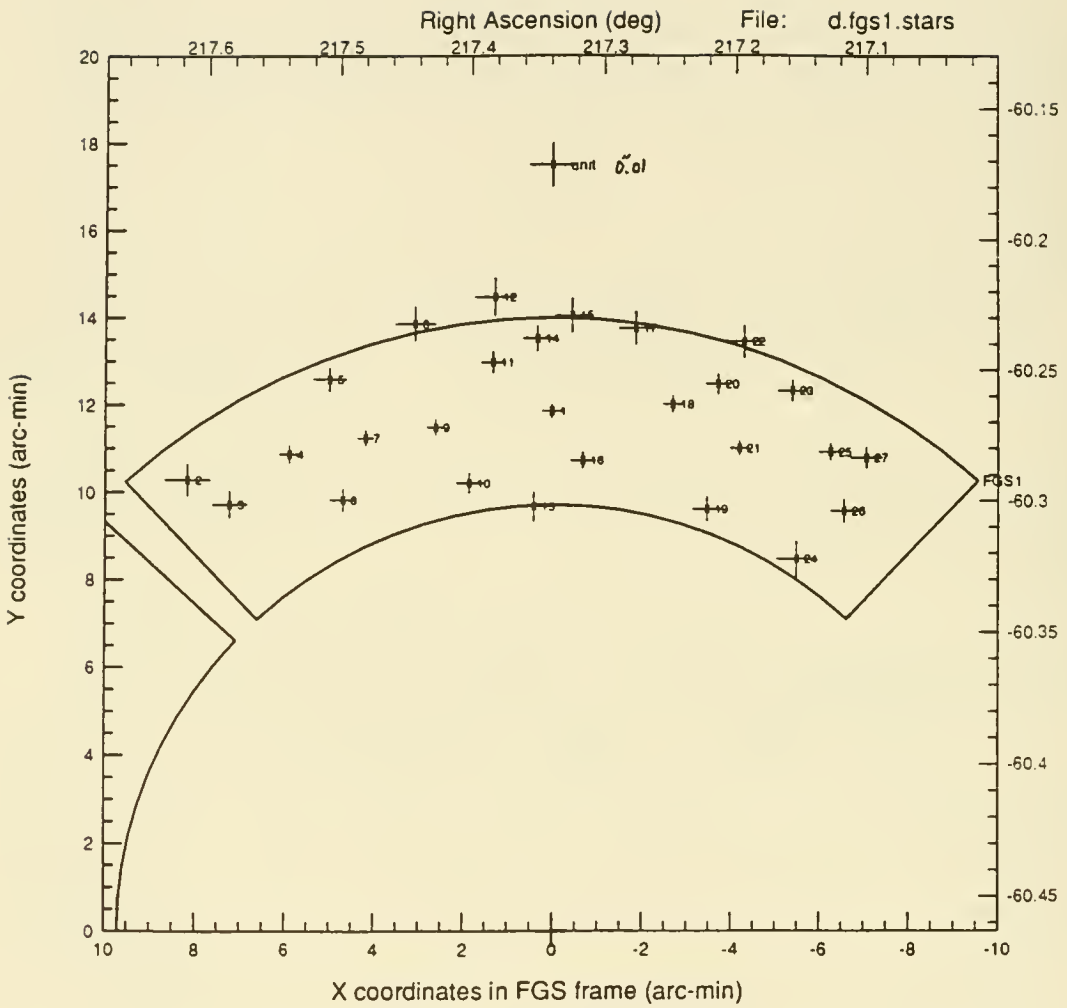

Figure 8 - X and y residuals as a function of position within FGS 1 for a preliminary OFAD study.

3.2 The Binary ADS 11300

For another contribution to the ERO program, we chose a known double, very close to periastron. One accurate measurement near periastron may serve to define its orbit. The details of this successful observation can be found in Franz et al. (1991a). The Astrometry Science Team will continue to monitor this star to better define the orbit and use it as a test of the FGS, since the separation is predicted to go below 0.01 arcsec in 1992.

4. Summary

HST will likely have (after final collimation) one fully capable astrometer, probably one fully capable guider in addition to the astrometer, and one guider capable of 7 mas guiding using the 2/3 aperture.

Jitter is ultimately a soluble problem. The interim solution of control law modification will eventually render some parts of all orbits quiet enough to reach our original relative position accuracy goal. The replacement of the existing solar arrays will provide a permanent fix, and a continuously stable platform.

The preliminary OFAD results are encouraging. We have demonstrated the logic and utility of our basic approach.

Finally, transfer scan mode double star science looks very promising, although we may have to restrict our observations to a particular location within one FGS.

References

Bradley, A., Abramowicz-Reed, L., Story, D., Benedict, G., and Jefferys, W. 1991, PASP, **103**, 317.

Franz, O.G., Kreidl, T.J.N., Wasserman, L.W., Bradley, A.J., Benedict, G.F., Hemenway, P.D., Jefferys, W.H., McArthur, B., McCartney, J.E., Nelan, E., Shelus, P.J., Story, D., Whipple, A.L., Duncombe, R.L., Fredrick, L.W., and van Altena, Wm. F. 1991a, ApJ, **377**, L17.

Franz, O.G., Wasserman, L.H., Nelan, E., Lattanzi, M.G., Bucciarelli, B., and Taff, L.G. 1991b, to appear in AJ

Hester, J., Light, R., Westphal, J., Currie, D., Groth, E., Holtzman, J., Lauer, T., and O'Neil, E. 1991, AJ, **102**, 654

Jefferys, W., McArthur, B., and McCartney, J.E. 1991, BAAS, **23**, 997.

Wang, Q., Jefferys, W. 1991, "Bootstrap statistical analysis of the Hubble Space Telescope Optical Field Angle Distortion", in preparation

A REVIEW OF PLANETARY OPPORTUNITIES AND OBSERVATIONS WITH THE HUBBLE SPACE TELESCOPE

Reta Beebe
Department of Astronomy, New Mexico State University
P.O. Box 30001/ Department 4500
Las Cruces, New Mexico 88003-0001
U.S.A.

Abstract

This review discusses the anticipated capabilities of the Hubble Space Telescope for observations of solar system bodies, reviews the results achieved from preliminary observations, suggests future observations and addresses improvements that will simplify and enhance planetary observations.

1. INTRODUCTION

The possibility of obtaining near simultaneous high resolution, multispectral images and ultraviolet spectra of selected regions of solar system bodies provides us with opportunities to obtain both spatial and spectral information concerning links between chemistry and dynamics of solar system bodies. But, obtaining desired observations is complicated by the differential motion of solar system objects relative to background stars. Although full implementation of software to track moving targets has not yet been completed, progress is being made. So far we have obtained data that expand our knowledge concerning temporal variability of planetary atmospheres and supplements earth-based observations of comets. This review:

1) addresses the effectiveness of deconvolution of the Wide Field/ Planetary Camera (WF/PC) images,
2) considers the anticipated capabilities of Hubble Space Telescope (HST) for a variety of solar system objects,
3) reviews early observations of Pluto, Comet Levy, Mars, and Jupiter,
4) presents a preliminary analysis of the Saturn data obtained in November 1990,
5) previews future observations and
6) concludes with a summary of problems yet to be solved and goals we expect to attain.

2. DECONVOLUTION OF WIDE FIELD/PLANETARY CAMERA IMAGES

The WF/PC team obtained multispectral images of Saturn in the wide-field mode on August 26, 1990. At this time, less than 6 weeks after opposition, Saturn was easily accessible and the globe showed typical east-west banding and color-dependent limb-darkening similar to that observed by the Voyager spacecraft. Because the structure of the rings was known, these data could be used to evaluate artifacts introduced by the deconvolution. The resolution of Encke's division, which is at the limit of earth-based resolution, was convincing evidence that HST could provide useful imaging data.

In late September a major disturbance developed in Saturn's equatorial region. In mid-November a series of multispectral images were obtained with the WF/PC. Figure 1 uses one of these images to illustrate the deconvolution problem. The image on the left is the original raw image from the planetary mode (chip P6) of the WF/PC and the image on the right is the reduced product, generated by the Lucy method (Lucy, 1974), assuming a constant theoretical point spread function over the image. Careful inspection of the images reveals that deconvolution is limited by uncertainties in the flat-field and noise in the data and that the assumption of a constant point spread function is not the limiting factor at this time (*i.e.*, there is no discernible distortion of Saturn's rings).

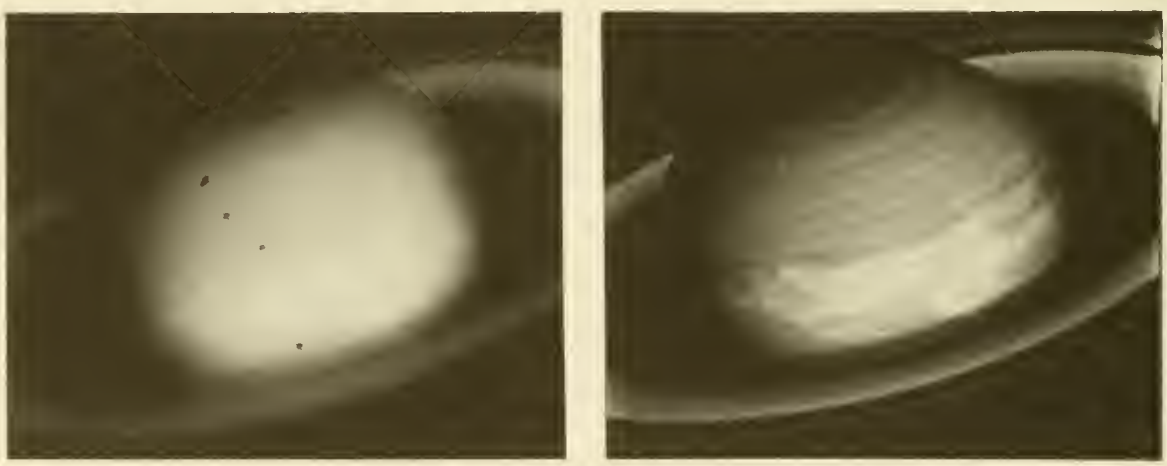

Figure 1. Deconvolution of WF/PC Data. This image was obtained with the F588N filter at 1:39:53 UT on Nov. 17, 1990. The raw image is on the left and the deconvolved image is on the right. (North is at the top and east to the right in all images in this article.)

3. ANTICIPATED CAPABILITIES OF THE HUBBLE SPACE TELESCOPE

The initial specifications for the HST and its associated camera and spectrographs promised the opportunity to obtain observations that would enhance our knowledge of both short term and longer term variable phenomena associated with solar system objects. The opportunity to sample at 1.5 hour intervals, to obtain high spatial resolution through relatively broad-band filters and to acquire high spectral resolution of areas on

solar system bodies would provide enhanced capabilities. We will consider some of the opportunities for some important targets.

3.1 Pluto

The fact that Pluto and Charon have recently completed a series of mutual occultations (which occur every 124 years) has enabled us to determine the radii and masses of the two bodies and has revealed that the albedo and spectral response of the two bodies differ. This new information, coupled with the fact that the two bodies have recently passed through perihelion and developed thin atmospheres due to maximum insolation, motivates us to seek evidence of atmospheric absorption on the two bodies. Although the expected lifetime of HST is short (15-17 yrs) relative to Pluto's seasons, the possibility of establishing surface conditions on the two bodies at a time near maximum solar heating is challenging.

The radii of Pluto and Charon are 1,150 km and 595 km, respectively, and the separation of their centers-of-mass is 19,640 km (see reliable tables in Beatty and Chaikin, 1990). At their current distance from earth (see the Astronomical Almanac, U.S. Gov. Printing Office), the diameter of Pluto would subtend a little more than 0.1" and Charon about half that. Near perihelion these two bodies have a maximum separation of about 0.9". The angular size of a pixel in the planetary mode (PC) of the WF/PC is 0.043". therefore the two bodies would be separated by about 20 pixels and the diameters of Pluto and Charon would span about 2.5 pixels and 1.3 pixels, respectively. Thus, the system would be a desirable target for multispectral imaging, as well as astrometric measurements to refine our knowledge of the system. But, even though WF/PC images have been successfully deconvolved and maximum separation of the two bodies, 0.9", occurs every 3.2 days, the current point-spread function presents an obstacle in the way of obtaining individual spectra.

3.2 Comets

Observations of comets from ground-based sites are fraught with problems. When the comet is bright enough to obtain many of the desired observations its proximity to the sun severely limits the length of the observing window and requires daylight observations or dealing with a large zenith angle. These observing aspects reduce spatial resolution and severely hamper photometric observations.

There is increasing evidence that the rotation rate of cometary nuclei is on the order of hours. When the patterns of outgasing of Comet Halley are considered, it is apparent that the possibility of observing a comet every orbit of HST, at 1.5 hour intervals. for multiple orbits several times during a period of weeks would be highly desirable. These observations, obtained under constant viewing conditions would greatly enhance our understanding of the composition and dynamics of a selected set of representative comets. H. Weaver will present WF/PC observations of Comet Levy elsewhere in this conference proceedings.

3.3 Mercury and Venus

Although, in 1974-75, Mariner 10 encountered Mercury three times, the nature of

the orbit was such that half of the surface area of the planet was not observed. When Mercury is at maximum elongation a pixel of the PC mode of the WF/PC would span only 30 km on the surface of Mercury, but the angle between Mercury and the sun is 17 to 28 degrees. This geometry places Mercury well inside of the HST safety limit for near-sun observations. Venus is also within the safety limit at about 46 degrees maximum elongation. Therefore, even though the PC mode would yield 22 km/pixel, observations of Venus are not possible without relaxing the HST sun safety limit.

3.4 Mars

The Earth-Mars distance of 0.666 to 0.381 AU at opposition makes Mars a likely target for HST. Because the synodic period is 2.135 years, favorable observing conditions will occur biannually.

Again, the ability to observe the planet at 1.5 hour intervals is useful for monitoring events associated with the onset of global dust storm which occur on time scales of hours and days. Because Mars and Earth rotate in the same direction with periods of 24.6229 and 23.9345 hr, respectively, the planet appears to rotate less than 10 degrees per day, providing poor coverage of planet-wide events from earth-based stations.

The last Martian opposition occurred in late November 1990, with a minimum Earth-Mars distance of about 0.52 AU. At this distance, an image of Mars spans 420 pixels in the PC mode of the WF/PC, and each pixel corresponds to about 16 km on the Martian surface. The fact that a second favorable opportunity would not arise for more than two years led Philip James and his co-investigators to ask for special consideration. They were granted the first General Observer time on HST. James will report on early results from the WF/PC and spectroscopic observations in this section of the conference proceedings.

3.5 The Outer Planets

Even though Jupiter, Saturn, Uranus and Neptune are more remote, the large scale of their atmospheric features recommends them as desirable HST targets. Table 1 summarizes the anticipated resolution of features within these cloud decks.

Table 1. The Resolution of the Giant Planets with the Planetary Mode of the Wide Field Planetary Camera

Planet	Apparent(1) Equatorial Diameter	Pixels Subtending	km/pixel
Jupiter	31.5 to 46.8"	735 - 1090	196 - 132
Saturn	15.2 to 18.7	353 - 435	342 - 277
Uranus	3.5 to 3.9	81 - 90	646 - 581
Neptune	2.1 to 2.3	50 - 53	990 - 934

(1) The equatorial diameters represent an annual range given in the Astronomical Almanac

With temperatures less than 150 K , the thermal response times of the visible cloud decks of these planets are on the order of years and it seems that occasional sampling

would probably suffice to define their atmospheric state. Although this appears to be true for Uranus, it is not the case for Jupiter, Saturn or Neptune. These planets have sizable internal heat sources, with Jupiter, Saturn and Neptune emitting 1.65, 1.82 and 2.70 times more energy than the absorbed solar radiation. As a result, convective processes play a large role in determining the state of the visible cloud deck. The resulting cloud features are controlled by the strong zonal (east-west) wind patterns and planet-encircling phenomena can develop in days. Wave phenomena, which change on the scale of minutes and hours, are also present. Therefore, HST opportunities, when combined with the historical ground-based data sets, the short term coverage by Pioneer and Voyager flybys and the hoped for Galileo and Cassini observations, will enhance our understanding of these giant planets.

Table 2. Observational Constraints for the Giant Planets

	Jupiter	Saturn	Neptune
Revolutions of HST per Rotation of the Planet	6 - 7	6 - 7	10 - 11
Exposure Time(1) per Pixel of Smear (sec)	10	30	450
Dilution Factor(2)	1.00	0.30	0.03
Maximum Measurement(3) Accuracy (m/sec)	4	8	14

(1) based on observed rotation rates at low latitudes.
(2) assumes distance from sun = semimajor axis of orbit.
(3) assumes it is possible to reach one pixel accuracy in location of a cloud feature on 2 consecutive rotations of the planet.

An unanswered fundamental question involves the degree of variability of the zonal winds as a function of latitude (Beebe and Youngblood, 1979; Ingersoll and Cuzzi, 1969; Ingersoll, *et al.* , 1981)). Conflicting models of the mechanisms that maintain the global circulation include a thin shell model, essentially a scaled model of the earth's atmosphere, and a deeper model that includes the convective envelope and assumes the winds are generated by the tendency for the rapid rotation to force rising convective cells into a cylindrical flow. The WF/PC in PC mode will allow short enough exposures to avoid smearing due to rotation of the planet while providing adequate spatial resolution to identify small cloud features moving with the winds. Unlike the Voyager video cameras that were insensitive to red light, the WF/PC can provide observations with an 889 nm narrow-band filter that spans a wavelength interval dominated by methane absorption in the upper atmosphere. These data, when combined with other filters and selected spectroscopic observations, will supply information about the vertical structure of cloud systems. Table 2 summarizes the observing constraints for resolving longitudinally varying cloud structure on Jupiter, Saturn and Uranus. The period of revolution of Jupiter and Saturn are 11.86 and 29.458 years and the inclination of the equators to their orbits are 3.12° and 26.73°, respectively. When the time scales associated with the seasonal aspects of the atmospheres of these two planets are considered, it is easy

to see that the data that can be acquired with HST will contribute a valuable archive for atmospheric studies.

4. SELECTION OF TARGETS FOR EARLY DATA ACQUISITION

The arrival of Comet Levy prompted early observations of a cometary target. These observations (see H. Weaver, *et al.* this proceedings) have shown that multispectral imaging in time steps on the order of hours can be used to determine the periods of rotation of comets. The brightening of the inner coma varies as active regions rotate in and out of our line-of-sight and periodic behavior can be derived from time sequences.

Sequences of observation which include multispectral imaging and ultraviolet spectra of Mars (see P. James, *et al.* this proceedings) and imaging of Titan (see J. Caldwell this proceedings) have been acquired and problems of deconvolution and calibration of the P6 chip in the WF/PC have been investigated.

Early multispectral imaging of Jupiter, which utilizes all four chips of the PC mode of the WF/PC, has been acquired by the WF/PC team. Problems of flat-fielding, deconvolving and mosaicking the data are being addressed. The initial results will be discussed in the next section.

In late September 1990, a major disturbance occurred in Saturn's equatorial region. Only two other major equatorial disturbances had ever been observed. They occurred in 1876 and 1933. The fact that the 1990 disturbance grew rapidly and the three events were separated by intervals of 57 years (two Saturnian years = 58.92 years) suggested that they might be seasonally induced convective disturbances. STScI responded to this event by granting a group of us, J. Westphal, W. Baum, R. Beebe, J. Caldwell, E. Danielson and A. Ingersoll, a target of opportunity which allowed us to acquire 6-color imaging for two rotations of the planet, spaced to allow 20 to 30 hours between observations of the same portion of the cloud deck. Early results from these observations will be discussed in the next section.

No observations of Neptune have been acquired. Ground-based imaging in red (619 nm) and near infrared (890 nm) by H. Hammel (1989) reveals the white clouds associated with the Great Dark Spot. In 1989, Voyager measurements established a rotational period of 18.33 h for the Great Dark Spot near 20°S latitude while the Voyager rotation period at 42°S was 16.76 hours (Hammel, *et al.* , 1989). In comparison, Belton *et al.* (1981) derived a dominant period of 17.73 hours and secondary periods of 18.56 and 18.29 hours from whole disk photometry. Whether this indicates that there was an additional large feature at mid-latitudes in 1981 or whether the Great Dark Spot decelerated before 1989 by moving northward or by some other mechanism is not known. It does indicate, however, that changes occur, not only on a time scale of minutes, hours and days (Smith, *et al.* , 1989), but also years. The resolution that HST can obtain on this 2.2" disk would be adequate to monitor the Great Dark Spot, especially with the 889 nm filter where the high white clouds would have a maximum brightness.

No observations of Uranus have been attempted. The bland, near featureless cloud deck that was observed by Voyager 2 (Smith, *et al.* ,1986) relegates it to low priority. However, it should be noted that Uranus and Neptune cannot be assumed to be similar to Jupiter and Saturn. With masses more than five times smaller than Saturn and average densities 1.8 to 2.4 times greater, this pair of planets represents an intermediate type planet when compared to the terrestrial or jovian planets. In contrast with Jupiter and Saturn, Uranus and Neptune have westward equatorial winds. These differences make the more accessible Neptune an interesting target for HST.

5.1 Jupiter

When Voyager 1 and 2 spacecraft were at a range of 20 million km from the planet, about 20 days before nearest encounter, the narrow-angle camera images had a resolution that was equal to the original specification of the PC mode of WF/PC. Figure 2 shows a Voyager 1 view of Jupiter on the left that has a viewing aspect similar to the HST image on the right. The Voyager image was obtained on Jan 26, 1979, 38 days before closest encounter when the resolution was 350 km/pixel, half the optimum PC

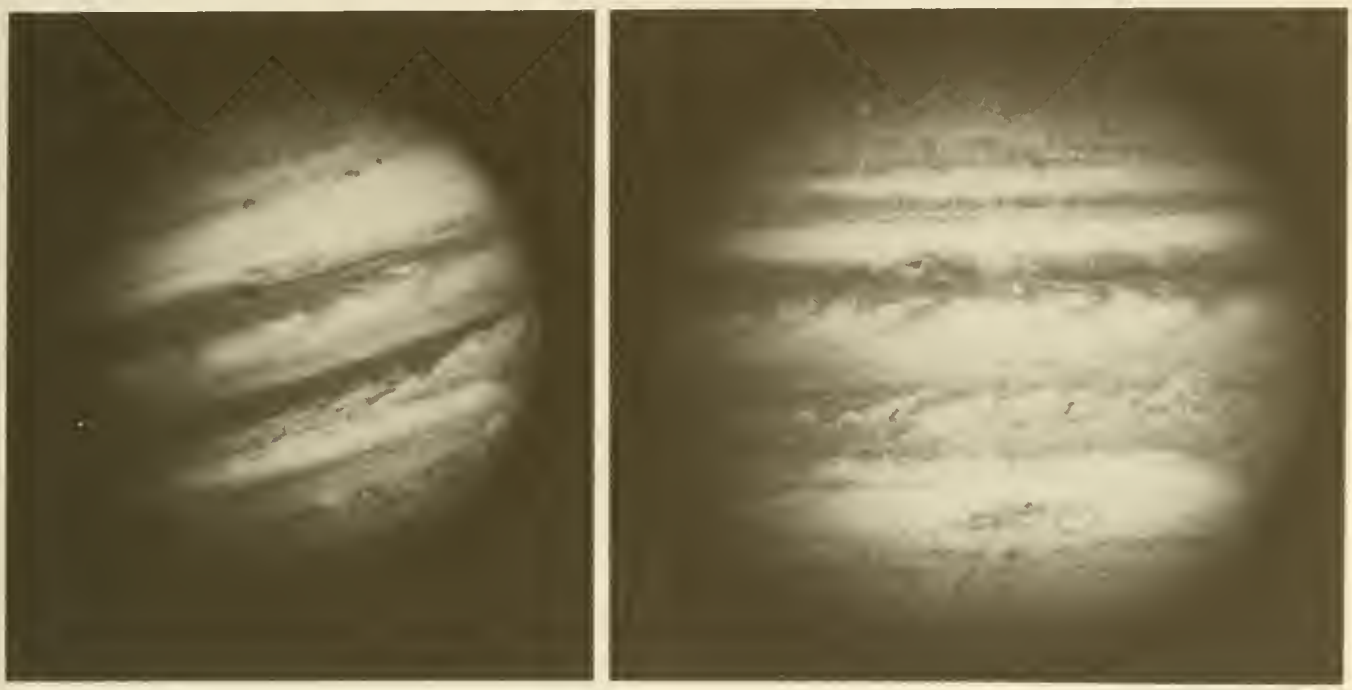

Figure 2. A Comparison of Voyager and Hubble Space Telescope Images. The Voyager 1 image was obtained on Jan 26, 1979 with a resolution of 350 km/pixel and the HST image was obtained with the F547M filter on Mar 11, 1991.

resolution. The Red Spot is rotating off the visible disk and one of three white ovals, located near 30°S latitude, is west of the Red Spot. (These three ovals formed in 1938, from an overall increase in the reflectivity of this latitudinal region. As the white clouds evolved, they separated into three storm centers where the dark intervening regions were designated A-B, C-D, and E-F. The white storm centers retained this designation as they contracted and still bear the unlikely names of FA, BC and DE.) The oval in the Voyager image is BC, with FA located to the east and DE to the west (Beebe, *et al.* , 1989). These ovals drift eastward relative to System III (870.536°/day, Riddle and Warwick, 1976) at 2.6 to 5.5 m/sec (Beebe and Youngblood, 1979). Not only do the ovals catch up and pass the Red Spot in about two and a half years, but the spacing between them varies. The image on the right in Fig. 2 is a deconvolved, green image (F547M) that was obtained with HST on March 11, 1991, almost one Jovian year after the Voyager image. Again the Red Spot is at the limb, however, this time the white oval

is FA, 50° to the west of the Red Spot, while DE and BC are 66° and 87° east of the Red Spot, respectively. Although the turbulence to the west of the Red Spot appears very similar in the Voyager and HST images, this region experienced a general brightening, where the entire dark belt became white and featureless in June 1989, similar to the aspect during the 1973-74 Pioneer 10 and 11 encounters. When Jupiter emerged from conjunction in late summer 1990, the belt had returned to the Voyager-like appearance seen in Fig. 2. The HST image serves as a test to determine how many small eddies are available as markers of atmospheric motion. Based on our experience with the Voyager images, the resolution is adequate to obtain a new map of zonal (east-west) wind velocities. Images separated by about 20 hours, will be used to derive zonal winds as a function of latitude. The results can be compared with a similar set of Voyager data, obtained one Jovian year earlier (Ingersoll, *et al.* , 1981) during the same season, to determine the extent to which the zonal winds have changed. The WF/PC team has already obtained a preliminary data set which will allow this comparison.

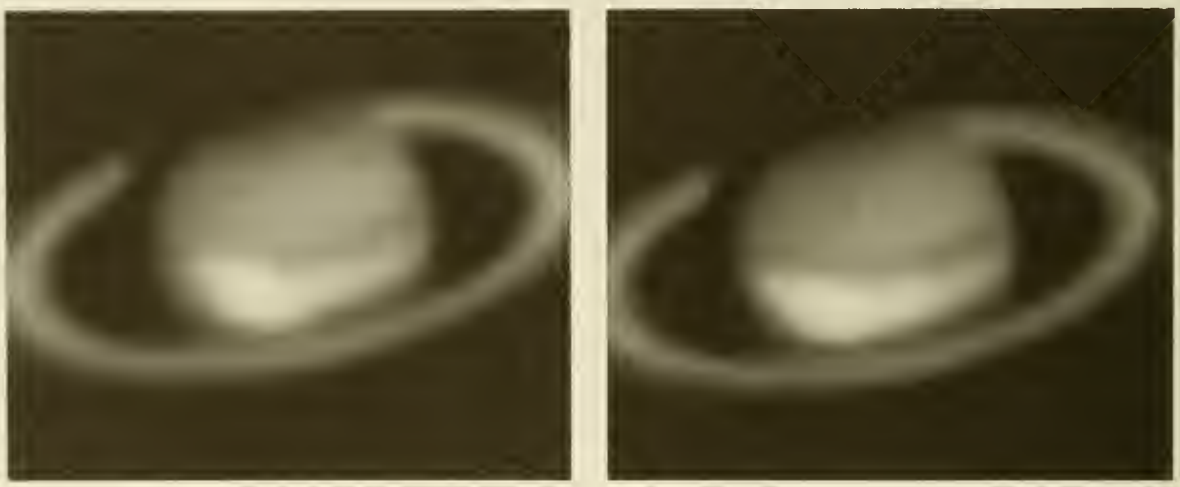

Figure 3. Ground-based Images of the Onset of the Saturnian Storm. The image on the left was obtained at 1:49:03 UT on Oct 4 and the image on the right was recorded at 1:31:41 UT on Oct 7, 1990. Both images were obtained at New Mexico State University with a broadband blue filter and 0.2" sampling.

5.2 Saturn

On September 25, 1990, amateur observers reported a bright white spot in Saturn's northern equatorial region. Subsequent ground-based observations obtained at New Mexico State University (see Fig. 3) revealed that, although the storm expanded rapidly, it retained an identifiable nucleus that translated eastward at a rate of 400.25 +/- 0.82 m/sec (Beebe, *et al.* , 1991) relative to System III longitude (System III is based on the modulation of the radio signal and presumably the planet core. See the The Astronomical Almanac, Section E79, Gov. Printing Office for definition of this system.) This translation rate results in an eastward displacement of the storm system relative to the core of the planet of -32.884 +/- 0.067 deg/day. At 0 h October 16, 1990, the nucleus was located at 212.1 +/- 1.6 deg. west longitude. This information was used to predict the location of the storm nucleus on November 9-18, when it was possible to develop an observing sequence for the planet as a moving target.

5.2.1. The HST Data Set

The multispectral data set, obtained during the November 1990 Saturn Target of Opportunity, consisted of exposures with the P6 chip of the PC mode of the WF/PC. The planet was nearly centered on the chip and the plate scale was such that the ansae of the rings were not imaged (see Fig. 1). The sequence included images for two consecutive orbits on November 9 and 11, 1990. They were followed on Nov. 17 and

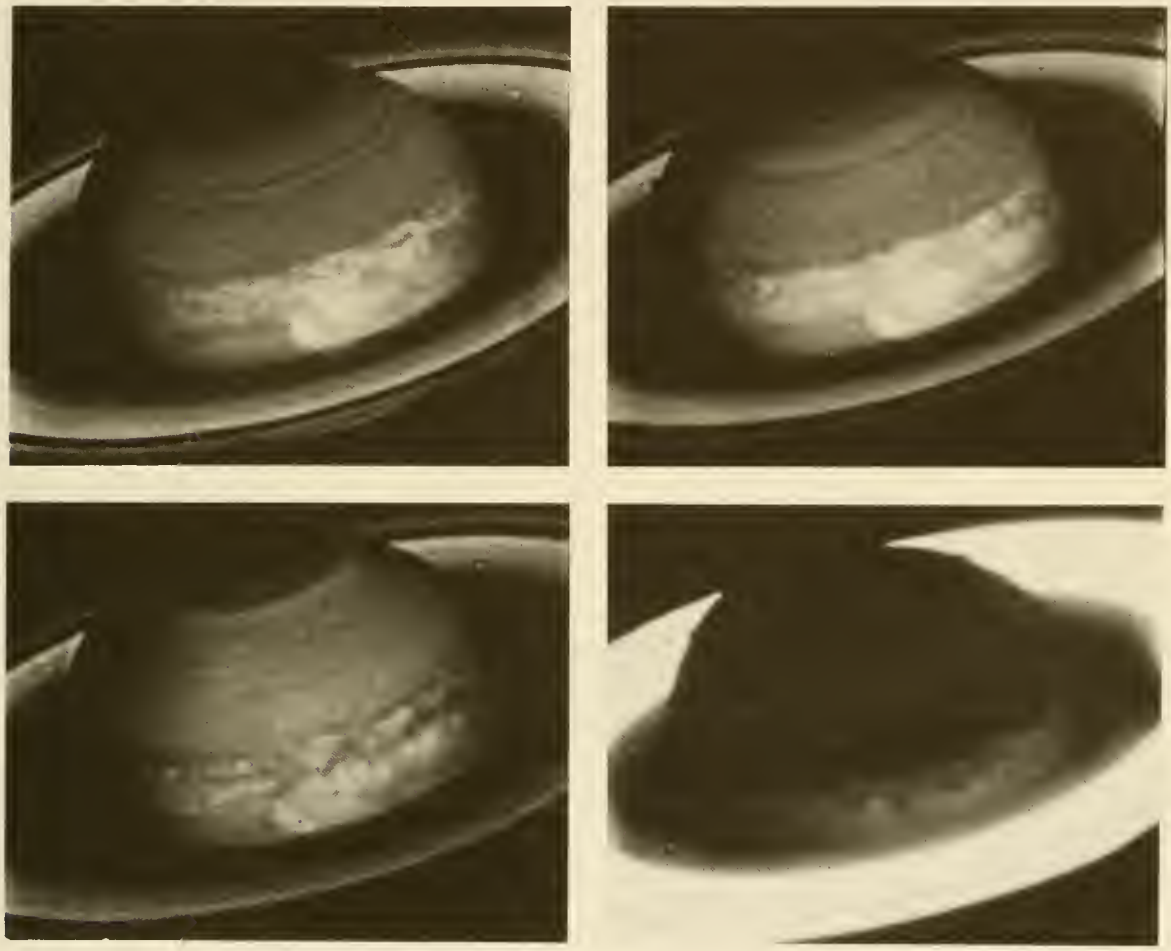

Figure 4. Multicolor HST Images. These images were obtained with the F439W, F547M, F889N and F718M filters, clockwise from upper left. The original storm nucleus is visible.

18 with a more extensive set of observations that included filters F439W, F547M, and F718M. Not only would these broad-band filters allow color composites to be generated, but the short exposures ranging from 0.8 to 4.0 sec would also minimize rotational smearing and allow determination of wind speeds and wave motion in the atmosphere. Two narrow-band filters, F889N, centered within a strong methane absorption band, and F588N, a continuum reference, were selected to form a discriminator of vertical structure. A final filter, F336W, was included to provide insight into the aerosol properties of the upper atmosphere. Data were obtained over 7 orbits of HST on November 17 from 1h 36m to 13h 13m UT. On November 18 observations from 0h 12m to 13h 27m, and an additional set at 22h 48m to 22h 58m, were obtained to maximize the total

time interval and better define drift rates of the clouds. Figure 4 illustrates the color dependence of clouds associated with the Saturn disturbance. This figure contains images obtained with broad-band blue, green and red filters that show large differences in structure. A fourth image illustrates the extent of absorption by atmospheric methane at 889 nm. Because the rings contain no methane, there is a large difference in surface brightness between the globe and rings. This creates problems during the deconvolution process and reduces the use of this filter as an indicator of vertical structure.

5.2.2 The Equatorial Wind Field

Pairs of broad-band blue and green images separated by approximately 20 hours, containing the same large-scale cloud features, were registered and map-projected. This allowed controlled measurements of observed translations of cloud features which were converted to zonal and meridional wind speeds. Preliminary analysis of the data revealed that the rates of translations of clouds in the equatorial region were less than those at the time of the Voyager encounters (Smith, *et al.* , 1981; Smith *et al.* ,1982).

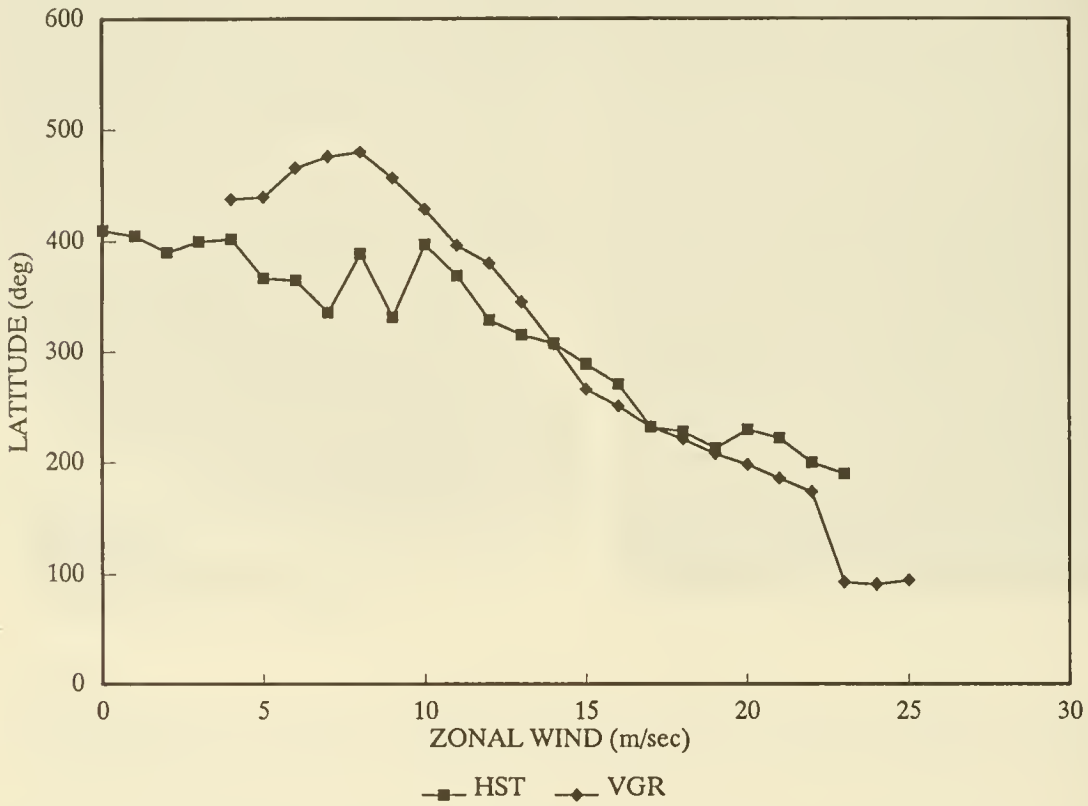

Figure 5. A Comparison of the Average HST and Voyager 2 Winds. These data are averaged zonal winds where all points within +/-0.5 degrees latitude are assigned equal weight and averaged.

Figure 5 illustrates the differences. At the time of the Voyager flybys there was little longitudinally dependent structure in the equatorial region. The few visible features were quickly sheared apart by the latitudinal variation in the zonal wind. The data are plotted in Fig. 5 as a function of planetographic latitude (the angle formed when a normal to the local surface on an ellipsoidal planet intersects the equatorial plane of

the planet).

Many of the features in the HST data are obviously associated with a planet-encircling wave pattern that has been generated as a consequence of the initial disturbance. Due to the fact that small wisps, not well-formed cloud systems, were measured in the Voyager images, an obvious interpretation of the discrepancy between the two data sets in Fig. 5 is that the Voyager 2 data represent the unperturbed zonal wind, and the difference between the HST and Voyager translation rates represents the phase velocity of the equatorial waves. If this is the case, the storm would be bounded on the poleward side by an eastward wind with a relative speed of about 75 m/sec. The fact that ground-based observations yield no evidence of additional convective disturbances similar to the initial disturbance (Beebe, *et al.* , 1991) supports this interpretation. Thus, we assume that our analysis of the cloud structure is justified.

5.2.3. Wave Analysis of the Cloud Structure

Broad-band green images from November 17, 1990, selected to span all longitudes, were processed to remove the limb darkening and then map-projected. The data were obtained over a period of 9.85 hours during seven HST orbits as the planet rotated in

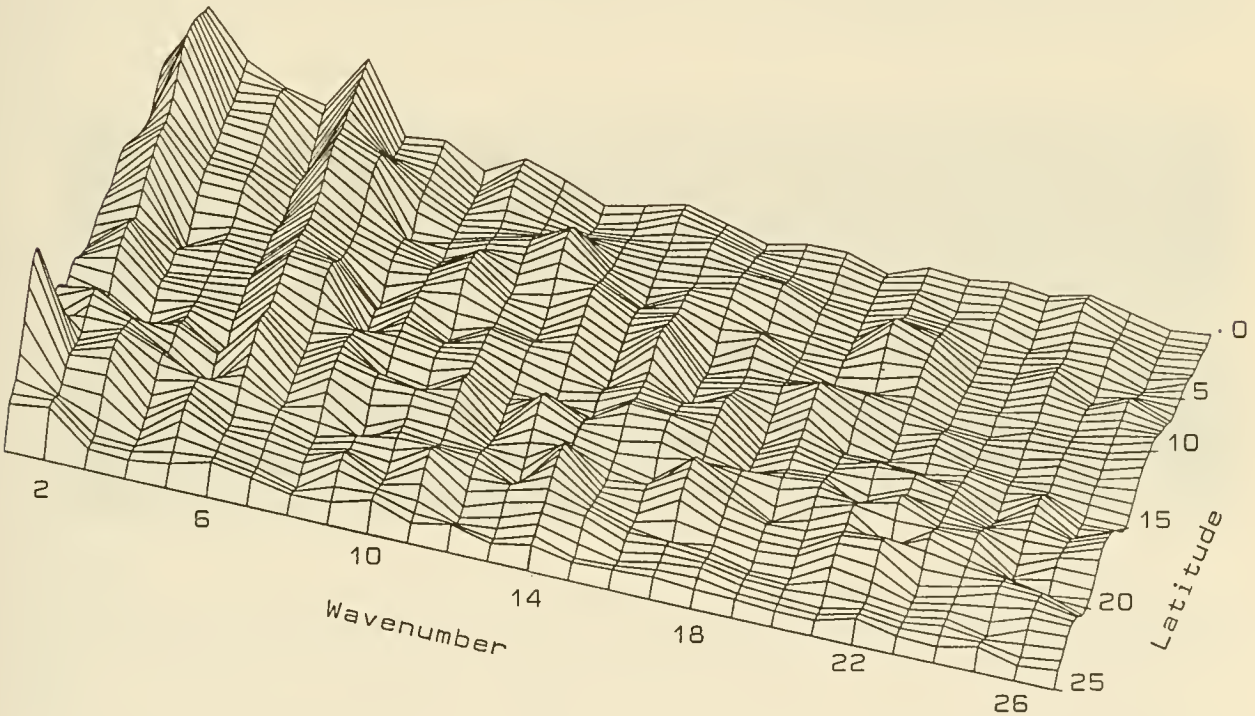

Figure 6. The Amplitudes of Components of Fourier Series. The amplitudes were obtained by fitting the variation in surface brightness in bins spanning 1 degree latitude and 360 degrees longitude. Both phase and amplitude were free parameters.

front of the camera. In order to reduce these images to some instant in time, the HST wind profile in Fig. 5 was utilized to correct each image for the latitudinal distortion that would occur over the intervening time interval. All seven images were remapped to reduce them to the time when the fourth image was obtained. This resulted in shifts as large as 6.7 degrees in the equatorial regions and half that at 20°N in images

1 and 7. The mosaic of the map-projected images, corrected to a standard time, was achieved. In regions where the maps overlapped, we selected the image that minimized the incident and emergent angles, reducing residuals from removal of limb darkening with the Minnaert function.

The resulting mosaic spans 360 degrees with a resolution of 0.5 degrees in longitude and latitude. Each latitudinal bin, 0.5 degrees wide, was fit with a Fourier series that contained up to 36 terms, where the phase and amplitude of each term was calculated. The 3-D plot in Fig. 6 illustrates the results for wavenumbers less than 27 (representing standing wave structure with wavelengths greater than 13 deg. longitude). Here the amplitude, which corresponds to surface brightness is plotted as a function of wavenumber on the x-axis and latitude on the y-axis.

Figure 7 is the corresponding mosaic. The dominance of wavenumber 2 is caused by the two bright regions that are bracketed along the top of the mosaic in Fig. 7, while the reality of the enhanced amplitudes for n = 6 is illustrated by the arrows that show a repeating pattern in the cloud structure. Although there are definite wave-like structures near 15°N latitude, there is no evidence from this analysis that they form a standing wave. Instead, inspection of these latitudes on map-projections separated in time by about 20 hours reveals that these features are behaving as expected. There is a strong latitudinal gradient in the zonal winds and they are responding to this shear by twinning and recombining. Thus, although they tend to span about 15 degrees, they do not constitute a standing wave.

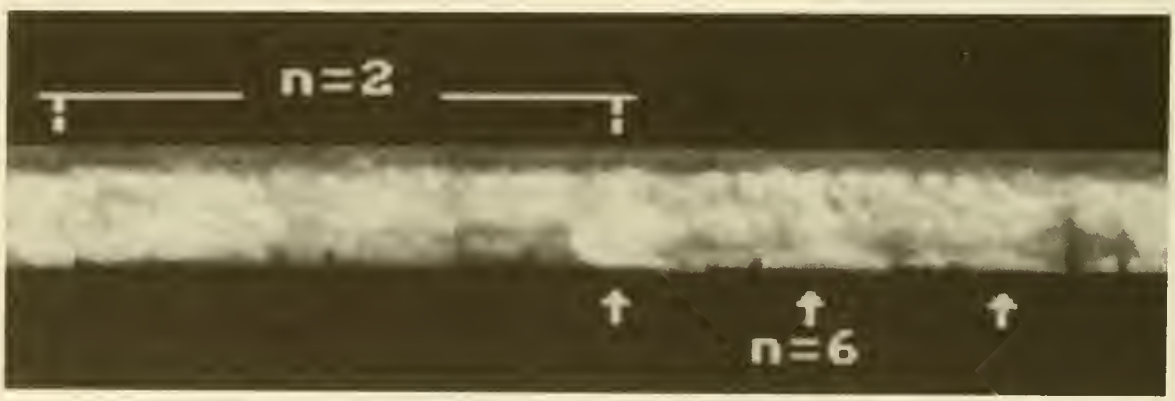

Figure 7. An F547M Map-Projection. These data were obtained on Nov 11, 1990, and show the cloud structures that yield the enhanced n = 2 and 6 amplitudes. The original storm nucleus is indicated by the first arrow on the left.

This preliminary analysis indicates that wavenumber 6 characterizes the gross wave structure. Surprisingly n = 6 is present in the polar hexagon at 76°N latitude (Allison, Godfrey and Beebe, 1990). The significance of this value is not obvious and there is much to be done to understand the November 1990 data set. To enhance our understanding of the equatorial region's response to a convective disturbance, additional observations of its dying stages and the subsequent recovery of the atmosphere are needed.

6. PREVIEW OF OBSERVATIONS TO COME

Already the WF/PC team has acquired multispectral imaging of Jupiter that will provide complete longitudinal coverage of the planet as well as a preliminary check on the stability of the zonal winds. In June 1991, they acquired 3 multispectral data sets of Saturn that spanned 6 HST orbits, providing a post-conjunction map of the wave structure of the abating disturbance. These data are now being reduced and analyzed and indicate that no additional disturbances have occurred.

In addition to these preliminary observations, systematic sets of observations that combine imaging and observations with the FOS or HRS to define temporal variations within the Martian, Jovian, Saturnian and Neptunian atmospheres are desirable. Because these bodies span 15" to 48" and have no extreme contrasts across the visible disks they can be deconvolved into useful data. In addition, prevailing zonal winds tend to cause molecular variations to be latitudinally dependent and to extend over large enough areas of the planet that spectra obtained with arcsecond apertures will reveal differences in molecular concentrations. When these observations are combined with multispectral imaging, they will provide insight into coupling between the troposphere and stratosphere of these planets. Limited observations of this sort are planned for Cycle 1 and later.

The usefulness of HST observations to investigate the dynamical properties of comets has been demonstrated. Unfortunately, the reluctance of comets to announce their arrival dates will tend to require that we be granted Targets of Opportunity to observe them. In a like manner, the abrupt development of Saturn's equatorial storm and the speed with which Jupiter's belts can mix and change dramatically will cause the planetary community to be strong contenders, along with novae watchers, for director's discretionary time.

7. CONCLUSIONS

The aberration associated with the mirrors has made it more difficult to acquire spatially resolved multispectral imaging and has increased exposures with the FOS and HRS. However, we have shown that HST will contribute vitally needed long-term data sets that will provide insight into the structure, dynamics and energy balance of planetary atmospheres and comets. There are still problems associated with reducing the effort necessary to obtain the data and to optimize their quality. The urgent problem of tracking moving targets, will be solved by completing planned software enhancements at the Institute. Other factors, such as improving our capability to flat-field the WF/PC data are being worked on. We, the planetary community, look forward to utilizing this facility for acquiring unique observations, as well as systematic acquisition of data sets that will enhance our understanding of the temporal variability within the Solar System.

ACKNOWLEDGEMENTS

I thank J. Westphal and R. Light for their efforts to deconvolve the data, A.S. Murrell for his dedication to obtaining ground-based observations to define the storm for targeting HST and C. Barnet, L. Huber and P. Sada for their support in reducing and analyzing the Saturn data. Ground-based observations used for targeting and interpreting this data were supported by NASA grant NAGW-1802.

REFERENCES

Allison, M., D.A. Godfrey, and R.F. Beebe 1990, *Science*, **247**, 1061.

Beatty, J.K. and A. Chaikin 1990, *The New Solar System* (Sky Publishing Corporation, Cambridge, Mass.) 298-291.

Beebe, R.F. and L.A. Youngblood 1979, *Nature*, **280**, 771.

Beebe, R.F., G.S. Orton and R.A. West 1989, in *Time Variable Phenomena of the Jovian System*, NASA SP-494, ed. M.S. Belton, R.A. West and J. Rahe, (U.S. Government Publication) p. 245.

Beebe, R.F., C. Barnet, P.V. Sada and A.S. Murrell 1991, Submitted to *Icarus*.

Belton, M.J., L. Wallace and S. Howard 1981, *Icarus*, **46**, 263.

Hammel, H.B. 1989, *Science*, **244**, 1165.

Hammel, H.B., R.F. Beebe, E. M. De Jong, C.J.Hansen, C. D. Howell, A.P. Ingersoll, T.V. Johnson, S.S. Limaye, J. A. Magalhaes, J.B. Pollack, L.A. Sromovsky, V.E. Suomi and C.E. Swift 1989, *Science*, **245**, 1367.

Ingersoll, A.P. 1990, in *The New Solar System*, ed. J.K. Beatty and A. Chaikin (Sky Publishing Corporation, Cambridge, Mass) p. 139.

Ingersoll, A.P. and J.N. Cuzzi 1969, *J. Atmos. Sc.*, **26**, 981.

Ingersoll, A.P., R.F. Beebe, J.L. Mitchell, G.W. Garneau, G.M. Yagi and J. Muller 1981, *J. Geophys. Res.*, **86**, 8733.

Lucy, L.B. 1974, *A. J.*, **79**, 745.

Riddle, A.C. and J.W. Warwick 1976, *Icarus*, **27**, 457.

Smith, B.A., et al. 1981, *Science*, **212**, 163.

Smith, B.A., et al. 1982, *Science*, **215**, 504.

Smith, B.A., et al. 1986, *Science*, **233**, 43.

Smith, B.A., et al. 1989, *Science*, **246**, 1422.

OBSERVATIONS OF MARS USING HUBBLE SPACE TELESCOPE OBSERVATORY

Philip B. James, Univ. Toledo, R. Todd Clancy and Steven W. Lee, Univ. Colorado, Ralph Kahn and Richard Zurek, Jet Propulsion Laboratory, Leonard Martin, Lowell Observatory, and Robert Singer, Univ. Arizona.

1. INTRODUCTION

The lack of a continuous record of martian meteorology or of volatile cycles on Mars for extended periods of several martian years seriously hinders efforts to understand the physics of the martian atmosphere - surface system. Despite the fact that Mars has received relatively intense scrutiny from spacecraft, these observations are limited to only a few isolated time periods; and, inasmuch as these missions were primarily interested in high resolution geology, more than a small fraction of the planet's surface was rarely covered during a particular time period. The earth based record is limited by the relatively short periods surrounding oppositions when telescopic observations can yield useful data. Because of the incommensurability of the orbital periods of Earth and Mars, the martian season seen during one opposition will not be observable again for eight martian years.

The lack of a continuous synoptic record of the planet is a serious impediment to understanding the martian weather and climate (for an up to date review of martian phenomena consult Mars, U. Arizona Press). For example, the martian global duststorms are a meteorological phenomenon which seems to be unique to Mars. Large storms were observed from Earth in 1956, from Earth and Mariner 9 in 1971, from Earth in 1973, and by Viking twice in 1977 and in 1982. There is no documentation for any other global duststorm event, leading to the facetious hypothesis that "spacecraft cause duststorms." A more reliable record is needed in order to determine the nature of a longer term cycle as well as to establish mechanisms which can lead to such events in some years but not in others. Our incomplete knowledge of the temporal distribution of major dust storm events on Mars is the best known consequence of the lack of such a record, but the situation is much the same for interannual variability in the behavior of surface condensates in the polar regions and for the behaviors of clouds in different years.

To test one possible technique for remedying this situation, we have embarked on a three year program of Mars observations using the Hubble Space Telescope. Although the solar pointing constraint eliminates 45% of the 780 day synodic cycle from possible observation, this is still a great improvement over the two to five months of each cycle (depending on the orbital geometry of the two planets at opposition) that can be profitably be used for earth based observations. During the initial phase of the project we have imaged Mars on five dates in a variety of spectral bands; the observations completed during Cycle 0 are listed in the following table:

Date	Ls (deg)	Size (arcsec)	Scale (km/px)	LCM (deg)	Filters
12-13-90	349	16.5"	17.7 km/px	190 300 70	890N,673N,588N,502N 439W,336W,230W
01-02-91	359	13.5"	21.7 km/px	300	673N,413M,FOS
02-07-91	16	9.4"	31.1 km/px	300	673,413,336,230,FOS
03-20-91	35	6.6"	44.3 km/px	300	673N,413M
05-15-91	60	4.8"	60.9 km/px	190 300 70	673N,413M 502N,336W,230W

Due to the fact that the Solar System Target software was not yet active, these observations were entered as fixed targets; the co-ordinates of Mars at the exact time of the observations were required for this. Much of the credit for the successful scheduling of this program can be traced to Marc Buie who performed these calculations. Most of the integration times were very short, less than 1 second. Therefore, scans were generally not needed despite the large apparent motion of Mars. In fact, three exposures were often made on a single target, producing a drift of ~100 pixels during the time interval between exposures. The 2 minute F230W exposures did require a scan, which was successful in all cases.

All of the Mars exposures were successful except for the first three targets which were to have imaged the 190 central meridian. These images were located at the outer edge of PC 6 so that only 50% - 33% of each exposure was recovered. Subsequent December exposures were recovered by uplinking a command to HST in real time to adjust its pointing by 15"; the success of this remedy, without which the December data would have been worthless, illustrates the advantage of having investigators at the Space Telescope Science Institute during observations. The error was ultimately traced to an aberration correction which had been inserted at two different steps in the preparation of instructions for HST.

Unfortunately, attempts to acquire images of a solar type star for photometric calibration and for point spread function proved to be much less successful. Images of HD23169, a G2V star, were acquired in December but were underexposed and therefore not useful for PSF's. Analysis of the failure was inconclusive; the images seemed consistent with a star which was one magnitude fainter than catalog values. The second attempt failed in February when a cosmic ray event in the South Atlantic Anomaly caused a safing. The final attempt on HD23169 failed in March when a properly exposed image of the star was found on PC 5 rather than PC 6.

2. SCIENTIFIC OBJECTIVES

The scientific interests of the observing team focus on the atmosphere of Mars and the interactions between the atmosphere and surface of the planet. The primary objective of the investigation is to monitor seasonal changes on the planet through as much of its annual cycle as possible. As noted above, Hubble Space Telescope is a potentially valuable tool for monitoring Mars. Near oppositions, the expected scale of HST images was comparable to that of the Viking approach images which provided resolution of the martian surface similar to a terrestrial weather satellite (Figure 1). Even more important, the resolution expected for images acquired when Mars is near solar conjunction was comparable to Planetary Patrol images acquired near oppositions (Figure 2). Therefore, except for the solar elongation constraint, HST could reliably monitor conditions on Mars throughout the seasonal cycle.

More focused scientific goals for the project include:
1. Observing the surface albedos of various units on the planet and seasonal variations in these albedos. The shapes and albedos of various surface units of Mars change as a function of time. Part of the variation is seasonal; originally ascribed to polar melting and to possible vegetation, these changes are now thought to be a result of shifting dust cover on the planet. Part of the variation is not seasonal but responds to changes over a longer time scale, perhaps related to a longer dust storm cycle. We have intentionally chosen the Syrtis Major area, where some of the most prominent albedo features occur, for frequent monitoring with HST in order to attempt to quantify the albedo changes which occur and to separate seasonal and longer term variations.
2. Observations of dust storms on Mars. As noted above, the dust cycle on the planet is still relatively unknown. Dust phenomena on the planet span the range of scales from dust devils to huge storms that completely envelop the planet. Many intermediate scale storms, 100-1000 km in size, were observed by Viking orbiters. Only the larger storms are generally picked up by terrestrial observers, and the statistics on these are modulated by the 15 year opposition cycle acting on the dust storm season, which spans the spring-early summer seasons in the south. Frequent monitoring of regions with the potential to initiate dust storms by HST during the next dust storm season, in HST Cycle 2, is proposed as a continuation of this work.
3. Measurement of atmospheric opacities. The background opacity of the atmosphere is affected by both condensate hazes and by aerosols. The opacity observed by Viking varied substantially during the mission being affected mainly by the dust cycle. Observed surface reflectances will be analyzed using a radiative transfer model in order to derive optical depths and properties of scatterers in the atmosphere.
4. Measurements of seasonal and interannual variations in the distribution of ozone on Mars. Ozone is a trace ingredient in

Figure 1: This approach image was taken by Viking Orbiter 1 shortly before its orbit insertion in 1976. The scale of the approach images is similar to that which was expected for HST observations of Mars near favorable oppositions. These images, similar in scale to terrestrial weather satellite views, are ideal for synoptic monitoring of the planet. Photo credit: NASA.

Figure 2: This photographic image of Mars was acquired from Mauna Kea in 1986 during the excellent opposition of that year, when the angular size was about 24 arc secs. WFPC images acquired when Mars is only 3-5 arc seconds, which is true during most of its synodic cycle, are expected to have better resolution than this image. Deconvolved WFPC images obtained when Mars was 4.8 secs in May, 1991, have proven that this is still the case despite the optical problems. Photo credit: Lowell Observatory and National Geographic Society.

Mars' atmosphere which displays substantial geographic and temporal variability. Ozone is destroyed through chemical reactions involving the OH radical, so ozone concentration is (anti) correlated with water vapor abundance. The driest regions of the planet, e.g. the winter polar regions, are therefore places where maximum ozone is expected. Ozone can be detected through absorptions near 230 nm. FOS scans of the planet were performed to provide spectra in this region which can be used to determine the concentration of ozone molecules in various regions of the planet. In addition, comparison of WFPC images using the 230W and 336W filters is being used to attempt to map ozone on the planet.

5. Multispectral mapping of surface units on Mars. The reflectance spectra of the surface of Mars contain features which are diagnostic of the minerals which are present on the surface. Comparisons of the spectra of various surface units contributes to understanding the geological history of the planet. Though the set of filters used does not provide the spectral resolution available using other techniques, the surface resolution possible is generally greater than in other experiments. The HST results will be used in concert with other data sets to map the compositions of surface units on the planet.

6. Seasonal changes in polar caps and polar hoods. Numerous polar regressions have been observed by earth based astronomers and by spacecraft. It has been shown that the polar regressions in different martian years are different, and there has been some speculation about possible relationships between these variations and those associated with the dust cycle. HST will enable determinations of polar cap boundaries during years in which these data cannot otherwise be obtained. In addition, monitoring in red and blue filters will permit separation of the atmospheric hood from the surface cap; though the hood is possibly the most dynamic phenomenon on the planet, it is one of the least understood.

7. Observation of diurnal and seasonal development of clouds. Condensate clouds occur in various regions of the planet. These are often diffuse hazes which appear near the limbs due to condensation in a cold atmosphere. There are regions which display discrete, optically thick clouds: Tharsis, Elysium, and Hellas are examples. The distribution of these clouds seems to be determined by topography, but there are substantial variations from year to year. HST will provide ample resolution to document these clouds at all times in Mars' synodic cycle. Limited diurnal data can be obtained by imaging on consecutive orbits.

3. PROCESSING WFPC IMAGES OF MARS

The scientific benefit of scheduling our GO program so early in Cycle 0 was only slightly negated by various practical difficulties associated with being the first GO program. The images were to receive initial processing which included flat fielding. The images which were emitted from the end of the processing "pipeline" in some cases had as many apparent defects as the raw images, and in all cases the images contained blemishes due to dust particles on components of the optical system. Post launch flat fields taken on PC 6 with the various N series filters which were used to image Mars in the visible and near infrared portions of the spectrum did not exist, and in some cases there were not even any pre launch flats available. The default for the processing software in the absence of any flat was to divide the raw image by a unit image and to proceed as if the image had been properly flatted. Valid flat field images were acquired for several of the filters which we used through the generosity of members of the WFPC team. A raw, unflatted image of the Syrtis Major region acquired using F588N is shown in Figure 3a.

Even images which had been divided by the appropriate flat field had residual blemishes due to dust specks on the pyramid and filters. These appeared as bimodal light-dark, nearly circular blotches roughly 5-10 pixels in diameter. They occurred in regions where there were large intensity gradients in the image, especially near the limbs of the planet. Particular care was needed to remove these blemishes since their scale is similar to the features on the martian surface which are of interest and since the deconvolution routines will further extend their influence. An example using the 588N filter of an image which has been flat fielded is shown in Figure 3b; the image has been greatly stretched to reveal the blemishes near the limb.

The method used to remove the blemishes is as follows:
1. The image is carefully compared to the flat field image to make certain that the blemish to be removed is indeed a residual of the optical system rather than a feature on the planet.
2. A square image generally 20-25 pixels on a side centered on the blemish is extracted from the main image.
3. The IRAF routine IMSURFIT is used to create an image from a two variable polynomial fit to the unblemished border of the extracted image. Generally a third or fourth order polynomial has proved to be sufficient to give a consistent image.
4. The polynomial fit is not adequate to replace the undesired portion of the image because it is mathematically smooth and stands out if used to replace the blemish. The IRAF routine MKNOISE is used to make a suitably noisy image out of the polynomial fit.
5. The "patch" is reinserted into the image to replace the blemish.

Inasmuch as most of the blemishes occurr in the relatively featureless limbs of the planet, we do not believe that this

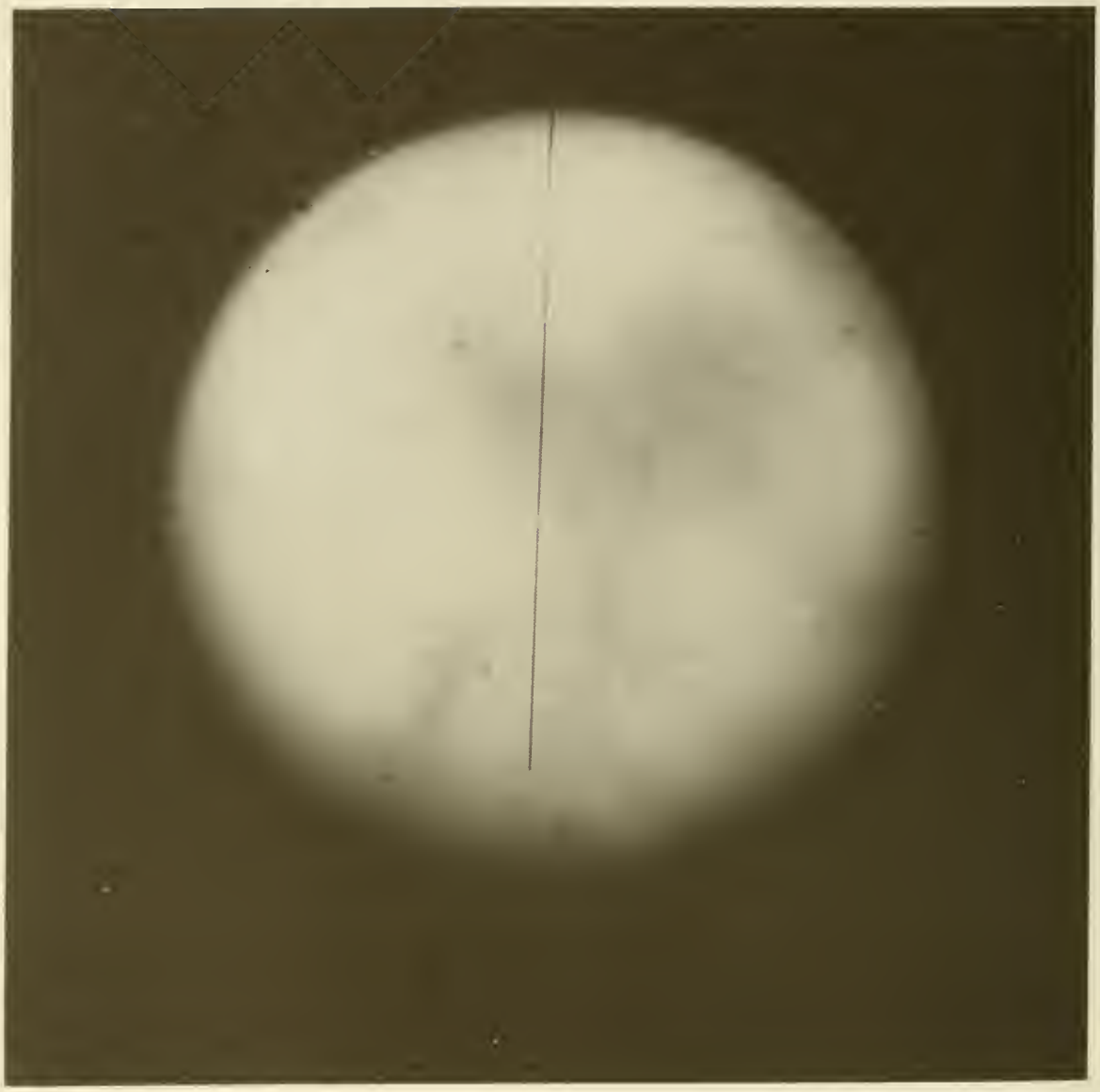

Figure 3a. This WFPC image of Mars through the 588N filter has not been flat fielded. In addition to a blocked column, numerous blemishes caused by dust on the pyramid and filter are present; inasmuch as their scale is similar to the surface features on Mars that are of interest, their careful removal is essential.

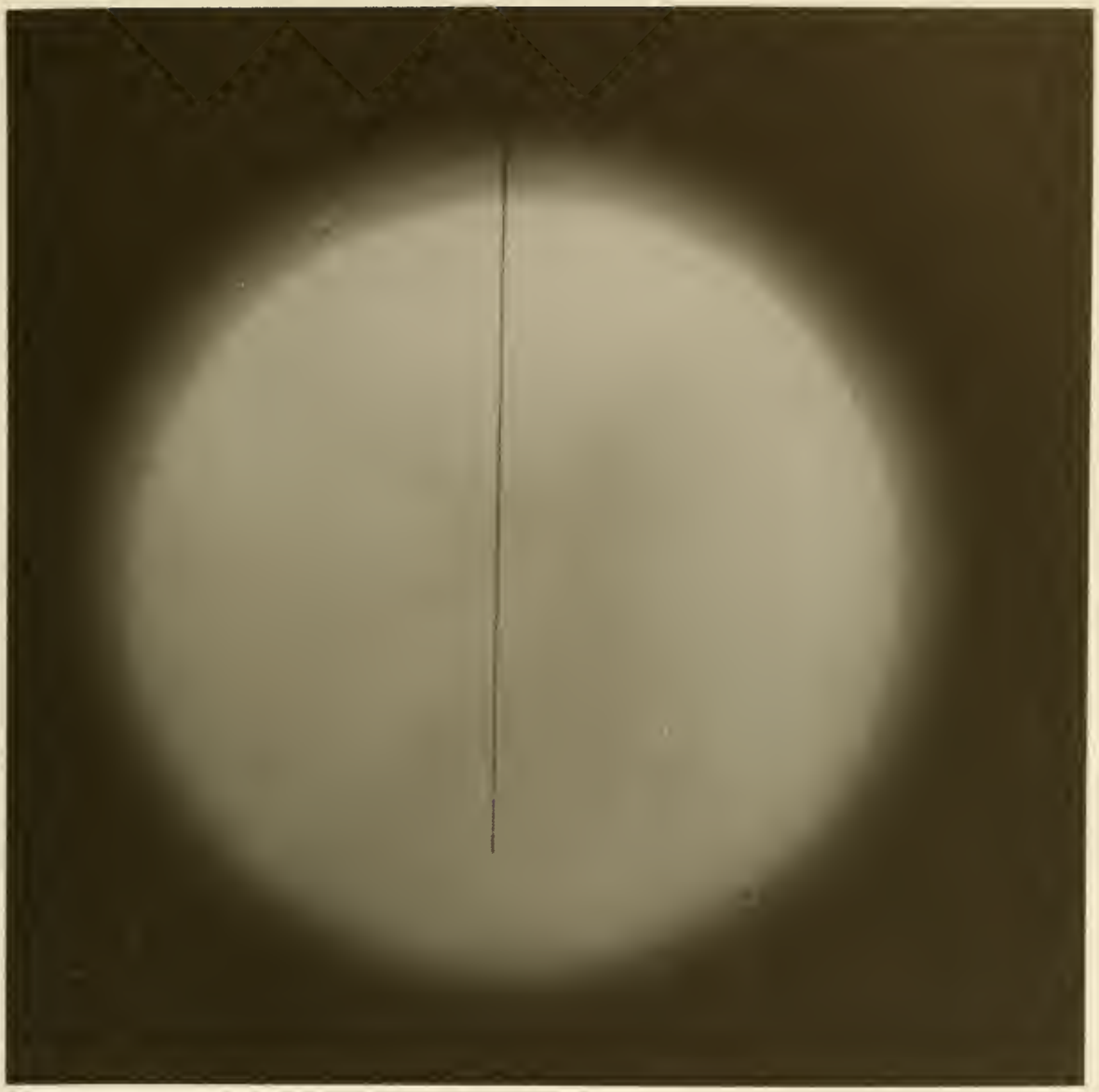

Figure 3b. After flat fielding, blemishes still remain in regions of large intensity gradient; this can be seen in the 588N picture of Figure 3a which has been stretched to bring out these features near the limb. This image also reveals that the point spread function has greatly extended the limbs of the planet; this effect makes determinations of limb profiles suspect.

cosmetic procedure has any detrimental effect on the validity of the scientific data contained in the images. The result of this process for the 588N Syrtis image is shown in Figure 3c.

Because the three attempts to acquire images of a solar type star on PC 6 to use as a photometric calibration and as a point spread function failed to provide the necessary data, computer generated point spread functions supplied by James Westphal were used to deconvolve the images. The implementation of the Richardson Lucy deconvolution procedure which is contained in the x version of the STSDAS package was used to deconvolve the images. This routine assumes that the point spread function is constant across the image. This is clearly not true for the early Mars images which are 400 pixels in diameter. However, except for the first set, the images are centered in the chip; and star field images suggest that large distortions appear mainly near the edge of the chip.

Forty to sixty iterations of Lucy were performed on the images. Less iterations led to reductions in resolution while more iterations produced little perceptible increase in resolution but made the images noticably more noisy. Estimation of resolution is somewhat subjective since the visibility of a surface feature depends on albedo contrast as well as on size; even a large crater is invisible if there is little contrast between it and the surrounding terrain. Surface features on the planet suggest that the sub earth resolution is at least 50-75 km, i.e slightly better than 0.2" The Richardson Lucy routine therfore restores the resolution to within a factor of two of the actual surface resolution which might have been expected in the absence of spherical aberration. The final, deconvolved 588N image which has been used as an example herein is shown in Figure 3d.

Color composits are useful scientifically in identifying yellow dust clouds which have only small contrast in brightness at individual wavelengths. However, the public appeal of color composits is probably their greatest asset. One of the first tasks facing the team was production of such a color image from the available data.

There are two potential problems in color compositing: registration and color balance. Both of these proved to be present in producing the color image which appeared in Life, Astronomy, Sky & Telescope, etc. Registration was a problem because Mars rotated perceptably between the exposures. The exposures which were used for blue and green were obtained on the same fixed target and were only slightly displaced from each other in time; the 889N image, used for red, was exposed on a different fixed target and was displaced by a greater amount from the other two. Registration at the limbs of the identically sized images would lead to fuzziness and color halos at the boundaries of major albedo features, such as Syrtis. Registration on the albedo features, which was finally used in the published composite, leaves a color halo around the limb of

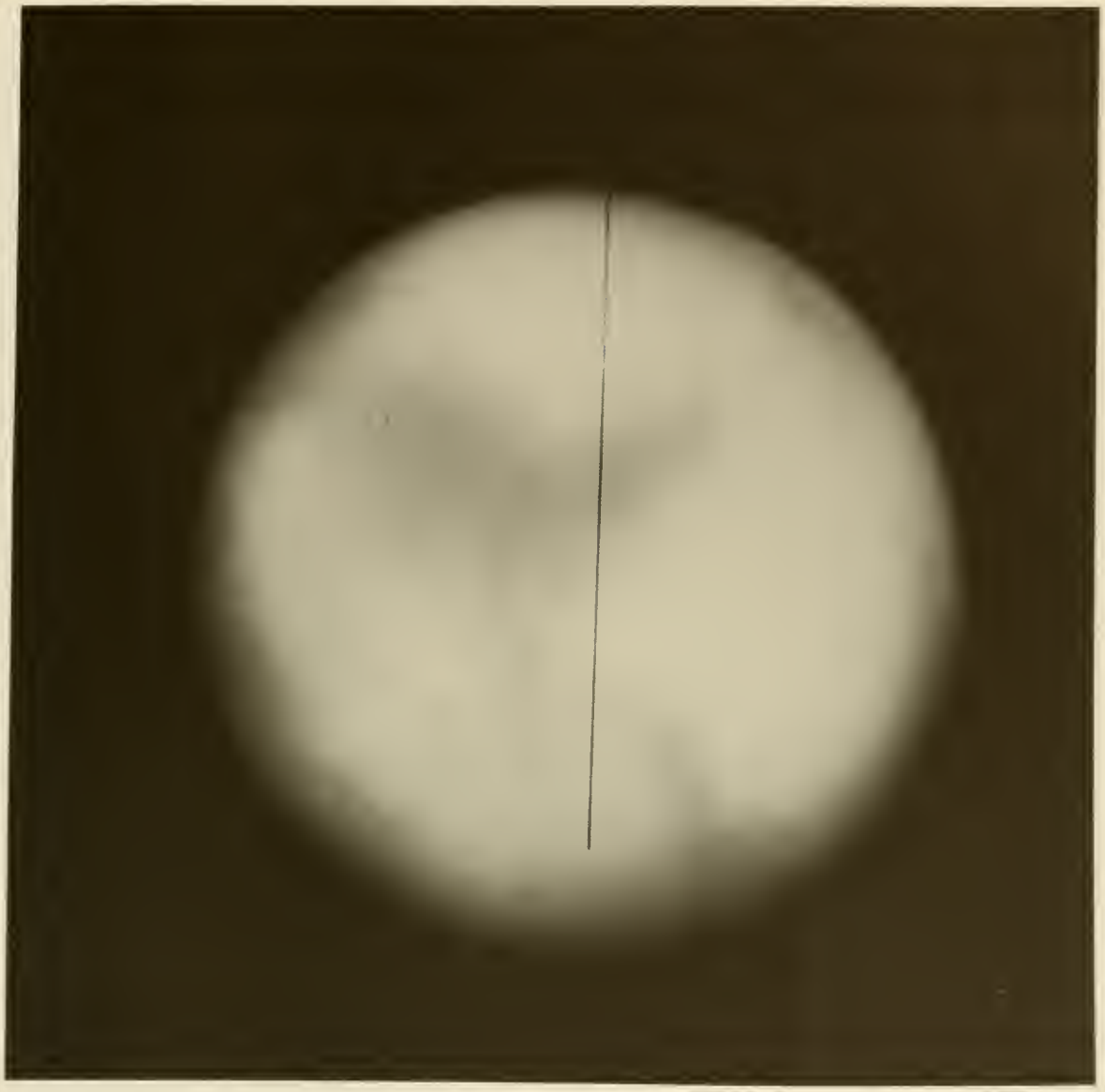

Figure 3c. The blemishes have been cosmeticly removed from the image of Figure 3b using techniques described in the text. Without further processing, the resolution of this image, acquired when Mars was 16.5 arc seconds, is similar to Planetary Patrol photographs.

Figure 3d. The same image in as in Figure 3c is shown after 40 iterations of the Richardson-Lucy algorithm. The surface resolution has been restored to within a factor of two of what was originally anticipated.

the planet.

Availability of flat fields for the various filters forced us to use 889N as red and 588N as green. Because the surface reflectance of Mars is quite steep between 500 and 600 nm, the latter situation caused considerable problems in attaining correct color balance. Mars is considerably brighter at 588nm than at 502nm, and the contrast between light and dark areas is much greater in the "yellow" filter than in green. The result is that the image is somewhat greener than most color images of the planet. Subsequently, we have composited images from May using 673N for red and 502N for green, and the color in the resulting image is much closer to what is expected for Mars.

4. PRELIMINARY RESULTS

Preliminary analysis of the images obtained by HST during the five observation sequences has rewarded our optimism concerning the potential scientific value of HST for monitoring martian phenomena. Even the 4.8 arc second images acquired in May have sufficient resolution to reveal details of the albedo boundaries on the surface. The images taken in May, when L_s equaled 60^0, clearly reveal the multicomponent "W" clouds in the Tharsis - Valles Marineris region as well as clouds associated with Elysium Mons. They also show the north polar surface cap, which is tilted earthward at this season; the coverage from three different central meridians will permit a detailed comparison of thee boundary of the cap with excellent spacecraft data at the same L_s from Mariner 9 and Viking for three martian years as well as with earth based regression data. The potential scientific value of these 4.8 arc second images augurs well for the investigation of the 1992 "classic dust storm" season which will use the similar scale images planned when Mars again emerges from the 50^0 solar interdict.

Processed images from December, January, February, and March are shown together in Figure 4; all of these were taken throught the 673N filter and were processed using a flat field for the "nearby" 656N filter. The use of the flat for the spectrally adjacent filter with a similar bandwidth does a reasonable job, at least superficially. This is probably because the size and structure of blemishes produced by dust in the optics is mainly wavelength dependent. The 656N flat did have an artifact not apparent in our 673N images which may be due to a pinhole leak in the former filter. The prominent dark feature which looks like an inverted map of Africa is Syrtis Major; this area is thought to slope from the bright Arabia region on the west to the Isidis impact basin on the east. The region is probably dark because of slope induced winds which scour dust from the surface. Syrtis is a region which exhibits many wind induced streaks which support this hypothesis. The bright region to the south of Syrtis is the huge Hellas impact basin. This is often the site of dust or condensate clouds, and during southern winter the basin is covered with bright carbon dioxide frost. The dark, east to west arc which bisects Hellas is a relatively new albedo feature which has not appeared on most past albedo maps; likewise, the dark knob to the west of Hellas is darker than it usually appears.

Figure 5 displays the corresponding blue images of the Syrtis region. Surface contrasts are reduced in blue, and Syrtis Major is barely visible. The filter 413M, which had been selected as our "blue" filter was replaced in December only by 439W because the CCD chips had not yet had a UV flood; the sensitivity of 413M was more suspect than that of the W series selection. The early pictures show the north polar hood prominently as well as extensive clouds to the north of the south polar region. This season, which is near the equinox, is historically one of the least active times on the planet from a meterological point of

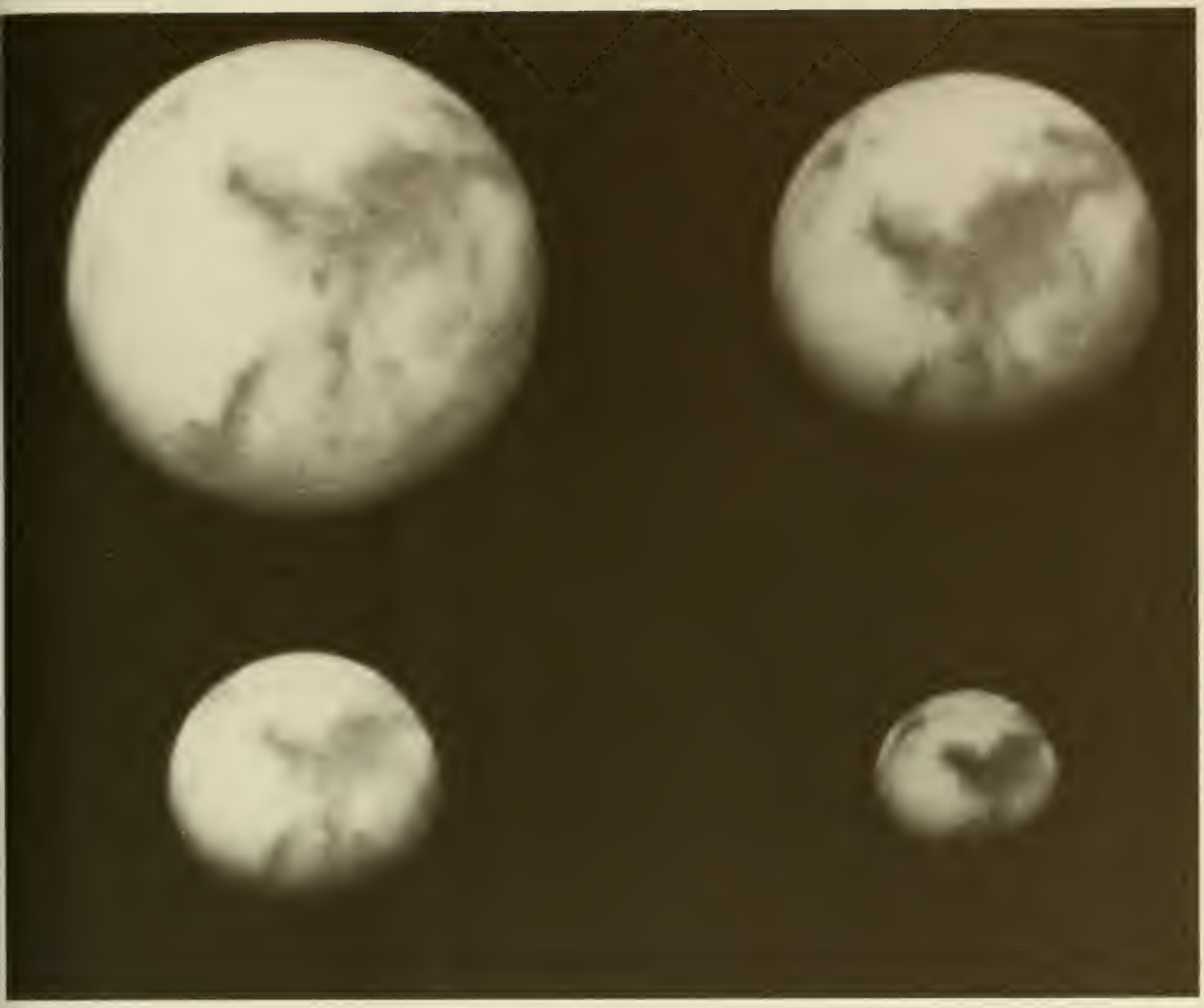

Figure 4: Four images of the Syrtis Major face of Mars acquired in December, January, February, and March when the angular diameters were 16.5, 13.5, 9.4, and 6.6 arc secs respectively. The images, which used the 673N filter, are shown at the correct relative scale. Even the smallest size images reveal detail comparable to very good terrestrial photographs, making them scientifically useful. Credit: STSCI/NASA and Univ. Colorado.

Figure 5: These are the blue filter (F413M) images corresponding to the red images in Figure 4. The shorter wavelengths show primarily atmospheric features on the planet, and surface contrast is much reduced. Credits: Same as Figure 4.

view.

The ultraviolet imaging capabilities of HST provide a unique opportunity to study the surface and atmosphere of Mars in this relatively unexploited wavelength region. In particular, the strong ozone absorption near 230 nm makes it possible to map ozone concentration through differencing the 230 and 336 nm images. Preliminary use of this method reveals strong ozone absorption in the north polar region during late winter, as expected from the low water vapor content in the atmosphere at that time, and reveals other interesting correlations with various topographic and surface features. The differencing technique will be verified and calibrated using spectral scans of the planet in the ultra violet portion of the spectrum using the Faint Object Spectrograph (FOS); the latter data have been inspected to verify that signal to noise is as expected, but detailed analysis of those data has not yet been undertaken. Inasmuch as Mars is much brighter at wavelengths in excess of 600 nm than at ultra violet wavelengths, red leaks in the ultraviolet filters could easily jeopardize this part of the experiment. Inspection of the 230N images strongly suggests that the red leak is no worse than indicated in Figure 4.7.3.1 of Version 2.1 of the WFPC Instrument Handbook. There is no apparent residual of the albedo patterns which would be produced by exposure to the longer wavelengths.

The two sequences of pictures in Figures 4 and 5 clearly illustrate that our expectations regarding the potential value of these images for monitoring Mars have been confirmed. Even the smallest images, acquired in May (not shown here) show detail comparable to Planetary Patrol images acquired at times of opposition. HST's Cycle 2 will encompass a major portion of the next dust storm season, and frequent monitoring of the planet has been proposed for that period. That Cycle will also afford the opportunity of revisiting the same seasons imaged during the last few months in order to search for existence and causes of interannual variability. Cycle 2 will provide monitoring of Mars leading into the Mars Observer Mission. We hope that, using the new instrumentation to be installed on HST in 1993, it will be possible to make observations which will complement the experiments to be conducted on that mission.

We wish to express appreciation to the large number of people at Space Telescope Science Institute whose assistance has been invaluable. We especially thank Ed Smith, who has worked with us in our attempts to overcome data analysis problems since the first day of the project. We also appreciate the assistance of James Westphal, who supplied much needed flat fields and psfs early in the project.

Reference

B. Jakosky, H.H. Kieffer, M. Matthews, and C. Snyder editors, MARS, University of Arizona Press, Tucson (1991).

DECONVOLUTION AND PHOTOMETRY ON HST-FOC IMAGES

C. Barbieri, G. De Marchi, R. Ragazzoni
Astronomical Observatory of Padova
Vicolo dell'Osservatorio, 5
35122 Padova, Italy

Abstract. Due to the peculiar characteristics of the PSF of HST, a careful analysis with many deconvolution experiments must be performed on HST-FOC images in order to understand their property. We briefly present some aspects of our work on the subject.

1. INTRODUCTION

The strongly aberrated PSF of HST requires a large amount of effort in the field of image deconvolution, under conditions quite unusual if compared with those found in ground-based optical and radio data analysis.

In fact, generally from the ground and before HST the equivalent PSF of an astronomical instrument (telescope plus atmosphere) was known only with a rough approximation, due to the stochastic behaviour of the atmosphere itself and of its perturbations. On the other hand, the reconstruction of images taken with radiotelescopes is fundamentally based on deconvolution techniques; in this latter case, though, the PSF is known with high accuracy (because it essentially coincides with the instrumental beam) and the collected raw images are characterized by a high signal-to-noise ratio (SNR).

In the HST case, a rather complex PSF is known with a good degree of accuracy and it seems to be fairly stable (apart from *human* modifications, like those arising from the changes of the focus setting, and so on). However, most of the images (especially FOC's) are strongly photon-limited, *i.e.* characterized by a high poissonian noise.

2. FOC FRAMES DECONVOLUTION USING CLEAN

Using IDL as a framework (because of its flexibility), two different implementations of the CLEAN algorithm were performed and extensively tested: a standard one, based on Högbom (1974) and Segalovitz et al. (1978), and an enhanced version, capable also to treat extended objects, based on Steer et al. (1984) and Wakker et al. (1988).

In order to test the efficiency of the procedure and to see what happens *inside* the procedure, a real time control of the behaviour both of the raw and of the cleaned image is allowed in our implementation.

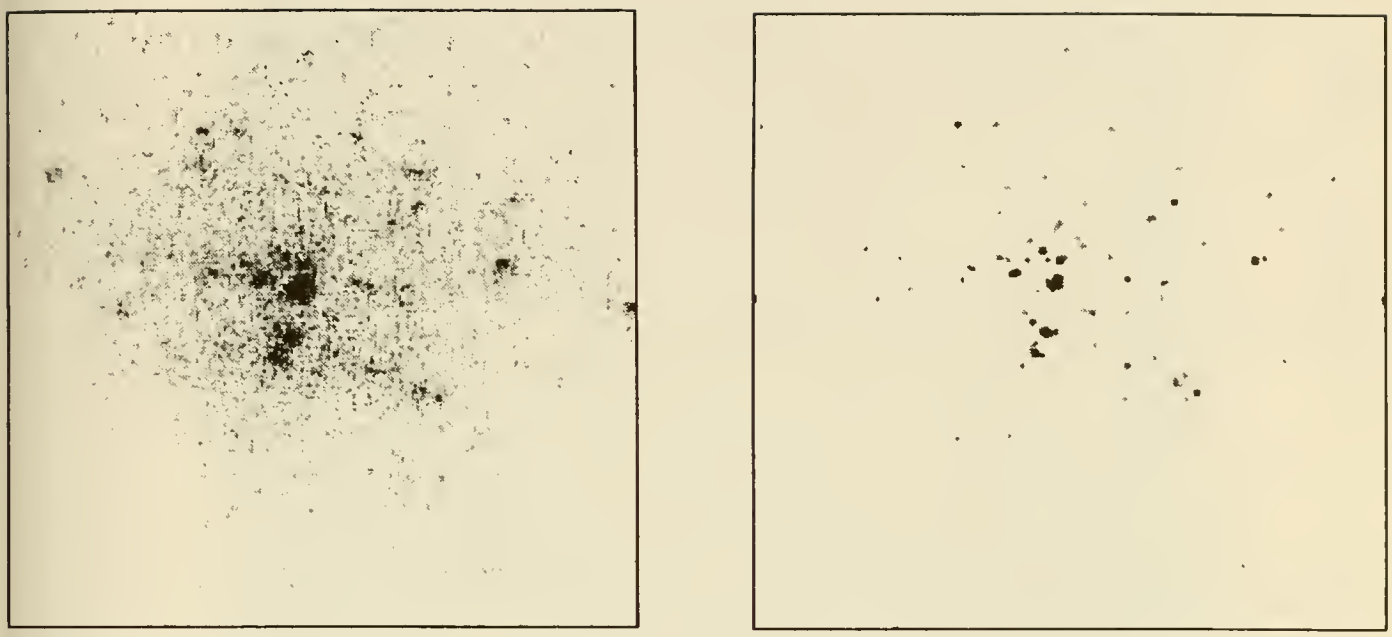

Figure 1: Action of Clean on an HST-FOC frame of R136a. See the text for an explanation. North is bottom-left to top-right. East on the right.

The operator, looking at the display, can interactively see the cursor moving from a point to another, indicating where objects are found and subtracted in the raw frame and simultaneously added in the cleaned one.

In other words, the growth of the stars in the cleaned frame and their corresponding disappearence in the raw one can be inspected *during* the execution of the procedure.

In our opinion, this step is of great importance, because programme execution can be thus interactively checked, avoiding the use of a *black-box* like procedure in deconvolution.

The typical run of this algorithm takes few minutes to some hours, depending on the choices for the loop gain, on the threshold and on the complexity of the treated image. In this case, the interactive display procedure becomes unuseful and so the option can be conveniently switched off.

Figure 1 shows one of the first results obtained on R136a. The raw image is treated with Clean, producing a set of locations where peaks arising over a certain threshold have been found. Each location is characterized by both positional and intensity information, since the latter is retrieved by subtracting the PSF from the raw frame and adding back the residual. As a matter of visualization, the final cleaned image is produced convolving the location data with the nominal PSF characterized by a FWHM typically of the order of the expected HST diffraction limited performances.

3. USING CLEAN TO SUBTRACT SINGLE UNRESOLVED SOURCES

In the case of a frame containing few unresolved sources, such as bright foreground stars, not scientifically interesting, Clean can be forced to remove them and their deleterious halo, even if the star peaks themselves are slightly saturated.

Actually, FOC is a photon counting device and the occurrence of the saturation effect can become so heavy that one of the statements which Clean techniques are based on (*i.e.* the fact that the height of the peak is proportional to the brightness of the star as it is for its optical halo) can fail.

In such cases (in practice easily detectable by simple inspection of the raw frame) Clean can be modified using, instead of the peak value, the average properly scaled value of a group of pixels, falling within an annulus surrounding the star.

This procedure, applicable to non crowded fields, allows one to perform subtractions of single stars in a very efficient way. Actually, the positional information is retrieved, as always, using the location of the peak, while the brightness information can be obtained fitting a zone of the PSF free of saturation.

Moreover, the effects of a slight blurring or of the oversampling can become negligible, thanks to the fact that peaks locations are allowed to vary during the numerous iterated subtractions in order to match the *shape* and the sub-pixel position of the star to be subtracted.

An example of application can be seen in Fig. 2

4. BLURRING PSFs IN ORDER TO CLEAN BLURRED IMAGES

Even if the great part of HST observations are taken in fine-lock mode, sometimes a loss of lock can happen. As a consequence finding a way to perform restoration and deconvolution even in such conditions is, in our opinion, of fundamental interest.

In fact, even when the frames clearly *look trailed* it is not so easy to give a detailed

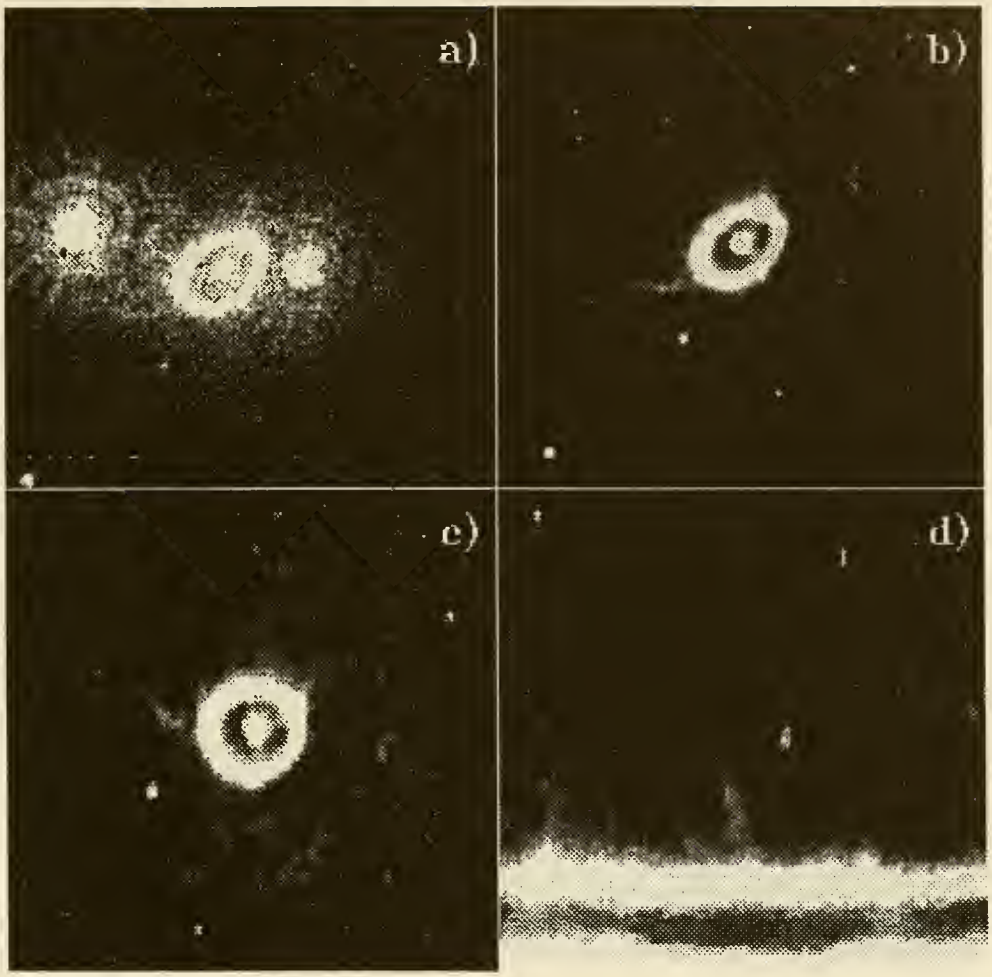

Figure 2: An example of image processing in IDL environment: **a)** The original SN1987a image; **b)** the same with the two bright stars subtracted; **c)** stretched in order to circularize the bright ring and **d)** converted to polar coordinates.

description of the blurring. Such information can be retrieved, with high signal to noise ratio and using array manipulation based on FFT, comparing the Auto Correlation Function (ACF) of an unblurred (*i.e.* collected in Fine Lock mode) PSF with the ACF of the whole frame (supposed trailed). This is rigorously true if there are neither extended sources nor crowding effect in the image; anyway, due to the weighting nature of ACF, a small number of close stars in a rich frame does not essentially modify the whole ACF.

Comparison could be possibly obtained following two methods. The first requires deconvolution of the ACF of the raw image using the ACF of the untrailed PSF as synthesized beam. It is very simple, for instance, to deconvolve via standard Clean: this allows one to immediately see the presence of trailing, since Clean associates to the main peak of the image ACF a set of displaced position instead of only one single well defined location (as it would have been if the image had not been trailed). On the other hand it is also possible to analyze the shape of the isolevels in the main peak of the trailed image ACF, comparing them with the shape of the isolevels of the PSF ACF.

This latter method is very simple and we found its results (amount and direction of trailing) are in good agreement with respect to those given by the former.

An important consequence follows: any strongly PSF-based deconvolution technique can get advantage from the preparation of a PSF blurred in the same way as the whole raw frame. So, we have found it possible to produce a synthetically trailed PSF (knowing both the amount and the direction of image trailing) and to use that, instead of the normal one, to deconvolve the raw image, for instance by Clean or Lucy algorithm.

Results are shown in Figure 3.

More difficult is the treatment of images taken with HST in oscillating conditions, for the trailing due to the spacecraft oscillation translates into a space-invariant blurring component plus a rotation of the field. Such latter effect is space-variant and so the described technique is not able to take it into account.

5. COMBINED ACTION OF LUCY AND CLEAN

The Richardson-Lucy iterative technique is able, at least in principle, to perform the deconvolution of HST-FOC frames. Our experiments, that are similar to those obtained by others (Adorf, 1990), show that the effects of a restoration of this kind are essentially significative on the outer halo of the PSF.

Only a very large number of iterations, with particular additional constraints, seems to produce point-like sources if performed on an image of point-like sources convolved with a typical FOC PSF.

In such a framework, we have made some simple attempts to merge the Lucy algorithm with Clean. It is worth noting that this approach is quite similar to Meier's (1990), who proposes a merging between MEM (Maximum Entropy Method) and Clean.

Lucy's capability of enhancing SNR is very good, but the algorithm requires many iterations to reach a high degree of resolution. So we have thought to apply Lucy (for instance 20 iterations) to both the raw image and the PSF and then use the lucy-ed PSF to deconvolve via Clean the lucy-ed image.

Due to the space-variant effect of the Lucy algorithm on the raw image, the reliability of the method (as far as the photometric precision is concerned) is quite low. As a consequence the method is recommended only for obtaining positional information

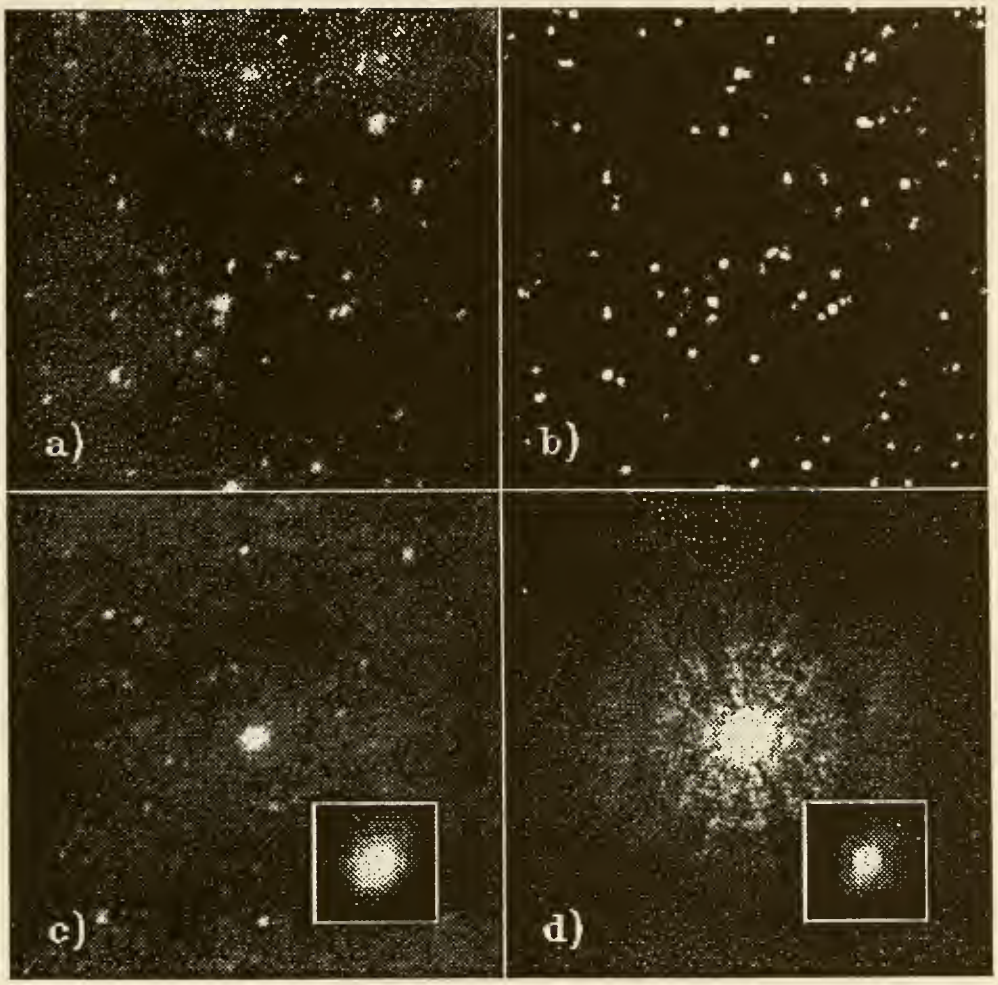

Figure 3: a): The *trailed* raw frame (M14), b) deconvolution using a *blurred* PSF, c) and d) the ACF of the raw frame and of an unblurred PSF; in the inset a magnification of the peak of the ACF is shown.

for single low SNR unresolved sources.

An example of application is shown in Figure 4.

6. A PHOTOMETRIC APPROACH

As a main consequence of the spherical aberration, the large halo of the HST-PSF requires a special care when any sort of aperture photometry is attempted.

A minimal mathematical description of the aperture photometry in presence of large PSF halo suffices to give insight into a possible way to overcome the problem and suggests useful photometric procedures.

Aperture photometry on position x, y can be efficiently described introducing the window function W (see Figure 5).

Saying R the raw frame, the sum of counts falling within the aperture defined by W centered in x_j, y_j can be expressed by

$$F_j = \int W(x - x_j, y - y_j) \cdot R(x, y) dx dy \tag{1}$$

The true sky, assumed composed by N single unresolved sources of intensity I_i, can be described by the function S:

$$S = \sum_{i=1}^{N} I_i \cdot \delta(x - x_i, y - y_i) \tag{2}$$

while the collected distribution is given by the following convolution:

$$R = S \otimes PSF = \sum_{i=1}^{N} I_i \cdot PSF(x - x_i, y - y_i) \tag{3}$$

Once locations x_j, y_j of the found stars are known, the aperture photometry procedure gives the following set of N measurements:

$$F_j = \int W(x - x_j, y - y_j) \cdot R dx dy = \sum_{i=1}^{N} I_i \int W(x - x_j, y - y_j) \cdot PSF(x - x_i, y - y_i) dx dy \tag{4}$$

So, defining the matrix $P_{i,j}$ as:

$$P_{i,j} = \int W(x - x_j, y - y_j) \cdot PSF(x - x_i, y - y_i) dx dy \tag{5}$$

while

$$F = [F_1, F_2, \ldots, F_N]; \quad I = [I_1, I_2, \ldots, I_N] \tag{6}$$

equation (4) becomes:

$$F^T = P \# I \tag{7}$$

where # indicates the row by column product between matrices. Note that no halo means $P = 1$. This suggests a way to perform aperture photometry, via inversion of the P matrix, since from equation (7):

$$I = P^{-1} \# F^T \tag{8}$$

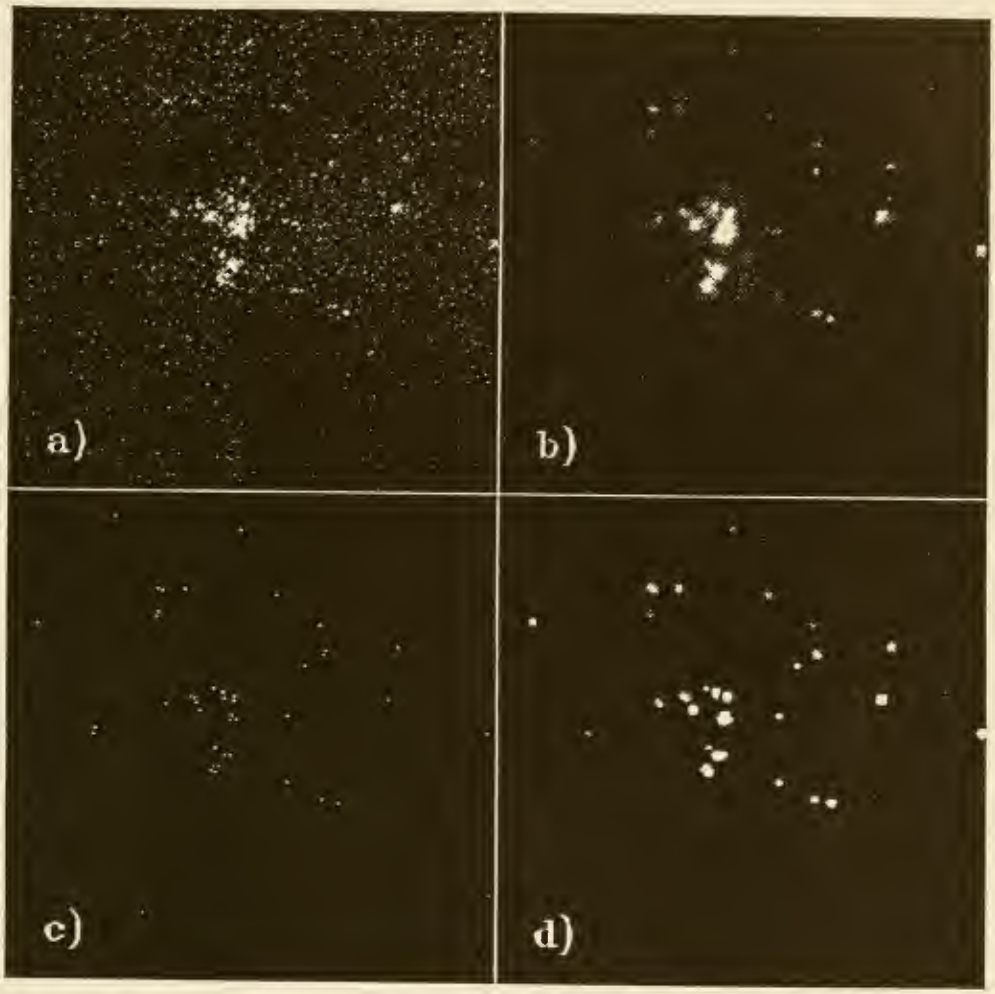

Figure 4: **a)**: Raw frame (R136a), **b)**: the same *Lucy-ed*, **c)**: Cleaning, and **d)** convolution with a gaussian beam.

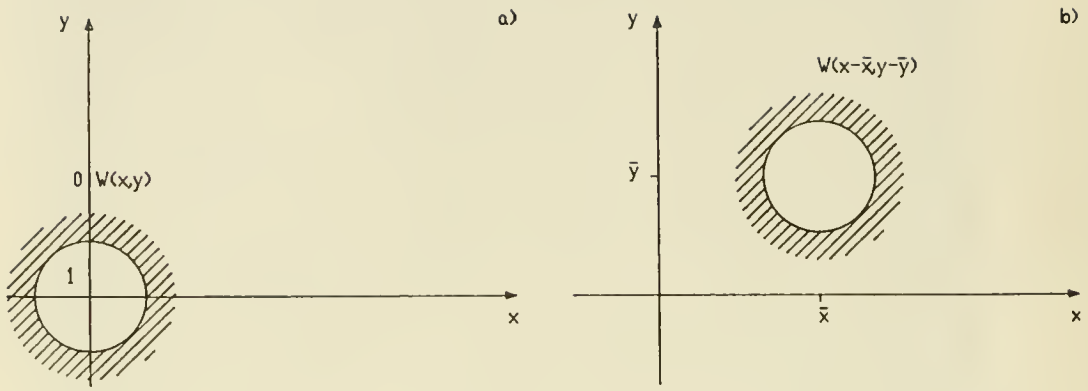

Figure 5: a): Definition of the function $W(x, y)$, b): the function $W(x - \bar{x}, y - \bar{y})$ is able to define the aperture location in any point $(\bar{x}, \bar{y})$.

Extensive testing of this method is now in progress. The estimation of the reachable photometrical accuracy is the subject of a future work, where a comparison between this and other methods is performed, via some numerical simulations with various degrees of crowding and different shapes of the luminosity function.

Initial tests show, as expected from a rough analytical estimation of the error (forthcoming), that satisfactory results can be obtained even with a high degree of crowding, provided the luminosity function is narrow enough.

7. CONCLUSIONS

Feasibility of a typical radioastronomical technique, like Clean, has been shown to be effective on the images of HST-FOC. However, some problems arise when the SNR is very low and, unless one is interested only in the brightest objects, the use of Clean becomes difficult, because it can produce false detections. This can be avoided following the suggestions given in section 5, although the non-linearity of Lucy's algorithm produces some minor problems related to the positional dependance of the PSF. Anyway, this is really not a severe problem, as we are interested in deconvolution primarily as a mean for locating objects positions in the frame and not in the evaluation of fluxes in deconvolved images. Finally, a new way to perform photometry on HST-FOC images is here indicated.

ACKNOWLEDGEMENT

Thanks are due to prof. F.Bortoletto for his kind advices and help in data analysis. We are indebted to Dr. A.Nota and Dr. F.Rampazzi for useful suggestions and careful reading of the manuscript.

REFERENCES

Adorf, H.M. : 1990, *ST-ECF Newsletter*, **14**, 8.

Högbom, J.A. : 1974, *Astron. Astrophys. Suppl.*, **15**, 417.

Meier, D.L. : 1990, *The restoration of HST images and spectra, STScI workshop, 20-21 August 1990 eds. R.L.White and R.J.Allen*, 113-120.

Segalovitz, A., Frieden, B.R. : 1978, *Astron. Astrophys.*, **70**, 335.

Steer, D.G., Dewdney, P.E., Ito, M.R. : 1984, *Astron. Astrophys.*, **137**, 159.

Wakker, B.P., Schwartz, U.J. : 1988, *Astron. Astrophys.*, **200**, 312.

FOC Images of the Gravitational Lens System G2237+0305

P. Crane[1,7], R. Albrecht[1,2,3], C. Barbieri[1,4], J. C. Blades[1,5], A. Boksenberg[1,6]
J. M. Deharveng[1,8], M. J. Disney[1,9], P. Jakobsen[1,3], T. M. Kamperman[1,10]
I. R. King[1,11], F. Macchetto[1,3,5], C. D. Mackay[1,12], F. Paresce[1,3,5], G. Weigelt[1,13]
D. Baxter[5], P. Greenfield[5], R. Jedrzejewski[5], A. Nota[5,4], W. B. Sparks[5]

[1]Member FOC Investigation Definition Team
[2]Space Telescope European Coordinating Facility
[3]Astrophysics Division, Space Science Department of ESA
[4]Observatorio Astronomico di Padova
[5]Space Telescope Science Institute
[6]Royal Greenwich Observatory
[7]European Southern Observatory
[8]Laboratoire d'Astronomie Spatiale du CNRS
[9]Department of Physics, University College of Cardiff, Wales
[10]Laboratory for Space Research, Utrecht
[11]Astronomy Department, University of California, Berkeley
[12]Institute of Astronomy, Cambridge
[13]Max Planck Institut fur Radioastronomie, Bonn

1. Introduction

The gravitational lens G2237+0305, discovered by Huchra *et al.* (1985), appears as a result of an extremely fortuitous alignment of a background QSO at $z = 1.695$ with the nucleus of a 14th magnitude foreground galaxy at $z = 0.039$. This lens produces four distinct QSO images (see Racine, 1991, for the best ground-based images) arranged in a roughly symmetrical cross, centered on the nucleus of the galaxy. Models of this lens presented by Schneider *et al.* (1988) and Kent and Falco (1988) imply the alignment is better than 0.1 arcseconds.

Although ground-based images of this lens with excellent seeing ($\approx$ 0.48 arcsec FWHM) have resolved the four QSO images, clearly better resolution is required to (a) improve or confirm their positions and magnitudes, (b) better determine the galaxy's nuclear structure which has an important effect on the QSO images, and (c) search for the fifth image predicted near the nucleus by current lensing theory.

2. Observations

The observations reported here were obtained through the f/96 camera on 27 August 1990 and 19 December 1990 and comprise three images. The first image was a 597s

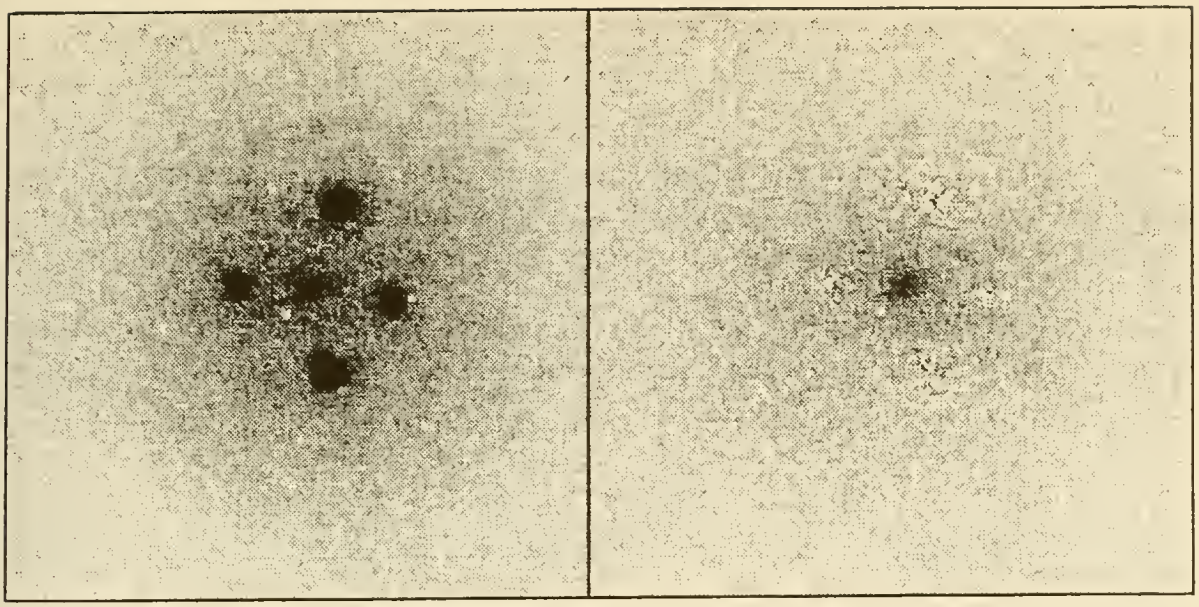

Figure 1: (a) *(left)* The central 256x256 ($\sim 5.5''$x$5.5''$) region of the F502M image. (b) The residual image obtained after subtracting the lensed quasar images. [Note: The cores of the quasar images do not come away cleanly because of differing amounts of non-linearity compared to the PSF used.]

acquisition exposure taken through the F430W filter (close to a Johnson B Filter). This image has 512x1024 pixels, where the pixels are rectangular and have a size of ≈ 0.044x$0.022''$, resulting in a field size of $\approx 22''$x$22''$. The second image (see Figure 1a) is a 512x512, 1496s exposure taken through the F502M filter, (approximately a Gunn *g* filter). In this image the pixels are $\approx 0.022''$ square, giving a field of $\approx 11''$x$11''$. The third image was also an f/96 exposure through the F342W filter for 3 x 1200s. The results from the first two images were reported by Crane *et al.*,1991.

The brightest of the lensed images, B, has a peak count of 430 counts in the F502M image and the corresponding count rate is well within the FOC linear range for point sources (Paresce, 1990). The diffuse source seen between the QSO images is the nucleus of the lensing galaxy and has a peak count of ~45 counts per pixel. Figure 1b shows the residual image of the galaxy with the quasars subtracted.

3. Results

These images allow us to determine the relative magnitudes of the individual images of the quasar, the galaxy, and to set an upper limit on the brightness of any fifth image. We also determine the positions of the individual images with very high precision. Except for the result on the fifth image, these results are reported in greater detail by Crane *et al.*(1991).

3.1. Positions

The positions of the individual quasar images were measured using a simple centroiding algorithm in IRAF. The results are given in Table 1 below, and are compared

Object	ΔX	ΔY	ΔE	ΔN
A	0.000	0.000	0.000	0.000
B	0.108	1.796	-0.672	1.673
B-Yee			-0.68	1.68
B-Racine			-0.671	1.682
C	-0.976	0.941	0.626	1.202
C-Yee			0.62	1.20
C-Racine			0.617	1.203
D	0.646	0.761	-0.854	0.517
D-Yee			-0.85	0.530
D-Racine			-0.853	0.530
Galaxy	-0.209	0.917	-0.093	0.936
G-Yee			-0.08	0.94
G-Racine			-0.073	0.938

Table 1: Relative Positions (in arcsec).

to the results of Yee(1988) and Racine(1991). The agreement with the results of Racine is quite good, except for the position of the galaxy nucleus which is off by about a FOC pixel. The center determined in the FOC image is closer to the D quasar image.

3.2 Photometry

The relative brightness of the individual quasar images was determined by summing the flux inside fixed apertures. The details of the procedures used are given in Crane *et al.*(1991) The results are summarized in Table 2. We note that the reported brightening of image B reported by Pettersen(1990) is confirmed.

Table 2: Relative Magnitudes.

Object	Δg (1)	ΔB (1)	ΔU (1)	ΔR (2)	Δg (3)	Δr (4)
A	0.00	0.00	0.00	0.00	0.00	0.00
B	-0.14	-0.14	-0.12	0.53	0.21	-0.10
C	0.67	0.70	0.78	1.14	0.69	0.33
D	0.89	1.02	0.80	1.37	0.92	0.83
Date	27 Aug 90	27 Aug 90	19 Dec 90	18 Aug 88	25 Sep 87	13 Oct 85

Notes: (1) This paper. The relative magnitudes have an error bar of ± 0.05 for component B and ± 0.10 for components C and D. An estimate of the g and B magnitudes of the A component is 17.74 ± 0.10 and 17.96 ± 0.07 respectively, (2) Irwin *et al.* (1989), (3) Yee (1988), (4) Schneider *et al.* (1988).

3.3 Fifth Image

The 3600s image in the UV was searched for a fifth image at or near the position of the galaxy nucleus. A careful subtraction of the quasar images resulted in no detectable image brighter than 250 times fainter than image B. This corresponds to 5.8 magnitudes fainter that image A. This result is uncorrected for the relative difference in extinction between the center of the galaxy and image A. Using the extinction law found of Nadeau *et al.*, 1991, the extinction might be as much as one magnitude greater at 3450Å than at the wavelength where Racine(1991) claims to have found a fifth image. Thus our limit would be 4.8 magnitudes fainter than image A and is just consistent with Racine's claimed detection at 4.5 magnitudes fainter than image A.

REFERENCES

Crane, P., *et al.*, 1991, *Ap. J. (Letters)*, **369**, L59.

Huchra, J., Gorenstein, M. Kent, S., Shapiro, I., Smith,G. Horine, E,. and Perley, R., 1985, *A. J.*, **90**, 691.

Irwin, M.J., Webster, R.L., Hewett, P.C., Corrigan, R.T., and Jedrzejewski, R.I., 1989, *A. J.*, **98**, 1989

Kent, S.M., and Falco, E.E., 1988, *Ap. J.*, **96**, 1570.

Paresce, F., 1990, The Faint Object Camera Handbook (Baltimore: Space Telescope Science Institute)

Pettersen, B.R., 1990, I.A.U. Circ. No 5099.

Nadeau, D., Yee, H.K.C., Forrest, W.J., Garnett, J.D., Ninkov, Z., Pipher, J.L., *Ap. J.*, **376**, 430.

Racine, R., 1991, *A. J.*, , 102, 454.

Schneider, D.P., Turner, E.L., Gunn, J.E., Hewitt, J.N., Schmidt, M., and Lawrence, C.R., 1988, *A. J.*, **95**, 1619.

Yee, H.K.C., 1988,*A. J.*, **95**, 1331.

REDUCTION OF PG1115+080 IMAGES

Edward J. Groth, Jerome A. Kristian, S. P. Ewald, J. Jeff Hester,
Jon A. Holtzman, Tod R. Lauer, Robert M. Light, Edward J. Shaya,
and the rest of the WFPC Team: William A. Baum, Bel Campbell,
Authur Code, Douglas G. Currie, G. Edward Danielson, S. M. Faber,
John Hoessel, Deidre Hunter, T. Kelsall, Roger Lynds, Glen Mackie,
David G. Monet, Earl J. O'Neil, Jr., Donald P. Schneider,
P. Kenneth Seidelmann, Brad Smith, and James A. Westphal

1. THE DATA

The data are three exposures in PC6 through F785LP obtained on March 3, 1991. The exposure times are 120, 400, and 400 seconds. The data are reduced with the "standard" WFPC reduction scheme: A-to-D correction, DC bias subtraction, AC bias subtraction, dark current subtraction, preflash subtraction, and flat field normalization, using the best available calibration data. The exposures are combined into a weighted average normalized to 400 seconds exposure time, so one DN (data number) is about 17.25 electrons. At this step, cosmic rays are removed by intercomparison of the three images.

2. THE GOAL

The lensing object can be seen in the processed image. One would like to subtract the four QSO images to leave behind a clear picture of the lens.

3. THE PROBLEM

Due to various glitches there is no high signal-to-noise PSF observation contemporaneous with the PG1115+080 observations. Since the data were obtained, the secondary mirror has been moved several times in an attempt to improve the performance of the FGSs, so it is unlikely that a PSF suitable for subtraction will *ever* be obtained.

4. THINGS THAT DON'T WORK: A "THEORETICAL" PSF

One of the things we tried was a PSF from the STScI library of PSFs. The library

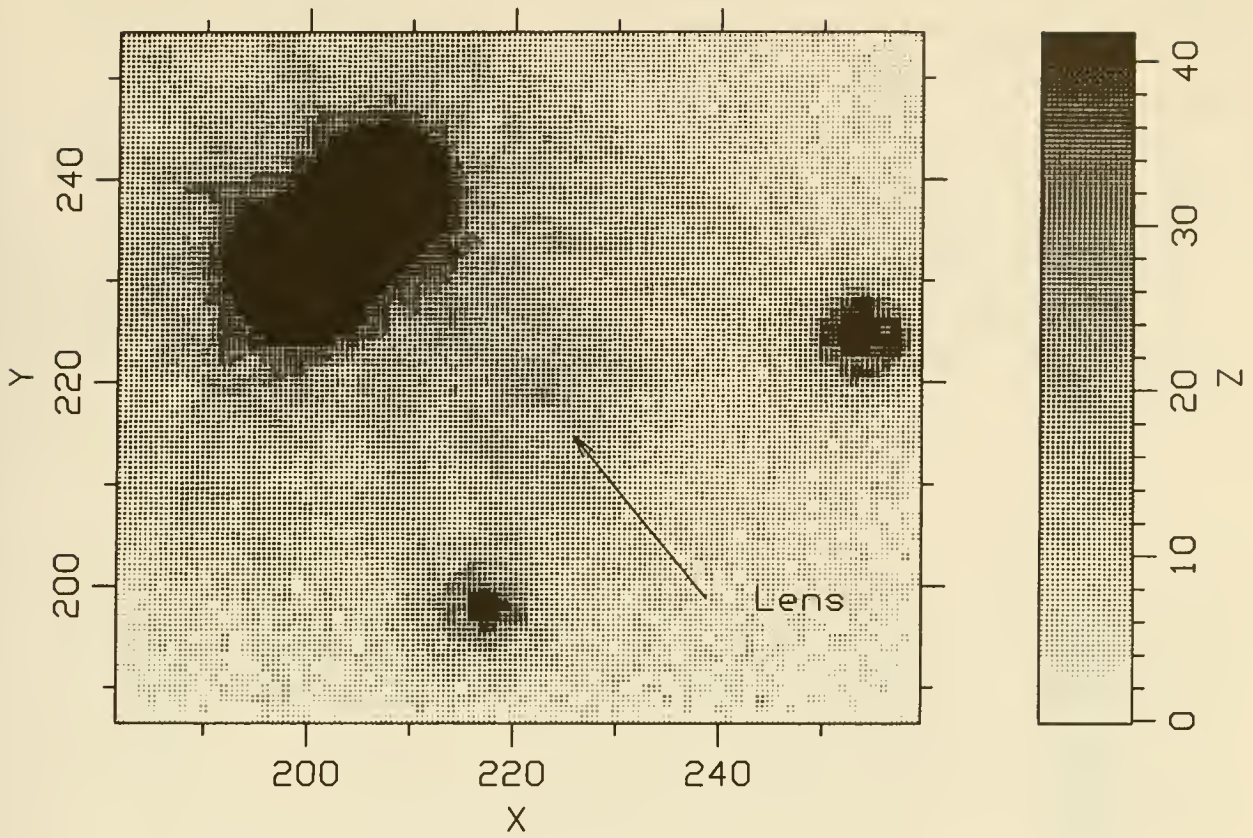

contains PSFs calculated "from first principles." While the library PSFs are qualitatively similar to the actual PSFs—one can make correspondences between the tendrils and rings, etc.—the library and actual PSFs differ in quantitative details which are important for the kind of subtractions required here.

The subtractions of the library PSF yields an image in which the lens is obscured by incomplete removal of the outer parts of the PSF. We attempted to calculate more accurate PSFs but were not successful.

5. THINGS THAT DON'T WORK: A LOW S/N PSF

Observations of Q0957+561 were obtained the same day as those of PG1115+080. One of the QSO images in these exposures is sufficiently well separated from the lens and the other image that it can be used as a PSF. Unfortunately, one of the two exposures with F785LP was badly jittered, leaving only a single 350 second exposure to be used for the PSF. Although the core of the PSF is well exposed, the halo is not. Using this object for subtraction introduces so much noise in the resulting image that the lens is obliterated.

6. SOMETHING THAT WORKS: AP LIB (BUT IT'S HARD)

Observations of AP Lib were obtained the same day as those of PG1115+080. These

observations include three exposures through F785LP in PC6. The exposure times are 30, 500, and 500 seconds. These data were processed through the standard reduction in the same way as the PG1115+080 observations. In this case, the combination of the images into a weighted average also takes account of the fact that the central four pixels of the 500 second exposures are saturated and uses only the data from the 30 second exposure for these pixels.

An advantage of the AP Lib exposure is that it's very high signal-to-noise: a saturated core means that the halo is well exposed. Another advantage is that AP Lib is centered on PC6 only about 55 pixels from the center of the PG1115+080 images.

A big disadvantage is that AP Lib is not a point source: there is a galaxy underneath that fills the entire detector!

However, it appears that AP Lib can be well approximated as a point source plus a concentric, circularly symmetric galaxy. It should be possible to take advantage of this symmetry.

7. ASSUMPTIONS AND PROCEDURES

Assume that the AP Lib image is a circularly symmetric smooth galaxy concentric with a point source manifested as the PSF. Note that this assumption is probably not quite correct. The convolution of the PSF with a smooth function should give back a smooth function. But, at the center, the galaxy in AP Lib may have structure on scales comparable to the structure in the PSF. Thus, the validity of this assumption must be judged by how well the procedure works.

In any case, with this assumption, the model is that everything in the PG1115+080 image with the exception of the lens can be represented as:

$$s(\mathbf{r}_j) = \sum_i a_i \left(A(\mathbf{r}_j - \mathbf{r}_i) - G(|\mathbf{r}_j - \mathbf{r}_i|) \right)$$

where $s(\mathbf{r}_j)$ is the signal in pixel $\mathbf{r}_j$, $\mathbf{r}_i$ is the center of QSO image $i, i = 1, 2, 3, 4$, a_i is the relative strength of QSO image i, A is the AP Lib image, and G is the circularly symmetric galaxy profile in the AP Lib image.

This model is fit to the PG1115+080 image using weighted least squares. The AP Lib image is translated to each QSO position with bi-cubic interpolation. The galaxy profile, G, is represented as 101 numbers giving the value of the profile at radii from 0 to 100 pixels; linear interpolation is used to center G at each QSO image. Altogether there are 105 parameters estimated by the fit: four QSO amplitudes and 101 numbers in the profile. Errors are determined by propagation of errors using the read and photon noise in the PG1115+080 image. The fit is performed for three cases: In case 1, a patch of 12 pixel radius centered on the lens is excluded from the fit. In case 2, the lens is not excluded, case 3 is a fit to a simulation, whose description is omitted due to space considerations. The following table summarizes results from the fits:

Case	Pixels in Fit	Degrees of Freedom	χ^2 Before	χ^2 After
1. Lens Excluded	46180	46075	815738	48772
2. Lens Included	46621	46516	861359	50097
3. Simulation	46180	46075	832000	47856

and the following shows the QSO parameters

QSO	a_i (Case 1)	a_i (Case 3)	Case 1 Rescaled
A1	0.1180 ± 0.0017	0.1159 ± 0.0013	0.1150
A2	0.0819 ± 0.0012	0.0795 ± 0.0009	0.0798
B	0.0204 ± 0.0003	0.0199 ± 0.0003	0.0199
C	0.0315 ± 0.0005	0.0301 ± 0.0004	0.0307

8. RESULTS OF THE SUBTRACTION

Once the QSO amplitudes, a_i, and the galaxy profile, G, are determined, the QSOs can be subtracted, leaving a picture that contains only the lens (and possibly the fifth image!). The results shown are for case 1, the lens excluded fit. The results for case 2, the lens included fit, are similar, except that the galaxy profile is a little higher at radii corresponding to the distance of the lens from the two brighter QSO images. The subtraction then leaves the lens slightly fainter and leaves a slight hole to the upper left of the two brighter QSO images at about the same distance as the lens.

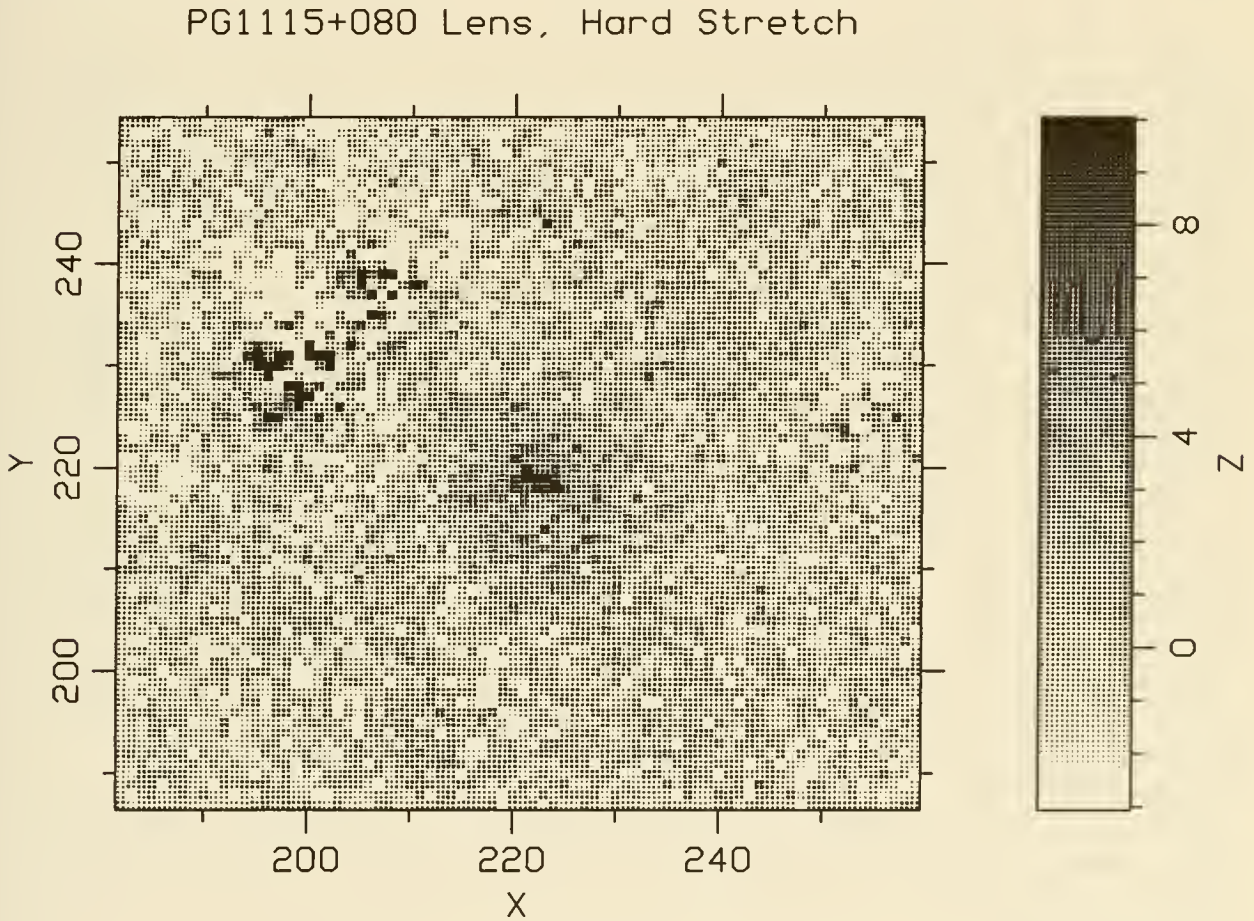

9. FUTURE WORK

Future work will attempt to improve the subtraction, to deconvolve the lens, and then to improve the lens model based on these data. Additional observations will be proposed in order to obtain a higher signal-to-noise image of the lens.

OPTICAL AND UV POLARIZATION OBSERVATIONS OF THE M 87 JET

P. E. Hodge, F. Macchetto, W. B. Sparks
Space Telescope Science Institute
3700 San Martin Dr
Baltimore, MD 21218
USA

The f/96 relay of the Faint Object Camera (FOC) contains three linearly polarizing filters with nominal position angles of 0, 60, and 120 degrees. These filters are described in some detail by Paresce (1990). Observations of the knot A region of the jet of M 87 were taken with the FOC in the blue and ultraviolet through the polarizing filters for the purpose of determining the orientations of the filters. Polarization maps were created from these data, and the results were compared with 2 cm VLA observations (Owen, Hardee, Cornwell, 1989).

The observations were taken on 1991 April 3. Each of the six exposures for polarization was of 1500 seconds duration. Three exposures were taken through the F430W filter, one with each of the polarizing filters, and then three exposures were taken through the F220W filter, one with each polarizing filter. The approximate peak wavelength and bandwidth of the F430W filter are 396 nm and 87 nm respectively, while for F220W the values are 226 nm and 47 nm (Paresce 1990).

The results are shown in Figures 1 and 2, both of which show polarization vectors, with the orientation indicating the magnetic field direction, and the length proportional to the polarized flux. The horizontal and vertical axes are labeled in image pixel coordinates. Figure 1 shows the data taken through the F430W filter, and Figure 2 shows the data taken through the F220W filter. The image orientation and scale are shown to the right of the plot border. The scale of polarized flux is indicated by a line at the lower right within the plot border showing the length of a bar for a polarized flux of 100 counts detected by the FOC during the full exposure of 4500 seconds.

The polarization map taken with the F430W filter is smaller than that with the F220W filter because the telescope was moved between the second and third of the F430W images in order to include knot C in the field of view. A common section within the overlap region was extracted. All three of the F220W images were taken at the same location.

The basic calibration of these images was performed by the Post Observation Data Processing System at the Space Telescope Science Institute. For FOC images, this calibration includes dividing by a flat field and correcting for the geometric distortion of the optics and camera. For further details, see Greenfield *et al.* (1991).

The background level was measured for each image by taking averages in regions away from the jet, and the values of about 15 counts per pixel for F430W and one

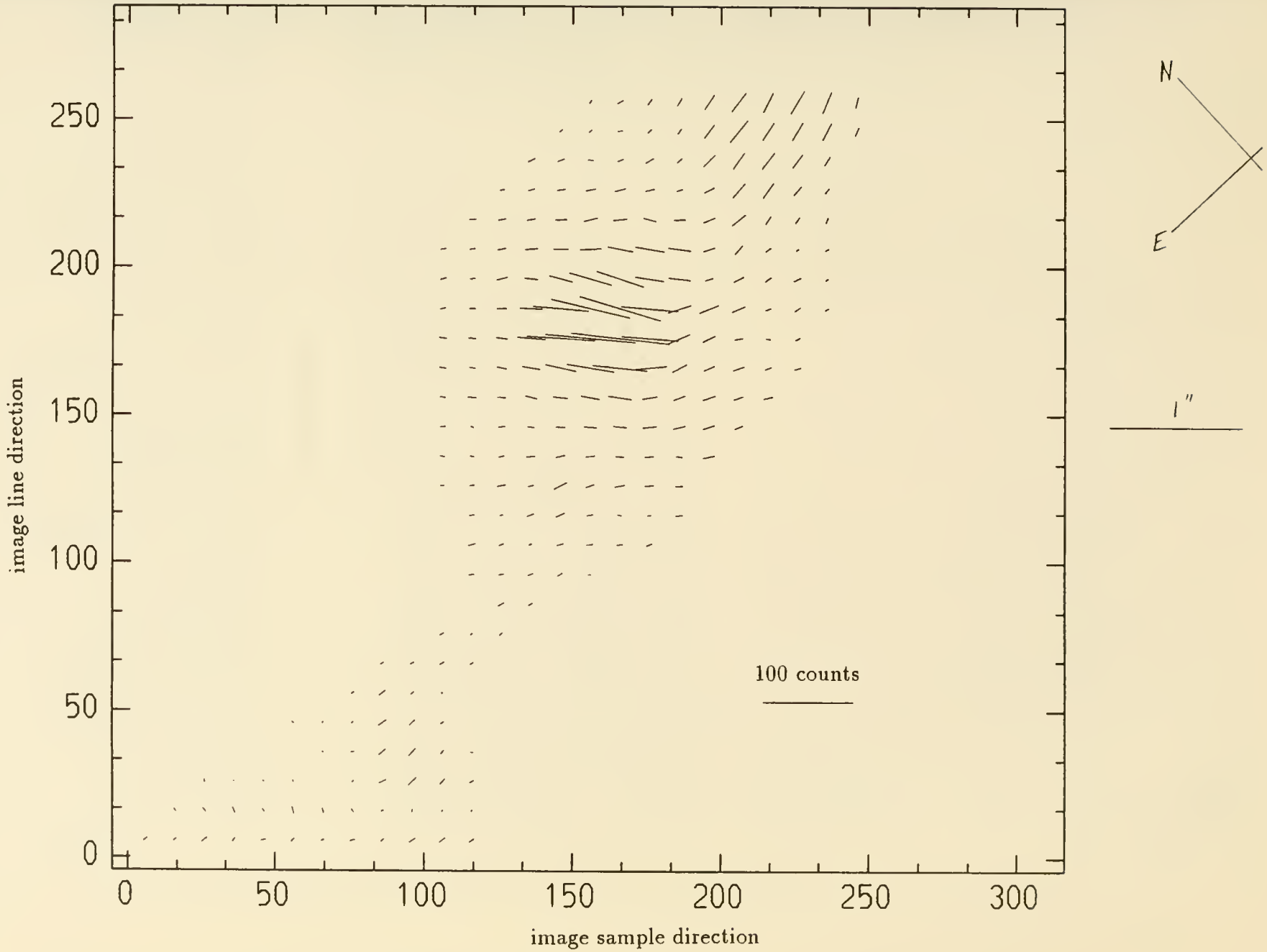

Figure 1. Polarized flux through F430W filter - magnetic field direction.

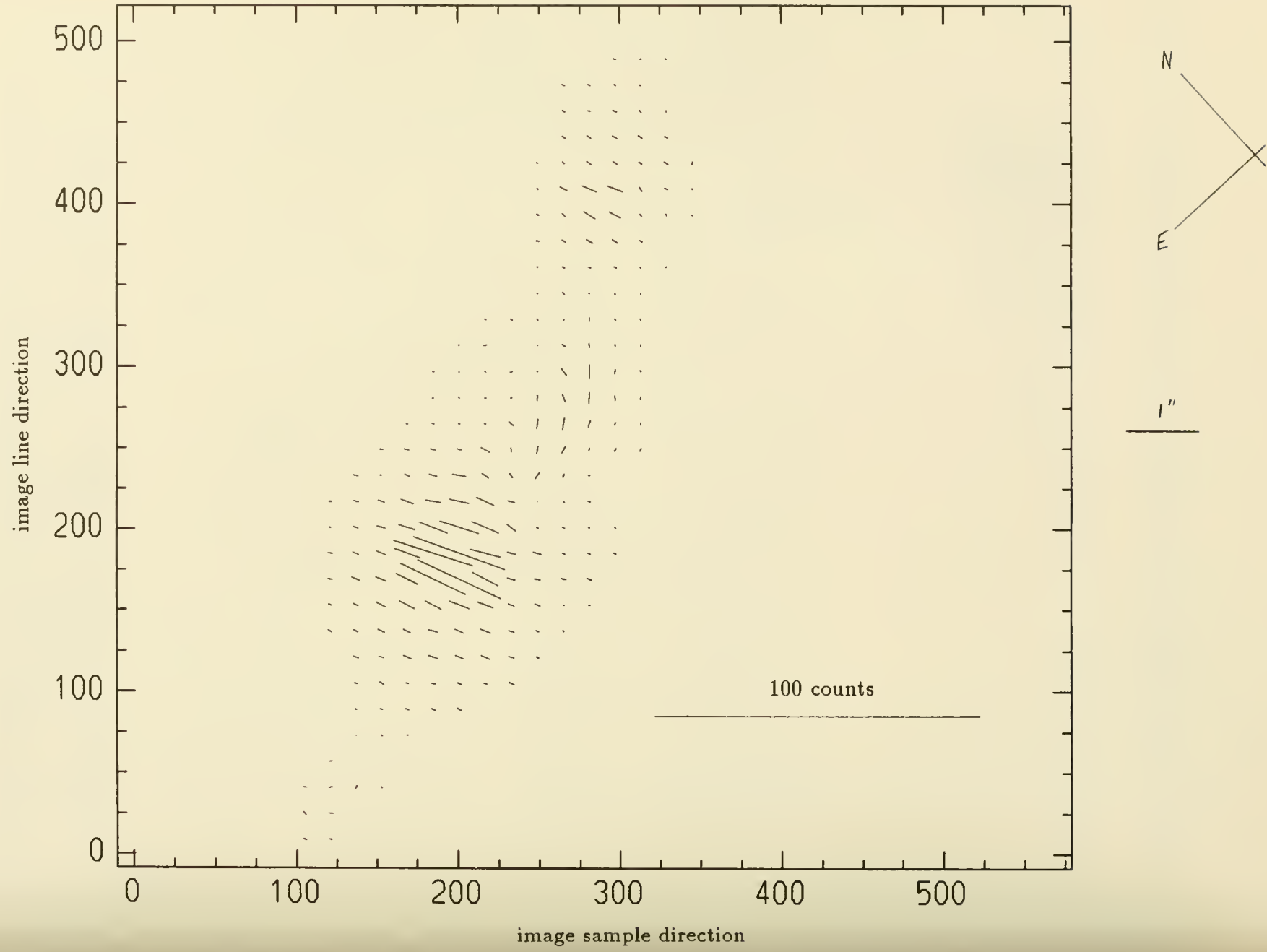

Figure 2. Polarized flux through F220W filter - magnetic field direction.

count per pixel for F220W were subtracted from the images. To improve the signal-to-noise, the F430W images were block averaged with a 10 x 10 pixel box, and the F220W images were block averaged with a 16 x 16 pixel box. The image scale of the FOC at f/96 is 0.02217 arcsecond per pixel (Greenfield *et al.* , 1991). These images have not been deconvolved.

The three polarizing filters differ somewhat in throughput. The 60-degree filter has a short-wavelength cutoff near 220 nm, while the 0 and 120-degree filters extend below 150 nm (Paresce 1990). When the polarizing filters are combined with F430W, the difference in throughput is less than one percent. With the F220W filter, on the other hand, the throughput of the 60-degree filter is only about 2/3 that of the other two polarizing filters. In order to have any confidence in the polarization measurement for F220W, this factor must be accurately determined. The reflectivities of the HST mirrors, the transmission curves of the various filters, and the sensitivities of the detectors were measured prior to launch. Horne (1990) has written a program called XCAL to calculate the throughput of the HST with various instrument configurations and different spectral distributions of the incident light. We used XCAL to calculate the relative throughput of the three polarizing filters together with either the F430W or F220W filter, and then we used these values to normalize the images. When running XCAL, we specified that the input light was unpolarized and had a power-law spectral distribution. We estimated that the spectral index was +1 (F-lambda increases with decreasing wavelength), based on the F430W and F220W fluxes in knot A.

The maximum flux was in the knot A region, with 334 counts through the F430W filter and 67 counts through the F220W filter. The maximum amplitude of polarization was 111 counts for F430W and 30 counts for F220W. Thus the degree of polarization in knot A was of order 30 to 40 percent. Note that the figures show polarized flux rather than percent polarization, and the direction shown is that of the magnetic field.

The position angles of polarization in the strongly polarized regions in these images are predominantly either parallel or perpendicular to each other. In this situation there are two arrangements of the polarizing filters that give identical results. The two arrangements are mirror images of each other around the direction of polarization. This ambiguity would not be an issue during routine observations because the filter positions would already have been calibrated, but these data were taken for the purpose of verifying the orientations of the polarizing filters. One arrangement agrees with the engineering drawing for the filter wheel, and we assume it is correct, but the other arrangement is not ruled out by these observations.

REFERENCES

Greenfield, P., et al., In-Flight Performance of the Faint Object Camera of the Hubble Space Telescope, Proc. Soc. Photoopt. Instrum. Eng., in press.

Horne, K., 1990, XCAL Users Manual, Space Telescope Science Institute, Baltimore.

Owen, F. N., Hardee, P. E., Cornwell, T. J., 1989, *Ap. J.*, **340**, 698.

Paresce, F., 1990, Faint Object Camera Instrument Handbook, Space Telescope Science Institute, Baltimore.

THE NON-PROPRIETARY SNAPSHOT SURVEY: A Search for Gravitationally-Lensed Quasars Using the HST Planetary Camera

D. Maoz[1], J.N. Bahcall[1], R. Doxsey[2], D.P. Schneider[1], N.A. Bahcall[3], O. Lahav[4], and B. Yanny[1]

1. Institute for Advanced Study
2. Space Telescope Science Institute
3. Princeton University Observatory
4. Institute of Astronomy

The Snapshot Survey is an imaging survey of bright quasars using HST's Planetary Camera (PC). Short exposures (2 or 4 minutes) are taken during gaps in the scheduled observing program, when the telescope would otherwise be idle. All images are obtained using only the gyroscopes for pointing and guiding, thus saving the time necessary to acquire guide stars, and also allowing us to monitor routinely the gyro performance. Targets are distributed throughout the sky, so only short slews (a few degrees) are required to move the telescope from any approved science target to a nearby Snapshot target. Snapshot targets are assigned only after all other programs have been scheduled. The resulting data are non-proprietary, and can be obtained from the STScI User Support Branch. Further details can be found in Bahcall *et al.* (1991).

The scientific purpose of the currently operating Snapshot Survey is to search for evidence of gravitational lensing among known distant, intrinsically luminous quasars. Despite the spherical aberration of HST's primary mirror, the sharp core of the point-spread function, containing $\sim 15\%$ of the light, permits high spatial resolution studies of closely separated bright point sources. The existing point-spread function permits the detection of multiple images at subarcsecond separations, which cannot be easily probed from the ground.

As of mid-April 1991, 89 short exposures, through two filters, of high luminosity quasars from a well-defined sample have been obtained. Useful high-resolution images of 30 quasars have resulted. None show evidence of multiple images caused by

gravitational lensing. Simulations show that multiple images with brightness ratios of up to several magnitudes would have been detected, if present, down to image separations of $\approx 0.1''$. This seems to be in conflict with several ground based surveys (*e.g.*, Crampton *et al.* 1989, Surdej *et al.* 1989) who reported that a large fraction of quasars have subarcsecond multiple images. The paucity of lensed quasars found so far (0 out of 30) suggests lensing is a rare phenomenon, and argues against recently popular-again cosmologies involving a universe dominated by a cosmological constant. In such cosmologies (Fukugita and Turner 1991) multiple images would be detected in about 10% of our sample. As more improved-quality data are obtained, this study will allow a stronger confrontation with the ground-based surveys and the theoretical models.

The Snapshot Survey has uncovered several engineering problems in the observatory's performance, which have already been corrected. In particular, we have encountered large telescope pointing errors (typically 20″) and drift rates (typically 4.5 milli-arcseconds/sec, or 3 to 4 times that expected) when solely under gyro control. We have determined that stellar aberration corrections are not applied in the current control system when HST is operating solely on gyros. The stellar aberration due to the motion of the earth around the sun is

$$\theta = \frac{v}{c} \sin\phi = 20.5'' \sin\phi \ , \tag{1}$$

where v is the earth's velocity around the sun, c is the speed of light, and ϕ is the angle between the earth's velocity vector and the direction of the object being observed. The orbital motion of HST about the earth contributes an additional aberration term with an amplitude of 5″. The spacecraft's centripetal acceleration around the earth will cause the object's position to drift at a rate

$$\frac{d\theta}{dt} = \frac{1}{c}\frac{dv}{dt} \sin\theta \approx 5.5 \sin\theta \text{ mas s}^{-1} \ , \tag{2}$$

where θ is the angle between the spacecraft's acceleration vector and the direction of the object.

Comparing these relations to the observations above, we see that the lack of stellar aberration correction can account for much of the pointing error and of the drift rate. Since April 1991, the HST operation procedures have been modified to invoke

the on-board stellar aberration corrections for observations carried out under gyro control. The correction of this problem will probably shorten the time required to acquire guide stars in FGS-guided observations. The low intrinsic gyro drift rate (now that the stellar aberration correction has been implemented) may make gyro-guided observations attractive to other observers as well. We will continue to monitor the performance of the gyros throughout HST's Cycle 1 of observations.

REFERENCES

Bahcall, J.N., Maoz, D., Doxsey, R., Schneider, D.P., Bahcall, N., Lahav, O., and Yanny, B. 1991, ApJ, in press

Crampton, D., McClure, R.D., Fletcher, J.M., and Hutchings, J.B. 1989, AJ, 98, 1188

Fukugita, M. and Turner, E.L. 1991, MNRAS, in press.

Surdej, J. 1989, in "Gravitational Lensing" eds. Y. Mellier, B. Fort, and G. Soucail, (Berlin: Springer-Verlag), p88

FIGURE CAPTION

Segments of typical Planetary Camera exposures of five Snapshot Survey quasars, with a variety of brightnesses and trail lengths. The image scale is 0.043″ pixel^{-1}, and the field for each panel is 8.6″ on a side. The orientation of the images is random, according to the HST roll angle at the time of the exposure. The gray scale is set individually for each image, such that the darkest hue corresponds to the number of counts pixel^{-1} in the brightest part of the quasar. The numerous dark specks in the images are charged-particle events. The filter used is indicated following the object name ("V" for F555W, and "I" for F785LP). The lower right-hand panel shows a simulated image of a quasar and a secondary image 2 magnitudes fainter, separated by 0.3″. The primary image corresponds to a 17th magnitude object trailed at a rate of 4.6 mas s^{-1} in the 120 s exposures, or a 17.8 magnitude object trailed at a rate of 2.4 mas s^{-1} in the 230 s exposures.

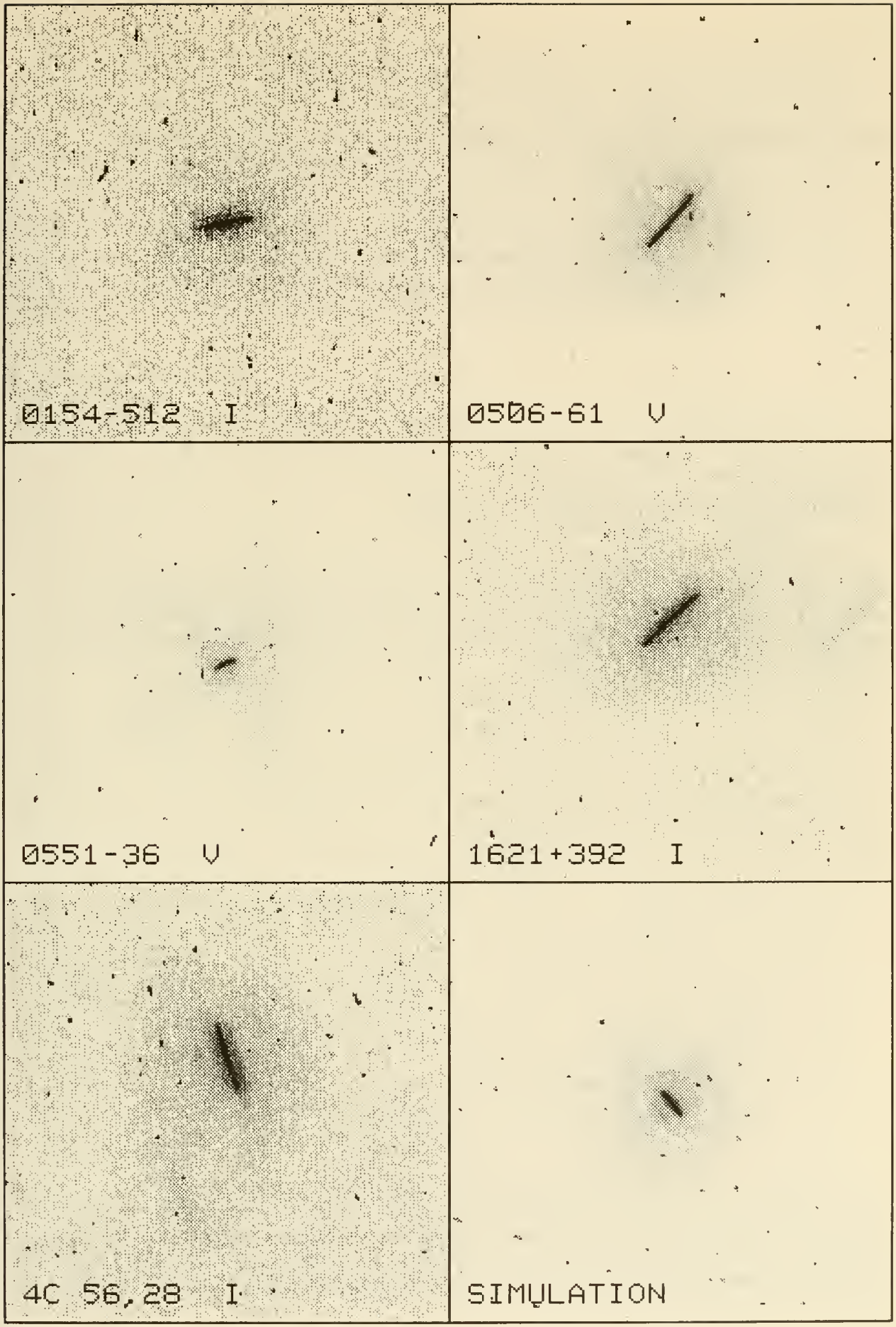
0154-512 I
0506-61 V
0551-36 V
1621+392 I
4C 56,28 I
SIMULATION

FAINT OBJECT SPECTROGRAPH OBSERVATIONS OF CSO 251

R.D. Cohen, E.A. Beaver, E.M. Burbidge,V.T. Junkkarinen,
R.W. Lyons, and E. I. Rosenblatt
Center for Astrophysics and Space Sciences, UCSD
La Jolla, CA 92093-0111

1. OBSERVATIONS AND REDUCTIONS

The QSO CSO 251 (z=0.0788, $F_\lambda(5500Å) = 2 \times 10^{-15}$) was observed as an early release observation (3065) with the FOS. Observations with the G130H grating, with 1Å per diode, and the "blue" Digicon detector were made on January 7, 1991. Sampling is improved by quarter-diode sub-pixel steps. In this mode the spectrum spans the full array sampling from 1150Å to 1600Å.

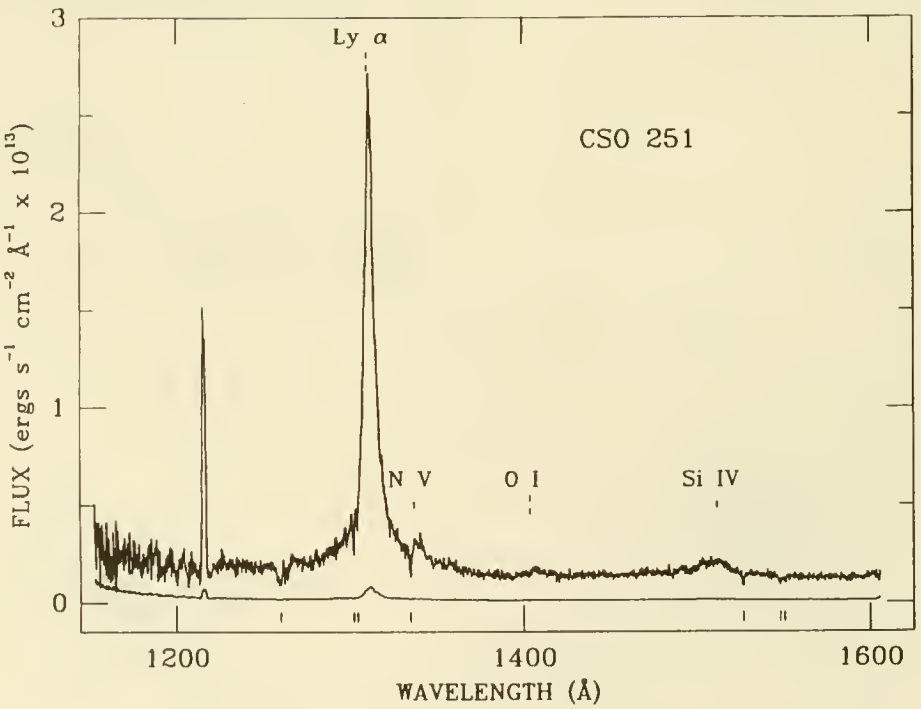

Fig. 1 – Observed spectrum of CSO 251 obtained with the FOS on the HST. Identified emission lines at z = 0.0788 are marked above the spectrum and absorption lines in the Galaxy are marked below the spectrum. The trace at the bottom of the figure shows the 1σ error. The emission line at 1215Å is geo-coronal Lyα.

Four spectral exposures were made with the 1.″0 circular aperture, selected as the best compromise between resolution and throughput efficiency. The exposure time per pixel is 1680 seconds. This UV spectrum is shown in figure 1. A fifth exposure was 100 seconds using the 4.″3 square aperture. The flux calibration of the large and small aperture data is consistent to better than 5%. Observations of Hα were taken at Lick Observatory within two weeks of the FOS observations, and observations of Hβ were made less than two months prior. While previous tests had shown a cyclic drift in position for the FOS red detector due to an interaction with the earth's magnetic field (Junkkarinen et al., 1991) no conclusive evidence has been found that such an effect exists in the blue detector. The background was scaled to match that predicted for the geomagnetic coordinates of our observations (Rosenblatt et al., 1991).

2. EMISSION LINES

The broad emission lines present in QSO spectra are probably produced by material, either in clouds or in an accretion disk, moving at velocities around 10000 km s^{-1} at distances of order one to ten parsecs from the source of continuum radiation. The emission-line profiles produced by this gas depend on both the dynamics of the clouds and the emission properties of the individual clouds. Several models for the broad-emission-line region have been developed that predict shapes for line profiles which are in reasonable agreement with observations. These models include: radiatively accelerated clouds (Blumenthal and Mathews, 1979), clouds accelerated by quasar winds (Weymann et al., 1982), and cloud motion along parabolic orbits (Kwan and Carroll, 1982). Because the overall line parameters do not provide a definitive test of the possible dynamical models, more subtle systematic properties of the emission-line profiles must be considered. Systematic QSO emission-line profile differences (Mathews and Wampler, 1985) and redshift differences (Gaskell, 1982 and Wilkes, 1984, 1986) have been observed. The interpretation of these data in terms of the dynamics, internal obscuration, and geometry of the broad-emission-line region is limited by the quality of the observations and the statistical nature of the problem. These data already provide direct evidence for an inhomogeneous, multi-component broad-emission-line region; with further observations, our understanding will improve.

Wilkes found that, on average, the high-ionization lines were blue-shifted with respect to Hβ, while the low-ionization lines were red-shifted. Observations of Hα in the IR by Espey et al. (1989) show a median redshift difference of 1000 km s^{-1} between Hα and C IV λ1549. Lyα is usually near the C IV redshift. This difference might be the result of a broad-emission-line region that contains a low-ionization region that is optically thick and a separate optically thin high-ionization region (see for example Mathews 1986). The Lyα emission-line profile compared to Hα can be used to estimate the Lyα/Hα ratio in different regions. One prediction of this model is that at velocities where the optically thin component dominates, the Lyα/Hα ratio should be near the recombination value i.e. large. Alternatively, some of the emission can come from the margins of the accretion disk (Collin-Souffrin et al., 1988).

Normalized emission line pairs can be divided to compare line flux ratios as a function of velocity (Shuder, 1982, 1984). With simple assumptions, Shuder showed that the Hα and Hβ profiles indicate that velocity increases inwards in the broad-line region of Seyfert galaxies, although the effects were less pronounced in QSOs. Detailed comparisons of several lines, including those from both the fully and partially ionized zones, combined with predictions from photo-ionization models may allow us to reach

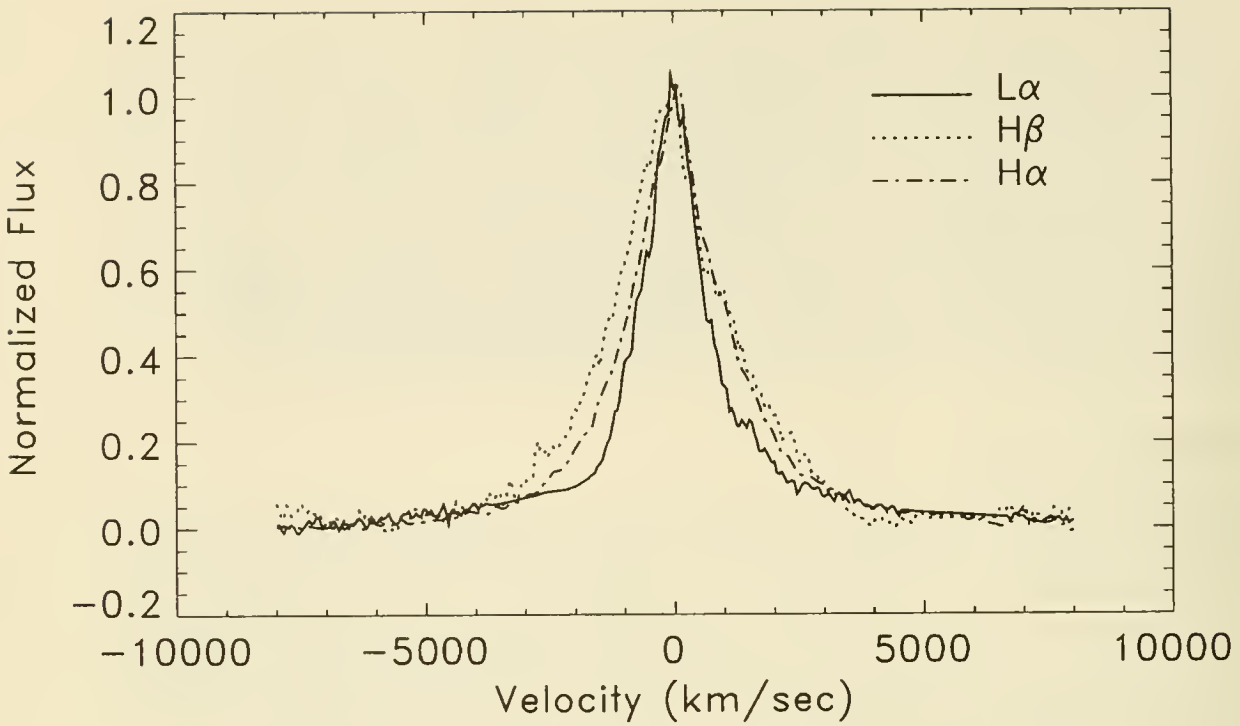

Fig. 2 – Broad emission lines in CSO 251 normalized and plotted on a velocity scale. The obvious smooth area in the wing of Lyα indicates where N V has been removed. Other lines have been removed as described in the text.

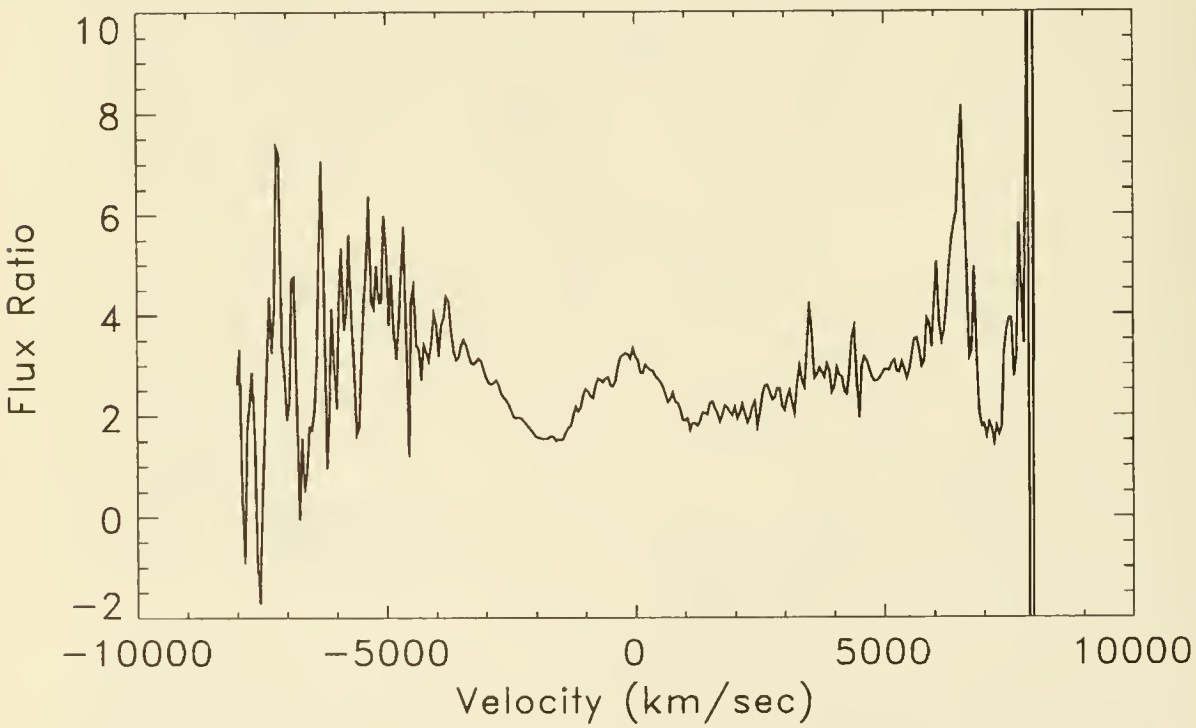

Fig. 3 – The profile of Lyα divided by the profile of Hα. The vertical scale shows true relative fluxes.

more detailed conclusions. Such comparisons require lines observed in the UV and optical or optical and IR. To date, the optical emission lines in such comparisons have been of higher resolution and signal–to–noise than the other lines. However, with the FOS and HST, emission lines from O VI out to Hα can be observed in low–redshift QSOs with comparable resolution and signal–to–noise. An additional advantage is that Lyα in low–redshift QSOs is not severely cut up by Lyα forest absorption lines.

Our analysis for these lines is not complete. However, although the peaks of all lines occur at almost the same velocity, profile differences between the lines are evident. Normalized profiles of Lyα, Hβ, and Hα are shown in figure 2, and the division of the Lyα profile by Hα is shown in figure 3. Broad emission lines at the positions of N V and Fe II were removed from the profiles of Lyα and Hβ respectively, while a smooth continuum was fit through all UV absorption lines. Narrow lines of [N II] are not seen, nor were any narrow components of the permitted lines. Profile comparisons made after subtracting our best estimates of the narrow lines are similar to those shown here.

While the division of Hβ by Hα (not shown) is reminiscent of the profile divisions shown by Shuder, the Lyα division is surprising. This line ratio first falls with increasing velocity, and then rises again. This behavior is similar to that shown in Carroll and Kwan (1985), but we hesitate to draw broad conclusions based on observations of three lines in a single object.

REFERENCES

Blumenthal, G. R., and Mathews, W. G. 1979, *Ap. J.*, **233**, 479.

Collin–Souffrin, S., Hameury, J.–M., and Joly, M. 1988, *Astron. and Astroph.*, **205**, 19.

Espey, B. R., Carswell, R. F., Bailey, J. A., Smith, M. G., and Ward, M. J. 1989, *Ap. J.*, **342**, 666.

Gaskell, C. M. 1982, *Ap. J.*, **263**, 79.

Junkkarinen, V. T., *et al.* 1990, *B.A.A.S.*, **22**, 1282.

Kwan, J., and Carroll, T. J. 1982, *Ap. J.*, **261**, 25.

Mathews, W. G. 1986, *Ap. J.*, **305**, 187.

Mathews, W. G., and Wampler, E. J. 1985, *P.A.S.P.*, **97**, 966.

Rosenblatt, E. R., *et al.* 1990, *B.A.A.S.*, **22**, 1283.

Shuder, J. M. 1982, *Ap. J.*, **259**, 48.

Shuder, J. M. 1984, *Ap. J.*, **280**, 491.

Weymann, R. J., Scott, J. S., Schiano, A. V. R., and Christiansen, W. A. 1982, *Ap. J.*, **262**, 497.

Wilkes, B. J. 1984, *M.N.R.A.S.*, **207**, 73.

Wilkes, B. J. 1986, *M.N.R.A.S.*, **218**, 331.

FOC OBSERVATIONS OF R136a IN THE 30 DORADUS NEBULA[1]

G. Weigelt[2,3], R. Albrecht[2,4,5], C. Barbieri[2,6], J. C. Blades[2,7], A. Boksenberg[2,8], P. Crane[2,9], J. M. Deharveng[2,10], M. J. Disney[2,11], P. Jakobsen[2,5], T. M. Kamperman[2,12], I. R. King[2,13], F. Macchetto[2,5,7], C. D. Mackay[2,14], F. Paresce[2,5,7], D. Baxter[7], P. Greenfield[7], R. Jedrzejewski[7], A. Nota[6,7], W. B. Sparks[7]

[1]Based on observations with the NASA/ESA *Hubble Space Telescope*, obtained at the Space Telescope Science Institute, which is operated by AURA, Inc., under NASA contract NAS 5-26555, [2]Member FOC Investigation Definition Team, [3]MPI für Radioastronomie, [4]Space Telescope European Coordinating Facility, [5]Astrophysics Division, Space Science Department of ESA, [6]Osservatorio Astronomico di Padova, [7]Space Telescope Science Institute, [8]Royal Greenwich Observatory, [9]ESO, [10]Laboratoire d'Astronomie Spatiale du CNRS, [11]Department of Physics, University College of Cardiff, [12]SRON - Space Research Utrecht, [13]Astronomy Department, University of California, Berkeley, [14]Institute of Astronomy, Cambridge.

1. OBSERVATIONS AND DISCUSSION

R136a is the central object in the 30 Doradus nebula (see Walborn 1973; 1986; 1990 and references therein). The physical nature of R136a has been the subject of controversy over the last few years. One suggestion was that R136a might be a single object with a mass of the order of 1000 solar masses. The other suggestion was that R136a is a compact star cluster and that it consists of several O and WR stars. Observations of R136a by speckle techniques have resolved 8 stars within 0.7 arcsec diameter (Weigelt and Baier 1985; Neri and Grewing 1988). The HST observations described here (Weigelt et al. 1991) confirm that R136a is a compact star cluster. There is good agreement with the speckle observations.

The raw image shown in Fig. 1 was taken on 1990 Aug. 23 (filter F346M and neutral density (ND) filter F8ND; FOC f/96 mode; coarse track mode; exposure time 600 s). The count number in the brightest pixel is only 136 since too many ND filters were used. The background light is caused by the wings of the psf (spherical aberration). Fig. 2 shows the same R136 image after application of the image restoration method CLEAN.

Fig. 3 shows a high-resolution image of R136a reconstructed from a FOC f/288 exposure (1990 Aug. 23; f/288 mode; 1.7 arcsec region; filter F253M plus ND filter F4ND; exposure time 900 s; count number in the brightest pixel is only 27; CLEAN reconstruction). The photometric accuracy of the reconstructed image is not very good since the raw image is very noisy. The separation of the bright, close double star a1-a2 is $\sim$ 0.11 arcsec. In the f/288 raw image the star R136a2 is $\sim$ 0.4 ($\pm$0.2) magnitudes fainter than R136a1, while the stars R136a3 and R136a6 are $\sim$ 0.6 ($\pm$0.3) magnitudes fainter than R136a1. All 8 stars resolved by holographic speckle interferometry can be found in both the f/96 and the f/288 FOC images.

Walborn (1986) has calculated the mass of the brightest component a1 on the assumption that the V-magnitudes of a2 and a3 are not more than $\sim$ 0.3 mag fainter than a1. In this case he finds an upper limit for the mass of a1 of $\sim$ 250 solar masses. The speckle observations have shown that in the red the magnitude differences of a1, a2, and a3 are $\sim$ 0 to 0.3. From the HST observations we now know in addition that at 2550 Å the magnitude differences of

Figure 1. FOC f/96 raw image of R136 (filter F346M + F8ND).

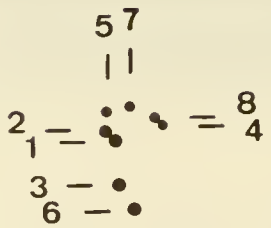

Figure 2. Image of R136 reconstructed from the FOC f/96 image shown in Fig. 1.

a1, a2, a3, a6 are only $\sim$ 0.4 to 0.6. This means that the HST observations support Walborn's conclusion that the upper limit for the mass of R136a1 is $\sim$ 250 solar masses.

ACKNOWLEDGEMENTS. The FOC is the result of many years of hard work and important contributions by a number of highly dedicated individuals. In particular, we wish to thank ESA *HST* Project Manager R. Laurance, the ESA/*HST* Project Team, and the European contractors for building an outstanding scientific instrument. The FOC IDT Support Team, D. B., P. G., R. J., and W. B. S., acknowledge support from ESA through contract 6500/85/NL/SK. P. C. and I. R. K. acknowledge support from NASA through contracts NAS5-27760 and NAS5-28086.

REFERENCES

Neri, R. & Grewing, M. 1988, A&A, **196**, 338
Walborn, N.R. 1973, Ap. J. (Letters), **182**, L21
Walborn, N.R. 1986, in IAU Symp. 116, p.185, Walborn, N.R. 1990, in IAU Symp. 148, p.145
Weigelt, G. & Baier, G. 1985, A&A, **150**, L18
Weigelt, G., Albrecht, R., Barbieri, C., Blades, J.C., Boksenberg, A., Crane, P., Deharveng, J.M., Disney, M.J., Jakobsen, P., Kampemann, T.M., King, I.R., Macchetto, F., Mackay, C.D., Paresce, F., Baxter, D., Greenfield, P., Jedrzejewski, R., Nota, A., & Sparks, W.B. 1991, Ap. J. (Letters), **378**, L21

Figure 3. Image of R136a reconstructed from a FOC f/288 exposure (filter F253M+F4ND).

GHRS CHROMOSPHERIC EMISSION LINE SPECTRA OF THE RED GIANT α TAU

Kenneth G. Carpenter (NASA - Goddard Space Flight Center)
Richard D. Robinson (Astronomy Programs - Computer Sciences Corporation)
Dennis C. Ebbets (Ball Aerospace System Group)
Alexander Brown and Jeffrey L. Linsky (JILA - Univ. of Colorado & NIST)

1. INTRODUCTION

The K5 III non-coronal giant α Tau was observed during the GHRS Science Assessment Observation (SAO) Program to assess capabilities of the spectrograph important to the study of narrow emission line sources. A region near 2325 Å was chosen since it contains intercombination lines of C II and Si II, which have very small intrinsic widths (no opacity broadening), as well as stronger lines of Fe II, Ni II, and Co II. The observations were made through both the Large and Small Science Apertures (LSA and SSA) in both medium (G270M) and high (Echelle-B) resolution modes to allow a determination of the relative instrument performance in the four observing configurations. The initial scientific results of the program are presented in Carpenter et al. (1991). In this paper, we discuss the instrument performance in more detail and present additional scientific results .

2. INSTRUMENT PERFORMANCE

2.1 Wavelength Calibration

Figure 1 shows typical results from the default wavelength calibration procedure compared with those based on calibration lamp exposures taken at the same carousel position and close in time to the science observations. The top figure (a) shows the Pt wavelength calibration spectrum for the G270M SSA exposure, where a default calibration has been applied. The dashed lines indicate the expected locations of the calibration lines. An offset of 2.83 diodes (36 km/s) was identified between the two. A careful reduction of the data using a near-simultaneous internal lamp exposures allows the computation of more accurate dispersion constants and wavelength offsets. The residuals from a second order polynomial fit to the measured line positions are shown in the lower panel (b) and are seen to be on the order of 0.1 diode-widths (1.2 km/s). Table I summarizes the precision of various levels of wavelength calibration, obtained from these and other SV/SAO observations.

2.2. Effect of Spherical Abberation on Sensitivity

Figure 2 shows the relative throughput of the Small and Large Science Apertures (SSA/LSA) versus wavelength. This curve is based on all SAO/SV/GTO observation sets where data were taken at the same wavelength in the same grating mode through both apertures **and** where we believe the target was well-centered in the SSA. The point at 2325 Å is based on the α Tau observations, while the targets used at the other

data points are indicated on the plot. Table II shows the counts rates seen through the four grating/aperture combinations used in the Alpha Tau program and compares them to each other and to pre-launch (pre-spherical aberration) expectations.

2.3. Comparative Line Profiles

Figure 3 illustrates the differences in the observed line profiles in four different observing modes. The line profiles obtained in modes G270M/LSA, G270M/SSA, and Ech-B/LSA are compared to the 'true' profiles obtained with Ech-B/SSA (dashed-line). The wavelength shift of the G270M/LSA data can be attributed to a relatively poor calibration, since this observation is the only one of the four without a cal-lamp exposure at a nearby wavelength. The lines shown here are almost fully resolved in the G270M/SSA mode, although a few very minor differences can be still be seen between it and the Echelle SSA observation.

3. SCIENTIFIC RESULTS

3.1. Detection of Non-photospheric UV Continuum

The ability to confidently detect the presence of a weak continuum in cool stars is one of the major advantages of GHRS over IUE. Figure 4 shows the G270M LSA observation (which has the highest photometric precision of the four observations), along with the expected photospheric flux (from a standard Kurucz line-blanketed LTE model with T_{eff} of 4000 K) from α Tau. Log(flux) is plotted to clearly display the weak and strong flux regions of the spectrum on a single plot. The factor used to scale the computed fluxes to flux-at-earth was derived by forcing agreement between the IUE and model fluxes at 3200 Å. The observed stellar spectrum, which is well-above background even between the strong emission features, is substantially above the 4000 K photospheric flux. This excess flux is most likely the first detection of chromospheric continuum emission from a cool giant star.

3.2. Line Profile Analysis

The top panel in Figure 5 shows gaussian fits to a Co II line and a self-reversed Fe II line. The former is well-fit with a single gaussian, the latter by a combination of an emission plus absorption gaussians, where the absorption gaussian is shifted by about 1.5 km/sec to the red of the emission gaussian. The lower panel shows gaussian fits to two of the C II] (UV 0.01) lines found in the Echelle data. The lines cannot be fit by single gaussians, but are well-represented by a two-gaussian fit, where the gaussians have the same central wavelength, but substantially different FWHM and maxima. However, the nearby Si II] (UV 0.01) lines (not shown) are well-represented by single gaussians. The profiles exhibited by the C II] lines are similar to those which can be generated, as discussed by Gray (1988), by the full-disk integration of an anisotropic velocity field. Alternatively, Harper (1991) has shown that such profiles can be generated using models of hybrid bright giants in which v_{turb} increases with T_e in the line formation region. Similar physics may be responsible for the profiles seen in α Tau. The differences in the Si II] and C II] profiles suggests differences in the extent and/or location of the line formation regions for the two species.

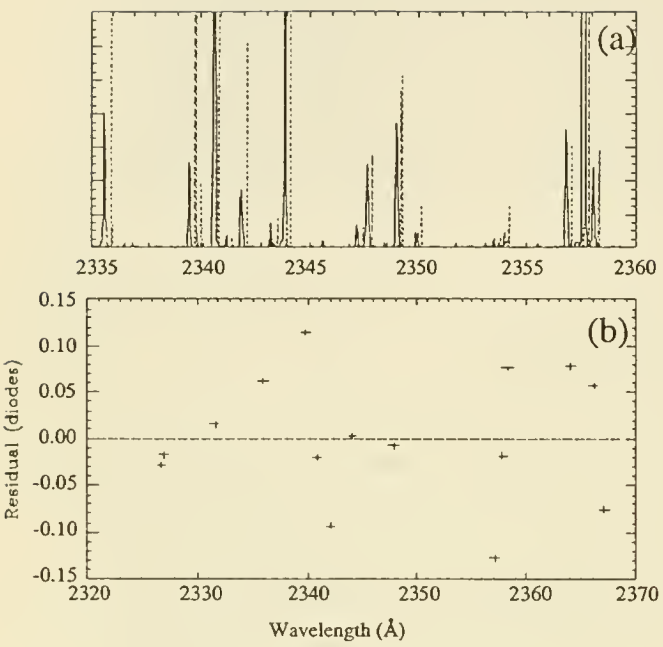

Figure 1

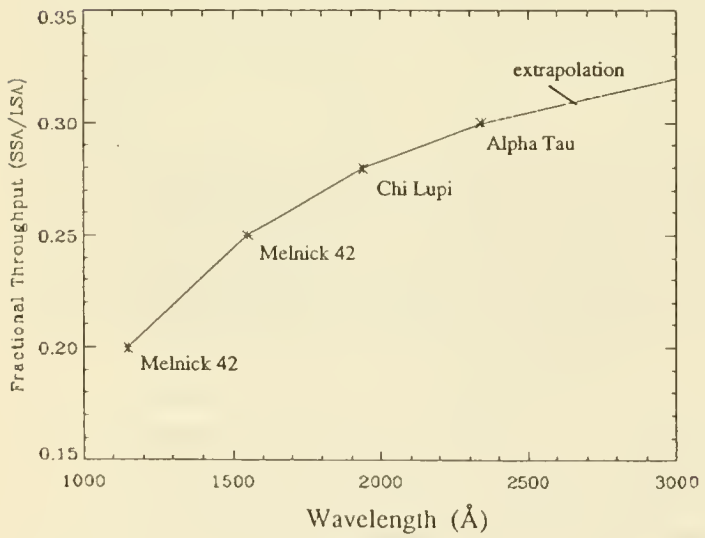

Figure 2

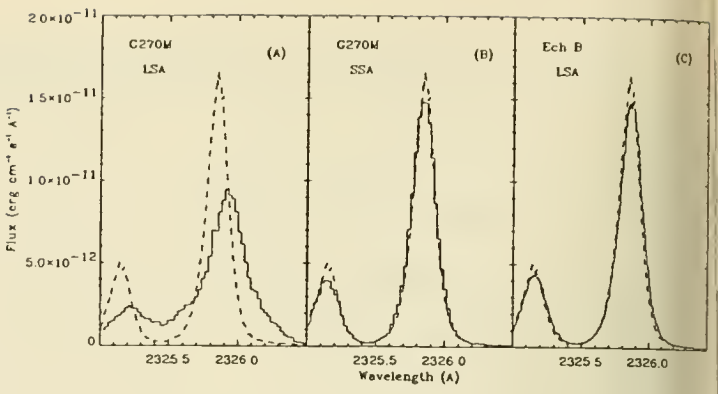

Figure 3

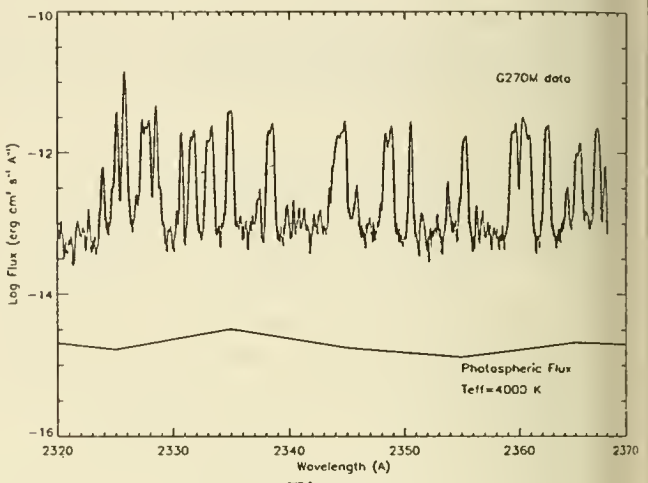

Figure 4

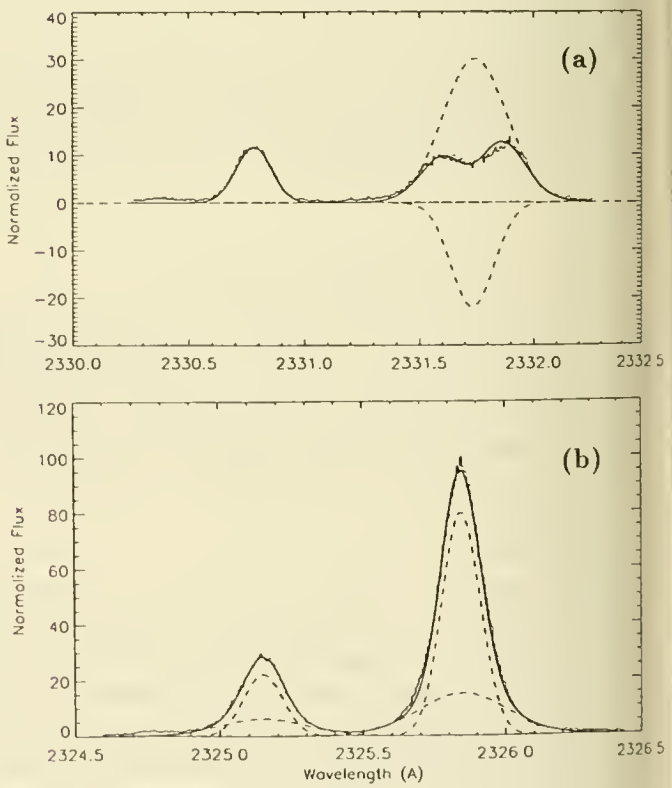

Figure 5

Table I
Properties of the Wavelength Calibrations

Grating	Dispersion (Å/diode)	Wavelength Range (Å)	Accuracy of Wavelength Scale*					
			Default Calib.		SPYBAL Calib.		Full Calib.	
			max offset (diodes)	max error (km/s)	max offset (diodes)	max error (km/s)	max offset (diodes)	max error (km/s)
G140L	0.572-0.573	1050-1800	3	470-285	0.5	78-48	0.1	15-10
G140M	0.056-0.052	1150-1700	3	46-28	0.5	7.6-4.5	0.1	1.5-0.9
G160M	0.072-0.066	1200-2000	3	54-30	0.5	9.0-5.0	0.1	1.8-1.0
G200M	0.081-0.075	1600-2400	3	46-28	0.5	7.6-4.7	0.1	1.5-0.9
G270M	0.096-0.087	2200-3200	3	39-24	0.5	6.5-4.0	0.1	1.3-0.8
Ech A	0.011-0.017	1050-1730	3	10.	0.5	1.6	0.1	0.33
Ech B	0.019-0.035	1680-3200	3	10.	0.5	1.6	0.1	0.33

* Maximum expected error in the absolute wavelength scale caused by thermal and magnetic drifts in the detector. Improvements can be expected if a known fiducial wavelength exists in the spectrum

Table II
Effects of the Spherical Aberration
Throughput for the Large and Small Aperture

grating	aperture	peak count (2325.8 Å)	total counts per Å	SSA/LSA throughput	degradation†
G270M	LSA	21.5	76.0	-	2.0
G270M	SSA	11.3	22.6	0.30	4.5
Ech B	LSA	14.5	117.3	-	2.0
Ech B	SSA	5.0	36.6	0.31	4.5

† Degradation relative to the pre-launch expectations

REFERENCES

Carpenter, K. G., Robinson, R. D., Wahlgren, G. M., Ake, T. B., Ebbets, D. C., and Walter, F. M. 1991, *Ap. J.*, **377**, L45.

Gray, David F. 1988, chapter 1 in 'Lectures on Spectral Line Analysis: F, G, and K Stars' (The Publisher: Arva, Ontario).

Harper, G. 1991, MNRAS, submitted.

We acknowledge support of NASA to NIST through grant S-56460-D. J. Linsky is a Staff Member, Quantum Physics Div., NIST.

IUE FAR-ULTRAVIOLET SPECTRA OF CAPELLA AND γ DRACONIS FOR COMPARISON TO HST/GHRS GTO OBSERVATIONS

Thomas R. Ayres[1]
Center for Astrophysics and Space Astronomy
University of Colorado
Campus Box 389
Boulder, CO 80309-0389
USA

Abstract. I present reference spectra from the IUE Archives to compare with recent HST/GHRS observations of Capella and γ Draconis. The comparison demonstrates graphically the enormous increase in sensitivity and spectral resolution afforded by the GHRS. At the same time, the HST tracings reveal that much of the faint structure in coadded IUE spectra is genuine: structure that seasoned IUE observers would tend to dismiss as noise.

1. INTRODUCTION

A previous paper (Linsky, Brown, & Carpenter 1991: this volume) reported the results of low-, moderate-, and high-dispersion spectroscopy of two bright late-type stars using the GHRS of HUBBLE during Science Verification and early GTO activities. The two targets – Capella (α Aurigae A [G9 III + G0 III]) and γ Draconis (K5 III) – present very different energy distributions in the vacuum ultraviolet. Capella – the archetype "active-chromosphere" giant – is dominated by bright, high-excitation emissions (like C IV $\lambda\lambda$1548,50). In contrast, γ Dra – a typical "non-coronal" giant – is dominated by low-excitation species (like the O I 1305 Å multiplet), and its high-excitation spectrum is quite weak (in fact, thought to be entirely absent prior to HST). The observational work described by Linsky and collaborators consisted of G140L low-resolution spectra of both stars, covering the range 1150–1750 Å; medium-resolution (G140M, G160M, & G200M) spectra of selected intervals of Capella containing diagnostically-important emission lines; and ECH-A & ECH-B spectra of the bright chromospheric emissions of H I (λ1215 Lyα) and Mg II ($\lambda\lambda$2795,2802 doublet) of Capella. The low-dispersion GHRS spectra have a factor of $\approx$ 5 higher spectral resolution than the comparable SWP-LO mode of the IUE; the medium gratings of the GHRS are comparable in spectral resolution (through the LSA) to the IUE echelle ("HI") mode; and the GHRS echelles have a factor of $\approx$ 8 higher resolving power (through the SSA) than the IUE SWP-HI or LWP-HI modes. Furthermore, the HST/GHRS is considerably more sensitive than the IUE by virtue of its 25× larger collecting area, high-throughput spectrometers, and low-noise detectors. Nevertheless, the IUE has been accumulating spectrograms of a diverse set of cosmic targets for nearly a decade and a half. Thus, a comparison between HST/GHRS and IUE spectra is useful not only to demonstrate the extraordinary advance represented by the new Great Observatory, but also as an independent validation of the data quality of the aging but prolific Explorer.

[1]Guest Observer, International Ultraviolet Explorer.

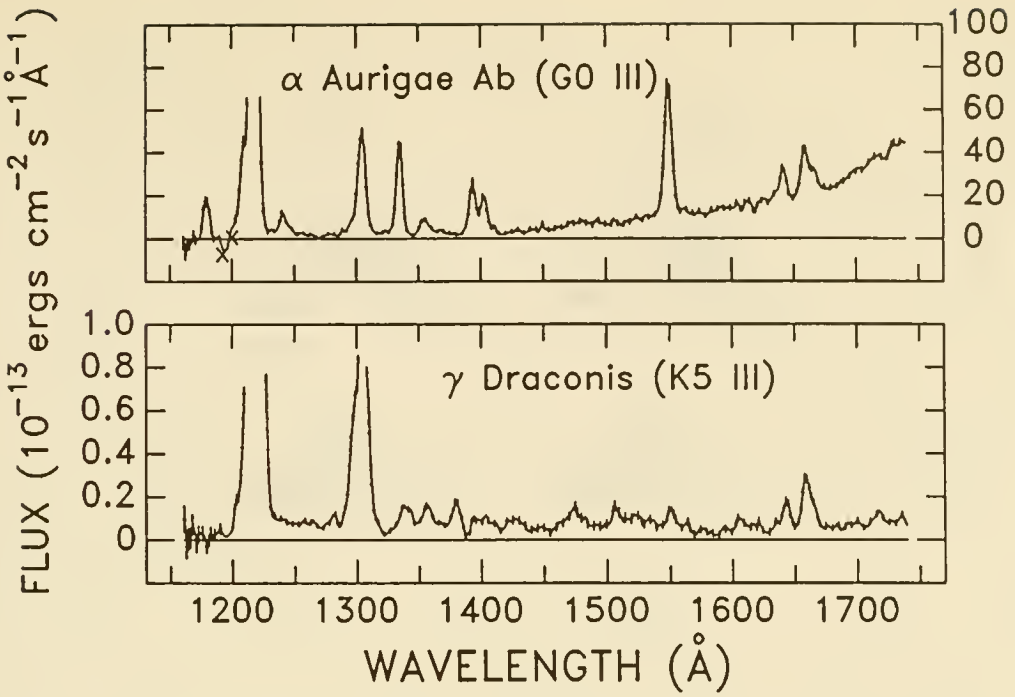

Figure 1: – Coadded SWP-LO spectra of Capella and γ Dra from the IUE Archives. Crosses flag a reseaux mark. Error bars indicate the statistical uncertainties of the coadded fluxes. Line identifications are provided in the Linsky et al. paper in this proceedings.

2. LOW-DISPERSION IUE SPECTRA

There are a large number of SWP-LO, SWP-HI, and LWP-HI spectra of Capella in the IUE Archives. I selected 4 representative SWP-LO images for the present work, with exposure times of 0.5–2.5M (5M total) to increase the effective dynamic range. For γ Dra, there are 4 SWP-LOs in the Archives: the 3 reliable spectra total 500M. Fig. 1 illustrates the coadded SWP-LO spectra of the two stars. These tracings should be compared with Figs. 1–4 from the Linsky et al. paper: the G140L exposure times were of order 0.5M for Capella and 10M for γ Dra. The difference in sensitivity of the two low-resolution modes is much greater than the simple ratio of the exposure times, because the S/N is higher in the HUBBLE spectra, and the noise refers to pixels that are 5× smaller in wavelength than those of the IUE. Encouragingly, the overall spectral structure in the 1150–1750 Å is qualitatively the same in the GHRS and IUE tracings. Nevertheless, a seasoned IUE observer would certainly hesitate to identify the 3σ feature near 1550 Å in the IUE coadded spectrum of γ Dra as C IV; whereas the feature is highly significant in the GHRS spectrum, and the identification as C IV is made all the more secure because both components of the doublet are present, in the expected intensity ratio, at the higher dispersion of the G140L mode.

3. HIGH-DISPERSION IUE SPECTRA

I reduced a series of IUE SWP and LWP echelle spectra of Capella, taken near opposite radial-velocity extrema in the orbit. The original observations were conducted using a number of techniques (including pseudo-trailing, multiple Offset Reference Points, and graded exposures) to push the S/N and dynamic range of coadded spectra beyond the usual limits.

Fig. 2 illustrates the Mg II h and k lines observed near the opposite orbital quadratures.

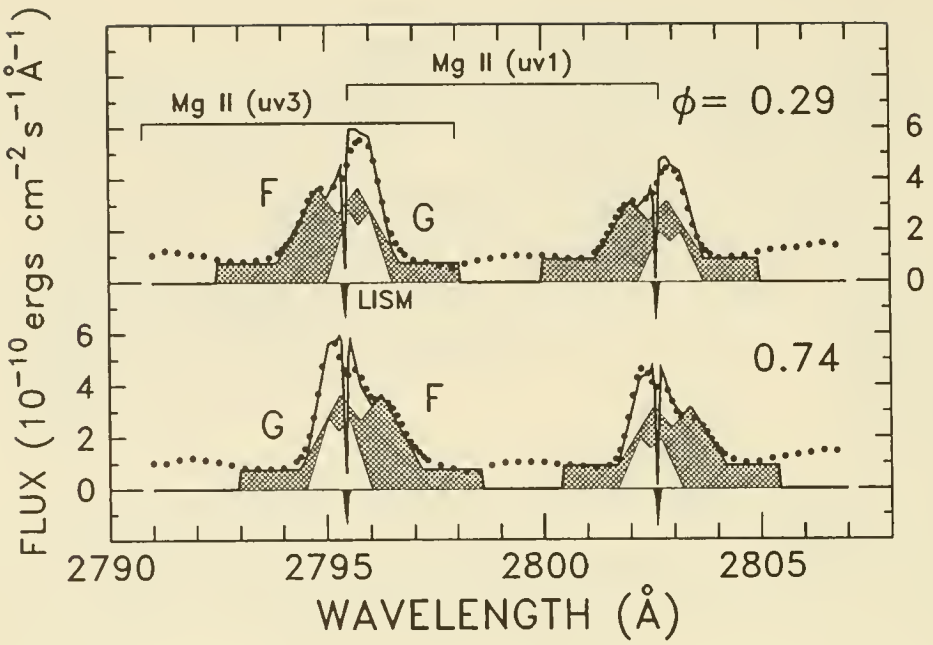

Figure 2: – LWP-HI spectra of Capella in vicinity of Mg II h and k resonance lines.

The S/N in these spectra is high (> 50:1): each tracing represents the sum of at least three independent pseudo-trailed spectra, and 10M of total integration time. Also shown is a simple model of the relative contributions of the active G0 III secondary ("F"), the less-active G9 III primary ("G"), and the interstellar Mg II absorption components ("LISM"). The solid curve depicts the sum of the three model contributions: it is similar (at phase 0.29) to the HST/GHRS ECH-B spectra (see Fig. 10 in Linsky et al.) and schematically illustrates the origins of the distinct spectral structure in the high-resolution profiles. While the GHRS ECH-B spectrum also required about 10M of integration, the S/N (and the noise characteristics) are better than the coadded IUE spectrum; again the noise refers to smaller wavelength steps; and the factor of ≈ 8 better resolution permits a whole new regime of scientific inquiry unavailable to the IUE.

Fig. 3 illustrates several intervals in the sub-2000 Å IUE spectrum of Capella coinciding with the medium-resolution (or ECH-A in the case of Lyα) GHRS spectroscopy reported by Linsky et al. Here, the IUE tracings represent the coaddition of two or more independent pseudo-trailed SWP-HI's with a total exposure time of 400M ($\lambda < 1800$ Å) or $\gtrsim$ 60M (Lyα & $\lambda > 1800$ Å). The solid curves refer to phase 0.29 (similar to that of the GHRS work), while the dashed curves refer to the opposite orbital quadrature. The overall shift of the high-excitation emissions between the opposite velocity extrema is clear: they follow the fast-rotating chromospherically-active secondary star. Panel (a) should be compared with Figs. 11 and 9 of Linsky et al.; panel (b) with Figs. 8 and 5; panel (c) with Fig. 7; and panel (d) with Fig. 6. Aside from the stunning GHRS echelle spectrum of Lyα, the medium-resolution spectra of Capella are comparable in resolution to those of the IUE, although the S/N is clearly higher in most of the HUBBLE observations (in about 1/50-th the equivalent IUE exposure time!). This is particularly true of the fainter emissions in each interval: compare, for example, the diagnostically-critical O IV] lines in the 1400 Å region.

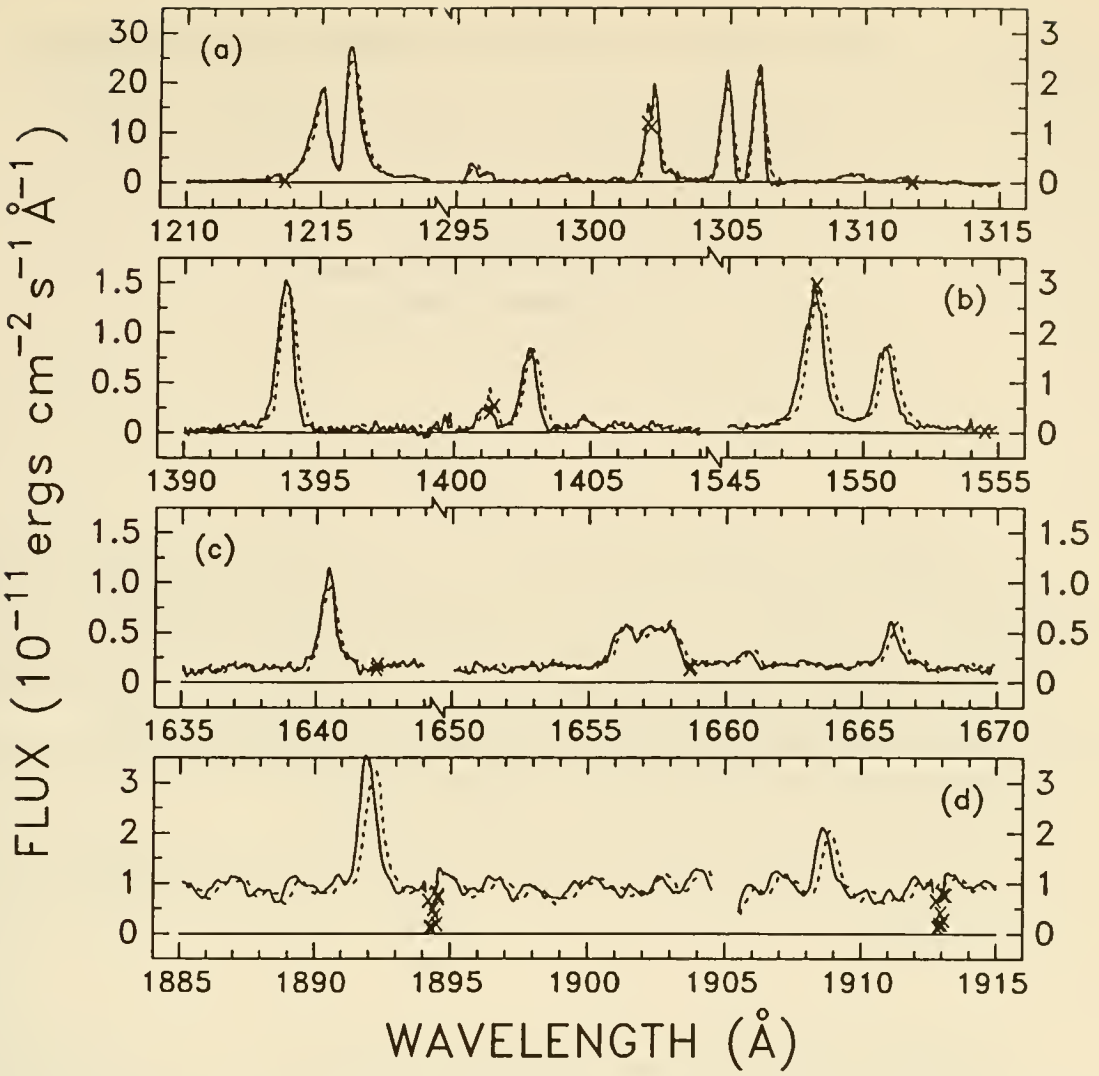

Figure 3: – Coadded SWP high-dispersion spectra of Capella in selected wavelength intervals near opposite quadratures in the binary orbit. Crosses flag reseau marks or saturation.

4. CONCLUSIONS

Space limitations prevent a more exhausive comparison than this. Nevertheless, one can safely conclude the following: (1) A large-aperture space telescope with a modern spectrograph and detectors produces beautiful (dare I say, solar-quality) vacuum-ultraviolet spectra; and (2) even so, the quality of the IUE spectrograms is surprisingly good, at least with respect to the preconceptions of this all-too-knowledgeable observer. Thus, the HST/GHRS presents not only a powerful new spectroscopic tool for the nineties, but also a critical validation of the quality of the spectral material in the extensive archives of the IUE, the workhorse UV space observatory of the eighties.

This work was supported by NASA Grants NAG5-199 and NAG5-1215.

Faint Object Camera In-flight Performance

Geometric Distortion, Stability and Plate Scale.

Dave Baxter
Space Telescope Science Institute
3700 San Martin Drive
Baltimore, MD. 21218.

Abstract

The geometric distortion characteristics of the Faint Object Camera have been analysed in great depth and it has been found that the distortion pattern is remarkably stable. The positional variations in the reseau pattern, over the central 512x512 region of the photocathode, from image to image, have an RMS value of ~1 pixel, (~40mas, 20mas and 7mas for the f/48, f/96 and f/288 modes, respectively). Of this, 0.25 pixel represents the uncertainty in the individual reseau position caused by the effects rebinning and photon noise on the reseau itself.

Low levels of saturation appear to have little or no effect on the stability of the detectors, however high flux rates across the full area of the photocathode, (particularly through the f/48 relay), can cause a permenent change to the distortion pattern.

The plate scales of the 3 imaging modes have been determined and are found to be very close to nominal. The values obtained are; **f/48:** 0.04526″/pixel, **f/96:** 0.02217″/pixel, and, **f/288:** 0.00746″/pixel.

1. Geometric Stability

In order to carry out geometric correction of FOC data, *i.e.* to recover an image in which the spatial relationships between objects are restored, a necessary requirement is that the geometric distortion field, shown in Figure 1, must be stable. By this we mean that there must be no significant change in the observed reseau positions with time.

It has been noted that short term variation of the geometric distortion pattern occurs during the period immediately following FOC high voltage switch-on. During this time the observed reseau positions show an RMS deviation from the stable positions of approximately 3→1 pixels. This period however, extends for only about 40 minutes, by which time the reseau positions have stabilised to within ~0.25-1.00 pixels. In order to avoid this period of instability, the scheduling software automatically inserts a time delay of 40 minutes immediately following high voltage switch-on, which prevents exposures being taken during this time.

Long term variation could possibly occur as a result of out-gassing in the instrument, however monitoring of the geometric distortion pattern over the last nine months has shown that, in general, both cameras are remarkably stable. As an example, in Figure 2 we show the RMS deviation of the **F/96** reseau positions from the mean positions. The mean positions are obtained by averaging the measured positions (from the central

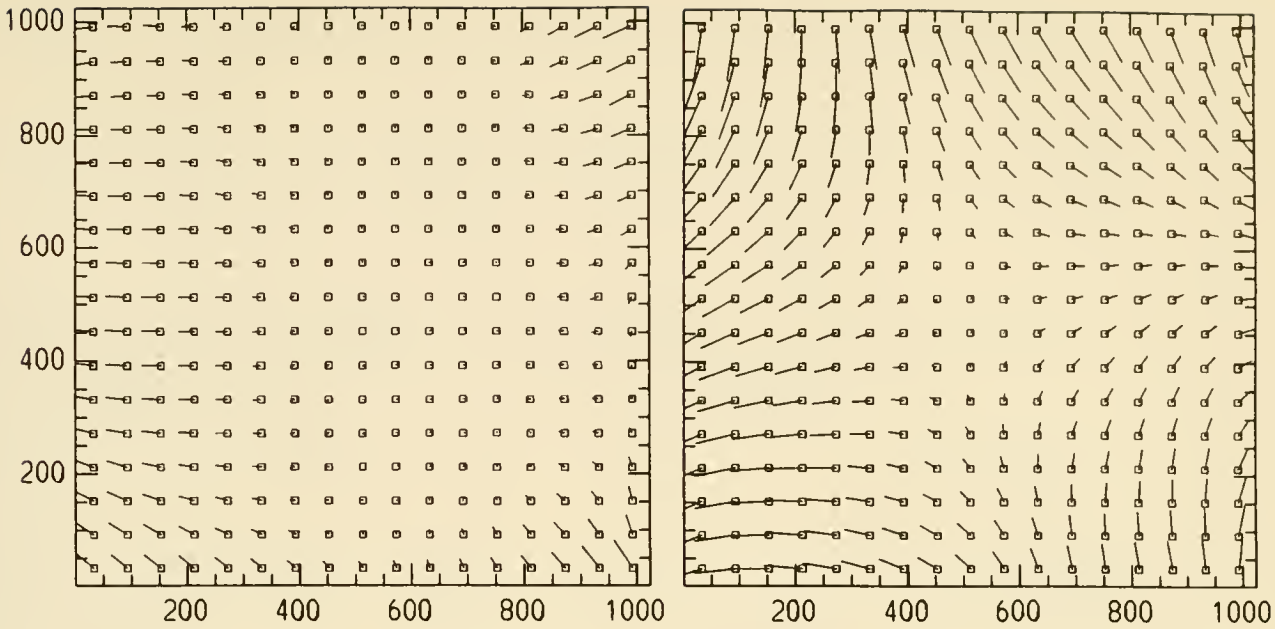

Figure 1: The total (*i.e.* optical+detector) geometric distortion pattern of both the **F/48** (*left*), and the **F/96** detectors (*right*). The full 1024x1024 distortion field is show, sampled on a grid interval of 60x60 pixels, with the vectors at a magnification of x2 for clarity.

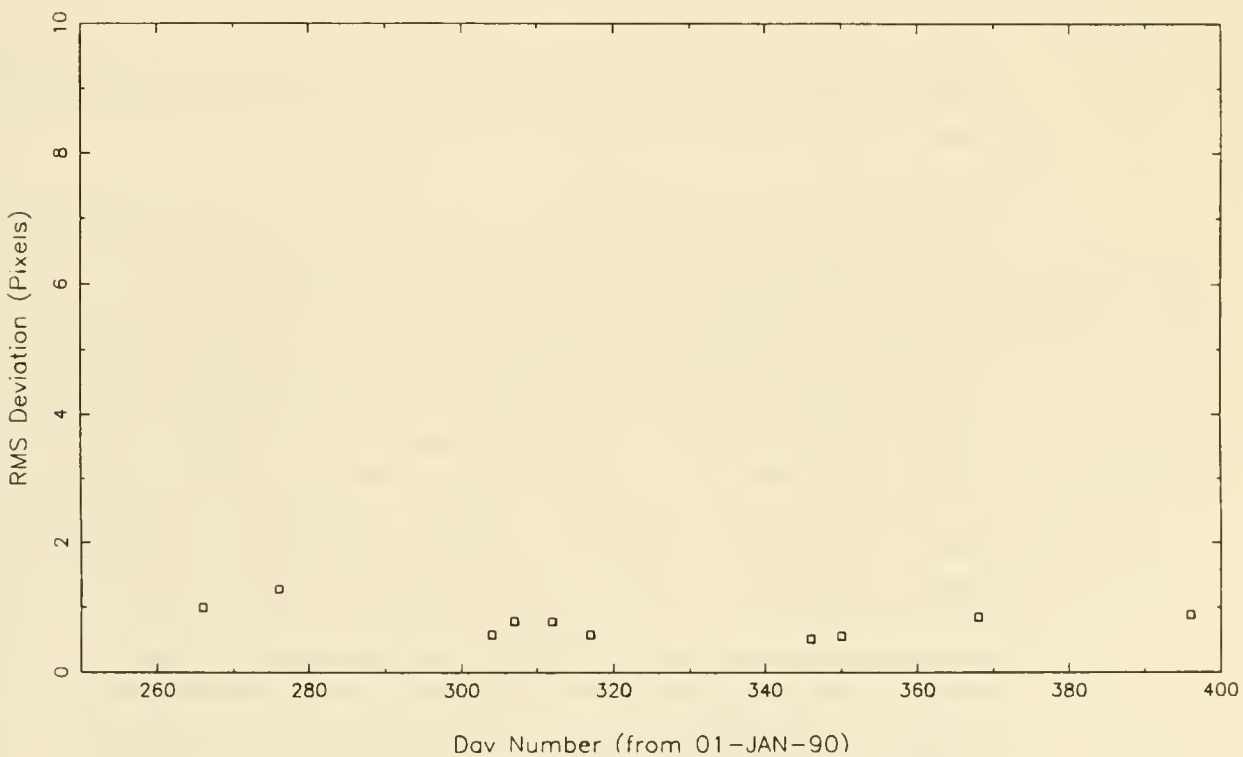

Figure 2: The RMS deviation of the reseau positions, from the mean, over the period 1st September 1990, to present.

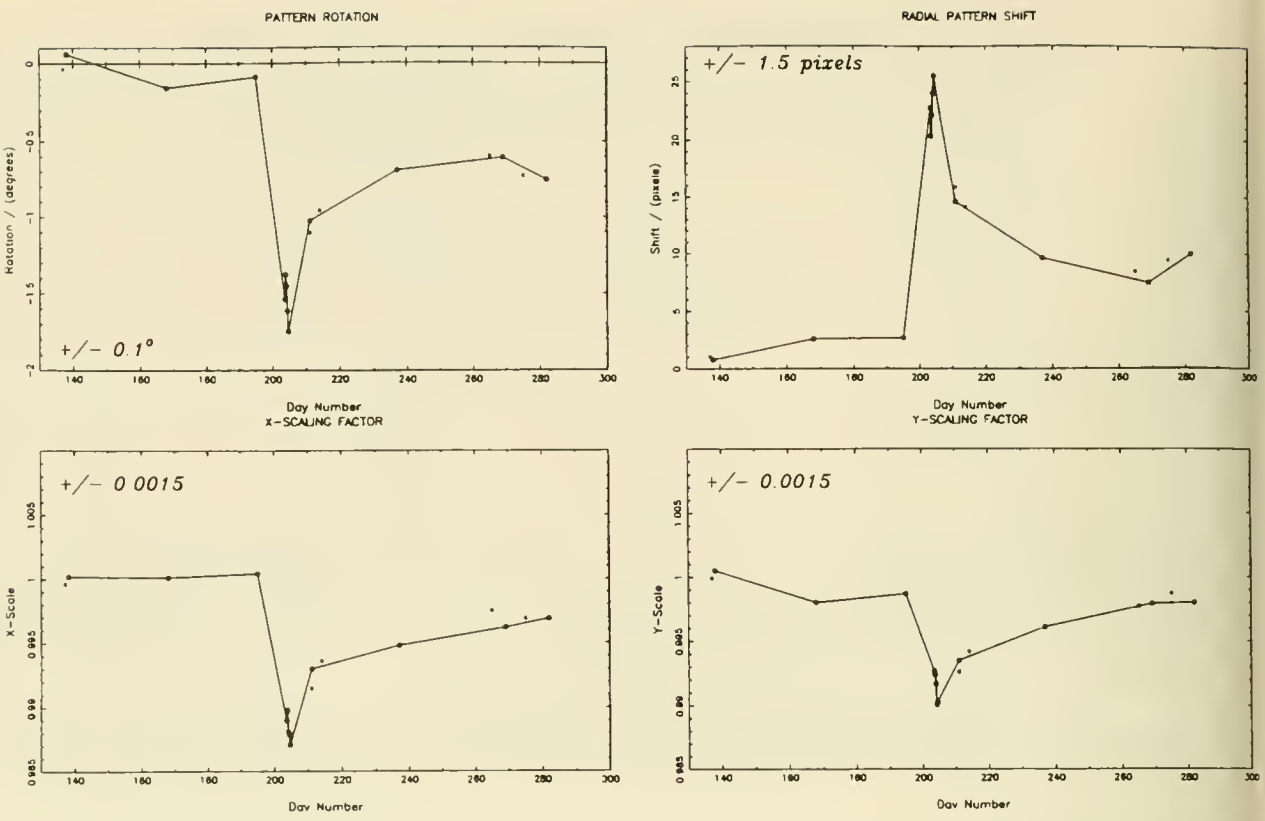

Figure 3: The effect of high saturation levels on the **F/48** detector. This event took place on 22 July 1990 and caused a large change in the distortion field, involving $\sim$ 1.5° of rotation, a 25 pixel pattern shift and a 1-2% change in the platescale.

512x512 region) over the period from 1st September 1990, up to the present. It can be seen that the deviation is small, ($\approx$ 0.85 pixels), and of this, $\sim$ 0.25 is the intrinsic uncertainty in an individual reseau position due to rebinning and photon noise.

One effect which has been noted however, is that the detector stability is rather suseptable to change if highly saturated. An event of this type occurred on 22nd July 1990 when both the F/48 and F/96 detectors were illuminated by the bright Earth to obtain a series of external flatfields. The resulting f/48 images were very highly saturated (>10 times the nominal saturation rate) and showed a sudden, and dramatic change in the distortion pattern amounting to a rotation of about 1.5 degrees and a shift of about 25 pixels (Figure **3**). This change recovered gradually over the subsequent 5-6 weeks and the F/48 geometric distortion pattern is now stable again, although not in the same position as prior to the saturation event. The current 'stable' position is offset by $\sim$10 pixels from its pre-saturation position. The F/96 detector also showed a disruption of the geometric stability at that time, however since the F/96 pixel has a smaller angular area, (by a factor of 4) than the f/48 pixel, the incident count rate was smaller by the same factor and hence, the level of saturation was much lower. The **F/96** detector returned almost immediately to the former stable position.

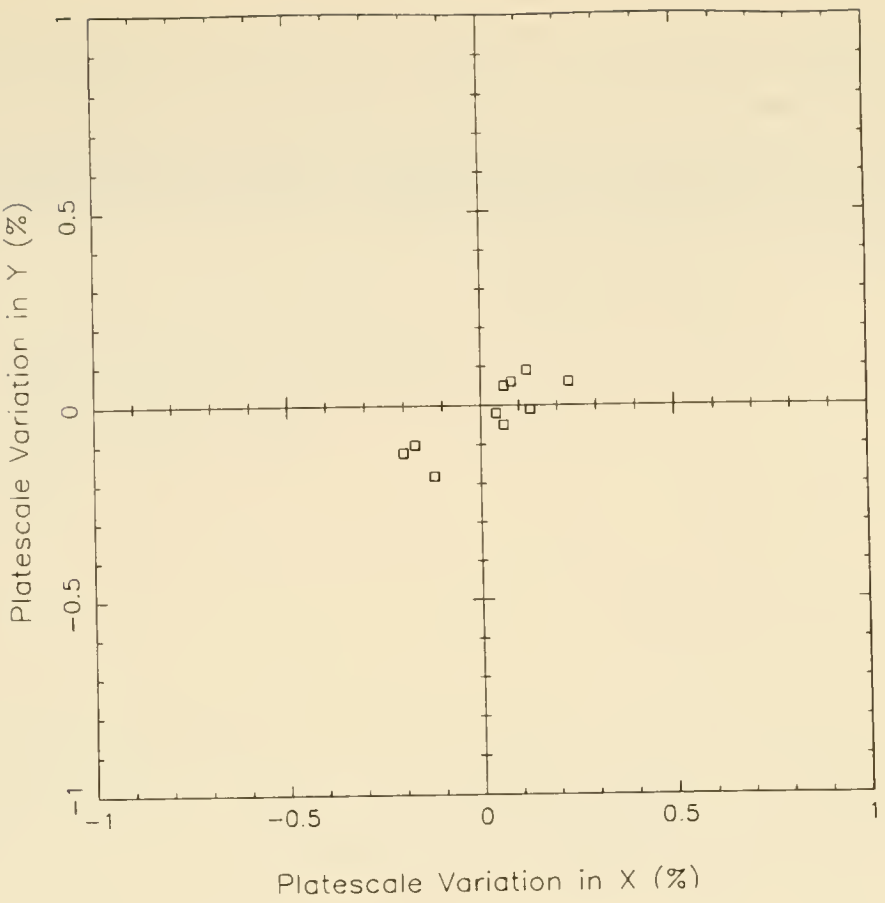

Figure 4: Variation of the **F/96** platescale since 1st September 1990.

2. Plate Scale

The plate scale (*i.e.* the size of the pixels in arc seconds) has been determined for the two cameras in the FOC. This is done by taking a series of overlapping images of a crowded star field, moving the telescope between exposures by a known angular offset. The measured distances (in pixels) between the same stars on adjacent exposures combined with the known offset (in arc seconds) then give us the plate scale.

For the F/96 relay this was determined to be 0.02217 arcseconds pixel^{-1} ($\pm$ 0.00010) and for the F/48, 0.04514 arcseconds pixel^{-1} ($\pm$ 0.0005). These values are 'radial' plate scales and are within a few percent of the nominal values, *vis.* 0.022 arcsecond pixel^{-1} for F/96, and 0.044 arcsecond pixel^{-1} for F/48. Figure **4** shows that the platescale (at least for F/96), has remained very stable over the report period, staying within $\pm$0.2% ($\sim$ 5x10^{-5} ″/pixel) of nominal. This is equivalent to an uncertainty in relative positions of $\approx$0.025″ over the width of the F/96 512x512 format. Although the analysis of the F/48 data indicated a possible difference in the x- and y-platescales, subsequent examination of other data does not confirm this. Because of this discrepancy however, the F/48 platescale is assigned a somewhat higher uncertainty than F/96. A new proposal has been designed to determine unambiguously the absolute values for the platescales in the F/48 and F/96 relays. This should be completed by late 1991.

The F/288 relay has a nominal value of 0.007 arcsecond pixel^{-1} and a derived value of 0.00746 arcsecond pixel^{-1}. Because of the degraded optical performance of the HST, due to spherical aberration, an isolated pointsource scatters significant amounts of light out to a radius of $\sim 2''$. This, combined with the small field size and the need for image restoration techniques, severely limits the usefulness of the imaging mode through the F/288 relay, and therefore we have no plans to investigate further, the platescale for this relay.

IN-FLIGHT PERFORMANCE OF THE FOC: EARLY ASSESSMENT OF THE ABSOLUTE SENSITIVITY.

W.B. Sparks and the FOC IDT
Space Telescope Science Institute,
3700 San Martin Drive,
Baltimore, MD 21218,
USA.

Abstract. Observations with the Faint Object Camera on the Hubble Space Telescope in the f/96 imaging mode indicate an absolute sensitivity consistent with nominal (as given in the Instrument Handbook) for wavelengths longward of about 2500 to 3000Å. Shortward of that, there is a smooth decline reaching approximately 60% relative to the baseline by 1200Å. No secular changes have been identified at this stage.

1. INTRODUCTION

Knowledge of the absolute efficiency of the FOC in combination with the OTA is essential in estimating program feasibility. Here, observations of UV photometric standard stars observed during the OV phase (up to February 1991) are analysed to provide an initial assessment of the absolute sensitivity of the FOC as a function of wavelength and of time. The analysis procedure is simply to derive total count rates for each observation and to compare the result to a prediction using the best estimate of the input spectrum together with all component throughput curves and instrument DQE. Departures of 'observed/predicted' count rates from 1.0 indicate inconsistencies between the simulations and the observations. See Greenfield *et al.* 1991.

The present analysis is based on data acquired for other purposes — focus monitoring, UV first light, UV throughput monitoring (OLT) and FOC SAO PSFs (Science Assesment Observation Point Spread Functions). It is therefore incomplete in wavelength coverage and has sparse time coverage. More recent science verification observations (proposal 1511 in particular) together with continued UV throughput and focus monitoring will enable a more thorough study of these issues to be undertaken in the future.

2. OBSERVATIONS AND ANALYSIS

2.1. UV standard star observations

Two UV photometric standard stars were observed during the period from launch to Day 51, 1991: BPM 16274 and GRW+70°5824, Bohlin *et al.* 1987, Turnshek *et al.* 1989, Turnshek *et al.* 1990. Spectrophotometry from the visible through to the UV is available within CDBS. The stars were observed at a variety of wavelengths and for a variety of purposes. There are a total of 72 images.

2.2. Analysis Procedure

The principle observable is total count rate. To estimate this, the *iraf* implementation of *daophot* was used together with IDL. Counts interior to 3.3 arcsec were used for the total, while the sky level was estimated from the outer region of the stellar intensity profile. Simulations of *expected* count rate assuming particular throughput curves were made using the *iraf/stsdas* package *synphot*, and the two were compared.

3. RESULTS

There is very strong Lyman α absorption situated within the peak transmission of the F120M filter for these UV photometric standards. The far-UV response estimate must therefore be considered more uncertain than the others, although both stars do give the same value for the sensitivity at F120M. Figure 1 shows the ratio of observed to predicted counts as a function of wavelength (the *pivot wavelength*, Koornneef *et al.* 1986). A fourth order polynomial modification to the DQE curve using a least squares fit to these data (excluding the uppermost outliers) is also included, derived using the *synphot* program *fitband*.

For wavelengths longer than about 2500 to 3000Å there is no evidence for departures from the nominal DQE as given in the Instrument Handbook, and assumed for the 'prediction'. There are some data points above a value of unity. The two reddest are also the observations with the narrowest filters. Because of this, the simulation becomes more uncertain and these two points should at this stage only be used as indicative that there are no serious problems in the red part of the spectrum. Shortward of 2500Å there appears to be a fairly smooth decline with wavelength, reaching about 60% of baseline with the F120M ($\approx$ 1200Å) filter.

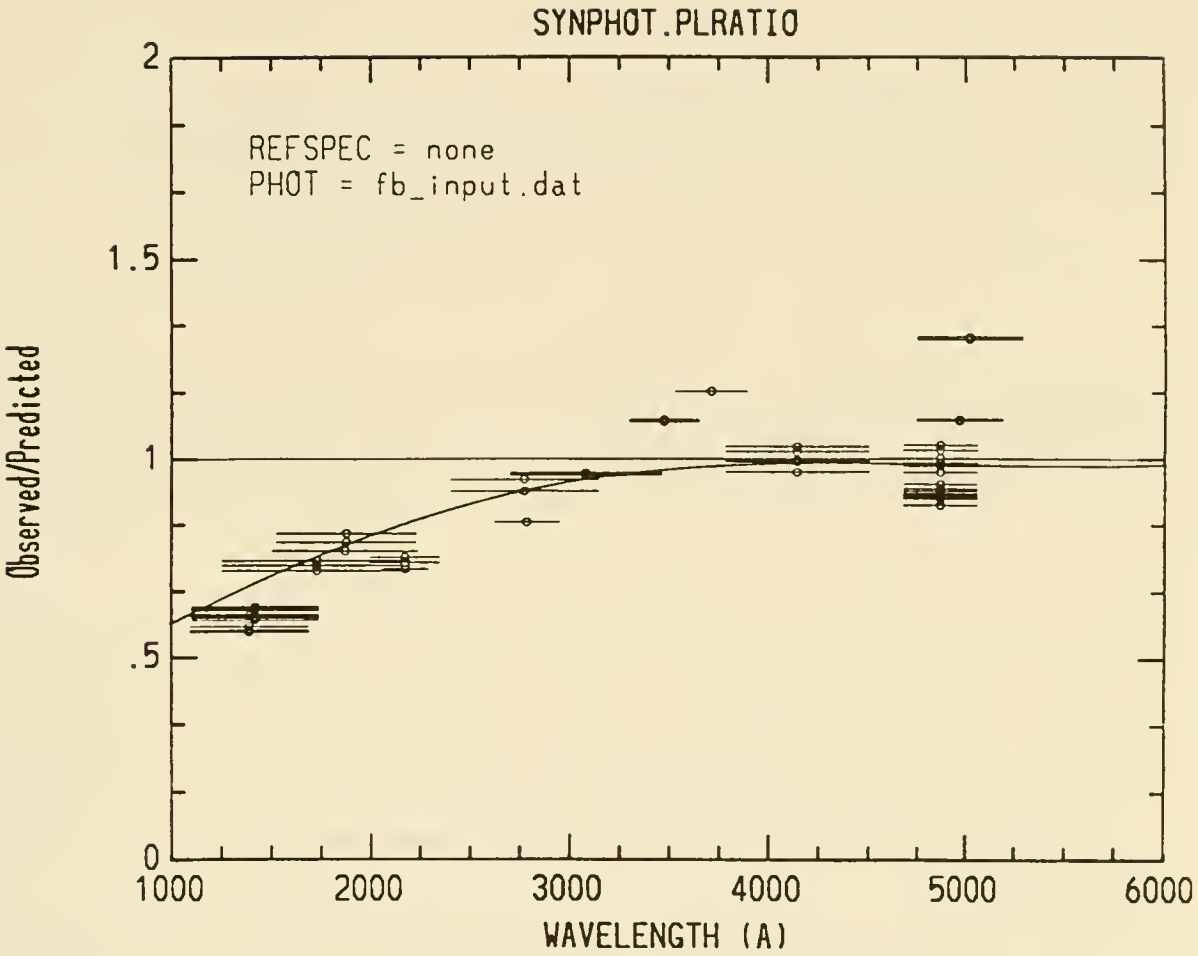

Figure 1. The ratio of observed to calculated count rate as a function of wavelength.

A potential source for apparent reduced UV sensitivity is large angle scattering from mirror micro-roughness. In order to assess whether this is a likely factor, the average of 15 F120M profiles from GRW+70°5824 was derived. Relative to the flux interior to 4.2 arcsec, by 2.5 arcsec the profile has reached 97% and by 3.3 arcsec, it has reached 99% of the total. There is no evidence therefore for much scattering into radii of order two to four arcsec.

The values of 'observation/prediction' versus time were analysed for visible and far UV filters. The visible data have no significant trends at all, while in F120M there is marginal evidence for an early decrease, although again the statistical significance is poor. Continued UV throughput monitoring will be carried out.

4. CONCLUSIONS

Results of a preliminary investigation into the f/96 absolute sensitivity of the FOC have been presented along with a description of the analysis techniques used. The results indicate that the DQE is consistent with nominal (as given in the Instrument Handbook) for wavelengths longward of about 2500 to 3000Å. Shortward of there, there is a smooth decline reaching approximately 60% relative to the baseline by 1200Å.

REFERENCES

Bohlin, R.C., Blades, J.C., Holm, A., Savage, B.S., Turnshek, D.A. 1987, *Standard Astronomical Sources for HST: 1. UV Spectrophotometric Standards.* STScI Publication.

Greenfield, P., Paresce, F., Baxter, D., Hodge, P., Hook, R., Jakobsen, P., Jedrzejewski, R., Nota, A., Sparks, W.B., Towers, N., Laurance, R., Macchetto, F. 1991, *SPIE Conference on Space Astronomical Telescopes and Instruments,* in press, STScI preprint 536.

Koorneef J., Bohlin, R.C., Buser, R., Horne, K.D., Turnshek, D.A. 1986, *Synthetic Photometry and the Calibration of the Hubble Space Telescope, Highlights of Astronomy,* **7**, p.833, ed. J.-P. Swings.

Turnshek, D.A., Baum, W.A., Bohlin, R.C., Dolan, J.F., Horne, K., Koornneef, J., Oke., J.B., Williamson, R.L. 1989, *Standard Astronomical Sources for HST: 2. Optical Calibration Targets.* STScI Publication.

Turnshek, D.A., Bohlin, R.C., Williamson, R.L., Lupie, O.L., Koornneef, J., Morgan, D.H. 1990, *Astron. J.*,**99**,1243.

IN-FLIGHT PERFORMANCE OF THE FOC: FLAT FIELD RESPONSE.

P. Greenfield and the FOC IDT.
Space Telescope Science Institute
3700 San Martin Drive
Baltimore, Maryland 21218

1. DETERMINING THE FLAT FIELD RESPONSE

This paper addresses the spatial response of the FOC detectors. Details of the FOC's operation and other aspects of FOC performance may be found in Paresce (1990) and Greenfield et al. (1991) as well as other papers at this conference.

The spatial response of the FOC's detectors, like most other photon counting detectors, is not constant over the field of view. Determining the flat field response is simple in principle, more difficult in practice. An ever present difficulty is the relatively limited linear count rate of the detectors. The full field video format ($512z \times 1024$) becomes more than approximately 10% nonlinear at count rates above 0.05 counts pixel^{-1} s^{-1} using flat field illumination. This results in very long exposure times if counts of several hundreds or thousands are required which, in turn, means that data related to flat field response will be limited either in the number of counts, wavelengths, or formats obtained.

In the visible, the onboard LEDs provide a convenient means of illumination, but, in the ultraviolet, it is more difficult to find a suitable source of illumination. The two candidates for UV flat field illumination have been the bright earth and a selected area of the inner Orion nebula. Although flat fields using the bright earth are attractive in the sense that illumination should be relatively flat because they are "streaked" over long paths on the ground and can be taken when the telescope would otherwise be idle, they have large variability in brightness, possible visible light contamination through the filters, and require a large attenuation of the light level. This is especially a problem for $f/48$ where the filter selection is relatively limited and there are no neutral density filters, thus ruling out this source as a method of obtaining UV flat fields for this optical relay. Flat fields using the Orion nebula are complicated by

the fact that the field illumination is not uniform. Fortunately, this region of the nebula looks relatively smooth in the UV and future observations should be able to determine the brightness distribution of the nebula, and therefore determine the UV spatial response. Nevertheless, so far virtually all information about the flat field response has been obtained from LED exposures or ground-based flat fields.

2. FLAT FIELD PROPERTIES

Figures 1 and 2 show $f/96$ and $f/48$ full format (512×1024 using "zoomed" pixels) flat fields. The $f/96$ flat field was taken using the inner region of the Orion nebula and the F140W filter, and as a result the occulting fingers are visible. The $f/48$ flat field was obtained using an LED. The nonuniform spatial response of the detectors is primarily due to the varying response of the bialkali photocathode which is evidenced by large and small scale variations (such as scratches), but there are other effects also. Variations in the camera tube target response also results in localized nonuniformity of response. The most obvious of these is the apparent outline of the smaller 512×512 video format within the larger video formats. This is apparently caused by degradation of the camera tube target by the extra dwell time of the electron read beam at the edges of the 512×512 format when it is in use. This format "burn-in" appears to worsen with time; however, it affects a relatively small part of the total detector area. Also noticeable, but usually minor in its effect except for the smallest video formats, is the read-beam flyback after each frame scan. The photocathode response tends to vary the most in the far UV where areas and scratches may show up to 30% drops in sensitivity.

Much of the apparent nonuniformity of the raw images is a result of detector geometric distortion where $\pm 10 - 20\%$ variations may result, mostly near the format's corners. Compare for example a $f/96$ 512×512 flat field shown in Figure 3 with the full format $f/96$ flat field. There are clearly areas in the 512×512 image where there is noticible nonuniformity that do not appear in Figure 2 because the geometric distortion characteristics vary with the format being used. For that reason, flat fields obtained in one format cannot be applied to other formats without correction for geometric distortion effects. Except for areas near the edges where the distortion is severe, this component can be removed by applying a flux-conserving geometric correction to the images. Figure 4 is a plot of a row of Figure 3 to show more quantatively the size of nonuniformities in the flat field (note however, the relatively large photon noise because of the relatively low counts). Figure 5 shows the size of the effect of the geometric distortion on the $f/96$ full format flat field response as a function of position.

Both detectors exhibit a couple of forms of "pattern noise." One is believed to result from a moiré fringe effect involving the camera tube's read beam interacting with

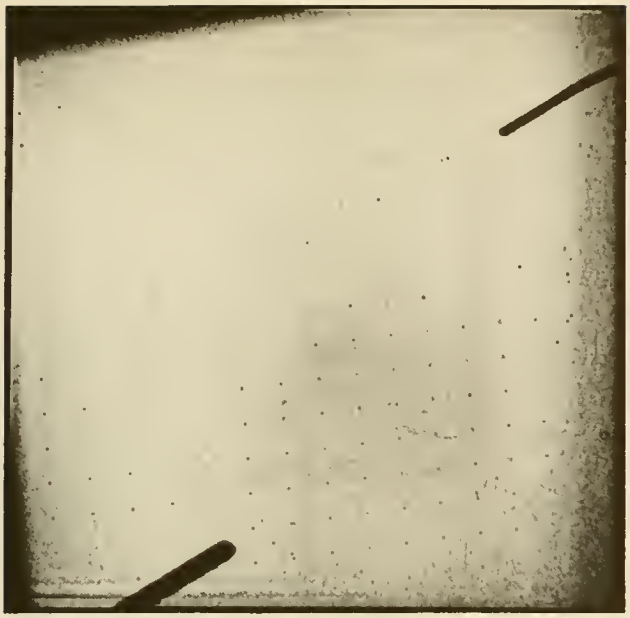

Figure 1— An *f*/96 full format exposure of the inner region of the Orion nebula taken with the F140W filter. The two coronographic fingers can be seen as well as the reseau marks, scratches, and the "burn-in" of the 512 × 512 format in the center. The exposure has typically 40 counts per zoomed pixel and is somewhat nonlinear.

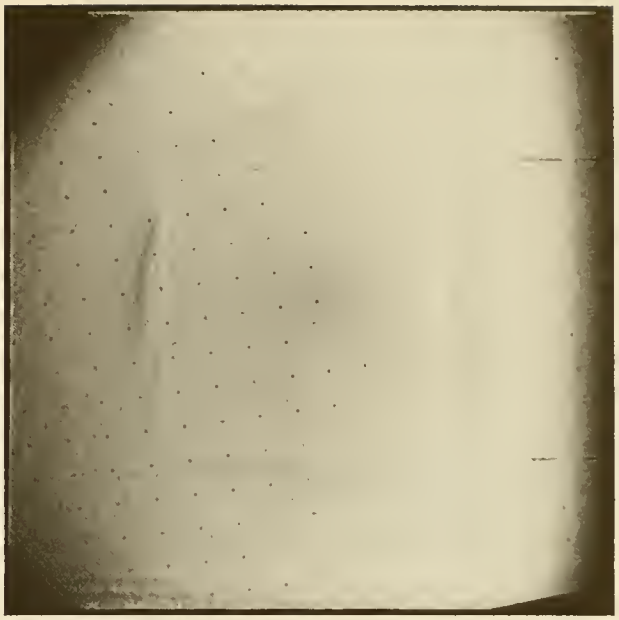

Figure 2— An *f*/48 full format exposure taken using an onboard LED. The dark corner in the upper left is a result of vignetting of the LED and does not appear in external exposures.

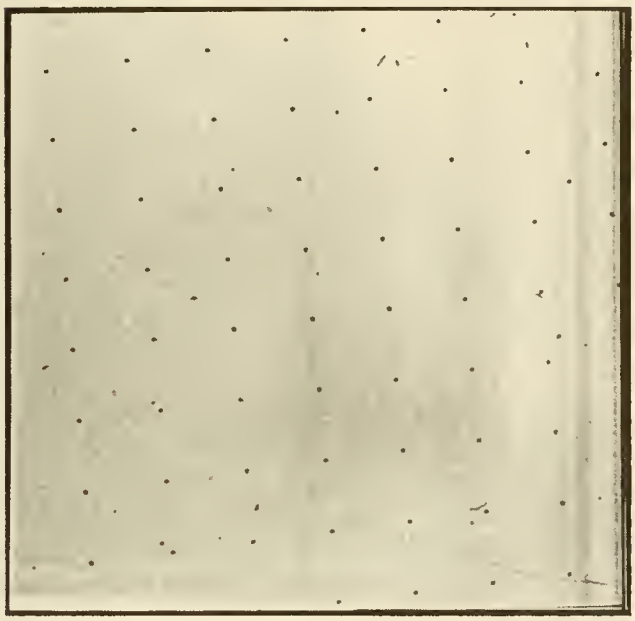

Figure 3— An *f*/96 512 × 512 pixel format exposure taken using an onboard LED.

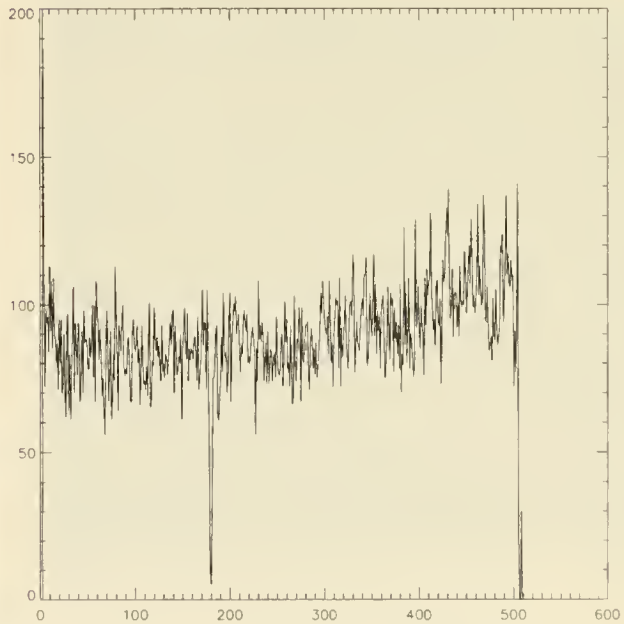

Figure 4— A plot of row 300 of figure 3.

Figure 5— This image shows the effect of the geometric distortion on the photometric response. Displayed is the result of geometrically correcting a perfectly flat full format image. Those areas that are brighter correspond to areas on the detector that had been stretched out and had larger than average pixels. The overlaid contours (the solid lines) are spaced every 5% in intensity relative to the center.

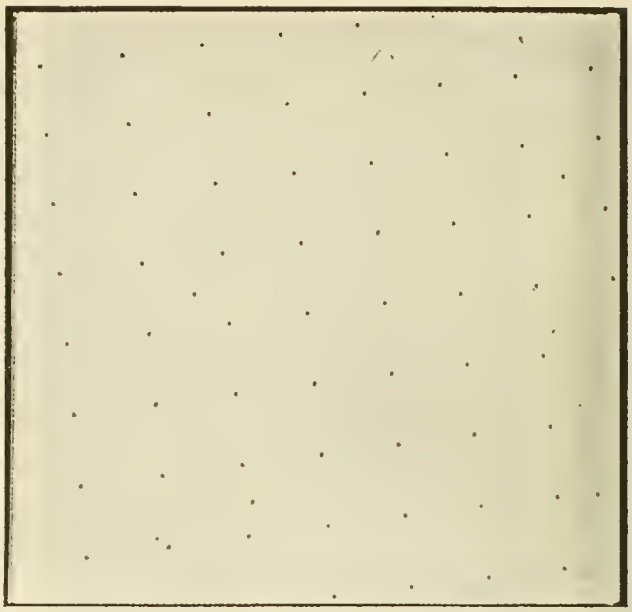

Figure 6— An f/96 512 × 512 pixel format exposure taken using an onboard LED at a high intensity setting to highlight the diagonal pattern noise which is enhanced when the detector is driven into its nonlinear regime.

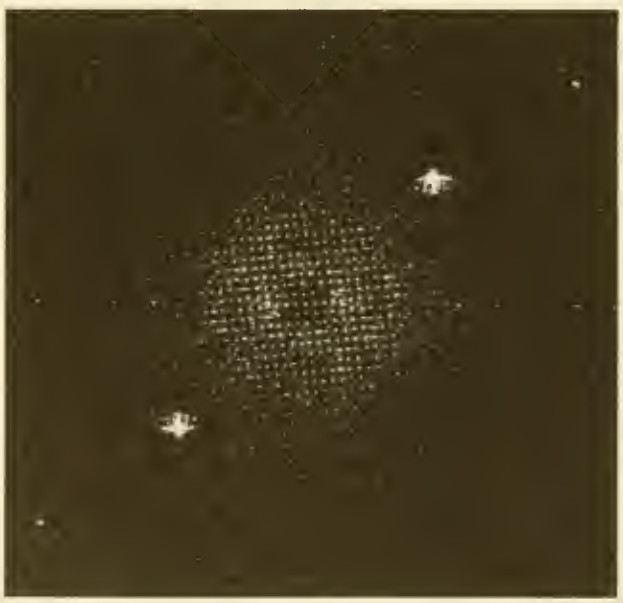

Figure 7— The amplitude of a two-dimensional FFT showing the presence of a 512 × 512 format *f*/96 image. The grid in the center is due to the reseaux. The diagonal pattern noise shows as extended peaks in the upper left and lower right while the 4-pixel pattern can be seen as sharp spikes in the center row.

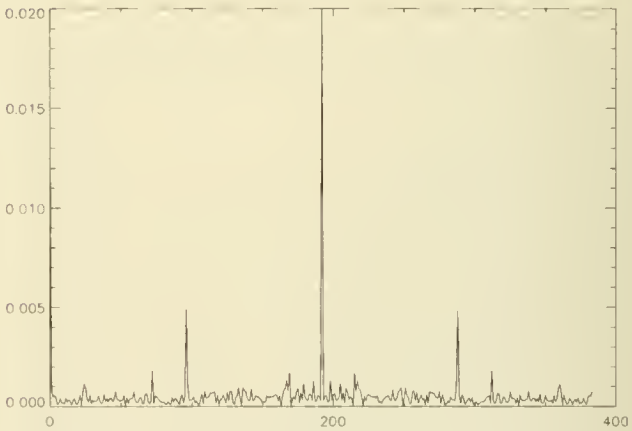

Figure 8— The plot of the amplitude of the central row of the FFT showing the presence of the 4-pixel pattern. This pattern is believed to result from a digital clock in the electronics that has a 4-pixel period.

both a tube grid and the target diode array. The end result is a roughly sinusoidal modulation of the response with a spatial frequency of 3.3 pixels running in a nearly diagonal direction for the $f/96$ detector with a $\sim 5\%$ RMS amplitude. The amplitude for the $f/48$ detector is approximately half that. This pattern is generally enhanced when nonlinear count rates are encountered, and for that reason can easily be seen in Figure 6 which is an $f/96$ LED exposure taken at relatively high count rates. The other pattern consists of vertical stripes appearing with a horizontal period of 4 pixels and originates from a digital clocking signal. The RMS amplitude of this pattern is $2 - 3\%$ for both detectors. Figure 7 shows the amplitude of the FFT of a $f/96$ flat field where the presence of both types of patterns can be seen. Figure 8 is a plot of the center row of the FFT showing the characteristics of the vertical pattern. Finally, there is evidence that there is a significant fine scale pixel-to-pixel variation in response not characterized by any of the previous effects. It is most likely an intrinsic granularity of the photocathode, but that has not been clearly shown and has not been well characterized.

Our estimates are that relative fluxes are currently accurate to only about the $\sim 10\%$ level if they are determined from an area of at least 10 pixels. Our long range goal is to improve the flat field calibration so that relative fluxes can be determined to the 3% level.

3. ACKNOWLEDGEMENTS

The Faint Object Camera is the result of many years of hard work and important contributions by a number of highly dedicated individuals far too numerous to list individually. In particular, we wish to thank the ESA HST Project Team and the European contractors for building an outstanding scientific instrument. All of the FOC images were taken using the NASA/ESA Hubble Space Telescope, obtained at the Space Telescope Science Institute, which is operated by AURA, Inc., under NASA contract NAS 5-26555. The FOC IDT Support Team: D. Baxter, P. Greenfield, and R. Jedrzejewski, acknowledge support from ESA through contract 6500/85/NL/SK.

REFERENCES

F. Paresce, *Faint Object Camera Instrument Handbook*, Space Telescope Science Institute, Baltimore, 1990.

Greenfield, P., Paresce, F., Baxter, D., Hodge, P., Hook, R., Jakobsen, P, Jedrzejewski, R., Nota, A., Sparks, W. B., Towers, N., Laurence, R., Macchetto, F., Proceedings of the SPIE Conference on Space Astronomical Telescopes Instruments, Orlando, Florida, 1 April 1991.

BACKGROUND NOISE REJECTION IN THE FAINT OBJECT SPECTROGRAPH

Rosenblatt, E.I., Beaver, E.A.,
Linsky, J.B., and Lyons, R.W.
Center for Astrophysics and Space Sciences
University of California, San Diego
La Jolla, CA 92093-0111

Abstract. We have modeled the background noise of the FOS "blue" MgF_2 detector to investigate the optimal strategies for reducing the noise level in spectra. Background observations made with the FOS during the Orbital and Science Verification periods (June 1990 to the present) have shown that the dominant source of noise is of a non–poisson burst character most likely produced by Cerenkov radiation. This radiation will be emitted whenever a high energy particle traverses the detector faceplate, and can result in large portions of the diode array being flashed nearly simultaneously. We have modeled the effects of Cerenkov radiation in image tube faceplates by means of a Monte Carlo numerical simulation. This model produces images and count statistics which are in good agreement with actual data. This simulated background data has allowed us to determine the rejection thresholds and frame times that yield the highest S/N ratio for a stellar source of any given flux level.

1. MONTE CARLO SIMULATIONS OF FOS BACKGROUND NOISE

A detailed analysis of FOS dark data has shown that the dominant source of background noise produced in the low altitude orbit of the HST results from Cerenkov radiation (Rosenblatt *et al.* 1991). This noise occurs whenever a high energy particle ($E \gtrsim 300$ MeV) such as a cosmic ray traverses the window of the Digicon detector and produces a burst of photons that can flash large portions of the diode array simultaneously. This source of noise generates at least 90% of the FOS background both inside and outside of the South Atlantic Anomaly.

Without an accurate subtraction of the background, measurement of the shape and absolute level of the continuum of astronomical objects is compromised. Figure 1 shows an uncalibrated spectrum of the quasar CSO 251 recently observed with the FOS. A third order polynomial fit to the diode response is also shown for the estimated background level. Note that even for this relatively bright quasar, the background is significant compared to the continuum flux level. For fainter objects, it is even more important to estimate and subtract the background accurately.

In order to better understand FOS dark background noise, we have developed a Monte Carlo model which closely simulates the FOS detector and the physical characteristics of Cerenkov radiation. This model allows a large number of particle events to be simulated and analyzed. The code first generates random impact positions and angles (weighted by solid angle) with respect to the faceplate. Since the number of Cerenkov photons produced depends on the atomic number of the incident particles, a cosmic ray abundance consisting of 91% protons and 9% alpha particles is input. Cones of Cerenkov light are generated along the particle path in the faceplate. These cones are divided into narrower sub-cones for greater resolution and accuracy in calculating MgF_2 absorption effects. The sub-cones are then projected down onto the photocathode and Poisson statistics are used to determine the number of photons incident on the photocathode within the solid angle subtended by any given diode. Binomial statistics (based on photocathode Q.E.) are then used to determine whether a photoelectron is emitted from a specific area of the photocathode. Since the Digicon employs one-to-one imaging, when a photoelectron is emitted directly in line with a diode, a count is registered in that diode. In this way, the differential and cumulative hits on each diode in the array can be traced throughout the simulation.

One major advantage of this technique is that the counting statistics (*i.e.*, the number of counts registered on the diode array per particle event) of the background noise can be analyzed. This information is difficult to acquire directly with the FOS due to the short time sampling required to separate one event from another. Our largest simulation to date includes over 16,600 particle events. Surprisingly, the vast majority of these events (~14,500) did not produce any counts in the array whatsoever. This result is due to a combination of factors including absorption in the faceplate, geometric dilution of photons, and poisson statistics. Another reason is simply that many of the projected conic sections did not intersect the diode array and therefore do not generate hits. Of the ~2000 events that did produce one or more counts, most generated 1–5 counts. However, a small number of events produced many hits at the array which qualitatively resemble the streaks observed in FOS dark data. The average count rate of this simulation (0.0056 cts s^{-1} $diode^{-1}$) agrees well with the observed rate (0.0062 cts s^{-1} $diode^{-1}$) at low geomagnetic latitude where the background is at a minimum.

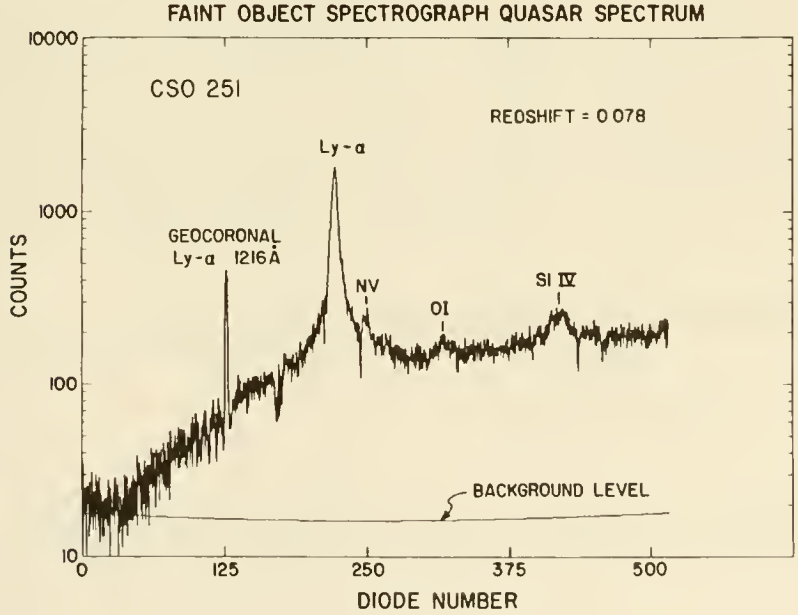

Fig. 1— An uncalibrated spectrum of the quasar CSO 251 recently observed with the FOS is shown together with a third order polynomial fit to the estimated background level. Note that even for this relatively bright quasar, the background is significant compared to the continuum flux level. For fainter objects, it would be even more important to estimate and subtract the background accurately.

2. BACKGROUND NOISE REJECTION

Due to the burst character of Cerenkov light, there is a potentially powerful tool available onboard the FOS that will eliminate a significant amount of the dark background noise from astronomical data. This rejection capability is supplied by a burst rejection algorithm (known as REJLIM) that can be set to different thresholds such that any noise burst (summed over the entire diode array) registering at or above the threshold within some specified live time will be rejected from the data stream (all data within this time interval will be rejected). The FOS rejection software allows a minimal live time of 20 ms in which the total number of counts for the array are summed. Following each live time is a deadtime of 10 ms in which the electronics are reinitialized. Simulated background data from our Monte Carlo model has allowed us to determine rejection thresholds and live times that yield the highest S/N ratio for a stellar source of any given flux level.

An example of our study is presented in Table 1. The background noise count rate was set to 0.01 cts s^{-1} $diode^{-1}$ in this simulation (corresponding to low geomagnetic latitudes). A stellar source was modeled using poisson statistics with a mean of 0.004 cts s^{-1} $diode^{-1}$. For each stellar flux level, the live time was varied from 20 to 500 ms and the threshold that resulted in the highest S/N ratio in each case was determined. Column 1 of Table 1 gives the live time in milliseconds, Col. 2 is the threshold (in units of counts per live time per array) that yielded the highest S/N ratio which is given in Col. 3, Col. 4 is the total time removed from the data stream due to rejected frames and deadtime, Col. 5 is the total deadtime, Col. 6 is the total live time rejected, Col. 7 gives the actual exposure time after the reject time of Col. 6 is subtracted from the original integration time, Col. 8 is the fraction of stellar counts rejected, and Col. 9 is the fraction of dark counts rejected.

Table 1

Simulated Burst Noise Rejection Data

Exp time = 1158s		Stellar flux = 0.004 c/s/d			Dark noise = 0.01 c/s/d			
frametime (ms)	threshold	S/N (d^{-1})	time lost (sec)	deadtime (sec)	rej time (sec)	live time (sec)	% star rejd	% dark rejd
(1)	(2)	(3)	(4)	(5)	(6)	(7)	(8)	(9)
20.0	2	1.31	396.6	386.0	10.6	761.4	0.02	0.72
100.0	2	1.45	184.3	105.3	79.0	973.7	0.12	0.78
300.0	3	1.33	247.4	37.4	210.0	910.6	0.28	0.77
500.0	4	1.21	322.7	22.7	300.0	835.3	0.36	0.77

To illustrate the improvement in S/N that optimal burst rejection can provide we note that in the example above the S/N ratio found with a frame time of 100 ms and a rejection threshold of 2 is 25% higher than the S/N ratio that would be obtained without any noise rejection. Moreover, only 12% of the stellar flux was rejected, while 77% of the noise was eliminated.

During the Spring 1991, the FOS obtained dark data with REJLIM enabled at threshold settings of 2, 3, 8, and 10. Figure 2 compares our Monte Carlo simulation (filled dots) with these observed data (asterisks). Although the Cerenkov model agrees fairly well with the observations, the addition of a 0.002 cts s^{-1} d^{-1} poisson noise source (open dots) results in the best fit. The figure clearly shows that threshold settings of 8–10 or greater will have little effect on the observed count rate (roughly 90% of the counts registered relative to what would have been detected with REJLIM disabled). Thus, large thresholds will not reduce the background noise significantly. However, if the astronomical source is faint, the threshold can be set to small values, eliminating a substantial fraction of the background.

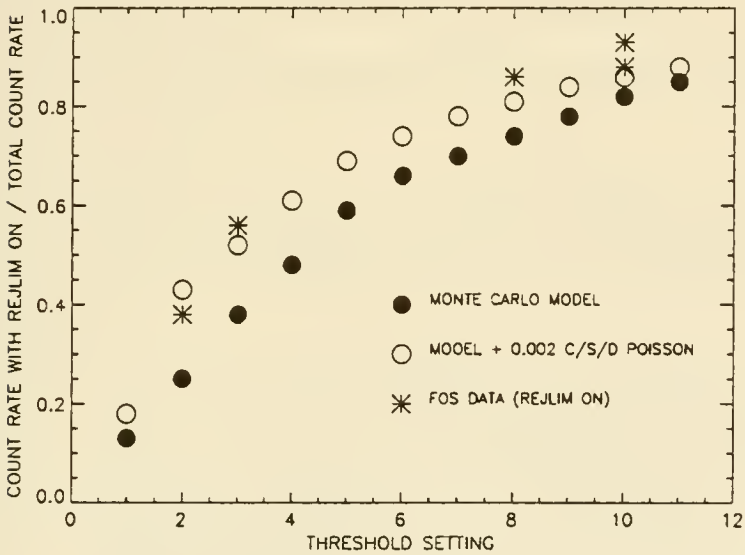

Fig. 2— The Monte Carlo background noise simulation (filled dots) data is compared to actual FOS dark data with REJLIM enabled (asterisks) at threshold settings of 2, 3, 8, and 10. Although the agreement is fairly good, the best fit is achieved with the inclusion of a 0.002 cts s^{-1} d^{-1} poisson noise source. Significant noise reduction is achieved at small thresholds for faint astronomical sources.

An important point to consider when applying REJLIM is zeroth order light, which in some observing configurations will register onto the diode array. Although the zeroth order light falls on a different section of the array than the spectrum, it will still be summed within a frame time and compared to the threshold. Thus, with zeroth order light included, an otherwise correct threshold setting might reject all frames and no data will be acquired. For this potential problem to be avoided requires the specific diodes on which the zeroth order light falls to be turned off so that these counts are not included.

The authors thank Rick Hier for useful discussions. This research was supported by NASA NAS 5-24463/NAS 5-29293.

REFERENCES

Rosenblatt, E. I., Beaver, E. A., Cohen, R. D., Linsky, J. B., and Lyons, R. W. 1991 *SPIE Proceedings on Electron Image Tubes and Image Intensifiers II*, ed. I. P. Csorba (Bellingham, WA: SPIE), **1449**, p. 72.

DETECTION OF BINARIES WITH THE FGS: THE TRANSFER FUNCTION MODE DATA ANALYSIS.

B. Bucciarelli, M. G. Lattanzi, and L. G. Taff

Space Telescope Science Institute

3700 San Martin Drive, Baltimore, MD 21218

O. G. Franz and L. H. Wasserman

Lowell Observatory

Mars Hill Road 1400 W., Flagstaff, AZ 86001

E. Nelan

University of Texas

Dept. of Astronomy, Austin, TX 78712-1083

1. TRANSFER FUNCTION MODE GENERALITIES AND A DESCRIPTION OF THE DATA

The Science Assessment Observations program (SAO) has given each scientific instrument on board the HST the first real opportunity to gather data usable for assessing, to a reasonable level of confidence, their scientific potential shortly after the problem in the telescope optics was found and well before the Science Verification (SV) had started. For what follows, it is therefore important to bear in mind that FGS3, the astrometer unit used to take our SAO observations was a totally uncalibrated device.

The FGS SAO program was devoted to the detection of possible, yet undiscovered, binaries among the bright members of the Hyades cluster. Out of 21 candidates, 16 targets were successfully observed in the so-called Transfer Mode, which consists of multiple scans through the target object executed in the following fashion. The FGS star selectors are driven in such a way that the aperture sweeps over the star at an angle of 45° to the X,Y FGS reference frame. The effect is to sample the visibility fringes (or Transfer Functions-TFs) of both the Koester prism interferometers in the FGSs (one per axis). The length of the scans is approximately 1.5" (on both axes) with an average sampling step of about 1 mas. Two representative scans, one taken with the neutral density

filter (Neut/ND5) and the other with the clear filter (Clr/583W), are shown in Figs. 1a and 1b (dashed curve) for the X-axis.

The TF scan raw data consist of a time series of photomultiplier counts and star selector encoder readings. These data must be transformed into the proper units and corrected for instrumental and other effects before the curves shown in Fig. 1 are obtained. The corrections include PMTs mismatch, sky background, spacecraft jitter, and velocity aberration. The imbalance between the two PMTs on the same axis is easily accounted for by averaging a set of the samples drawn from both tails of the TF scan. Sky background is not an issue since the targets are quite bright stars. Finally, given the early stage of the Science Verification observing, the refinements of jitter removal and velocity aberration were not considered (and only differential aberration really counts).

2. REDUCTION PROCEDURES AND EVALUATION OF THE RESULTS

Assume now we know the form of the Single Star (SS) TF. The hypothesis that the incoming light from two different sources, close by in the sky, is incoherent and the application of the superposition principle yield the expected Double Star (DS) TF $[D(x)]$ in the form of a linear combination of two SS TFs, i.e.,

$$D(x) = A(\Delta m)[S(x) + B(\Delta m)S(x + dx)] \tag{1}$$

(and its analogue for the Y-axis), where the second SS TF $[S(x + dx)]$ is identical to the first $[S(x)]$ but displaced along the X-axis by dx, the DS projected separation. $A(\Delta m)$ is a normalization factor, and B is the intensity ratio of the primary to the secondary star. Both quantities are, of course, functions of the magnitude difference (Δm). The model just described is fitted to the observed TF curve and the parameters dx and Δm derived. It is worth noticing here that two independent estimates of Δm are available, one for each FGS axis. In practice, a grid of models is generated by varying dx and Δm. Each model is cross-correlated wih the observed TF by computing the correlation integral

$$\int D(t - u)\, TF(t)dt\,, \tag{2}$$

where the template function D is being cross-correlated with the actual visibility fringe TF; the sought value for u, which maximizes Eq. 2, represents the shift along the horizontal axis between the two functions.

The best-fit model is chosen as the cross-correlation that minimizes the sum of the squares of the differences between the model and the observed one., *viz.*

$$\int [D(t - u_0) - TF(t)]^2 dt = min\,, \tag{3}$$

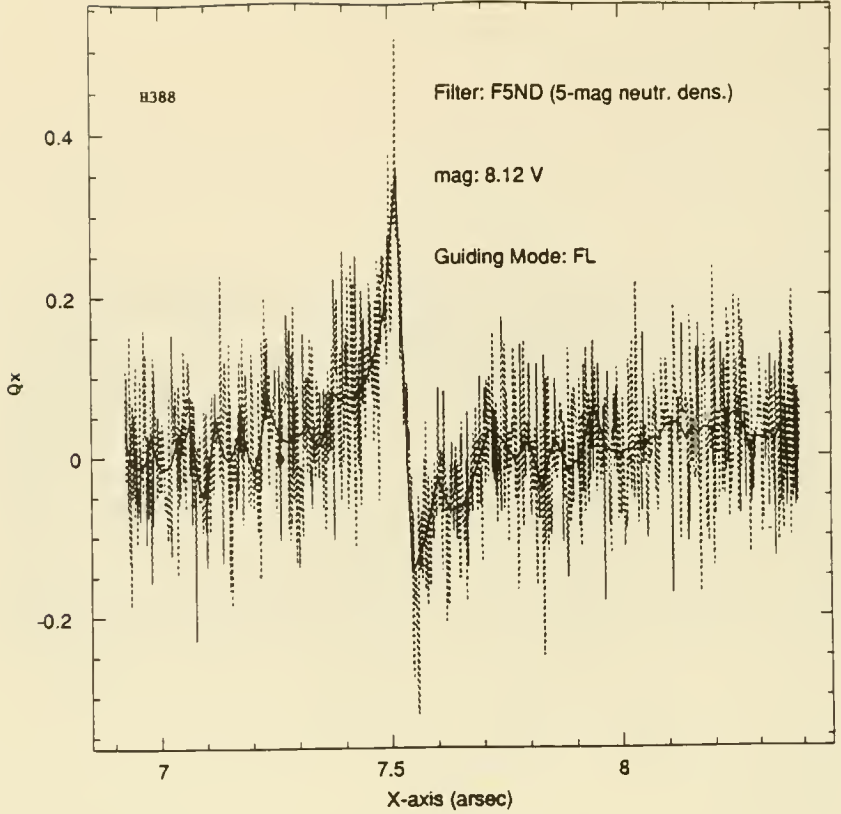
H388
Filter: F5ND (5-mag neutr. dens.)
mag: 8.12 V
Guiding Mode: FL
0.4
0.2
0
-0.2
Qx
7
7.5
8
X-axis (arsec)

Fig. 1(a)

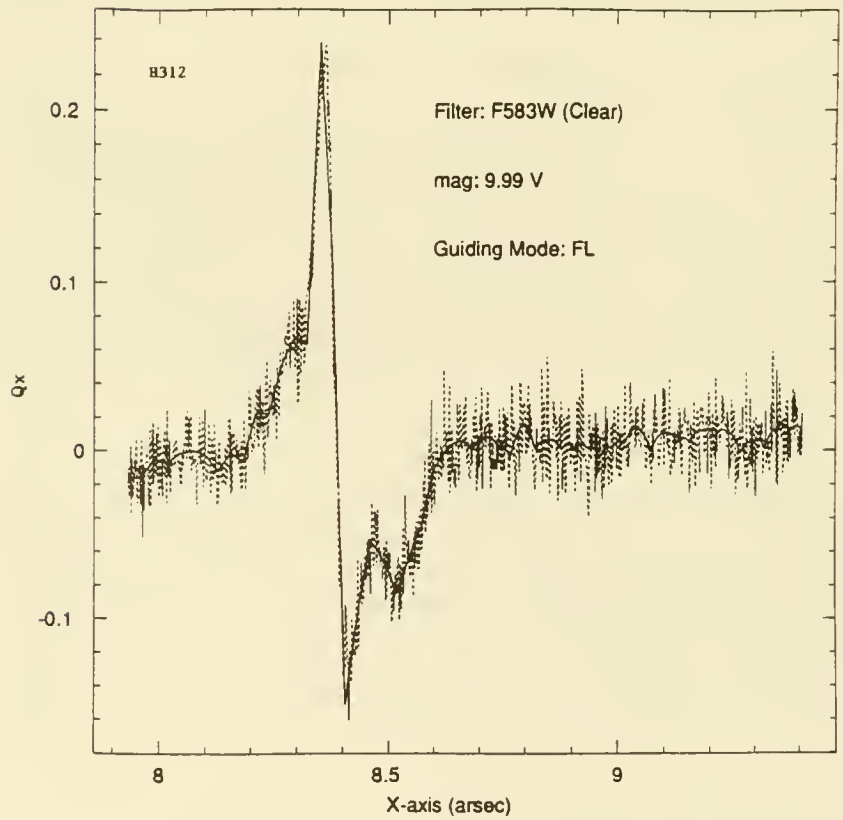
H312
Filter: F583W (Clear)
mag: 9.99 V
Guiding Mode: FL
0.2
0.1
0
-0.1
Qx
8
8.5
9
X-axis (arsec)

Fig. 1(b)

where u_0 is the value maximizing Eq. 2. This approach has been preferred to direct applications of least-squares-like schemes for its robustness, in relation to the range of narrow separations (from 100 mas down to about 10 mas) where the astrometer FGS will make its most interesting detections, and the independent difficulty of giving sufficiently accurate initial guesses for dx and Δm. However, if felt necessary, the accuracy of the fit can be improved, now using the answers from the correlation technique, as initial guesses for the least-squares final adjustment.

Before running the cross-correlation, the noise in the observed TF is smoothed via a piecewise low-order polynomial fit, where continuity is imposed at the bin boundaries up to the specified derivative order (continuous lines in Fig. 1). This polynomial smoothing increases the resolution of the subsequent cross-correlation, and makes it possible to compute the correlation integral *analytically*.

The current OTA and, possibly, residual aberrations and misalignments within the FGSs are producing field dependent aberrations across the FGS fields of view. In terms of a single star TF, this means that, at the moment, we are unable to successfully predict either its shape or its marked variation across the field of view. The nice properties of the theoretical, pre-launch, TF are gone. To find the actual signatures of a single star TF as a function of the position in the field of view, one must resort to in-flight calibrations, or, as for the SAO analysis, bootstrap one's way to find a single-star TF. To do so, we used data taken from the 9 POINTS OF LIGHTS experiment, a series of engineering observations aimed to monitor the OTA-FGS optical characteristics as function of the secondary mirror position. Noticing that all the Hyades transfer scans were taken approximately in the same spot of the FGS field of view (FOV), we selected the single-star TFs on the basis of their resemblance with the 9 POINTS OF LIGHT TF taken in the nearest position of the FGS FOV.

After having inspected all the scans of all the 16 targets (grouped per filter), we started our boostrap procedure by *defining* some scans to be single-star TFs. All these scans were co-added to produce an initial single-star TF template; then, each single scan was kept or rejected, on the basis of its resemblance to the template. Finally, the resulting single-star TF model was constructed by co-adding all the accepted scans. The templates obtained for the X-axis and the two filters used are shown in Figs. 2a and 2b.

All the remaining stars, which observed TF had not contributed to the definition of the single-star TF, were tested for duplicity through the technique described above, and one binary was found. The complete results, together with other relevant information, are reported in Table 1.

Based on the experience made with the SAO data analysis, we believe that FGS Transfer Function Mode astrometry can give binary star component separations with a precision of about 5 mas, and derive magnitude differences to about 0.15 mag. After SV and Cycle 1 calibrations are carried out, we should be able to improve upon the present situation.

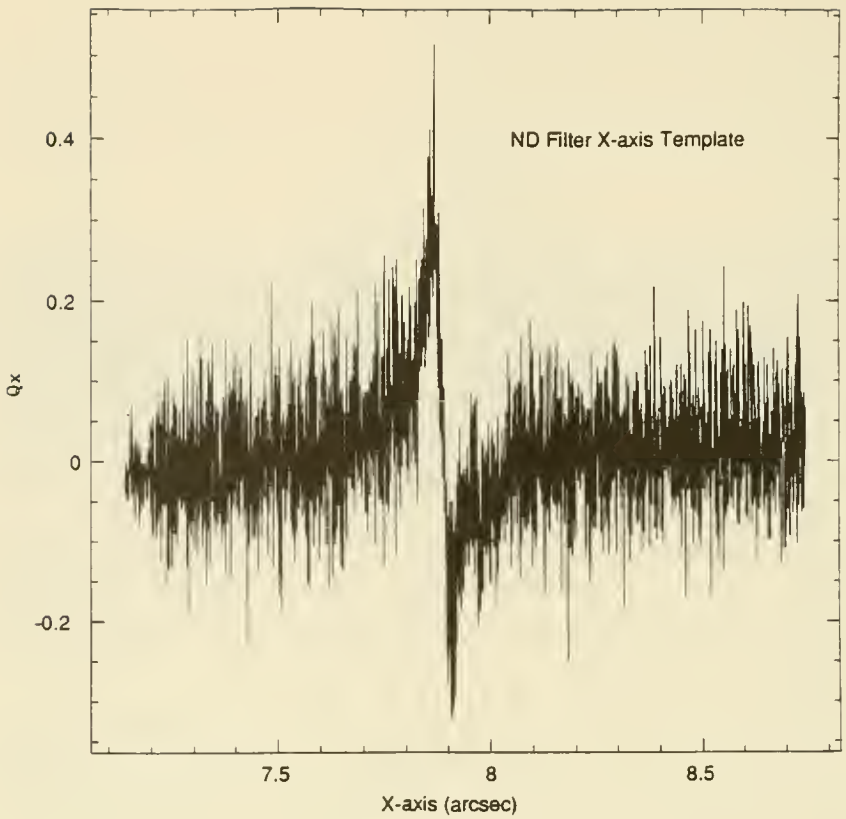
ND Filter X-axis Template
0.4
0.2
0
-0.2
Qx
7.5
8
8.5
X-axis (arcsec)

Fig. 2(a)

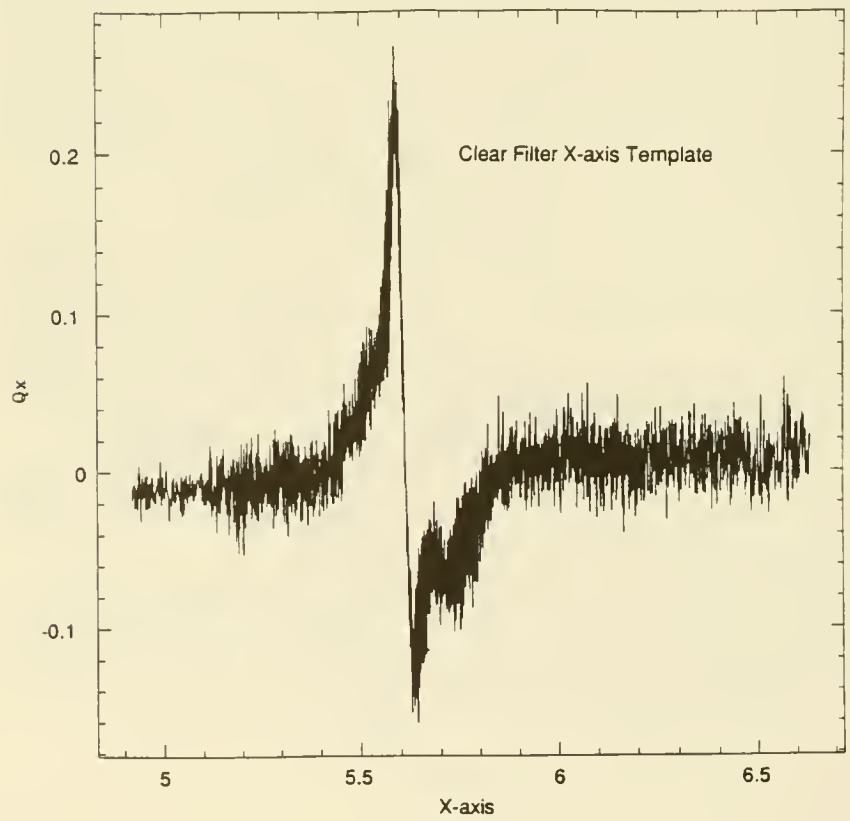
Clear Filter X-axis Template
0.2
0.1
0
-0.1
Qx
5
5.5
6
6.5
X-axis

Fig. 2(b)

TABLE 1. Summary of Observations

Star Name[a]	V	$B-V$	Status	Filter	Guiding Mode
H115	$11^m.56$	$+1^m.38$	I[b]	Clear[e]	G[f]
H198	8.46	0.72	I	Clear	CT[f]
H230	6.17	0.46	S[c]	ND[e]	CT
H246	6.61	0.41	I	ND	CT
H292	9.11	0.87	S	Clear	CT
H307	7.15	0.22	S	ND	CT
H312	9.99	1.06	S	Clear	FL[f]
H316	6.97	0.44	S	ND	CT
H379	7.49	0.54	S	ND	FL
H388	8.12	0.66	S	ND	FL
H417	9.52	0.93	S	Clear	CT
H420	9.03	0.84	S	Clear	FL
H429	5.90	0.84	S	ND	CT
H507	7.78	0.54	S	ND	FL
H554	8.66	0.74	S	Clear	CT
H578	8.51	0.84	D[d]	Clear	CT

[a]From Hansen (1975).

[b]I = Indeterminate but probably single.

[c]S = Single.

[d]D = Double.

[e]ND = F5ND neutral density filter (5 mag); Clear = F583W clear filter (λ_e = 5830Å FWHM = 2340Å).

[f]Guidance Modes were FL = Fine Lock, CT = Coarse Track, or G = Gyroscopes.

REFERENCES

Bradley, A., Abramowicz-Reed, L., Story, D., Benedict, G., and Jefferys, W. 1991, *PASP*, **103**, 317.

Franz, O. G., Wasserman, L. H., Nelan, E., Lattanzi, M. G., Bucciarelli, B., and Taff, L. G. 1991, *A. J.*, submitted.

Restoration of Images Degraded by Telescope Aberrations

T. Reinheimer, D. Schertl and G. Weigelt
Max-Planck-Institut für Radioastronomie
Auf dem Hügel 69
D-5300 Bonn 1
Germany

1. Introduction

The spherical aberration of the Hubble Space Telescope (HST) causes a point spread function (psf) which consists of a central core of about 0.1 arcsec diameter and a halo of several arcsec diameter. The core contains only about 12% of the total psf intensity. We have performed laboratory simulations of images degraded by telescope aberrations and photon noise (10 000 photon events per image). Spherical aberration was produced by suitable optics. The aberrated images were used to investigate the dependence of the reconstructed image on the applied image restoration method. The image reconstruction methods Wiener filtering, Clean, Gerchberg method, Lucy-Richardson method and MEM were compared.

2. Image Restoration Experiments with Laboratory Raw Data

The laboratory setup for the simulation of HST data is shown in Fig. 1. Spherical aberration is produced by using an achromatic telescope lens with the wrong orientation in the setup (plain surface on the side of the parallel beam). In front of the telescope lens a mask similar to the HST pupil function was inserted . The aberrated images in the focal plane of the telescope were recorded with a high-gain image intensifier (gain about 10^5) coupled to a CCD camera. The system was able to record individual photon events. Fig. 2 shows a diffraction-limited image of the laboratory object. The intensity ratios of the 4 stars are 1:0.61:0.53:0.23 . Fig. 3 shows the point spread function of the optical setup (spherical aberration). Fig. 4 is an aberrated raw image of the star cluster (Fig. 2) recorded with our optical setup. The image is degraded by spherical aberration and photon noise. The total number of photon events per image is $\sim$ 10 000, the number of photon events in the brightest pixel is $\sim$ 70. Figures 5-9 show the images reconstructed from the aberrated raw image (Fig. 4) by Wiener filtering (Helstrom 1967; Fig. 5), by the iterative image restoration method Clean (Högbom 1974; Fig. 6), by the iterative Gerchberg method (Gerchberg 1974; Fig. 7), by the Lucy-Richardson method

(Richardson 1972, Lucy 1974; Fig. 8) and by MEM (MEMSYS-3 package, Gull and Skilling 1984; Fig. 9).

The reconstruction of star 4 has the biggest error since it is faint and close to bright stars. A comparison of the reconstructed images, the aberrated raw image and the original object shows that most of the restoration methods were quite successful. In all reconstructed images all stars are clearly visible, whereas they are not visible in the aberrated image (see Reinheimer and Weigelt, 1992 for more quantitative details). The conclusion may be different if photon noise is more severe or if other object classes are observed. In future experiments we will study other object classes.

REFERENCES

Helstrom, C.W., 1967, J. Opt. Soc. Am. 57, 297

Högbom, J.A., 1974, Astron. Astrophys. Suppl. 15, 417

Lucy, L.B., 1974, Astron. J. 79, 745

Gerchberg, R.W., 1974, Opt. Acta 21, 709

Reinheimer, T., Weigelt, G., "Deconvolution of Hubble Space Telescope Data: Computer Simulations and Laboratory Experiments", Conf. Proc. on "Restoration of HST Images and Spectra", 1990, ed. R. Allen (STScI), p. 88

Reinheimer, T., Weigelt, G., "Restoration of Images Degraded by Telescope Aberrations" submitted to Pure and Applied Optics

Richardson, W.H., 1972, J. Opt. Soc. Am. 62, 55

Gull, S.F., Skilling,J., 1984, "The maximum entropy method" in Indirect Imaging, ed. J.A. Roberts, Cambridge Univ. Press

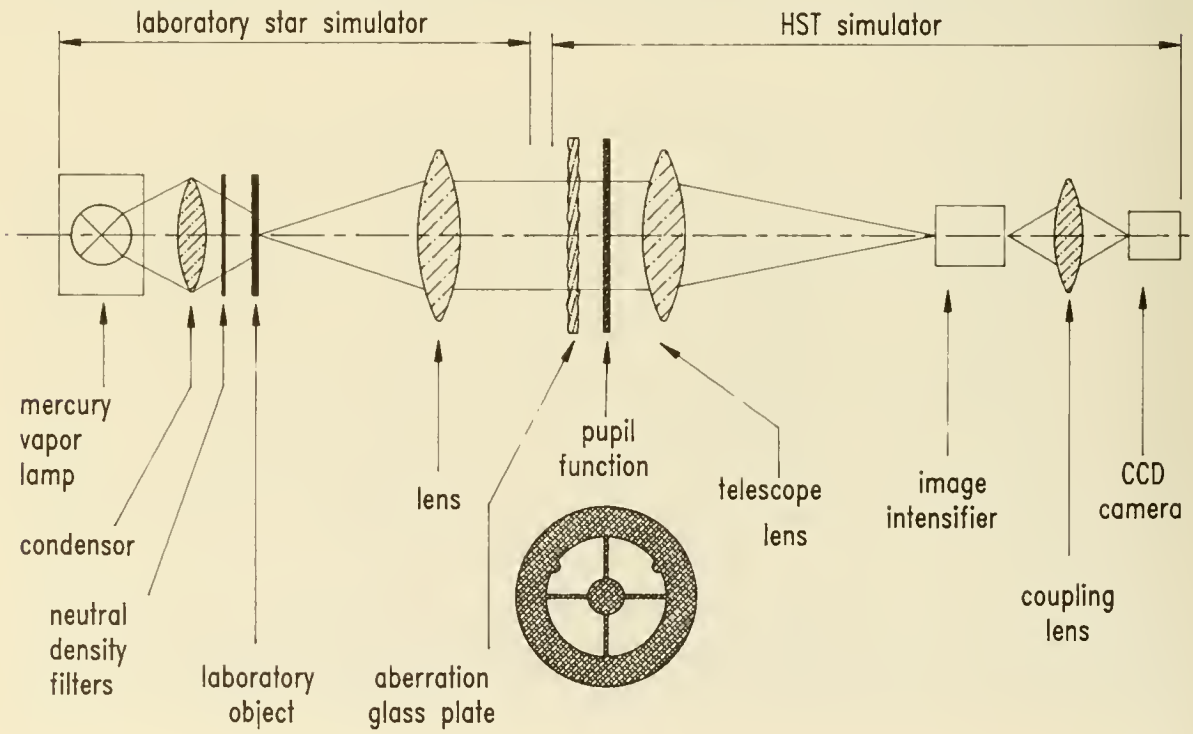

Fig. 1: Optical setup

Fig. 2: Diffraction-limited object, a star cluster. The stars are called 1, 2, 3, and 4 from top to bottom.

Fig. 3: Laboratory point spread function (simulated spherical aberration and HST FOC f/288 pupil function)

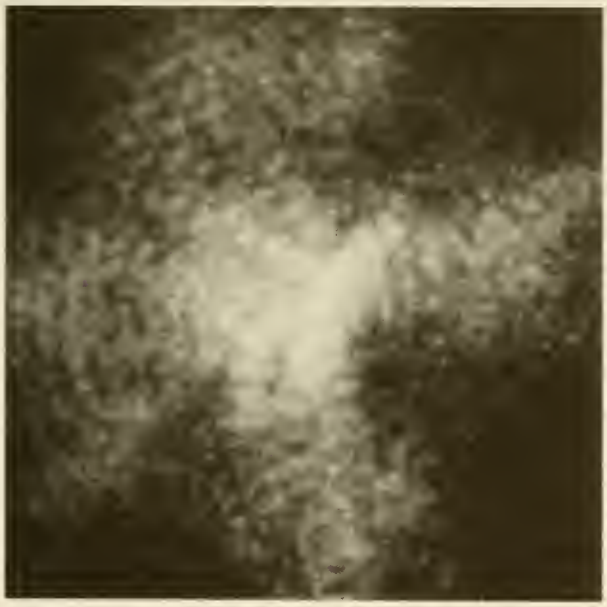

Fig. 4: Laboratory image of the object degraded by spherical aberration and photon noise ($\sim$ 10000 photon events/frame or $\sim$ 70 photon events in the brightest pixel)

Fig. 5: Image reconstructed from Fig. 4 by Wiener filtering

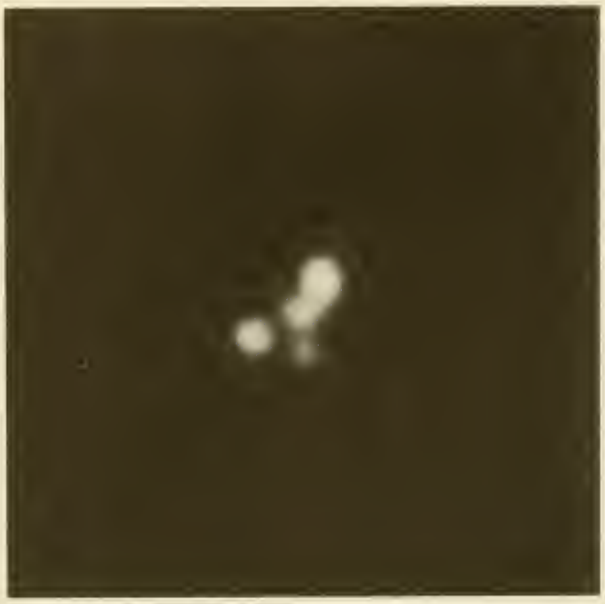

Fig. 6: Image reconstructed from Fig. 4 by Clean

Fig. 7: Image reconstructed from Fig. 4 by the Gerchberg method (30 iterations)

Fig. 8: Image reconstructed from Fig. 4 by the Lucy- Richardson method (140 iterations)

Fig. 9: Image reconstructed from Fig. 4 by MEMSYS-3 (140 iterations)

Coping with the Hubble Space Telescope's PSF: Crowded Field Stellar Photometry

Eliot M. Malumuth
Computer Sciences Corporation
James D. Neill AND Donald J. Lindler
Advanced Computer Concepts
AND
Sara R. Heap
Goddard Space Flight Center

1 Introduction

The spherical aberration of the Hubble Space Telescope, HST, presents astronomers with a Point Spread Function, PSF, unlike any that they have had to deal with in the past. The PSF has a sharp core of approximately 0.″1 and broad low surface brightness wings which have rings and tendrils that extend to over 2.″0 in diameter. Figure 1, a shaded surface plot of a PSF star taken from a Planetary Camera image, illustrates how much higher the surface brightness of the core is compared with the wings. Another complication is that the PSF varies with position in the field of view of the Wide Field Camera, WFC, and the Planetary Camera, PC.

While the PSF is tantalizing to the astronomer who wishes to do photometry of crowded fields because of the sharp core, it is disappointing because the wings of nearby stars introduce a variable and unknown background.

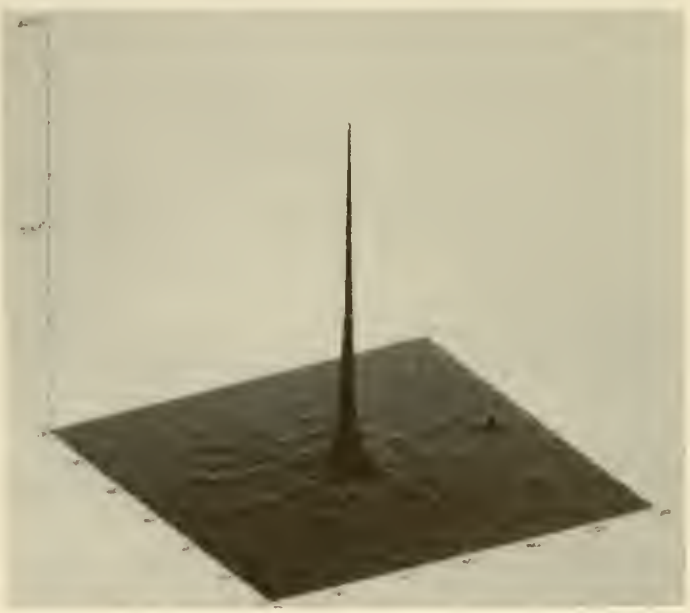

Figure 1. A shaded surface plot of the PSF star taken from the PC image of 30 Doradus. It illustrates how sharp the core is, and how much higher surface brightness than the wings it is.

2 Observations

As part of the Science Assessment Program, PC images of the 30 Doradus region of the Large Magellanic Cloud, LMC, were obtained with two different filters. Five 300 second exposures were taken with the F368M (hereafter U) filter and five 100 second exposures were taken with the F547M (hereafter V) filter. A further complication was that the V images all had saturated pixels in the cores of the brightest stars. We have repaired the V images as best we could by matching the unsaturated parts of the core with the same star in the U image. The compact cluster of stars at the center of 30 Doradus is known as R136. In these data R136 is located near the bottom center of the P6 CCD chip. In this work we only consider the data located on PC chip P6.

Figure 2 shows the final U image displayed on a logarithmic scale. It is a median of the 5 individual images. Inspection of the R136 region shows that there are $\sim$ 150 stars in an area about the size of the PSF wings. The light between the stars in R136 is due to the overlapping of the wings of the PSFs of all of the stars. It is this background which must be correctly accounted for in order to use the cores to do accurate photometry. The average sky background has been subtracted

off of this image.

3 Method

In order to do stellar photometry in crowded fields with the HST, we have developed a simple approach that uses the known properties of the HST PSF. The following is a brief step by step description of this technique.

1. Prepare a list of stars and their x, y positions. We used DAOPHOT (Stetson 1987) as modified by Holtzman (1990) to find 402 stars brighter than the local maxima in the PSF of the brightest stars. We found an additional 259 stars by inspecting the image. The positions of these additional stars were measured by fitting gaussians to the cores in both the x and y directions.

2. Extract images of stars to use as PSFs. In the case of 30 Doradus, there is one bright, isolated star in the field. It is the star designated by the letter A, somewhat to the left of center in figure 2. The PSF derived from this stellar image has an area of 120x120 pixels or 5.″16x5.″16.

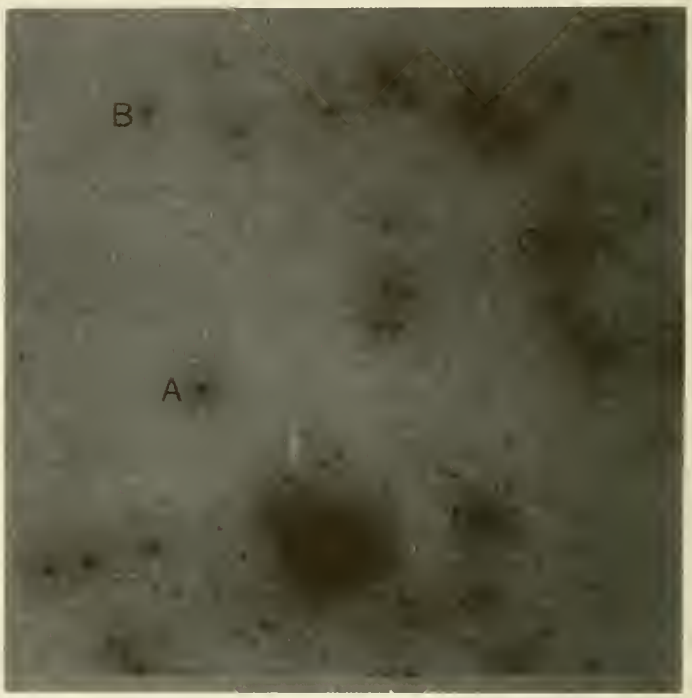

Figure 2. PC image of 30 Doradus. This image is the median of five 300 second exposures using the F368M filter.

3. Make an initial guess of the relative flux of each star, F_i. The ratio of the counts in the core of each star to the counts in the core of the PSF star is used for the initial guess of the relative flux. In practice we used the central 5x5 pixels (0.″22x0.″22) to give us the counts in the core. This will give an overestimate of the relative flux in the most crowded regions because the central 5x5 pixel box will contain light due to the wings of the neighbouring stars.

4. Produce a model of the field. We start with an image of the same size as the data image (800x800 for one PC chip) that has a data value of zero in each pixel. For each star, i, we register precisely the PSF image with the star's position using a bilinear interpolation, scale it by F_i, and add it to the model image pixel by pixel. When this has been done for each star we have a model of the field which can be compared with the data frame.

5. Adjust the relative flux scale factor for each star. Once a model image is made the scale factors for each star is adjusted using the following equation.

$$F_i' = F_i \times \frac{\sum_{x_i-2}^{x_i+2} \sum_{y_i-2}^{y_i+2} O(x,y)}{\sum_{x_i-2}^{x_i+2} \sum_{y_i-2}^{y_i+2} M(x,y)}$$

Where F_i' is the new scale factor of the i^{th} star, O is the observed image and M is the model image.

The last two steps are repeated using the new scale factors until the convergence criterion is met. For these data we used a convergence criterion of 98% of the star scale factors change by less

than 3% between iterations. The behavior of the estimates of the scale factors is that stars which are isolated reach their final value quickly (1 or 2 iterations), while stars in crowded regions start out with an overestimate on the initial guess, drop below the final value after the first iteration, and then approach their final value asymptotically. For the crowded inner region of R136 it takes about 15 iterations to reach the final values of the relative flux scale factors.

4 RESULTS

The final model for the U image is shown in figure 3. This can be directly compared to figure 2. On casual inspection it appears to be a very good representation of the observed image. A more quantitative way to evaluate the results is to produce a residual image. This is done by subtracting the final model image from the observed image. Figure 4 is the U residual image. This image reveals the problem of not having positional information for the PSF. For example the mismatch between the PSF and the stellar image is evident for the bright stars on the right side of the image. Otherwise, the residuals are fairly small.

Figure 3. Final model image of the U image of 30 Doradus. This image can be compared with figure 2.

Another way of looking at the results is to compare cross-sectional plots of the observed image and the final model image. Figure 5 shows a row plot which crosses the stars R136c and Melnick 42 (Melnick 1985). The dotted line shows the data from the PC image and the dashed line is from the model image. Aside from the excellent overall agreement, notice how well the model matches the background between the stars in the crowded region of R136.

One of the advantages to this method is that it is a simple matter to use many PSFs. In theory, as many PSFs as there are stars may be used. To illustrate this, we have repeated the procedure using 4 PSF stars. The PSF stars used are shown in figure 2, and are labeled by letters A, B, C and D. The original photometry was used to clean stars from the vicinity of stars C and D. Figure 6 is the U residual image using the 4 PSF stars. Notice how the residuals of the stars on the right have decreased.

Figure 7 is a comparison of the derived magnitudes using 1 PSF star and 4 PSF stars. In addition to the random errors at fainter magnitudes, small systematic differences between the photometry done with different PSF stars are evident. The differences for the fainter stars in the lower left quadrant, for which the PSF star was the same, are due to changes in the stars in neighboring quadrants.

Figure 4. Residual image formed by subtraction figure 3 from figure 2. The effect of the spacial variation of the PSF is seen as the worsening residuals in the upper right hand corner of the image. Notice the residuals of the rings and tendrils.

Figure 6. Residual image formed using the model made with 4 PSF stars. The residuals in the lower left corner are identical to those in figure 4 because the same PSF stars (star A) was used for this quadrant. The residuals on the right hand side of the image are much better than in figure 4. This is especially true for the rings and tendrils of those stars.

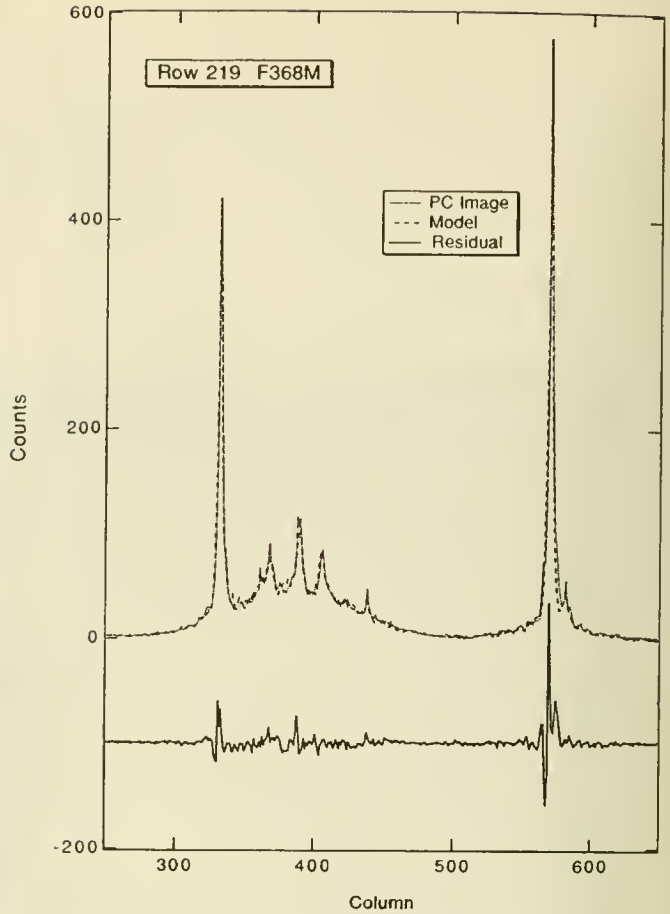

Figure 5. A plot of row 219 crossing R136c and Melnick 42 (star D in fig. 2) in the PC image of 30 Doradus. The Observed image (fig. 2) is shown as the dotted line. The model image (fig. 3) is shown as the dashed line. The residual is shown as the solid line offset by -100. Notice how well the background light in the region of R136 is matched.

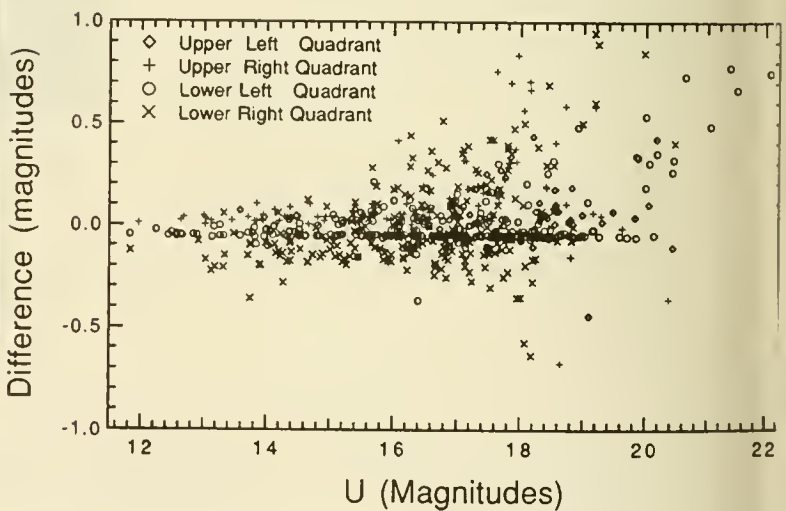

Figure 7. Comparison of the results for 1 PSF star and 4 PSF stars. In addition t the random errors at the fainter magnitudes there are small systematic difference between the photometry done with different PFS.

REFERENCES.

Holtzman, J. 1990, PASP, 102, 806

Melnick, J. 1985, A&A, 153, 235

Stetson, P. 1987, PASP, 99, 191

SOME ALGORITHMS AND PROCEDURES USEFUL TO ANALYSE HST-FOC IMAGES

C. Barbieri, G. De Marchi, R. Ragazzoni
Astronomical Observatory of Padova
Vicolo dell'Osservatorio, 5
35122 Padova, Italy

Abstract. Four procedures are briefly described among those we have developed for the reduction of HST-FOC frames.
Emphasis is given to those algorithms we think particularly useful for this kind of space-based images.

1. INTRODUCTION

Images collected by the Faint Object Camera need some particular procedures in order to be properly handled. Actually, most of the problems normally encountered analysing ground-based images are different from those arising while treating space-based images.

In this poster we want to point out, with some examples, that a special care is required even for simple operations, like recentering, smoothing, background subtraction, peak location and so on.

2. FRAME RECENTERING VIA SHIFT AND ROTATION USING AUTOCORRELATION TECHNIQUES

This section will discuss the problem of comparing and superimposing images taken from the ground and from the space. Ground-based images are characterized by approximately the same degree of resolution, and the problem of comparing two or more of them is relaxed.

Furthermore, the PSF is undersampled in space-based images while it is oversampled in ground-based, so the precise matching of HST with ground-based images becomes a difficult task (even ignoring strong colour differences).

Even the comparison of two FOC frames is not a trivial operation: actually, in Coarse Track mode we are never sure to be justified in ignoring field rotation. Due to the sharpness of the PSF core, even a slight rotation can destroy the precise alignment of stars in a crowded field.

Precise and robust procedures capable of matching two generic images are therefore

needed. Recentering of frames via X-Y shifting, using auto correlation techniques, is more or less a common method. An extension of this method, allowing also for unknown relative rotation of frames, is here briefly described.

The full procedure is shown in Figure 1 and is here summarized step by step:

1. Each image is split into two areas: the **inner** one, with a radius of 1/6 of the image size, and the **outer** one, an annulus with internal and external radii respectively 1/6 and 1/2 of the image size. The internal size of 1/6 has been somewhat arbitrarily chosen in order to have enough area in the center and at the same time a not excessive rotation effect inside it.

2. On the inner area the usual 2D auto correlation function (ACF) is performed. The position of the ACF's main peak gives the relative X-Y shifting;

3. The outer areas are projected, using polar coordinates, on strips with height 1/3 of the image size and width π times the size;

4. Auto Correlation is performed on the couple of strips **line-by-line**;

5. The sum of columns is performed, weighting each line by the value of the corresponding radius.

6. Finally, the amount of relative rotation (radians) is obtained multiplying by 2 the position of the peak in the latter sum and dividing it by the size.

It should be noted that performing auto correlation on the full image (instead of on the inner part only) in order to get the X-Y shift does not produce any improvement on the overall accuracy. Moreover, X-Y recentering is to be performed **before** projection and following rotation detection.

Actually, each rotation around a point different from the centre of the frame translates into an additive blurring of the final rotational Auto Correlation Function, *i.e.* in a loss of accuracy.

The reached precision is of the order of some fraction of pixel, both for X-Y displacement and rotation. For the latter quantity, this linear error translates into a rotational error at the radius distance where the ACF is not negligible. In a typical crowded FOC frame 512×512 this means an error in the estimation of $\Delta\theta \approx 5'$.

3. SOME SIMPLE ADAPTIVE FILTERS

Smoothing frames in order to enhance the signal to noise ratio (SNR) is a common and useful operation.

Working with photon limited images means sometimes dealing with abrupt SNR changes on the frame itself. In order to retain a SNR level approximately equal over the whole frame, some adaptive smoothing must be performed.

Such adaptive filtering, while retaining the SNR constant on the entire image, leaves a varying resolution. In fact, a poor SNR calls for a strong smoothing, *i.e.* a loss in resolving power. We think that such a loss is due to physical and unavoidable reasons, and so no real information is lost.

In Figure 2 some examples of such smoothing are shown.

Given an estimation of the spatial resolution at a given SNR (for istance the FWHM of the typical PSF where SNR is greater than 10) the method can produce a map

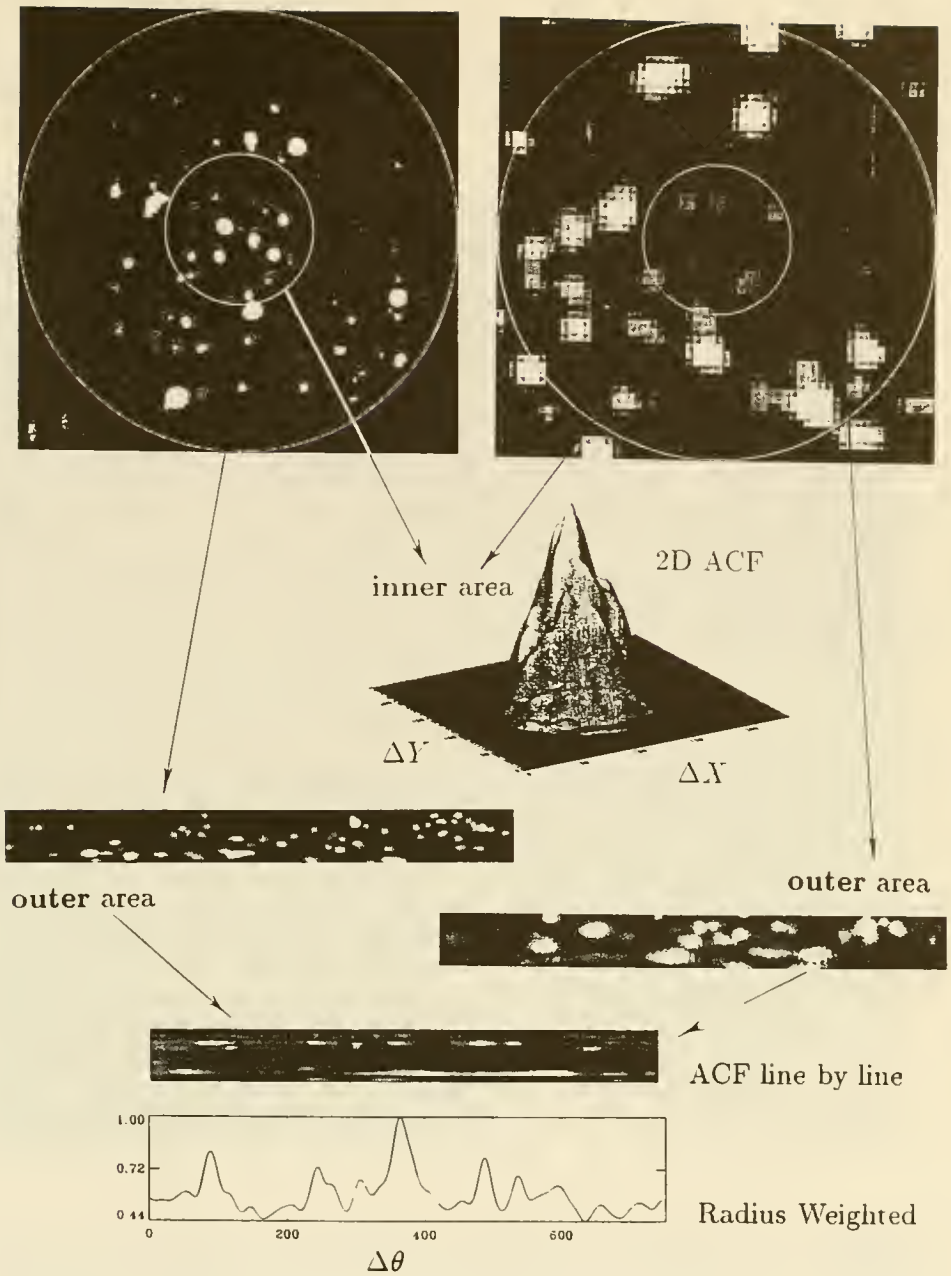

Figure 1: Auto Correlation helps to solve the problem of recentering two frames shifted and rotated one with respect to the other. In this example the centre of a globular cluster taken with HST-FOC and convolved with a gaussian shaped beam is compared with a ground based frame in order to properly match the two observations.

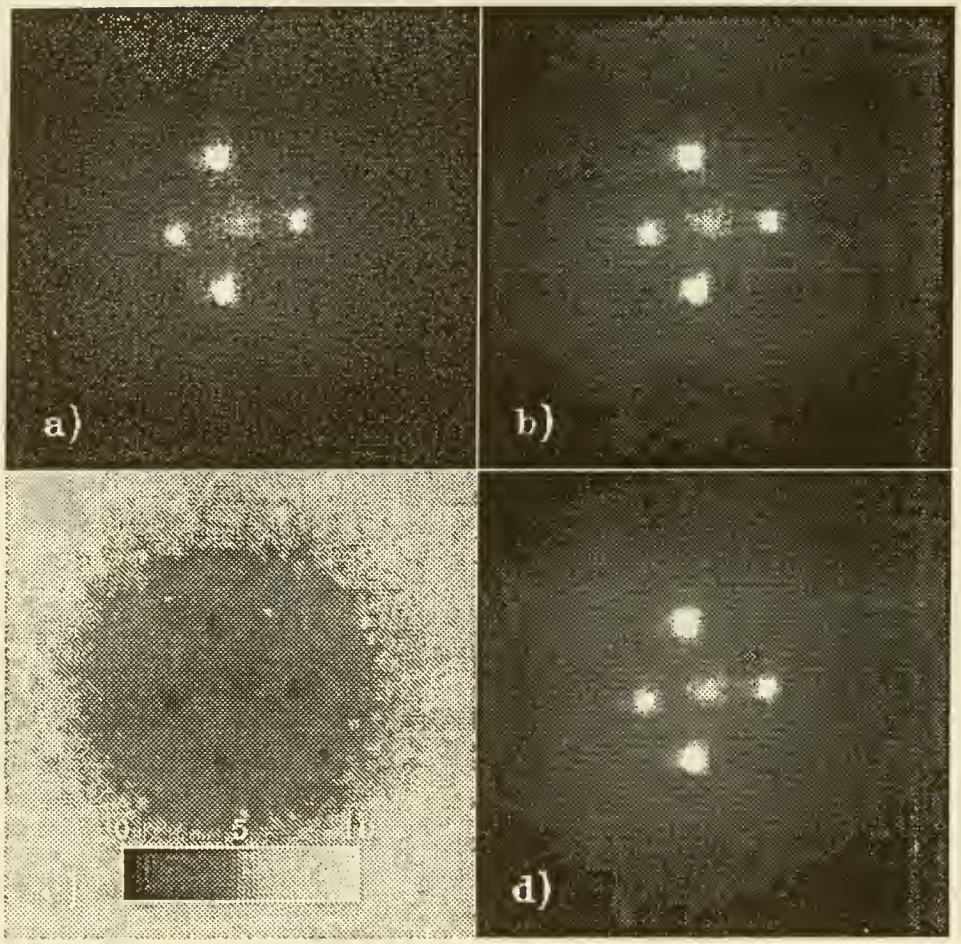

Figure 2: a):Raw frame (G2237, the Einstein cross), b): the same filtered in an adaptive way, c): the adopted gaussian beam size for any point of the frame, d): a normal (space invariant) smoothing, for comparison.

showing the resolution for each point of the frame, in order to estimate the significance of faint, photon limited details in the raw frame.

4. ABOUT THE SUBTRACTION OF UNDERLYING DIFFUSE OBJECTS

Thanks to the sharp core of the HST PSF, a very simple technique can be used to subtract an underlying and diffuse object, like a nebulosity in a point-like field.

The procedure can be summarized step by step as follows:

1. Place a grid of assigned size on the image;
2. Evaluate the lowest pixel value in each sub-image defined by the grid;
3. The diffuse object is described as a smooth approximation to this set of values.

The procedure is based on the assumption that there should be *a priori* no reason to have, on a sub-image defined by the grid, lower values than those given by the underlying object.

In order to meet such requirements, care must be paid to the size of the gridding and to some initial smoothing in order to avoid exceedely low values due to Poisson fluctuations rather than to the real background.

In Figure 3, as an example, the gridding is operated in a circular manner, in order to subtract the underllying galaxy in the assumption that its photometric behaviour is, at least approximately, only radial.

From this example one can easily detect a typical drawback of the application to HST-FOC frames, *i.e.* the presence of reseau marks. At these locations the counts are lower than in the neighborhood. These extremely dark reseau marks are seen in the figure as circular dark rings. On the other hand the position of the reseau marks is well known in advance and it would be easy to remove them before applying the procedure.

5. 2D CENTERING VIA DERIVATIVE TECHNIQUES

This simple procedure originates from the observation that the core of the PSF is undersampled in the FOC frames and some positional capability can be lost.

In spite of the geometrical stability of the camera (which is very good, anyway) it can be useful to get precise positions of point-like sources **on the frame** as accurately as possible, even if this could not be related to an analogous position in the sky (for purposes of recentering, subtraction of stars, and so on).

We have adopted a technique somewhat common in line centering, using derivatives of the third order (see, as an example, Figure 4).

It is well known, in fact, that such an approach takes automatically into account any background described by a quadratic polynomial.

This feature is particulary interesting in the case of crowded fields, where one needs an accurate centering of stars embedded in the halos of the other stars.

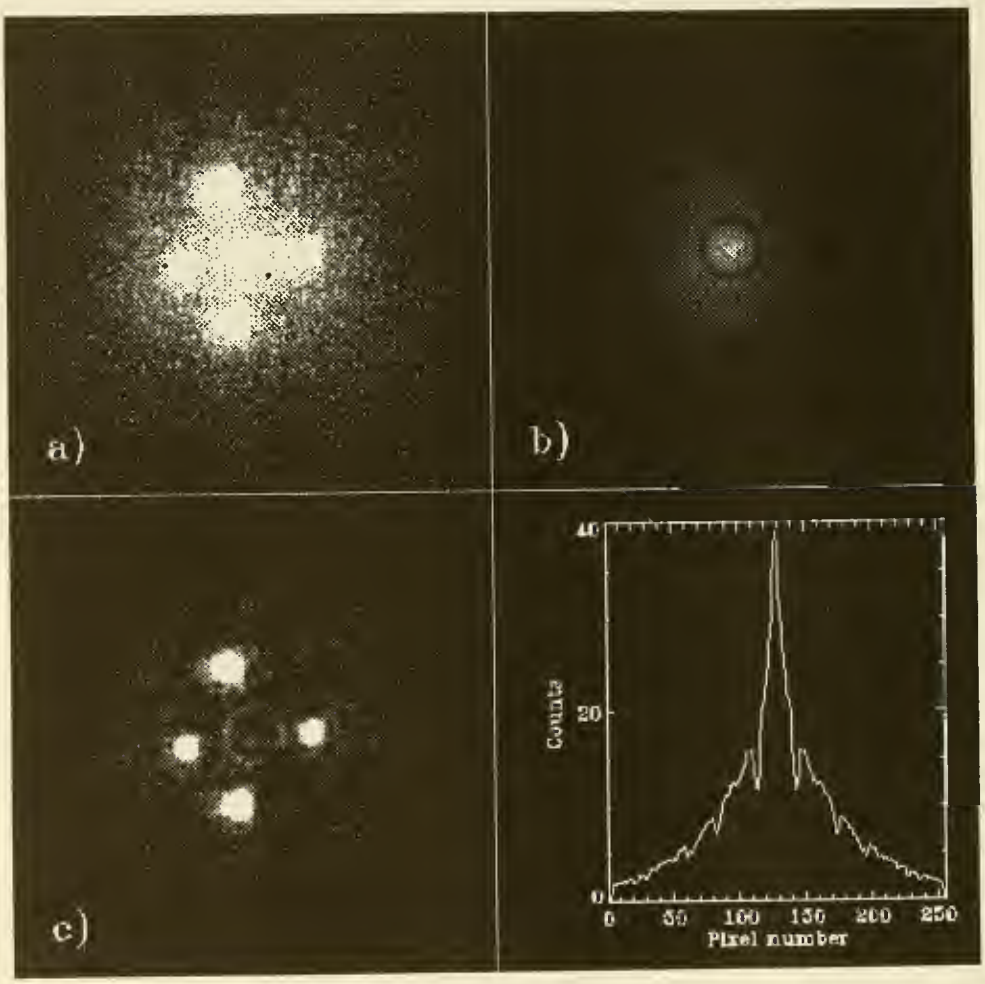

Figure 3: **a)**:Raw frame (G2237), **b)**: circular background estimation (see the text), **c)**: results of the subtraction of the background from the raw frame. In the lower right plot a trace along the background estimation is shown. Note the dark rings due to the *reseau-marks*.

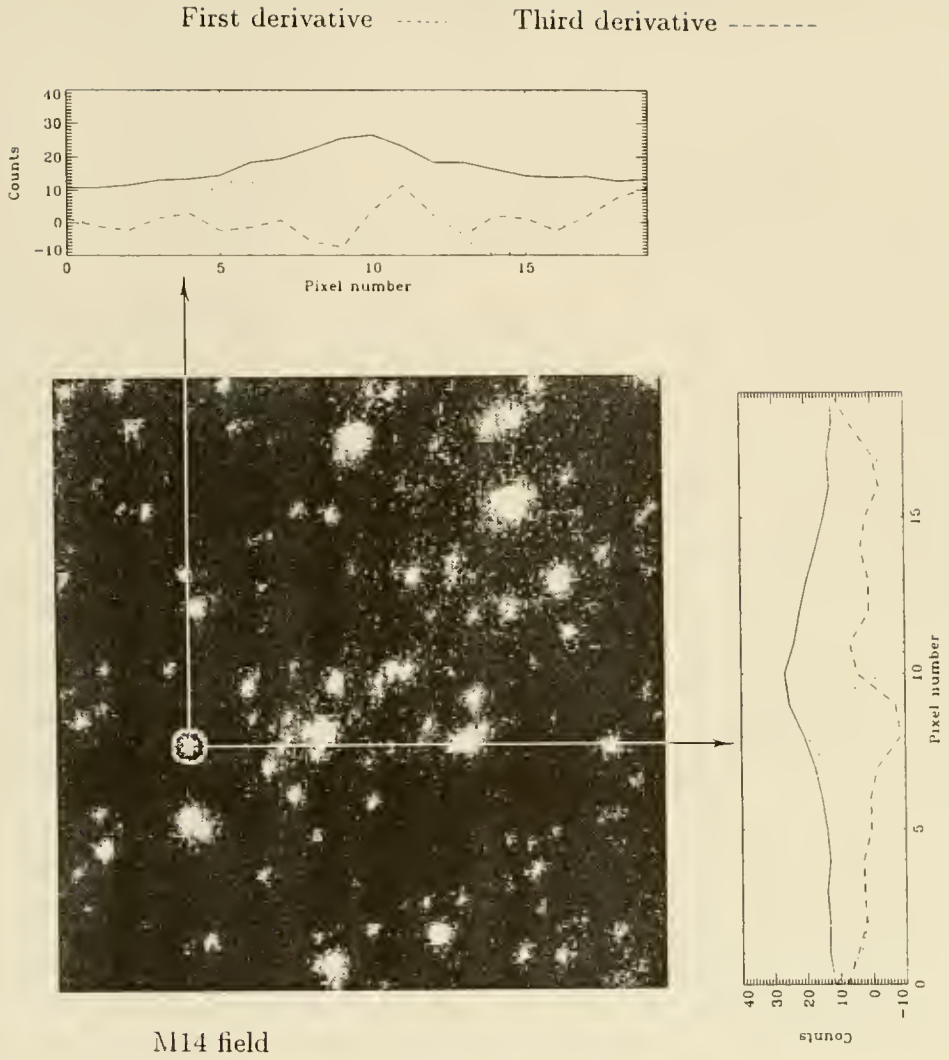

Figure 4: Centering of a star in a crowded field can take advantage from the use of the first and third order derivative of the image itself.

DECONVOLUTION OF AN FOC IMAGE USING A TIM-GENERATED PSF

P. E. Hodge
Space Telescope Science Institute
3700 San Martin Dr
Baltimore, MD 21218
USA

Science Data Analysts at the STScI have already computed a number of PSFs using the Telescope Image Modelling (TIM) software of Burrows and Hasan. These PSFs are the first of a catalog of PSFs that are to be prepared so that observers may deconvolve images taken with the Hubble Space Telescope. In order to get some feeling for the usefulness of these initial PSFs for deconvolving images taken with the f/96 relay of the Faint Object Camera (FOC), an image of a single star was deconvolved using the Lucy-Richardson algorithm with the appropriate TIM PSF. The central brightness increased by a factor of eight, but some structure in the wings was accentuated rather than suppressed.

The image selected for deconvolution was a 900-second exposure of the star BPM 16274 taken through the F210M filter plus a two magnitude neutral-density filter. The TIM PSFs are oversampled by a factor of two, so the IRAF blkrep task was run on the FOC image to match the pixel scales. The computed PSFs in this first set do not include aberrations other than spherical and focus offset. The PSF for F210M is one of the polychromatic PSFs, however, so it does include contributions from several wavelengths. We can expect substantially better agreement between the computed and observed PSFs as we develop a better understanding of the optical characteristics of the HST.

The image was deconvolved using the lucy task in the stsdas playpen package in IRAF. Fewer than 30 iterations were required to bring chi-squared below one. The parameter values adu=1 and noise=0 were used.

Figures 1 and 2 show the original image and the deconvolved image using a grey scale that emphasizes the outer portions of the PSF. The same range of pixel values was used for both displays, even though the maximum value of the deconvolved image was much higher. Figure 3 shows a radial profile plot of the deconvolved image. The profiles of the original (not included here due to lack of space) and deconvolved images differ by a factor of eight in scale, and the original is a half pixel larger in radius, but otherwise both profiles are virtually identical in form.

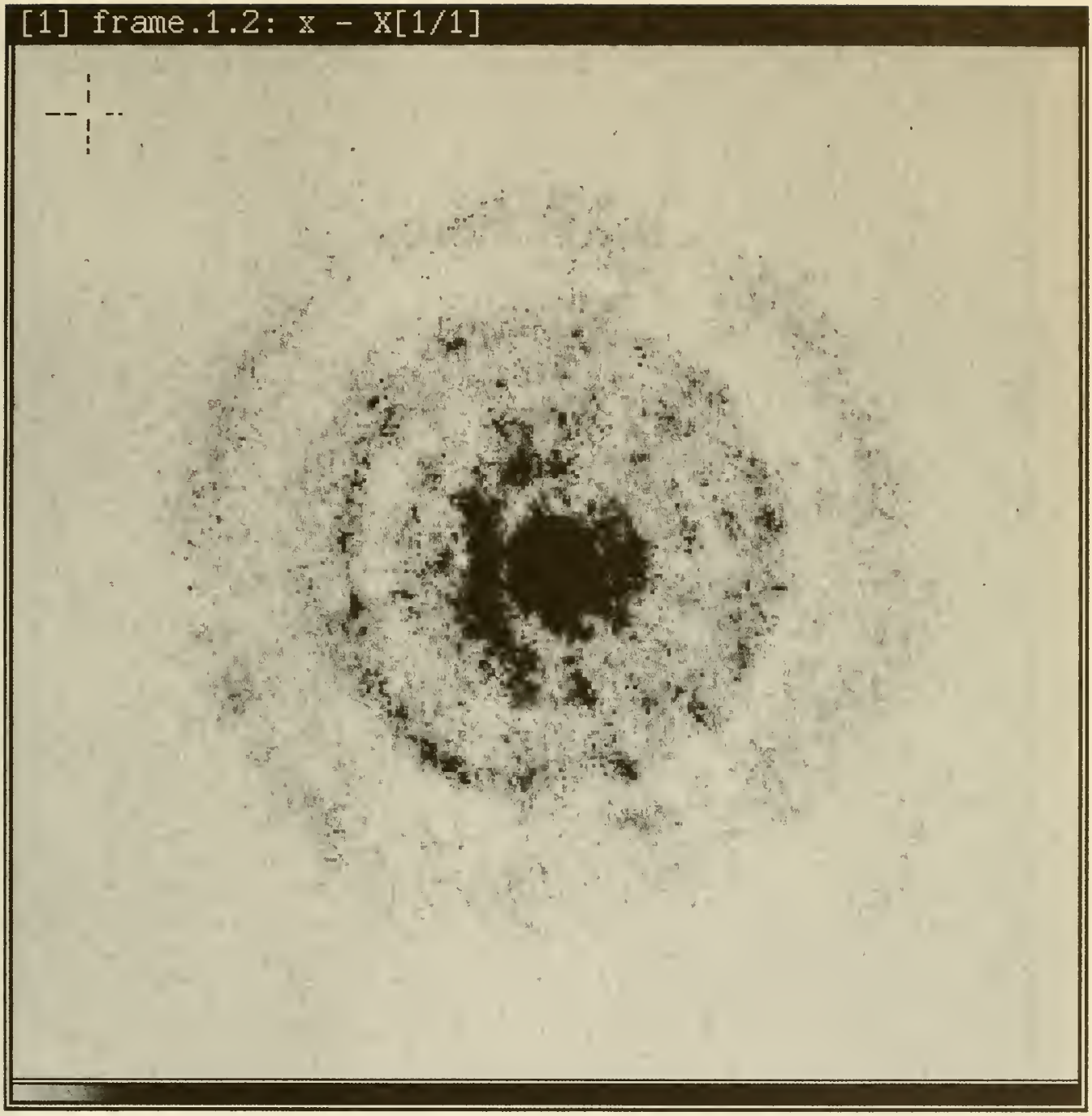

Figure 1. FOC f/96 image of BPM 16274 with F210M filter, scaled to show the outer portions of the PSF.

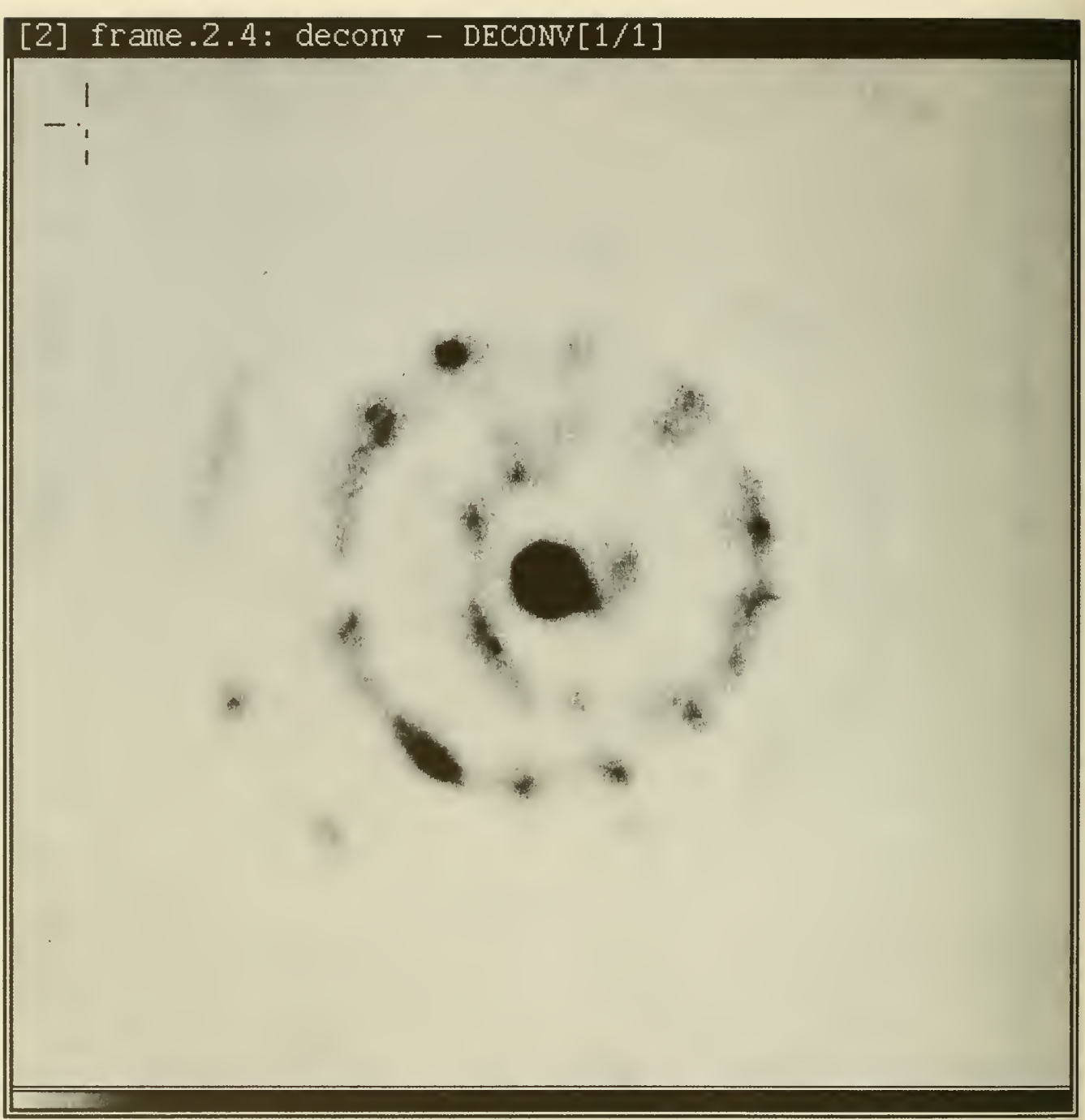

Figure 2. Deconvolved image of BPM 16274, using the same display minimum and maximum and grey scale as Fig 1.

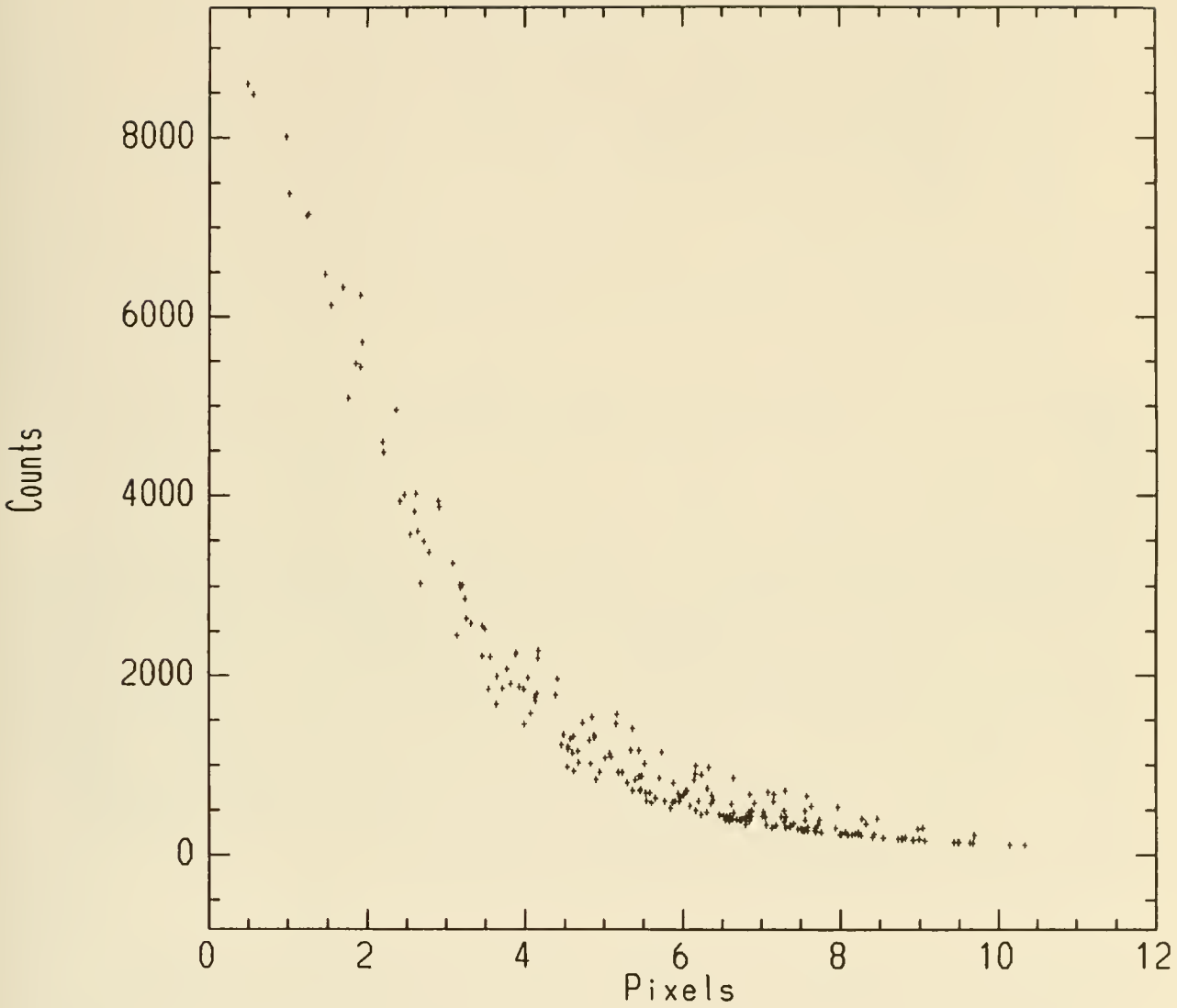

Figure 3. Radial profile plot of the deconvolved image.

RAPID DECONVOLUTION OF HUBBLE SPACE TELESCOPE IMAGES ON THE NRL CONNECTION MACHINE

Paul Hertz and Michael L. Cobb
E. O. Hulburt Center for Space Research
Naval Research Laboratory
Washington, DC 20375-5000
USA

Abstract. We have developed a rapid, highly parallel image space based convolution algorithm for use on the NRL 16k processor Connection Machine. This supports an image reconstruction program which uses standard iterative algorithms, such as the Maximum Entropy Method or Richardson-Lucy Method; thus, when given a constant point spread function (PSF) it yields reconstructed images identical to those run on serial computers and workstations. Our parallel implementation offers two advantages. (1) The highly parallel Connection Machine allows us to use a PSF which varies across the field of view, more closely approximating the true HST PSF. Our current implementation uses a 512×512 image and 256 PSFs, each of which is a 61×61 image array. We can handle up to 16k PSFs with no loss of throughput. (2) Image deconvolution is a highly parallel operation so our program runs very rapidly. A single MEM or RLM iteration requires less than 3 seconds of clock time and maintains a sustained performance of 1.1 Gflops. HST images can be deconvolved in a few minutes, rather than many hours as required on serial machines. This is an advantage when many different PSFs, background subtractions, etc., are being considered.

1. DECONVOLUTION OF HUBBLE SPACE TELESCOPE IMAGES

The spherical aberration errors associated with HST still produce diffraction limited information in the final images. The core, or Airy disk, of stellar images is the size of the diffraction limit of the HST mirror but contains only 20% of the photons (Burrows *et al.* 1991). The remaining 80% of the photons are distributed in a halo on the arcsecond scale size. For bright objects, deconvolution techniques can restore the images to the full diffraction limit creating images comparable to an unaberrated optical system (White and Allen 1990). Unfortunately the deconvolution techniques will not be able to push the faint end of the images to larger limiting magnitudes because the halo becomes lost in the noise of the images.

Most iterative deconvolution methods take a current guess of the true image, convolve with a PSF, and compare with the observed image. A correction term based on the residuals is determined and applied to the current guess; the process continues until

some convergence criteria are met. Common iterative techniques include the Maximum Entropy Method (MEM) (Cornwell and Evans 1985) and the Richardson-Lucy Method (RLM) (Richardson 1972; Lucy 1974).

From a deconvolution point of view, HST images have two atypical characteristics. First, because of the reimaging optics in the WF/PC imaging system, the point spread function is space variant. A space variant PSF is one where the shape of the PSF depends on the location in the final image; thus no single PSF can be used to accurately characterize the image. The most computationally intense process in iterative image reconstriction techniques is the convolution of image and PSF. For space invariant PSFs, the convolution of two arrays is the product of their Fourier transforms, and the fast Fourier transform (FFT) is an integral part of most deconvolution efforts. FFTs can not be used for the convolution of WF/PC images since the PSF is space variant.

The second atypical characteristic of WF/PC images is that, though PC images are sampled at the Nyquist frequency, WFC images are undersampled by a factor of two. Implicit in the use of FFTs is the assumption of Nyquist sampled images. If Fourier techiniques are used on undersampled images, aliasing becomes a problem and frequencies higher than the sampling frequency are aliased into lower spatial frequencies creating low frequency artifacts. In order to limit aliasing, the original image resolution must be degraded until the image becomes Nyquist sampled.

2. A PARALLEL SOLUTION

The Connection Machine is a massively parallel, single–instruction–multiple–data (SIMD) computer (Hillis 1987). The NRL CM-2 contains 16k processors, each with 128 kbyte of memory and access to floating point coprocessors. The geometry of the processors is hardware configured as a hypercube, and is software configured to mimic the geometry of the problem. Additional hardware includes a data vault of striped disks connected by high speed parallel buses, video frame generation capabilities, 14 inch removable optical disks, Sun and VAX front-end machines, and a T1 link into the University of Maryland internet node.

Our implemetation of an image space convolution algorithm on the CM-2 addresses both the issues of space variable PSFs and undersampled images in a robust, user friendly way. Our algorithm works in image space and does not use FFTs, thus the aliasing problem is minimized. We assume that there is a scale size over which the PSF can be considered space invariant. Each of these isoplanatic patches is assigned its own PSF. In the current implementation, isoplanatic patches range in size from 32×32 to 2×2 pixels with the PSF in these patches being 61×61 pixels. In the case of a space invariant PSF, all isoplanatic patches are assigned the same PSF. The convolution subroutine is microcoded in CMIS, the CM instruction set, and relies on detailed knowledge of the CM geometry and communication hardware. The subroutine is C or FORTRAN callable, and the calling program, which executes the iterative image reconstruction algorithm, is currently written in C*, a parallel extension of C++.

3. RESULTS

The code was benchmarked using both the MEM and RLM iterative techiniques. The MEM code was based on FORTRAN code provided by T. Cornwell of NRAO. WFC images of Saturn and the LMC open cluster NGC 1850 were provided by J. Westphal

and the WF/PC Instrument Development Team for testing of the algorithm. The limiting factor in our deconvolution efforts is a detailed knowledge of the PSF across the field of view. We have used PSF modeling software provided by P. Miller of Hughes Danbury. The TIM code developed at STScI is more accurate, but can not currently calculate the 256 PSFs required in a reasonable amount of time.

A total of 8 runs were made with the CM deconvolution/reconstruction package. These runs include all combinations of two images (Saturn and NGC 1850), two PSFs (observed and modeled), and two iterative techniques (MEM and RLM). The observed PSF was obtained by clipping an isolated stellar image from near the center of a sparse WFC image. The clipped PSF is then replicated 256 times to create our observed PSF. The modeled PSF consists of 256 calculated PSFs evenly spaced throughout the 512×512 image.

In the table we indicate the final values of χ^2, which is calculated from the difference between the raw image and the deconvolved image convolved with the PSF, as well as the number of iterations and the run time for the calculation. I/O takes another 40–90 seconds depending on whether the data is stored on the frontend disk of the CM datavault and on whether video or graphics output is desired. For comparison purposes, comparable runs on serial computers would require between 1 and 16 hours.

Note that the currently modeled space variant PSF gives results comparable to the observed space invariant PSF, but not significantly better. This is an indication of the lack of knowledge of the space variant properties of the PSF at the $< 10\%$ level. As understanding of the HST PSF improves, the results from the modeled PSF will be superior to those from the observed PSF. At that time, algorithms using space variant PSFs, such as the one described here, will yield results superior to those using a constant PSF.

Parallel Image Reconstruction Test Runs

Target	PSF	Method	χ^2	N_{iter}	Run Time
NGC 1850	observed	MEM	1.391	30	89 sec
NGC 1850	observed	RLM	1.229	20	
NGC 1850	modeled	MEM	1.533	30	
NGC 1850	modeled	RLM	1.358	20	
Saturn	observed	MEM	1.009	20	90 sec
Saturn	observed	RLM	0.865	20	
Saturn	modeled	MEM	1.000	20	
Saturn	modeled	RLM	0.860	20	

REFERENCES

Burrows, C. J., *et al.* 1991, *Ap. J. (Letters)*, **369**, L21.

Cornwell, T. J., and Evans, K. F. 1985, *Astr. Ap.*, **143**, 77.

Hillis, W. D. 1987, *Sci. Am.*, **256**, 108.

Lucy, L. B. 1974, *A. J.*, **79**, 745.

Richardson, W. H. 1972, *J. Opt. Soc. Am.*, **62**, 55.

White, R. L., and Allen, R. J. 1990, *The Restoration of HST Images and Spectra* (STScI: Baltimore).

ON ORBIT MEASUREMENT OF HST BAFFLE REJECTION CAPABILITY

by Pierre Y. Bély, Doris Daou and Olivia Lupie

Space Telescope Science Institute
3700 San Martin Drive
Baltimore, MD21218

1. HST BAFFLE DESIGN

HST is extremely well baffled against the effect of off-axis bright sources such as the sun, moon and bright earth. Pointing restrictions and the aperture door fully protect against any effect from the sun. Light from the moon and bright earth is allowed to enter HST's tube, but baffles prevent direct illumination of the focal plane. Light can reach the focal plane only after deflection by several baffles or via scatter due to mirror dust.

The mechanisms producing straylight in the focal plane fall into three regimes.

At angles, larger than 27 degrees, light only reaches the focal plane after bouncing several times between the outer baffles or when scattered by the primary mirror dust. The effect is essentially proportional to the dust coverage on the primary mirror.

For the middle angles, 15 to 27 degrees, light can reach the focal plane after bouncing from the rear of the outer baffle and secondary mirror baffle and subsequent reflection by the secondary mirror. In this regime, the focal illumination is essentially independent of the mirror dust.

For smaller angles, 15 degrees and below, light strikes the primary mirror, is scattered by dust, and reaches the focal plane after reflection by the secondary mirror. Light scattered or diffracted by other surfaces (e.g. secondary mirror spider) also contributes to focal plane straylight.

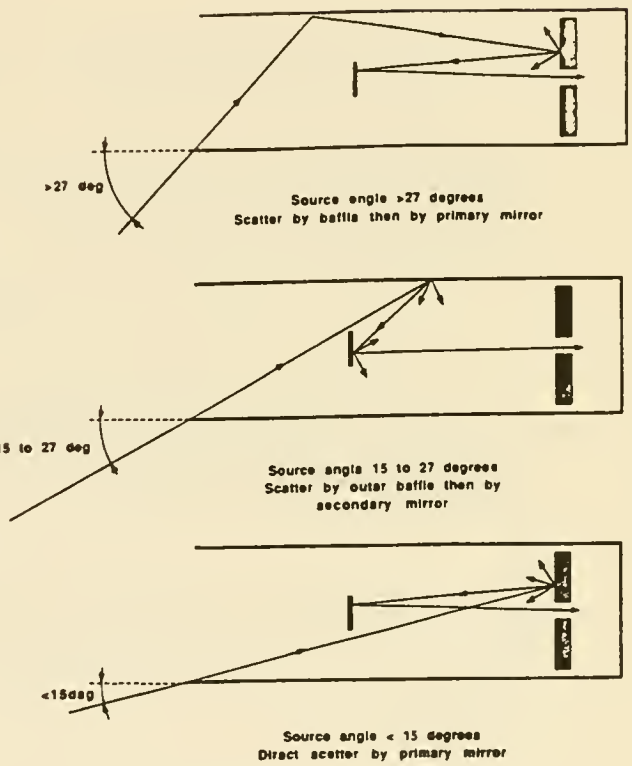

Figure 1 Scattering Regimes

The pre-launch determination of attenuation of off-axis light sources was made by Perkin Elmer and the Marshall Space Flight Center using computer modelling with the APART package and laboratory measurement of mirror dust scatter. The predicted attenuation factor is shown in Figure 2. The APART detailed model was not run for angles smaller than 15 degrees. In this domain, light from the off-axis source hits the primary mirror directly and the resulting scatter by dust on the mirror becomes the dominant source of straylight. We have determined the attenuation at angles smaller than 15 degrees by using a simplified analytic model for the mirror scatter and extrapolating the APART model for the other scattering sources.

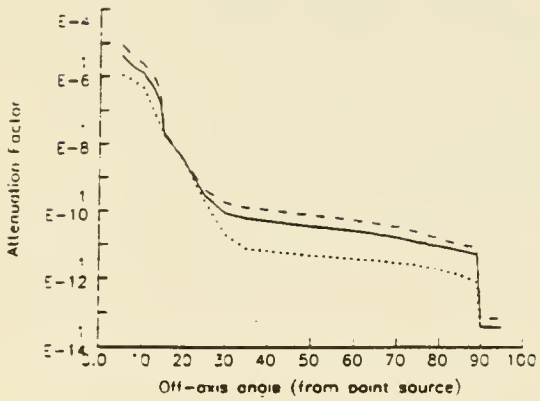

Figure 2 Predicted Baffle attenuation factor. The curves are for 0% (dotted), 2% (solid) and 5% (dashed) dust coverage on the primary mirror. The predicted pre-launch dust coverage was estimated at about 2% .

2. ON-ORBIT MEASUREMENTS OF STRAYLIGHT DUE TO OFF-AXIS SOURCES

For angles less than 30 degrees the attenuation of the baffling system was measured on orbit using the moon as a source and the Wide Field Camera as an area photometer. The test consisted of measuring the focal plane illumination as a function of wavelength (F284W(VUV), F336W(UV), F569W(V) and F675W(R)) at 4, 8 20 and 30 degrees from the full moon. The sky background for the faintest exposure levels (20 and 30 degrees) was measured at the subsequent new moon.

The results are summarized in Figure 3.

The on orbit data essentially confirms the validity of the detailed model in the 15 to 30 degree domain. At 30 degrees, straylight from the moon is negligible compared to the zodiacal light level, as it was required by HST specifications.

The 8 degree data confirms the prediction made with the simplified model but the 4 degree measurement is about 3 times brighter. This is likely explained by an underestimation of the complex scattering processes by surfaces other than the mirror (baffle,spider etc..) at very low angles.

These results obtained at low angles where dust on the primary mirror is a primary source of straylight suggest that the amount of dust on the primary mirror is not substantially different from pre-launch estimates (2%).

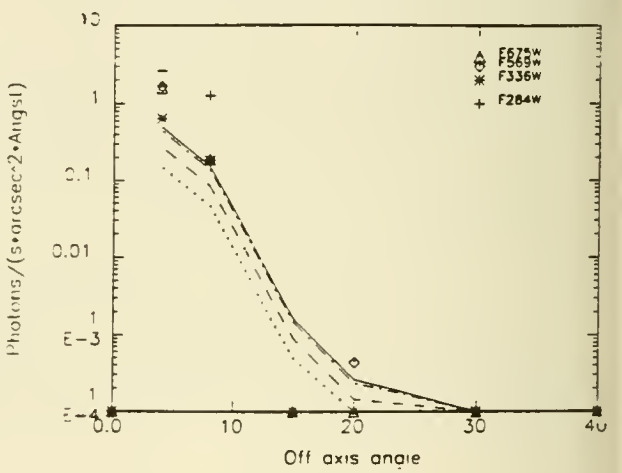

Figure 3 Illumination of the focal plane by the full moon as a function of the off-axis angle. The on-orbit measured data is shown by point symbols for the various wavelengths and is to be compared to the predicted level shown as lines (solid:V, dotted:VUV, dashed:UV, dot-dashed:R). The UV data (F284W) is affected by red leak in the WFPC and should not be relied upon.

3. CONCLUSION

In conclusion, the results of this test indicate that the design requirement concerning straylight from the moon has been met. The test confirms the validity of the model in the 15 to 30 degree range, and hence suggests that the design requirement for the bright earth has also been satisfied (straylight less than the zodiacal light at 70 degrees from the bright earth limb). However, we intend to confirm the level of straylight at large angles by measuring the background in selected WFPC frames taken over the bright earth.

APPENDIX

Scheduling of Science Observations and Subsequent Data Processing

TRANSFORMATION: THE LINK BETWEEN THE PROPOSAL AND THE HUBBLE SPACE TELESCOPE DATABASE

M.L. McCollough, H.H. Lanning, and K.E. Reinhard
Computer Sciences Corporation/Space Telescope Science Institute

Overview

In order for a scientific program, specified in a proposal, to be executed by HST the information in the proposal must be translated into a set of parameters which can be interpreted and used by the Science Planning and Scheduling System (SPSS), Science Commanding System (SCS), Observation Support System (OSS), and Post Observation Data Processing System (PODPS). The conversion of the proposal is performed by the "Transformation" software. Transformation is a rule based body of software, written in LISP, designed to convert the proposal into a series of relations which can be loaded into the Proposal Management Database (PMDB). In addition, Transformation provides products which are used by Science Planning Interactive Knowledge Environment (SPIKE) to do long term science planning. Figure 1 shows the flow of information from the proposal through Transformation into SPSS:

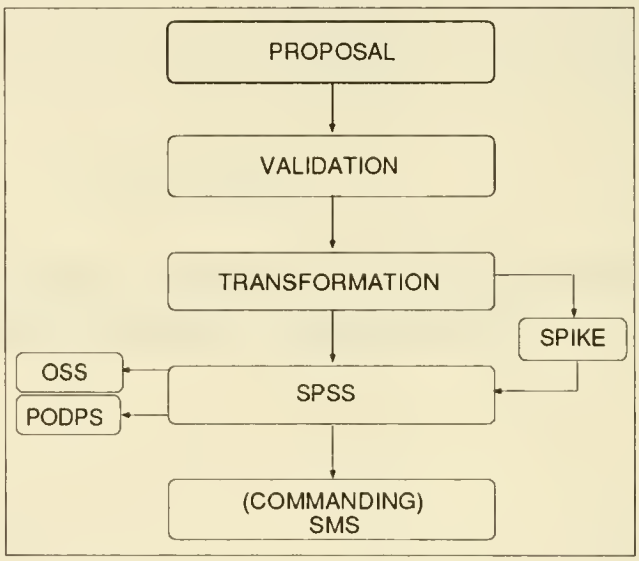

Figure 1. This diagram shows how information from the proposal flows through Transformation to the various operational systems.

The Proposal and Validation

Observers initially enter their observing projects into the system through the proposal. An example of a proposal is shown in Figure 2. The format and outline of how to create a proposal are contained in the "Hubble Space Telescope Proposal Instructions". The major points of information from the proposal are the following:

(A) Target Information: All the information necessary to observe the target of interest must be given (position, positional uncertainty, magnitude, etc.). It is from this information that the pointing of the spacecraft and the guide stars used are determined.

(B) Exposures: These are the basic building blocks of the proposal and represent the observations which will be performed by the spacecraft.

(1) **Instrument:** The scientific instrument used (*WFPC, FOC, FOS, GHRS, HSP, or FGS*).
(2) **Mode of Operation:** The way in which the instrument is used (*IMAGE, ACCUM, RAPID, etc.*).
(a) *Optional Parameters*: Adjustments to various instrument parameters for each mode of operation.

(3) **Number of Observations:** A single line can result in a multiple number of observations.
(4) **Exposure Time:** This is the length of time that the instrument will collect photons. This can critically determine how an observation is performed and if the observation is possible.
(5) **Special Requirements:** These determine how and when the observations are performed.
(a) *Structure*: The order in which exposures are executed relative to one another is determined (*SEQ, GROUP, etc.*).
(b) *Timing*: When exposures occur relative to each other and relative to an absolute time (*AT, AFTER, etc.*).
(c) *Real Time Contacts*: The use of real time contacts (*TDRSS:Tracking and Data Relay Satellite System*) with the spacecraft are determined (*INT ACQ, RT ANALYSIS, etc.*).
(6) **Logsheet Comments:** It is through exposure level comments that special scheduling and commanding requirements of exposures can be noted (not always completely describable by the special requirements).

(C) Proposal Abstract and Description: In addition to the logsheet comments the proposal abstract and description relay much of the intent of the proposal to the people doing the scheduling and commanding of the spacecraft.

EXPOSURE LOGSHEET Id = 251(P)
Page: 0 of 0

1 Ln Nm	2 Seq Nam	3 Target Name	4 Instr Config	5 Oper. Mode	6 Aper orFOV	7 Spectral Element	8 Centrl Waveln	9 Optional Parameters	10 Num Exp	11 Time	12 S/N Rel.Time	13 Flx Ref	14 Pr	15 Special Requirements
1		NGC224	FOS/BL	ACQ	4.3	MIRROR			1	100S	1			INT ACQ FOR 2
2		NGC224	FOS/BL	ACCUM	0.5-PAI	G270H	2700	STEP-PATT=STAR-SKY-BKG	3	200S	1			
3		NGC224	FOS/BL	ACCUM	0.5	G190H	1900	STEP-PATT-DEF	1	100S	1			
4		NGC224	FOS/BL	ACCUM	0.25-PA	G130H	1300	STEP-TIME=1.5	1	300S	1			
5		NGC224	FOS/BL	ACCUM	0.3	G190H	1900	POLSCAN-0B	1	80S	1			
6		NGC224	FOS/RD	ACQ/FIRMWARE	4.3	MIRROR		MAP=BOTH, BRIGHT=4500.0 FAINT=300.0, SKY=20.0	1	300S	1			ONBOARD ACQ FOR 7
7		NGC224	FOS/RD	ACQ/PEAK	0.3	G570H	5700	TYPE=UP, SEARCH-SIZE=3, SCAN-STEP=0.2	1	15S	1			ONBOARD ACQ FOR 8
8		NGC224	FOS/RD	ACCUM	0.3	G570H	5700		1	300S	1			
9		NGC224	FOS/RD	ACCUM	0.3	G570H	5700	POLSCAN-4A	2	100S	1			
10		NGC224	FOS/RD	RAPID	0.3	G570H	5700	SUB-STEP=2, COMB=NO, READ-TIME=2.5	1	90S	1			
11		HZHER	FOS/RD	ACQ/BINARY	4.3	MIRROR		BRIGHT=4120.0 FAINT=25.0, NTHSTAR=3	1	300S	1			ONBOARD ACQ FOR 12
12		HZHER	FOS/RD	ACQ/PEAK	2.0-BAR	G780H		TYPE=DEF	1	20S	1			ONBOARD ACQ FOR 13
13		HZHER	FOS/RD	PERIOD	2.0-BAR	G780H	7800	BINS=6, SUB-STEP=2, CYCLE-TIME=500, DATA-RATIO=5.0	1	1500S	1			AT21-AUG-89:13:08
15		HZHER	FOS/RD	IMAGE	4.3	G780H		Y-SIZE=18, Y-SPACE=18, X=5, Y=-3	1	600S	1			

Figure 2. The table above is an example of a typical exposure logsheet. The exposure logsheet is how the observer expresses what observation needs to be performed. It is from this information that Transformation will create the observing structure and populate the PMDB.

The proposal is submitted into the system through the Proposal Entry Processor (PEP) System. It is while the proposal is in PEP that exposures and defined sequences are expanded. Also, linkages between exposures are determined (both in ordering and timing of observations). Before the proposal reaches Transformation, it must be processed by "Validation" in the PEP system. Validation is software that checks the proposal syntax and populates the Internal Database (IDB). It is from the IDB that Transformation gets the files, containing the proposal information, with which it will populate the PMDB.

Observing Structure

It is necessary for Transformation to create the observing structure which will be used by SPSS. The hierarchy created by Transformation is (from the smallest to largest structure):

I.	Exposure (Ex)
II.	Alignment (Al)
III.	Obset (Ob)
IV.	Scheduling Unit (SU)

(I) Exposure:

This is the basic building block of a proposal. Normally there is a one to one correspondence between an exposure and a logsheet entry on the proposal. Information on the observation such as, Scientific Instrument (SI) used, mode of operation, spectral element used, and aperture used are determined at this level. It is at this level most of the information necessary to command the SIs is contained. Also contained at this level is the information that PODPS finds necessary to do the post-processing of the observations.

(II) Alignment:

Exposures are grouped into alignments. An alignment deals primarily with the pointing of the V1 axis of the spacecraft. Target position, roll of the spacecraft, and the timing of the observation which are used for scheduling are determined at this level. Also, the operational states of the detectors are fixed at the alignment level.

(III) Obset:

Alignments are in turn grouped into larger structures called Observation sets (Obsets). Obsets are groups of alignments which use the same type of pointing control. In particular, groups of alignments which can use the same guide stars are often grouped together into the same Obsets.

(IV) Scheduling Unit:

Finally, Obsets are built into large units called Scheduling Units (SUs). SUs are sets of Obsets which can be scheduled all at one time. SUs are the basic units which are used to build calendars in SPSS. It is between SUs that time linkages are done.

Transformation takes exposures created from the proposal and orders and merges them to form the observing structure. Once the order has been determined by Transformation, adjacent exposures are merged into alignments by a set of merging rules. In turn, Transformation will merge adjacent alignments into Obsets, and Obsets into SUs. The merging rules consist of reasons to merge and reasons not to merge. If there is any reason not to merge (no matter how many reasons there are to merge) the exposure (alignment or Obset) is not merged. Also, a lack of a reason to merge or not to merge is treated as a reason not to merge. For the test proposal given above a summary of the structure (and timing) determined by Transformation is shown in Figure 3.

Alignment Times

Another task of Transformation is to calculate the time it takes to perform the observation. This includes not only the exposure time but also all of the overhead necessary to operate the SI. The basic alignment time calculations for an observation are given by the algorithm shown in Figure 4.

TRANSFORMATION VERSION 12.0
GENERATED 6-26-1991 14:34:46
PROPOSAL 251 VERSION P
TRANSFORMED USING FULL-TRANS

PEPSI EXPOSURE	SEQU LINE NUM	OBSET ID	ALIGN ID	EXP ID	EXP TIME	AL TIME	SU ID	PRIM SU	TOLERANCE	DELTA
1.0000000		01	01	01	492	492	0025101	002501	000:00:00:00	000:00:00:00
INT-ACQ-DEC		01	02	01		960		0025101	000:00:00:00	000:00:00:00
INT-ACQ-UPLINK		01	03	01		510		0025101	000:00:00:00	000:00:00:00
2.0000000#001		01	04	01	464	464		0025101	000:00:00:00	000:00:00:00
2.0000000#002		01	05	01	407	407		0025101	000:00:00:00	000:00:00:00
2.0000000#003		01	06	01	407	407		0025101	000:00:00:00	000:00:00:00
3.0000000		01	07	01	454	454		0025101	000:00:00:00	000:00:00:00
4.0000000		01	08	01	689	689		0025101	000:00:00:00	000:00:00:00
5.0000000		01	09	01	1078	1077		0025101	000:00:00:00	000:00:00:00
HOME		01	0A	01		292		0025101	000:00:00:00	000:00:00:00
6.0000000C		02	01	01	1041	1040	0025102	0025102	000:00:00:00	000:00:00:00
6.0000000F		02	02	01	1025	1024		0025102	000:00:00:00	000:00:00:00
SETUP		02	03	01		948		0025102	000:00:00:00	000:00:00:00
7.0000000		02	03	02	948	948		0025102	000:00:00:00	000:00:00:00
8.0000000		02	04	01	535	534		0025102	000:00:00:00	000:00:00:00
9.0000000#001		02	05	01	568	567		0025102	000:00:00:00	000:00:00:00
9.0000000#002		02	06	01	594	593		0025102	000:00:00:00	000:00:00:00
10.0000000		02	07	01	276	276		0025102	000:00:00:00	000:00:00:00
HOME		02	08	01		234		0025102	000:00:00:00	000:00:00:00
11.0000000		03	01	01	862	862	0025103	0025103	000:00:00:00	000:00:00:00
SETUP		03	02	01		1235		0025103	000:00:00:00	000:00:00:00
12.0000000		03	02	02	1235	1235		0025103	000:00:00:00	000:00:00:00
HOME		03	03	01		151		0025103	000:00:00:00	000:00:00:00
13.0000000		04	01	01	1957	1957		0025103	000:00:00:00	000:00:00:00
15.0000000		04	02	01	999	4342		0025103	000:00:00:00	000:00:00:00
HOME		04	03	01		0		0025103	000:00:00:00	000:00:00:00

Figure 3. The example above (Summary File) shows the structure and timing which resulted from the logsheet shown in figure 2.

AL_TIME	=	AL_BEGIN + S (EXP_TIME) + AL_END
AL_BEGIN	=	Alignment specific overheads which occur at the beginning of the alignment.
EXP_TIME	=	Overheads and exposure time to complete a single exposure of the alignment (this quantity is summed over all the exposures in the alignment).
AL_END	=	Alignment specific overhead which occurs at the end of the alignment.
EXP_TIME	=	PRE_OVERHEAD + EXPTIME + POST_OVERHEAD
PRE_OVERHEAD	=	Exposure level overheads necessary to prepare the SI for the observation and command the SI to perform the observation.
EXPTIME	=	Time to perform the exposure and overheads incurred while taking the exposure.
POST_OVERHEAD	=	Exposure level overheads necessary to read out the detector and return the detector to a state necessary to perform the next observation.

Figure 4. Above is the basic algorithm used to calculate alignment times.

Populating the PMDB

The final product from Transformation which is used to load the PMDB is the assignment file. The assignment file consists of a set of relations (see list below) which describe the proposal, i.e. the way in which the observations will be done and how they will be scheduled. This file is in essence an IQL (Interactive Query Language) file [in the near future to be converted into an SQL (Standard Query Language) file] which is directly loaded into the PMDB. An example of the PMDB values is shown in Figure 5.

Relation	System Used By	Description
Exposure Level:		
QEXPOSURE	1,2,3	Exposure Level Information
QELOGSHEET	2	Logsheet Information
QESIPARM	2	SI Parameter Information
QECOMMENTS	1	Exposure Level Comments
QGACTINST	1,2	SPSS-SCS Interface
Alignment Level:		
QALIGNMENT	1	Alignment Level Information
QAPOSITION	1	Pointing Information
QASI_STATES	1,2	Detector State Information
QACOMMENTS	1, 4	Alignment Level Comments
Obset Level:		
QBS_OBSET	1	Obset Level Information
QBWINDOWS	1	Scheduling Time Windows
SU Level:		
QSCHEDULING	1	SU Level Linkage Information*
QSBRANCHING	1	SU Level Linkage Information*
Target Level:		
QTARGETS	1	Target Information
QTSYNONYMS	1	Target Related Information
QTCOMMENTS	1	Target Level Comments
Proposal Level:		
QPDESCRIP	1	Proposal Information
QPABSTRACT	3	Proposal Information
QPKEYWORDS	1	Proposal Information
QPCOPROPSER	3	Proposer Information
QPERSONNEL	1	Proposer Information
QPPCOMMENTS	1	Proposal Level Comments

1- SPSS 2- SCS 3- PODPS 4- OSS

* In the near future the time linkage between SUs currently contained in these relations will be placed in the new relations QSLINK_INFO and QSLINK_SPEC.

Test Scheduling and SMS Generation

After the assignment file has been loaded into the PMDB, the "Proposal Preparation Group" of SPSS personnel must complete the analysis and processing of the proposal for scheduling and execution. This consists of three things:

(1) Operational Problem Report (OPR) Fixups: Transformation has known problems and deficiencies. These issues must be addressed and fixed for proposals which are loaded into the PMDB. Also, as Transformation evolves and changes the new products must be examined for potential problems.

(2) Test Scheduling: Once all fixups are completed on a proposal it is then test scheduled. The proposal is scheduled by itself on a test calendar of one week (the week it is supposed to first be observed if possible). This will allow scheduling concerns and problems to be addressed in advance of scheduling on the Flight Calendar.

(3) Test Science Mission Specification (SMS) Generation: Once the test calendar has been made, it is then run through the SPSS software to produce a test SMS. The SMS is a detailed listing (in time) of the maneuvering and commanding of the spacecraft. It is during this stage that problems in the proposal which relate to the commanding of the SIs will be uncovered. If problems are found then fixes to remedy these problems are made to the proposal.

After all three of the above steps have been sucessfully completed the proposal is ready for scheduling for flight operations by SPSS.

Figure 5. Below is an example of a portion of an assignment file that is used to load the PMDB

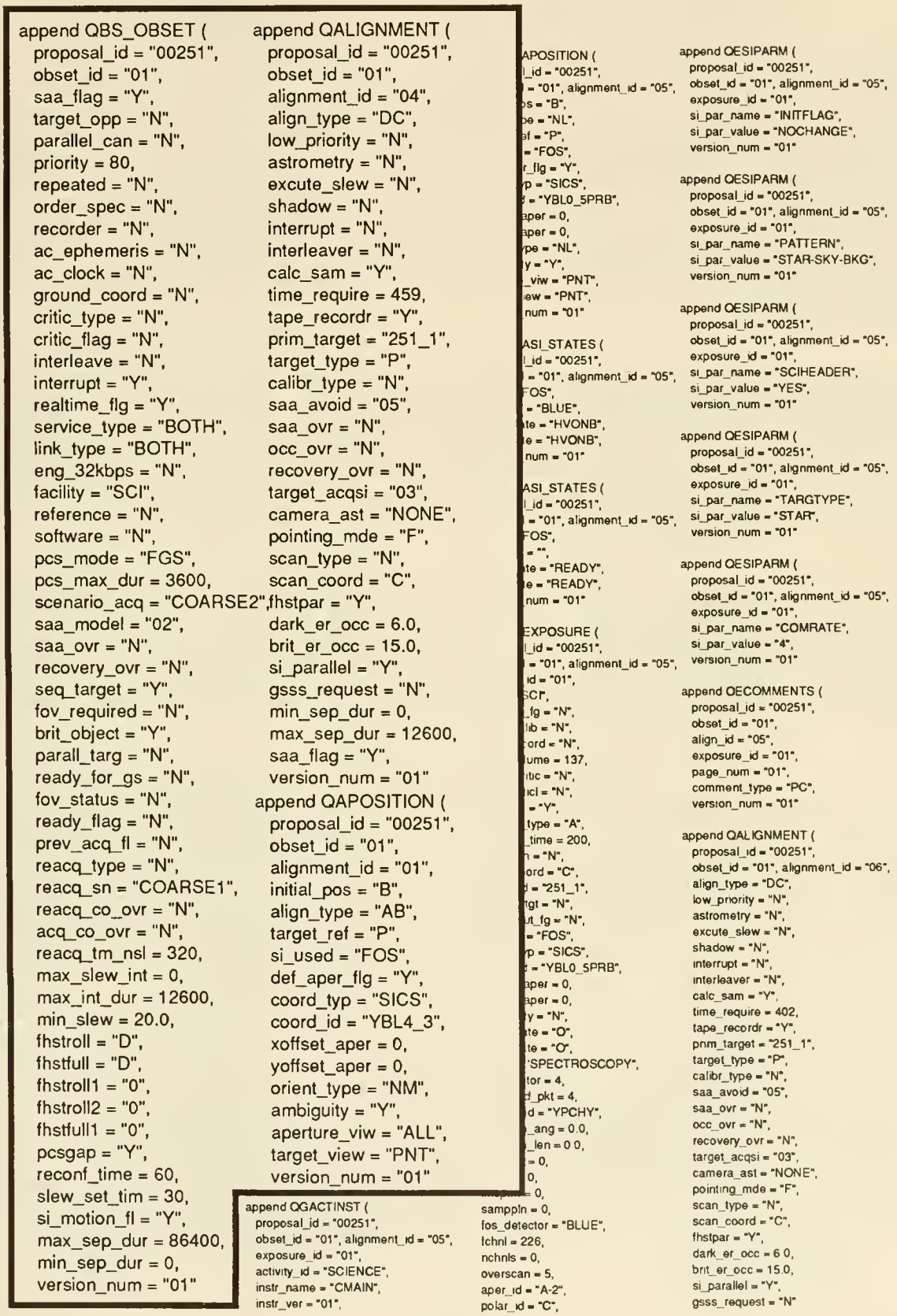

```
append QBS_OBSET (
  proposal_id = "00251",
  obset_id = "01",
  saa_flag = "Y",
  target_opp = "N",
  parallel_can = "N",
  priority = 80,
  repeated = "N",
  order_spec = "N",
  recorder = "N",
  ac_ephemeris = "N",
  ac_clock = "N",
  ground_coord = "N",
  critic_type = "N",
  critic_flag = "N",
  interleave = "N",
  interrupt = "Y",
  realtime_flg = "Y",
  service_type = "BOTH",
  link_type = "BOTH",
  eng_32kbps = "N",
  facility = "SCI",
  reference = "N",
  software = "N",
  pcs_mode = "FGS",
  pcs_max_dur = 3600,
  scenario_acq = "COARSE2",
  saa_model = "02",
  saa_ovr = "N",
  recovery_ovr = "N",
  seq_target = "Y",
  fov_required = "N",
  brit_object = "Y",
  parall_targ = "N",
  ready_for_gs = "N",
  fov_status = "N",
  ready_flag = "N",
  prev_acq_fl = "N",
  reacq_type = "N",
  reacq_sn = "COARSE1",
  reacq_co_ovr = "N",
  acq_co_ovr = "N",
  reacq_tm_nsl = 320,
  max_slew_int = 0,
  max_int_dur = 12600,
  min_slew = 20.0,
  fhstroll = "D",
  fhstfull = "D",
  fhstroll1 = "0",
  fhstroll2 = "0",
  fhstfull1 = "0",
  pcsgap = "Y",
  reconf_time = 60,
  slew_set_tim = 30,
  si_motion_fl = "Y",
  max_sep_dur = 86400,
  min_sep_dur = 0,
  version_num = "01"

append QALIGNMENT (
  proposal_id = "00251",
  obset_id = "01",
  alignment_id = "04",
  align_type = "DC",
  low_priority = "N",
  astrometry = "N",
  excute_slew = "N",
  shadow = "N",
  interrupt = "N",
  interleaver = "N",
  calc_sam = "Y",
  time_require = 459,
  tape_recordr = "Y",
  prim_target = "251_1",
  target_type = "P",
  calibr_type = "N",
  saa_avoid = "05",
  saa_ovr = "N",
  occ_ovr = "N",
  recovery_ovr = "N",
  target_acqsi = "03",
  camera_ast = "NONE",
  pointing_mde = "F",
  scan_type = "N",
  scan_coord = "C",
  fhstpar = "Y",
  dark_er_occ = 6.0,
  brit_er_occ = 15.0,
  si_parallel = "Y",
  gsss_request = "N",
  min_sep_dur = 0,
  max_sep_dur = 12600,
  saa_flag = "Y",
  version_num = "01"

append QAPOSITION (
  proposal_id = "00251",
  obset_id = "01",
  alignment_id = "01",
  initial_pos = "B",
  align_type = "AB",
  target_ref = "P",
  si_used = "FOS",
  def_aper_flg = "Y",
  coord_typ = "SICS",
  coord_id = "YBL4_3",
  xoffset_aper = 0,
  yoffset_aper = 0,
  orient_type = "NM",
  ambiguity = "Y",
  aperture_viw = "ALL",
  target_view = "PNT",
  version_num = "01"

append QGACTINST (
  proposal_id = "00251",
  obset_id = "01", alignment_id = "05",
  exposure_id = "01",
  activity_id = "SCIENCE",
  instr_name = "CMAIN",
  instr_ver = "01",

APOSITION (
l_id = "00251",
= "01", alignment_id = "05",
os = "B",
be = "NL",
ef = "P",
= "FOS",
r_flg = "Y",
/p = "SICS",
= "YBL0_5PRB",
aper = 0,
aper = 0,
/pe = "NL",
y = "Y",
_viw = "PNT",
iew = "PNT",
_num = "01"

ASI_STATES (
l_id = "00251",
= "01", alignment_id = "05",
FOS",
= "BLUE",
te = "HVONB",
e = "HVONB",
_num = "01"

ASI_STATES (
l_id = "00251",
= "01", alignment_id = "05",
FOS",
= "",
te = "READY",
e = "READY",
_num = "01"

EXPOSURE (
l_id = "00251",
= "01", alignment_id = "05",
id = "01",
SCI",
_fg = "N",
lib = "N",
ord = "N",
ume = 137,
ttic = "N",
ncl = "N",
= "Y",
_type = "A",
_time = 200,
n = "N",
ord = "C",
d = "251_1",
rgt = "N",
ut_fg = "N",
= "FOS",
/p = "SICS",
= "YBL0_5PRB",
aper = 0,
aper = 0,
y = "N",
te = "O",
te = "O",
"SPECTROSCOPY",
tor = 4,
d_pkt = 4,
d = "YPCHY",
_ang = 0.0,
_len = 0.0,
= 0,
0,
= 0,
samppln = 0,
fos_detector = "BLUE",
fchnl = 226,
nchnls = 0,
overscan = 5,
aper_id = "A-2",
polar_id = "C",

append QESIPARM (
  proposal_id = "00251",
  obset_id = "01", alignment_id = "05",
  exposure_id = "01",
  si_par_name = "INITFLAG",
  si_par_value = "NOCHANGE",
  version_num = "01"

append QESIPARM (
  proposal_id = "00251",
  obset_id = "01", alignment_id = "05",
  exposure_id = "01",
  si_par_name = "PATTERN",
  si_par_value = "STAR-SKY-BKG",
  version_num = "01"

append QESIPARM (
  proposal_id = "00251",
  obset_id = "01", alignment_id = "05",
  exposure_id = "01",
  si_par_name = "SCIHEADER",
  si_par_value = "YES",
  version_num = "01"

append QESIPARM (
  proposal_id = "00251",
  obset_id = "01", alignment_id = "05",
  exposure_id = "01",
  si_par_name = "TARGTYPE",
  si_par_value = "STAR",
  version_num = "01"

append QESIPARM (
  proposal_id = "00251",
  obset_id = "01", alignment_id = "05",
  exposure_id = "01",
  si_par_name = "COMRATE",
  si_par_value = "4",
  version_num = "01"

append QECOMMENTS (
  proposal_id = "00251",
  obset_id = "01",
  align_id = "05",
  exposure_id = "01",
  page_num = "01",
  comment_type = "PC",
  version_num = "01"

append QALIGNMENT (
  proposal_id = "00251",
  obset_id = "01", alignment_id = "06",
  align_type = "DC",
  low_priority = "N",
  astrometry = "N",
  excute_slew = "N",
  shadow = "N",
  interrupt = "N",
  interleaver = "N",
  calc_sam = "Y",
  time_require = 402,
  tape_recordr = "Y",
  prim_target = "251_1",
  target_type = "P",
  calibr_type = "N",
  saa_avoid = "05",
  saa_ovr = "N",
  occ_ovr = "N",
  recovery_ovr = "N",
  target_acqsi = "03",
  camera_ast = "NONE",
  pointing_mde = "F",
  scan_type = "N",
  scan_coord = "C",
  fhstpar = "Y",
  dark_er_occ = 6.0,
  brit_er_occ = 15.0,
  si_parallel = "Y",
  gsss_request = "N"
```

PROPOSAL PREPARATION BY SPSS FOR SCHEDULING ON THE HUBBLE SPACE TELESCOPE

K.E. REINHARD, H.H. LANNING, and W.M. WORKMAN, III
Computer Sciences Corporation / Space Telescope Science Institute

Overview

Preparation of a proposal for execution on board the Hubble Space Telescope encompasses a great deal of manually intensive work by Science Planning and Scheduling System (SPSS) personnel. The preparation task includes tracking of the work status, detailed analysis of the structure and contents of the proposal, modification of the database values as required for proper execution onboard, generation of scheduling windows, test scheduling, and incorporation of the commanding and proposal changes necessary for execution. This preparation process is shown in the flow diagram on the next page. Throughout the process, the products are analyzed for potential errors in order to deliver a schedulable proposal. The test products are reviewed internally, and upon approval, delivered to flight preparation personnel within SPSS for guide star processing and final preparation for flight.

PMDB Load

Upon receipt of a proposal Delivery Notice from the Science Planning Branch (SPB), the Assignment File and Summary File which contain the proposal structure information, science and spacecraft activities, etc. are transferred to the Science Operations Ground System (SOGS) by Science Planning & Scheduling System (SPSS) personnel. The Assignment File, an IQL/SQL language file, is then loaded into the Proposal Management Database (PMDB). As part of the loading process, Scheduling Windows are set for the planned scheduling time frame, link set information is established, and a number of standardized database values are input based upon current spacecraft/scheduling requirements.

Proposal Structure Review

Initial analysis of the proposal structure focuses on the evaluation of the correctness of the activities desired by the proposer. Such activities include looking for the proper arrangement of Interactive Target Acquisitions, the nature of Interruptions allowed, the combination of exposures in a given Observation Set (Obset), etc. If the structure is not consistent with the requirements of the proposal, or major Transformation problems are identified, the proposal will be returned to SPB along with the needed information to make the proposal schedulable. SPB then reworks the proposal and redelivers it to SPSS.

TRANSFORMATION OPRs

Transformation software problems or deficiencies identified with the products must be addressed prior to the final preparation and testing of the proposal to be scheduled. A list of Operations Problems Reports (OPRs) is reviewed in detail by examining the database values loaded into the various relations. If a problem is deemed to exist for a given case, the database is modified in accordance with the OPR. Following completion of the OPR analysis, the Obsets and Scheduling Units (SUs) may then be updated in order to prepare the data for test scheduling. The list of Transformation OPRs is updated as necessary as new OPRs are submitted and others fixed and installed in order to maintain as current and viable an operational system as possible. All stages of activities including the loading, review of OPRs, and subsequent preparation and testing are recorded in a History File in order to track all proposal work from input to final execution on board the spacecraft.

Updating

After the initial proposal preparation has been completed the Obset data must be updated. The updating process involves generation of Space Telescope pointing data for single or multiple Obsets. The pointing data consists of calculation of target RA and DEC and aperture position in the Space Telescope V2-V3 coordinate plane, and orientation data for all underlying alignments and exposures. The updating process has to be executed any time changes are made to targets, alignments, or exposures of an observation set. The SU updating process is executed to prepare scheduling windows, observation times and user entered Science Instrument reconfiguration data. User entered values reflecting the targeted scheduling time are used during updating to determine the available windows. The windows calculated are 1) TV - Target dependent general visibility windows, which include the Sun and

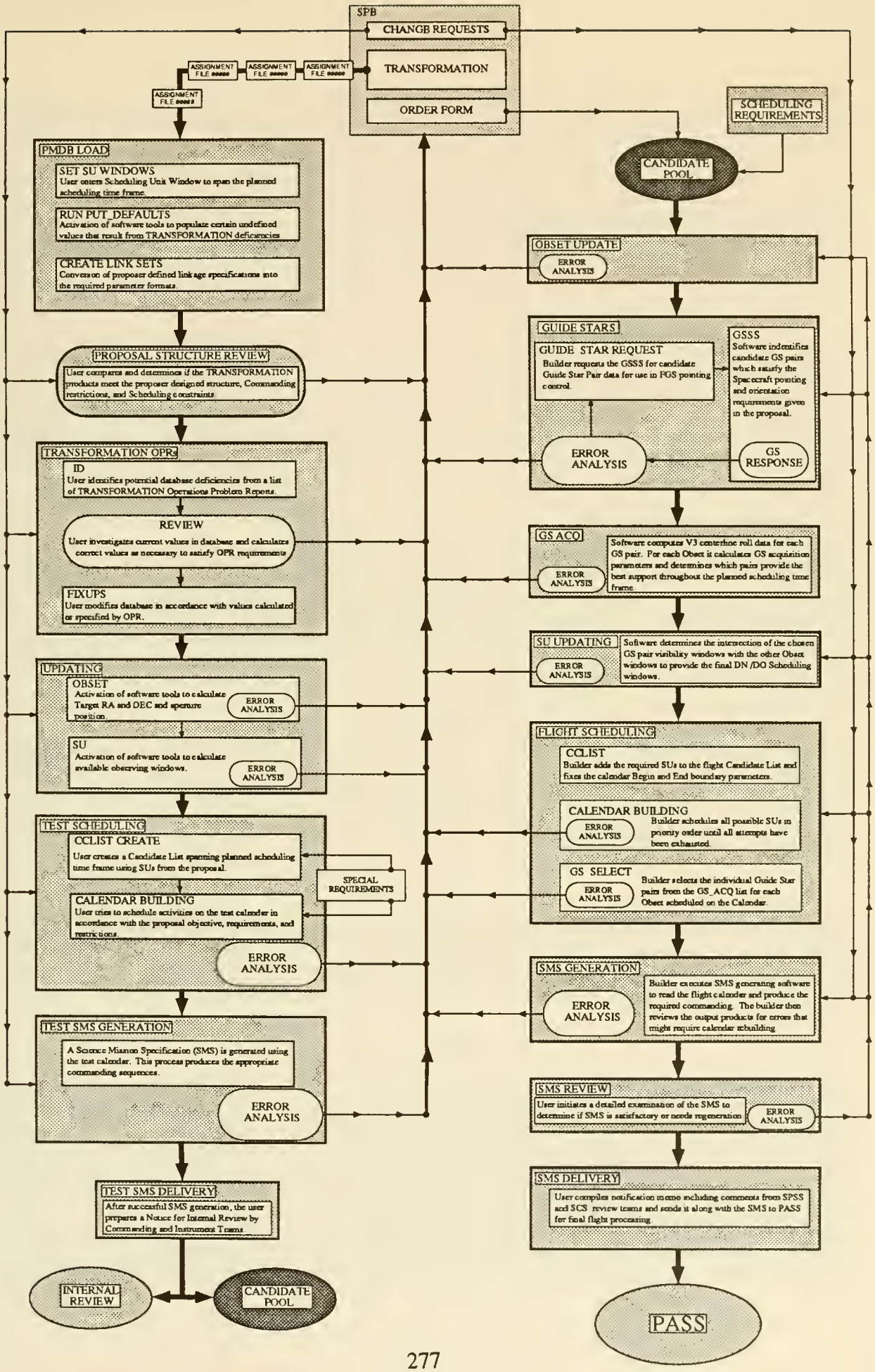
SPB
CHANGB REQUESTS
TRANSFORMATION
ORDER FORM
ASSIGNMENT FILE
ASSIGNMENT FILE
ASSIGNMENT FILE
ASSIGNMENT FILE
SCHEDULING REQUIREMENTS
CANDIDATE POOL
PMDB LOAD
SET SU WINDOWS
User enters Scheduling Unit Window to span the planned scheduling time frame.
RUN PUT_DEFAULTS
Activation of software tools to populate certain undefined values that result from TRANSFORMATION deficiencies
CREATE LINK SETS
Conversion of proposer defined linkage specifications into the required parameter formats.
OBSET UPDATE
ERROR ANALYSIS
PROPOSAL STRUCTURE REVIEW
User compares and determines if the TRANSFORMATION products meet the proposer designed structure, Commanding restrictions, and Scheduling constraints
GUIDE STARS
GUIDE STAR REQUEST
Builder requests the GSSS for candidate Guide Star Pair data for use in FGS pointing control.
GSSS
Software indentifies candidate GS pairs which satisfy the Spacecraft pointing and orientation requirements given in the proposal.
GS RESPONSE
ERROR ANALYSIS
TRANSFORMATION OPRs
ID
User identifies potential database deficiencies from a list of TRANSFORMATION Operations Problem Reports.
REVIEW
User investigates current values in database and calculates correct values as necessary to satisfy OPR requirements
FIXUPS
User modifies database in accordance with values calculated or specified by OPR.
GS ACQ
Software computes V3 centerline roll data for each GS pair. For each Obset it calculates GS acquisition parameters and determines which pairs provide the best support throughout the planned scheduling time frame
ERROR ANALYSIS
SU UPDATING
Software determines the intersection of the chosen GS pair visibility windows with the other Obset windows to provide the final DN /DO Scheduling windows.
ERROR ANALYSIS
UPDATING
OBSET
Activation of software tools to calculate Target RA and DEC and aperture position.
ERROR ANALYSIS
SU
Activation of software tools to calculate available observing windows.
ERROR ANALYSIS
FLIGHT SCHEDULING
CCLIST
Builder adds the required SUs to the flight Candidate List and fixes the calendar Begin and End boundary parameters.
CALENDAR BUILDING
Builder schedules all possible SUs in priority order until all attempts have been exhausted.
ERROR ANALYSIS
GS SELECT
Builder selects the individual Guide Star pairs from the GS_ACQ list for each Obset scheduled on the Calendar.
ERROR ANALYSIS
TEST SCHEDULING
CCLIST CREATE
User creates a Candidate List spanning planned scheduling time frame using SUs from the proposal.
SPECIAL REQUIREMENTS
CALENDAR BUILDING
User tries to schedule activities on the test calendar in accordance with the proposal objective, requirements, and restrictions.
ERROR ANALYSIS
SMS GENERATION
Builder executes SMS generating software to read the flight calendar and produce the required commanding. The builder then reviews the output products for errors that might require calendar rebuilding
ERROR ANALYSIS
TEST SMS GENERATION
A Science Mission Specification (SMS) is generated using the test calendar. This process produces the appropriate commanding sequences.
ERROR ANALYSIS
SMS REVIEW
User initiates a detailed examination of the SMS to determine if SMS is satisfactory or needs regeneration
ERROR ANALYSIS
SMS DELIVERY
User compiles notification memo including comments from SPSS and SCS review teams and sends it along with the SMS to PASS for final flight processing.
TEST SMS DELIVERY
After successful SMS generation, the user prepares a Notice for Internal Review by Commanding and Instrument Teams.
INTERNAL REVIEW
CANDIDATE POOL
PASS

Moon avoidance angle, 2) SN - Roll Normal windows and SO - Roll Off-Nominal windows which are based on the aperture position, target position, orientation type and V3 position angle, 3) RN - Restricted Normal windows and RO - Restricted Off-Nominal windows which are based on the guide star acquisition data set results. 4) PC - Phase Critical windows, 5) SF - Surface Feature windows, 6) DN - Derived Normal windows and DO - Derived Off-Nominal windows which are the intersection of TV, SN, SO, RN, RO, PC, and SF windows, and 7) SU - Scheduling Unit windows which are calculated to bound the DN and DO windows. The SU updating must be done before a candidate can be added to a Candidate List (CCLIST). SU updating must be repeated if any modifications are done to the underlying Obsets, alignments , and exposures such as a new Guide Star request, changes to science times, PCS Scenario usage, alignment parameters, etc.

Test Scheduling

Following the successful completion of Obset/SU updating, or resolution of updating problems, the candidate SUs contained within the proposal are placed onto a CCLIST. All candidates which can be scheduled usually will be, with the exception of large groups of identical SUs, in which case a small subset will be tested. Candidates whose target visibility windows are closed for the targeted timeframe must wait until their windows are open. The test calendar is reviewed and verified to be free of significant errors prior to generation of the command sequences. If scheduling problems are encountered or inconsistencies between scheduling requirements and the target time frame noted, problems must be resolved before proceeding. If severe enough, it may be necessary to return the proposal to SPB.

Test SMS Generation

A Science Mission Specification (SMS) is generated which contains the associated commanding required to execute the instrument operations and spacecraft maneuvers for the science observations. The SMS and all error output products are reviewed upon completion to verify that the timing of alignments is adequate, no errors exist in the target locations vs aperture locations, all planned exposures are present, and so on. If no significant errors are noted, the SMS may be sent out for Internal (STScI/Commanding) Review. On the other hand, if significant problems are encountered with timing, spatial scan parameters, etc., it may again be necessary to resolve the conflicts with SPB and/or the proposer.

Change Requests

SPB is notified of problems which have been identified in any of the error analysis processes of proposal preparation. These errors can result in one of two things; 1) the proposal being returned to SPB or 2) SPB sending a Proposal Change Request to be implemented that will correct the problem. Change Requests can also originate from the Proposer, and the Science Commanding System (SCS). These Change Requests can be implemented up to the point of Flight SMS Generation and have from minor to severe impact upon normal SPSS operations.

Test SMS Delivery

A Delivery Notice is prepared noting the proposal tested in the SMS to be reviewed. Special circumstances such as SUs which could not be tested due to closed windows or special scheduling requirements as provided in the proposal are described in the notice. At this point, specified SUs defined for the Flight SMS may be scheduled by the Flight Preparation crew. SPSS will be informed of any subsequent problems noted by the simultaneous Internal Review in progress.

Candidate Pool

Once a given proposal has passed proposal preparation, it is considered to be "flight ready"; that is, it is ready for flight SMS preparation activities as described below. Its associated SU's are now considered to be a part of the pool of scheduling candidates. At this stage nothing further is done with the SUs until SPSS is notified that they have been selected for scheduling on a specific flight SMS. SPB is responsible for providing the list of which usable candidate SU's from the existing pool are to be executed on each flight SMS. Currently, this notification is being done via the Flight SMS Order Form which is defined based partially on the Science Verification (SV) observing cycle requirements. The order form provides the list of SU's which are to be used from the candidate pool, as well as highlighting special proposal requirements such as scheduling priority, ordering of SU's relative to each other, pointing control requirements, etc. This form of notification has been in use from launch to the present. As the mission progresses into the General Observer (GO) cycles and the schedule

requirements become less rigid, SPB intends to provide a software-generated list of SU's from the pool of candidates.

Obset Updating

The updating requirements for making an Obset ready for flight scheduling are the same as those covered in the Proposal Preparation phase with the addition of guide star processing. The updating starts with the generation of a list of all Obsets to be added to the CCLIST. This list can be used with the Updating Command Procedure to ready the Obsets for Guide Star Requests. This procedure generates all of the pointing data and sets the "ready for guide star request" flag which allows guide stars to be requested for the Obsets. Once the updating is completed and all errors have been corrected the Obsets are ready for the next step which is Guide Star Requesting.

Guide Stars

A major part in the flight SMS preparation activity involves the selection of guide stars for Fine Guidance System (FGS) pointing control. In fact, guide star processing takes up at least 15% of the time required during the flight SMS generation activities. This is a three stage process involving: 1) The identification of those Obsets which require guide stars and generation of the request, 2) the processing of the request by the Guide Star Selection System (GSSS), and 3) the processing of the guide star response data to apply acquisition specific selection criteria to the pool of candidate guide stars in order to achieve selection of guide star pairs which have the highest probability of success for the given acquisition. Of the total guide star processing time required, Steps 2) and 3) involve the most in both the actual processing, results analysis, and troubleshooting. A majority of the Obsets can be processed automatically by the software from request through acquisition selection processing to provide satisfactory results the first time through. The remainder require the user to analyze processing results and interact with the software to produce the desired GS support. Problems due to physical constraints in the Field Of View (FOV) which limit the accessible guide star pair candidates using the default GSSS processing parameters are usually identified during step 2. These occur for sky regions which contain an extremely low density of field stars, extremely high density of field stars such as globular clusters, or fields which may be washed out in the GSSS catalog such as those near very bright stars, nebulosities, etc. Interactive processing may be used to modify the GSSS run time parameters in order to access other guide star candidates, or to generate diagnostics for analysis and documentation to show why a given observation cannot be supported due to real physical constraints. A recent quick survey of the PMDB and operations staff suggests that the ratio of the percent of Obsets per type of request to GS request/response processing time required breaks down approximately as follows:

Type	% Obsets	% Time
Automatic	85	60
Interactive	15	40

Once a pool of candidate GS's is returned to SPSS, the processing of step 3 computes sets of V3 roll ranges over which GS support is available. The candidate GS's which are used to make up these roll ranges are chosen based on a set of acquisition criteria. These ranges are then used by the SU updating function to compute the RN/RO GS support windows during the scheduling window computation. Following successful DN/DO window generation, the SU is ready for the next step; flight scheduling.

Flight Scheduling

This is the next manually intensive step in the SMS generation of activities. Creation of the CCLIST and the subsequent scheduling of activities are mechanically the same as described for the proposal preparation tasks. However, we are no longer working with SU's from just one proposal. In addition, there are special activities which must be prepared and scheduled to control Scientific Instrument (SI) states and Space Telescope (ST) pointing at the calendar boundaries. The scheduling scenario for the SU's listed on the Flight Order Form occurs in three basic passes as follows. First , the time critical and other SU's with special scheduling requirements are put on the calendar manually. Second, automatic scheduling software can be used to attempt scheduling of non-critical pointed SU's in priority order. This pass can be done in parallel with other SPSS activities (batch mode, etc.). The final pass is the most time consuming for the SPSS scheduler. It involves manual attempts to schedule the remaining pointed SU's. Problem SU's are analyzed to determine if the candidate can be scheduled on this calendar. Lower priority candidates may need to be removed at this time if that action would facilitate the

scheduling of higher priority "problem" SUs. The analysis results are reviewed and directed to the appropriate management levels for resolution. (For example, alignments whose science is too long to fit into an orbit are referred to SPB to see if a reduction in the time is possible.) Some candidates may be dropped from the Flight Order Form and rescheduled at a later date due to these types of problems. After all the problems with pointed candidates are resolved, any internal calibration SU's are scheduled. Again, this third scheduling pass is the most manually intensive and can be iterated many times over. Once completed, the calendar is reviewed in detail to verify that all scheduling requirements have been met, and that no known problems (software-created, etc.) exist.

GS Select

The guide star processing stage above generates a pool of candidate pairs which support the calendar timeframe. The actual selection of the specific guide star pairs which will be used in flight is done after the calendar is complete and the exact schedule time is known. Problems at this stage are rare since the major guide star support problems have been worked out during the request and response processing stage. Since this is the last step prior to generating the SMS, the selection results are reviewed in detail at this time to verify that they satisfy the chosen FGS acquisition scenario for the Obset. This is a low manual impact part of the Flight SMS preparation activities.

SMS Generation

While this step in the processing is not manually labor intensive, it is one of the most time consuming with an average runtime of 3-4hrs for a one week SMS. The SMS generation software basically reads the calendar and queries the PMDB to determine what activities are being requested in the schedule. As it reads the calendar, it then extracts the instructions from the PMDB which are necessary to provide the science instrument or pointing control commanding for each activity, and then builds that commanding into the SMS. There are literally hundreds of activities which are expanded into thousands of commands for each one week SMS that is processed. The limited manual effort at this step comes after the SMS generation has completed. Then a brief error analysis is done to identify any problems in the SMS processing itself due to either proposal data or commanding deficiencies. Problems which are identified are resolved via PMDB fixups to the proposal data, commanding, etc., and by iterating through the previous SMS preparation steps to get the schedule back to its SMS readiness state.

SMS Review

A more detailed SMS Review is conducted by SPSS and Science Commanding System (SCS) on a SMS after it has been generated by SPSS. The initial review by SPSS consists of a series of checks on the selected Guide Stars, SMS file and the Database information used to generate the SMS. Upon completion of the SPSS review, the SMS is either sent for commanding review or returned to SPSS for fixes and regeneration. All errors found during the review process are catalogued in an error summary log. These error summary logs contain the status of the error and the solutions to be used in fixing them. If the SMS passes the Review process a detailed Delivery Notice which accompanies the SMS to PASS is generated. The SMS is then sent by electronic means to PASS at Goddard and will go through additional analysis and eventual uplink to the Space Telescope.

Mailing address:

K. E. Reinhard, H. H. Lanning, and W.M. Workman, III
Computer Sciences Corporation
Space Telescope Science Institute
3700 San Martin Drive
Baltimore, Maryland 21218

THE SCHEDULING OF SCIENCE ACTIVITIES FOR THE HUBBLE SPACE TELESCOPE

D.K. TAYLOR[1], *K.E. REINHARD*[1], *H.H. LANNING*[1], *D.R. CHANCE*[1]
and
E.V. BELL, II[1,2]

Overview

The Science Planning and Scheduling System (SPSS) is the operational software portion of the Science Operations Ground System (SOGS) responsible for scheduling science activities onboard the Hubble Space Telescope (HST). In this presentation, we show a chronological order of the activities and features of SPSS that take an observing proposal from Transformation to execution.

Once a proposal is entered into the relational Proposal Management Database (PMDB) by conversion software known as Transformation, a proposal consists of Scheduling Units (SU), Observation Sets (Obset), Alignments, and Exposures. These represent the observing structure used by SPSS in which the exposure is the basic building block containing the proposal logsheet information including Science Instrument (SI) used, mode of operation, spectral element, and aperture. Exposures are merged into alignments which manage the pointing of the spacecraft including target position, roll, and the timing of the observations. The alignments are merged into Obsets which control the type of pointing and acquisition of guide stars. The SU controls the execution of the Obsets, Alignments, and Exposures and is the major building block used in the construction of a detailed timeline of science activities known as a Calendar. The scheduling of each SU on a calendar consists of calculating guide star acquisitions, slew activities, target visibility, science instrument transitions, orbital characteristics, etc. Whenever observational requirements permit, the ordering of SUs is chosen to minimize slews and other time consuming activities onboard the spacecraft.

After an acceptable calendar has been built, a Science Mission Specification (SMS) is generated. A SMS is an ASCII file consisting of the expanded commands from the calendar, calculated alignment times, expanded exposure commands, and orbit relative commanding. The SMS is then sent from the Space Telescope Science Institute (STScI) to the Payload Operations Control Center Application Software Support (PASS) at Goddard Space Flight Center where it is merged with engineering commands and converted to binary for spacecraft upload.

Shown below is a portion of the exposure logsheet from the proposal 03123, "Revised FOS Combined Mode II Target Acquisition", which was a Science Verification test proposal.

EXPOSURE LOGSHEET Id = 3123(P) Page: 1

1 Ln Nm	2 Seq Nam	3 Target Name	4 Instr Config	5 Oper. Mode	6 Aper orFOV	7 Spectral Element	8 Centrl Waveln	9 Optional Parameters	10 Num Exp	11 Time	12 S/N Rel.Time	13 Flx Ref	14 Pr	15 Special Requirements
1	DEF BIN	NGC-188-136	#	ACQ	4.3	MIRROR			1	33S		1	1	INT ACQ FOR 2;SEQ 1-4 NO GAP; CYCLE 0/1-213
2	^	^	^	ACQ/BINARY	^	^		BRIGHT=330000 ,FAINT=275	1	5.6S		1	1	ONBOARD ACQ FOR 3;
3	^	^	^	ACQ	^	^			1	33S		1	1	
3.5	^	TALED	^	ACQ/BINARY	0.3	^		BRIGHT=650000 ,FAINT=275	1	11S		1	1	ONBOARD ACQ FOR 4;
4	^	NGC-188-136	#	ACQ	4.3	MIRROR			1	33S		1	1	

Comments: LINE 1-4 DEFINE THE BINARY ACQUISITION MODE TEST

In the following section is a portion of the one week calendar pertinent to this test, a fraction of the SMS generated from this calendar, and various plots and charts showing the constraints and observing restrictions routinely encountered by SPSS. Certain sections of the calendar are circled and titled. In the following text, under the same headings, are descriptions of the calendar activities. Following the calendar descriptions are the same type of descriptions for the SMS portion of the example.

1 with Computer Sciences Corporation / Space Telescope Science Institute
2 with ST Systems Corporation / National Space Science Data Center - Goddard Space Flight Center

CALENDAR

SMS

```
                    Slews and FHST Updates
014:00:22:43  014:00:27:53   MF Slew (AN=  0,RA=  7,DE= 85,PA=250,OR=  0,)
014:00:27:53  014:00:33:23   MF FHST Updte (FULL ,MAN,E= 119,3, , )
014:00:49:05  014:00:49:06   SI UP   FOS        READY          03123-0G6:08:01 01
014:00:49:06  014:00:58:36   SI UP   FOS  RED   LVONA          03123-0G6:08:01 01
014:00:58:36  014:01:00:26   SI UP   FOS  RED   HVONA          03123-0G6:08:01 01
014:01:09:31  014:02:01:51      F/S_AVD     (EXT,L=  20.4)        03123:08:01 01

014:01:09:43 ********          Main SU 0312308 ********************************
**
014:01:09:43  014:01:30:26   MF PCS AQ(FGS ,E= 69,COARSE2 ) 03123-0G6:08:01
014:01:13:52                    NODE Crossing  3937
014:01:29:16  014:02:10:13       SLW_FHST 1 (EXT,L=  37.0)        03123:08:01 01
014:01:29:52  014:01:33:02   SI UP   FOC  DET   STDBY96        03028-0C1:52:01 01
014:01:29:58  014:02:05:17      SHADOW      (ENTRY)
014:01:30:26  014:01:37:31 * MF Com          (DN ,MA ,  ,E,2) 03123-0G6:08:01 01
014:01:30:26  014:01:37:35 * MF Tar  FOS  YRD4_3              03123-0G6:08:01 01
014:01:30:26  014:01:37:35 * MF Sci  FOS  YRD4_3            1 03123-0G6:08:01 01
014:01:32:02  014:02:01:28       SLW_FHST 2 (EXT,L=  37.1)        03123:08:01 01
014:01:33:02  014:01:33:03   SI UP   FOC        POWER          03028-0C1:52:01 01
014:01:37:35  014:01:53:35 * MF Sci  FOS                      2 03123-0G6:08:02 01
014:02:01:51  014:02:46:16      F/S_AVD     (ENT,L=  20.4)        03123:08:01 01
014:02:05:17
014:02:14:11    Science Instrument Transition                    03123:08:01 01
014:02:23:14  014:02:23:15   SI UP   HRS        STDBY          02168-0D6:01:01 01
014:02:23:15  014:02:23:16   SI UP   HRS  DET2  STDBY2         02168-0D6:01:01 01
014:02:23:16  014:02:51:46   SI UP   HRS  DET2  HVON2          02168-0D6:01:01 01
014:02:46:16  014:02:51:36   MF REAQ/N(FGS ,E= 50,COARSE2 ) 03123-0G6:08:01
014:02:46:16                    NODE Crossing  3938 (EXT,L=  20.4)        03123:08:01 01
014:02:50:35
014:02:51:36 * MF SAM  (ANG=  0.0000,ROLL=  0.07)
014:02:51:36  014:03:00:16      F/S_AVD     (EXT,L=  30.4)        03123:08:03 01
014:02:51:46  014:03:00:16 * MF Sci  FOS  YRD4_3            3 03123-0G6:08:03 01
014:02:51:46  014:03:00:16 * MF Com          (UP ,SSA,  ,W,1) 03123-0G6:08:03 01
014:03:00:16  014:03:00:26 * MF SAM  (ANG=  0.0000,ROLL=  0.08)
014:03:00:16  014:03:08:38      F/S_AVD     (EXT,L=  45.0)        03123:08:04 01
014:03:00:26  014:03:08:38 * MF Tar  FOS  YRD4_3              03123-0G6:08:04 01
014:03:00:26  014:03:08:38 * MF Sci  FOS  YRD4_3            4 03123-0G6:08:04 01
014:03:03:58  014:03:04:38   SI UP   HRS        WARM           02168-0D6:01:01 01
014:03:06:49  014:03:42:07      SHADOW      (ENTRY)
014:03:08:38  014:03:13:48      F/S_AVD     (EXT,L=  53.5)        03123:08:05 01
014:03:08:38  014:03:08:48 * MF SAM  (ANG=  0.0000,ROLL=  0.09)
014:03:08:48  014:03:13:48 * MF Sci  FOS  YRD4_3            5 03123-0G6:08:05 01
014:03:13:48  014:03:13:58 * MF SAM  (ANG=  0.0001,ROLL=  0.09)
014:03:13:48  014:03:38:35      F/S_AVD     (EXT,L=  54.4)        03123:08:06 01
014:03:13:58                                RD2_0BAR       03123-0G6:08:06 01
014:03:13:58    Target Visibility           RD2_0BAR     6 03123-0G6:08:06 01
014:03:38:35  014:04:22:59      F/S_AVD     (ENT,L=  20.4)        03123:08:06 01
014:03:42:07  014:04:43:39      SHADOW      (EXIT)
014:03:50:54  014:04:10:42      F/S_OCC     (BRIGHT EARTH)        03123:08:06 01
014:04:04:38  014:04:07:08   SI UP   HRS  DET2  READY2         02168-0D6:01:01 01
014:04:07:08  014:04:07:18   SI UP   HRS  DET2  OPER2          02168-0D6:01:01 01
014:04:22:59  014:04:28:19   MF REAQ/N(FGS ,E= 42,COARSE2 ) 03123-0G6:08:01
014:04:22:59  014:04:28:19      F/S_AVD     (EXT,L=  20.3)        03123:08:06 01
014:04:27:18                    NODE Crossing  3939
014:04:28:19  014:04:28:29 * MF SAM  (ANG=  0.0001,ROLL=  0.14)
014:04:28:19  014:04:54:12      F/S_AVD     (EXT,L=  30.4)        03123:08:07 01
014:04:28:29  014:04:36:00 * MF Sci  FOS  YRD4_3            7 03123-0G6:08:07 01
014:04:33:03  014:04:37:53   SI UP   FOC  DET   OPER96         03028-0C1:52:01 01
014:04:36:00  014:04:37:36 * MF Sci  FOS                      8 03123-0G6:08:08 01

014:04:37:36 ********          End  SU 0312308 ********************************

014:04:37:18  014:04:37:48   SI UP   HRS  DET2  OBS2          02168-0D6:01:01 01
014:04:37:36  014:04:38:16   SI DOWN FOS  RED   LVONA          03123-0G6:08:08 01
014:04:38:16  014:04:41:56   SI DOWN FOS  RED   HOLD           03123-0G6:08:08 01
014:04:41:56  014:04:41:57   SI DOWN FOS        HOLD           03123-0G6:08:08 0
\/\
\/\
016:01:11:08  016:01:11:09   SI UP   FOS        READY          03123-0G6:05:01 01
016:01:11:09  016:01:20:39   SI UP   FOS  RED   LVONA          03123-0G6:05:01 01
016:01:20:39  016:01:22:29   SI UP   FOS  RED   HVONA          03123-0G6:05:01 01
016:01:31:35  016:02:15:28      F/S_AVD     (EXT,L=  20.4)        03123:05:01 01

016:01:31:46 ********          Main SU 0312305 ********************************

016:01:31:46  016:01:52:29   MF PCS AQ(FGS ,E= 69,COARSE2 ) 03123-0G6:05:01
016:01:35:33                    NODE Crossing  3967
016:01:52:29  016:01:59:34 * MF Com          (DN ,MA ,  ,E,2) 03123-0G6:05:01 01
016:01:52:29  016:01:59:38 * MF Tar  FOS  YRD4_3              03123-0G6:05:01 01
016:01:52:29  016:01:59:38 * MF Sci  FOS  YRD4_3            1 03123-0G6:05:01 01
016:01:55:14  016:02:30:31      SHADOW      (ENTRY)
016:01:59:38  016:02:15:38 * MF Sci  FOS                      2 03123-0G6:05:02 01
016:02:15:28  016:02:15:38 * MF SAM  (ANG=  0.0000,ROLL=  0.03)
016:02:15:28  016:02:26:43      F/S_AVD     (EXT,L=  36.2)        03123:05:03 01
016:02:15:38  016:02:24:08 * MF Sci  FOS  YRD4_3            3 03123-0G6:05:03 01
016:02:15:38  016:02:24:08 * MF Com          (UP ,SSA,  ,E,2) 03123-0G6:05:03 01
016:02:26:43  016:03:08:19      F/S_AVD     (ENT,L=  14.8)        03123:05:03 01
016:02:30:31  016:03:32:04      SHADOW      (EXIT)
016:02:35:41  016:02:56:28      F/S_OCC     (BRIGHT EARTH)        03123:05:03 01
016:03:08:19  016:03:13:39   MF REAQ/N(FGS ,E= 40,COARSE2 ) 03123-0G6:05:01
016:03:08:19  016:03:13:39      F/S_AVD     (EXT,L=  20.4)        03123:05:03 01
016:03:12:16                    NODE Crossing  3968
016:03:13:39  016:03:13:49 * MF SAM  (ANG=  0.0000,ROLL=  0.07)
016:03:13:39  016:03:22:01      F/S_AVD     (EXT,L=  30.7)        03123:05:04 01
016:03:13:49  016:03:22:01 * MF Tar  FOS  YRD4_3              03123-0G6:05:04 01
016:03:13:49  016:03:22:01 * MF Sci  FOS  YRD4_3            4 03123-0G6:05:04 01
016:03:22:01  016:03:22:11 * MF SAM  (ANG=  0.0000,ROLL=  0.08)
016:03:22:01  016:03:36:53      F/S_AVD     (EXT,L=  45.2)        03123:05:05 01
016:03:22:11  016:03:27:11 * MF Sci  FOS  YRD4_3            5 03123-0G6:05:05 01
016:03:27:11  016:03:36:53 * MF Sci  FOS  YRD0_3            6 03123-0G6:05:06 01
016:03:32:04  016:04:07:22      SHADOW      (ENTRY)
016:03:36:53  016:03:37:03 * MF SAM  (ANG=  0.0000,ROLL=  0.09)
016:03:36:53  016:04:03:33      F/S_AVD     (EXT,L=  55.0)        03123:05:07 01
016:03:37:03  016:03:43:49 * MF Sci  FOS  YRD4_3            7 03123-0G6:05:07 01
016:03:40:31  016:04:25:37      SLW_FHST 3 (EXT,L=  21.3)        03123:05:07 01
016:03:43:49  016:03:45:25 * MF Sci  FOS                      8 03123-0G6:05:08 01

016:03:45:25 ********          End  SU 0312305 ********************************

016:04:34:44  016:05:24:13      TORS        (WEST,MA ,RET,VIS )
016:04:34:44  016:05:24:13      TORS        (WEST,MA ,FWD,VIS )
016:04:36:36  016:05:22:17      TORS        (WEST,SSA,RET,VIS )
016:04:36:36  016:05:22:17      TORS        (WEST,SSA,FWD,VIS )

016:04:49:42 *  PCS Acquistion  0312306 ********************************
016:04:49:42  016:05:10:25   MF PCS AQ(FGS ,E= 52,COARSE2 ) 03123-0G6:06:01
016:05:08:55  016:05:44:12      SHADOW      (ENTRY)
016:05:10:25  016:05:17:30 * MF Com          (DN ,MA ,  ,W,1) 03123-0G6:06:01 01
```

```
SMS00MV  :TEXT,TIME=(ORB,3966,EASCNCR,01H21   SI Transition
         BEGINTEXT;
               RECON- FOS RED Low Voltage To High Voltage
         ENDTEXT                                              ;;
         ;SMSTIME=1991.016:01:20:39.000
         ;BEGINNING A&V COMMAND BLOCK YSHVON
SMS00MW  :RTSCTRE,FUNC(ACT),RTSID(YHVON094),TIME=(ORB,3966,EASCNCR;;
         ,01H21M49.000S)                                      ;;
         ;SMSTIME=1991.016:01:20:39.000
SMS00MX  :GROUP,PYHV_20,TIME=(ORB,3966,EASCNCR,01H21M51.000S)  ;;
         ;SMSTIME=1991.016:01:20:41.000
         ;BEGINNING A&V COMMAND BLOCK YSHVSET
SMS00MY  :GROUP,PYFOCUS,FOCUS(2.88),TIME=(ORB,3966,EASCNCR     ;;
         ,01H23M31.000S)                                      ;;
         ;SMSTIME=1991.016:01:22:21.000
SMS00MZ  :GROUP,PYHV_DAC,KVOLTS(2.22E+01),TIME=(ORB,3966,EASCNCR ;;
         ,01H23M32.000S)                                      ;;
         ;SMSTIME=1991.016:01:22:22.000
         ;BEGINNING A&V COMMAND BLOCK YSREFO
SMS00NO  :GROUP,PYREFDAC,REFDAC(4.185E+01),TIME=(ORB,3966,EASCNCR ;;
         ,01H23M33.000S)                                      ;;
         ;SMSTIME=1991.016:01:22:23.000

SMS00N1  :GSACQ,ASTID(1),CENTER(BOTH),CPNAME(PQ   Guide Star   ;;
         ,GS11DEC(8.534364004831777E+01),GS11FG   Acquisition  ;;
         ,GS11ID(0461901205),GS11MAG(1.27621E+01)              ;;
         ,GS11RA(9.966343148855716),GS11RAD(6.5                ;;
         ,GS12DEC(8.539605644938104E+01),GS12FGS(2)            ;;
         ,GS12ID(0461900995),GS12MAG(1.29619E+01)              ;;
         ,GS12RA(9.661870114189522),GS12RAD(6.685134547995373E+01);;
         ,GS1DOM(2),GS21DEC(8.513335446334971E+01),GS21FGS(3)  ;;
         ,GS21ID(0461900434),GS21MAG(1.05773E+01)              ;;
         ,GS21RA(7.962712834845506),GS21RAD(1.5E+01)           ;;
         ,GS22DEC(8.511983525969107E+01),GS22FGS(3)            ;;
         ,GS22ID(0461900520),GS22MAG(1.13659E+01)              ;;
         ,GS22RA(6.987715709971109),GS22RAD(1.5E+01),GS2DOM(2) ;;
         ,NOSLEW,NUM_PAIR(2),ACQTYPE(2),FHSTBIAS(1),GS11FT(F583W) ;;
         ,GS11K1K(3.222746806750257E-02)                       ;;
         ,GS11K1Y(4.042746903905828E-02)                       ;;
         ,GS11K3K(4.707391076601762E-01)                       ;;
         ,GS11K3Y(4.315245459492814E-01),GS11ML(114),GS12FT(F583W);;
         ,GS12K1K(3.254703190550703E-02)                       ;;
         ,GS12K1Y(4.074703287706274E-02)                       ;;
         ,GS12K3K(4.660931454559664E-01)                       ;;
         ,GS12K3Y(4.282305822068399E-01),GS12ML(97),GS21FT(F583W) ;;
         ,GS21K1K(2.400658945090792E-02)                       ;;
         ,GS21K1Y(2.570658848707524E-02)                       ;;
         ,GS21K3K(6.178924269269839E-01)                       ;;
         ,GS21K3Y(5.613451652511787E-01),GS21ML(1207)          ;;
         ,GS22FT(F583W),GS22K1K(2.413789333687464E-02)         ;;
         ,GS22K1Y(2.583789359590676E-02)                       ;;
         ,GS22K3K(6.137563655248157E-01)                       ;;
         ,GS22K3Y(5.582595153709073E-01),GS22ML(589),PLNTPRLX(0) ;;
         ,RCHVM(0.0),TARGETAQ(PRIMARY),WHICHACQ(BASELINE),END=(ORB;;
         ,3966,EASCNCR,01H53M39.000S),START=(ORB,3966,EASCNCR   ;;
         ,01H32M56.000S)                                       ;;
         ;SMSTIME=1991.016:01:31:46.000

0G605001 :TEXT,TIME=(ORB,3966,EASCNCR,01H53M39  Science
         BEGINTEXT;                              Activities
         START PROP=03123 ,PROG=0G6 ,OBSET=05       A          ;;
         NGC-188-13 , FOS/RD , ACQIMAGE , 37.0                 ;;
         NOCHANGE , A4_3 , MIRROR , G780H ,                    ;;
              Begin Observation
         ENDTEXT                                               ;;
         ;SMSTIME=1991.016:01:52:29.000
         ;BEGINNING A&V COMMAND BLOCK YSFGWP
0G605002 :RTSCTRL,FUNC(ACT),RTSID(YMOTR094),TIME=(ORB,3966,EASCNCR;;
         ,01H53M39.000S)                                       ;;
         ;SMSTIME=1991.016:01:52:29.000
0G605003 :GROUP,PYFMTCD,FMTCODE('73'X).FORMAT(2),TIME=(ORB,3966  ;;
         ,EASCNCR,01H53M39.000S)                               ;;
         ;SMSTIME=1991.016:01:52:29.000
0G605004 :GROUP,PYFILTER,DIR(FWD),FILTER(MIRRORA),TIME=(ORB,3966 ;;
         ,EASCNCR,01H53M40.000S)                               ;;
         ;SMSTIME=1991.016:01:52:30.000
0G605005 :SCIHDR,INST_ID(FOS),OBS_ID(01),OBS_SET(05),PROG_ID(0G6) ;;
         ,WORD11(32),TIME=(ORB,3966,EASCNCR,01H53M41.000S)     ;;
         ;SMSTIME=1991.016:01:52:31.000

0G605007 :COMCON,INST_ID(FOS),OBS_ID(01),OBS_SET(05),P  COMCON ;;
         ,RATE(4.0),SERVICE(MAR),TAPE_OPT(BACKUP),END=(ORB,3966  ;;
         ,EASCNCR,02H00M12.000S),START=(ORB,3966,EASCNCR        ;;
         ,01H53M49.000S),TAPE_BEG=(ORB,3966,EASCNCR,01H56M49.000S);;
         ,TAPE_END=(ORB,3966,EASCNCR,02H00M31.000S)             ;;
         ;SMSTIME=1991.016:01:52:39.000

0G605008 :GROUP,PYHCSTEP,DIR(CW),TIME=(ORB,39  Science         ;;
         ,01H53M51.000S)                         Activities    ;;
         ;SMSTIME=1991.016:01:52:41.000             B          ;;
0G605009 :TABLE,YOCKHI,OVERLITE(3000000),TIME                   ;;
         ,01H53M55.000S)                                       ;;
         ;SMSTIME=1991.016:01:52:45.000
0G60500A :TABLE,YOCKLO,OVERLITE(3000000),TIME=(ORB,3966,EASCNCR ;;
         ,01H53M56.000S)                                       ;;
         ;SMSTIME=1991.016:01:52:46.000
         ;BEGINNING A&V COMMAND BLOCK YSPTRNS
         ;BEGINNING A&V COMMAND BLOCK YSDEFL
0G60500B :GROUP,PYDEFLEC,XOFFSET(0),X_BASE(AS  Science         ;;
         ,YOFFSET(-496),Y_BASE(ASCMIRO),Y_PI     Activities    ;;
         ,Y_RANGE(1024),TIME=(ORB,3966,EASCNC       C          ;;
         ;SMSTIME=1991.016:01:52:47.000
         ;BEGINNING A&V COMMAND BLOCK YSDEFP
0G60500C :GROUP,PYPATTRN,INTS(1),OVERSCAN(5),                   ;;
         ,Y_STEPS(64),TIME=(ORB,3966,EASCNCR,01H54M02.000S)    ;;
         ;SMSTIME=1991.016:01:52:52.000
         ;BEGINNING A&V COMMAND BLOCK YSDAQP
0G60500D :GROUP,PYACQPAR,CHNNL1(256),CHNNLS(20),DEAOTIME(1.0E+01) ;;
         ,INIT_HYS(HYSTER),INIT_SLI(SLICE),INIT_XOF(XDEF)      ;;
         ,INIT_YOF(YDEF),LIVETIME(2.00625E+01),REJLIMIT(NOREJLIM) ;;
         ,TIME=(ORB,3966,EASCNCR,01H54M07.000S)                ;;
         ;SMSTIME=1991.016:01:52:57.000
         ;BEGINNING A&V COMMAND BLOCK YSORP
0G60500E :GROUP,PYPATTS,PATTERNS(1),TIME=(ORB,3966,EASCNCR     ;;
         ,01H54M16.000S)                                       ;;
         ;SMSTIME=1991.016:01:53:06.000
0G60500F :GROUP,PYREADS,READOUTS(1),TIME=(ORB,3966,EASCNCR     ;;
         ,01H54M17.000S)                                       ;;
         ;SMSTIME=1991.016:01:53:07.000
0G60500G :GROUP,PYCLEARS,CLEARS(1),TIME=(ORB,3966,EASCNCR      ;;
         ,01H54M18.000S)                                       ;;
```

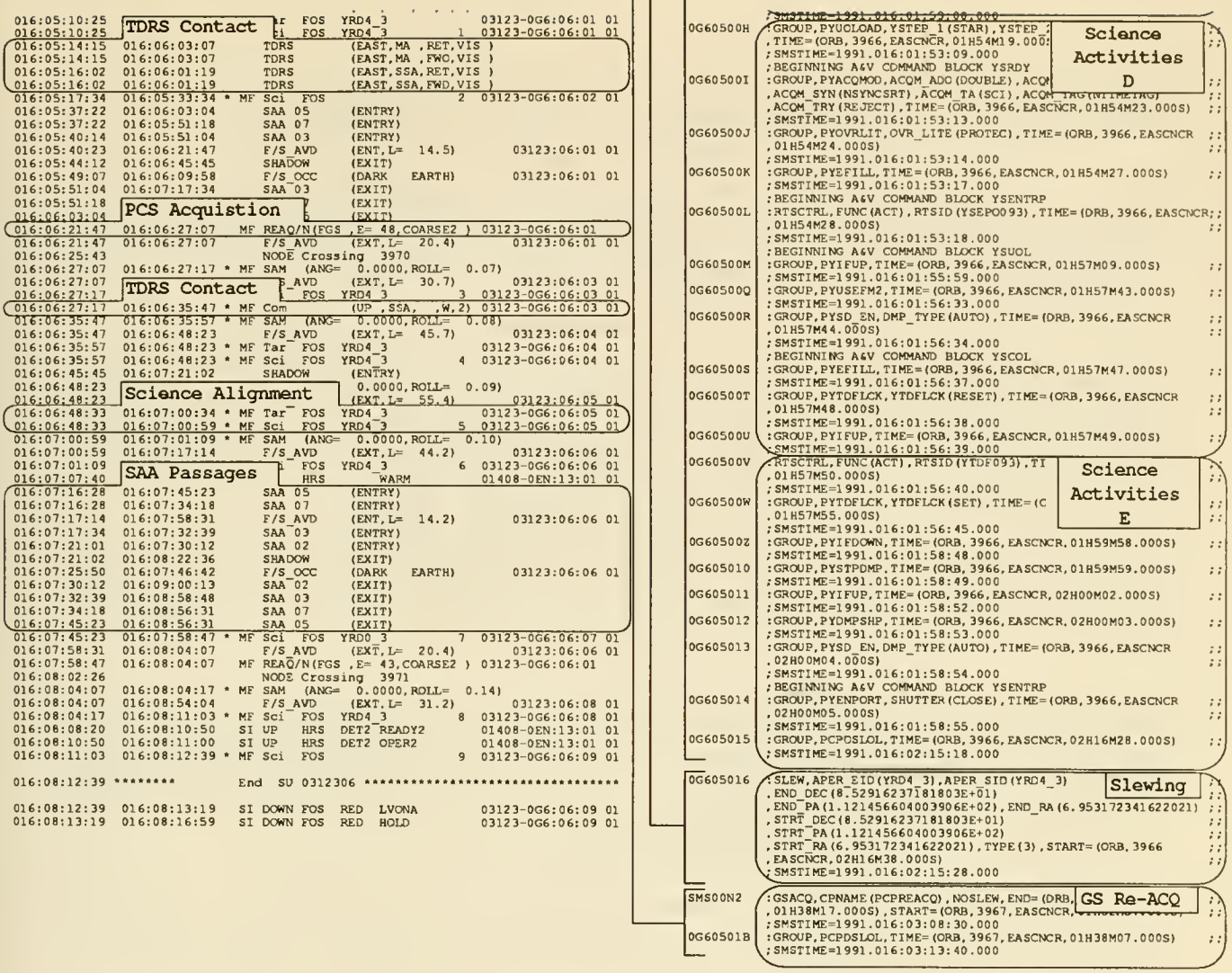

CALENDAR INFORMATION

Slews and FHST Updates

A basic attribute of HST is its ability to slew to any position in a reasonable amount of time (approximately 6 degrees of arc per minute of time). Given the target coordinates, an eigenslew is calculated, allowing the spacecraft to maneuver in all three axes (pitch, yaw, and roll) simultaneously. In the example shown here, the slew angle is zero, meaning that the previous pointing was essentially identical to the new pointing. The position angle for nominal roll (defined as the sun lying in the half-plane given by the +V3 axis) is determined along with the solar avoidance angle.

The coarsest pointing control mechanism is the Fixed Head Star Trackers (FHST). These are wide field imaging devices placed off the main optical axis of the telescope. The FHSTs are used to update the HST position uncertainty after maneuvers. This updating provides sufficient pointing accuracy such that the guide star acquisition to follow will have a high probability of succeeding.

A very small slew which can occur within an Obset but between alignments is the Small Angle Manuever (SAM). These usually involve a small offset to place the target in a particular aperture of the SI or at a specific position within an aperture.

Science Instrument Transitions

The calendar building software determines the appropriate time for the science instruments (SI) to transition to a higher state before the exposures occur and down to a lower state after observation completion. Frequently, however, the SIs will not transition down completely if succeeding observations using the same instrument

follow closely in time. This can result in groups of SUs scheduling differently than each one separately. Also, other SIs for other proposals can transition during this SU if the observation permits.

Target Visibility

All target and geometrical information is incorporated at calendar building time. For a given target, the bright and dark limb avoidance angles are calculated, thereby determining when the Fine Guidance Sensors (FGS) can begin a guide star acquisition. The duration of target visibility (a function of the day on which the observation is scheduled), can be determined by when the target enters occultation. The calendar also shows Earth shadow crossings and node crossings.

PCS Acquisition

For all observations, a Pointing Control System acquisition (PCS ACQ) occurs before data taking begins. The acquisition can be done in GYRO mode (as is done for internals) or with the FGS (as is usually done for external observations). The calendar allots sufficient time for the PCS ACQ depending on the scenario: coarse track or fine lock and whether it is a one or two pair acquisition (cf. Figures 3 - 5). The expected pointing error in arcseconds is calculated knowing the previous pointing , the length of the slew to the new position, estimated drift, and time since the last update.

After an observation has been interrupted due to Earth occultation or South Atlantic Anomaly (SAA) passage a re-acquisition (REACQ) occurs. The REACQ acquires the same set of guide stars used in the previous acquisition. Since the pointing has not changed, the probability of a successful acquisition is quite high and the time allocated for the REACQ is much less than that for the initial PCS ACQ.

TDRS Contact

From ephemeris data processed in SPSS, the visibility of the Tracking and Data Relay Satellite (TDRS) is calculated. Important information regarding the TDRS include: which satellite (East or West), the type of service (multiple access [MA] or single service access [SSA]), and whether it is a forward or return link. When determined by the proposal, communication contacts (COMCONs) are established with the TDRS for either uplinks or downlinks. COMCONs are established at the alignment level, therefore requiring the alignment time to be sufficient for the COMCON (and any other activities).

Science Alignment

The designation "MF Sci" on the calendar refers to the Main Fixed Science alignment within an obset. Within this time span all exposures under this alignment must occur (unless the alignment is interruptible, in which case it may stop and resume at a later time). In the example shown, a target acquisition is also being executed. Obviously, if the alignment is pointed, the target must be visible for the duration of the alignment.

SAA Passages

A major constraint in scheduling science instrument activities is the passage of HST through the SAA. Because the different SIs respond differently to the varying radiation intensities within the SAA, several models of the SAA are used (cf. Figure 1). A passage through one of the larger models (e.g., Model 05) can last as much as 30 minutes (cf. Figure 2). During the SAA passage, instruments such as the WFPC should not take data due to the higher background noise. Another major scheduling constraint depends on the geometrical interaction of the SAA with the target visibility windows. If the two occur at the same time the desired observations may not be possible for many hours until HST's orbit does not intersect the SAA at all. This non-intersection happens about once a day and can last as long as 9 to 10 hours. Many observations that are SAA sensitive are targeted for these times.

SMS INFORMATION

SI Transition

The statement at time 016:01:20:39 indicating the FOS transitioning from low to high voltage (HV) is expanded into the SMS block shown in the figure. Included are various command groups (essentially command subroutines with their arguments), comment blocks, and absolute and orbit relative times. The commanding following the Text Block starts with the HV turn on by ramping up the HV to 20 KV in 2 KV steps. The next step is the setting of the focus followed by the final adjustment of the HV value. The last commanding in this block is the calibration of the Digital to Analog converter.

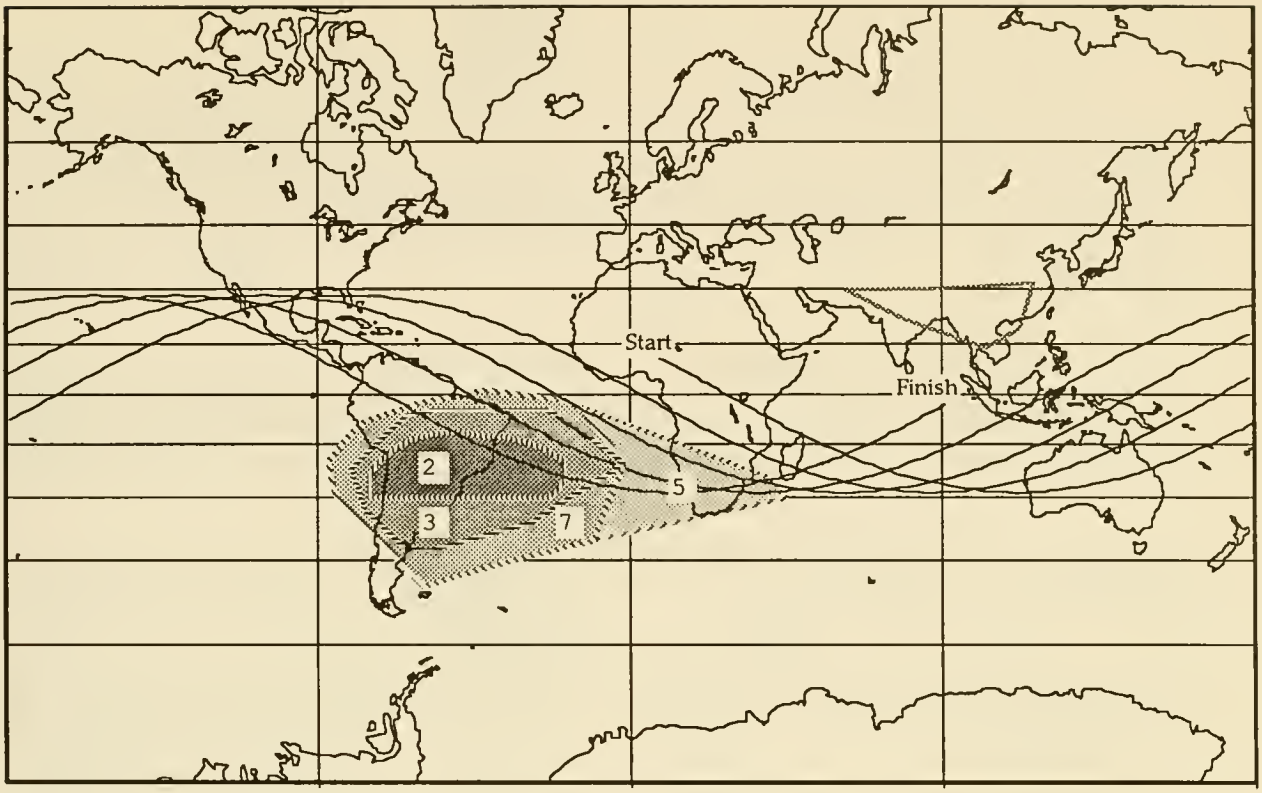

Figure 1
Plot of four South Atlantic Anomaly (SAA) models and the orbit of HST over an eight hour time span. Model 2 is relevant to the FGS, Model 3 for the FOC, Model 5 for the FOS, HSP, WFPC, and FGS for astrometry, and Model 7 for the GHRS.

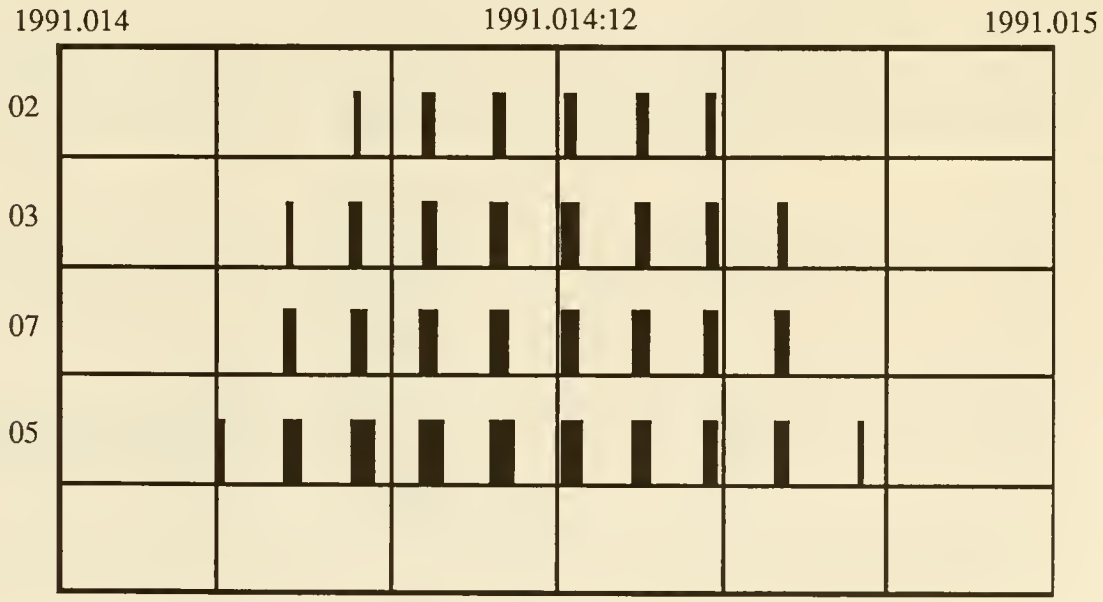

Figure 2
Duration of HST passage through four SAA models over the the course of one day.

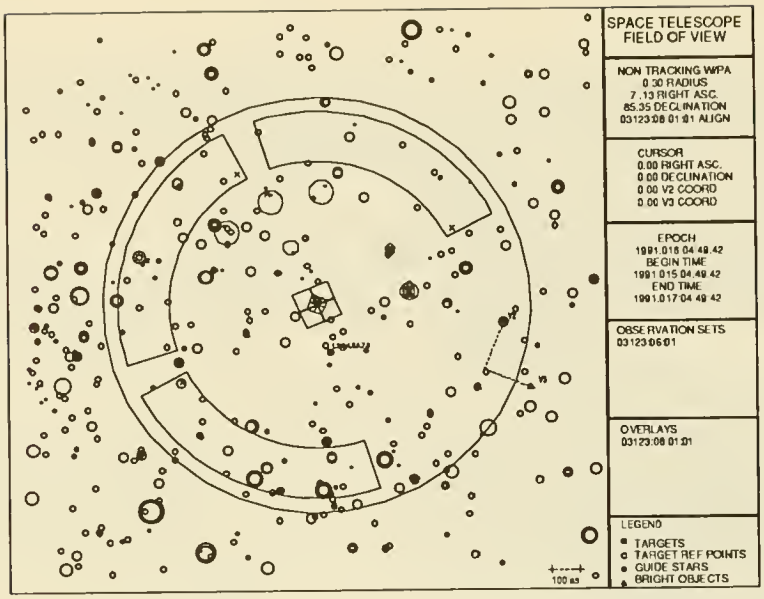

Figure 3
Display of the stars from the Guide Star Catalog for the pointing of the Obset 03123:06.

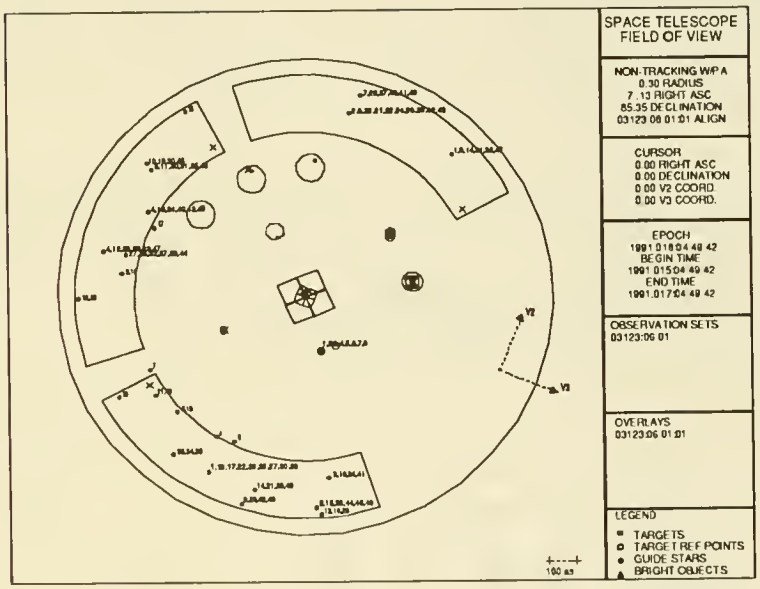

Figure 4
Guide Stars returned from GSSS for the Guide Star Reques t sent for Obset 03123:06. GSSS returns stars which have a high probability of acquisition (e.g., no close binaries, stars of a limited magnitude range, etc.). However, only a small fraction (~ 20 %) pass further criteria imposed by the scheduling software.

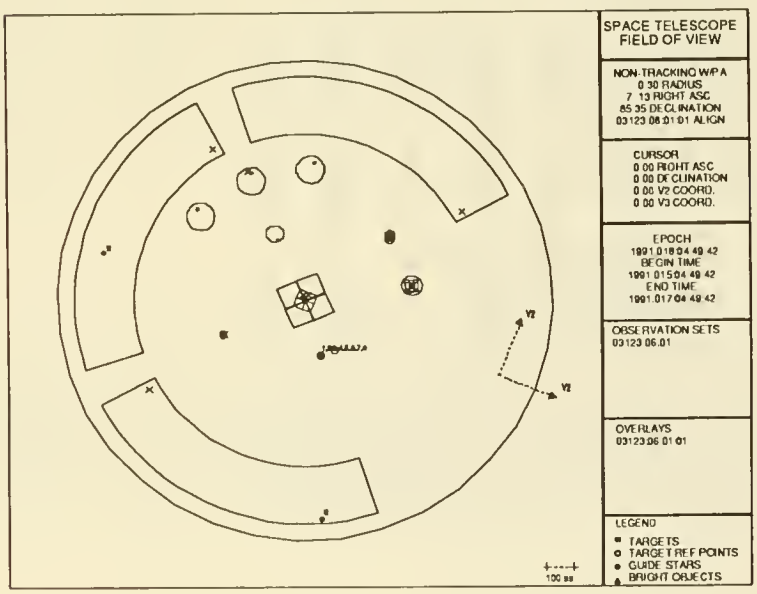

Figure 5
FOV display showing the Guide Star pair selected for the use in the acquisition for the Obset 03123:06.

Guide Star Acquisition

The guide star acquisition occuring at 016:01:31:46 becomes this rather lengthy block on the SMS. All necessary information regarding the acquisition is pulled from the PMDB and displayed as parameters and arguments. Included are the guide star pair identifications taken from the Guide Star Selection System (GSSS) catalog, coordinates of the stars in right ascension and declination, magnitudes, which star is the dominant (star that controls pitch and yaw), which is the sub- dominant (controls the roll), and other information controlling the actual guide star acquistion. Also included is the acquistion type (baseline, two step, and list), the Guide Star search radius values (upper search radius limit), the filters to be used by each of the FGS and the guide control scenario (coarse or fine lock).

Science Activities - A

The science activity for the alignment 03123:05:01 begins thirty minutes after the SI transition block. This warmup time is standard for the FOS. The Text Block describes the values that will be set in the following commands and is equivalent to line 1 of the Exposure Log Sheet. The next activity is the setting of the Filter Grating Wheel (FGW) which is followed by a format code setup used by Post Observation Data Processing System (PODPS) for picture processing.

COMCON

The COMCON on the calendar at 016:01:52:39 now becomes the block shown on the SMS. The data rate is specified (here, 4 kb per second), the type of service (multiple access, return link), whether a science tape recorder backup will be done, and start and end times for the tape use.

Science Activities - B

The science activities continue after the COMCON with the final setting of the FGW. The following commands then sets the OVERLIGHT LIMIT value which is used to safe the instrument if the count reaches this value.

Science Activities - C

The next activity is setting up the magnetic deflection. This process determines where the spectrum is located on the photocathode and also sets the scale of the spectrum on the photocathode. The remaining part of the block sets up the pattern that is desired on the photocathode. OVERSCAN shifts the spectrum I diode to compensate for dead diodes. CHNNL1 and CHNNLS determine the first diode and the number of diodes to use for imaging the spectrum. READOUT sets the number of readouts of the pattern but does not clear the diodes. CLEARS is the same as READOUT except it clears the diodes after the readout.

Science Activities - D

The beginning of this block is a setup for PODPS. It tells them what to expect in the frame (sky, star, background). This is followed by a formating of the FOS and the turn on of the OVERLIGHT protection which was set earlier. After this has completed a command is given to read out the engineering data. The last group of this block is the commanding to open the entrance port followed by another readout of the engineering data.

Science Activities - E

This block begins with the command PYTDFLCK which sets up the Take Data Flag (TDF) management governing when taking data is allowed. This is then followed by the SET parameter which is where data take begins. The remainder of the block is a cleanup after the observation. For the FOS this is known as the "Fire Break" which insures that the observation stops when it is supposed to.

Slewing

The type 3 slew block, a small angle maneuver at 016:03:13:50, is shown. The start and end aperture ids are given, along with starting and ending coordinates and position angle. Orbit relative time is given in addition to absolute time.

GS Re-ACQ

The guide star re-acquisition occuring at 016:03:13:50 on the calendar is expanded on the SMS. Much less information is needed for a re-acquisition than for the initial acquisition due to the fact that the same guide stars are being used.

THE SCHEDULING EFFICIENCY FOR THE HUBBLE SPACE TELESCOPE DURING THE FIRST YEAR OF OPERATION

E.V. BELL, II [1,2], K.E. REINHARD[2], and H.H. LANNING[2]

Introduction

Prior to the launch of the Hubble Space Telescope (HST), estimates were made as to the ability of the Science Operations Ground System (SOGS) to schedule observations efficiently. These estimates ranged from the extremely pessimistic (0%), for those who thought SOGS incapable of the task, to optimistic values around 35%. These latter estimates were based on several factors including the ability of HST to see the Tracking and Data Relay Satellites (TDRS), the penetration of HST's orbit into the South Atlantic Anomaly (SAA), target visibility, etc. HST completed the Orbital Verification (OV) phase of the mission in November 1990 and is currently in the Science Verification (SV) portion. Although the observations made during these early phases are not, in general, representative of the majority of the mission, they are indicative of the scheduling software's ability to cope with many of the extreme cases likely to be seen during the mission. This paper presents the results of the first year of scheduling observations on HST.

General Overview of Scheduling Efficiency Since Launch

Shown in Figure 1 is the total scheduling efficiency since launch (shown as the (percent) fraction of time during which the spacecraft performed some activity relative to the total time span of a given calendar). These activities include the total alignment time for each separate observation as well as numerous overheads (e.g., guide star acquisitions, target acquisitions, FHST updates, etc.). The efficiencies of the calendars generated by SPSS in this period range from a low value of 13% to a high of 62% with the majority of calendars falling in the 37-47% range. There are several features about these efficiency plots which need to be pointed out at this time. First, very early scheduling operations for HST were different than has been true more recently, both in terms of the type of proposals being scheduled as well as the time spans of the calendars. Characteristic of the first 20 days or so of scheduling are short interruptions between calendars created at STScI. These calendars contained planned gaps during which teams of engineers and scientists would analyze data and then upload new information to thespacecraft. During these gaps, spacecraft attitude was maintained by "Health and Safety" SMSs (Science Mission Specifications) generated by the Payload Operations Control Center (POCC) at the Goddard Space Flight Center. Second, there are visible gaps in between calendars which are of a longer duration (on the order of 1-3 days). These are spacecraft safing events, times during which the spacecraft placed itself in a mode wherein it could not be damaged. Note that most of the safing events which have so far occurred happened within the first four months of operations, although two other events have happened fairly recently. Also, note that these do not include individual science instrument (SI) safing events. SI safing events do not affect the overall functioning of the spacecraft, just the ability to perform observations with that instrument. Because the instrument is only recovered once the safing event has been fully analyzed and at such a time that the recovery can be performed without disrupting the operation of all the other instruments, these SI safing events are not visible on these plots. Third, early calendars generated by SPSS were of short duration (~18 hours to several days), whereas the current schedule (one expected to last for the duration of the mission) is to produce calendars covering seven days and running from Sunday midnight to Sunday midnight. This is driven not due to limitations in the ground support software, but because of the scheduling time periods for TDRSS. Finally, we wish to address how the actual observing timeline has reflected the timeline planned prior to launch.

Originally, the OV period consisted of two equal portions, covering a four week period, during which the Marshall Space Flight Center was to have control of the spacecraft in the first half and Goddard Space Flight Center was to have control in the latter half. This orbital verification phase was intended to be used to check out the general health of all onboard support systems (the batteries, solar panels, on-board attitude control, etc.) as well as an initial checkout of the general health of the SIs. This period was to be followed by an eight month period of science verification (SV) during which the various operating modes of the SIs would be checked out. Shown above Figure 1 (and all subsequent plots) is the planned duration of OV and SV as well as the original planned start of the GO/GTO (General Observer/Guaranteed Time Observer) program. Also shown is the actual duration of OV and the beginning of SV. Although OV officially ended 202 days after launch (on Nov. 12, 1990), some portions of OV were still being executed until very recently. Likewise, several SV proposals began to be executed some 60 days or more prior to the official beginning of SV (as the initial OV checkouts of some instruments were completed before others). The current timeline plans for the end of SV to be sometime late in 1991. There are several reasons for the extension of both the OV and SV phases of the mission. First, several

1 with ST Systems Corporation / National Space Science Data Center - Goddard Space Flight Center
2 with Computer Sciences Corporation / Space Telescope Science Institute

weeks of activity were involved in attempting to focus the telescope. Once it was discovered that the aberration of the mirror was to blame for the inability to find a single optimum focus, it was necessary to continue to

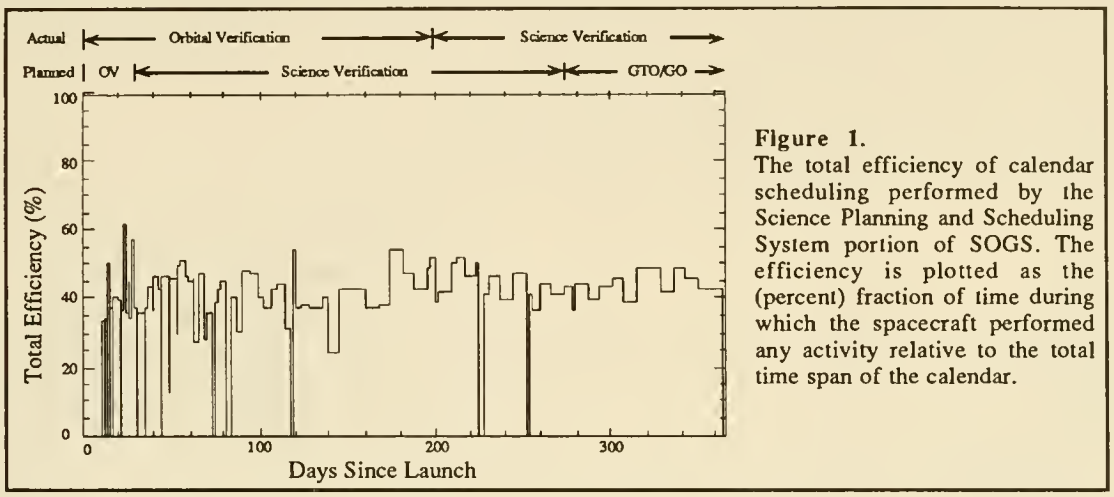

Figure 1.
The total efficiency of calendar scheduling performed by the Science Planning and Scheduling System portion of SOGS. The efficiency is plotted as the (percent) fraction of time during which the spacecraft performed any activity relative to the total time span of the calendar.

perform observations with the WF/PC and FOC to determine the amount of aberration so that a point spread function could be determined. This greatly expanded the duration of OV. In addition, it was decided to perform several observations for early release to the astronomical community and the media in order to provide evidence of the capabilities of the telescope in spite of the spherical aberration.

Time Spent in Various Activities

Included in Figure 1 are several different activities which are overhead activities. These are such things as target and guide star acquisitions, FHST updates, and slews and settling time. Several of these activities are broken out in the following figures. There are three main types of observing activities into which a calendar can be broken. These are main fixed observations (these include not only targeted observations but internal and earth limb observations), interleavers (activities which do not alter the attitude of the spacecraft and so can be scheduled during large gaps within a scheduling unit of another observation), and parallel observations. So far, interleavers have only been used on a few calendars (fewer than 20) and have accounted for less than 5% of the total time span of any given calendar. In addition, the current version of the ground-support software does not support the use of parallel observations. Therefore, these are not presented herein. Figure 2 shows the amount of time spent on each calendar in main fixed observations. Main fixed observations account for the majority of the total time presented in Figure 1. The amount of time since launch spent in main fixed activities (essentially the total of all the individual alignment times) has ranged from a low of 12% of the calendar span to a high of 52% with the bulk of the calendars ranging from 25- 30%. Little difference is seen in the efficiency between the OV period

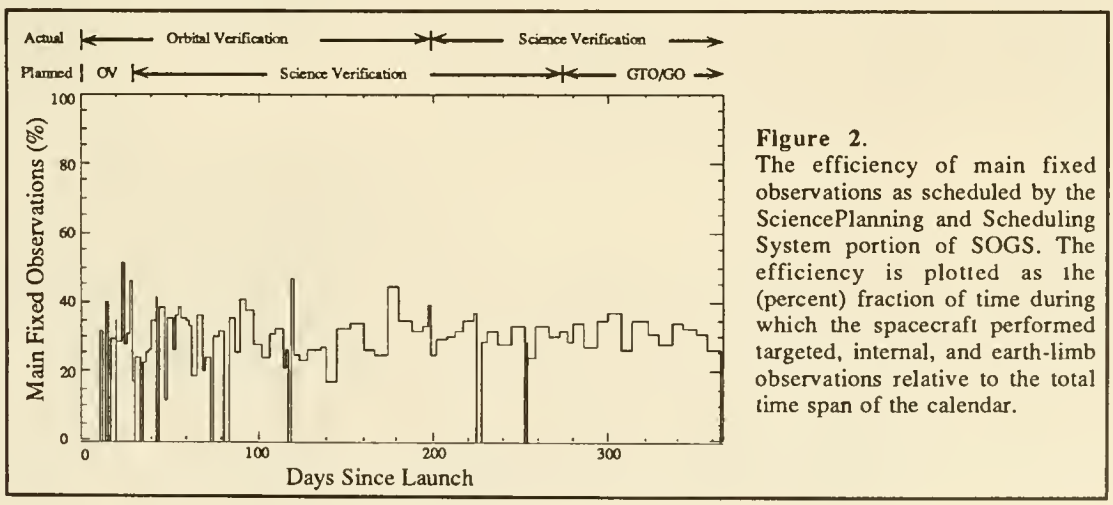

Figure 2.
The efficiency of main fixed observations as scheduled by the SciencePlanning and Scheduling System portion of SOGS. The efficiency is plotted as the (percent) fraction of time during which the spacecraft performed targeted, internal, and earth-limb observations relative to the total time span of the calendar.

(where much of the observing timeline was determined by committees of individuals) and the SV period to date (where the timeline is "optimized" by the use of the artificial intelligence program SPIKE). Shown in Figures 3-5 are the percent time spent per calendar in the (re)acquisition of guide stars, the (re)acquisition of targets, and in slews and settling, respectively. Important to note in Figures 3 and 5 are the relatively consistent amount of

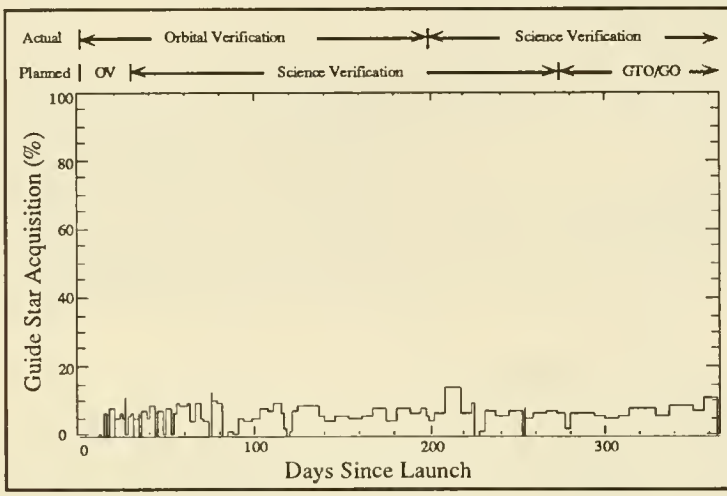

Figure 3.
The amount of time spent in guide star (re)acquisition for calendar spanning the first year of observations by HST. The time is plotted as the (percent) fraction of time which the pointing control system (PCS) spent acquiring or reacquiring guide stars relative to the total time span of the calendar.

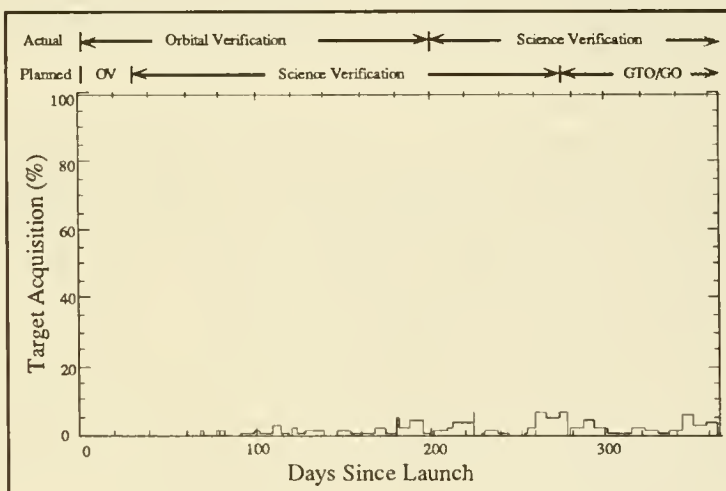

Figure 4.
The amount of time spent in target (re)acquisition for calendars spanning the first year of observations by HST. The time is plotted as the (percent) fraction of time which the pointing control system (PCS) spent acquiring or reacquiring targets relative to the total time span of the calendar.

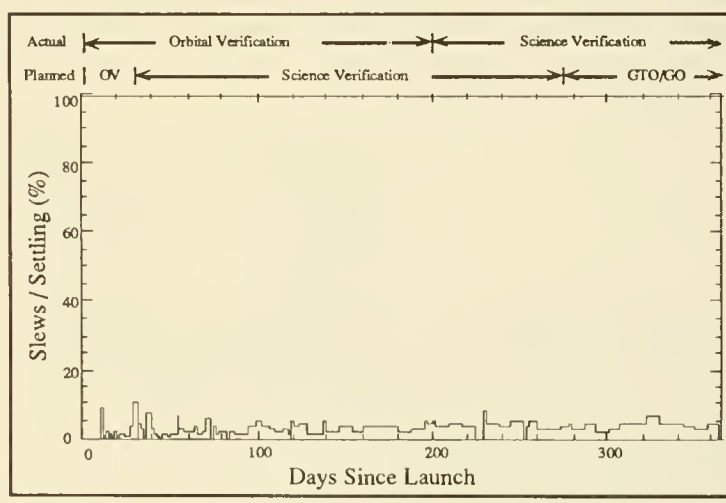

Figure 5.
The amount of time spent in slewing the spacecraft for calendars spanning the first year of observations by HST. The time is plotted as the (percent) fraction of time which the spacecraft spent slewing relative to the total time span of the calendar.

time spent in performing guide star acquisitions and in slewing the telescope (~5-10% and ~5%, respectively). Most of the variation of these three activities can be attributed to the amount of time spent pointed at a particular target, as well as the number of internal observations scheduled on a given calendar. Figure 4, however, shows one of the primary differences between OV and SV activities, that is that much of the early OV observations did not require much time for target (re)acquisition. Much of the early timeline involved remaining at a particular attitude for extended periods of time, but few targets were actually involved. This was necessary to perform many of the checkouts of the pointing control system (PCS) which is involved not only in slewing and guide star acquisition, but in maintaining attitude. Target acquisitions have become a larger fraction of the calendar activities as the spacecraft spends more time in instrument checkouts and can probably be expected to account for 5-10% of the calendar time as a norm. Not shown is the amount of time spent performing updates of the fixed-head star trackers (FHSTs) which accounts for less than 3% of the total calendar time.

The Impact of TDRS Contact Time on Efficiency

Another quantity which has a potential effect on scheduling efficiency is the amount of time required by a calendar to be in contact with one of the two Tracking and Data Relay Satellites (TDRS). The Tracking and Data Relay Satellite System (TDRSS) is the sole means of communicating with the spacecraft. The amount of time required for an observation and the availability of time on a given TDRS, as well as the ability of HST to see the TDRS, can have a significant impact on it's schedulability. SPSS can take all of this into account, but all final resolutions of conflicting requests for TDRSS time must be resolved between POCC, STScI, and the NCC (Network Control Center). The NCC is responsible for scheduling time on TDRSS. Shown in Figure 6 is the percent TDRSS request time for HST to date. Note that this is not the amount of time given to HST during final conflict negotiations nor does it take into account the additional time for monitoring the spacecraft which is requested by POCC nor the time allocated on an emergency basis during spacecraft safemode events. This time does include the total amount of time required by the calendar for uplinks requested by the institute (for spacecraft and SI commanding), downlinks requested for real time activities (e.g., interactive acquisitions), and decision time needed by the observer. Only a minor fraction of the total calendar time (<<1%) is taken by decision time. Note that during early OV, a large fraction of time was needed to perform the necessary spacecraft commanding and to obtain data. During the latter portion of OV, however, and into early SV, requested TDRS time has settled down to a nearly constant rate of ~5%. There is very little correlation, however, between the overall efficiency of a given calendar with how much TDRS time is requested (cf. Figures 1 and 6). Shown in Figure 7 is the amount of time during which either TDRS east was not available (generally during shuttle missions) or that TDRSS was

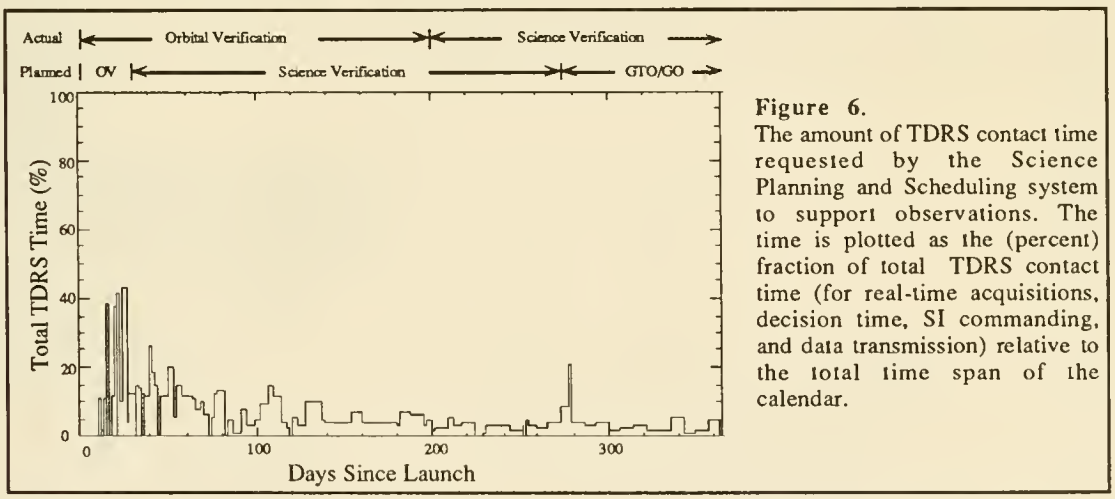

Figure 6.
The amount of TDRS contact time requested by the Science Planning and Scheduling system to support observations. The time is plotted as the (percent) fraction of total TDRS contact time (for real-time acquisitions, decision time, SI commanding, and data transmission) relative to the total time span of the calendar.

down (for upgrade or maintenance). TDRS east has the largest potential impact because during shuttle missions it is used exclusively for communications between the shuttle and mission control. These dead zones were calculated as a percentage of the total available TDRS east visibility during the span of the calendar. Note that during each time that a shuttle mission was launched or expected to take place, TDRS east was completely unusable for spacecraft like HST. Smaller periods of TDRS unavailability (varying from around 2 to 6 hours) are usually the result of maintenance or upgrade of equipment or software at White Sands. These have little effect, however, on the overall efficiency of calendars (as can be seen by comparing Figures 1 and 7). This is because many observations requiring TDRS can be satisfied by simply requesting time on the remaining TDRS

(for which there are no extensive periods of dead time) or by scheduling the observation during an earlier or later time for which the TDRS down time is not a problem. This is a quite convenient feature of the manner in which the telescope is operated, since launch delays in the shuttle manifest can affect several weeks of TDRS east availability.

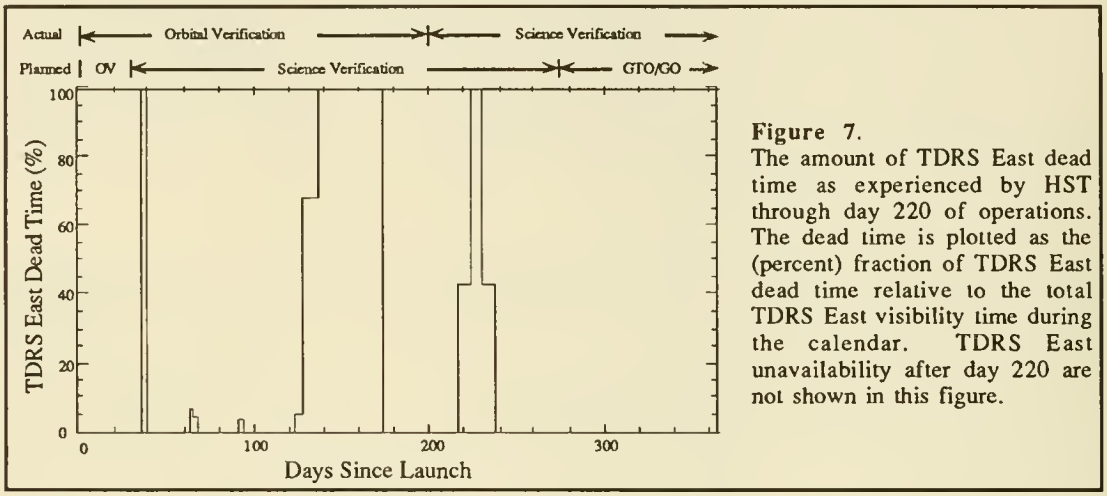

Figure 7.
The amount of TDRS East dead time as experienced by HST through day 220 of operations. The dead time is plotted as the (percent) fraction of TDRS East dead time relative to the total TDRS East visibility time during the calendar. TDRS East unavailability after day 220 are not shown in this figure.

Data Volumes

The last topic to be examined is the amount of data so far generated by HST. This has a direct bearing on the efficiency of scheduling observations since one can very efficiently schedule activities on a spacecraft, but if no useful science activities are being performed or no data are being transmitted to the ground, it isn't a very efficient system. Shown in Figure 8 is the expected average daily data volume (in Gbits/day) for each calendar as calculated by the SPSS scheduling software. Note that this and the subsequent figure do not represent the actual data return of HST, but are expected returns. Very little data were being generated early in the mission. Figure 8

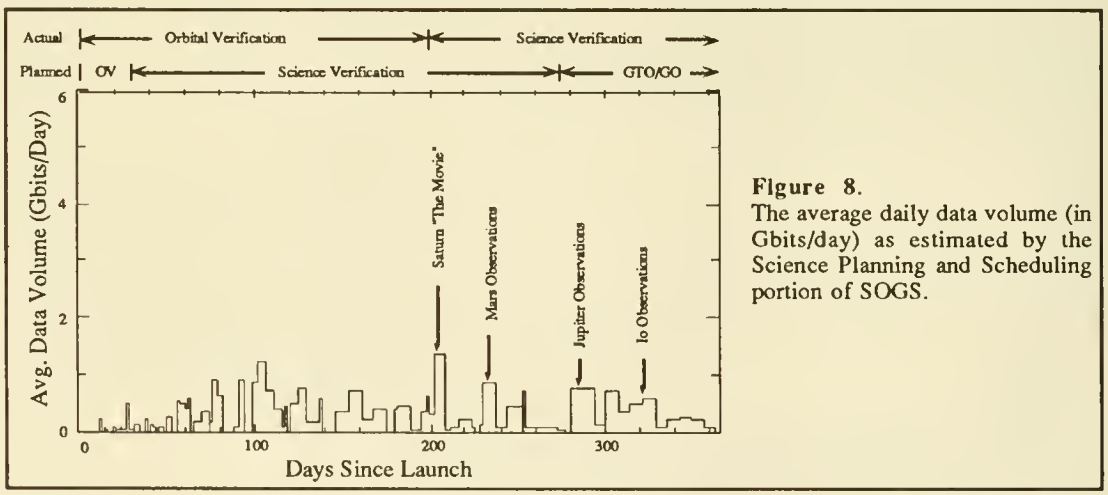

Figure 8.
The average daily data volume (in Gbits/day) as estimated by the Science Planning and Scheduling portion of SOGS.

has denoted on it four special observations, the first a "movie" of Saturn's white spot which occupied a major portion of one calendar, the second a series of Mars observations, the third several scheduled observations of Jupiter, of which all but the first acquisition failed, and lastly some exposures of Io. Most of the early larger features were either the result of repeated data takes with the WF/PC and/or FOC to characterize the mirror or to support the early release observations (EROs). Shown in Figure 9 is the anticipated maximum daily data volume (to the same scale as Figure 8) for each calendar. Note the large peak for the Saturn movie. Even with this large value, however, HST has still not generated the amount of data expected on a daily basis once the observatory is fully operational (somewhere in the neighborhood of 6 Gbits/day).

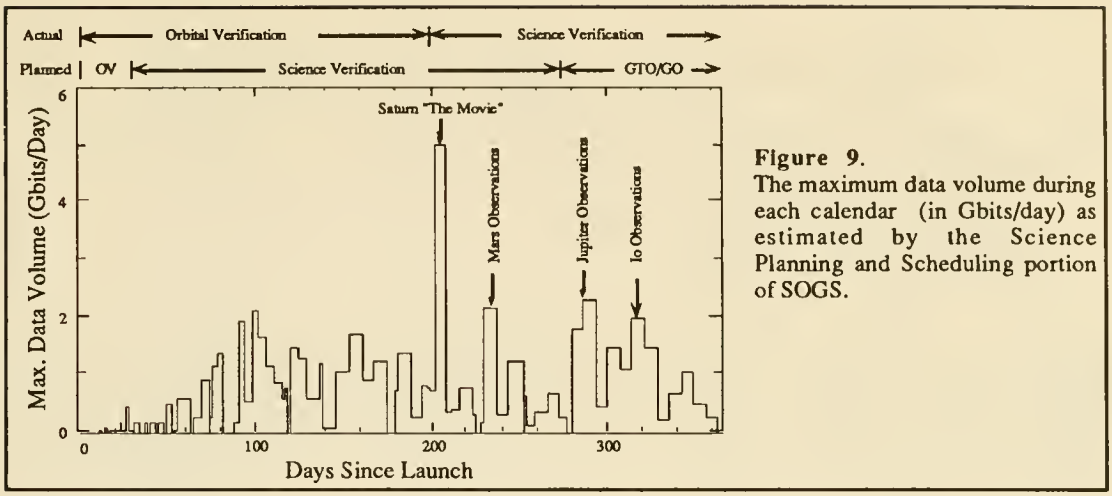

Figure 9.
The maximum data volume during each calendar (in Gbits/day) as estimated by the Science Planning and Scheduling portion of SOGS.

Summary

The scheduling efficiency of SOGS has so far supported the most optimistic estimates made prior to the launch of HST, around 30-40%. The overhead for each calendar amounts to some 15-20% necessary for supporting the science (guide star and target acquisition), a figure which is unlikely to change much during the course of the mission. It is expected that the overall efficiency of these calendars will improve from these values as more interleaver activities are available for inclusion and as SOGS is modified to support parallel observations. TDRSS availability, although not a major impact on the efficiency of a given calendar, can affect whether or not a given proposal will schedule during a particular period, and the TDRS time required by a given proposal can, of course, make the difference between an observation which is easy to schedule and one which is impossible. In addition, although no evidence currently exists to support the claim that artificial intelligence pre-scheduling of observations can improve the efficiency (this may be due to the largely manual effort still required to schedule many of these early observations) it may be that this will change as the nature of the proposals being scheduled have more to do with the more "normal" GO/GTO observations.

Mailing address:
E. V. Bell, II
Code 933.9
National Space Science Data Center
NASA-Goddard Space Flight Center
Greenbelt, Maryland 20771

K. E. Reinhard and H. H. Lanning
Computer Sciences Corporation
Space Telescope Science Institute
3700 San Martin Drive
Baltimore, Maryland 21218

ROUTINE SCIENCE DATA PROCESSING OF HST OBSERVATIONS

Daryl A. Swade[1], Sidney B. Parsons[1], Phil Van West[1], Sylvia Baggett[1], Mark Kochte[1], Daryl Macomb[1], Al Schultz[1], and Ian Wilson[1]

Computer Sciences Corporation
3700 San Martin Drive
Baltimore, MD 21218

Abstract. All science observations performed by the Hubble Space Telescope (HST) will be automatically processed by the Routine Science Data Processing (RSDP) pipeline at the Space Telescope Science Institute (STScI). Monitoring and maintenance of pipeline activity is the responsibility of the Post Observation Data Processing System (PODPS) branch.

1. HST TO PODPS DATA FLOW

Data from the Hubble Space Telescope are transmitted from the spacecraft to White Sands [TDRSS (Tracking and Data Relay Satellite System)] ground station by telemetry through a Tracking and Data Relay Satellite. From there the data are transmitted to NASA communication (NASCOM) at GSFC (Goddard Space Flight Center) by domestic communications satellite and to the DCF (Data Capture Facility) at GSFC. DCF transmits the packetized data to the PODPS RSDP pipeline at STScI via ground links which are maintained at STScI by the Computer Operations Branch (COB).

2. RSDP PIPELINE PROCESSING

In the absence of any errors, RSDP reception and processing of data through Calibration will proceed automatically once data receipt has been initiated. Therefore all processing described in this section below requires no operator intervention. RSDP pipeline processing of HST science observations is supported by a Science Support Schedule from the Science Planning and Scheduling System (SPSS) and real-time activity and observer comment files from the Observation Support System (OSS). If a problem occurs at any step in the pipeline processing the observation is sent to "trouble" where the problem can be investigated and hopefully repaired by PODPS personnel before the observation is reinserted into the pipeline. A schematic representation of PODPS is shown in Figure 1.

2.1 Data Partitioning

For every observation received the data are partitioned into packetized information sets with one packet equal to one VAX record. These records are sorted by Packet Format Code into files to form an EDT data set with a Standard Header Packet, Unique Data Log, and science data. Other informational and trailer files are created by PODPS. These files are assigned a rootname which is derived from programmatic information in the SHP and follows the convention ipppssoot where i is the science instrument (v=HSP, w=WFPC, x=FOC, y=FOS, and z=GHRS), ppp is the program id, ss is the obset id, oo is the observation number within the obset, and t is the version (T=tape-recorded, R=real-time...).

Data Partitioning then performs a time ordered sort of the science packets, checks for the correct number of packets received to detect

[1]Staff member of the Space Telescope Science Institute

POST OBSERVATION DATA PROCESSING SYSTEM

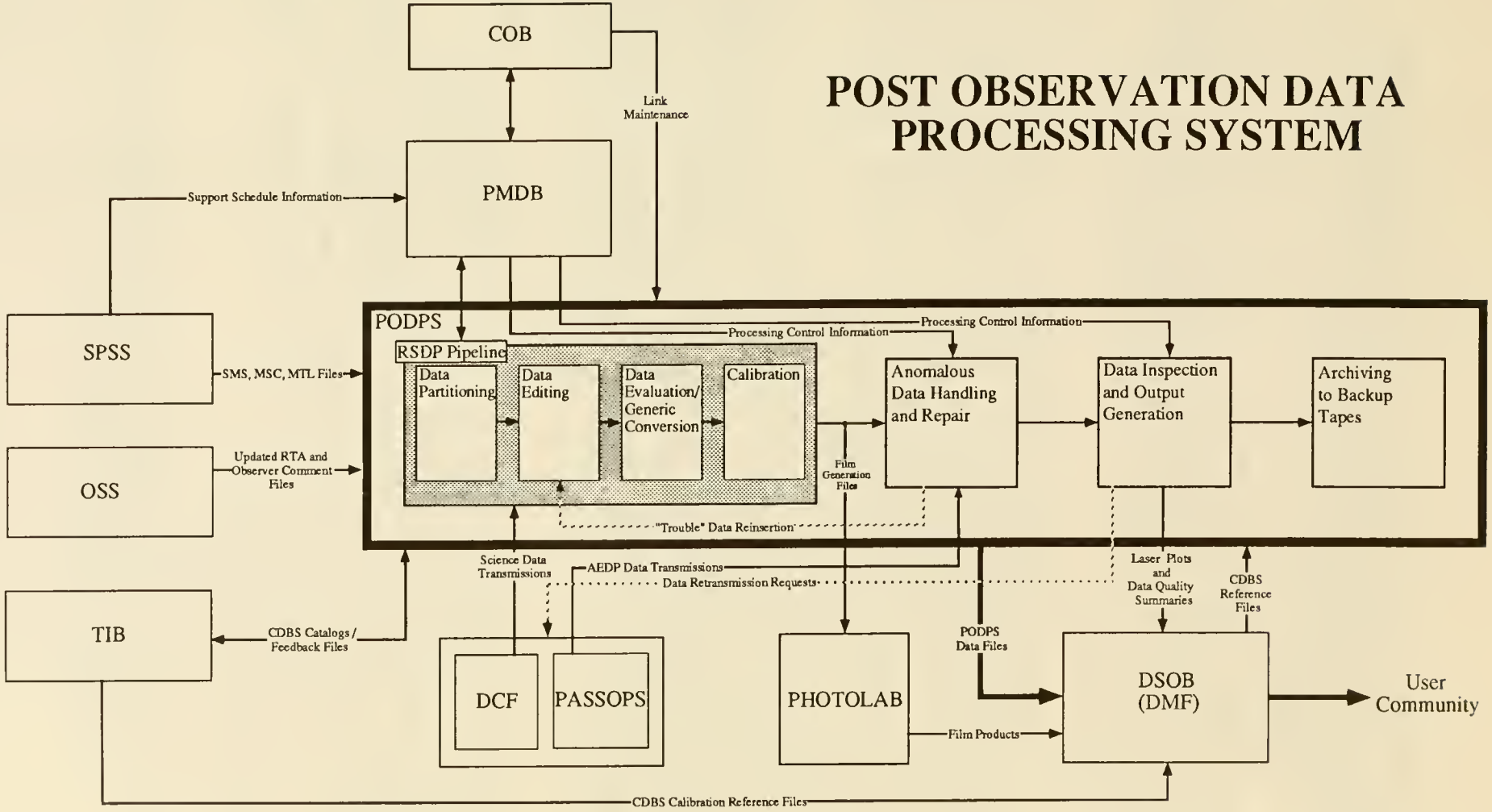

Figure 1

missing packets, and processes the DCF Quality Accounting Capsule to compute a total quality weighted error sum for each observation. If this error sum exceeds a database specified threshold value all files pertaining to the observation are removed from the RSDP pipeline and transferred to the appropriate trouble directory.

2.2 Data Editing

The output products of Data Partitioning are analyzed by the Data Editing process. Among the activities carried out here are insertion of PODPS fill data to serve as place holders of missing packet segments and detection of DCF fill data and Reed-Solomon corrections. If Data Editing is successfully completed an Edited Information Set is created and the observation is queued for Generic Conversion. The Edited Information Set is retained and archived to the EDT class.

2.3 Generic Conversion

The first step in Generic Conversion is Data Evaluation. The flags and indicators (F&I) required for the unique specification of the parameters which control the reformatting of the packetized data into a waivered FITS structure are dredged from the telemetry and compared to those specified in the Project Management Data Base (PMDB). If a flags and indicators mismatch between the telemetry (actual) and the PMDB (predicted) occurs, the telemetry values are used. Invalid F&I as well as F&I mismatches contribute towards the total weighted error sum. Once again, if the sum exceeds a database specified threshold the observation is removed from the RSDP pipeline and the observation's files are transferred to trouble.

If the error sum is less than the threshold value, the packetized information set is reformatted into a waivered FITS structure, i.e., data and header files, called a Generic Edited Information Set (GEIS). This conversion uses bit locations specified in the Project Data Base. If any problems are encountered during this process the observation is removed from the RSDP pipeline and transferred to trouble.

Upon successful completion of Generic Conversion any observation flagged as requiring calibration is sent through the calibration process.

2.4 Calibration

The individual HST Science Instrument Teams will supply through the Telescope Instrument Branch (TIB) all the information for calibration performed by the RSDP pipeline. Pipeline calibration consists of instrument specific algorithms such as wavelength calibration, flat-fielding, absolute flux, etc. As calibration standards change based on knowledge gained through observational experience or evolution of instrument performance, PODPS will update calibration reference files and tables. In addition, the observer will have the capability of recalibrating an observation from the GEIS files with Space Telescope Science Data Analysis System (STSDAS) tools.

At the end of calibration all files produced in Generic Conversion and Calibration (uncalibrated GEIS files and calibrated data) are queued for archiving to the CAL class.

3. STANDARD OUTPUT PRODUCTS

At the end of RSDP pipeline processing PODPS produces either film files from which a print is made or a laser plot of the first group in a spectral observation. Generated for each science instrument are -

FOC & WFPC: calibrated images on film
HRS & FOS: uncalibrated plot of counts vs. channel number

and calibrated plot of flux vs. wavelength
HSP: plot of raw counts vs. time

In addition to film products and plots PODPS creates a data quality report which is distributed along with the hardcopy output and is archived as ancillary data (class ASA). The PDQ (PODPS Data Quality) file contains the predicted as well as the actual observation parameters. Three keyword fields within the PDQ file contain information about the usefulness of the observation:

QUALITY - one word or one phase that describes the overall quality
QUALCOM1 - comments about the usefulness of the observation
QUALCOM2 - summarized significant OSS comments

The choice of QUALITY keyword is based upon the intrinsic merits of the observation and geared for the archival user. The standard PODPS quality keywords are:

OK	No apparent problems
NOISY	High background, low S/N
WEAK-SIGNAL	No target seen with decent S/N (if a targetted observation)
DATA-DROPOUTS	More than ca. 2% missing, or affecting probable area of interest
SATURATED	Majority of pixels "overexposed"
NO-COUNTS	Zero-level data
BLANK-IMAGE	No features visible
POOR	Other problems affecting probable scientific usefulness
UNKNOWN	Unable to judge usefulness
NOT-DISPLAYED	Undisplayable with current software, not enough time during shift, or a calibration exposure.

4. DATA DISPERSION

EDT and CAL data sets are archived to the Data Management Facility (DMF) optical disk and this data will normally be available to the General Observer (GO) from the HST archives within two days after the observation is performed. FITS tapes will be made for the GO and these tapes along with hardcopy output will be available to the GO from DSOB (Data Systems Operations Branch) within five days of the observation. Data loses proprietary status after one year at which time it is available for use by the astronomical community.

Astro qQB 500.268 .F57 1991

The First year of HST
observations